GEOCHEMICAL SIGNATURES OF STABLE PLANETARY SURFACES: OXIDATIVE WEATHERING PROCESSES ON EARTH AND MARS

by

MARK ROBERT SALVATORE

B.Sc., The Pennsylvania State University, 2008
Sc.M., Brown University, 2010

A DISSERTATION SUBMITTED IN PARTIAL FULFILLMENT OF THE REQUIREMENTS FOR THE DEGREE OF DOCTOR OF PHILOSOPHY IN THE DEPARTMENT OF GEOLOGICAL SCIENCES AT BROWN UNIVERSITY

PROVIDENCE, RHODE ISLAND
MAY 2013

This dissertation by Mark Robert Salvatore is accepted in its present form by the Department of Geological Sciences as satisfying the dissertation requirements of the degree of Doctor of Philosophy.

_____	_____
Date	**John F. Mustard**, Brown University Advisor
_____	_____
Date	**James W. Head III**, Brown University Advisor

Recommended to the Graduate Council

_____	_____
Date	**Reid F. Cooper**, Brown University Reader
_____	_____
Date	**Alberto E. Saal**, Brown University Reader
_____	_____
Date	**A. Deanne Rogers**, Stony Brook University Reader

Approved by the Graduate Council

_____	_____
Date	**Peter M. Weber**, Brown University Dean of the Graduate School

MARK ROBERT SALVATORE

Curriculum Vitae

Planetary Geosciences Group
Dept. of Geological Sciences
Brown University
324 Brook Street, Box 1846
Providence, RI 02912

Office: 310 Lincoln Field Bldg.
Email: Mark_Salvatore@brown.edu
Telephone: (401) 863-3379
Fax: (401) 863-3978
http://planetary.brown.edu/grad_pages/Salvatore

EDUCATION

2013	**Ph.D.** (exp.), Geological Sciences, Brown University *Dissertation*: Geochemical signatures of stable planetary surfaces: Oxidative weathering processes on Earth and Mars *Advisors*: Dr. John F. Mustard and Dr. James W. Head III
2010	**Sc.M.**, Geological Sciences, Brown University *Thesis*: Definitive evidence of Hesperian basalt in Acidalia and Chryse planitiae *Advisors*: Dr. John F. Mustard and Dr. Michael B. Wyatt
2008	**B.Sc.**, Geography, *Student Marshal*, The Pennsylvania State University *Thesis*: Relationship between transverse aeolian ridges and climate on Mars *Advisor*: Dr. Derrick J. Lampkin

RESEARCH SUMMARY

- Oxidative weathering in hyper-arid and hypo-thermal environments
- Characterization of recent chemical alteration on Mars
- Field, laboratory, and orbital studies in the McMurdo Dry Valleys of Antarctica
- Reflectance and emission spectroscopy (orbital- and laboratory-based)

PROFESSIONAL EXPERIENCE

2013-	**Postdoctoral Research Associate** (accepted position), Arizona State University *Advisor*: Dr. Philip Christensen
2008-present	**Graduate Student**, Brown University *Advisors*: Dr. John F. Mustard, Dr. James W. Head III, and Dr. Michael B. Wyatt
2011	**Imagery Lead**, Desert Research and Technology Studies, NASA Lyndon B. Johnson Space Center *Science Operations Lead*: Dr. Dean B. Eppler
2009-2010	**Field Work**, McMurdo Dry Valleys, Antarctica *Principal Investigators*: Dr. Michael B. Wyatt and Dr. James W. Head III
2008	**Research Assistant**, NASA Lyndon B. Johnson Space Center *Advisor*: Dr. M. Justin Wilkinson
2007	**Research Intern**, Lunar and Planetary Institute *Advisors*: Dr. Carlton C. Allen and Dr. Dorothy Z. Oehler
2006	**Research Intern**, Center for Earth and Planetary Studies, Smithsonian Institution *Advisors*: Dr. James R. Zimbelman and Dr. Thomas R. Watters

TEACHING EXPERIENCE

2011	**Teaching Assistant**, GE1350 (Weather and Climate), Brown University *Instructor*: Dr. Meredith G. Hastings
2010	**Teaching Assistant**, GE1350 (Weather and Climate), Brown University *Instructor*: Dr. Meredith G. Hastings
2009	**Teaching Assistant**, GE0050 (Mars, Moon and the Earth), Brown University *Instructors*: Dr. Michael B. Wyatt and Dr. Caleb I. Fassett
2009	**Instructor**, Brown University SPARK Program *Course*: Hello from Mars (Introduction to Martian Geoscience)

PEER-REVIEWED PUBLICATIONS

Accepted & Published

2. **Salvatore M. R.**, Mustard J. F., Head J. W., Marchant D. R. and Wyatt M. B. (2013), Characterization of spectral and geochemical variability within the Ferrar Dolerite of the McMurdo Dry Valleys, Antarctica: Weathering, alteration, and magmatic processes. *Antarctic Science*, accepted.
1. **Salvatore M. R.**, Mustard J. F., Wyatt M. B. and Murchie S. L. (2010), Definitive evidence of Hesperian basalt in Acidalia and Chryse planitiae. *J. Geophys. Res.* **115**, *E07005*, doi:10.1029/2009JE003519.

Submitted & In Review

2. **Salvatore M. R.**, Mustard J. F., Head J. W. and Cooper R. F. (2013), Oxidative weathering in Antarctica and evidence for a cold and dry Amazonian Mars. *Nature Geoscience*, submitted.
1. **Salvatore M. R.**, Mustard J. F., Head J. W., Cooper R. F., Marchant D. R. and Wyatt M. B. (2013), Development of alteration rinds by oxidative weathering processes in Beacon Valley, Antarctica, and implications for Mars. *Geochimica et Cosmochimica Acta*, in review.

In Preparation

2. Jackson C. R. M., Cheek L. C., Williams K. B., Dyar M. D., Breves E. A., **Salvatore M. R.**, Prissel T. C., Dhingra D., Pieters C. M., Parman S. W. and Cooper R. F. (2013), Spectral properties of aluminate spinels and application to lunar remote sensing.
1. **Salvatore M. R.**, Mustard J. F., Head J. W., Cooper R. F. and Wyatt M. B. (2013), The spectral influence of oxidative weathering on martian low albedo terrain.

SELECTED PRESENTATIONS & PUBLISHED ABSTRACTS

Invited Talks

- Stony Brook University, Department of Geosciences, February 2013
  Title: Oxidative weathering on Earth and Mars: Laboratory and orbital analyses

First-Authored Abstracts (Since 2011)

- **Salvatore M. R.**, Mustard J. F., Head J. W., Cooper R. F., Marchant D. R. and Wyatt M. B. (2013), Oxidative weathering on Mars and implications for chemical alteration during the Amazonian epoch. *LPSC* **XLIV**, abstract 1339.
- **Salvatore M. R.**, Mustard J. F., Head J. W., Marchant D. R., Cooper R. F. and Wyatt M. B. (2013), Spectral and chemical characterization of hyper-arid and hypo-thermal oxidation processes as an analog for Amazonian alteration on Mars (*Invited*). *AGU Fall Mtg.*, abstract P11F-06.
- **Salvatore M. R.**, Mustard J. F., Head J. W., Marchant D. R. and Wyatt M. B. (2012), Compositional remote sensing of the McMurdo Dry Valleys: Integrated analyses of primary and secondary processes within the Ferrar Dolerite. *SCAR Open Sci. Conf.* **XXXII**, abstract 654.
- **Salvatore M. R.**, Mustard J. F., Head J. W., Cooper R. F., Marchant D. R. and Wyatt M. B. (2012), Characterizing widespread oxidation processes on Mars: Alteration rind development and effects on spectroscopic investigations. *LPSC* **XLIII**, abstract 1597.
- **Salvatore M. R.**, Mustard J. F., Head J. W., Marchant D. R., Wyatt M. B. and Seeley J. (2012), Linking orbital, field, and laboratory analyses of dolerites in the McMurdo Dry Valleys of Antarctica: Terrestrial studies and planetary applications. *LPSC* **XLIII**, abstract 1590.
- **Salvatore M. R.**, Mustard J. F., Head J. W., Cooper R. F., Marchant D. R. (2011), Widespread, juvenile alteration of the Ferrar Dolerite in Beacon Valley, Antarctica. *AGU Fall Mtg.*, abstract P31C-1717.
- **Salvatore M. R.**, Mustard J. F., Head J. W. and Seeley J. (2011), Verification of spectral mapping of the McMurdo Dry Valleys using in situ and laboratory techniques. *GSA Joint Ann. Mtg.*, abstract 284-7.
- **Salvatore M. R.**, Wyatt M. B., Mustard J. F., Head J. W., Cooper R. F. and Marchant D. R. (2011), Constraining the chemical alteration of rock surfaces of the Ferrar Dolerite in Beacon Valley, Antarctica. *11th Intl. Symp. on Ant. Earth Sci.*, Br. Geol. Surv., Edinburgh, U.K.
- **Salvatore M. R.**, Wyatt M. B., Mustard J. F. and Head J. W. (2011), Development of alteration rinds on the Ferrar Dolerite of the Antarctic Dry Valleys: Initial characterization. *LPSC* **XLII**, abstract 1479.

- **Salvatore M. R.**, Wyatt M. B., Mustard J. F., Head J. W., Marchant D. R. (2010), Near-infrared spectral diversity of the Ferrar Dolerite in Beacon Valley, Antarctica: Implications for martian climate and surface compositions. *LPSC* **XLI**, abstract 2290.
- **Salvatore M. R.**, Mustard J. F., Wyatt M. B., Murchie S. L. and Barnouin-Jha O. S. (2009), Assessing the mineralogy of Acidalia Planitia, Mars, using near-infrared orbital spectroscopy. *LPSC* **XL**, abstract 2050.
- **Salvatore M. R.**, Wilkinson M. J., Allen C. C. and Oehler D. Z. (2008), Terrestrial megafans as an analog for ridged unit of SW Arabia Terra, Mars: Current observations and future analysis. *LPSC* **XXXIX**, abstract 1455.
- **Salvatore M. R.**, Allen C. C., Oehler D. Z. and Wilkinson M. J. (2007), Geomorphologic interpretation of southwest Arabia Terra, Mars: Evidence for regional, long-duration fluvial activity. *AGU Fall Mtg.*, abstract P13B-1293.
- **Salvatore M. R.** and Zimbelman J. R. (2006), Investigation of martian transverse aeolian ridges. *AGU Fall Mtg.*, abstract P31B-0129.

OUTREACH & SERVICE

- **Co-Convener**, American Geophysical Union Annual Fall Meeting, 2011.
  Session: Nanocrystalline Materials on Earth and Mars (P20)
- **Undergraduate Advising**
  Andrea Weber (2012): Inorganic approaches to climate reconstruction in Lake Towuti, Indonesia.
- **Graduate student leadership positions**, Brown University
  Board of Governors, Brown University Faculty/Graduate Student Club, 2010-present.
  Representative, Professional Development Seminars, 2010-2012.
  Graduate student liaison, faculty search committees, 2010-2011.
  President, Geosciences Graduate Student Association, 2009-2010.
- **Guest speaker**, 2006-2012.
  Recent Locations: Cresskill High School (Cresskill, NJ), Lincoln Elementary School (Ridgefield Park, NJ), Civil Air Patrol Pennsylvania Wing (Fort Indiantown Gap, PA).
  Recent Lectures: Past, Present, and Future of Manned Spaceflight; Global Warming and Future Impacts; Exploring Mars: Rovers and Landers; The Antarctic Environment.
- **Volunteer**, Greene County Habitat for Humanity, Waynesburg, PA, 2001-2012.
- **President**, Geography International Honor Society *Gamma Theta Upsilon*, 2007-2008.
  The Pennsylvania State University Chapter.
- **Volunteer**, *Mars Day! 2006*, Smithsonian Institution, 2006.

HONORS & AWARDS

- **Best Poster**, Scientific Committee on Antarctic Research (SCAR) Open Science Conference, 2012.
- **U.S. Congressional Antarctic Service Medal**, United States Antarctic Program, 2012.
- **Outstanding Student Paper Award**, American Geophysical Union Annual Fall Meeting, 2011.
- **Honorary Mention**, Stephen E. Dwornik Award – Best Paper, Lunar and Planetary Science Conference, 2009.
- **Student Marshal**, College of Earth and Mineral Sciences, The Pennsylvania State University, 2008.
- **Schreyer Honors Scholar – Highest Distinction**, The Pennsylvania State University, 2008.

PROFESSIONAL ASSOCIATIONS

- **American Geophysical Union (AGU)**, 2006 – present.
- **Geological Society of America (GSA)**, 2011 – present.
- **Association of American Geographers (AAG)**, 2007 – 2009.

Acknowledgements

To my advisors, **Jack Mustard** and **Jim Head**, for teaching me how to think critically and to harness my enthusiasm into disciplined and productive energy. You have both provided me with many wonderful opportunities during my tenure as a graduate student. In particular, you taught me to be an independent researcher and to pursue my own research interests. You never hesitated to nudge me in the right direction, which is certainly a major reason why I have been able to make it to this point in my academic career. Your combined generosity in providing guidance and stability throughout my time at Brown also ensured that my research and career goals remained intact, and for that I will be forever grateful.

To my defense committee, for all of the wonderful scientific discussions over the past five years, in addition to the helpful comments and suggestions still to come. To **Reid Cooper**, for your countless hours and tireless efforts to teach a macroscale-thinking planetary geologist the wonders of nanoscale material properties and analytical techniques. To **Alberto Saal**, for your endless encouragement and support, both academic and non-academic. To **Deanne Rogers**, for laying the foundation upon which much of this dissertation is rooted, and for the motivation and guidance that you have selflessly provided. I'm excited to see what more there is to learn regarding martian surface compositions!

To all of my **professors** and **mentors** at Brown University and other institutions, thank you for the advice, suggestions, and support over the past five years. To **Mike Wyatt**, for helping me to mature from an undergraduate student, and for the opportunity to take an active role in the designing and execution of two successful field seasons in Antarctica. To **Meredith Hastings**, for sharpening my teaching skills and for allowing me to grow and develop as an instructor. To **Jim Russell**, for your generosity and guidance both in the classroom and in the field.

Thank you for all of the technical assistance and mentoring that I have received throughout my tenure at Brown University, particularly from **Dave Murray**, **Joe Orchardo**, **Takahiro Hiroi**, and **Bill Collins**. Thank you all for spending that extra time to teach me not only *how* things work, but also *why* things work.

A special thank you is reserved for all of my **professors**, **advisors**, and **mentors** prior to my time at Brown University, particularly those at **Penn State University** (especially **Derrick Lampkin** and **Jim Kasting**), the **Center for Earth and Planetary Studies** (especially **Jim Zimbelman** and **Tom Watters**), **NASA Johnson Space Center** (especially **Carl Allen**, **Dorothy Oehler**, and **M. Justin Wilkinson**), and the **Lunar and Planetary Institute**.

Hall of Fame pitcher Bob Lemon once said, "I've come to the conclusion that the two most important things in life are good friends and a good bullpen." I couldn't agree more. To my teammates on the **Fall River Blue Jays** and the **East Greenwich Coyotes**, especially **Jose**, **Jeremy**, **Chris**, **Tom**, **Adam**, and **Shawn**. It's hard to describe the relationship that I have developed with my teammates, but it's underscored by a mutual dedication, commitment, and loyalty that I have yet to experience anywhere else. Let's just say that I wouldn't step into a 2-seam fastball for anybody.

To my friends from **Penn State University**, particularly **Allison O'Black**, for nine years of continuous encouragement.

To **Theresa Stone**, for helping me stay sane through these difficult times, for your patience and understanding, and for assuring me that my heart is not about to suddenly stop or explode on more than a handful of occasions.

To my **friends** and **colleagues** from Brown University, particularly my friends, roommates, and fellow students that I've known for 5+ years. This includes (but is certainly not limited to) **Danny** and **McCall Burau**, **Rocio Caballero Gill**, **Leah Cheek**, **Jay Dickson**, **Kerri Donaldson Hanna**, **Bethany Ehlmann**, **Caleb Fassett**, **Heather Ford**, **Chris Havlin**, **David Hollibaugh Baker**, **Alex Kasprak**, **Laura Kerber**, **Bronwen Konecky**, **Shannon Loomis**, **Linda Meyers**, **Gareth Morgan**, **Edgard Rivera-Valentin**, **Jess Rodysill**, **Jeff Salacup**, **Victor Schmidt**, **Angela Stickle**, and **Chen Sun**. Thank you for accompanying me on this academic, professional, and personal marathon and helping me to grow and mature along the way. And to the **continuing graduate students** in the Department of Geological Sciences, thank you for your friendship and support, and I look forward to watching your continued success in the future.

To **Colin Jackson**, while not the best PlayStation2 NASCAR teammate, I can't think of anyone more selfless or willing to offer guidance, suggestions, or advice. I look forward to a long future of collaborative science that is rivaled only by our even longer friendship.

To my friends from Cresskill, many of whom I've known for more than a quarter of a century. I wish there were some way that I could repay you for your encouragement and support throughout the years. Here's to closing out the rest of that century as close friends. Thank you, **Liz Beck**, **TJ Berardo**, **Erin Goldrick**, **Neil Hartmann**, **Jackie Knight**, **Lauren Luciani**, **Shaun Mitchell**, **Jayme Moran**, **Melissa Rosario**, **Gwenn Santoro**, **Carolyn Thomasma**, and **Katie Zanone**.

Finally, to my loving and caring family, whose support has been my backbone throughout my graduate studies. To **Chris**, for our continuance as the "babies" of the family and for preceding me to Rhode Island and showing me where all of the best inexpensive restaurants reside. I'm extremely proud of your hard work and look forward to your continued success. To **Brian** and **Erin**, for being quick to provide comfort and encouragement, and for listening to my countless tirades without hesitation or criticism. I hope that our long discussions about the New York Mets and tacky television continue, either on your couch or via Skype. To **Amelia**, my wonderful Goddaughter, for disproving my hypothesis that there exists nothing more beautiful in the universe than a well developed alteration rind. And finally, to my parents, **Lois** and **Vinnie**, for absolutely everything. Words cannot begin to describe my appreciation, gratitude, or love for you both.

This dissertation is dedicated to a very special person whose presence remains with me today and every day. Her commitment to her family, both immediate and extended, was truly inspirational. Unfortunately, she passed away before the completion of my graduate studies, but not before making a lasting impact on my life and the life of so many other people. She will be remembered forever in the hearts and minds of her friends and family, and in the compassion that she instilled upon everyone who knew her. To **Adrienne Murphy**, for your courage, your love, and your omnipresence in our family. We miss you dearly.

TABLE OF CONTENTS

Title Page i
Copyright Page ii
Signature Page iii
Curriculum Vitae iv
Acknowledgements vii
Table of Contents ix

Chapter One: Geochemical investigations of cold and dry chemical weathering in desert landscapes: An introduction 1

1.0 Motivation 2
1.1 Characterizing hyper-arid and hypo-thermal chemical alteration on Earth 5
1.2 Understanding recent weathering on Mars 8
2.0 Approach 10
2.1 Field studies 11
2.2 Remote sensing 12
2.3 Laboratory analyses 12
3.0 Dissertation Summary 13
References 16
Figure Descriptions 24
Figures 26

Chapter Two: Development of alteration rinds by oxidative weathering processes in Beacon Valley, Antarctica, and implications for Mars. 29

Abstract 30
1.0 Introduction 31
2.0 Background 34
3.0 Geographic Setting 36
4.0 Methods 39
5.0 Results 44
5.1 Chemistry 45
5.2 Mineralogy 47
5.3 Morphology 52
6.0 Discussion 54
7.0 Implications for Surface Alteration on Mars 65
8.0 Conclusions 71
Acknowledgements 72
References 73
Figure and Table Descriptions 89
Figures 96
Tables 111

Chapter Three: Characterization of spectral and geochemical variability within the Ferrar Dolerite of the McMurdo Dry Valleys, Antarctica: Weathering, alteration, and magmatic processes 115

Abstract 116
Key Words 116
1.0 Introduction and Geologic Setting 117
2.0 Methods 123
2.1 Laboratory spectral investigations 123
2.2 Orbital data acquisition, calibration, and atmospheric removal 124
2.3 Identification of spectrally pure dolerite using ASTER TIR data 132
2.4 Identification of spectral variability within the Ferrar Dolerite using ASTER TIR data 134
2.5 Resultant spectral products 135
3.0 Results 135
3.1 Laboratory spectroscopy 136
3.2 Lithological mapping from orbit 139
3.3 Spectral variability of pure dolerite 140
3.4 Chemical variability within the Ferrar Dolerite 143
4.0 Discussion 144
4.1 Identification and distribution of doleritic signatures 144
4.2 Geochemical evolution of the Ferrar Dolerite 148
5.0 Conclusions 149
Acknowledgements 151
References 152
Figure and Table Descriptions 158
Figures 164
Tables 182

Chapter Four: Oxidative weathering in Antarctica and evidence for a cold and dry Amazonian Mars. 185

Main Text 186
Methods 193
Spectral analyses of dolerite samples 193
Orbital data retrieval and calibration 193
Assembly of endmember library and linear unmixing 195
References 195
Figure and Table Descriptions 200
Figures 202
Tables 205

Chapter Five: The spectral influence of oxidative weathering on martian low albedo terrain. 207

Abstract 208
1.0 Introduction 209

2.0 Methods 212
2.1 Laboratory spectroscopy 212
2.2 Visible/Near-infrared orbital spectroscopy 215
2.3 Thermal infrared orbital spectroscopy 217
3.0 Results 219
3.1 Laboratory analyses (Table 2) 219
3.2 Orbital analyses (Regional) 221
3.3 Orbital analyses (Local) 225
3.3.1 Acidalia Planitia 226
3.3.2 Syrtis Major 228
3.4 Summary 231
4.0 Discussion 232
4.1 Assumptions regarding oxidative weathering products and processes 232
4.2 Effects of oxidative weathering on apparent surface composition 234
4.3 Distribution of oxidative weathering products on Mars 237
4.4 Implications for Amazonian climate 240
5.0 Conclusions 243
References 246
Figure and Table Descriptions 257
Figures 264
Tables 281

Chapter Six: On the current and future investigation of pervasive oxidative alteration processes on Earth and Mars. 286

1.0 Summary and Significance of Work 287
2.0 Outstanding Questions 290
2.1 What is the primary mechanism for the migration of cations to rock surfaces during oxidative weathering in Beacon Valley, Antarctica? 291
2.2 What is the cause of the large amount of variability observed in X-ray diffraction data and what is the relationship to spectroscopic measurements? 291
2.3 What is the origin of the spectral variations observed in oxidative weathering products? 293
2.4 How does oxidative weathering influence the spectral signatures of different primary compositions? 294
2.5 How does oxidative weathering progress under different climatic conditions? 296
2.6 What is the rate of oxidative weathering in terrestrial and martian environments? 297
3.0 Future Work and Concluding Remarks 298
3.1 Future work 298
3.1.1 Field studies 300
3.1.2 Laboratory analyses 301
3.1.3 Remote analyses 302
3.2 Concluding remarks 304

References 304
Figure Descriptions 308
Figures 310

Appendix A: Multispectral map of the McMurdo Dry Valleys: Description, methodology, and parameterization. 314

Main Text 315
References 319
Figure and Table Descriptions 321
Figures 323
Tables 340

Appendix B: Database of samples collected during the 2009-2010 and 2010-2011 field seasons supporting National Science Foundation grant ANT-0739702. 361

Main Text 362
Figure and Table Descriptions 365
Figure 367
Table 368

Chapter One:

Geochemical investigations of cold and dry chemical weathering in desert landscapes: An introduction.

M. R. Salvatore[1]

[1]Department of Geological Sciences,

Brown University, Providence, RI 02912, USA

1.0 Motivation

The martian surface represents an ancient and preserved landscape that provides information about the evolution of climatic and geologic environments during the early history of our solar system (Fig. 1). Compared to the Earth, Mars has undergone a relatively rapid geologic and climatic evolution that has resulted in the barren and geologically dormant surface that we observe today. The cause, timing, and duration of this rapid evolution are largely unknown, but are likely related to a combination of events including the declining strength of the martian magnetic field, the end of heavy impactor bombardment, the formation of the Tharsis volcanic province, and the hydrodynamic loss of volatiles to space (Jakosky and Phillips, 2001). Even less constrained are the geochemical and environmental precursors and results associated with these transitions. It is predicted that the Earth will undergo a similar evolutionary fate as a result of cooling of the planet's interior and solidification of our multifaceted liquid outer core. Therefore, understanding the timing, duration, magnitude, and geochemistry associated with these transitions will help to elucidate how and when these significant transitions may occur on Earth.

Using crater counting and stratigraphic relationships, it is estimated that more than 70% of the exposed martian surface is older than 3 Ga (Scott and Tanaka 1986, Greeley and Guest 1987, Tanaka and Scott 1987). The oldest of these terrains also exhibit geomorphic and spectral evidence for widespread aqueous activity, indicating that liquid water was present and active within our solar system during the earliest history of the terrestrial planets. However, the information stored within these ancient geologic units is only as valuable as our abilities to identify, measure, and interpret it. For more

than a century, the capabilities available to investigate the martian surface have continuously improved in terms of spatial, radiometric, temporal, and spectral resolution. Visible imagery is now able to easily resolve a golf cart-sized object on the martian surface, while hyperspectral VNIR spectrometers are capable of acquiring fifteen three-dimensional (two spatial and one spectral) pixels within the area of a single American football field. These higher quality datasets provide the information necessary to ask and answer complex questions related to the evolution of the martian geologic and climatic system, which can provide crucial details regarding the evolution of the other terrestrial planets within our solar system.

The effects of exposing these landscapes to the martian environment for billions of years have gone largely unstudied. Our current understanding of the martian climate system suggests that the latter half of martian history has been dominated by extremely cold and arid environmental conditions (Fig. 1). Most studies of these ancient terrains have overlooked the influence of recent environmental conditions on the chemical and spectral evolution of the martian surface since the exposure of these geologic units. However, a critical questions remain unanswered: What are the effects of cold, dry, and oxidizing environments on the observed surface spectra, and what (if any) are the underlying chemical and/or mineralogical consequences of these conditions?

This dissertation details our investigation of the effects of cold, dry, and oxidizing environments on the modification of surface compositions and spectral signatures, with particular emphasis on remote detection and the accompanying spectral modifications. We utilize the McMurdo Dry Valleys (MDV) of Antarctica as a natural laboratory to investigate these alteration processes given their pervasive hyper-arid and hypo-thermal

environmental conditions. Our laboratory investigations focus on samples collected from Beacon Valley, the coldest and driest of the primary MDV (Doran et al., 2002) where the products of cold and dry alteration processes are well preserved throughout the extremely stable landscape (Salvatore et al., 2013b) (Fig. 2). The floor of Beacon Valley is also dominated by clasts of the Ferrar Dolerite, a quartz-normative shallow intrusive tholeiitic basalt that has been regarded as a good analog to martian basalts (Harvey, 2001; Chevrier et al., 2006). This fortuitous pairing of analog environmental and geochemical conditions provides the framework necessary to associate recent chemical alteration in both environments.

Comparisons between the MDV and Mars is not a novel idea; the MDV have been long regarded as an analog for martian surface processes due to the extremely cold and dry environmental conditions. Investigations of this analog locale have included studies on geomorphology (e.g., Marchant and Head, 2007), soil formation (e.g., Gibson et al., 1983), microbial ecosystems (e.g., McKay et al., 1992), lacustrine environments (e.g., Andersen et al., 1993), and primary mineralogy (e.g., Harvey, 2001). While localized chemical alteration products in the MDV have been compared to potential martian weathering processes (e.g., Allen and Conca, 1991; Bishop et al., 1996), few studies have sought to characterize the relationship between cold, dry, stable, and oxidizing conditions and pervasive rock weathering on broad spatial scales. Furthermore, the use of orbital spectroscopy to identify hyper-arid and hypo-thermal chemical alteration products on both Earth and Mars is a significant and novel contribution to both terrestrial and martian geochemical studies (Salvatore et al., 2013a).

The outline of the contributions reported in this dissertation are prefaced with a brief overview of our current understanding of cold and dry chemical alteration processes on Earth and the evolution of chemical alteration processes on Mars:

1.1 Characterizing hyper-arid and hypo-thermal chemical alteration on Earth

Chemical weathering is a fundamental aspect of surface modification on any planetary surface, with the nature, extent, and resultant alteration products varying widely depending on a plethora of environmental conditions. The lunar surface, for example, undergoes chemical weathering as a result of micrometeorite impact processes and interactions with the solar wind, producing nanometer-sized particles of metallic iron that significantly modifies our spectral investigations of surface compositions (Pieters et al., 2000, and references therein). Due to the presence of an atmosphere and the surplus of near-neutral water, subaerial chemical weathering on Earth is dominated by water-rock interactions (Lasaga, 1984). Under the traditional chemical alteration paradigm, primary crystalline materials are broken down into poorly crystalline secondary alteration products, consisting largely of amorphous aluminosilicate gels with high chemical reactivities (Wada, 1989; Schwertmann and Taylor, 1989; Shoji et al., 1993). These poorly crystalline components are then transformed into less reactive but more crystalline alteration products (Vitousek et al., 1997). While specific alteration pathways vary widely due to the composition of the parent material, the amount and chemistry (e.g., pH) of liquid water, the age of the surface, the presence and activity of biological materials, and other factors, this alteration pathway is a well characterized framework with which to base studies of subaerial chemical alteration on Earth.

Desert environments, though, are substantially different in terms of their routes of chemical alteration. In most desert environments, rates of physical erosion tend to dominate relative to rates of chemical weathering (Stoffer, 2004). Despite these slow rates, the influence of chemical weathering in these environments is clearly evident on a variety of scales. For example, rock coatings and alteration rinds are prevalent in desert environments where highly stable surfaces are exposed for longer durations than in regions with greater amounts of precipitation and physical erosion (Dorn, 2009). Elemental chemistries of soils in desert environments have also shown unique geochemical trends as a result of the paucity of liquid water and the limited extent of chemical alteration (Gibson et al., 1983).

The MDV of Antarctica are unique in their extreme environmental conditions as well as their antiquity ($\geq$ 8.1 Ma in some locations; Marchant et al., 2002). The sub-freezing mean annual temperatures, desiccating and frequent hurricane-force winds, and extremely low water-equivalent mean annual precipitation are unlike any other geomorphic or environmental location on Earth (Doran et al., 2002; Marchant and Head, 2007; Fountain et al., 2009). Considerable attention has been given to the interaction between surface and subsurface waters with the valley soils, with particular emphasis on biogeochemical consequences (e.g., Lyons et al., 2003; Gooseff et al., 2003; Gooseff et al., 2006). Less attention has been dedicated to the effects of chemical weathering on rock surfaces, although pivotal research has laid the foundation required to investigate these unique processes and resultant products. This work was spearheaded by Glazovskaya (1958), who was the first to identify the presence of staining in iron-bearing minerals on rock surfaces in Antarctica. Additional studies that characterize rock

weathering processes in the Antarctic are nicely summarized by Campbell and Claridge (1987). Of particular note are the studies by Glasby et al. (1981) and Allen and Conca (1991). Glasby et al. (1981) were the first to document the diffusive nature of alteration rinds (referred to in their study as "desert varnish") on the surfaces of the Ferrar Dolerite, a shallow intrusive igneous lithology of basaltic composition that is the focus of our Antarctic studies throughout this dissertation. Though the means of dolerite alteration was declared "ambiguous" from their study, their thorough laboratory investigations and documentation of the relationship between the rock surfaces and the local environments was an inspiration for the work presented in this dissertation. Allen and Conca (1991) focus primarily on chemical alteration that occurs within etch pits that form on dolerite surfaces. While the maturity of alteration documented in their study exceeds the pervasive and ubiquitous surface oxidation described in this work, and while this study was not the first to relate the Antarctic environment to that of Mars, their work was the first to link infrared spectroscopic measurements to other laboratory analyses in the MDV. This association provides the foundation for the work presented in this dissertation and for linking spectroscopy with the complex relationship between geology and climatology in the MDV.

Since the work of Glasby et al. (1981), few studies have investigated the nature of dolerite surface alteration in the MDV, and those that have did not focus on the nature of the alteration process itself (e.g. Chevrier et al., 2006). Several critical questions have remained unanswered: Can we better understand the alteration process at work on the Ferrar Dolerites in the MDV? How well developed or mature are these alteration products? What are the resultant chemical, mineralogical, and spectral signatures

associated with alteration in cold and dry terrestrial environments? Lastly, what is the relationship between cold and dry alteration on Earth and Mars, where the entire surface can be considered a cold and dry desert?

1.2 Understanding recent weathering on Mars

Extensive evidence suggests that Mars was once a warmer, wetter, and more geologically active planet than the present. Integrated valley networks (Fassett and Head, 2008) and striking outflow channels (Baker et al., 1992) indicate regional- (if not global-) scale systems of fluvial activity, possibly resulting in the presence of one or more extensive bodies of standing water (Parker et al., 1993). More recent spectral evidence also confirms the geochemical effects of aqueous activity. The identification of Fe-/Mg-bearing smectite clays (Poulet et al., 2005), mono- and poly-hydrated sulfates (Gendrin et al., 2005; Langevin et al., 2005), opaline silica (Milliken et al., 2008), carbonates (Ehlmann et al., 2008), crystalline hematite (Christensen et al., 2000), and a range of other hydrated phases (e.g. Ehlmann et al., 2009) through the use of VNIR and TIR orbital spectroscopy has confirmed that not only has liquid water interacted with the martian crust, but it was capable of chemical alteration through its interaction with *in situ* geologic materials. While the exact timing and geologic provenance of these alteration products has been extensively debated, it is clear that the majority of chemical alteration took place during the first half of martian history, followed by a near-complete desiccation and cessation of aqueous alteration.

The cold and dry surface conditions that we presently observe on Mars are the result of the tenuous martian atmosphere (Lammer et al., 2009). The bulk of martian aqueous activity likely terminated contemporaneously with the evolution of the martian

atmosphere, with the last episodes of widespread fluvial activity dated at roughly 3.5 Ga (Hartmann, 2005; Fassett and Head, 2007). The evolution from an ancient warmer and wetter climate to one that has remained cold and dry for the most recent ~3.0 Ga of martian history is also supported by orbital spectral datasets (Bibring et al., 2006). These observed morphological and geochemical signatures likely signify the effective termination of widespread aqueous alteration and the preservation of the martian surface.

However, TIR orbital data from the Thermal Emission Spectrometer (TES) instrument on the Mars Global Surveyor (Christensen et al., 2001) have been interpreted to indicate that large extents of the martian surface have experienced chemical alteration since the termination of extensive aqueous activity. The high-latitude Surface Type 2 (ST2) spectral unit, as initially reported by Bandfield et al. (2000), has since been interpreted to represent the spectral contribution from a range of proposed alteration mineralogies, most of which require substantial quantities of liquid water. Smectite clays (Wyatt and McSween, 2002), micron-thick amorphous silica coatings (Kraft et al., 2003), palagonite (Morris et al., 2003), zeolites (Minitti and Hamilton, 2010), Al- or Fe-rich opaline silica (Michalski et al., 2005), Si-rich mineraloids (Michalski et al., 2005), and allophane (Rampe et al., 2012) have all been proposed as potential sources of the TIR spectral signatures observed across the martian high latitudes. These proposed compositional components are seemingly at odds with VNIR spectral data because (1) their associated VNIR spectral features have not been identified, and (2) their distribution within terrain that has been dated as Amazonian (~3.1 Ga to present; Hartmann and Neukum, 2001) in age suggests that considerable aqueous alteration has occurred since Mars has transitioned into the hyper-arid and hypo-thermal desert observed today.

The nature and abundance of this surface component has direct implications for the evolution of the martian surface over its geologic history. If significant amounts of chemical alteration have occurred, what environmental conditions must have been present? Why are these alteration products confined to the high latitudes, particularly in the northern hemisphere? If the altered component is hydrated, why is there no evidence for hydration in the VNIR wavelength region? Can hyper-arid and hypo-thermal chemical alteration account for the observed spectral signatures?

2.0 Approach

This work investigates the geochemical evolution of planetary surfaces as they interact with their hypo-thermal, hyper-arid, and hyper-stable climatic environments. These environmental conditions are pertinent to the polar regions of the Earth, with particular emphasis on the MDV of Antarctica, as well as the majority of the martian surface, which has not experienced substantial aqueous activity throughout most of its geologic history (Bibring et al., 2006). In order to investigate the geochemical nature and evolution of these surfaces, we use a variety of analytical tools to obtain, extract, and process data followed by subsequent verification and interpretation. This dissertation details the use of a multitude of different datasets and techniques to investigate alteration products and processes, and demonstrates how the use of multiple datasets at a variety of analytical scales and resolutions can provide key insights into the geochemical evolution of weathering products in cold and dry environments.

To investigate the processes and products of chemical alteration in cold and dry conditions on Earth, we have developed a multifaceted research strategy that operates on

a variety of spatial, temporal, and spectral scales (Fig. 3). We have used this strategy to effectively identify and interpret alteration products of the Ferrar Dolerite as products of oxidative chemical alteration. In addition, we engaged in extensive analyses of martian orbital datasets to further characterize both the VNIR and TIR spectral signatures and relate them to our understanding of martian climate evolution. Below, we detail the analytical approach utilized in both our terrestrial and martian investigations:

2.1 Field studies

Aside from the samples themselves, *in situ* data and sample collection provide invaluable contextual information. Experiencing the hyper-arid and hypo-thermal environmental conditions prevalent in Beacon Valley provides a uniquely personal connection to the evolution of the Ferrar Dolerite and its oxidative weathering processes. The dearth of aqueous activity and hydrous alteration is also realized during field studies. Other climate variables, including wind speed and direction, the amount of solar radiation incident upon rock surfaces, and variations in the temperature of rock surfaces can all change significantly over short temporal durations. As a result, in situ data collection and analysis is crucial for determining the magnitude and frequency of this variability and its relationship to the otherwise fossilized landscape.

Aerial and orbital remote sensing, while providing an unprecedented amount of spatial coverage, suffers from limitations in spatial resolution. Variables such as surface roughness, rock cover, and subsurface properties are typically only estimated using remote datasets. The ability to ground truth these datasets establishes the link between properties beyond the resolution of the remote sensors and the large spatial scales beyond the capabilities of traditional field work. In tandem, this pairing provides the confidence

in extracting a range of valuable information over vast spatial expanses with remote datasets.

2.2 Remote sensing

On the other end of ground truthing, remote sensing exploits the properties inherent to liquid, gaseous, and solid materials and records them with their associated spatial information. In this dissertation, we primarily utilize multi- and hyper-spectral spectroscopic datasets, which record energy either reflected or emitted from the surface following interactions with the surface materials. While characterizing the surface composition is the desired outcome of these analyses, many other factors contribute to these remote datasets. For example, planetary atmospheres contribute significantly to the recorded spectral signatures measured by remote instruments. As a result, steps must be taken to remove both the additive and multiplicative contributions from these remote datasets due to atmospheric contamination.

2.3 Laboratory analyses

One such way to assess the performance of remotely acquired data is to calibrate these datasets using laboratory investigations. Laboratory analyses of a suite of diverse surface samples provide well calibrated data that should reflect that obtained using remote datasets over regions of similar properties. For example, the spectral signatures of basalts measured in a laboratory setting should be comparable to those signatures obtained from orbit over basaltic terrains, following calibration and correction of the remote dataset.

Laboratory analyses exploit the compositional, structural, and textural properties of materials and their relationship to each other. For instance, in Chapter Three, we show

that MgO content of dolerites is directly related to the abundance of orthopyroxene (opx) within the samples. Opx has unique spectral signatures that can be measured from orbit. As a result, laboratory measurements can be used to relate the spectral properties of opx in collected samples to the MgO content of the same samples, and this relationship can then be used to estimate MgO content throughout the pure dolerite surfaces in the MDV (Salvatore et al., 2013a). In such instances, and through laboratory analyses, it is possible to map and analyze different properties of surfaces that cannot be directly measured using remote datasets.

Laboratory analyses, along with sample collection and contextual information collected during field work, can also help to reconstruct the temporal evolution of a surface. In the case of surface alteration and chemical weathering, the progression of these processes with time is of critical importance. Stratigraphic relationships and other methods can be used in the field to reconstruct the relative ages of materials. With this information, laboratory analyses can be used to identify a range of differences between these samples and provide information as to the temporal evolution of alteration products. Establishing an understanding for the alteration trends can help to constrain the conditions necessary for that material to evolve in such a fashion. However, it is only through this detailed laboratory characterization that such information regarding temporal evolution can be ascertained.

3.0 Dissertation Summary

The first half of this dissertation focuses on investigating the processes and products of chemical alteration of a particular lithology in the MDV of Antarctica

(Chapter Two). The resultant spectral signatures associated with these alteration products enable us to investigate the distribution of these alteration products throughout the MDV using multispectral VNIR and TIR orbital datasets (Chapter Three). The second half of this dissertation expands upon this work in the MDV by investigating the spectral and chemical signatures of the martian surface using both VNIR and TIR orbital spectroscopic datasets (Chapters Four and Five). The cold and dry environmental conditions of both the MDV and Mars, in addition to the presence of a "Mars-relevant" lithology in the MDV (the Ferrar Dolerite; Harvey, 2001), make this association possible. The wealth of both VNIR and TIR spectral data also provide the near-global coverage of the martian surface necessary to investigate trends in the spatial distribution of geochemical signatures. These spatial trends provide additional information regarding the climatic and volcanic evolution of Mars.

Identifying an analytical technique that is capable of identifying the products of oxidative chemical weathering is necessary to associate the cold and dry chemical alteration processes in the MDV with those occurring on the martian surface. In Chapter Two, we demonstrate how VNIR and TIR spectroscopic datasets provide the clearest evidence for oxidative alteration processes. While neither the VNIR reflectance signatures nor the TIR emission signatures of oxidative alteration are individually unique, their concordance and mutual occurrence is unique from any other known alteration process. In Chapter Three, these spectroscopic signatures are investigated from orbit throughout the MDV using both VNIR and TIR multispectral orbital datasets, which reveal their heterogeneous distribution throughout the study region.

The last fifteen years have seen a momentous increase in the volume of VNIR and TIR orbital observations of the martian surface. These high-resolution global datasets provide the data necessary to investigate the distribution of these unique spectral signatures associated with oxidative alteration processes. In Chapter Four, we present the initial dual VNIR and TIR (termed "pan-spectral") investigation of the martian surface, focusing on two characteristic yet disparate spectral terrains. The identification of significant abundances of oxidative alteration products, in addition to the non-detection of hydrated mineral phases, emphasizes the cold and dry nature of the martian surface during the Amazonian geologic epoch (~ 3.1 Ga to present, Hartmann and Neukum, 2001). This investigation is further expanded in Chapter Five, where all nine unique spectral shapes associated with martian low albedo (dust-free) terrains (as identified by Rogers et al. (2007) and Rogers and Christensen (2007)) are characterized using both VNIR and TIR orbital spectroscopy. The modeled mineral abundances associated with this new investigation provide new information regarding both the primary and secondary geochemical evolution of the martian surface. More localized investigations of the two regions initially studied in Chapter Four (Acidalia Planitia and Syrtis Major) reveal spatial variations and trends that further our understanding of the ancillary spectral variations associated with oxidative alteration. These additional spectral variations provide further insight into the interpretation of planetary surface compositions from orbit given the altered spectral signatures as a result of oxidative weathering processes.

This dissertation concludes with a summary of regional- and global-scale VNIR and TIR spectral investigations, with implications for the evolution of the martian surface as a function of time, chemical alteration, and climate change. Outstanding questions and

future research directions are also highlighted, as the characterization of the martian surface is a continuous process that is dependent upon the available datasets and the imagination of planetary scientists to pose new and exciting hypotheses.

References

Allen C. C. and Conca J. L. (1991), Weathering of basaltic rocks under cold, arid conditions: Antarctica and Mars. *Proc. Lunar Planet. Sci.* **21**, 711-717.

Andersen D. W., Wharton Jr. R. A. and Squyres S. W. (1993), Terrigenous clastic sedimentation in Antarctic dry valley lakes. *Ant. Res. Ser.* **59**, 71-82.

Baker V. R., Carr M. H., Gulick V. C., Williams C. R. and Marley M. S. (1992), Channels and valley networks. In *Mars* (eds. H. H. Kieffer, B. M. Jakosky, C. W. Snyder and M. Matthews). Space Science Series, University of Arizona Press, p. 493-522.

Bandfield J. L., Hamilton V. E. and Christensen P. R. (2000), A global view of martian surface compositions from MGS-TES. *Science* **287**, 1626-1630.

Bibring J.-P., Langevin Y., Mustard J. F., Poulet F., Arvidson R., Gendrin A., Gondet B., Mangold N., Pinet P., Forget F. and the OMEGA Team (2006), Global mineralogical and aqueous Mars history derived from OMEGA/Mars Express data. *Science* **312**(5772), 400-404.

Bishop J. L., Koeberl C., Kralik C., Fröschl H., Englert P. A. J., Andersen D. W., Pieters C. M. and Wharton R. A. (1996), Reflectance spectroscopy and geochemical analyses of Lake Hoare sediments, Antarctica: Implications for remote sensing of the Earth and Mars. *Geochim. Cosmochim. Acta* **60**(5), 765-785.

Campbell I. B. and Claridge G. G. C. (1987), *Antarctica: Soils, weathering processes and environment*. Elsevier, Amsterdam, 406 pp.

Carr M. H. and Head III J. W. (2010), Geologic history of Mars. *EPSL* **294**, 185-203.

Chevrier V., Mathé P.-E., and Gunnlaugsson H. P. (2006), Magnetic study of an Antarctic weathering profile on basalt: Implications for recent weathering on Mars. *Earth & Planet. Sci. Lett.* **244**, 501-514.

Christensen P. R., Bandfield J. L., Clark R. N., Edgett K. S., Hamilton V. E., Hoefen T., Kieffer H. H., Kuzmin R. O., Lane M. D., Malin M. C., Morris R. V., Pearl J. C., Pearson R., Roush T. L., Ruff S. W. and Smith M. D. (2000), Detection of crystalline hematite mineralization on Mars by the Thermal Emission Spectrometer: Evidence for near-surface water. *J. Geophys. Res.* **105**(E4), 9623-9642.

Christensen P. R., Bandfield J. L., Hamilton V. E., Ruff S. W., Kieffer H. H., Titus T. N., Malin M. C., Morris R. V., Lane M. D., Clark R. N., Jakosky B. M., Mellon M. T., Pearl J. C., Conrath B. J., Smith M. D., Clancy R. T., Kuzmin R. O., Roush T., Mehall G. L., Gorelick N., Bender K., Murray K., Dason S., Greene E., Silverman S. and Greenfield M. (2001), Mars Global Surveyor Thermal Emission Spectrometer experiment: Investigation description and surface science results. *J. Geophys. Res.* **106**(E10), 23823-23871.

Doran P. T., McKay C. P., Clow G. D., Dana G. L., Fountain A. G., Nylen T. and Lyons W. B. (2002), Valley floor climate observations from the McMurdo dry valleys, Antarctica, 1986-2000. *J. Geophys. Res.* **107**, doi:10.1029/2001JD002045.

Dorn R. I. (2009), Desert rock coatings. In *Geomorphology of Desert Environments 2nd Edition* (eds. A. J. Parsons and A. D. Abrahams). doi:10.1007/978-1-4020-5719-9_7, p. 153-186.

Ehlmann B. L., Mustard J. F., Murchie S. L., Poulet F., Bishop J. L., Brown A. J., Calvin W. M., Clark R. N., Des Marais D. J., Milliken R. E., Roach L. H., Roush T. L., Swayze G. A. and Wray J. J. (2008), Orbital identification of carbonate-bearing rocks on Mars. *Science* **322**, 1828-1832.

Ehlmann B. L., Mustard J. F., Swayze G. A., Clark R. N., Bishop J. L., Poulet F., Des Marais D. J., Roach L. H., Milliken R. E., Wray J. J., Barnouin-Jha O. and Murchie S. L. (2009), Identification of hydrated silicate minerals on Mars using MRO-CRISM: Geologic context near Nili Fossae and implications for aqueous alteration. *J. Geophys. Res.* **114**, doi:10.1029/2009JE003339.

Ehlmann B. L., Mustard J. F., Murchie S. L., Bibring J.-P., Meunier A., Fraeman A. A. and Langevin Y. (2011), Subsurface water and clay mineral formation during the early history of Mars. *Nature* **479**, 53-60.

Fassett C. I. and Head J. W. (2008), The timing of martian valley network activity: Constraints from buffered crater counting. *Icarus* **195**(1), 61-89.

Fountain A. G., Nylen T. H., Monaghan A., Basagic H. J. and Bromwich D. (2009), Snow in the McMurdo Dry Valleys, Antarctica. *Intl. J. Climatol.* **30**(5), 633-642.

Gendrin A., Mangold N., Bibring J.-P., Langevin Y., Gondet B., Poulet F., Bonello G., Quantin C., Mustard J., Arvidson R. and LeMouélic S. (2005), Sulfates in martian layered terrains: The OMEGA/Mars Express view. *Science* **307**, 1587-1591.

Gibson E. K., Wentworth S. J. and McKay D. S. (1983), Chemical weathering and diagenesis of a cold desert soil from Wright Valley, Antarctica: An analog of martian weathering processes. *J. Geophys. Res.* **88**, A912-A928.

Glasby G. P., McPherson J. G., Kohn B. P., Johnston J. H., Keys J. R., Freeman A. G. and Tricker M. J. (1981), Desert varnish in southern Victoria Land, Antarctica. *N. Z. J. Geol. & Geophys.* **24**(3), 389-397.

Glazovskaya M. A. (1958), Weathering and primary soil formation on the Antarctic continent. *Nauchnoye Doklady Vyeshey Shkoly: Geolicheskiy-Geographicheskie Nauki*, No. 1.

Gooseff M. N., Barrett J. E., Doran P. T., Fountain A. G., Lyons W. B., Parsons A. N., Porazinska D. L., Virginia R. A. and Wall D. H. (2003), Snow-patch influence on soil giogeochemical processes and invertebrate distribution in the McMurdo Dry Valleys, Antarctica. *AAAR* **35**(1), 91-99.

Gooseff M. N., Lyons W. B., McKnight D. M., Vaughan B. H., Fountain A. G. and Dowling C. (2006), A stable isotopic investigation of a polar desert hydrologic system, McMurdo Dry Valleys, Antarctica. *AAAR* **38**(1), 60-71.

Greeley R. and Guest J. E. (1987), Geologic map of the eastern equatorial region of Mars. *USGS Map 1-1802-B*, 1:15M scale.

Hartmann W. K. (2005), Martian cratering 8: Isochron refinement and the chronology of Mars. *Icarus* **174**(2), 294-320.

Hartmann W. K. and Neukum G. (2001), Cratering chronology and the evolution of Mars. *Space Sci. Rev.* **96**, 165-194.

Harvey R. P. (2001), The Ferrar Dolerite: An Antarctic analog for martian basaltic lithologies and weathering process. *Wkshp. Martian Highlands & Moj. Des. Analogs*, abstract 4012.

Jakosky B. M. and Phillips R. J. (2001), Mars' volatile and climate history. *Nature* **412**, 237-244.

Kraft M. D., Michalski J. R. and Sharp T. G. (2003), Effects of pure silica coatings on thermal emission spectra of basaltic rocks: Considerations for martian surface mineralogy. *Geophys. Res. Lett.* **30**(24), doi:10.1029/2003GL018848.

Lammer H., Kasting J. F., Chassefière E., Johnson R. E., Kulikov Y. N. and Tian F. (2008), Atmospheric escape and evolution of terrestrial planets and satellites. *Space Sci. Rev.* **139**, 399-436.

Langevin Y., Poulet F., Bibring J.-P. and Gondet B. (2005), Sulfates in the north polar region of Mars detected by OMEGA/Mars Express. *Science* **307**, 1584-1586.

Lasaga A. C. (1984), Chemical kinetics of water-rock interactions. *J. Geophys. Res.* **89**(B6), 4009-4025.

Lyons W. B., Welch K. A., Fountain A. G., Dana G. L., Vaughn B. H. and McKnight D. M. (2003), Surface glaciochemistry of Taylor Valley, southern Victoria Land, Antarctica and its relationship to stream chemistry. *Hydrol. Proc.* **17**(1), 115-130.

Marchant D. R., Lewis A. R., Phillips W. M., Moore E. J., Souchez R. A., Denton G. H., Sugden D. E., Potter N. and Landis G. P. (2002), Formation of patterned ground and sublimation till over Miocene glacier ice in Beacon Valley, southern Victoria Land, Antarctica. *Geol. Soc. Amer. Bull.* **116**(6), 718-730.

Marchant D. R. and Head J. W. (2007), Antarctic dry valleys: Microclimate zonation, variable geomorphic processes, and implications for assessing climate change on Mars. *Icarus* **192**(1), 187-222.

McKay C. P., Friedman E. I., Wharton R. A. and Davies W. L. (1992), History of water on Mars: A biological perspective. *Adv. Space Res.* **12**(4), 231-238.

McKay D. S., Gibson E. K., Thomas-Keprta K. L., Vali H., Romanek C. S., Clemett S. J., Chillier X. D., Maechling C. R. and Zare R. N. (1996), Search for past life on Mars: Possible relic biogenic activity in martian meteorite ALH84001. *Science* **273**, 924-930.

Michalski J. R., Kraft M. D., Sharp T. G., Williams L. B. and Christensen P. R. (2005), Mineralogical constraints on the high-silica martian surface component observed by TES. *Icarus* **174**(1), 161-177.

Milliken R. E., Swayze G. A., Arvidson R. E., Bishop J. L., Clark R. N., Ehlmann B. L., Green R. O., Grotzinger J. P., Morris R. V., Murchie S. L., Mustard J. F. and Weitz C. (2008), Opaline silica in young deposits on Mars, *Geology* **36**(11), 847-850.

Minitti M. E. and Hamilton V. E. (2010), A search for basaltic-to-intermediate glasses on Mars: Assessing martian crustal mineralogy. *Icarus* **210**, 135-149.

Morris R. V., Graff T. G., Mertzman S. A., Lane M. D. and Christensen P. R. (2003), Palagonitic (not andesitic) Mars: Evidence from thermal emission and VNIR spectra of palagonitic alteration rinds on basaltic rock. *6th Intl. Conf. Mars*, abstract 3211.

Nyquist L. E., Bogard D. D., Shih C.-Y., Greshake A., Stöffler D. and Eugster O. (2001), Ages and geologic histories of martian meteorites. *Chron. & Evol. Mars* **96**, 105-164.

Parker T. J., Gorsline D. S., Saunders R. S., Pieri D. C. and Schneeberger D. M. (1993), Coastal geomorphology of the martian northern plains. *J. Geophys. Res.* **98**(E6), 11061-11078.

Pieters C. M., Taylor L. A., Noble S. K., Keller L. P., Hapke B., Morris R. V., Allen C. C., McKay D. S. and Wentworth S. (2000), Space weathering on airless bodies: Resolving a mystery with lunar samples. *Met. Planet. Sci.* **35**, 1101-1107.

Poulet F., Bibring J.-P., Mustard J. F., Gendrin A., Mangold N., Langevin Y., Arvidson R. E., Gondet B., Gomez C. and the OMEGA Team (2005), Phyllosilicates on Mars and implications for early martian climate. *Nature* **438**, 623-627.

Rampe E. B., Kraft M. D., Sharp T. G., Golden D. C., Ming D. W. and Christensen P. R. (2012), Allophane detection on Mars with Thermal Emission Spectrometer data and implications for regional-scale chemical weathering processes. *Geology* **40**(11), doi:10.1130/G33215.1.

Rogers A. D. and Christensen P. R. (2007), Surface mineralogy of martian low-albedo regions from MGS-TES data: Implications for upper crustal evolution and surface alteration. *J. Geophys. Res.* **112**(E01003), doi:10.1029/2006JE002727.

Rogers A. D., Bandfield J. L. and Christensen P. R. (2007), Global spectral classification of martian low-albedo regions with Mars Global Surveyor Thermal Emission Spectrometer (MGS-TES) data. *J. Geophys. Res.* **112**(E02004), doi:10.1029/2006JE002726.

Salvatore M. R., Mustard J. F., Head J. W., Marchant D. R. and Wyatt M. B. (2013a), Characterization of spectral and geochemical variability within the Ferrar Dolerite of the McMurdo Dry Valleys, Antarctica: Weathering, alteration, and magmatic processes. *Antarctic Sci.*, accepted.

Salvatore M. R., Mustard J. F., Head J. W., Cooper R. F., Marchant D. R. and Wyatt M. B. (2013b), Development of alteration rinds by oxidative weathering processes in Beacon Valley, Antarctica, and Implications for Mars. *Geochim. Cosmochim. Acta, in review.*

Schwertmann U. and Taylor R. M. (1989), Iron oxides. In *Minerals in Soil Environments 2nd Edition* (eds. J. B. Dixon and S. B. Weld). Soil Science Society of America, Madison, Wisconsin, p. 379-438.

Scott D. H. and Tanaka K. L. (1986), Geologic map of the western equatorial region of Mars. *USGS Map I-1802-A*, 1:15M scale.

Shoji S., Nanzyo M. and Dahlgren R. A. (1993), *Volcanic ash soils.* Elsevier, Amsterdam.

Stoffer P. (2004), Desert landforms and surface processes in the Mojave National Preserve and vicinity. *USGS Report 2004-1007*.

Tanaka K. L. and Scott D. H. (1987), Geologic map of the polar regions of Mars. *USGS Map I-1802-C*, 1:15M scale.

Treiman A. H. (2005), The nakhlite meteorites: Augite-rich igneous rocks from Mars. *Chemie der Erde – Geochem.* **65**(3), 203-270.

Vitousek P. M., Chadwick O. A., Crews T. E., Fownes J. H., Hendricks D. M. and Herbert D. (1997), Soil and ecosystem development across the Hawaiian islands. *GSA Today* **7**(9), 1-8.

Wada K. (1989), Allophane and imogolite. In *Minerals in Soil Environments 2nd Edition* (eds. J. B. Dixon and S. B. Weld). Soil Science Society of America, Madison, Wisonsin, p. 1051-1087.

Wyatt M. B. and McSween Jr. H. Y. (2002), Spectral evidence for weathered basalt as an alternative to andesite in the northern lowlands of Mars. *Nature* **417**, 263-266.

Figure Descriptions

Figure 1. A synopsis of the geological and geochemical history of Mars. The majority of martian morphological evolution and geochemical alteration occurred prior to 3.0 Ga. The martian surface has been relatively stable and quiescent after this timeframe. In this dissertation, we aim to characterize the role of chemical alteration during this geologically dormant era. References include [1] Hartmann and Neukum (2001); [2] McKay et al. (1996); [3] Treiman (2005); [4] Nyquist et al. (2001); [5] Carr and Head (2010); [6] Fassett and Head (2008); [7] Ehlmann et al. (2011); [8] Bibring et al. (2006).

Figure 2. A multispectral map of the McMurdo Dry Valleys, highlighting the location of Beacon Valley, from Salvatore et al. (2013a). The map colors represent the following spectral parameterizations: Red maps the strength of the broad 1 μm absorption feature, which is unique to the Ferrar Dolerite. Green maps the spectral slope in the near-infrared, which is strongest in the quartz- and feldspar-bearing lithologies of the Beacon Supergroup and the basement granites, granodiorites, and gneisses. Blue

maps the thermal infrared spectral feature associated with the presence of quartz, and is uniquely high in the Beacon Supergroup where quartzites dominate. Ice and snow has been masked from the multispectral map and is overlain for effect. The floor of Beacon Valley is dominated by quartz-normative doleritic clasts, which are characteristically purple in this color scheme.

Figure 3. A conceptual model of the analytical techniques used in this dissertation.

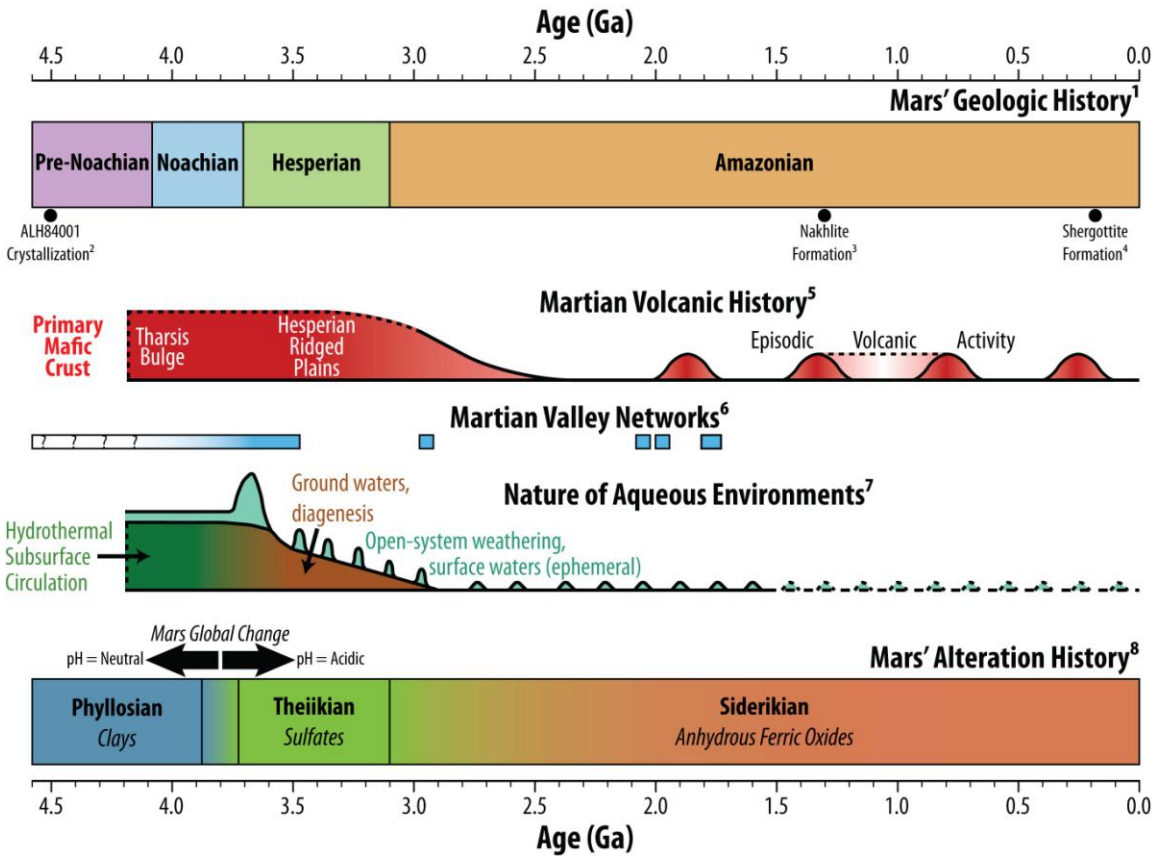

Chapter 1, Figure 1.

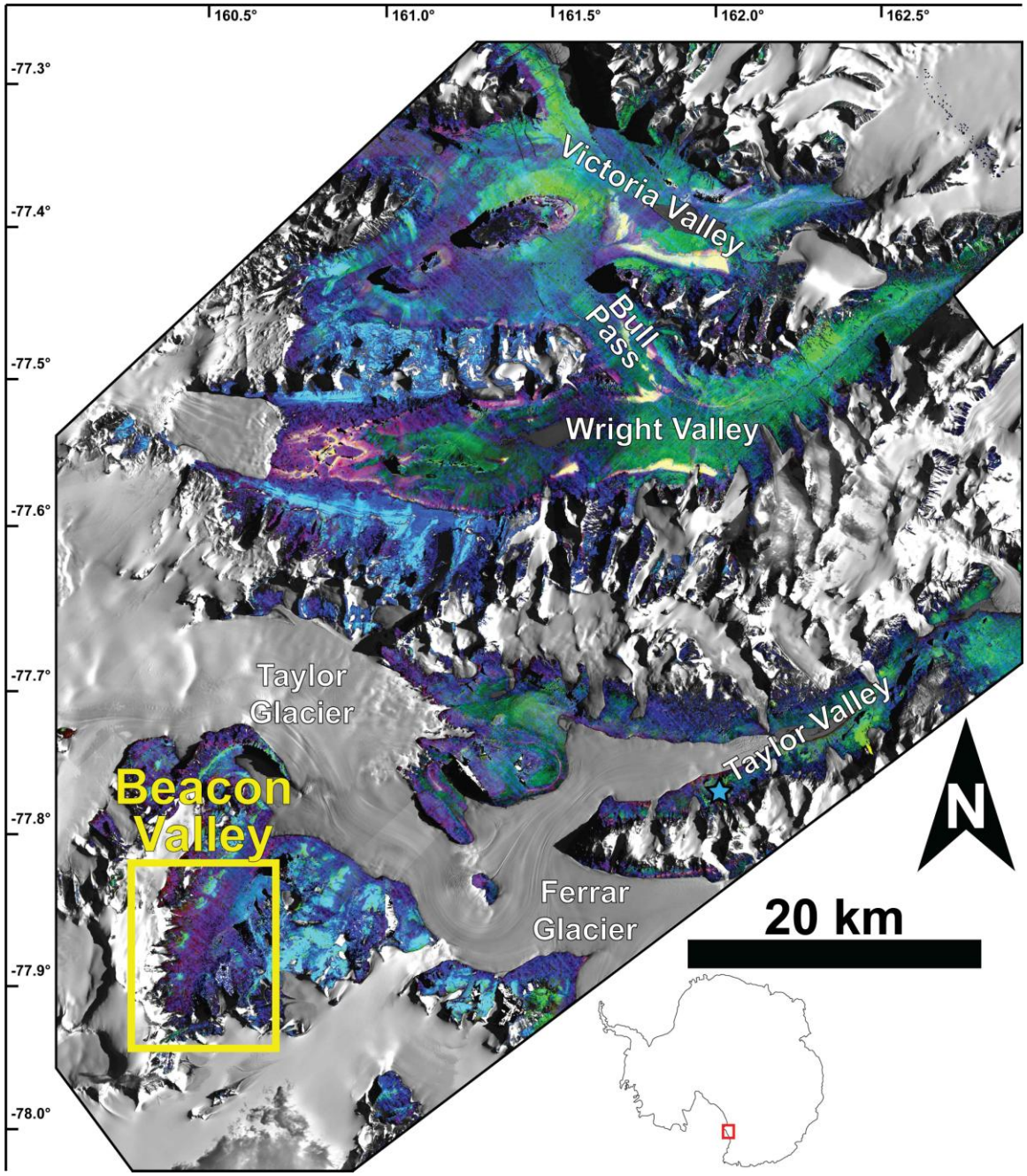

Chapter 1, Figure 2.

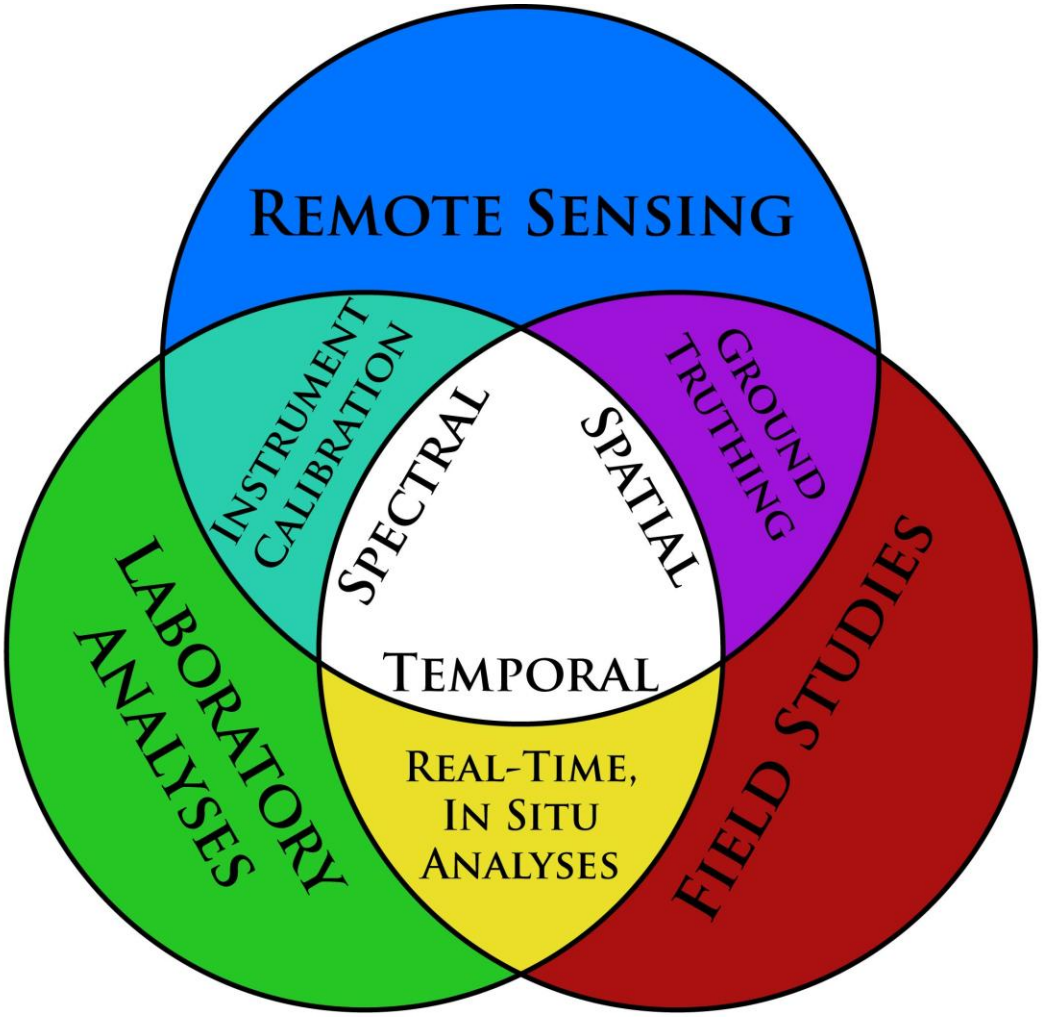

Chapter 1, Figure 3.

Chapter Two:

Development of alteration rinds by oxidative weathering processes in Beacon Valley, Antarctica, and implications for Mars.

M. R. Salvatore[1], J. F. Mustard[1], J. W. Head[1], R. F. Cooper[1], D. R. Marchant[2], and M. B. Wyatt[1]

[1]Department of Geological Sciences,

Brown University, Providence, RI 02912, USA

[2]Department of Earth Sciences,

Boston University, Boston, MA 02215, USA

In press in its current form in:

Geochimica et Cosmochimica Acta

DOI: 10.1016/j.gca.2013.04.002

Abstract

Alteration of fresh rock surfaces proceeds very rapidly in most terrestrial environments so that initial stages of modification of newly exposed surfaces are quickly masked by subsequent aqueous weathering processes. The hyper-arid and hypo-thermal environment of Beacon Valley, Antarctica, is limited in terms of available liquid water and energy available for alteration, which severely slows weathering processes so that the initial stages of alteration can be studied in detail. We report on the nature of initial chemical alteration of the Ferrar Dolerite in Beacon Valley, Antarctica, using a multiplicity of approaches to characterize the process. We suggest that initial chemical alteration is primarily driven by cation migration in response to the oxidizing environment. Morphological studies of altered rock surfaces reveal evidence of small-scale leaching and dissolution patterns as well as physical erosion due to surface weakening. Within the alteration front, mineral structures are largely preserved and alteration is only indicated by discrete zones of discoloration. Mineralogical investigations expose the complexity of the alteration process; visible/near-infrared reflectance and mid-infrared emission spectroscopy reveal significant variations in mineralogical contributions that are consistent with the introduction of oxide and amorphous phases at the surfaces of the rocks, while X-ray diffraction analyses reveal no definitive changes in mineralogy or material properties. Chemical analyses reveal large-scale trends that are consistent with cation migration and leaching, while small-scale electron microprobe analyses indicate that chemical variations associated with magmatic processes are still largely preserved within the alteration rind. This work confirms the incomplete and immature chemical alteration processes at work in the McMurdo Dry

Valleys. Liquid water is not a significant contributor to the alteration process at this early stage of rind development, but assists in the removal of alteration products and their local accumulation in the surrounding sediments. These results also suggest that the McMurdo Dry Valleys (and Beacon Valley, in particular) are relevant terrestrial analogs to hyper-arid and hypo-thermal alteration processes that may be dominant on the martian surface.

1.0 Introduction

Igneous rocks are immediately susceptible to chemical alteration upon exposure to the terrestrial atmosphere (Wilson, 2004). The rate of alteration is directly related to the temperature and chemistry of both the water and the atmosphere to which these precursor materials are exposed (Lasaga, 1984). These variables also control the relative solubility of the constituent minerals and the transport coefficients for the mineral ionic components and, consequently, the types of products that will form during chemical alteration. Identifying locales where the resultant alteration products are in relative equilibrium with the environment in which they formed can yield valuable information regarding the climatic variables and starting compositions from which the weathering products were derived. In warm and wet climates, mineral dissolution and elemental leaching occur rapidly and on relatively short geologic timescales. For example, in the Hawaiian Islands, > 90% of Ca, Mg, and Si are leached from their basaltic precursor soils after approximately 20,000 years during subaerial weathering in warm and wet tropical climates, resulting in heavily leached oxisols (Chadwick et al., 1999). Cold and/or arid climates, however, experience much slower rates of chemical alteration. For example, mature coatings and varnishes form on rock surfaces in arid environments on the order of

$10^{-6} – 10^{-5}$ m ka^{-1} and often contain immature alteration products (i.e., silica glaze, Fe/Mn oxides) (Dorn, 2009; Liu and Broecker, 2000).

Modest amounts of chemical alteration have also been observed in the coldest and driest locations on Earth. Previous studies have shown that the tholeiitic Ferrar Dolerite of the McMurdo Dry Valleys (MDV) of Antarctica has undergone relatively minor chemical alteration despite prolonged (up to 10^6 yr) exposure to the environment (Campbell and Claridge, 1987). The most substantial alteration products observed on dolerites in the MDV are pervasive, red/brown alteration rinds on rock surfaces (Glasby et al., 1981) with more soluble salt species present where the evaporation of liquid water is focused (Bockheim, 2002). However, debates continue as to whether these rinds are depositional in nature (e.g., Staiger et al., 2006) or the result of leaching and alteration of the primary lithology to secondary products (e.g., Chevrier et al., 2006).

Throughout this manuscript, the term "rind" will be used to describe internally derived alteration horizons, while the term "coating" will be reserved to describe externally derived depositional features (Fig. 1). Desert varnishes and other depositional coatings are commonly found in terrestrial desert environments and their chemistry and formation mechanism are highly variable (Dorn, 2009). The presence of lithobionts can result in the formation of biofilms and other biological coatings where conditions allow (Viles, 1995). Abiotic mechanisms include the cementation of dust, clays, metals, or other mobile element species to rock surfaces (Dorn, 2009). Most coatings lie uncomfortably on the surfaces of rocks, which can be easily identified in thin section. Rinds, however, do not exhibit a discontinuity between the underlying unweathered rock and the altered surface above. Instead, rinds are characterized by a gradational transition

from unaltered rock interiors to their altered surfaces (e.g., Sak et al., 2004; Hausrath et al., 2008), as was first described in Antarctic dolerites by Glasby et al. (1981). Glasby et al. (1981) therefore conclude that alteration rinds must be derived from leaching of material from the inner regions of rocks and subsequent oxidation and alteration, rather than an accretionary or externally derived mechanism. This definition of an alteration rind is adopted throughout this study and the mechanism of alteration rind formation is investigated further.

Building on the significant contributions of these previous works, we have integrated morphological, chemical, and mineralogical analyses of a suite of representative dolerites in a well-characterized environmental setting in order to bring a range of new techniques to this problem. This integrated approach is designed to address the following questions: What are the alteration processes and products associated with the chemical alteration of tholeiites under hyper-arid and hypo-thermal conditions? Additionally, what is the nature of the pervasive alteration rinds on doleritic clasts and how are these rinds related to the environment under which they formed? How do rinds differ from coatings and what are the fundamental differences in processes and timescales? In this study, we investigate the chemical weathering of the Ferrar Dolerite in Beacon Valley, the coldest, driest, and most stable of the MDV (Marchant and Head, 2007) (Fig. 2). We both qualitatively and quantitatively compare the altered surfaces of 14 doleritic clasts to their unaltered interiors by integrating morphological, chemical, and mineralogical analyses. This further understanding of the unaltered and altered lithologies, in conjunction with an established understanding of the geologically recent

environmental conditions, allows us to unravel the process of initial chemical alteration that is dominating dolerite surfaces in Beacon Valley.

2.0 Background

Chemical alteration throughout the MDV and the resultant alteration products have been extensively studied for more than 50 years. Early studies of dolerite alteration and the development and preservation of alteration rinds is synthesized in Campbell and Claridge (1987) and references therein, where they are primarily described as desert varnishes or "staining". None of the early studies identified a biological contribution to the alteration process, which differs from mid-latitude desert varnishes that commonly contain a significant biological component (Dorn, 2009). These early investigations describe how Fe is weathered out of ferromagnesian minerals and redeposited as coatings on quartz and feldspar grains on the rock surface (Campbell and Claridge, 1987). Initial chemical studies revealed that the rinds and coatings on dolerites are enriched in Fe and Si, but not Mn, which also suggests that they are not genetically related to traditional desert varnishes in hot desert regions (Glasby et al., 1981; Talkington et al., 1982).

Allen and Conca (1991) focused on the formation and development of etch pits on dolerite surfaces. They document that solar heating of dark rock surfaces results in the melting of snow trapped in surface cracks and pits. As liquid water is focused and concentrated in surface etch pits, evaporation results in the precipitation of a variety of soluble salt species, followed by the crystallization of illite and quartz (Allen and Conca, 1991). This material is then easily scoured and removed by aeolian processes. A subsequent analysis of etch pits and their relationship to martian surface observations

(Head et al., 2011) corroborates these earlier studies and discusses how more extensive physical and chemical alteration and the resultant formation of etch pits is dominated by transient episodes of surface wetting controlled by snowmelt and solar heating. These transient processes can potentially dominate the physical and chemical properties of rock surfaces in locations where chemical and physical erosion are limited (Head et al., 2011). Other recent alteration studies have focused on the Ferrar Dolerite largely due to its compositional similarities to martian basalts (Harvey, 2001; Chevrier et al., 2006). In contrast to the results of Glasby et al. (1981), Chevrier et al. (2006) identify a decrease in Si in the altered surface of a weathered dolerite relative to its unweathered interior, in addition to the formation of (oxy)hydroxides and "porous" textures at the surface of their analyzed sample. Staiger et al. (2006) analyzed several dolerites from Vernier Valley and concluded that "varnish" thickness increases with increasing exposure age. In addition, VNIR reflectance and MIR emission spectroscopic studies have been performed by Wyatt et al. (2008) and Salvatore et al. (2010a; 2011a; 2011b; 2011c) in conjunction with various other analytical techniques. Their results indicate substantial spectral variations between dolerite interiors and their altered surfaces with only minor mineralogical or chemical variations.

Many outstanding questions remain following these foundational studies: (1) What is the true morphologic nature of these alteration rinds (coatings, staining, varnishing)? Such information would help to determine the formation mechanism and extent of chemical alteration and leaching experienced by the dolerites in Beacon Valley. (2) What are the chemical and mineralogical signatures of the alteration products and how do they differ from the unaltered rock interiors? The alteration and leaching of

distinct mineral and elemental species can help to constrain the necessary environmental conditions. Lastly, (3) what is the process that forms the observed alteration signatures and what can it tell us about the environment under which these signatures formed? Our detailed analyses of samples from the McMurdo Dry Valleys aim to address these questions.

3.0 Geographic Setting

Beacon Valley, Antarctica (77º 49' S, 160º 39' E), is the southernmost of the McMurdo Dry Valleys (Fig. 2). In addition, its latitude, distance from the Ross Sea (~ 70 km), mean elevation of approximately 1200 m HAE (height above the World Geodetic System 1984 (WGS84) ellipsoid), and proximity to the East Antarctic Ice Sheet make Beacon Valley one of the coldest, driest, and, as a result, most stable valleys of the MDV (Marchant and Denton, 1996; Marchant and Head, 2007). It has a mean annual temperature of -22º C (Doran et al., 2005) and mean annual water equivalent precipitation of less than 10 mm yr^{-1} (Schwerdtfeger, 1984; Fountain et al., 2009). Beacon Valley is largely dominated by atmospheric conditions generated over the East Antarctic Ice Sheet; deposition of snow derived from the ice sheet and frequent gravity-driven katabatic wind events are two such examples. This is confirmed by the widespread distribution and abundance of nitrate salts, which are derived from snow blown off of the East Antarctic Ice Sheet and are different from the sulfates and chlorides found in valleys closer to the Ross Sea (Bao and Marchant, 2006). Stratified and undisturbed ash deposits found on the floor of Beacon Valley have been dated to 8.1 Ma by Sugden et al. (1995), verifying the antiquity and stability of the valley surface. The stability of the surface and the absence

of fluvial activity make Beacon Valley an ideal natural laboratory for weathering experiments in cold and hyper-arid terrestrial environments.

The walls of Beacon Valley are composed of Devonian-Triassic Beacon Supergroup sandstones, siltstones, and orthoquartzites and intrusive sills of the Jurassic Ferrar Dolerite (McElroy and Rose, 1987). These dolerites are shallow intrusive igneous rocks composed primarily of plagioclase and pyroxene that underwent minor deuteric alteration during their emplacement (McAdam, 2008). The chemistry and mineralogy of the Ferrar Dolerite has been extensively studied (e.g., Gunn, 1962; 1963; 1965; 1966; Kyle et al., 1981; Heimann et al., 1994; Marsh, 2004; Bédard et al., 2007). The exposure of these sills was initiated by substantial uplift and tilting of the Transantarctic Mountains that began ~50 Ma (Gleadow and Fitzgerald, 1987) and continued through the late Oligocene and early Miocene (~25 Ma) (Denton et al., 1993). Beacon Valley is partially filled by a cold-based (dry) debris-covered glacier with a till dominated by doleritic clasts, fragments, and sediments, the age and structure of which has also been extensively studied in previous investigations (e.g., Sugden et al., 1995; Marchant et al., 2002). In upper Beacon Valley, the till material originates from rockfall near the head of several tributary glaciers (e.g., Mullins Valley and Friedman Valley) and is transported downhill into Beacon Valley as a sublimation till (Levy et al., 2006; Marchant and Head, 2007; Kowalewski et al., 2010; Kowalewski et al., 2012). As a result, this "geologic conveyor belt" provides the opportunity to study alteration and erosion with constraints on surface exposure age.

Marchant and Head (2007) designated Beacon Valley as the archetype of the Stable Upland Zone (SUZ) in their microclimate architecture of the MDV (Fig. 2). In

this zone, liquid water is limited to minor amounts of snowmelt, typically only on rock surfaces that have been heated by solar radiation, with no fluvial activity present. Pitted rocks are common in the SUZ and are the result of snowmelt accumulation on rock surfaces, localized aqueous alteration, and scouring by aeolian processes (Allen and Conca, 1991; Head et al., 2011). Sublimation polygons, formed by thermal contraction of subsurface glacial ice or permafrost with excess ice, dominate surfaces in the SUZ as a result of the lack of significant surface melting and saturated active layer cryoturbation. At lower elevations and closer to the coast, the valleys transition from the SUZ to the Inland Mixed Zone (IMZ), characterized by localized transient fluvial activity and associated intermittent subsurface fluvial activity, discontinuous ice cement, and sand-wedge polygons. The warmest and wettest of the microclimate zones is the Coastal Thaw Zone (CTZ), which is located at the lowest elevations and closest to the Ross Sea. Seasonal fluvial activity results in channelized flow, evaporative salt accumulations, and ice-wedge polygons. All of the rock samples analyzed in this study are from central Beacon Valley, well within the SUZ, and have experienced only transient liquid water from snowmelt and no fluvial activity. However, the presence of some minor amounts of liquid water is required to explain the observed surface pitting on many samples (Allen and Conca, 1991; Head et al., 2011) as well as the salt accumulations and horizons present under many rocks and within the underlying regolith, respectively, as is discussed in Bao and Marchant (2006), Marchant and Head (2007), Bao et al. (2008), and Head et al. (2011).

4.0 Methods

Fourteen dolerite float samples (largely flat-lying and approximately 10^3-10^4 cm^3 in size) were collected along a 2.5 km transect through upper Beacon Valley. Landscape age in the study area is determined from a combination of cosmogenic-nuclide analyses of surface clasts (Marchant et al., 2007; Schaefer et al., 2000) and $^{40}Ar/^{39}Ar$ dating of undisturbed ash fall deposits (Marchant et al., 1996; 2002). Using these methods, Marchant et al. (2007) determined that the minimum duration for rock exposure in the study area is ~0.64 Ma, and may be considerably greater (Fig. 2). This finding is consistent with measured horizontal ice flow velocities (as derived from repeat satellite interferometry (Rignot et al., 2000)), which suggest that transport of supraglacial debris from the headwall source in Mullins Valley to the study site in upper Beacon Valley could take hundreds of thousands of years. Each of the fourteen dolerite samples were selected based on their apparent antiquity, estimated based on the visual extent of rind development (continuous oxidized surface, no evidence of flaking, glossy and specular sheen), the presence of a horizontal surface with ventifaction along the edges of the sample, and surface pitting, which is expected to increase in abundance and depth as a function of age (e.g., Staiger et al., 2006; Marchant and Head, 2007).

Rocks were subsampled into chips, powders, and thick/thin sections at Brown University for subsequent morphological, mineralogical, and chemical analyses. Rock chips were created by fragmenting larger samples using a rock hammer to avoid the influence of saw abrasion on the different spectroscopic techniques, and also to avoid the use of water or solvents to help prevent the dissolution of soluble species. Thin and thick sections were created using standard practices, which include preparation using water as

a cleaning and lubricating agent. Although the epoxies used during this process were not impregnated with hardening agents, the coherent crystalline nature of the samples, both within and away from the alteration rind, prevented any flaking, cracking, or other types of damage to the samples.

In an attempt to isolate the uppermost altered surfaces of these rocks, powders were created using a diamond-tipped rotary drill to abrade the outer surface and to remove the alteration rind from the underlying unaltered rock. This procedure was done without the use of water or solvents, preventing the possibility of mineral or chemical dissolution during the sample preparation process. Based on visual observations and test samples, it was determined that the average sampling depth of this method is roughly 500 μm. The test samples, which consisted of dolerites not analyzed in this study, were optically inspected to determine rind thickness prior to abrasion. Following abrasion and surface removal, thick sections were created to determine the extent of surface material that was removed. The average sampling depth was found to be approximately 500 μm. It should be noted that, in some instances, unaltered rock interiors may contribute to the rock powders derived from the altered surfaces. This inevitable consequence of sample preparation should not influence the analyses, as we are investigating the nature of chemical alteration and not the terminal products of alteration. Powders derived from the unaltered centers of the rocks were produced using the same method to ensure consistency and homogeneous sampling.

Several laboratory techniques were implemented to investigate the formation processes and nature of alteration rinds on the Ferrar Dolerite (Table 1). Rind morphology was investigated using a combination of thin and thick section optical

microscopy and scanning electron microscopy (SEM), which was used to investigate the character and variability of natural rock surfaces. Chemical analyses were performed using a combination of electron microprobe analyses (EPMA), inductively coupled plasma atomic emission spectroscopy via flux fusion (FF/ICP-AES), and Mössbauer spectroscopy to determine iron oxidation state. These techniques characterize the chemical composition of the samples at a variety of scales to define both the primary chemical properties of the dolerites under investigation as well as the extent and nature of chemical modification in the alteration rinds. Sample mineralogy was assessed using visible/near-infrared (VNIR) reflectance and mid-infrared (MIR) emission spectroscopy, X-ray diffraction (XRD) analyses, and Mössbauer spectroscopy. The combination of both intrusive (e.g., XRD and Mössbauer spectroscopy) and non-intrusive (e.g., VNIR and MIR spectroscopy) mineralogical analyses helps to link remote observations with laboratory measurements.

SEM analyses were performed at the University of Minnesota's LacCore Facility using a Hitachi TM-1000 Table-top SEM with a Tungsten filament and an accelerating voltage of 15 kV. Backscattered electron (BSE) images ranging from 20x – 10,000x magnification were collected to investigate the morphology of the altered surfaces as well as broad compositional variations between mineral grains and surface features.

EPMA analyses were performed at the Massachusetts Institute of Technology's Electron Microprobe Facility using wavelength dispersive spectrometry (WDS) on a JEOL JXA-8200 Superprobe with a LaB_6 electron gun, an accelerating voltage of 15 kV, and a 10 nA beam current. Quantitative chemical analyses were collected in addition to

qualitative elemental mapping products to identify spatial variations in major element chemistry.

ICP-AES analyses were performed at the Brown University Environmental Chemistry Facility. These analyses were utilized to measure the geochemistry of powdered samples in the fashion described by Murray et al. (2000). Powdered rock surfaces and interiors were divided into 40 mg aliquots, mixed with 160 mg $LiBO_2$, and fused for 10 minutes at 1050° C. The melts were quenched in 20 mL of 10% HNO_3 and agitated for one hour. The samples were then filtered through 0.45 µm filters and diluted in additional 10% HNO_3. The resultant liquids were analyzed using a JY2000 Ultrace ICP Atomic Emission Spectrometer. Samples were analyzed for Si, Al, Fe, Mg, Ca, Na, K, P, Mn, and Ti using a Gaussian peak search technique and the results were calibrated and converted to weight percentages using a series of blanks and geochemical standards that were processed in the same fashion as the samples. All samples, standards, and blanks were run in duplicate to increase the robustness of the measurements. Twenty two standard measurements were run concurrently with the sample analyses to both assess the analytical uncertainty and to convert the sample measurements to oxide weight percentages.

Mössbauer spectroscopy was performed at the Mount Holyoke College Department of Astronomy on three pairs of sample powders. Seventy-five mg powdered aliquots were analyzed at a temperature of 295 K on a WEB Research Co. model WT302 spectrometer using a ^{57}Co source. The ability for Mössbauer spectroscopy to identify iron-bearing phases, to quantitatively assess the distribution of iron among these phases,

and to determine the distribution of iron among its oxidation states makes it a powerful tool to assess both the chemistry and mineralogy of samples.

VNIR reflectance spectroscopy was performed at the Brown University Keck/NASA Reflectance Experiment Laboratory (RELAB) using a bidirectional reflectance (BDR) spectrometer, which acquires spectra between 0.32 and 2.55 μm at a 5 nm spectral sampling interval using a photomultiplier and InSb detectors (Pieters, 1983; Mustard and Pieters, 1989). Illumination and emergence angles were fixed at 30° and 0°, respectively. Both rock chips and powders were measured in the BDR spectrometer under identical experimental setups, although rock chips were slowly rotated to reduce artifacts associated with viewing or illumination geometries. MIR emission spectroscopy was performed at the Stony Brook University Vibrational Spectroscopy Laboratory using a Nicolet 6700 FTIR Spectrometer, which utilizes a deuterated L-alanine doped triglycine sulfate (DLaTGS) detector and CsI window. Measurements were made between 2000 cm^{-1} and 200 cm^{-1} at a resolution of 4 cm^{-1} using a CsI beamsplitter. As is standard in MIR emission spectroscopy, samples were held at 80º C to improve signal. Additional information regarding MIR measurements and calibrations can be found in Ruff et al. (1997). Only macroscopically flat rock fragments were analyzed using VNIR and MIR spectral techniques, minimizing the effects of microscale sample topography on these analyses.

XRD measurements were performed at Brown University's XRD Facility (Siemens D5000 Diffraktometer, Cu radiation source, all samples) and the University of Minnesota's LacCore Facility (Rigaku MiniFlex CRD, Cu radiation source, all samples). XRD patterns were collected at Brown University in an attempt to perform quantitative

analyses, and patterns were collected at the LacCore Facility to understand and better quantify the potential contributions from smectite clays. The D5000 instrument at Brown University has been enhanced by the addition of a Gobel mirror assembly to increase the system intensity and resolution. The system utilizes a standard powder XRD setup, with the powder loaded into a sample holder that is positioned between an X-ray tube and detector. The sample stage and detector are rotated during the analysis to sweep through the full 2θ range. This setup has a 2θ range and resolution of 3° - 85° and 0.1°, respectively, and the scanning interval for each analysis was 0.2° per minute. Sample sizes were approximately 100 mg and sieved to < 63 μm. Sample preparation for the MiniFlex instrument at the University of Minnesota included agitation and suspension of a powdered sample (~250 mg, sieved to < 63 μm) in ethanol and evaporated onto an aluminum sample holder. Each sample was prepared with a calcite spike to improve quantitative statistics. Samples were run both before and after spiking to ensure that no data were lost during the sample preparation process. The MiniFlex instrument geometry is nearly identical to that of the D5000, has a 2θ range and resolution of 4° - 65° and 0.05°, respectively, and a scanning interval of 1° per minute.

5.0 Results

The petrography of the samples analyzed in this study is consistent with prior studies of the Ferrar Dolerite (e.g., Elliot and Fleming, 2004). Mean grain size throughout our sample suite is highly variable, from equigranular subophitic textures with grain sizes less than 100 μm, to 800 μm subhedral and unoriented ophitic textures. This variability is due to the initial location of the dolerite clast within the sill; finer grained

textures are derived from the rapidly cooling sill margins, while coarser grained textures are derived from the interior of the sills. Mineral proportions are also variable at the scale of the thin sections, with ratios varying between 3:1 plagioclase feldspar and pyroxene, and vice versa. Interstitial glass is common throughout the sample suite, and quartz is present as a minor interstitial phase in some of the samples, and the abundance of these phases (up to ~25% in the least crystalline samples) is highly variable. Largely euhedral chlorite pseudomorphs have also been observed in some samples and confirmed through EPMA analyses. However, the observed chlorite abundances are minor (less than 1 vol.%, based on optical and EPMA analyses) and, as a result, their spectral, chemical, and mineralogical contributions are likely to be minor as well.

5.1 Chemistry

The bulk chemistry of interior and surface powders was determined by FF/ICP-AES. These analyses show only subtle variations in major element chemistry between the rock interiors and their corresponding alteration rinds (Fig. 3; Table 2). Of particular interest are the trends of Ca and Mg, which are systematically depleted in the alteration rinds relative to their unaltered interiors, and Na and K, which are systematically enriched in the alteration rinds relative to their unaltered interiors (Fig. 4). While the Ca and Na interior and alteration rind measurements are within one standard deviation, the Mg and K measurements are outside of one standard deviation.

The calculated Mössbauer isomer shift relative to metallic iron (δ), quadrupole splitting (ΔE_Q) parameters, and spectral peak information are provided in Table 3. Mössbauer spectroscopy of three sample pairs (Sample 04, Sample 10, Sample 12) confirms a systematic increase in Fe^{3+}/Fe_{Total} from an average of 0.21 to 0.35 from rock

interiors to the alteration rinds, respectively (Fig. 5; Table 3). This technique identifies the ferrous iron component as principally pyroxene or chlorite (indistinguishable in Mössbauer spectroscopy due to their similar crystal structures), with no indication of ferrous iron in feldspar due to its low total Fe content. Based on other spectroscopic, chemical, and optical analyses, we conclude that pyroxene and not chlorite is the dominant ferrous component present in the dolerite samples. This technique is also able to determine that the ferric iron is present in either its original primary mineral phases or in nanophase ferric iron oxides; crystalline iron oxides and oxy-hydroxides including hematite and goethite have not been identified, indicating that mature phases are not being produced during the alteration process. The nearly pristine crystalline morphologies observed within the alteration rinds by optical microscopy and SEM confirm that no mature alteration phases (e.g, hematite, goethite) are present as large crystals within the altered zones.

The subtlety of chemical alteration is also confirmed in EPMA analyses, which verifies that, on the basis of these measurements and analyses, the relative abundances of major cations are indistinguishable between the interiors and alteration rinds (Fig. 6). In addition, compositional zoning associated with an evolving magmatic chemistry during crystallization are visible both within the unaltered rock interiors and the alteration rinds (white arrows, Fig. 6). More intense alteration processes likely would have masked the minor chemical variations that we observe, and their preservation within the alteration rinds of several samples supports the interpretation that the rinds are only minimally altered.

5.2 Mineralogy

XRD analyses on sample powders were utilized to determine the mineralogical constituents of the sample interiors and alteration rinds. XRD patterns (Fig. 7) show diagnostic peaks that correspond to the presence of quartz, plagioclase, and pyroxene. No additional peaks were definitively identified in alteration rinds that were not present in the unaltered interiors. Additionally, no peaks disappeared in the patterns of the alteration rinds when compared to those of the unaltered interior. These observations are consistent with the EPMA analyses, which indicate that the major mineralogy and mineral chemistries both within and outside of the alteration rind are identical. Weak, broad, and diffuse peaks associated with either poorly crystalline materials (e.g., glassy intergranular matrix) or amorphous materials (e.g., amorphous Fe-O-H phases, amorphous or pre-crystalline clay minerals) are present in the XRD patterns of both interiors and alteration rinds centered at approximately 23º 2θ (Fig. 7). The relative strengths of these broad peaks are similar, indicating that the volumetric component of amorphous or poorly crystalline components does not significantly vary within alteration rinds relative to rock interiors. These results suggest that no detectable changes are apparent between rock surfaces and their corresponding interiors.

Attempts at performing quantitative mineralogical analyses on these XRD data proved problematic for several reasons. First, the signal associated with most individual measurements was low compared to instrumental noise. Second, quantitative modeling utilizing Rietveld refinement (Bish and Post, 1993; Hillier, 2000) suggested that nontronite should be present at abundances greater than 30% in both dolerite interior and surface powders despite no additional evidence for the presence of nontronite in any

other analytical dataset. Chlorite, which can sometimes be mistaken for nontronite in XRD analyses (e.g. Granger and Raup, 1969), was also modeled at ~5% abundance in both interiors and surfaces, suggesting that the identification of nontronite was not solely a false identification of chlorite at similar abundances. The presence of nontronite and/or chlorite at these abundances can be identified with great confidence using VNIR spectroscopy by their diagnostic absorptions at 2.29 μm and 2.35 μm, respectively, and using MIR spectroscopy by their diagnostic absorptions at 530 cm^{-1} and 1026 cm^{-1}, respectively. The absence of these diagnostic features suggests that neither nontronite nor chlorite are abundant at spectrally significant quantities (> 20%; Ehlmann et al., 2012; Ruff and Christensen, 2007). No evidence of microscopic fracture networks was observed in any of the samples, suggesting that the modeled nontronite abundances are not the result of complex microfracture network formation and alteration. Third, significant inter-laboratory variability in measured sample patterns precludes the definitive quantification of mineral abundances. This inter-laboratory variability results in considerable variations in modeled mineral abundances. For these reasons, quantitative analyses of these XRD data proved indeterminate. We therefore rely on several other proven techniques to constrain the geochemical and mineralogical variations between sample surfaces and their unaltered interiors.

VNIR reflectance spectroscopy reveals substantial variations between rock interiors and their corresponding surfaces (Fig. 8). Rock interiors are characterized by a broad and complex absorption feature centered near 1.0 μm that is attributed to pyroxene with possible contributions from plagioclase and/or chlorite (Clark, 1999). A weaker and broader absorption feature centered near 2.0 μm is also attributable to pyroxene. Narrow

absorptions near 1.4 μm, 1.9 μm, and 2.3 μm indicate minor amounts of OH^-- and H_2O-bearing phases (e.g., Bishop et al., 2002). While preserving the broad 1.0 μm absorption feature, VNIR spectra of rock surfaces exhibit a substantial strengthening of the Fe^{2+}-Fe^{3+} charge-transfer absorption feature present at wavelengths < 0.6 μm (Morris et al., 1985), resulting in a strongly positive spectral slope between 0.5 μm and 0.7 μm. The relative lack of structure associated with this broad absorption feature is indicative of a weakly crystalline or non-crystalline ferric iron phase(s) or the presence of Fe^{3+} within a primary crystal structure, consistent with our Mössbauer results. The presence of crystalline ferric iron phases, including hematite and/or goethite, would produce diagnostic absorption features between 0.5 μm and 0.8 μm that are not observed in the spectra of dolerite surfaces. The 2.0 μm pyroxene absorption feature is largely masked by a negative spectral slope, which is strongly suggestive of the presence of strong OH and H_2O fundamental absorption near 3.0 μm (Clark et al., 1990). The 1.4 μm and 1.9 μm hydration features in the spectra of rock surfaces are stronger than those observed in the rock interiors. However, the 2.3 μm absorption, which is a combination tone of metal-OH bends and stretches (Clark et al., 1990; Bishop et al., 2002), remains extremely weak (measured band depths of 0.33% and 0.68% for average interiors and surfaces, respectively), suggesting that the increased hydration is not associated with a significant increase in smectite clays.

MIR emission spectroscopy is sensitive to the vibrational motions that occur at fundamental frequencies within crystal lattices that are indicative of crystal structure and chemical composition (e.g., Farmer, 1974; Christensen et al., 2001). MIR emission spectra of sample interiors and surfaces are shown in Figure 9. Emission spectra of rock

interiors show broad and complex reststrahlen bands (regions of maximum absorption due to high absorption coefficients) indicative of the presence of several primary igneous phases. Conversely, rock surface spectra have much narrower reststrahlen bands centered near 1090 cm^{-1} and 475 cm^{-1} that lack the structure and complexity found in the interior spectra, indicating that the primary igneous mineral signatures are being masked by another spectral component.

MIR emission spectra of mineral components in a mixture, such as in a rock, are shown to combine linearly (Gillespie, 1992; Adams et al., 1993) and has been demonstrated for laboratory spectra of minerals (Ramsey and Christensen, 1998) and rocks (Feely and Christensen, 1999). As shown in these studies, MIR emission spectra of mineral mixtures reflect the areal abundance of the mineral components. As a result, MIR emission spectra can be modeled using linear retrieval algorithms and a suite of spectral endmembers. We have used the linear spectral deconvolution algorithm developed by Ramsey and Christensen (1998) and a customized spectral library (Table 4) to estimate the relative spectral contributions from different endmember minerals.

Our endmember library is derived from the Rogers and Christensen (2007) skeleton library used to unmix martian basaltic terrains from orbit, although our library also contains several additional phyllosilicate and glass endmembers. The reduction of spectral endmember libraries is a widely used strategy to (1) reduce the number of endmembers that exhibit similar spectral shapes and to (2) only incorporate those components that are potentially present as to avoid spurious mineral identifications (e.g., Feely and Christensen, 1999; Hamilton and Christensen, 2000; Wyatt et al., 2001; Rogers and Christensen, 2007). The exclusion of a significant spectral endmember will result in

high RMS errors and the overprinting of those spectral signatures on the residual spectrum. The absence of either of these indicators suggests that our modeling is accounting for the majority of spectral variations. The results of this linear unmixing model are presented in Figure 10, along with the modeled endmember abundances for both averaged dolerite interiors and averaged dolerite surfaces. Dolerite interiors are best modeled by a combination of plagioclase (52 vol.%), pyroxene (21 vol.%), and synthetic Si- and K-rich glass ("SiK-Rich Glass", 16 vol.%). While mineral proportions at the scale of the MIR measurements (~ 1 cm) are highly variable, this mineral assemblage is consistent with thin section observations and with qualitative analyses of XRD patterns. Dolerite surfaces are best modeled as pyroxene (32 vol.%), SiK-Rich Glass (21 vol.%), smectite clays (20 vol.%), and feldspar (13 vol.%). Similar to the modeled mineralogy of dolerite interiors, the combination of pyroxene and feldspar is consistent with other mineralogical and optical analyses. The modeled abundance of smectites, which is almost entirely modeled as Ca-rich montmorillonite (19 vol.%), is inconsistent with other analyses, particularly VNIR spectroscopy. In the VNIR, montmorillonite exhibits a strong absorption feature present at 2.2 μm, which is absent in VNIR spectra of dolerite surfaces. In the MIR, montmorillonite is being preferentially selected by the unmixing model to account for the strong absorption feature present at 465 cm^{-1}. However, this spectral feature is not unique to smectites, but is common in both amorphous materials (such as glasses) and smectites. The lack of a strong dioctahedral smectite absorption feature at 530 cm^{-1}, as well as the lack of a strong 2.2 μm absorption feature in the VNIR, strongly suggests that montmorillonite (and, more generally, smectites) is not a significant spectral phase and can instead be accounted for by the presence of additional

amorphous materials. To test this hypothesis, smectites were excluded from the endmember library and dolerite surfaces were remodeled. SiK-Rich Glass was indeed used to replace the previously modeled smectite component, increasing in modeled abundance from 21 vol% to 39 vol.%, and only slightly decreasing the model's overall goodness of fit (indicated by the root-mean-squared error (RMSE)) from 0.507% to 0.581%.

SEM analyses were also able to observe unique mineralogical features on dolerite surfaces. The white arrows in Figure 11a and 11b highlight etching morphologies that appear to be targeting lamellae within primary mineral grains. Lamellae have been observed in both pyroxene and plagioclase grains within our sample suite; however, we are unable to ascertain the host mineralogy of these etch patterns based on these SEM analyses. Additionally, the small scale of these lamellae (on the order of 1 μm wide, Figure 11b) precludes analyses using traditional EPMA analytical techniques, which have a resolution on the order of 5 μm. The small scale of these lamellae prevents us from determining the exact chemistry of the etched material.

5.3 Morphology

Thin and thick section optical analyses of all fourteen samples clearly exhibit alteration rinds that are characterized by at least one discolored zone that, while locally variable, gradationally terminates at a near-uniform depth in each sample. The rinds transition to the unaltered interior several hundred micrometers to several millimeters within each sample (Fig. 12). These rinds can vary in thickness across very short spatial scales (< 1 mm), although their thickness typically parallels the morphology of the rock surfaces. The thickness of the discolored zones appears to be partially controlled by

underlying grain size, with coarser grained samples exhibiting thicker alteration rinds than finer grained samples. In all of the analyzed samples, primary crystal structures are preserved within the alteration rinds and there are no apparent discontinuities between the rock interior and the rinds (Fig. 12), consistent with the absence of depositional coatings. The gradational transition between the altered surfaces and unaltered interiors also suggests an alteration process that modifies the underlying rock in response to its surrounding environment. Figure 12 shows zones of moderately oxidized dolerite just beneath the rock surfaces (A"). These zones grade into zones of lesser oxidation (A'), which extend several millimeters into the rock interiors. A' is identified by its less discolored nature, which is intermediate between the highly discolored A" zone and the underlying and unaltered (U) zone that exhibits no discoloration. Primary crystal structure is observed throughout both the oxidized and unoxidized zones, consistent with inward alteration of the primary rock texture, and not the depositional morphology expected from a secondary rock coating. The dolerite in Figure 12b has a slightly larger grain size than the other examples (~700 μm average length, as compared with ~225 μm average length in Figure 12d). As a result, the area of maximum discoloration is substantially thicker (~2.60 mm) in Figure 12b than that observed in the other examples (~0.85 mm for Figure 12d).

SEM measurements of dolerite surfaces show pit development on a variety of spatial scales (~20 – 300 μm), flaking, and etching and dissolution morphologies (Fig. 11). Figure 11c shows evidence for extensive surface cracking (white arrow) and flake development (black arrow). Surface cracks appear to develop through individual mineral grains, as is apparent near the white arrow. The variations in contrast apparent

throughout the BSE image are indicative of different types of mineral grains present at the surface. Near the white arrow, a bright grain is shown to be dissected by a surface crack. Within the surface flake (indicated by the black arrow), mineral faces are clearly visible. The coalescence of surface cracks and the raised nature of the surface suggest that this surface is in the process of dislocation and removal. These observations confirm that surface cracking is occurring in the absence of a depositional coating, despite the glossy and specular sheen present on the rock surfaces. Figure 11d illustrates pitting on the sub-millimeter scale. Similar to Figure 11c, contrast variations in the BSE image represent the chemical and mineralogical variations observed throughout the sample. The appearance of primary plagioclase and pyroxene crystals (as confirmed through energy-dispersive X-ray spectroscopy (EDS)) at the sample surface confirms the absence of a chemically homogeneous surface layer and further refutes the presence of a depositional coating. The occurrence and morphology of these micro-pits suggest that they could be the precursors to the larger pits observed on dolerites (white arrow, Fig. 11d) and described by Allen and Conca (1991), Staiger et al. (2006), and Head et al. (2011).

6.0 Discussion

The data obtained for rock interiors and surfaces are consistent with diffusive oxidation (Fig. 13) being the dominant chemical alteration process in Beacon Valley, in which an oxidizing environment drives the migration of cations to the free surface of the sample, resulting in distinct structural, chemical, and mineralogical signatures. The driving force behind this alteration process is the strong oxidation gradient established between the unaltered dolerites (which, like most terrestrial igneous lithologies, were

emplaced near the quartz-fayalite-magnetite (QFM) redox buffer) and the oxidizing Antarctic environment (f_{O2} = 0.21). Although the resultant products of anhydrous oxidation-driven alteration are not entirely unique, the presence of two reaction interfaces (A" and A') in our samples, in addition to the multitude of chemical, mineralogical, and morphological observations, strongly suggest that oxidation is the dominant process that has altered these samples. Previous work has discussed the morphological and chemical signatures of such oxidation processes in basaltic glasses in both laboratory (Cooper et al., 1996a, 1996b; Smith and Cooper, 2000) and natural settings (Burkhard and Müller-Sigmund, 2007). The complex nature of poly-mineralic samples has, however, not been widely investigated in laboratory environments, and so direct comparison of Beacon Valley samples to previous reference studies is difficult.

Cooper et al. (1996a, 1996b) discuss the structures and products associated with cation migration and subsequent oxidation in basaltic glass. The relatively weak morphological and compositional signatures associated with these products are easily overprinted by more mature alteration products. Only under unique circumstances are the products of this oxidation process preserved. Burkhard & Müller-Sigmund (2007) identified these metastable oxidation signatures in lobes of basaltic pahoehoe lava in Hawaii, where the altered margins between lobes were uniquely preserved as a result of rapid burial by subsequent flow lobes following the initiation of surface oxidation. This process effectively sequestered the metastable products of oxidation and protected them from physical erosion or subsequent chemical alteration. In Beacon Valley, the hyper-arid and hypo-thermal conditions prevent the formation of widespread mature alteration products (i.e., smectite clays) on rock surfaces. Transient episodes of liquid water

produced by snowmelt (e.g. Marchant and Head, 2007) are able to exploit defects on rock surfaces, resulting in localized concentrations of clay minerals (Allen and Conca, 1991; Head et al., 2011) and the accumulation of mobile salt species (Marchant and Head, 2007). However, the short-lived nature of this liquid water is unable to produce and preserve mature alteration phases across the majority of rock surfaces, resulting in the widespread preservation of metastable products of oxidation. Although physical erosion plays a significant role in the redistribution of material throughout Beacon Valley, the climate and valley surface in Beacon Valley are some of the most stable in the world (Marchant and Head, 2007), making Beacon Valley an ideal natural laboratory to identify the metastable products of oxidation-driven alteration.

The products of oxidation-driven alteration have been carefully studied in laboratory environments (Cooper et al., 1996a, 1996b; Smith and Cooper, 2000) and, with the identification of Beacon Valley as an appropriate natural laboratory, this process (Fig. 13) can be investigated with respect to the observed chemical, mineralogical, and morphological signatures identified in the Ferrar Dolerite. When exposed to an oxidizing atmosphere, divalent cations are able to effectively migrate to the free surface of dolerites in response to the oxidation potential between the dolerite interior and the surrounding environment (Cooper et al., 1996a). The primary migrating species will be highly dependent on the chemistry and mineralogy of the dolerites, especially in dealing with complex poly-mineralic samples, although divalent cations are most susceptible to migration. The migration of cations to the free surface is charge-compensated by the inward flux of electron holes ($h^{\bullet}$, electron "vacancies" in the valence band of the mineral, specifically associated with Fe^{3+} occupying a site on the lattice "normally" occupied by a

Fe^{2+} cation, e.g., the M1 site in clinopyroxenes) which, in this instance, are manifested as the conversion of Fe^{2+} to Fe^{3+}. The ensuing outward flux of electrons caused by the oxidation of Fe results in the transfer of electrons to environmental oxygen, which allows the oxygen ions to combine with the migratory cations to form soluble oxide species on the free surfaces of the samples. Oxidation thus occurs as the removal of cations increases the oxygen/cation ratio within the sample, not by the addition of oxygen into the sample itself. This process most efficiently dissipates the Gibbs energy despite causing significant micrometer- to millimeter-scale textural changes in the process. Here, the noted textures refer to the morphologies of the interfaces between grains as well as the spatial differences in composition (Cooper 2010). These metastable products have disrupted crystal structures that are depleted in divalent cations and are relatively enriched in Fe^{3+}. We believe that this process and the resultant chemical and textural variations are responsible for the chemical and spectral signatures associated with these dolerite samples.

The dolerite samples are characterized by the presence of two oxidation fronts (Fig. 12). These oxidation fronts are defined by distinct variations in color (i.e., apparent oxidation) in the absence of visible morphological or structural changes in crystal structure. Similar zones of discoloration are observed by Smith and Cooper (2000) and are indicative of regions of variable extents of cation migration. As the oxygen/cation ratio increases, the concentration of Fe^{3+} locally exceeds different redox buffers, resulting in visible heterogeneities within these mobilized zones. In addition to the total FeO content of the protolith dolerites, the thickness and sharpness of the discolored zones appear to be at least partially controlled by grain size, with coarser grained samples

exhibiting thicker zones of discoloration and more diffuse boundaries than finer grained samples (Fig. 12).

The oxidation process detailed for glass was originally identified in crystalline oxide materials (Fehlner and Mott, 1970; Schmalzried, 1983) and further elucidated by Cooper et al. (1996a) and subsequent studies. The two fundamental properties associated with oxidation in crystalline materials (i.e., minerals) are (1) the presence of a semi-conductor condition, and (2) the presence of sufficient amounts of Fe. To establish a semi-conductor condition, the migration of divalent cations to the free surface of the minerals and rocks must be counter-balanced by a combination of the inward migration of electron holes ($h^{\bullet}$), the replacement by monovalent cations, and the presence of vacancies and point defects. Because the transport coefficient (the product of species concentration and species mobility) of $h^{\bullet}$ is exceedingly large compared to that of the divalent cations (a function of the extremely high mobility of $h^{\bullet}$), the electrochemical potential gradient of $h^{\bullet}$ must be equally as small in order to achieve electro-neutrality. By definition, this state satisfies the semi-conductor condition and is independent of the matrix in which the divalent cations and $h^{\bullet}$ exist. This model of oxidation driven alteration is also well supported by the observed micrometer- to millimeter-scale textures and morphologies of the rocks themselves. As argued by Schmalzried (1983) and Cooper (2010) and reemphasized in this manuscript, rock textures are invaluable clues to their kinetic and alteration histories.

The presence of Fe at high enough abundances to effectively charge-balance the oxidation process is necessary to create the observed signatures. Basaltic glasses and most igneous minerals contain sufficient amounts of Fe to result in substantial and visible

modifications, plagioclase included. Cook and Cooper (2000) show that high abundances of Fe are not required for cation-diffusion oxidation to dominate geologic materials. This process is still dominant at Fe abundances as low as 0.3 wt.%, which is lower than the amount of Fe contained within the average plagioclase crystals measured by EPMA in our study (~0.5 wt.%) (Cook and Cooper, 2000). This suggests that the redox kinetics are rate-limited by the migration of the cations and not by the abundance of Fe in all mineral types present in the dolerite. Additionally, as temperature is lowered, even less Fe is required to achieve this semi-conductor condition. While 0.3 wt.% Fe was required for the high temperature experiments described in Cook and Cooper (2000), even less is likely required at near-ambient conditions.

The growth rate of alteration rinds, as presented here, should follow parabolic kinetics (Cooper et al., 1996a), where the square of thickness is proportional to the diffusivity of the rate-limiting cation and the thermodynamic driving force (normalized to RT) for oxidation. However, cation diffusion rates at the ambient conditions of Beacon Valley have not been measured, but are estimated to be extremely slow due to the extremely low temperatures despite the strong oxidation driving potential. Simple extrapolation of high-temperature volume diffusion data confirms this hypothesis (Manning, 1973). Despite these thermal difficulties, the growth kinetics are likely enhanced by other diffusive mechanisms with lower temperature sensitivities (e.g., grain boundary diffusion), by the extreme driving force for oxidation at ambient conditions, and by the surface stability and duration of exposure to the Antarctic environment.

In their oxidation experiments, Cooper et al. (1996a) found that Ca^{2+} and Mg^{2+} were the dominant mobile cations, forming measurable layers of surface precipitates.

This migration leaves a zone of oxidized basaltic glass that is depleted in CaO and MgO, as measured using Rutherford backscattering spectroscopy. The magnitude of these depletions for CaO and MgO were found to be 8.01 mol.% and 7.75 mol.%, respectively. However, this zone is enriched in Na^+ (by 16.96 mol.%) and, to a lesser extent, K^+ (by 0.11 mol.%), which migrate into the divalent-cation-depleted zone from the sample interior in response to the charge imbalances. Assuming a similar process occurs in a poly-mineralic sample of similar composition, the dolerites of Beacon Valley should exhibit similar zones of depletion and precipitated layers of enrichment (Fig. 13).

While no oxide coatings are visible on dolerite surfaces, the dolerites do exhibit systematic depletions of Ca and Mg in the alteration rind relative to their interiors (Table 2 and Fig. 4). In addition, Na and K are enriched in the alteration rinds relative to their respective interiors (Table 2 and Fig. 4). We interpret the lack of surface coatings enriched in oxide species on the dolerites as a result of physical erosion (i.e., aeolian abrasion) and dissolution, mobilization, and reprecipitation during transient wetting from melting snow. This interpretation is substantiated by the abundance of salt species found underneath rocks and within the regolith throughout Beacon Valley; the cations that form these salt species are derived from the overlying doleritic clasts. Claridge and Campbell (1977) identified that soils derived from dolerites are uniquely enriched in Ca and Mg relative to soils derived from other lithologies, an observation that is consistent with oxidation-driven alteration processes and subsequent oxide dissolution during transient wetting events. Following the removal of these oxide coatings, the dolerites in Beacon Valley simply exhibit alteration rinds defined by oxidation fronts that are depleted in divalent cations and enriched in monovalent cations. Optical microscopy and SEM

analyses show that depositional coatings are not present on rock surfaces and that primary crystal morphologies are instead present at the surfaces of these samples. The lack of coatings, which are predicted if migration, leaching, and subsequent precipitation are occurring, confirms that physical erosion and/or aqueous dissolution and mobilization away from the rock surfaces are significant processes in Beacon Valley. The specular appearance of the rock surfaces is also consistent with extensive aeolian modification and smoothing.

The diversity of surface textures observed in SEM analyses is likely due to a combination of the different exposure and alteration histories of each sample, heterogeneous alteration on each individual sample surface, and modest chemical differences in the protolith. For example, more intense chemical alteration and physical erosion is able to occur in micro-topographic hollows on rock surfaces (Marchant and Head, 2007; Head et al., 2011). Conversely, in areas where water is unable to accumulate, smooth textures are able to develop as the surface matures and is not subjected to extensive physical erosion.

Mineralogical observations of dolerites are largely consistent with this oxidation-driven alteration process. XRD analyses show no evidence for significant changes in mineralogy between sample interiors and the alteration rinds. Mössbauer spectroscopy confirms the significant oxidation of Fe, present solely as Fe^{3+} substituting for Fe^{2+} in the crystal structure of pyroxene or chlorite, and/or the formation of nanophase Fe oxides (npOx). Morris et al. (2006) define npOx as "a generally poorly crystalline product of oxidative weathering that contains nanometer-sized particles of Fe^{3+}-bearing material that is embedded in a matrix and is associated with unknown proportions of H_2O, O^{2-}, OH^-…,

and other species through the formation of chemical bonds or specific chemical adsorption." The presence of npOx species is likely, particularly due to the reddening of dolerite surfaces in response to oxidative weathering processes. However, the abundances of these phases are small, as npOx has not been definitively identified in EPMA or VNIR analyses. Additionally, Singer (1982) showed that even at abundances of 1 wt%, these phases exhibit clear and strong absorptions in the VNIR spectral region. These significant optical contributions from Fe^{3+} in dolerite surfaces are accompanied by minor increases in the strength of H_2O and OH^- hydration features near 1.4 μm and 1.9 μm, which may suggest minor and volumetrically insignificant abundances of nanophase Fe^{3+}-bearing hydroxide and oxyhydroxide phases or the presence of adsorbed water on the rock surface. Efforts to identify these phases using transmission electron microscopy (TEM) are ongoing, although initial results confirm the minor volumetric contribution of these optically dominant phases.

Bulk chemistries are also consistent with the absence of aqueous alteration products. All dolerite interior and surface data plot below the feldspar-(pyroxene, olivine) join on a ternary FeO_T + MgO, Al_2O_3, CaO + Na_2O + K_2O (FM/A/CNK) diagram (Fig. 3), which is widely considered to be a region indicative of unaltered basaltic compositions and primary igneous variability (e.g., Hurowitz and McLennan, 2007). While these authors recognize that chemical alteration under extremely acidic environments can mimic primary igneous chemical variations, such environmental conditions are not present in Antarctica, and therefore we do not consider strongly acidic aqueous alteration a likely possibility.

VNIR and Mössbauer spectroscopy, in tandem, indicate that Fe hydroxides/oxyhydroxides cannot be present at significant abundances near the surfaces of these samples. Mössbauer results indicate that hematite, goethite, or other crystalline Fe^{3+} oxides and oxyhydroxides are not present at significant abundances. The VNIR absorption features unique to these hydroxide and oxyhydroxide phases are not substantial spectral components in any of the dolerite surface spectra, indicating that they are not present in significant abundances. These phases have also not been identified in EPMA analyses, which would be capable of observing significant concentrations of sub-pixel nanophase ferric iron phases should they be present.

The increased spectral contribution of amorphous aluminosilicate material, as modeled in MIR emission spectra of rock surfaces (Fig. 10), is not directly identified in any other mineralogical or chemical analysis despite being predicted products of the alteration process. Evidence for the chemical etching of plagioclase, which is identified in SEM analyses, may influence the MIR spectroscopy of these altered surfaces. The limited occurrences of these etched morphologies, however, in addition to the ubiquity of the MIR emission signatures of altered surfaces, strongly suggest that the source of these MIR spectral signatures is not associated with the observed etched morphologies. Instead, the ubiquity of the discolored alteration rind indicates that they are the likely source of the observed spectral signatures. The preferentially etched lamellae are indicative of localized aqueous modification. Additional evidence of aqueous alteration can be seen on many rock surfaces throughout Beacon Valley that exhibit surface pits and depressions. These depressions (Fig. 11d, black arrows), originally created by physical (e.g., cracks) or chemical/mineralogical (e.g., dissolution pits) defects, preferentially

accumulate liquid water following the melting of snow. This water is able to cause significant structural weakening as minor amounts of chemical alteration occur. Subsequent aeolian activity then acts to scour and remove this altered material, which expands the topographic depressions and creates a positive feedback that can result in large pits (white arrow) that can frequently reach diameters greater than one centimeter (e.g., Allen and Conca, 1991, Head et al., 2011). We speculate that, with time, these pits will widen and deepen as liquid water is preferentially concentrated in these hollows, allowing for more intense chemical alteration to occur, as described in Marchant and Head (2007) and Head et al. (2011).

While the extent of oxidation and grain size of the sample are clearly related to the presence of multiple oxidation fronts and their depth and transition characteristics within the samples, respectively, other variables may also contribute to the morphologies observed in thin section. Considering that these samples were all selected based on the same selection criteria, we assume that they have undergone similar physical and chemical histories since their deposition. Based on cosmogenic data for nearby rocks (not analyzed in this study), we believe that all of the rocks examined here were exposed in the hyper-arid, hypo-thermal climate of Beacon Valley for at least 0.64 Ma. The rocks in the distal end of the transect may have been exposed for considerably longer time spans (Marchant et al., 2007). These data, therefore, suggest that alteration rind development is complete by 0.64 Ma. Subsequent alteration rind evolution would simply contribute to the thicknesses of the A’ and A” alteration zones, although grain size and protolith FeO content also play significant roles.

7.0 Implications for Surface Alteration on Mars

The alteration processes and products described here are not limited to the Earth's surface. The present day martian surface can be considered a hyper-arid and hypo-thermal desert similar to the MDV based on the work of previous climatic, lithological, and morphological analog studies (Marchant and Head, 2007, and references therein; Harvey, 2001; Glasby et al., 1981; Allen and Conca, 1991; Chevrier et al., 2006). While the oxygen fugacity of the martian atmosphere is much less than that of the Earth (f_{O2} = $1.3x10^{-3}$ on Mars (Owen, 1992), compared to f_{O2} = 0.21 on Earth), the atmosphere is still extremely oxidizing compared to the magmatic conditions experienced during the genesis of martian basalts (approximately QFM-3 to QFM-1 (Herd et al., 2002) which, for 1200º C magma, represent f_{O2} values of approximately 2×10^{-12} to 2×10^{-10}, respectively). Oxidation-driven alteration processes, therefore, are important components of chemical weathering on the martian surface. Whether the martian surface exhibits signatures of such anhydrous alteration processes or whether these signatures have been overprinted by subsequent aqueous alteration is paramount towards understanding the extent of chemical alteration on the martian surface and the evolution of the martian climate.

Aside from localized exposures of heavily weathered Noachian-aged terrain (e.g., Bibring et al., 2005; Mustard et al., 2008), VNIR and MIR spectroscopy of dust-free martian terrains has primarily identified unaltered to weakly altered basaltic landscapes (Christensen et al., 2000b; Mustard et al., 2005). These observed spectral signatures are similar to spectral measurements of the dolerites from Beacon Valley (Fig. 14). VNIR reflectance spectroscopy identifies a significant Fe^{3+} charge-transfer absorption feature in the visible portion of the electromagnetic spectrum, even in archetypical "unaltered" and

relatively dust-free basaltic regions (e.g., Singer et al., 1979), in addition to mafic signatures of varying strength (Mustard et al., 2005). Even in the representative unaltered basaltic locations (i.e., Syrtis Major), significant VNIR spectral variability has been observed and has been linked to minor amounts of surface alteration during distinct paleoclimatic episodes that ended 2.1 Ga ago (Skok et al., 2010). The spectral signatures of these altered regions are exemplified by weakened mafic signatures and the addition of a spectral slope that decreases from shorter to longer wavelengths (Skok et al., 2010). Based on this work and those performed by Minitti et al. (2007) and Fischer and Pieters (1993), Skok et al. (2010) conclude that weakly altered basalt, comparable to that observed in the basaltic plains of Gusev crater by the Mars Exploration Rover (MER) *Spirit*, is the likely candidate for the observed spectral features throughout Syrtis Major.

MIR emission spectra of Surface Type 2 locales (as identified by the Thermal Emission Spectrometer (TES) onboard the Mars Global Surveyor spacecraft and defined in Bandfield et al. (2000)) exhibit the same narrowing of the restrahlen bands and masking of igneous spectral components as is seen in MIR emission spectra of the surfaces of Beacon dolerites (Fig. 14). Although the Surface Type 2 signature was originally interpreted as andesitic in nature (Bandfield et al., 2000), subsequent studies presented an alternate model that fit the data: partially altered basaltic signatures enriched in a sheet silicate or an amorphous component (Wyatt and McSween, 2002). Because one of the diagnostic smectite absorption features at 530 cm^{-1} was excluded from modeling due to an atmospheric CO_2 absorption, Wyatt and McSween (2002) were unable to determine whether the spectral signatures were due to smectites or amorphous phases. However, the lack of significant concentrations of smectites seen in VNIR

reflectance spectra of areas dominated by Surface Type 2 (Mustard et al., 2005) and in subsequent MIR emission studies (Michalski et al., 2005; Ruff and Christensen, 2007) support the interpretation that amorphous phases are a reasonable explanation for the observed spectral signatures. The detection of olivine-bearing basalts in the immediate subsurface of Acidalia Planitia by VNIR spectroscopy (Salvatore et al., 2010b) in addition to basaltic elemental signatures in the uppermost tens of centimeters by the Gamma Ray Spectrometer onboard the Mars Odyssey spacecraft (Karunatillake et al., 2006) confirms the basaltic nature of the unaltered substrate of this archetypical Surface Type 2 locale.

Both VNIR and MIR orbital spectroscopy of the martian surface confirm that volumetrically minor contributions of spectrally distinct components can have significant effects on spectroscopic studies of the martian surface. This observation is supported by the spectral studies of the Beacon dolerites, which exhibit large spectral variations despite only minimal mineralogical and chemical variations. The sensitivity of VNIR and MIR spectroscopy to the uppermost tens of microns of the surface allows for processes that alter a volumetrically minor component (including surface etching and thin rinds and/or coatings) to potentially dominate the observed spectral signatures. The implications of non-volumetrically representative spectral signatures must be taken into account when interpreting orbital spectral signatures and putting them into geologic context.

Observations and analyses of the basaltic plains of Gusev crater by the MER *Spirit* are also suggestive of alteration that is potentially dominated largely by anhydrous processes. While multiple styles and products of alteration have been inferred or identified by *Spirit* within Gusev crater, we focused our study solely on the first two

Adirondack-class basalts investigated on the plains of Gusev crater. The basaltic rocks Adirondack and Humphrey (McSween et al., 2006) exhibit chemical trends between their alteration rinds (represented by surfaces that were brushed by the Rock Abrasion Tool (RAT)) and their interiors (represented by areas that were ground away by the RAT) that indicate the removal of divalent cations and the enrichment of monovalent cations (Gellert et al., 2006). The major element variations between the surfaces and interiors of these two rocks are nearly identical to the chemical trends observed in Beacon Valley as a result of oxidation-driven alteration processes (Fig. 15). Furthermore, VNIR multispectral data obtained from the Pancam instrument show a significantly stronger Fe^{3+} charge transfer absorption feature in the spectra of rock surfaces relative to their interiors (McSween et al., 2004). Lastly, Morris et al. (2004) state that the ubiquity of olivine in both the rocks and soils suggest that physical erosion (rather than aqueous alteration) dominate the materials analyzed by *Spirit* in the plains of Gusev crater. These rocks do not show any evidence for significant enrichments of Br, Cl, or S on their surfaces that cannot be accounted for by minor amounts of dust contamination (Gellert et al., 2006), confirming the absence of surface coatings containing these elemental species. The absence of oxide coatings on the surfaces of Adirondack and Humphrey also support the conclusion of Morris et al. (2004) and suggest that aeolian abrasion and/or minor aqueous activity (that is largely incapable of significant aqueous alteration) are able to remove these soluble oxide species from the rock surfaces. Although no spectral evidence for amorphous aluminosilicates were observed by the Mini-TES instrument on the surfaces of either Adirondack or Humphrey, there has been substantial difficulties in identifying amorphous phases and surface coatings even where other lines of evidence

exist (e.g., Hamilton and Ruff, 2012). This non-detection of amorphous phases by Mini-TES may be caused by several factors, including the incomplete removal of pervasive surface dust from rock surfaces, or the lack of spectral endmembers in unmixing libraries that match the observed alteration products (Hamilton and Ruff, 2012). Another possibility is that the different parental composition of the Gusev plains basalts and the Ferrar Dolerite result in varying spectral signatures associated with oxidation-driven alteration.

Mössbauer spectroscopy of Adirondack and Humphrey show slight increases in Fe^{3+}/Fe_{Total} between rock interiors and surfaces of 0.01 and 0.04, respectively (Morris et al., 2006). This increased oxidation is more subtle than that observed for the dolerites, which show an average increase in Fe^{3+}/Fe_{Total} between rock interiors and surfaces of 0.14. This subtle increase in Fe^{3+}/Fe_{Total} may be due to either geologically recent physical erosion of the oxidized surface, slower oxidation rates on Mars relative to Beacon Valley, more recent exposure of the rock surfaces to the oxidizing environment, or some unique combination or alternative process.

While the interior of the Gusev plains rock named Mazatzal is chemically and mineralogically similar to Adirondack and Humphrey, its surface exhibits multiple coatings that are enriched in Ni, Zn, and K (Gellert et al., 2006). Due to their similar charges and ionic radii (Shannon and Prewitt, 1969), Ni and Zn could easily substitute for Mg and Fe in olivine and clinopyroxene in basaltic rocks. As a result, the presence of coatings on Mazatzal may represent the soluble oxide coatings predicted to form during oxidation-driven alteration processes. However, Fe, Mg, and Ca are all depleted in these coatings relative to the interior of Mazatzal (Gellert et al., 2006) despite their predicted

enrichment in the coatings if they are the products of oxidation-driven alteration. As a result, the coatings on Mazatzal may not be indicative of such anhydrous alteration processes. Haskin et al. (2005) suggested that these coatings may have formed when Mazatzal was buried beneath soil or dirty snow, which would explain the concentration of soil-derived S and S-correlated elements in the coatings.

Aqueous alteration processes have also been proposed to explain the observed chemical trends in the plains of Gusev crater. Hurowitz et al. (2006) proposed an acidic aqueous alteration model to explain the relationship between rock surfaces. They identify that at low pH and low water:rock ratios, Fe, Mg, and Si are more mobile than Ca, Na, and K during aqueous alteration (Hurowitz et al., 2006), resulting in alteration trends that are distinct from those found in most temperate terrestrial environments (e.g., Nesbitt and Wilson, 1992; Nesbitt and Markovics, 1997). However, the surfaces of neither Adirondack nor Humphrey are enriched in Si relative to their interiors (Gellert et al., 2006), as would be predicted in the model of acidic aqueous alteration proposed by Hurowitz et al. (2006) (Fig. 15). The relative depletion of Ca in the surface of Humphrey as well as the relative enrichment of K and Na in both Humphrey and Adirondack, together with the uniform Si concentrations, strongly suggest that acidic aqueous alteration was not the dominant alteration mechanism acting upon the currently exposed surfaces of these two rocks. Additionally, Hurowitz et al. (2006) propose that olivine dissolution is the dominant control on the alteration of the Gusev basalts. However, the ubiquity of olivine in the fine-grained sediments throughout the Gusev Plains suggests that preferential dissolution of olivine is not a significant alteration process subsequent to the formation of the local soils (Morris et al., 2004). As a result, the data suggest that

oxidation-driven alteration processes where preferential mineral dissolution does not occur can better explain the available chemical and spectral data derived from basaltic rocks in Gusev crater. Aqueous activity, while necessary to explain the presence of accumulated salts in Gusev soils (Haskin et al., 2005) and to assist in the removal of oxide coatings on rock surfaces, does not appear to be a significant contributor towards the alteration of rock surfaces, similar to the role of liquid water in Beacon Valley. Mini-TES observations of the surface of Mazatzal do not exhibit evidence for amorphous aluminosilicates or surface coatings, which is inconsistent with Microscopic Imager observations (McSween et al., 2006). This indicates either that the alteration products are disparate from those expected from oxidation-driven alteration, or that the spectral signatures associated with oxidation-driven alteration on rocks of compositions that are significantly different from the Ferrar Dolerite exhibit comparably different MIR spectral signatures. The inability for Mini-TES to detect these surface coatings also bolsters the hypothesis that oxidative chemical alteration is occurring on the surfaces of Adirondack and Humphrey but is not detected by the Mini-TES instrument.

8.0 Conclusions

Chemical alteration in Beacon Valley, Antarctica, is driven by an oxidation potential that causes mobile divalent cations to migrate to the sample surface. The migration of these cations is charge-balanced by the inward migration of electron holes (manifested as an increase in Fe^{3+} that decreases from the rock surface into the unaltered rock interior), the migration of monovalent cations into the alteration rind from the sample interior, and the presence of point defects. At the near-surface, the presence of

ferric iron, metastable mineral structures, and surface etching results in significant spectral differences between the rock surfaces and the unaltered interiors. Deeper within the rock, mobile cation migration continues to result in oxidation, creating distinct oxidation fronts caused by the concentration of Fe^{3+} locally exceeding different redox buffers. No significant mineralogical variations exist between rock surfaces and interiors and chemical variations are consistent with the predicted depletion of divalent cations and enrichment of monovalent cations in the alteration rinds. The metastable products observed in Beacon Valley are the result of chemical alteration in extreme hyper-arid and hypo-thermal conditions where the products of these early stages of chemical alteration are uniquely preserved. This alteration process may also explain many of the global and local spectral and chemical observations of the martian surface. VNIR and MIR spectroscopy of the martian surface suggests the ubiquity of lightly altered basalts across the majority of relatively dust-free terrains. In addition, observations from the plains of Gusev crater suggest that similar spectral and elemental trends to those observed in Beacon Valley dominate the Adirondack and Humphrey basaltic rocks. Aqueous activity recorded in the plains of Gusev crater, like in Beacon Valley, appears to be limited to the remobilization of different elemental species rather than the significant aqueous alteration of rocks and soils.

Acknowledgements

This work was supported by the National Science Foundation (ANT-0739702). The authors would like to thank several people and institutions for their support and assistance with data collection, analyses, and interpretations: The National Science

Foundation, the United States Antarctic Program, Raytheon Polar Services Company, the staff of McMurdo Station, PHI Inc., Cherie Achilles, Nilanjan Chatterjee and the Electron Microprobe Facility at the Massachusetts Institute of Technology, M. Darby Dyar, Timothy Glotch and the Vibrational Spectroscopy Laboratory at Stony Brook University, Takahiro Hiroi and the Brown University RELAB Facility, Colin Jackson, the LacCore Facility at the University of Minnesota, Anthony McCormick, Douglas Ming, Richard Morris, David Murray, Joseph Orchardo, Stephen Parman, A. Deanne Rogers, Alberto Saal, and Paul Waltz and the School of Engineering at Brown University. We are also extremely grateful for the helpful reviews from Steve Ruff, Penelope King, and an anonymous reviewer.

References

Adams J. B., Smith M. O. and Gillespie A. R. (1993), Imaging spectroscopy: Interpretation based on spectral mixture analysis. In *Remote Geochemical Analysis: Elemental and Mineralogical Composition* (eds. C. M. Pieters and P. A. Englert). Cambridge Univ. Press, New York, pp. 145-166.

Allen C. C. and Conca J. L. (1991), Weathering of basaltic rocks under cold, arid conditions: Antarctica and Mars. *Proc. Lunar Planet. Sci. Conf.* **21**, 711-717.

Bandfield J. L., Hamilton V. E. and Christensen P. R. (2000), A global view of martian surface compositions from MGS-TES. *Science* **287**, 1626-1630.

Bao H. and Marchant D. R. (2006), Quantifying sulfate components and their variations in soils of the McMurdo Dry Valleys, Antarctica. *J. Geophys. Res.* **111**, doi:10.1029/2005JD006669.

Bao H., Barnes J. D., Sharp Z. D. and Marchant D. R. (2008), Two chloride sources in soils of the McMurdo Dry Valleys, Antarctica. *J. Geophys. Res.* **113**, doi:10.1029/2007JD008703.

Bédard J. H. J., Marsh B. D., Hersum T. G., Naslund H. R. and Mukasa S. B. (2007), Large-scale mechanical redistribution of orthopyroxene and plagioclase in the Basement Sill, Ferrar Dolerites, McMurdo Dry Valleys, Antarctica: Petrological, mineral-chemical and field evidence for channelized movement of crystals and melt. *J. Petrology* **48**, 2289-2326.

Bibring J.-P., Langevin Y., Gendrin A., Gondet B., Poulet F., Berthé M., Soufflot A., Arvidson R., Mangold N., Mustard J., Drossart P. and the OMEGA Team (2005), Mars surface diversity as revealed by the OMEGA/Mars Express observations. *Science* **307**, 1576-1581.

Bish D. L. and Post J. E. (1993), Quantitative mineralogical analyses using the Rietveld full-pattern fitting method. *Am. Mineral.* **78**, 932-942.

Bishop J. L., Murad E. and Dyar M. D. (2002), The influence of octahedral and tetrahedral cation substitution on the structure of smectites and serpentines as observed through infrared spectroscopy. *Clay Miner.* **37**, 617-628.

Bockheim J. G. (2002), Landform and soil development in the McMurdo Dry Valleys, Antarctica: A regional synthesis. *Arc. Antarc. & Alp. Res.* **34**, 308-317.

Burkhard D. J. M. and Müller-Sigmund H. (2007), Surface alteration of basalt due to cation-migration. *Bull. Volcanology* **69**, 319-328.

Campbell I. B. and Claridge G. G. C. (1987), *Antarctica: Soils, weathering processes and environment*. Elsevier, Amsterdam, 406 pp.

Chadwick O. A., Derry L. A., Vitousek P. M., Huebert B. J. and Hedin L. O. (1999), Changing sources of nutrients during four million years of ecosystem development. *Nature* **397**, 491-497.

Chevrier V., Mathé P.-E. and Gunnlaugsson H. P. (2006), Magnetic study of an Antarctic weathering profile on basalt: Implications for recent weathering on Mars *Earth Planet. Sci. Lett.* **244**, 501-514.

Christensen P. R., Bandfield J. L., Hamilton V. E., Howard D. A., Lane M. D., Piatek J. L., Ruff S. W. and Stefanov W. L. (2000a), A thermal emission spectral library of rock-forming minerals. *J. Geophys. Res.* **105**, 9735-9739.

Christensen P. R., Bandfield J. L., Smith M. D., Hamilton V. E. and Clark R. N. (2000b), Identification of a basaltic component on the martian surface from Thermal Emission Spectrometer data. *J. Geophys. Res.* **105**, 9609-9621.

Christensen P. R., Bandfield J. L., Hamilton V. E., Ruff S. W., Kieffer H. H., Titus T. N., Malin M. C., Morris R. V., Lane M. D., Clark R. L., Jakosky B. M., Mellon M. T., Pearl J. C., Conrath B. J., Smith M. D., Clancy R. T., Kuzmin R. O., Roush T., Mehall G. L., Gorelick N., Bender K., Murray K., Dason S., Greene E., Silverman S. and Greenfield M. (2001), Mars Global Surveyor Thermal Emission Spectrometer experiment: Investigation description and surface science results. *J. Geophys. Res.* **106**, 23823-23871.

Claridge G. G. C. and Campbell I. B. (1977), The salts in Antarctic soils, their distribution and relationship to soil processes. *Soil Sci.* **123**, 377-384.

Clark R. N., King T. V. V., Klejwa M., Swayze G. A. and Vergo N. (1990), High spectral resolution reflectance spectroscopy of minerals. *J. Geophys. Res.* **95**, 12653-12680.

Clark R. N. (1999), Chapter 1: Spectroscopy of rocks and minerals, and principles of spectroscopy. In *Manual of Remote Sensing, Vol. 3, Remote sensing for the Earth Sciences* (ed. A. N. Rencz). John Wiley & Sons, New York, p. 3-58.

Cook G. B. and Cooper R. F. (2000), Iron concentration and the physical process of dynamic oxidation in an alkaline earth aluminosilicate glass. *Am. Min.* **85**, 397-406.

Cooper R. F. (2010), On being a student of thermodynamics: Trust your eyes; use your imagination. *Elements* **6**, 282-283.

Cooper R. F., Fanselow J. B. and Poker D. B. (1996a), The mechanism of oxidation of a basaltic glass: Chemical diffusion of network-modifying cations. *Geochim. Cosmochim. Acta* **60**, 3252-3265.

Cooper R. F., Fanselow J. B., Weber J. K. R., Merkley D. R. and Poker D. B. (1996b), Dynamics of oxidation of a Fe^{2+}-bearing aluminosilicate (basaltic) melt. *Science* **274**, 1173-1176.

Denton G. H., Sugden D. E., Marchant D. R., Hall B. L. and Wilch T. I. (1993), East Antarctic Ice Sheet sensitivity to Pliocene climate change from a Dry Valleys perspective. *Geograf. Annal.* **75**A, 155-204.

Doran P. T., Dana G. L., Hastings J. T. and Wharton Jr. R. A. (1995), McMurdo Dry Valleys Long-Term Ecological Research (LTER): LTER automatic weather network (LAWN). *Antarctic J. of the U. S.* **30**, 276-280.

Dorn R. (2009), Desert rock coatings. In *Geomorphology of Desert Environments 2nd Edition* (eds. A. J. Parsons and A. D. Abrahams). Springer, 153-186.

Dyar M. D. (1984), Precision and interlaboratory reproducibility of measurements of the Moessbauer effect in minerals. *Am. Miner.* **69**, 1127-1144.

Ehlmann B. L., Bish D. L., Ruff S. W. and Mustard J. F. (2012), Mineralogy and chemistry of altered Icelandic basalts: Application to clay mineral detection and understanding aqueous environments on Mars. *J. Geophys. Res.*, doi:10.1029/2012JE004156, in press.

Elliot D. H. and Fleming T. H. (2004), Occurrence and dispersal of magmas in the Jurassic Ferrar large igneous province, Antarctica. *Gondwana Res.* **7**(1), 223-237.

Farmer V. C. (1974), *The Infrared Spectra of Minerals*. Mineral. Soc., London, 539 pp.

Feely K. C. and Christensen P. R. (1999), Quantitative compositional analysis using thermal emission spectroscopy: Application to igneous and metamorphic rocks. *J. Geophys. Res.* **104**, 24195-24210.

Fehlner F. P. and Mott N. F. (1970), Low-temperature oxidation. *Oxid. Metals* **2**(1), 59-99.

Fischer E. M. and Pieters C. M. (1993), The continuum slope of Mars: Bidirectional reflectance investigations and applications to Olympus Mons. *Icarus* **102**, 185-202.

Fountain A. G., Nylen T. H., Monaghan A., Basagic H. J. and Bromwich D. (2009), Snow in the McMurdo Dry Valleys, Antarctica. *Intl. J. Climatology*, doi:10.1002/joc.1933.

Gellert R., Rieder R., Brückner J., Clark B. C., Dreibus G., Klingelhöfer G., Lugmair G., Ming D. W., Wänke H., Yen A., Zipfel J. and Squyres S. W. (2006), Alpha Particle X-Ray Spectrometer (APXS): Results from Gusev crater and calibration report. *J. Geophys. Res.* **111**, doi:10.1029/2005JE002555.

Gillespie A. R. (1992), Spectral mixture analysis of multispectral thermal infrared images. *Remote Sens. Environ.* **42**, 137-145.

Glasby G. P., McPherson J. G., Kohn B. P., Johnston J. H., Freeman A. G. and Tricker M. J. (1981), Desert varnish in Southern Victoria Land, Antarctica. *New Zealand J. Geol. & Geophys.* **24**, 389-397.

Gleadow A. J. W. and Fitzgerald P. G. (1987), Uplift history and structure of the Transantarctic Mountains: new evidence from fission track dating of basement apatites in the Dry Valleys area, southern Victoria Land. *Earth Planet. Sci. Lett.* **82**, 1-14.

Glotch T. D., Morris R. V., Christensen P. R. and Sharp T. G. (2004), Effect of precursor mineralogy on the thermal infrared emission spectra of hematite: Application to Martian hematite mineralization. *J. Geophys. Res.* **109**, doi:10.1029/2003JE002224.

Granger H. C. and Raup R. B. (1969), Geology of the uranium deposits in the Dripping Spring Quartzite, Gila County, Arizona. *Geol. Surv. Prof. Paper* **595**, 106 pp.

Gunn B. M. (1962), Differentiation in Ferrar Dolerites. *New Zeal. J. Geol. & Geophys.* **5**, 820-863.

Gunn B. M. (1963), Layered intrusions in the Ferrar dolerites, Antarctica. *Mineral. Soc. Am. Spec. Paper* **1**, 124-133.

Gunn B. M. (1965), K/Rb and K/Ba ratios in Antarctic and New Zealand tholeiites and alkali basalts. *J. Geophys. Res.* **70**, 6241-6247.

Gunn B. M. (1966), Modal and element variation in Antarctic tholeiites. *Geochim. Cosmochim. Acta* **30**, 881-920.

Hamilton V. E. (2000), Thermal infrared spectroscopy of the pyroxene mineral series. *J. Geophys. Res.* **105**(E4), 9701-9716.

Hamilton V. E. (2010), Thermal infrared (vibrational) spectroscopy of Mg-Fe olivines: A review and applications to determining the composition of planetary surfaces. *Chemie der Erde* **70**, 7-33.

Hamilton V. E. and Ruff S. W. (2012), Distribution and characteristics of Adirondack-class basalt as observed by Mini-TES in Gusev crater, Mars and its possible volcanic source. *Icarus* **218**(2), 917-949.

Haskin L. A., Wang A., Jolliff B. L., McSween H. Y., Clark B. C., Des Marais D. J., McLennan S., Tosca N. J., Hurowitz J. A., Farmer J. D., Yen A., Squyres S. W., Arvidson R. E., Klingelhöfer G., Schröder C., de Souza Jr. P. A., Ming D. W., Gellert R., Zipfel J., Brückner J., Bell III J. F., Herkenhoff K., Christensen P. R., Ruff S., Blaney D., Gorevan S., Cabrol N. A., Crumpler L., Grant J. and Soderblom L. (2005), Water alteration of rocks and soils on Mars at the Spirit rover site in Gusev crater. *Nature* **436**, 66-69.

Harvey R. P. (2001), The Ferrar Dolerite: An Antarctic analog for martian basaltic lithologies and weathering process. *Wkshp. Martian Highlands & Moj. Des. Analogs*, abstract 4012.

Hausrath E. M., Navarre-Sitchler A. K., Sak P. B., Steefel C. I. and Brantley S. L. (2008), Basalt weathering rates on Earth and the duration of liquid water on the plains of Gusev crater, Mars. *Geology* **36**, 67-70.

Head J. W., Kreslavsky M. A. and Marchant D. R. (2011), Pitted rock surfaces on Mars: A mechanism of formation by transient melting of snow and ice. *J. Geophys. Res.* **116**, doi:10.1029/2011JE003826.

Heimann A., Fleming T. H., Elliot D. H. and Foland K. A. (1994), A short interval of Jurassic continental flood basalt volcanism in Antarctica as demonstrated by $^{40}Ar/^{39}Ar$ geochronology. *Earth Planet. Sci. Lett.* **121**, 19-41.

Herd C. D. K., Borg L. E., Jones J. H. and Papike J. J. (2002), Oxygen fugacity and geochemical variations in the martian basalts: Implications for martian basalt petrogenesis and the oxidation state of the upper mantle of Mars. *Geochim. Cosmochim. Acta* **66**, 2025-2036.

Hillier S. (2000), Accurate quantitative analysis of clay and other minerals in sandstones by XRD: Comparison of a Rietveld and a reference intensity ratio (RIR) method and the importance of sample preparation. *Clay Mineral.* **35**, 291-302.

Hurowitz J. A., McLennan S. M., Tosca N. J., Arvidson R. E., Michalski J. R., Ming D. W., Schröder C. and Squyres S. W. (2006), In situ and experimental evidence for acidic weathering of rocks and soils on Mars. *J. Geophys. Res.* **111**, doi:10.1029/2005JE002515.

Karunatillake S., Squyres S. W., Taylor G. J., Keller J. M., Gasnault O., Evans L. G., Reedy R. C., Starr R., Boynton W., Janes D. M., Kerry K. E., Dohm J. M., Sprague A. L., Hahn B. C. and Hamara D. (2006), Composition of northern low-

albedo regions of Mars: Insights from the Mars Odyssey Gamma Ray Spectrometer. *J. Geophys. Res.* **111**, doi:10.1029/2006JE002675.

Koeppen W. C. and Hamilton V. E. (2008), Global distribution, composition, and abundance of olivine on the surface of Mars from thermal infrared data. *J. Geophys. Res.* **113**, doi:10.1029/2007JE002984.

Kowalewski D. E., Marchant D. R., Swanger K. M. and Head III J. W. (2010), Modeling vapor diffusion within cold and dry supraglacial tills of Antarctica: Implications for the preservation of ancient ice. *Geomorphology* **126**, 159-173.

Kowalewski D. E., Marchant D. R., Head III J. W. and Jackson D. W. (2012), Modeling the effects of thermal contraction-crack polygons on sublimation of buried glacier ice, Antarctica. *Perm. & Peri. Proc.*, in review.

Kraft M. D., Michalski J. R. and Sharp T. G. (2003), Effects of pure silica coatings on thermal emission spectra of basaltic rocks: Considerations for martian surface mineralogy. *Geophys. Res. Lett.* **30**, doi:10.1029/2003GL018848.

Kyle P. R., Elliot D. H. and Sutter J. F. (1981), Jurassic Ferrar Supergroup tholeiites from the Transantarctic Mountains, Antarctica, and their relationship to the initial fragmentation of Gondwana. In *Gondwana Five (Proc. Intl. Gond. Symp., 5)* (eds. M. M. Cresswell and P. Vella). Rotterdam, Balkema. Wellington, New Zealand, 283-287.

Lane M. D. (2007), Mid-infrared emission spectroscopy of sulfate and sulfate-bearing minerals. *Am. Mineral.* **92**, 1-18.

Lasaga A. C. (1984), Chemical kinetics of water-rock interactions. *J. Geophys. Res.* **89**, 4009-4025.

Levy J. S., Marchant D. R. and Head III J. W. (2006), Distribution and origin of patterned ground on Mullins Valley debris-covered glacier, Antarctica: The roles of ice flow and sublimation. *Antarct. Sci.* **18**, 385-397.

Liu T. and Broecker W. S. (2000), How fast does rock varnish grow? *Geology* **28**, 183-186.

Manning J. R. (1973), Diffusion kinetics and mechanisms in simple crystals. In *Geochemical Transport and Kinetics* (eds. A. W. Hofmann, B. J. Giletti, H. S. Yoder Jr. and R. A. Yund). Carnegie Institution of Washington, Publication 634, pp. 3-13.

Marchant D. R. and Denton G. H. (1996), Miocene and Pliocene paleoclimate of the Dry Valleys region, southern Victoria Land: A geomorphological approach. *Marine Micropaleo.* **27**, 253-271.

Marchant D. R., Lewis A. R., Phillips W. M., Moore E. J., Souchez R. A., Denton G. H., Sugden D. E., Potter Jr. N. and Landis G. P. (2002), Formation of patterned ground and sublimation till over Miocene glacier ice in Beacon Valley, southern Victoria Land, Antarctica. *Geol. Soc. Am. Bull.* **114**, 718-730.

Marchant D. R. and Head III J. W. (2007), Antarctic dry valleys: Microclimate zonation, variable geomorphic processes, and implications for assessing climate change on Mars. *Icarus* **192**, 187-222.

Marchant D. R., Phillips W. M., Fastook J. L., Head III J. W., Schaefer J. M., Shean D. E. and Kowalewski D. E. (2007), Dating the world's oldest debris-covered glacier: Implications for interpreting viscous-flow features on Mars. *LPSC* **38**, abstract 1895.

Marsh B. (2004), A magmatic mush column Rosetta Stone: The McMurdo Dry Valleys of Antarctica. *Eos* **85**, 497-508.

McAdam A. C. (2008), Martian weathering processes: Terrestrial analog and theoretical modeling studies, *Ph.D. Thesis*, *Arizona State University*, 254 pp.

McElroy C. T. and Rose G. (1987), Geology of the Beacon Heights area, southern Victoria Land, Antarctica. *New Zeal. Geol. Surv.*, Misc. Map Series 15.

McSween H. Y., Arvidson R. E., Bell III J. F., Blaney D., Cabrol N. A., Christensen P. R., Clark B. C., Crisp J. A., Crumpler L. S., Des Marais D. J., Farmer J. D., Gellert R., Ghosh A., Gorevan S., Graff T., Grant J., Haskin L. A., Herkenhoff K. E., Johnson J. R., Jolliff B. L., Klingelhoefer G., Knudson A. T., McLennan S., Milam K. A., Moersch J. E., Morris R. V., Rieder R., Ruff S. W., de Souza Jr. P. A., Squyres S. W., Wänke H., Wang A., Wyatt M. B., Yen A. and Zipfel J. (2004), Basaltic rocks analyzed by the Spirit rover in Gusev crater. *Science* **305**, 842-845.

McSween H. Y., Wyatt M. B., Gellert R., Bell III J. F., Morris R. V., Herkenhoff K. E., Crumpler L. S., Milam K. A., Stockstill K. R., Tornabene L. L., Arvidson R. E., Bartlett P., Blaney D., Cabrol N. A., Christensen P. R., Clark B. C., Crisp J. A., Des Marais D. J., Economou T., Farmer J. D., Farrand W., Ghosh A., Golombek M., Gorevan S., Greeley R., Hamilton V. E., Johnson J. R., Joliff B. L., Klingelhöfer G., Knudson A. T., McLennan S., Ming D., Moersch J. E., Rieder R., Ruff S. W., Schröder C., de Souza Jr. P. A., Squyres S. W., Wänke H., Wang A., Yen A. and Zipfel J. (2006), Characterization and petrologic interpretation of

olivine-rich basalts at Gusev crater, Mars. *J. Geophys. Res.* **111**, doi:10.1029/2005JE002477.

Michalski J. R., Kraft M. D., Sharp T. G., Williams L. B. and Christensen P. R. (2005), Mineralogical constraints on the high-silica martian surface component observed by TES. *Icarus* **174**, 161-177.

Minitti M. E., Weitz C. M., Lane M. D. and Bishop J. L. (2007), Morphology, chemistry, and spectral properties of Hawaiian rock coatings and implications for Mars. *J. Geophys. Res.* **112**, doi:10.1029/2006JE002839.

Minitti M. E. and Hamilton V. E. (2010), A search for basaltic-to-intermediate glasses on Mars: Assessing martian crustal mineralogy. *Icarus* **210**, 135-149.

Morris R. V., Lauer Jr. H. V., Lawson C. A., Gibson Jr. E. K., Nace G. A. and Stewart C. (1985), Spectral and other physiochemical properties of submicron powders of hematite (α-Fe_2O_3), maghemite (γ-Fe_2O_3), magnetite (Fe_3O_4), goethite (α-FeOOH), and lepidochrosite (γ-FeOOH). *J. Geophys. Res.* **90**, 3126-3144.

Morris R. V., Klingelhöfer G., Bernhardt B., Schröder C., Rodionov D. S., de Souza Jr. P. A., Yen A., Gellert R., Evlanov E. N., Foh J., Kankeleir E., Gütlich P., Ming D. W., Renz F., Wdowiak T., Squyres S. W. and Arvidson R. E. (2004), Mineralogy at Gusev crater from the Mössbauer Spectrometer on the Spirit Rover. *Science* **305**, 833-836.

Murray R. W., Miller D. J. and Kryc K. A. (2000), Analysis of major and trace elements in rocks, sediments, and interstitial waters by Inductively Coupled Plasma-Atomic Emission Spectroscopy (ICP-AES). *Texas A&M University, ODP Technical Note* **29**, 21 pp.

Mustard J. F. and Pieters C. M. (1989), Photometric phase functions of common geologic minerals and applications to quantitative analysis of mineral mixture reflectance spectra. *J. Geophys. Res.* **94**, 13619-13634.

Mustard J. F., Poulet F., Gendrin A., Bibring J.-P., Langevin Y., Gondet B., Mangold N., Bellucci G. and Altieri F. (2005), Olivine and pyroxene diversity in the crust of Mars. *Science* **307**, 1594-1597.

Mustard J. F., Murchie S. L., Pelkey S. M., Ehlmann B. L., Milliken R. E., Grant J. A., Bibring J.-P., Poulet F., Bishop J., Noe Dobrea E., Roach L., Seelos F., Arvidson R. E., Wiseman S., Green R., Hash C., Humm D., Malaret E., McGovern J. A., Seelos K., Clancy T., Clark R., Des Marais D., Izenberg N., Knudson A., Langevin Y., Martin T., McGuire P., Morris R., Robinson M., Roush T., Smith M., Swayze G., Taylor H., Titus T. and Wolff M. (2008), Hydrated silicate minerals on Mars observed by the Mars Reconnaissance Orbiter CRISM instrument. *Nature* **454**, 305-309.

Nesbitt H. W. and Wilson R. E. (1992), Recent chemical weathering of basalts. *Am. J. Sci.* **292**, 740-777.

Nesbitt H. W. and Markovics G. (1997), Weathering of granodioritic crust, long-term storage of elements in weathering profiles, and petrogenesis of siliciclastic sediments. *Geochim. Cosmochim. Acta* **61**, 1653-1670.

Owen T. (1992), The composition and early history of the atmosphere of Mars. In *Mars* (eds. H. H. Kieffer, B. M. Jakosky, C. W. Snyder and M. S. Matthews). The University of Arizona Press, Tuscon & London, pp. 818-833.

Pieters C. M. (1983), Strength of mineral absorption features in the transmitted component of near-infrared reflected light: First results from RELAB. *J. Geophys. Res.* **88**, 9534-9544.

Ramsey M. S. and Christensen P. R. (1998), Mineral abundance determination: Quantitative deconvolution of thermal emission spectra. *J. Geophys. Res.* **103**, 577-596.

Rogers A. D., Christensen P. R. and Bandfield J. L. (2005), Compositional heterogeneity of the ancient martian crust: Analysis of Ares Vallis bedrock with THEMIS and TES data. *J. Geophys. Res.* **110**, doi:10.1029/2005JE002399.

Ruff S. W. (2004), Spectral evidence for zeolite in the dust on Mars. *Icarus* **168**(1), 131-143.

Ruff S. W. and Christensen P. R. (2007), Basaltic andesite, altered basalt, and a TES-based search for smectite clay minerals on Mars. *Geophys. Res. Lett.* **34**, doi:10.1029/2007GL029602.

Ruff S. W., Christensen P. R., Barbera P. W. and Anderson D. L. (1997), Quantitative thermal emission spectroscopy of minerals: A laboratory technique for measurement and calibration. *J. Geophys. Res.* **102**, 14889-14913.

Sak P. B., Fisher D. M., Gardner T. W., Murphy K. and Brantley S. L. (2004), Rates of weathering rind formation on Coasta Rican basalt. *Geochim. Cosmochim. Acta* **68**, 1453-1472.

Salvatore M. R., Wyatt M. B., Mustard J. F., Head J. W. and Marchant D. R. (2010a), Near-infrared spectral diversity of the Ferrar Dolerite in Beacon Valley,

Antarctica: Implications for martian climate & surface compositions. *LPSC* **41**, abstract 1533.

Salvatore M. R., Mustard J. F., Wyatt M. B. and Murchie S. L. (2010b), Definitive evidence of Hesperian basalt in Acidalia and Chryse planitiae. *J. Geophys. Res.* **115**, doi:10.1029/2009JE003519.

Salvatore M. R., Wyatt M. B., Mustard J. F. and Head J. W. (2011a), Development of alteration rinds on the Ferrar Dolerite of the Antarctic Dry Valleys: Initial characterization. *LPSC* **42**, abstract 1479.

Salvatore M. R., Wyatt M. B., Mustard J. F., Head III J. W., Cooper R. F. and Marchant D. R. (2011b), Constraining the chemical alteration of rock surfaces of the Ferrar Dolerite in Beacon Valley, Antarctica. *Intl. Symp. Antarct. Earth Sci.* **11**, abstract PO8.6.

Salvatore M. R., Mustard J. F., Head J. W., Cooper R. F. and Marchant D. R. (2011c), Widespread alteration of the Ferrar Dolerite in Beacon Valley, Antarctica. *AGU Fall Mtg.*, abstract P31C-1717.

Schmalzried H. (1983), Internal and external oxidation of nonmetallic compounds and solid solutions (I). *Ber. Bunsenges. Phys. Chem.* **87**, 551-558.

Schwerdtfeger W. (1984), *Weather and climate of the Antarctic*. Elsevier, Amsterdam, 327 pp.

Shannon R. and Prewitt C. (1969), Effective ionic radii in oxides and fluorides. *Acta Cryst.* **B25**, 925-946.

Singer R. B., McCord T. B., Clark R. N., Adams J. B. and Huguenin R. L. (1979), Mars surface composition from reflectance spectroscopy: A summary. *J. Geophys. Res.* **84**, 8415-8426.

Skok J. R., Mustard J. F., Murchie S. L., Wyatt M. B. and Ehlmann B. L. (2010), Spectrally distinct ejecta in Syrtis Major, Mars: Evidence for environmental change at the Hesperian-Amazonian boundary. *J. Geophys. Res.* **115**, doi:10.1029/2009JE003338.

Smith D. R. and Cooper R. F. (2000), Dynamic oxidation of a Fe^{2+}-bearing calcium-magnesium-aluminosilicate glass: The effect of molecular structure on chemical diffusion and reaction-morphology. *J. Non-Crys. Solids* **278**, 145-163.

Staiger J. W., Marchant D. R., Shaefer J. M., Oberholzer P., Johnson J. V., Lewis A. R. and Swanger K. M. (2006), Plio-Pleistocene history of Ferrar Glacier, Antarctica: Implications for climate and ice sheet stability. *Earth Planet. Sci. Lett.* **243**, 489-503.

Sugden D. E., Marchant D. R., Potter N., Souchez R., Denton G. H., Swisher C. C. and Tison J.-L. (1995), Preservation of Miocene glacier ice in East Antarctica. *Nature* **376**, 412-416.

Talkington R. W., Mayewski P. A. and Gaudette H. E. (1982), Geochemical and glacio-geomorphic implications of basalt weathering in the Queen Maud Mountains, Antarctica. *Geol. Mag.* **119**, 553-566.

Vandenberghe R. E., DeGrave E. and de Bakker P. M. A. (1994), On the methodology of the analysis of Mössbauer spectra. *Hyper. Int.* **83**, 29-49.

Viles H. A. (1995), Ecological perspectives on rock surface weathering: Towards a conceptual model. *Geomorph.* **13**, 21-35.

Wilson M. J. (2004), Weathering of the primary rock-forming minerals: Processes, products, and rates. *Clay Minerals* **39**, 233-266.

Wyatt M. B., Hamilton V. E., McSween H. Y., Christensen P. R. and Taylor L. A. (2001), Analysis of terrestrial and Martian volcanic compositions using thermal emission spectroscopy: 1. Determination of mineralogy, chemistry, and classification strategies. *J. Geophys. Res.* **106**(E7), 14711-14732.

Wyatt M. B. and McSween Jr. H. Y. (2002), Spectral evidence for weathered basalt as an alternative to andesite in the northern lowlands of Mars. *Nature* **417**, 263-266.

Wyatt M. B., Horodyskyj U. N., Kelley K. A. and Neal K. M. (2008), Comparisons of TIR and LA-ICP-MS derived bulk chemistries for natural surfaces of igneous rocks. *LPSC* **39**, abstract 2105.

Figure and Table Descriptions

Figure 1. The alteration rind of sample MS10_BV_06 (a), as compared to a traditional desert rock coating (b) (from Dorn, 2009). White arrows demarcate the sharp boundary between the underlying rock surface and the rock coating, while black arrows highlight layering parallel to the shape of the depositional surface.

Figure 2. Geographic setting of Beacon Valley, Antarctica. (a) The location of the McMurdo Dry Valleys. (b) The McMurdo Dry Valleys and their associated microclimate zones (modified from Marchant and Head (2007)). Beacon Valley, located well within the Stable Upland Zone, is highlighted and shown in detail in (c). (c) LIDAR hillshade and digital elevation model of Beacon Valley. Surface elevation is reported in

meters above the World Geodetic System 1984 (WGS84) ellipsoid. The locations of samples measured in this study are shown as yellow dots, with MS10_BV_01 being the furthest north and the sample number increasing to MS10_BV_13 to the south. Cosmogenic age dates (from Marchant et al., 2007) are shown as blue text and the approximate surface motion from Mullins Valley is indicated by the blue line.

Figure 3. Ternary FeO_T + MgO, Al_2O_3, CaO + Na_2O + K_2O (FM/A/CNK) diagram showing the chemistry of unaltered sample interiors (dark gray dots) and alteration rinds (red dots), in addition to the chemistry of Gusev plains basalt interiors (light gray dots) and surfaces (blue dots). (a) The Beacon Valley data cluster tightly in the center of the diagram. Largely unaltered basalts fall just below the olivine-feldspar join, which is where all of the Beacon Valley samples plot. The martian basalts fall towards slightly more mafic compositions along the feldspar–(FeOT + MgO) join. A traditional terrestrial alteration path via leaching is highlighted with the orange dotted line (Nesbitt and Wilson, 1992; Nesbitt and Markovics, 1997). The gray trapezoid is expanded in (b). (b) The data are tightly clustered and do not follow traditional terrestrial leaching trends through aqueous alteration, suggesting that aqueous processes do not significantly alter rock surfaces in Beacon Valley. Similarly, Gusev plains basalts also do not follow the traditional terrestrial leaching trend. Gusev plains basaltic rocks are labeled “H” for Humphrey, “A” for Adirondack, and “M” for Mazatzal.

Figure 4. Chemical ratios of oxide abundances (in wt.%) in rock surfaces relative to their interiors. Values greater than 1 indicate enrichments in rock surfaces, while values less than 1 indicate depletions in rock surfaces. Each of the 14 dolerite samples is plotted as a filled gray circle, while the average value is plotted as a filled maroon circle.

Of particular interest are the systematic depletions in divalent cations (Ca^{2+}, Mg^{2+}) and the systematic enrichments in monovalent cations (Na^{+}, K^{+}) in rock surfaces relative to their interiors.

Figure 5. Mössbauer spectra and modeled fits for a representative dolerite interior (a) and alteration rind (b). For this sample, the modeled ferric contribution in the alteration rind increases by 21.25%, as illustrated by the increased contribution of the ferric doublet (blue modeled line). Based on the current model, the ferric phase is consistent with nanophase Fe oxides or as Fe^{3+} retained within a pyroxene or chlorite structure. The ferrous phases present are best modeled as Fe^{2+} in pyroxenes or chlorites, with pyroxenes likely being the dominant carriers based on optical analyses of thin and thick sections. Calculated Mössbauer parameters are provided in Table 3.

Figure 6. (a) An optical micrograph of sample MS10_BV_05A. The location of the EPMA analysis is outlined in the yellow box, which encompasses both the alteration rind and the unaltered interior. (b) EPMA elemental map with Fe mapped as red, Al mapped as green, and Si mapped as blue. The approximate transition from the unaltered interior into the alteration rind is shown as the light yellow dashed line. There are no obvious chemical or morphological variations associated with this transition in this analysis. The white arrows highlight primary zoning in pyroxene grains, with Mg enriched in the grain interior and Fe enriched in the grain exterior. The preservation of this chemical zoning is further indication of the incomplete chemical alteration within the alteration rinds.

Figure 7. Averaged XRD patterns (from Brown University's XRD Facility) for sample interiors (black) and alteration rinds (red). Buffers of one standard deviation are

shown for both the interior (grey) and alteration rind (pink) patterns to highlight the magnitude of variability observed amongst the samples, which hinders quantitative XRD analyses. No filtering or background removal has been performed in order to preserve the spectral shape and to highlight the weak amorphous "hump" present in both patterns. Peak locations are identical in both the interior and alteration rind spectra, with only minor variations in peak heights, which may be due to sampling, preparation, or analyses biases or artifacts. Ab = albite, An = anorthite, Aug = augite, En = enstatite, Pl = plagioclase, Px = pyroxene, Qtz = quartz.

Figure 8. Visible/Near-infrared reflectance spectra of all 14 sample interiors (a) and surfaces (b), with average interior and surface spectra shown in (c). Sample labels are abbreviated to their identifying digits.

Figure 9. Mid-infrared emission spectra of all 14 sample interiors (a) and surfaces (b), with average interior and surface spectra shown in (c). Sample labels are abbreviated to their identifying digits.

Figure 10. Linear unmixing model results for (a) average dolerite interiors and (b) average dolerite surfaces. Modeled spectra are shown in green. Reported results with values in % abundance are shown and are normalized to exclude the blackbody component (which is also reported). The goodness of fit of the model is reported as the root-mean-squared error (RMSE).

Figure 11. Scanning electron microscope images of sample surfaces showing a variety of surface morphologies. (a) Etching and/or dissolution visible, apparently targeting lamellae or zones within individual grains (white arrows). (b) Additional etching and/or dissolution apparent along lamellae or zones (white arrows). (c) Surface

cracking (white arrow) and flaking (black arrow). The indicated flake (black arrow) is raised relative to the rock surface, suggesting that this portion of the surface has been at least partially dislodged. (d) Micro-pit development at the sample surface (black arrows) near a well-formed larger pit (white arrow).

Figure 12. Optical micrographs of four representative samples, highlighting their alteration rinds. Grain size and morphology greatly influence the preservation and appearance of the alteration rinds. Regions labeled at U, A', and A'' indicate unaltered, moderately oxidized/altered, and heavily oxidized/altered portions of the rock, respectively. Samples shown are (a) MS10_BV_06, (b) MS10_BV_03, (c) MS10_BV_04, and (d) MS10_BV_05A.

Figure 13. Schematic of alteration processes and products. The outward migration of cations is charge-balanced by the inward flux of electron holes (i.e., the conversion of Fe^{2+} to Fe^{3+}) and the flux of monovalent cations towards the surface. Soluble cation oxide species are not observed on the sample surfaces because of their removal by physical erosion and aqueous dissolution. Oxidation fronts are visible within the samples where the local concentration of Fe^{3+} exceeds different redox buffers. Regions labeled at U, A', and A'' indicate unaltered, moderately oxidized/altered, and heavily oxidized/altered portions of the sample, respectively.

Figure 14. (a) Visible/Near-infrared (VNIR) reflectance spectra of a representative dolerite interior (black) and surface (red) compared to two representative low albedo spectra (spectra from the Observatoire pour la Minéralogie, l'Eau, les Glaces et l'Activité (OMEGA) instrument). The effects of oxidation are clearly observed in both the terrestrial and martian spectra. (b) Mid-infrared (MIR) emission spectra of the

average dolerite interior (black spectrum) and surface (red spectrum) compared to TES Surface Type 1 (gray spectrum, from Bandfield et al. (2000)) and TES Surface Type 2 (pink spectrum, from Bandfield et al. (2000)) regions of Mars. The narrowing of the reststrahlen bands is visible in both TES Surface Type 2 and dolerite surfaces. The martian spectral signatures are consistent with those observed in Beacon dolerites as the result of oxidation-driven alteration processes. These spectra also show the sensitivity of both VNIR and MIR spectroscopy to small amounts of chemical alteration.

Figure 15. Chemical ratios for the Gusev basalts Adirondack (blue circle) and Humphrey (green circle), as measured by the APXS instrument on MER *Spirit* via Rock Abrasion Tool (RAT) brushing (surface measurements) and grinding (interior measurements). Dolerite data are also plotted (see Figure 6 for description). Adirondack and Humphrey trends are very similar to those observed in the dolerites of the MDV, suggesting that similar anhydrous alteration processes may be dominating the chemical alteration of the Gusev basalts in the hyper-arid and hypo-thermal martian environment.

Table 1. Analytical techniques used to investigate the primary composition and chemical alteration of the fourteen dolerite samples.

Table 2. Major element chemistry of dolerite interior and surface powders as determined by flux fusion and ICP-AES analyses, reported in oxide weight percentages. Standard deviations were calculated using 22 standards measured concurrently with the samples. Sample names are abbreviated and should be preceded by "MS10_BV_".

Table 3. Calculated Mössbauer parameters for the three analyzed dolerite sample pairs. Parameters include isomer shift relative to metallic iron (δ), quadrupole splitting (ΔE_Q), and the peak widths of the modeled fits, all reported in mm/sec. Errors associated

with these parameters are ±0.02-0.04 mm/sec (Dyar, 1984; Vandenberghe et al., 1994). Also provided are the peak areas of the modeled fits, presented as percent of total area. Errors are on the order of 1-3% (absolute) for relative areas of distributions. * denotes fixed parameters.

Table 4. Endmember library used in the linear spectral deconvolution of mid-infrared emission data. The spectral library was created using the ASU Spectral Library v. 1.1, available at speclib.asu.edu, and with the assistance of A. D. Rogers. [1] Christensen et al. (2001a); [2] Minitti and Hamilton (2010); [3] Lane (2007); [4] Hamilton (2000); [5] Hamilton (2010); [6] Koeppen and Hamilton (2008); [7] Glotch et al. (2004); [8] Ruff (2004); [9] Wyatt et al. (2001).

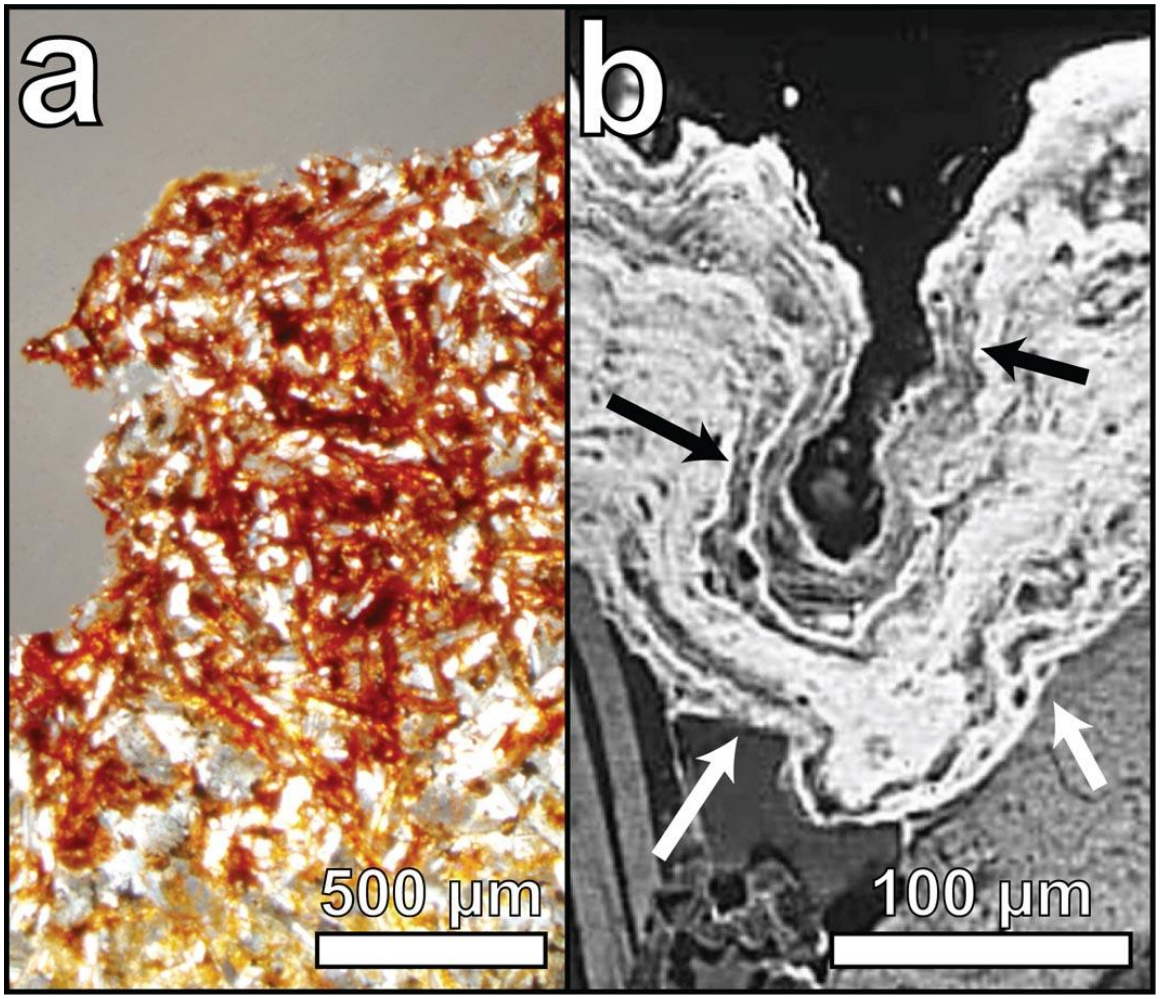

Chapter 2, Figure 1.

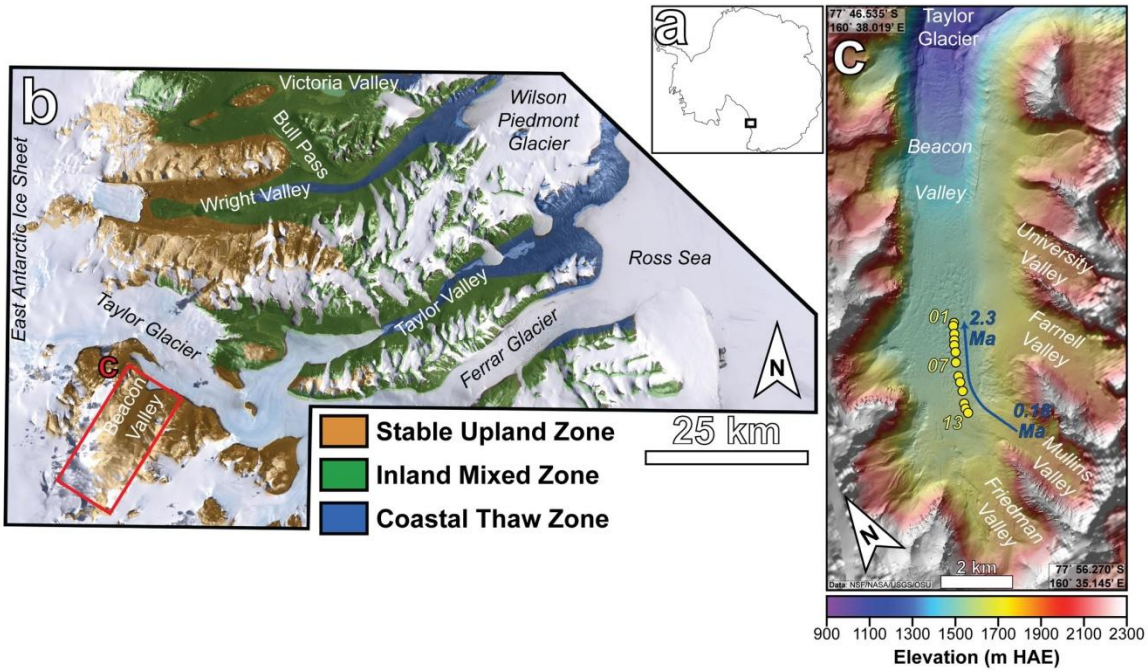

Chapter 2, Figure 2.

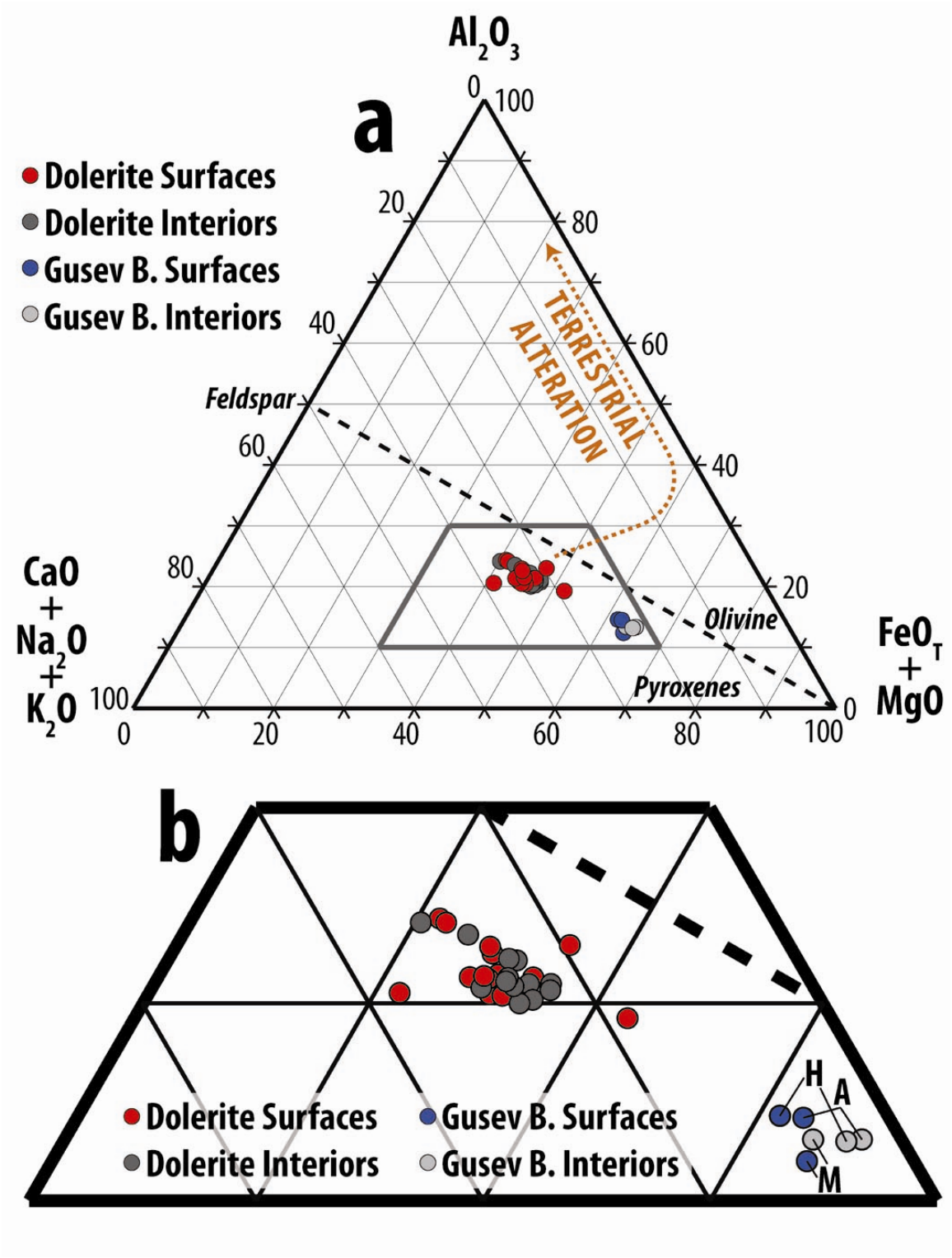

Chapter 2, Figure 3.

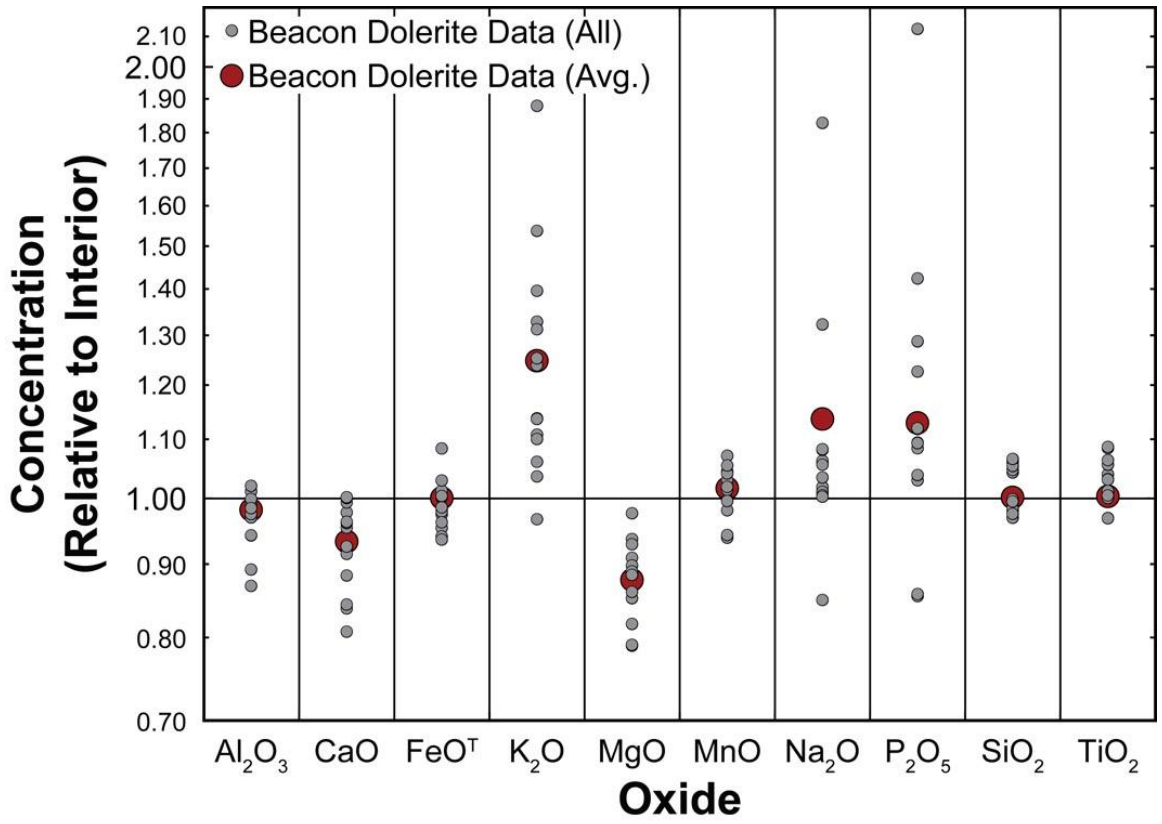

Chapter 2, Figure 4.

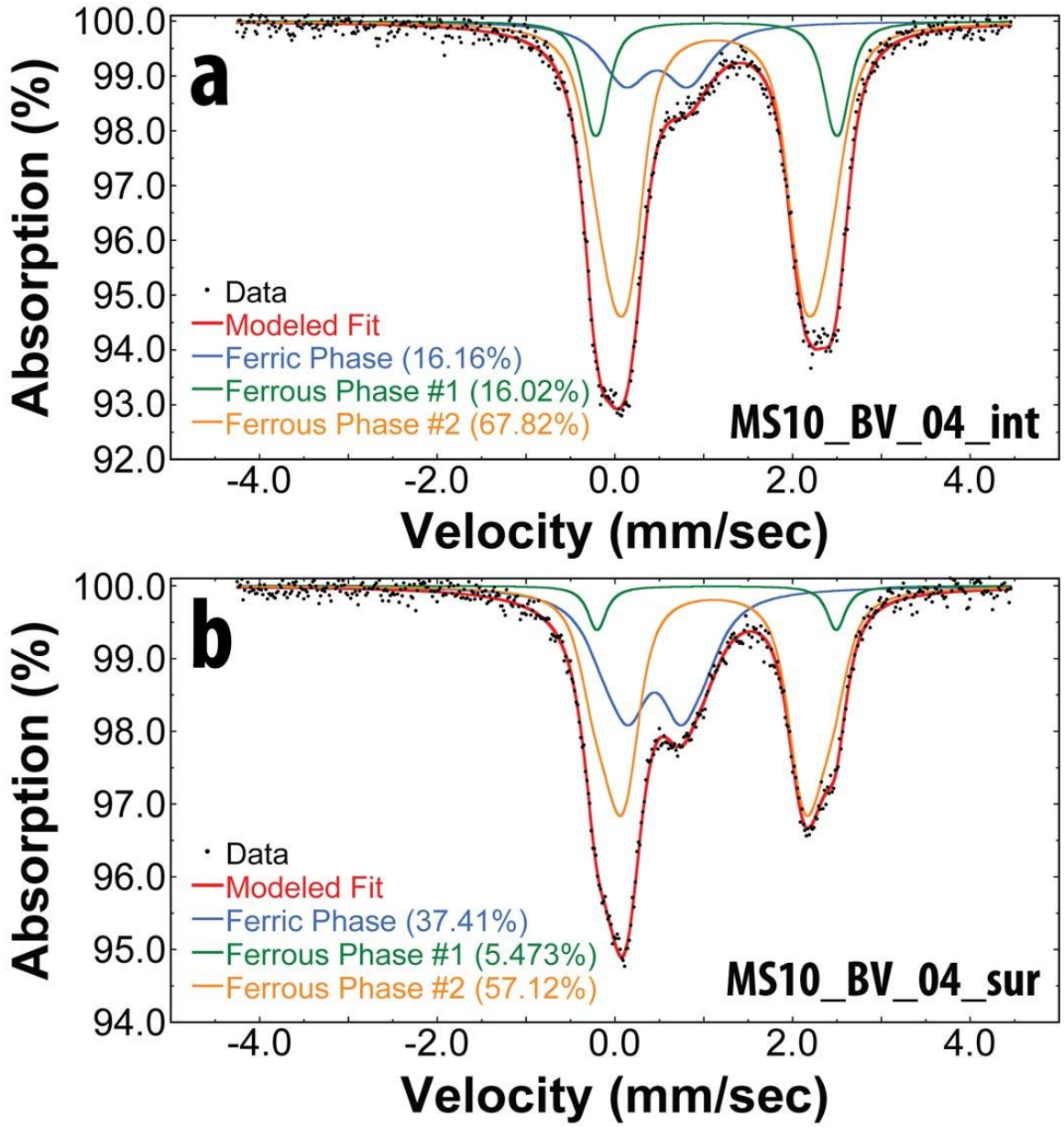

Chapter 2, Figure 5.

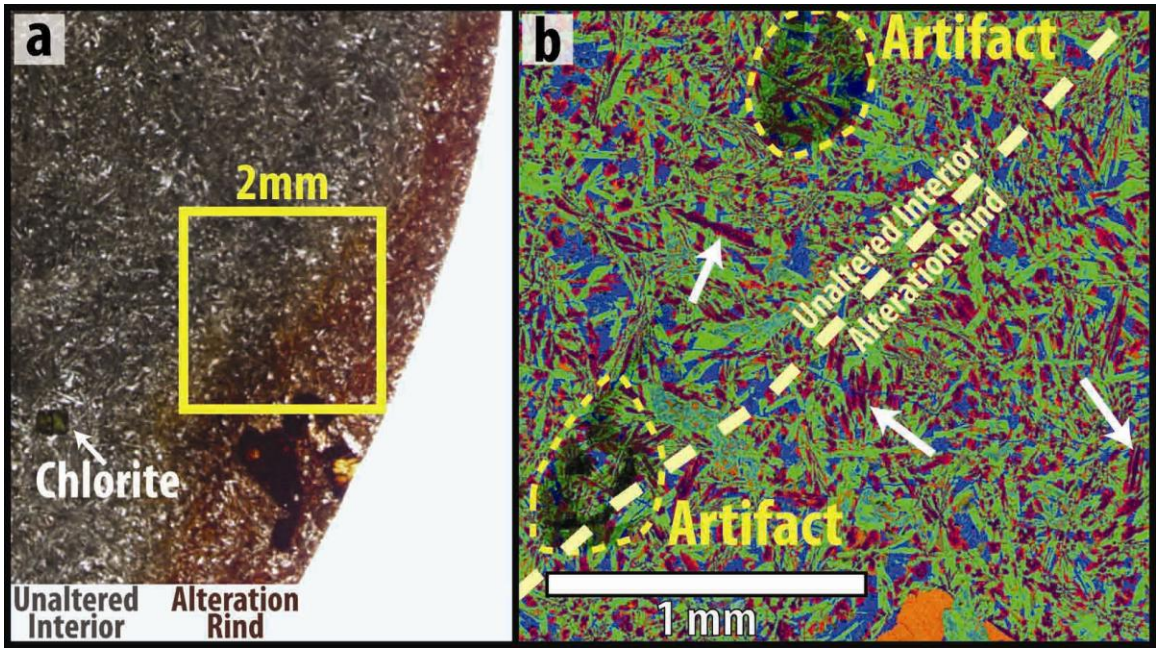

Chapter 2, Figure 6.

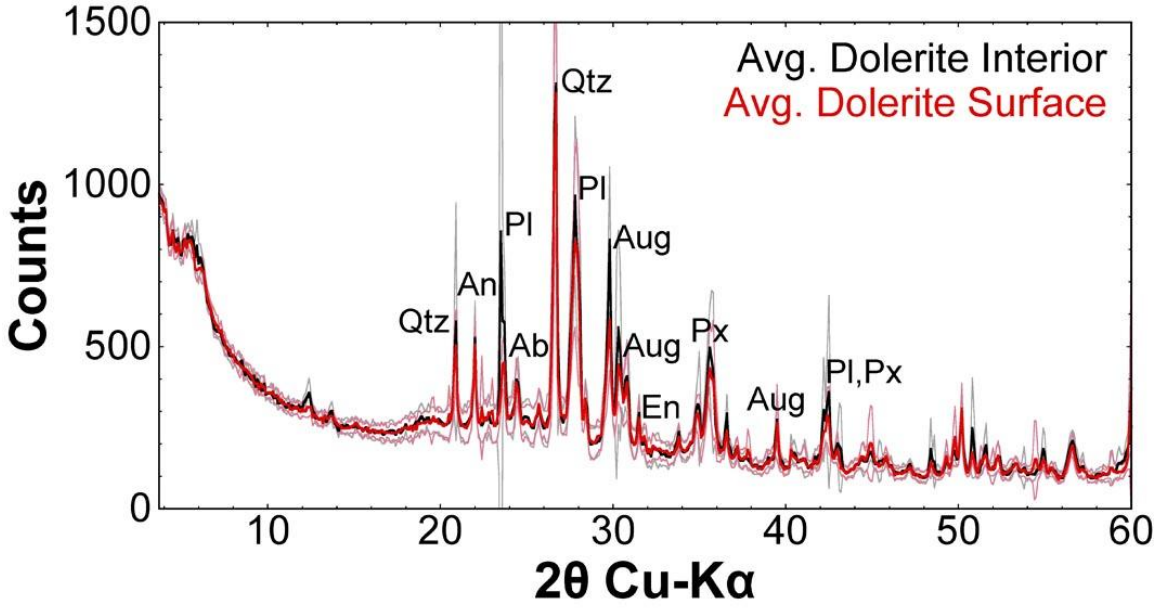

Chapter 2, Figure 7.

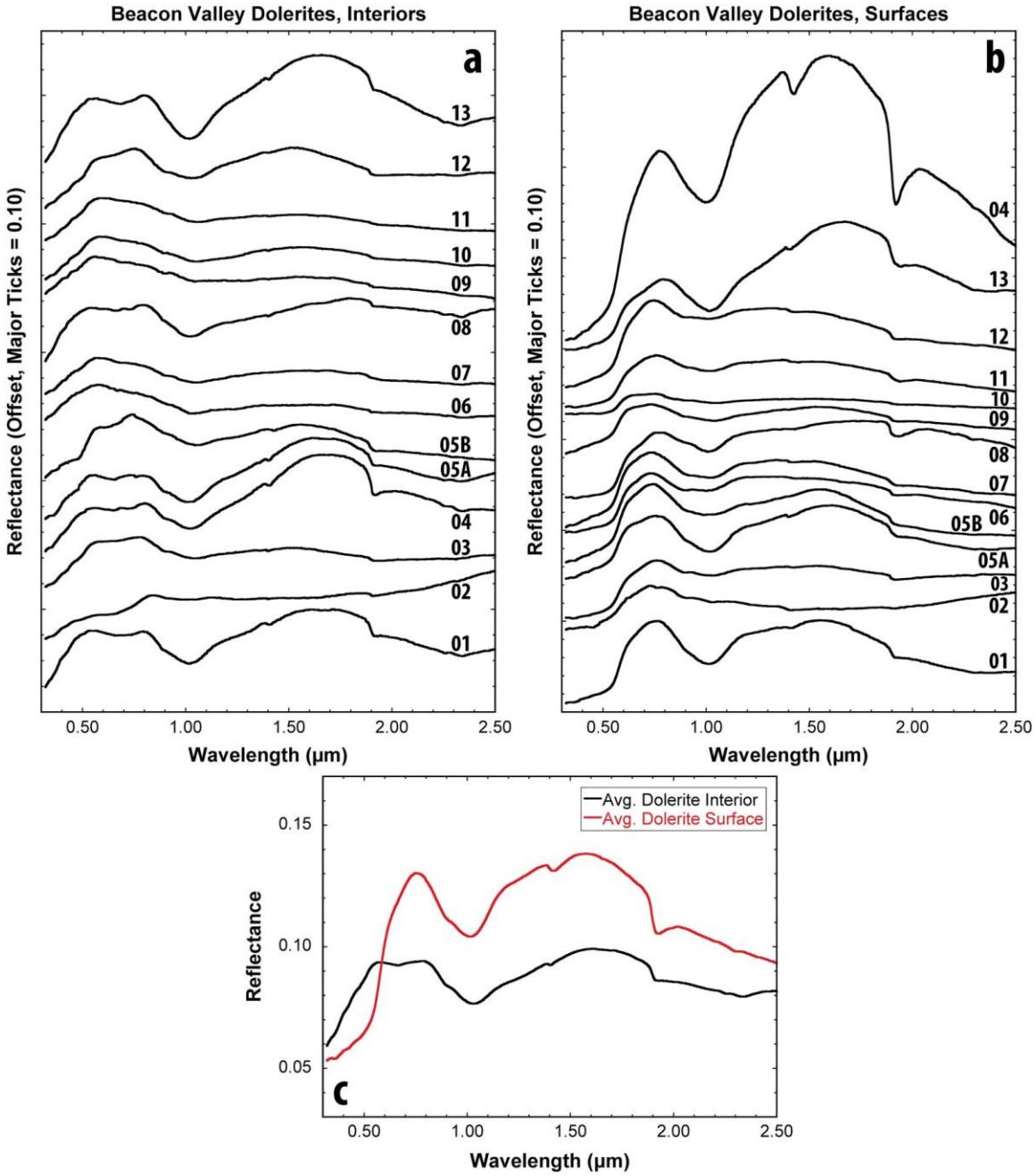

Chapter 2, Figure 8.

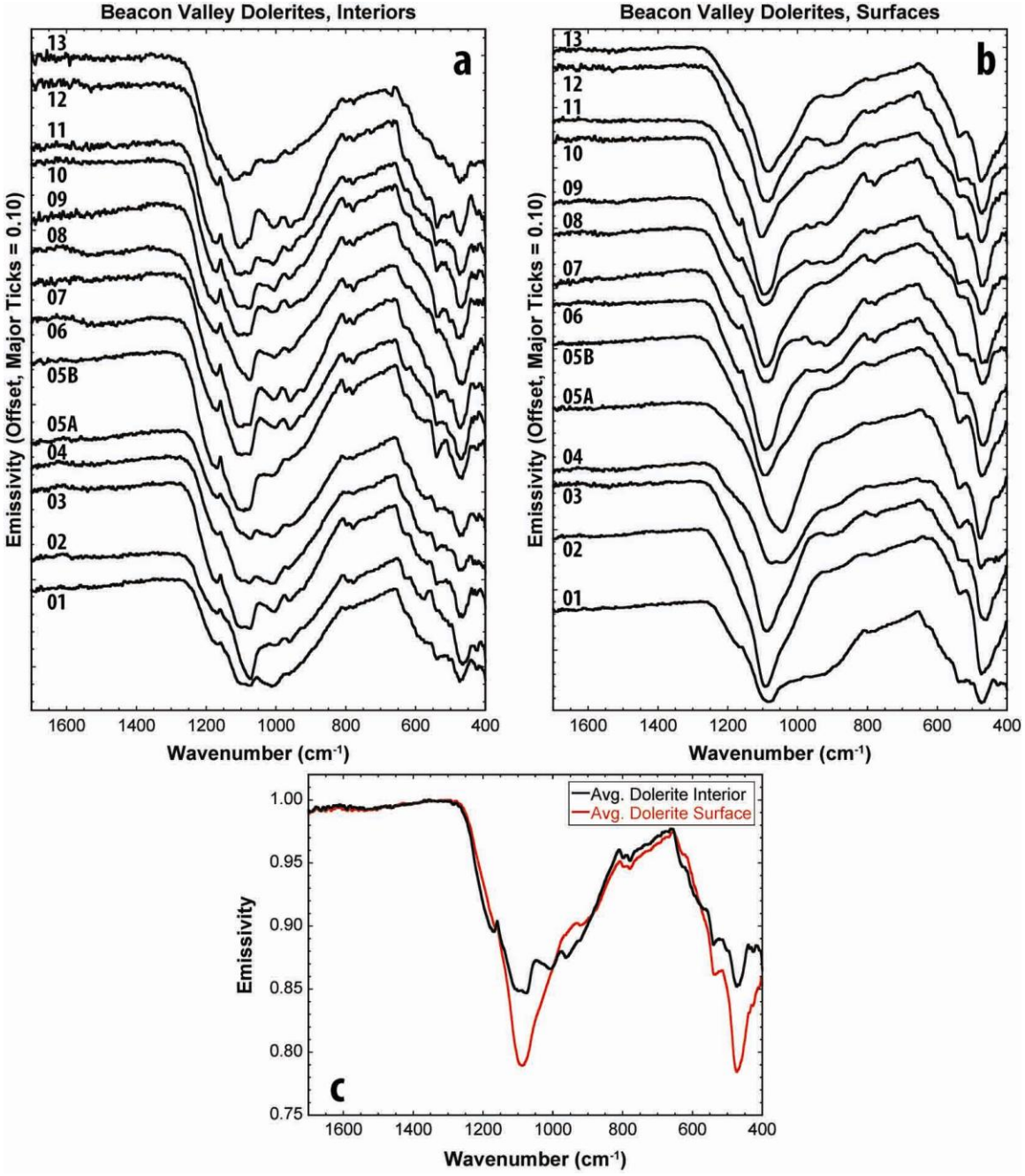

Chapter 2, Figure 9.

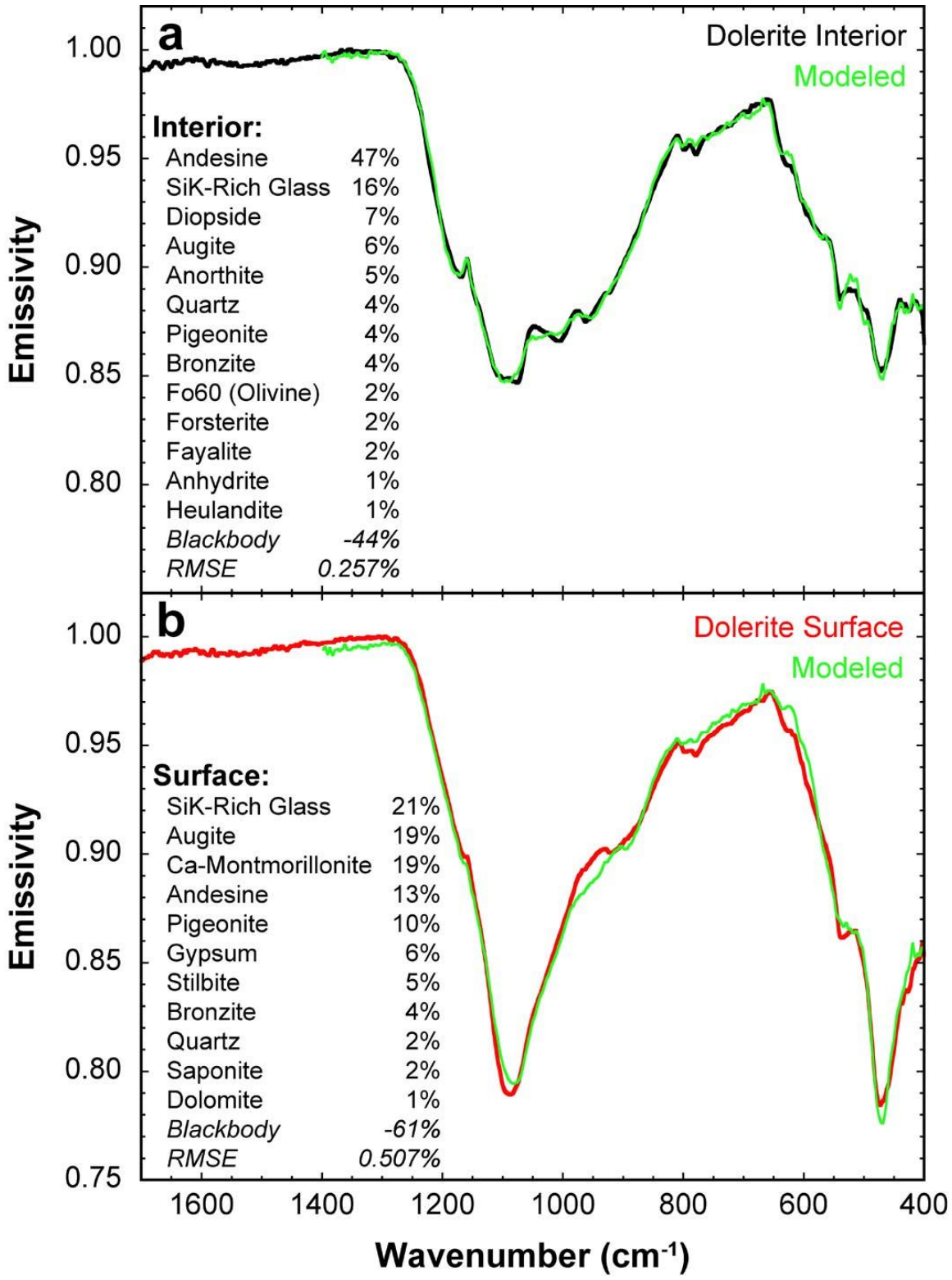

Chapter 2, Figure 10.

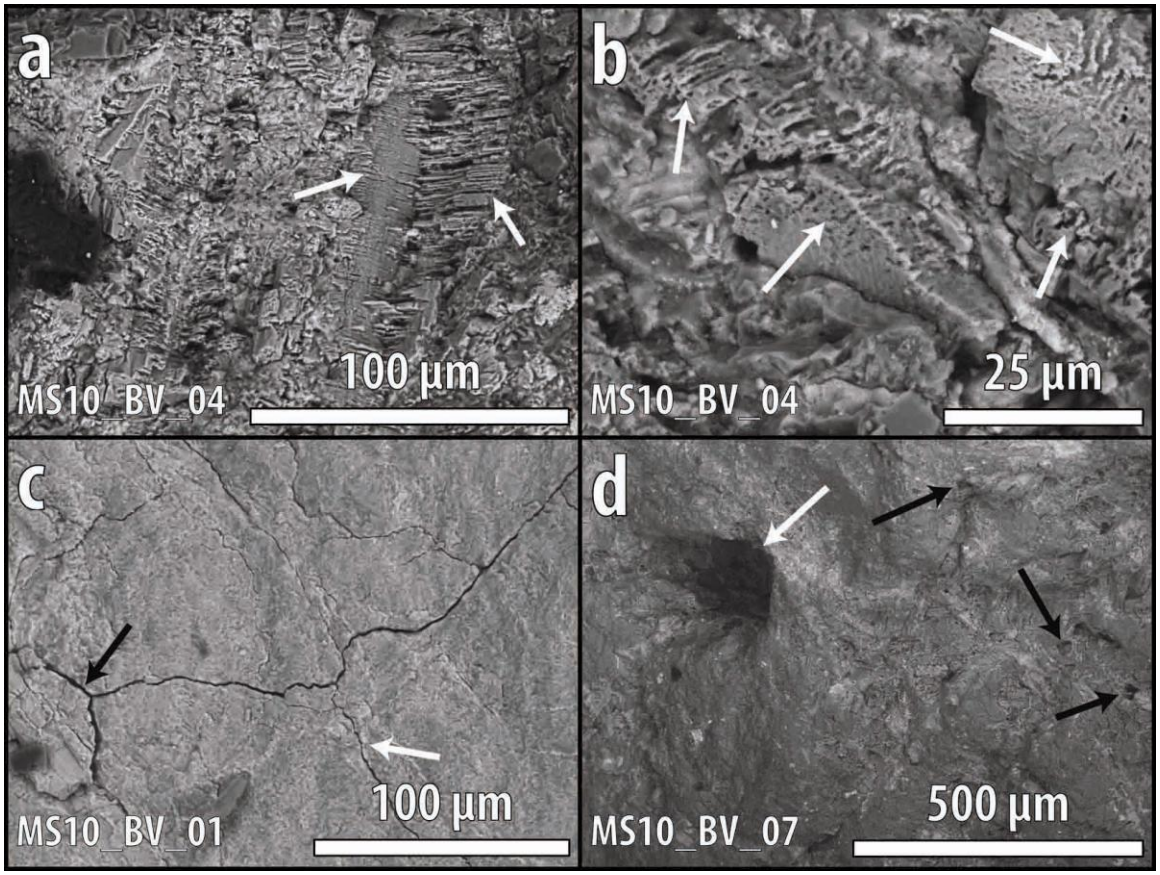

Chapter 2, Figure 11.

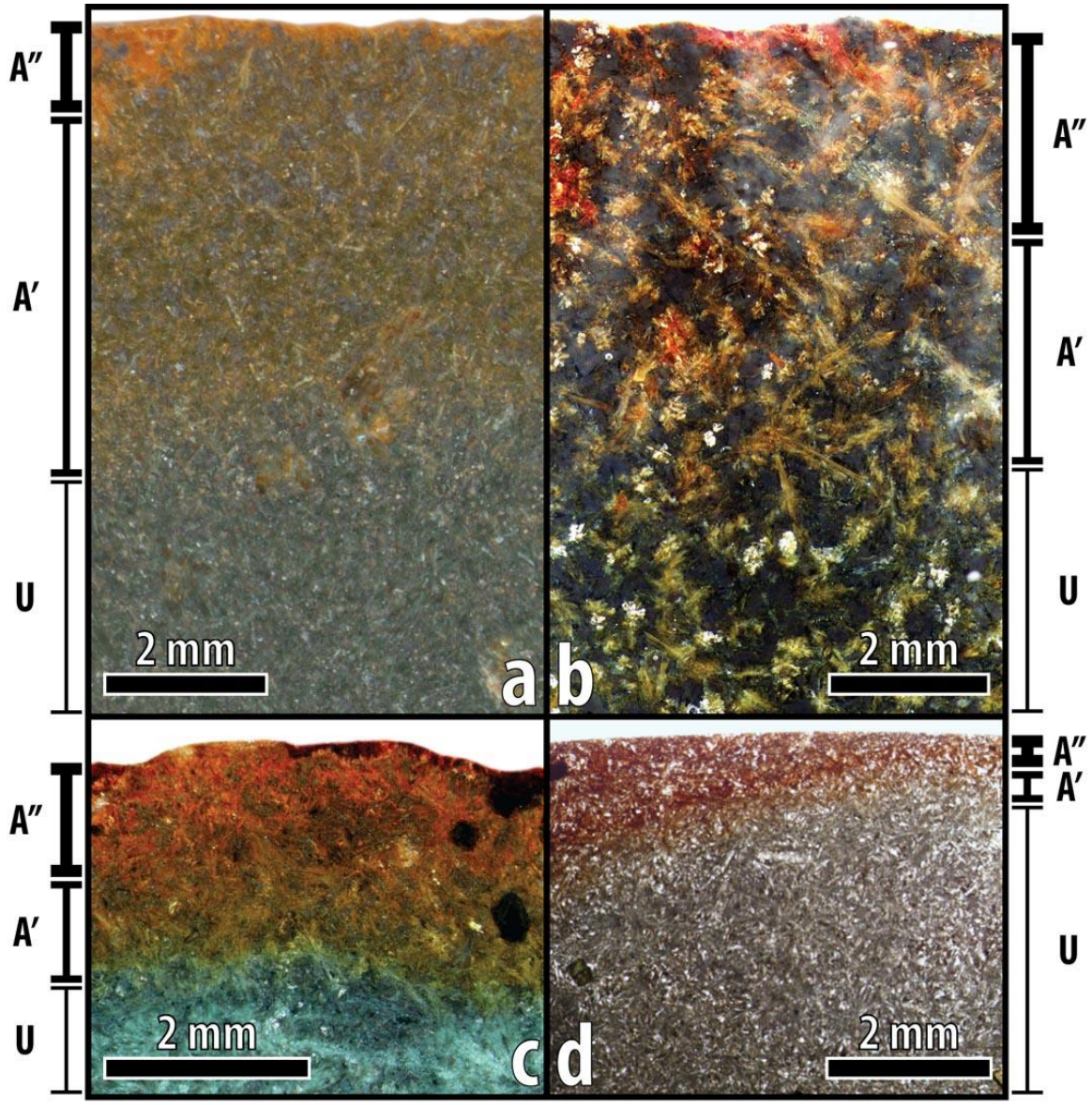

Chapter 2, Figure 12.

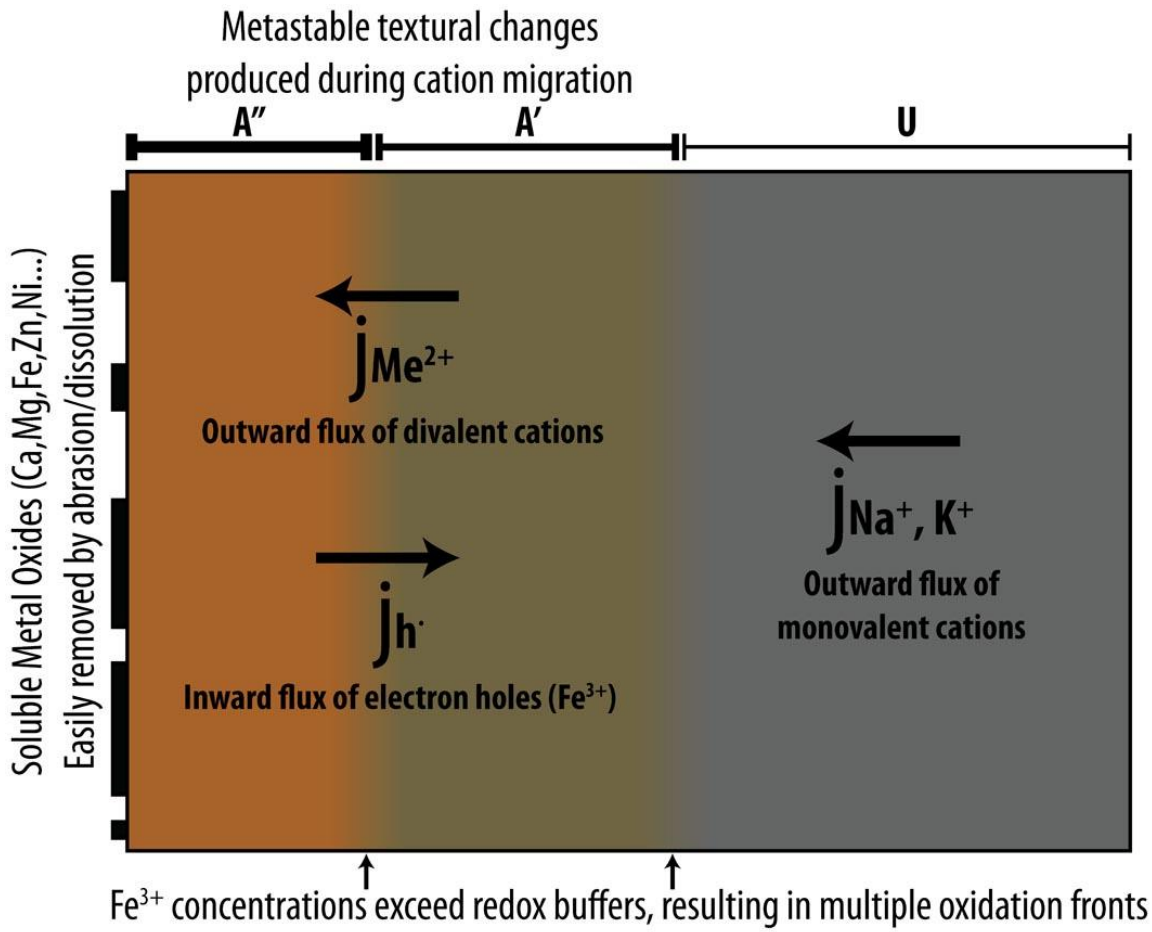

Chapter 2, Figure 13.

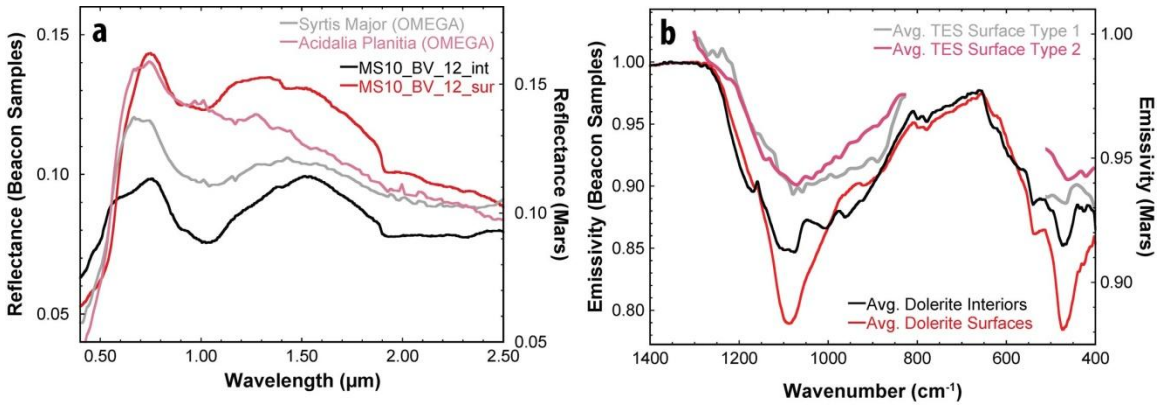

Chapter 2, Figure 14.

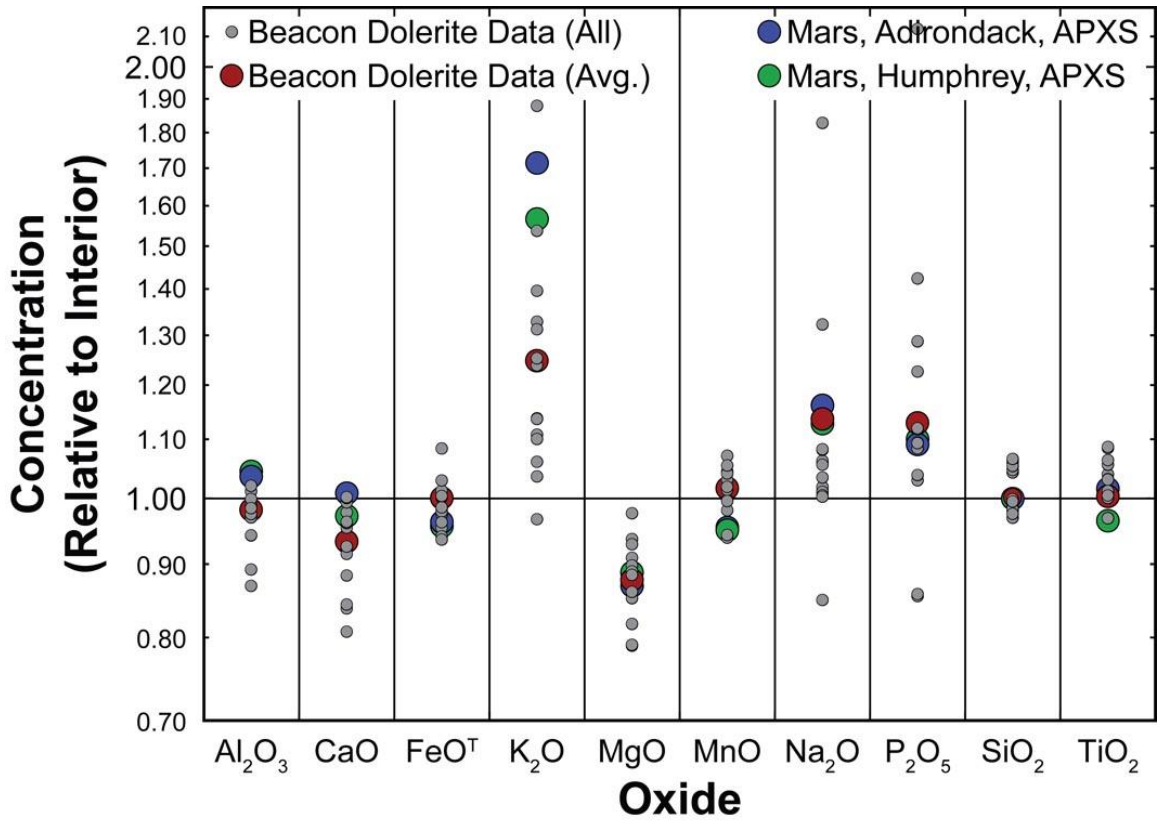

Chapter 2, Figure 15.

Chapter 2, Table 1.

Technique	Target	Sampling Depth	Description
Optical Microscopy	Thin Sections	30 μm	Investigate the morphology and structure of unaltered rock interiors and the alteration rinds. Determine whether coatings are present.
Visible/Near-Infrared (VNIR) Reflectance Spectroscopy (0.32 μm – 2.55 μm)	Rock Chips	~ 100 μm	Identify primary and secondary minerals using diagnostic absorption features resulting from electronic and vibrational processes.
Mid-Infrared (MIR) Emission Spectroscopy (2000 cm^{-1} – 200 cm^{-1})	Rock Chips	~ 100 μm	Identify primary and secondary minerals using diagnostic absorption features resulting from the fundamental vibrational frequencies within crystal lattices.
Scanning Electron Microscopy (SEM)	Rock Chips	< 5 μm	Characterize unaltered interior and alteration surface morphology.
X-Ray Diffraction (XRD)	Rock Powders	~ 500 μm*	Identify minerals based on the diagnostic diffraction of X-ray beams based on the principles of Bragg's Law.
Mössbauer Spectroscopy	Rock Powders	~ 500 μm*	Quantitatively assess the distribution and oxidation state of iron within samples.
Electron Microprobe Analyses (EMPA)	Thin Sections	< 5 μm	Determine the concentration of elements using X-ray spectrometry.
Inductively Coupled Plasma-Atomic Emission Spectroscopy (ICP-AES)	Rock Powders	~ 500 μm*	Quantitatively assess the concentration of elements using emission spectrophotometric techniques.

Chapter 2, Table 2.

Sample	Al_2O_3	CaO	FeO^T	K_2O	MgO	MnO	Na_2O	P_2O_5	SiO_2	TiO_2	Total
01_int	14.19	9.78	10.44	1.03	7.00	0.17	1.85	0.08	53.93	0.66	99.13
01_sur	14.19	9.33	10.46	1.17	6.37	0.16	1.87	0.07	53.28	0.64	97.54
02_int	14.03	8.16	10.11	1.51	4.57	0.17	2.14	0.12	59.33	0.90	101.04
02_sur	13.84	7.98	9.64	1.46	4.06	0.16	2.18	0.13	57.59	0.91	97.95
03_int	13.28	8.99	11.71	1.40	4.79	0.18	2.00	0.12	58.19	0.91	101.57
03_sur	13.15	8.64	11.85	1.59	4.09	0.19	2.11	0.12	57.18	0.95	99.87
04_int	14.22	9.22	10.41	1.29	6.99	0.17	1.98	0.08	53.64	0.63	98.63
04_sur	12.38	7.73	11.28	1.59	6.83	0.18	1.68	0.09	53.63	0.67	96.06
05A_int	14.48	9.23	9.08	1.16	6.72	0.17	1.89	0.07	56.36	0.61	99.77
05A_sur	14.67	9.17	8.93	1.23	6.30	0.16	1.91	0.06	55.53	0.61	98.57
05B_int	14.53	8.98	10.33	1.31	3.96	0.17	2.08	0.08	59.28	0.84	101.56
05B_sur	12.98	7.25	10.07	1.74	3.41	0.17	2.09	0.17	61.90	0.91	100.69
06_int	13.83	10.36	10.41	0.52	5.94	0.18	2.06	0.07	55.41	0.66	99.44
06_sur	13.05	9.57	10.19	0.73	4.69	0.17	3.77	0.08	54.14	0.67	97.06
07_int	13.44	10.43	10.88	0.86	6.29	0.18	1.58	0.07	54.94	0.67	99.34
07_sur	13.10	10.04	10.73	0.95	5.65	0.18	1.58	0.07	54.94	0.69	97.93
08_int	14.07	9.36	10.66	0.21	5.46	0.18	2.02	0.07	54.40	0.73	97.16
08_sur	14.07	7.90	11.55	0.39	5.07	0.19	2.09	0.09	54.22	0.75	96.32
09_int	13.14	9.05	12.22	1.30	5.12	0.18	2.01	0.11	56.20	0.94	100.27
09_sur	13.43	9.05	11.76	1.43	4.55	0.19	2.14	0.12	59.84	0.91	103.42
10_int	12.88	8.96	11.72	1.02	5.03	0.18	1.85	0.12	54.74	0.88	97.38
10_sur	12.51	8.98	12.06	1.28	4.12	0.19	2.00	0.15	58.09	0.95	100.33
11_int	12.93	8.73	11.55	1.38	4.92	0.18	2.16	0.11	55.60	0.89	98.45
11_sur	12.93	7.72	10.86	2.12	4.38	0.18	2.86	0.13	58.29	0.95	100.42
12_int	13.88	10.41	11.31	0.81	6.15	0.20	1.73	0.08	55.53	0.78	100.88
12_sur	13.56	9.52	11.35	1.07	4.87	0.21	1.87	0.09	58.59	0.79	101.92
13_int	13.97	9.62	10.42	1.19	6.00	0.18	1.83	0.06	53.21	0.66	97.14
13_sur	13.77	8.91	9.75	1.23	5.31	0.18	1.93	0.07	56.79	0.66	98.60
Avg. Interior	13.78	9.38	10.80	1.07	5.64	0.18	1.94	0.09	55.77	0.77	99.42
Avg. Surface	13.40	8.70	10.75	1.28	4.98	0.18	2.15	0.10	56.72	0.79	99.05
St. Dev.	±0.225	±0.465	±0.156	±0.047	±0.076	±0.004	±0.144	±0.013	±0.817	±0.052	

Chapter 2, Table 3.

Sample	Phase	δ (mm/s)	ΔE_Q (mm/s)	Width	Area	Fe^{3+}/Fe_{Total}
MS10_BV_04_int	Ferric Phase	0.475	0.691	0.579	16	0.16
	Ferrous Phase #1	1.136	2.067	0.303	68	
	Ferrous Phase #2	1.145	2.718	0.230*	16	
MS10_BV_04_sur	Ferric Phase	0.447	0.582	0.509	37	0.37
	Ferrous Phase #1	1.115	2.037	0.300*	57	
	Ferrous Phase #2	1.147	2.693	0.230*	5	
MS10_BV_10_int	Ferric Phase	0.460	0.717	0.694	26	0.26
	Ferrous Phase #1	1.150	2.047	0.324	40	
	Ferrous Phase #2	1.136	2.660	0.230*	34	
MS10_BV_10_sur	Ferric Phase	0.426	0.704	0.631	39	0.39
	Ferrous Phase #1	1.148	2.072	0.329	46	
	Ferrous Phase #2	1.130	2.698	0.230*	16	
MS10_BV_12_int	Ferric Phase	0.454	0.632	0.500*	21	0.21
	Ferrous Phase #1	1.144	2.030	0.376	53	
	Ferrous Phase #2	1.135	2.624	0.230*	26	
MS10_BV_12_sur	Ferric Phase	0.435	0.603	0.412	30	0.30
	Ferrous Phase #1	1.141	2.052	0.349	63	
	Ferrous Phase #2	1.130	2.714	0.300*	8	

Chapter 2, Table 4.

Mineral Name	Sample ID	Citation
Albite	WAR-0244	[1]
Andesine	BUR-240	[1]
Andesite interstitial glass	MEM-5	[2]
Anhydrite	ML-S9	[3]
Anorthite	BUR-340	[1]
Augite	NMNH-9780	[4]
Augite	NMNH-122302	[4]
Biotite	BUR-840	[1]
Bronzite	NMNH-93527	[1]
Calcite	C40	[1]
Ca-Montmorillonite	STx-1	[1]
Chlorite	WAR-1924	[1]
Dacite interstitial glass	MEM-4	[2]
Diopside	WAR-6474	[1]
Dolomite	C20	[1]
Fayalite	WAR-RGFAY01	[1]
Forsterite	BUR-3720A	[1]
Fo60 (Olivine)	KI 3362	[5] [6]
Gypsum	ML-S6	[3]
Hedenbergite (Manganoan)	DSM-HED01	[1]
Avg. Martian Hematite	TES-Derived	[7]
Heulandite	---	[8]
Illite	IMt-2	[1]
SiK-Rich Glass	---	[9]
Magnesiohastingsite	HS-115.4B	[1]
Nontronite	WAR-5108	[1]
Pigeonite	---	[4]
Quartz	BUR-4120	[1]
Quenched Basalt	---	[9]
Saponite	ASU-SAP01	[1]
Serpentine	HS-8.4B	[1]
Stilbite	---	[8]

Chapter Three:

Characterization of spectral and geochemical variability within the Ferrar Dolerite of the McMurdo Dry Valleys, Antarctica: Weathering, alteration, and magmatic processes.

M. R. Salvatore[1], J. F. Mustard[1], J. W. Head III[1], D. R. Marchant[2], and M. B. Wyatt[1]

[1]Department of Geological Sciences,

Brown University, Providence, RI 02912, USA

[2]Department of Earth Sciences,

Boston University, Boston, MA 02215, USA

Accepted in its current form in:

Antarctic Science

doi:10.1017/S0954102013000254

Abstract

Orbital spectroscopy and laboratory analyses are utilized to identify major geochemical variations throughout the Ferrar Dolerites exposed in the McMurdo Dry Valleys (MDV) of Antarctica. Our laboratory results highlight the range of primary and secondary chemical and spectral variations observed throughout the dolerite, and provide the necessary calibration for detailed orbital investigations. Pure dolerite units are identified and analyzed throughout the MDV using Advanced Land Imager (ALI) and Advanced Spaceborne Thermal Emission and Reflection Radiometer (ASTER) orbital datasets. In conjunction with our laboratory analyses, orbital analyses indicate that the dolerite sills are dominated by MgO concentrations of approximately 6 – 7 wt.% except where influenced by orthopyroxene-laden magmatic injections, where MgO concentrations can reach as high as 32.5 wt.%. ASTER analyses also indicate that spectrally significant alteration is limited primarily to surfaces dominated by fine-grained dolerites, which form and preserve well-developed alteration rinds due to their resistance to physical erosion. The archetype of these secondary signatures is Beacon Valley, where a combination of cold, dry, and stable environmental conditions and the presence of fine grained dolerites results in strong alteration signatures. This work provides unprecedented spatial coverage of meso- and macro-scale geochemical features that, until now, have only been identified in field and laboratory investigations.

Key Words

ASTER, ALI, spectroscopy, geochemistry, remote sensing, alteration rinds.

1.0 Introduction and Geologic Setting

The McMurdo Dry Valleys (MDV) of Antarctica are a series of predominantly east-west trending valleys located approximately 100 km to the northwest of McMurdo Station along the eastern flank of the Transantarctic Mountains (Fig. 1). The valleys are bordered to the west by the East Antarctic Ice Sheet and to the east by the Ross Sea and seasonal sea ice. The cold polar conditions and the glacioclimatic influences of the Transantarctic Mountains limit the mean annual water equivalent precipitation to < 50 mm yr^{-1}, the majority of which is lost to sublimation prior to its incorporation in the local and regional hydrologic system (Fountain et al., 2009). As a result of these hypo-thermal and hyper-arid conditions, the MDV are characterized by the absence of vascular vegetation and the abundance of coarse sediments, bedrock outcrops, and ephemeral meltwater channels originating from local alpine and outlet glaciers (Doran et al., 2002). Although subtle, the resulting differences in temperature and relative humidity produce local microclimatic variations that create diverse micro-, meso-, and macro-scale landforms. (Marchant and Head, 2007).

The valleys incise the Devonian-Triassic Beacon Supergroup, which are composed largely of sandstones, siltstones, and orthoquartzites, and the underlying Precambrian-Ordovician Granite Harbour Intrusives, composed of granites, granodiorites, gneisses, and orthogneisses (Isaac et al., 1995). Basaltic magmatism associated with the breakup of Gondwana at approximately 180 Ma (Fleming et al., 1997) intruded both the Beacon Supergroup and the Granite Harbour Intrusives and was emplaced in four prominent sills (the Ferrar Dolerite) and as surficial basaltic flows (the Kirkpatrick Basalt) throughout the region (Elliot and Fleming, 2004; Marsh, 2004) (Fig. 2). During

emplacement, the magmatic system experienced crustal assimilation (Fleming et al., 1995), complex differentiation processes (Bédard et al., 2007), and multiple injections that delivered slurries of phenocryst-laden magmatic "mush" into the lowermost portions of the intrusions (Marsh, 2004). Of the four major sills, the lower sills (Basement Sill and Peneplain Sill) exhibit the largest range of magmatic products and textures, whereas the upper sills (Asgard Sill and Mt. Fleming Sill) are characterized by near-liquid compositions and largely sub-ophitic textures (Fleming et al., 1995; Elliot and Fleming, 2004; Marsh, 2004). The dolerites within the MDV are most closely related to the Mount Fazio chemical type (MFCT) lavas of north Victoria Land, which are characterized by intermediate Mg# (~ 40-50) and MgO contents (4.5-7.5 wt.%), with higher values present where pyroxenes have accumulated (Fleming et al., 1995). The emplacement, modification, and subsequent cooling of the Ferrar Dolerite has resulted in significant chemical and mineralogical variations, which can be identified in the well-exposed outcrops throughout the MDV (Marsh, 2004; Bédard et al., 2007).

Prior to cooling, additional pulses of magmatic intrusion occurred and injected orthopyroxene- (opx-) laden magmatic slurries into the two lowermost sills. These slurries, however, were unable to infiltrate the uppermost sills or reach the surface, resulting in mineralogical, chemical, and textural variations throughout the different outcrops of the Ferrar Dolerite (Marsh and Wheelock, 1994; Heyn et al., 1995; Marsh, 2004; Bédard et al., 2007). Outside the zone of opx-enrichment, dolerites exhibit an average MgO concentration of 7.0 wt.%, whereas the MgO concentration can exceed 20 wt.% within opx-rich zones (Marsh, 2004). Additionally, exposures of the Basement Sill exhibit silicic segregations (Zavala et al., 2011) as well as massive cryptic layering that

alternates between anorthosite (~14 wt.% CaO, 10 wt.% MgO) and pyroxenite (~8 wt.% CaO, 16 wt.% MgO) (Marsh, 2004).

After emplacement of the dolerite sills, the Transantarctic Mountains underwent complex geological history that included deep burial and exhumation during the late Mesozoic and Cenozoic eras (e.g. Fitzgerald et al., 2006). Following exhumation and upon exposure to the hyper-arid and hypo-thermal Antarctic environment, the dolerites have undergone chemical alteration and micro-structural modification (e.g. Glasby et al., 1981; Head et al., 2011). In particular, dolerites undergo rapid surface modifications in response to the oxidizing Antarctic environment. In Beacon Valley, the southernmost and highest of the MDV, chemical alteration results largely from these anhydrous oxidation processes (Salvatore et al., unpublished data). In response to a strong oxidation gradient, divalent cations are preferentially removed from the rock surface, which results in the oxidation of Fe^{2+} to network-modifying Fe^{3+} and creates metastable structural changes in the rock surface (e.g. Cooper et al., 1996). These alteration products, while difficult to identify using most laboratory techniques due to the minute chemical and mineralogical variations, are easily observed in visible/near-infrared (VNIR) and thermal-infrared (TIR) spectroscopic analyses due to the near-surface modifications and the sensitivity of these techniques to the minor variations. Oxidation of iron in pyroxenes and the formation of metastable structures in response to cation migration are responsible for unique VNIR and TIR spectral signatures, respectively (Fig. 3). In the VNIR, a strong Fe^{2+}-Fe^{3+} intervalence charge transfer absorption forms in the spectra of dolerite surfaces, with only subtle variations observed throughout the rest of the spectrum. No evidence for the formation of additional hydration features (e.g. sharp OH^- vibrational

absorptions between 2.0 μm and 2.5 μm) were detected in the VNIR. In the TIR, a substantial narrowing of the primary reststrahlen features centered near 1100 cm^{-1} (9.1 μm) and 465 cm^{-1} (21.3 μm) is observed in dolerite surfaces relative to their interiors, which is thought to reflect the production of minor amounts of metastable and immature alteration products. Under the current hyper-arid and hypo-thermal environmental conditions in Beacon Valley, more mature and crystalline alteration phases (including smectite clays) are unable to form. As a result, these metastable, incomplete, and immature alteration products, which are typically overprinted in most terrestrial environments, are uniquely preserved in Beacon Valley.

Understanding the spatial distribution of both primary and secondary mineralogies throughout the dolerite units will shed light on the geochemical evolution and alteration history of the MDV. In this study, we characterize the mesoscale (10^1 – 10^4 m) compositional and spectroscopic variability within the Ferrar Dolerite due to both primary and secondary processes using the Advanced Land Imager (ALI) and Advanced Spaceborne Thermal Emission and Reflection Radiometer (ASTER) orbital datasets (Table 1). Orbital spectral datasets have not been widely utilized in compositional investigations of the MDV because of the difficulties associated with photometric calibration and atmospheric correction at such high latitudes. Additionally, spectral verification and ground truthing is a challenging in remote and mountainous environments where not all lithologies or geographic regions may be easily accessible. As a result, a large component of this work has focused on the calibration and correction of these orbital datasets to obtain georeferenced and mosaicked surface reflectance and emission signatures that are acceptable for geologic and geochemical investigations.

Laboratory spectroscopy and chemical analyses were performed to further validate these data, to provide additional hyperspectral information on representative dolerite samples, and to determine the range of chemical variability observed due to primary magmatic evolution and secondary alteration processes. At spatial resolutions of 30 m pix^{-1} and 90 m pix^{-1}, respectively, ALI and ASTER provide regional perspectives on the compositional nature of the Ferrar Dolerite across the majority of the ice-free portions of the MDV.

We focus on four main geographic regions within the MDV (Fig. 1). Samples from these locations have either been extensively analyzed in previous studies or were collected by the authors and subsequently analyzed for this study. These locations include Beacon Valley, the Labyrinth of Upper Wright Valley, Central Wright Valley (including the southwestern portion of Bull Pass), and Victoria Valley. These locations highlight both the spectral and igneous diversity observed in the Ferrar Dolerite and help to limit our subsequent analyses to regions that have been well characterized.

Beacon Valley is the coldest (mean annual temperature of -22º C (Doran et al., 2002)), driest (mean annual water equivalent precipitation of less than 10 mm yr^{-1} (Schwerdtfeger, 1984; Fountain et al., 2009)), and highest (mean elevation of approximately 1200 m above the World Geodetic System 1984 ellipsoid (Schenk et al., 2004)) of the MDV. Exposed along the valley walls are outcrops of the Asgard and Mt. Fleming sills in addition to a significant sedimentary component of the Beacon Supergroup. The valley floor, however, is composed almost entirely of doleritic clasts with only minor quartzitic and granitic components present in the northern half of the valley. The Labyrinth of Upper Wright Valley is thought to have formed as a result of

episodic and immense drainage of subglacial bodies of water (Lewis et al., 2006). The resultant canyon and plateau system exposes large outcrops of the Peneplain Sill of the Ferrar Dolerite. Upper Wright Glacier bounds this system to the west, the Dais of Wright Valley is present to the east, and large cliffs composed of the Beacon Supergroup flank both the northern and southern margins. Victoria Valley, in the region south of Lake Vida, hosts one of the most complete exposures of the Basement Sill and its contact with the underlying granitic basement. The shallow slope and large spatial extent reveal significant compositional diversity within the Basement Sill that is readily observable from orbit. The Basement Sill is also exposed in Central Wright Valley and Bull Pass, which exhibit some of the strongest mafic signatures identified from orbit throughout the MDV. There is a significant amount of laboratory data from samples collected in this region as a result of studies by Marsh and Wheelock (1994), Heyn et al. (1995), Fleming et al. (1995), Elliot and Fleming (2004), Marsh (2004), Bédard et al. (2007), and others, making this region particularly appealing for orbital investigations.

Following radiometric and atmospheric calibration and correction of the orbital datasets, we use TIR orbital data to identify regions that are spectrally dominated by doleritic signatures. This task was performed by utilizing laboratory-derived spectral endmembers and a linear unmixing algorithm to differentiate between doleritic, quartzitic, and granitic compositions. We then assess the range of observed spectral signatures in the dominantly doleritic regions using an additional least-squares linear unmixing algorithm to identify the distribution of unique doleritic endmembers and spectral components. The distribution of these doleritic signatures throughout the MDV

shed light on the characteristics of magmatic intrusion as well as the production, distribution, and preservation of secondary alteration phases.

2.0 Methods

2.1 Laboratory spectral investigations

Spectra of 64 altered and unaltered dolerites, granites, granodiorites, and quartzites from throughout the MDV were collected in both the VNIR (Brown University Reflectance Experiment Laboratory (RELAB) Facility and FieldSpec-3 portable VNIR spectrometer developed by Analytical Spectral Devices, Inc.) and TIR (Stony Brook University Vibrational Spectroscopy Laboratory) spectral regions. VNIR spectral measurements are sensitive to electronic transitions and vibrational processes within materials (Farmer, 1974), while TIR spectral measurements measure the fundamental vibrational motions associated with a range of geologically pertinent anion groups (SiO_4, CO_3, etc.) (Christensen et al., 2000). RELAB measurements were made using a bidirectional reflectance (BDR) spectrometer, which acquires spectra between 0.32 and 2.55 μm at a 5 nm spectral sampling interval using a photomultiplier and InSb detectors (Pieters, 1983; Mustard and Pieters, 1989). FieldSpec-3 measurements were made using an external light source and Spectralon white reference calibration targets. Both BDR and FieldSpec-3 illumination and emergence angles were fixed at 30º and 0º, respectively. TIR emission spectra were acquired using a Nicolet 6700 FTIR Spectrometer, which utilizes a deuterated L-alanine doped triglycine sulfate (DLaTGS) detector and CsI window. Measurements were made between 2000 cm^{-1} and 200 cm^{-1} (5 μm and 50 μm) at a sampling resolution of 4 cm^{-1} (variable depending on wavelength,

0.01 μm at 5 μm, 1.00 μm at 50 μm) using a CsI beamsplitter. All laboratory measurements were also resampled to orbital ALI and ASTER spectral bandpasses for direct comparison to these orbital datasets.

Bulk chemistry of 18 unaltered dolerite samples were obtained using inductively coupled plasma atomic emission spectroscopy (ICP-AES) via the flux fusion dissolution technique (Murray et al., 2000). To dissolve the materials into solution, powdered samples were divided into 40 mg aliquots, mixed with 160 mg $LiBO_2$, and fused for 10 minutes at 1050º C. The melts were quenched in 20 mL of 10% HNO_3 and agitated for one hour. The samples were then filtered through 0.45 μm filters and diluted in additional 10% HNO_3. The resultant liquids were analyzed using a JY2000 Ultrace ICP Atomic Emission Spectrometer. Elemental abundances were calculated using a Gaussian peak search technique and the results were calibrated and converted to weight percentages using a series of blanks and geochemical standards that were processed in the same fashion as the samples (Murray et al., 2000). All samples, standards, and blanks were run in duplicate to increase the measurement statistics. Each sample was measured for Si, Al, Ca, Fe, Mg, Mn, Na, K, Ti, and P.

2.2 Orbital data acquisition, calibration, and atmospheric removal

ALI is a pushbroom imaging system onboard the Earth Observing-1 spacecraft. The data consist of ten spectral bands (Mendenhall et al., 2000); nine multispectral bands ranging from 0.443 μm to 2.215 μm with an optimal spatial resolution of 30 m pix^{-1}, and one panchromatic band centered at 0.585 μm with an optimal spatial resolution of 10 m pix^{-1} that is not used in this study. Five ALI scenes were obtained from the U. S. Geological Survey (USGS) Earth Resources Observation and Science (EROS) Center

website at glovis.usgs.gov (date accessed: 14 June 2011) (Table 1). These data were then converted from their original raw digital number format (Q) to calibrated digital numbers (Q_{cal}), followed by conversion to at-sensor spectral radiance (L_λ) using the methods discussed in Chander et al. (2009):

$$L_\lambda = G_{rescale} \times Q_{cal} + B_{rescale}$$

where:

$$G_{rescale} = \frac{LMAX_\lambda - LMIN_\lambda}{Q_{calmax} - Q_{calmin}}$$

and

$$B_{rescale} = LMIN_\lambda - \left(\frac{LMAX_\lambda - LMIN_\lambda}{Q_{calmax} - Q_{calmin}}\right) Q_{calmin}$$

where L_λ is the spectral radiance at the sensor's aperture [W/(m^2 sr μm)], Q_{cal} is the quantized calibrated pixel value [DN], Q_{calmin} (Q_{calmax}) is the minimum (maximum) quantized calibrated pixel value corresponding to $LMIN_\lambda$ ($LMAX_\lambda$) [DN], $LMIN_\lambda$ ($LMAX_\lambda$) is the spectral at-sensor radiance that is scaled to Q_{calmin} (Q_{calmax}) [W/(m^2 sr μm)], $G_{rescale}$ is the band-specific rescaling gain factor [(W/(m^2 sr μm))/DN], and $B_{rescale}$ is the band-specific rescaling bias factor [W/(m^2 sr μm)].

Atmospheric contributions were then removed from the at-sensor spectral radiance through a hybrid dark object subtraction and regression (DOS-R) method (Chavez, 1996; Lu et al., 2002). This method estimates the atmospheric contributions to a surface spectrum by measuring homogeneous surfaces over a range of illumination conditions. Assuming the last spectral band (band 10, 2.215 μm) is devoid of scattered downwelling radiance, the other spectral bands are plotted against this last spectral band and regressions are found to identify the atmospheric contributions where those bands project to zero solar input. Multiple iterations of this technique are performed over multiple spectral sampling locations in each image to derive the average atmospheric contribution for each ALI scene. Each DOS-R sampling location was selected based on the identification of a range of illumination conditions (from bright to dark, typically on slopes where a range of shadow conditions are present) as well as the verification of a geologically homogeneous surface (e.g., glacial tills on valley floors, slopes with single lithologies present). The average contributions from these spectral sampling locations are then subtracted from the previously derived at-sensor spectral radiance for each individual band in each individual image. The locations used for this DOS technique are shown in Figure 1 (orange stars) and are provided, along with the derived average atmospheric contributions, in Table 2.

The assumption that ALI band 10 is devoid of scattered downwelling radiance is based on the Rayleigh equation, which predicts that the amount of scattered radiance at 2.215 μm is 0.03%. The paucity of scattered radiance and the relationship between band 10 and the other spectral bands is also shown in Figure 4. The frequency distribution of spectral radiance in 3,372 shadowed pixels measured in each band of ALI scene

EO1A0581152008022110KG is shown in Figure 4a and is scaled for each band. The high radiances measured in the lowest ALI bands represent the strong effects of scattering at the shortest wavelengths. However, at longer wavelengths, the contributions from scattered downwelling radiance become very small. Figure 4b is a magnified portion of Figure 4a (marked by a dashed line) and shows the scaled radiance values for the three ALI bands at wavelengths beyond 1 μm. The majority of spectral radiance values measured in band 10 are less than 0.1 W/(m^2 sr μm) and represent 0.057% of the scattered downwelling radiance. This example validates our assumption that band 10 is essentially devoid of scattered downwelling radiance.

An example of a DOS-R regression scatterplot is shown in Figure 4c, where 42 spectra (located near -77.75º N, 160.64º E) from a homogeneous surface under varying illumination conditions were extracted and plotted against their measured radiance values for band 10. Regressions modeled to these data exhibit good fits, and their y-intercept represents their theoretical radiance values when band 10 equals zero. In this example, the y-intercept value for band 8 is 0.7379 W/(m^2 sr μm), which is equal to the scattered downwelling radiance estimated at 1.25 μm.

Three in situ VNIR calibration sites were identified and measured in November of 2010. A 100 m x 100 m grid was demarcated by GPS coordinates at three different locations of varying surface albedo. Spectral measurements between 0.35 μm and 2.50 μm were made using a FieldSpec-3 portable field spectrometer every 10 meters throughout the gridded area, with calibration targets measured after every tenth measurement. These data were then averaged to produce a representative VNIR spectrum for each of the three calibration locations. However, two of the three

calibration locations overlap with pixels that were excluded from our spectral map due to the presence of snow and ice in the only ALI image covering these locales. To make it possible to utilize this valuable dataset, a Landsat image (Table 1) was calibrated (using the methods of Chander et al. (2009)) and atmospherically corrected using these three spectral grid locations. Spectra of four regions of overlap between the Landsat image and our multispectral map were acquired and compared to determine the agreement between the two datasets. The spectra of three doleritic regions and one quartzitic region are compared in Figure 5, which confirms that the DOS atmospheric correction technique appropriately removes the majority of atmospheric contributions from our spectral map despite the exclusion of these three calibration grids. This exercise also demonstrates the advantage of ALI data over Landsat in the ability to better resolve the diagnostic absorption features associated with the dolerites.

The DOS-R atmospheric correction technique was chosen over more complex physically-based modeling (e.g., FLAASH, MODTRAN, ATCOR3) because of (1) the amplification of scattering and aerosol contributions at high latitudes, (2) the difficulty in constraining atmospheric parameters for the remote and highly variable MDV, and (3) the good agreement between ground-truthed orbital datasets and the DOS-R-corrected ALI datasets. The longer atmospheric path lengths, due to the low solar elevations at high latitudes, significantly enhance the contributions of scattering and aerosols within an image. Small errors in aerosol estimates can also result in significant errors in retrieved surface reflection values as a result of these low solar elevations. Additionally, more sophisticated physically-based atmospheric modeling requires either the collection of considerable amounts of in situ atmospheric data (e.g., weather ballon observations)

and/or complex atmospheric simulations. Unfortunately for studies of the MDV, the nearest site of frequent atmospheric data collection (McMurdo Station) is located 80 – 160 km to the east. Weather conditions within the MDV are also highly variable over both spatial and temporal scales (Doran et al., 2002), making modeling of atmospheric parameters extremely difficult. Lastly, our DOS-R-corrected ALI data are in good agreement with our already ground-truth corrected Landsat scenes. The results showed very good agreement, particularly at wavelengths greater than 0.6 μm where the effects of atmospheric scattering are less pronounced (Fig. 5). Further use of the DOS-R method on additional ALI scenes also resulted in good inter-scene spectral agreement, indicating that, for the purposes of our spectral and geochemical investigations, the DOS-R technique performs well.

Atmospherically corrected at-sensor spectral radiance is then converted to surface reflectance using the following equation (Chander et al., 2009):

$$\rho_\lambda = \frac{\pi \times L_\lambda \times d^2}{ESUN_\lambda \times \cos\theta_s}$$

where ρ_λ is the planetary reflectance [unitless], L_λ is the spectral radiance at the sensor's aperture [W/(m^2 sr μm)], d is the Earth-Sun distance on the date of acquisition [astronomical units], $ESUN_\lambda$ is the mean exoatmospheric solar irradiance [W/(m^2 μm)], and θ_s is the solar zenith angle [degrees]. Atmospherically corrected reflectance measurements of compositionally pure locations in the MDV are in good agreement with laboratory measurements (Fig. 6a), which confirms the efficacy of the DOS-R technique.

Following the calculation of surface reflectance for each spectral band (after atmospheric correction, ρ_λ is equivalent to surface reflectance), the individual spectral bands were stitched and mosaicked using the Environment for Visualizing Images (ENVI) software developed by Exelis Visual Information Solutions.

ASTER thermal infrared images consist of five spectral bands ranging from 8.3 μm to 11.4 μm, have an optimal spatial resolution of 90 m pix^{-1}, and are acquired using a whiskbroom mechanism (ERSDAC, 2005). Five ASTER scenes were utilized in the production of the spectral mapping product (Table 1) and were acquired from the NASA Land Processes Distributed Active Archive Center (LP DAAC) at https://lpdaac.usgs.gov/lpdaac/get_data/wist (date accessed: 13 August 2010). Data were acquired as Level 2B AST_05 products, which have already been calibrated and converted to surface emissivity using the Temperature/Emissivity Separation (TES) algorithm described in Gillespie et al. (1998). These data were compared to laboratory derived emissivity measurements to ensure that the pre-calibration was effective. In all cases, the Level 2B AST_05 data of compositionally pure locales throughout the MDV were spectrally consistent with laboratory-derived spectra, confirming that further corrections or calibrations were not required (Fig. 6b). The five images were mosaicked with each other and to the five ALI images to create a single multispectral dataset.

The entire dataset was merged to accommodate the full spatial resolution of the ALI dataset. As a result, the ASTER dataset is highly pixilated in comparison to the ALI dataset, although no interpolation or data modification was applied during this process. The ten images were then geographically mosaicked in ENVI to produce a single image with fourteen spectral bands. All imagery was georeferenced prior to delivery, and

coregistration was manually verified before mosaicking. Pixels containing water, ice, snow, clouds, and shadows were removed from the spectral mosaic through isolation of their unique spectral properties, as discussed below. The resultant product consists of 1.57×10^6 multispectral data points over the ice-free MDV. A parameterization of this final spectral product is shown in Figure 1.

High latitude mountainous terrains are influenced by considerable variations in illumination angle in addition to the presence of pronounced shadows. Topography and illumination angle have been shown to not influence remote spectral identifications (Domingue and Vilas, 2007), although they have been shown to have minor effects on mineral abundance estimations using nonlinear modeling techniques (Cord et al., 2005).

Water, ice, snow, and clouds are easily separated from rocky surfaces using atmospherically corrected surface reflectance data. In the VNIR, water and ice have reflectance maxima in the visible wavelengths and their reflectance decreases significantly at longer wavelengths (Fig. 7a). In contrast, rocky surfaces generally exhibit relatively low reflectance values in the visible wavelengths as compared to longer wavelengths. To exploit these spectral disparities, a spectral parameter was established to identify water- and ice-rich pixels. If the corrected surface reflectance value at 0.565 μm is more than twice that at 1.65 μm, the pixel was removed from the scene. In the TIR, water and ice exhibit relatively high emissivity values across the entire ASTER spectral range relative to rocky surfaces, which exhibit large variations due to the presence of diagnostic structural vibrations (Fig. 7b). To exploit this spectral characteristic, pixels were determined to be contaminated by water or ice if the average emissivity value over

all five spectral bands was greater than 0.95. These pixels were identified and removed from the spectral mosaic.

Spectral parameters were also developed to identify shadowed regions following the removal of pixels contaminated by water and ice. In the VNIR, pixels dominated by rocky materials typically exhibit high reflectance values in the ALI band positioned at 1.65 μm. For example, the final spectral dataset has an average reflectance value at 1.65 μm of 0.183 with a standard deviation of 0.097. Shadowed regions, however, exhibit extremely low reflectance values following atmospheric correction. As a result, pixels exhibiting a reflectance at 1.65 μm less than 0.03 were identified and removed, as they are dominated by shadows. ASTER data were already corrected for the effects of shadows during TES processing and surface emissivity derivation (Gillespie et al., 1998), and the algorithm is capable of calculating emissivity values regardless of time of day or extent of shadowing.

2.3 Identification of spectrally pure dolerite using ASTER TIR data

Assessing the spectral variability within purely doleritic terrains requires that the data be limited exclusively to regions composed of dolerites and lack significant abundances of other lithologies. Deriving the areal abundance of surface compositions is theoretically straightforward using TIR emission spectroscopy due to the extremely high absorption coefficients exhibited by most geologic materials in this wavelength region. As a result, the observed spectral signal is derived from the uppermost surface and is a linear combination of the compositional constituents present on the surface (Ramsey and Christensen, 1998). Deconvolving complex mixtures in the VNIR spectral region is more complex due to the significant contribution of volume scattering of rays that have been

refracted into and out of individual mineral grains (Hapke, 1981). However, mineral identification and parameterization in the VNIR spectral region is a widely used technique that has been verified through both field and laboratory validation.

We ran a least squares linear retrieval algorithm (Ramsey and Christensen, 1998) using spectral endmembers derived from laboratory measurements to identify regions that are spectrally dominated by dolerite using in the TIR. Because this algorithm limits the number of endmembers to one fewer than the number of spectral bands, our library is limited to a maximum of four endmembers. The four selected endmembers highlight the extremes of lithological variation throughout the MDV (Fig. 8). Unaltered dolerites from Beacon Valley and Bull Pass were selected to represent the Mg-poor and Mg-rich endmembers of the Ferrar Dolerite, respectively, while a granite from Victoria Valley and quartzite from Wright Valley were chosen to represent the Si-rich lithologic endmembers (e.g., the Granite Harbour Intrusives and the Beacon Supergroup, respectively).

The results of this unmixing algorithm are reported in Fig. 9. The unmixing yields an average root-mean-squared (RMS) error of 0.0048 ± 0.0033, indicating that the majority of the spectral diversity within the scene can be accounted for by these four spectral endmembers. The highest RMS error values (0.041) appear to be associated with atmospheric contamination and clouds that were not properly removed during calibration, as the spectra do not appear consistent with any known geologic materials that are present within the MDV and are often tightly aggregated. The lack of areas with high RMS error associated with geographically coherent units indicates that no major lithologies are being excluded from our endmember library.

Areas identified as non-pure dolerite pixels (< 90% Mg-poor + Mg-rich dolerites, as modeled during linear unmixing) were removed from the rest of the spectral mapping product, leaving only those pixels mapped as having > 90% modeled dolerite. The sensitivity of thermal wavelengths to the presence of quartz makes the detection of even small amounts of granite and quartzite contamination possible. The 90% threshold for dolerite abundance was selected to minimize the spectral contribution of quartzites and granites; the number holds no geologic or geochemical significance. As a result, we utilized this constraint to qualitatively select our regions of spectrally pure dolerite.

2.4 Identification of spectral variability within the Ferrar Dolerite using ASTER TIR data

Subsequent to subsetting pure dolerite pixels from the rest of the image, an endmember library containing unaltered Mg-rich dolerite, unaltered Mg-poor dolerite, and altered Mg-poor dolerite was used to unmix the pure dolerite pixels to assess the primary mineralogy and the extent of surface alteration contributing to these pixels (Fig. 8). An altered Mg-rich dolerite was not included in this endmember library because of its absence from our sample suite, which will be discussed below. Altered dolerite surfaces exhibit strong Fe^{3+} absorption features at visible wavelengths, but lack any diagnostic near-infrared spectral signatures. In contrast, altered dolerite surface exhibit a dramatic sharpening of the major TIR absorption feature centered near 9.1 μm as a result of the breakdown of microscale mineral structures (Salvatore et al., unpublished data). While considerably different from the unaltered dolerite spectra, the overall spectral shape of the altered Mg-poor dolerite is also different from that of granites or quartzites. Accordingly, in the previous unmixing algorithm, units containing substantial quantities

of altered dolerites were mapped as unaltered dolerites with slightly higher RMS errors; this can be seen in Figure 9f in southern Beacon Valley. To ensure that granitic or quartzitic components were successfully eliminated from the pure dolerite pixels assessed here, both granite and quartzite endmembers were alternated into this second unmixing model. Only 74 pixels were modeled as including more than 10% granite or quartzite, with the highest abundance being 15.14%. These pixels were removed to ensure that the pixels under investigation consist of spectrally pure dolerite surfaces.

2.5 Resultant spectral products

Two spectral products result from the assembly of these datasets. The first product is a 14-band multispectral image of pure dolerite pixels throughout the MDV, which provides the spectral data necessary to create summary parameters (e.g., Table 3). The spatial resolution of the VNIR and TIR datasets are 30 m pix^{-1} and 90 m pix^{-1}, respectively. The second product is a 5-band linear unmixing product, mapping the relative percentage of Mg-poor unaltered dolerite, Mg-poor altered dolerite, and Mg-rich unaltered dolerite throughout the scene, normalized to 100%. The other two bands consist of a modeled blackbody component, which is used to scale the endmember spectra to fit the measured ASTER data, in addition to a band containing the modeled RMS error for each pixel. These three-dimensional products (two spatial dimensions, one spectral dimension) provide the ability to assess the spatial distribution of these spectral components throughout the MDV. Additionally, spectral profiles can be generated to highlight the observed and modeled spectral variability along transects.

3.0 Results

Granites, quartzites, and dolerites each have unique spectral properties that can be identified and measured in the VNIR (Fig. 10) and TIR (Fig. 8). Laboratory spectral measurements provide hyperspectral data with which to interpret our multispectral orbital datasets.

3.1 Laboratory spectroscopy

Laboratory VNIR spectra of samples from the Granite Harbour Intrusives (green spectrum, Fig. 10) show a relatively flat spectrum after a rapid increase in reflectance to approximately 0.6 μm with several sharp vibrational absorption features associated with OH^- and H_2O. These absorption features can be explained by a combination of an Al-OH phyllosilicate (likely muscovite; 1.4 μm, 1.9 μm, 2.2 μm) in addition to varying amounts of prehnite (1.5 μm, 2.35 μm), a Ca-Al silicate hydroxide that forms in specific metamorphic environments (Ehlmann et al., 2009). The TIR is dominated by a broad absorption feature near 9 μm with variable quartz signatures and a lack of mafic mineral absorptions present at wavelengths between 10 μm and 12 μm. When convolved to orbital bandpasses, the VNIR spectra of granites and granodiorites are relatively featureless with a steady increase in reflectance to 1.65 μm, whereas the TIR exhibits low emissivity values short of 10 μm followed by a rapid increase in emissivity beyond 10 μm (green spectrum, Fig. 8).

Most outcrop-forming exposures of the Beacon Supergroup consist of quartzites with occasional shale, siltstone, and mudstone interbeds (Isaac et al., 1995). The quartzites exhibit a similar spectral shape to the granites and granodiorites in the VNIR, exhibiting a relatively flat spectrum that steadily increases in reflectance until a maximum at approximately 1.7 μm (blue spectrum, Fig. 10). The vibrational absorption

features associated with OH^- and H_2O are much stronger than those observed in the granites and can be explained by the presence of opaline silica (1.4 μm, 1.45 μm, 1.9 μm, 2.2 μm) and illite (1.4 μm, 1.9 μm, sharp 2.2 μm). The TIR emission spectra are dominated by the diagnostic quartz absorptions centered near 8.4 μm and 8.9 μm with an emissivity peak between the two absorptions near 8.62 μm. The remainder of the TIR spectrum is relatively featureless until approximately 12.5 μm, where a second pair of absorption features unique to quartz is present. Convolved to the orbital bandpasses, the quartzites exhibit a similar VNIR spectral shape to that of granites and granodiorites, except that the increase in reflectance up to 1.65 μm and the decrease in reflectance beyond 1.65 μm are both typically of greater magnitude. In the TIR, the first three ASTER bands are able to capture the absorption doublet and emission peak unique to quartz, while the last two bands exhibit significantly higher emissivity values (blue spectrum, Fig. 8).

Two distinct classes of the Ferrar Dolerite are evident in the laboratory VNIR dataset. The first class of dolerites exhibits a low albedo and a relatively weak 1 μm and 2 μm absorption features associated with opx (Adams, 1974) (purple spectrum, Fig. 10). Additionally, the presence of a relatively broad absorption feature at 1.2 μm due to the Fe present in the M1 site of pyroxenes (Klima et al., 2008) causes the reflectance peak beyond 1 μm to be located at approximately 1.6 μm. The second class of dolerites is characterized by strong 1 μm and 2 μm absorption features and a masking of the weaker 1.2 μm absorption feature that is present in the first class of dolerites, causing the local reflectance maximum to be located near 1.3 μm (orange spectrum, Fig. 10). When convolved to orbital bandpasses, the spectral shapes of these classes are easily

distinguished by (1) the strength of the broad 1 μm and 2 μm opx absorption features (regarded as VNIR mafic band strength (MBS), see Table 3) and (2) the position of the local reflectance maximum at either 1.25 μm or 1.65 μm. The TIR signatures of these dolerite classes are also unique. The emissivity spectra from the first class of dolerites exhibit a broad and complex absorption feature between 8 μm and 12 μm with evidence for quartz, plagioclase, opx, and other minor phases (purple spectrum, Fig. 8). The second class of dolerites, however, exhibits stronger opx absorptions centered near 9.1 μm and 11 μm. When convolved to orbital bandpasses, the second class of dolerites exhibit a stronger decrease in emissivity between 8.6 μm and 9.1 μm, in addition to a less pronounced increase in emissivity between 9.1 μm and 10.65 μm, which reflect the additional opx contribution (orange spectrum, Fig. 8).

While plagioclase fractionation and variability has been previously studied (e.g., Fleming et al., 1995), this component is difficult to assess using our spectroscopic techniques. In the VNIR, crystalline plagioclase exhibits a relatively weak and broad crystal field absorption near 1.25 μm due to the substitution of trace amounts of Fe^{2+} for Ca^{2+} (Adams and McCord, 1971). This feature, however, is commonly masked by the 1.2 μm pyroxene absorption feature (Klima et al., 2008). The minor TIR spectral variations expected for varying degrees of plagioclase fractionation are also difficult to observe in our analyses due to the broad and complex absorptions caused by multiple overlapping silicate mineralogies. However, the strong and diagnostic pyroxene absorption features are readily distinguishable in both VNIR and TIR spectral regions.

The altered surfaces of many fine grained dolerites exhibit unique TIR spectral signatures. These signatures are dominated by a strong decrease in emissivity between

8.6 μm and 9.1 μm, followed by a sharp increase in emissivity from 9.1 μm to 10.65 μm (red spectrum, Fig. 8). This spectral shape is diagnostic of the breakdown of mineral structures at the rock surface as a result of surface oxidation and alteration and will be discussed further below.

3.2 Lithological mapping from orbit

Laboratory spectra provide the necessary validation for interpreting orbital spectral signatures. Spectral parameters were heavily used to exploit unique spectral features (Table 3). In Figure 1, MBS is mapped in red, the intensity of the reflectance increase between 1.25 μm and 0.79 μm is mapped in green, and the height of the quartz emissivity peak at 8.62 μm relative to the depth of the two adjacent absorption features is mapped in blue. When combined into a single image, these parameters prominently highlight the lithologic diversity throughout the MDV (Fig. 1).

Figure 11 compares the MBS relative to the strength of the quartz emissivity maximum for all of the pixels in the final spectral mapping product. Dolerites plot towards stronger MBS, whereas granites and quartzites plot at intermediate and strong quartz emissivity maximum values, respectively. The dense data cloud representative of weak values for each parameter represents the widespread and homogeneous sediments present in the valley floors and along mixed talus slopes, which comprise most of the image. When values for representative in-scene endmembers (boxes with widths and heights of one standard deviation) are plotted, it is evident that the representative laboratory measurements (circles) accurately represent the lithologies present throughout the MDV. The largest offset between laboratory and in-scene endmembers is associated with the dolerites, although there is a slight offset with quartzite measurements as well.

Sub-pixel mixing of quartz- and opx-rich material with the Mg-rich dolerites and quartzites, respectively, can explain the observed offset between laboratory and in-scene endmembers. The Mg-poor dolerite laboratory endmembers measured in this study were obtained from Beacon Valley, which is composed largely of quartz-normative dolerites, whereas portions of the lower sills are composed of hypersthene-normative dolerites (Fleming *et al.* 1995). As a result, the Mg-poor dolerites selected for laboratory measurements are expected to be the quartz-rich dolerite endmembers, as is confirmed in Figure 11.

3.3 Spectral variability of pure dolerite

Purely doleritic pixels show a range of spectral variability associated with diagnostic compositional properties. Mapping the MBS in ALI reveals widespread variability throughout the Labyrinth, Victoria Valley, and Central Wright Valley, whereas Beacon Valley exhibits uniformly low values with little variability (Fig. 12). The strong MBS values are restricted to the middle of the lower dolerite sills and are absent from any surfaces dominated by dolerites from the upper sills. A similar distribution can be identified by mapping the location of the local reflectance maximum at either 1.25 μm or 1.65 μm, which was shown earlier to be diagnostic of pyroxene content. The centers of the lower sills exhibit the reflectance maximum at 1.25 μm, whereas the margins of the lower sills and the entirety of the upper sills exhibit the reflectance maximum at 1.65 μm (Fig. 13).

While ALI only has one spectral band located in the region dominated by OH^- combination tones (band 10, 2.215 μm), its broad full width at half maximum (0.135 μm) and the lack of other nearby spectral bands also make the identification of hydrated

alteration phases difficult. As a result, in the absence of additional mineralogical information, ALI cannot be used to determine the presence or abundance of hydrated alteration phases. However, none of the dolerites investigated in this study exhibit vibrational absorption features between 2.0 μm and 2.5 μm. All dolerite surfaces instead exhibit strong absorption features at wavelengths shorter than 0.7 μm that are associated with Fe^{3+}. Unfortunately, these features are also difficult to characterize using ALI due to the unavoidable influences of Rayleigh scattering in the remote investigations of high latitudes. As a result, we have not considered quantitatively assessing the degree of surface oxidation using this spectral region.

Significant variability in TIR spectra is observed throughout the Ferrar Dolerite, as is evident from the linear unmixing of purely doleritic pixels (Fig. 14). The low average RMS error (0.0043 ± 0.0016) confirms the goodness of fit of the model. In Beacon Valley, the most significant spectral contributor is the altered Mg-poor dolerite, with only minor contributions from the unaltered endmembers. In the Labyrinth, unaltered mafic dolerite signatures dominate the central regions with perhaps the strongest signatures present along the scree slopes. Altered dolerite signatures are modeled along the western, northern, and southern margins. The Labyrinth shows the largest RMS errors associated with the unmixing algorithm, although the values still represent good spectral fits. These high RMS errors are likely to be a result of the Mg-rich dolerite endmember spectrum being derived from samples largely collected from Victoria Valley and Bull Pass, with only a few samples collected from the Labyrinth. Central Wright Valley and Bull Pass are also dominated by unaltered mafic dolerites, with less mafic dolerite contributing significantly to the dolerite lobe along the

southeastern portion of Central Wright Valley and altered dolerite signatures modeled along the eastern edge of Bull Pass. Lastly, Victoria Valley is largely characterized by unaltered mafic materials, while substantial altered components are modeled along the northwestern portion of Victoria Valley as well as along the central portion of the exposed sill.

The alteration signatures observed in the Labyrinth are particularly intriguing due to their distribution only along the western, northern, and southern margins (Fig. 14d), where the current surface elevations are highest. To test the relationship between alteration signatures and surface elevation, an average of fifteen south-to-north profiles was made across the Labyrinth with the surface elevation (as measured by airborne LIDAR measurements (Schenk et al., 2004)) and the modeled abundance of altered dolerite values extracted. There is a clear relationship between higher elevations and higher modeled abundances of altered dolerites (Fig. 15a). The Pearson correlation coefficient of the relationship between these two parameters is 0.56, with a Student's t-test value confirming to a 95% confidence level that the elevation of the surface provides information to the prediction of the modeled altered surface abundance. In addition, the sum of the chi-square value is equal to 35.5 with 181 degrees of freedom, verifying that there is a probability of less than 1% that the data can be explained by randomness alone. Together, these statistical tests conclude that areas of higher elevation in the Labyrinth are correlated with regions of higher modeled altered dolerite abundances. A single representative topographic profile is provided in Figure 15b to highlight the topographic variability within the Labyrinth and along its margins. Background colors are consistent

with the stratigraphic profile in Figure 2 and demarcate the approximate locations of the sill chilled margins and the opx-enriched interior.

3.4 Chemical variability within the Ferrar Dolerite

Bulk rock MgO and CaO concentrations follow similar trends to those identified in Marsh (2004), with more evolved magmas showing an increase of CaO with increased MgO below ~ 7 wt.% MgO, representing the near-liquid compositions of the upper sills and the sill margins of the lower sills (Fig. 16a). At MgO concentrations greater than ~ 7 wt.%, CaO decreases with increasing MgO concentration, representing the addition of more primitive opx-bearing magmas. A similar relationship is also seen when plotting the MBS against MgO (Fig. 16b); below ~ 7 wt.%, the strength of the MBS remains relatively constant, whereas samples with MgO concentrations greater than 7 wt.% show a systematic increase in MBS. Because ALI bandpasses were used to calculate the MBS in laboratory data, this relationship can be used in the analysis of orbital datasets to approximate the MgO concentration in different doleritic regions throughout the MDV by applying the equation in Figure 16b to the map shown in Figure 12. This equation converts the low and high MBS values identified in Figure 12 to 6.6 wt.% MgO and 32.5 wt.% MgO, respectively, which are broadly consistent with MgO abundances measured in rocks from Central Wright Valley presented by Marsh (2004). These values should be regarded as estimates, as several potential sources of error exist, including the effects of topography, illumination angle, and shadows, although these effects are likely to be minor (Cord et al., 2005; Domingue and Vilas, 2007).

4.0 Discussion

4.1 Identification and distribution of doleritic signatures

The spectral signatures of purely doleritic regions of the MDV can be effectively characterized using an endmember library derived from laboratory measurements of dolerite samples documented and collected in key areas of the MDV. Variations in both primary mineralogies and secondary alteration products are identified in laboratory measurements, which can then be linked to spectral signatures observed from orbit. For example, TIR orbital data indicates that the majority of the variability in the lower sills is due to variations in the primary mineralogy of the dolerite (Fig. 14a-c). However, in the upper sills, the presence and abundance of alteration products account for the majority of the observed spectral variability (Fig. 14d). In the VNIR, the lower sills exhibit a range of MBS values that are associated with the presence and abundance of opx-rich dolerites (Fig. 12a-c). However, the upper sills exhibit little variability in MBS, as these dolerites consist largely of fine-grained dolerites of minimal chemical variability (Fig. 12d).

Variations in primary igneous compositions are in good agreement with previous studies that have identified major chemical variations within the Ferrar Dolerites exposed throughout the MDV. The zones of opx-enrichment identified by Marsh (2004) are clearly visible in VNIR orbital data as the regions of heightened MBS values. Significant exposures of opx-rich dolerites that were not detailed in Marsh (2004) can also be observed and characterized from orbit, particularly in Victoria Valley and the Labyrinth (Fig. 12). The identification of these variations in primary mineralogy add spatial context to the studies of Marsh (2004), Bédard et al. (2007), and other works that use laboratory investigations to identify local mineralogical and chemical heterogeneities. Spectral

effects associated with silicic segregations were not observed in our orbital datasets due to their small spatial scales and extents (typically ≤ 2 m thick (Zavala et al., 2011)).

The distribution of secondary alteration products is also in good agreement with previous studies of chemical weathering in the MDV. The VNIR and TIR spectral signatures of dolerite surfaces from Beacon Valley exhibit unique spectral signatures, as compared to their unaltered interiors (Fig. 3), that represent anhydrous oxidation in response to the oxidizing Antarctic environment (Salvatore et al., unpublished data). While Fe^{3+} absorption features in the VNIR are difficult to characterize from orbit, the shape and characteristics of ASTER TIR spectra are consistent with the presence of altered dolerites throughout Beacon Valley (Fig. 6). These signatures are strongest along the valley floor and weakest along the western walls, suggesting that the exposed walls of Beacon Valley are younger and less altered than the floors, which have had sufficient time to develop and preserve alteration products.

Why are TIR chemical alteration signatures almost exclusively concentrated in Beacon Valley? The development of alteration products is not likely to be limited to certain rock chemistries; opx-rich lithologies are just as (if not more) susceptible to chemical alteration than those of near liquid composition (Lasaga, 1984). The maturation and preservation of alteration products is more likely to be related to variations in sill properties as exposed in the different valleys. The upper sills, which are devoid of mafic intrusions and were intruded into cold sedimentary rocks, are characterized by fine grained igneous textures. As suggested by Glasby et al. (1981), fine grained dolerites are the best hosts for alteration rinds due to their resistance to physical weathering. The lower dolerite sills were both intruded at a greater depth and were subject to multiple

episodes of magmatic injection, providing a heat source and ample time for prolonged crystal growth. Whereas some coarse grained dolerites do effectively preserve alteration rinds and their associated spectral signatures, most coarse grained dolerites are easily weakened by aeolian abrasion, thermal cycling, freeze-thaw cycling, and other means of physical breakdown and erosion (Marchant et al., 2013). As a result, alteration products that form on coarse grained dolerites are easily lost to flaking or disintegration before they can become significant spectral components of the rock surfaces.

The western, northern, and southern margins of the Labyrinth also show evidence of altered dolerite signatures in ASTER data (Fig. 14a). These areas are associated with the upper margin of the Peneplain Sill, which is relatively fine grained (as compared to the central regions of the Peneplain Sill) and has a composition similar to the near liquid dolerites from Beacon Valley (Marsh and Wheelock, 1994). Transitioning to lower elevations and into the opx-enriched portion of the Peneplain Sill, alteration signatures are modeled at lower abundances due to the difficulties associated with preserving alteration rinds (Fig. 16).

The other localized area of altered TIR signatures includes portions of Victoria Valley. The exposure of the Basement Sill in Victoria Valley is bisected by a narrow valley that connects the topographically higher Bull Pass to Lake Vida in Victoria Valley (Fig. 1). The margins of this valley exhibit TIR alteration signatures that may be associated with erosion from this ancient channel, which masks the underlying mafic compositions. However, no samples were collected from this location and so identifying the cause of the narrow reststrahlen bands is purely speculative. The northwestern margin of Victoria Valley also exhibits narrow reststrahlen bands typical of altered

dolerites (Fig. 14b). This locale appears to be a portion of the lower margin of the Basement Sill, which is thought to be associated with finer grained rocks of near liquid compositions. As a result, these signatures are likely to be associated with the preferential preservation of alteration rinds on fine grained dolerites. Lastly, a portion of the center of the Basement Sill exhibits evidence of TIR alteration signatures where the MBS values are particularly high (Fig. 12c and Fig. 14c). No samples were collected from this particular region in Victoria Valley, and only one sample collected from Victoria Valley exhibits both alteration signatures in the TIR as well as a strong 1 μm opx absorption feature, although the 2 μm feature is absent (W10_VV_D1_008, Fig. 17). This sample, although coarse grained, has a well-preserved alteration rind on its surface. A possible explanation for these orbital VNIR and TIR signatures is that the surface is dominated by rocks similar to W10_VV_D1_008, where alteration rinds are able to develop and remain preserved on the surfaces of mafic, coarse grained dolerites. Why this portion of Victoria Valley is unique, however, has yet to be constrained and will likely require future *in situ* investigations.

The spectral signatures in Victoria Valley were further investigated using a second ASTER scene obtained over Victoria Valley. This additional scene is in agreement with the one used in the MDV spectral map regarding the distribution of altered dolerites (Fig. 18). This observation confirms that the identification of alteration signatures is not an instrumental artifact or due to the presence of transient sub-pixel ice, snow, or clouds. Rather, these spectral signatures represent fundamental mineralogical and structural properties of the doleritic surfaces.

4.2 Geochemical evolution of the Ferrar Dolerite

The geochemical and mineralogical signatures associated with the emplacement of dolerite sills, and the chemical weathering following exposure to the Antarctic environment, both produce distinct spectral signatures that can be identified from orbit. During emplacement, the parental magmas of the Ferrar Dolerite were intruded into the subsurface at various depths, resulting in a range of cooling histories and initial grain sizes (e.g. Marsh, 2004; Bédard et al., 2007; Elliot and Fleming, 2008). The lower sills were then intruded with additional, more primitive magmatic slurries of liquid and opx crystals, which also acted to reheat the surrounding doleritic material and create unique crystallization patterns and cryptic banding within these sills (Marsh and Wheelock, 1995; Heyn et al., 1995). The two upper sills were never modified by subsequent injections of magmatic slurry, resulting in a preservation of the initial stages of magma intrusion, near-liquid compositions, rapid quenching, and the resultant fine grained crystals (Marsh, 2004). As we have shown in our spectroscopic investigations, the influence and distribution of these primary magmatic processes can be readily observed from orbit using both VNIR and TIR multispectral datasets due to the spectrally unique signatures of opx. These spectral data provide valuable information regarding the spatial distribution of opx enrichment and chemical variability throughout the sills.

Long after emplacement, burial, and exhumation (Fitzgerald et al., 2006), the dolerite sills were exposed throughout the MDV through a series of physical processes dominated by fluvial and glacial erosion (Sugden et al., 1995, and references therein). Once exposed to these hyper-arid and hypo-thermal environmental conditions (Marchant and Head, 2007), chemical alteration of the dolerites was able to commence. Recent

studies suggest that anhydrous alteration products dominate dolerite surfaces (Salvatore et al., unpublished data). These processes, which can proceed in the absence of liquid water, are the only known explanation for the observed geochemical and spectral signatures. Whereas the majority of the VNIR spectral modifications are difficult to quantify due to the residual effects of Rayleigh scattering, TIR spectral variations are very sensitive to these alteration processes and readily capture their variability and distribution throughout the MDV. Localized aqueous alteration has also been observed throughout the MDV (e.g., Allen and Conca, 1991; Head et al., 2011), although the preservation of mature alteration products on rock surfaces appears to be the exception rather than the norm.

The products of this chemical alteration are best preserved on fine grained dolerites, which are less susceptible to physical erosion, and result in unique spectral and chemical signatures. In contrast, coarse grained dolerites, including most of the opx-rich dolerites that underwent slow cooling at depth, lack alteration signatures because of their susceptibility to physical erosion. Regardless of grain size, rock ventifaction and disintegration as a result of freeze-thaw and thermal cycling (Glasby et al., 1981; Marchant et al., 2013) are widespread throughout the MDV and confirm the dominance of physical erosion over chemical alteration.

5.0 Conclusions

We have presented the results of a combined laboratory and orbital investigation to identify and interpret geochemical signatures of the Ferrar Dolerite throughout the MDV. Our analyses conclude that:

(1) Dolerites exhibit unique VNIR and TIR spectral signatures as a result of both primary geochemical properties as well as secondary chemical alteration;

(2) Linear unmixing of ASTER data using a laboratory-derived endmember library is able to identify spectrally pure dolerite pixels in orbital datasets based on their diagnostic TIR spectral signatures;

(3) Laboratory investigations reveal an association between the strength of the strength of opx absorption features in the VNIR and the bulk MgO content of the dolerites. When applied to ALI data, the measured MgO contents throughout the dolerite sills are consistent with previous studies. Additionally, this analysis is the first complete assessment of the spatial distribution of exposed opx-rich sill interiors throughout the MDV;

(4) TIR signatures of altered dolerites are largely restricted to Beacon Valley and the margins of the Labyrinth. Only fine grained dolerites are capable of preserving mature alteration rinds that result in these spectral signatures. This observation explains the scarcity of altered Mg-rich dolerites in our collected sample suite.

Future use of additional multispectral and hyperspectral datasets can provide critical information regarding the presence, nature, and distribution of crystalline alteration products throughout the MDV. For example, ASTER shortwave-infrared (SWIR) datasets can provide additional spectral resolution between 2.0 – 2.5 μm, which could help to identify the presence and distribution of phyllosilicates, sulfates, and carbonates throughout the MDV. These data were excluded from this study largely due to the incomplete spatial coverage of cloud-free images. While absorption features have not been identified in this wavelength region as a result of dolerite alteration processes,

the analysis of glacial till and the other prominent lithologies may benefit greatly from the addition of these spectral bands. The acquisition of additional cloud-free ASTER SWIR imagery would be beneficial to these types of studies. Additional *in situ* reflectance and emissivity measurements of doleritic surfaces would help to reduce some of the short wavelength scattering and aerosol contributions associated with remote sensing at high latitudes. These in situ measurements may help to better study the nature and distribution of Fe^{3+} phases and could help to assess the effects of oxidation outside of Beacon Valley.

Our analyses demonstrate that multispectral orbital datasets can be used to better characterize the magmatic, climatic, and alteration histories of the Ferrar Dolerite within the MDV. The identification and characterization of pure doleritic terrains throughout the MDV has helped to constrain the spatial distribution of complex magmatic and alteration products, which has significant implications for the geologic and weathering histories within the Transantarctic Mountains.

Acknowledgements

This work was funded by the National Science Foundation Antarctic Science Division (Office of Polar Programs) through grants to James W. Head (ANT-0739702) and David R. Marchant (ANT-0944702), which are gratefully acknowledged. Logistical support for this project was provided by the U.S. National Science Foundation through the U.S. Antarctic Program. The authors would also like to thank Raytheon Polar Services Company, the United States Air Force 62nd Airlift Wing, and PHI, Inc., for their assistance and support during the 2009-2010 and 2010-2011 austral summer field

expeditions. We thank James Dickson, Laura Kerber, Gareth Morgan, Brandon Boldt, Sylvain Piqueux, David Hollibaugh Baker, J. R. Skok, Sean Mackay, Jennifer Lamp, Jack Seeley, Sandra Wiseman, Tim Goudge, Rebecca Greenberger, Kevin Cannon, Paul Morin, Tim Glotch, Deanne Rogers, Takahiro Hiroi, Dave Murray, Joe Orchardo, Andrea Weber, the Keck/NASA Reflectance Experiment Laboratory (RELAB) at Brown University, and the Vibrational Spectroscopy Laboratory at Stony Brook University for their assistance with field work, orbital analyses, and laboratory measurements. This manuscript benefitted greatly from the reviews by Christian Haselwimmer, Teal Riley, and Alan Vaughan, for which we are sincerely grateful.

References

Adams J. B. (1974), Visible and near-infrared diffuse reflectance spectra of pyroxenes as applied to remote sensing of solid objects in the solar system. *J. Geophys. Res.* **79**, 4829-4836.

Adams J. B. and McCord T. B. (1971), Optical properties of mineral separates, glass, and anorthositic fragments from Apollo mare samples. *Proc. Lunar Planet. Sci. Conf.* **3**, 2183-2195.

Allen C. C. and Conca J. L. (1991), Weathering of basaltic rocks under cold, arid conditions: Antarctica and Mars. *Proc. Lunar Planet. Sci. Conf.* **21**, 711-717.

Bédard J. H. J., Marsh B. D., Hersum T. G., Naslund H. R. and Mukasa S. B. (2007), Large-scale mechanical redistribution of orthopyroxene and plagioclase in the Basement Sill, Ferrar Dolerites, McMurdo Dry Valleys, Antarctica: Petrological,

mineral-chemical and field evidence for channelized movement of crystals and melt. *J. Petrol.* **48**, 2289-2326.

Chander G., Markham B. L. and Helder D. L. (2009), Summary of current radiometric calibration coefficients for Landsat MSS, TM, ETM+, and EO-1 ALI sensors. *Rem. Sens. of Env.* **113**, 893-903.

Chavez Jr. P. S. (1996), Image-based atmospheric corrections – Revisited and improved. *Photogram. Eng. & Rem. Sens.* **62**, 1025-1036.

Christensen P. R., Bandfield J. L., Hamilton V. E., Howard D. A., Lane M. D., Piatek J. L., Ruff S. W. and Stefanov W. L. (2000), A thermal emission spectral library of rock-forming minerals. *J. Geophys. Res.* **105**, 9735-9739.

Cooper R. F., Fanselow J. B. and Poker D. B. (1996), The mechanism of oxidation of a basaltic glass: Chemical diffusion of network-modifying cations. *Geochim. Cosmochim. Acta* **60**(17), 3253-3265.

Cord A. M., Pinet P. C., Daydou D. and Chevrel S. D. (2005), Experimental determination of the surface photometric contribution in the spectral reflectance deconvolution processes for a simulated Martian crater-like regolith target. *Icarus* **175**, 78-91.

Domingue D. and Vilas F. (2007), Local topographic effects on photometry and reflectance spectra of planetary surfaces: An example based on lunar photometry. *Met. & Planet. Sci.* **42**(10), 1801-1816.

Doran P. T., McKay C. P., Clow G. D., Dana G. L., Fountain A. G., Nylen T. and Lyons W. B. (2002), Climate observations from the McMurdo Dry Valleys, Antarctica, 1986-2000. *J. Geophys. Res.* **107**, doi:10.1029/2001JD002045.

Ehlmann B. L., Mustard J. F., Swayze G. A., Clark R. N., Bishop J. L., Poulet F., Des Marais D. J., Roach L. H., Milliken R. E., Wray J. J., Barnouin-Jha O. and Murchie S. L. (2009), Identification of hydrated silicate minerals on Mars using MRO-CRISM: Geologic context near Nili Fossae and implications for aqueous alteration. *J. Geophys. Res.* **114**, doi:10.1029/2009JE003339.

Elliot D. H. and Fleming T. H. (2004), Occurrences and dispersal of magmas in the Jurassic Ferrar large igneous province, Antarctica. *Gondwana Res.* **7**(1), 223-237.

ERSDAC, SNM (2005), ASTER Users Guide, Part 1 General, Version 4. http://www.science.aster.ersdac.or.jp/en/documents/users_guide/part1/pdf/Part1_4E.pdf, Date Accessed: 12 June 2012.

Farmer V. C. (1974), *The Infrared Spectra of Minerals*, Mineralogical Society, London, 539 pp.

Fleming T. H., Foland K. A. and Elliot D. H. (1995), Isotopic and chemical constraints on the crustal evolution and source signature of Ferrar magmas, north Victoria Land, Antarctica. *Contrib. Min. & Petr.* **121**, 217-236.

Fleming T. H., Heimann A., Foland K. A. and Elliot D. H. (1997), $^{40}Ar/^{39}Ar$ geochronology of Ferrar Dolerite sills from the Transantarctic Mountains, Antarctica: Implications for the age and origin of the Ferrar magmatic province. *Geol. Soc. Am. Bull.* **109**(5), 533-546.

Fitzgerald P. G., Baldwin S. L., Webb L. E. and O'Sullivan P. B. (2006), Interpretation of (U-Th)/He single grain ages from slowly cooled crustal terranes: A case study from the Transantarctic Mountains of southern Victoria Land. *Chem. Geol.* **255**(1-2), 91-120.

Fountain A. G., Nylen T. H., Monaghan A., Basagic H. J. and Bromwich D. (2009), Snow in the McMurdo Dry Valleys. *Int. J. Climat.* **30**, doi:10.1002/joc.1933.

Gillespie A., Rokugawa S., Matsunaga T., Cothern S., Hook S. and Kahle A. B. (1998), A temperature and emissivity separation algorithm for Advanced Spaceborne Thermal Emission and Reflection radiometer (ASTER) images. *Inst.Elect. & Electr. Eng. Trans. on Geosci. & Rem. Sens.* **36**, 1113-1126.

Glasby G. P., McPherson J. G., Kohn B. P., Johnston J. H., Freeman A. G. and Tricker M. J. (1981), Desert varnish in Southern Victoria Land, Antarctica. *N. Z. J. Geol. & Geophys.* **24**, 389-397.

Hapke B. (1981), Bidirectional reflectance spectroscopy 1: Theory. *J. Geophys. Res.* **86**, 3039-3054.

Head J. W., Kreslavsky M. A. and Marchant D. R. (2011), Pitted rock surfaces on Mars: A mechanism of formation by transient melting of snow and ice. *J. Geophys. Res.* **116**, doi:10.1029/2011JE003826.

Heyn J., Marsh B. and Wheelock M. (1995), Crystal size and cooling time in the Peneplain sill, dry valley region, Antarctica. *Ant. J. of the U. S.* **30**, 50-51.

Isaac M. J., Chinn T. J., Edbrooke S. W. and Forsyth P. J. (1995), Geology of the Olympus Range area, southern Victoria Land, Antarctica. Scale 1:50,000. *N. Z. Inst. of Geol. & Nucl. Sci.*, geol. map 20.

Klima R. L., Pieters C. M. and Dyar M. D. (2008), Characterization of the 1.2 μm M1 pyroxene band: Extracting cooling history from near-IR spectra of pyroxenes and pyroxene-dominated rocks. *Met. & Planet. Sci.* **43**, 1591-1604.

Lasaga A. C. (1984), Chemical kinetics of water-rock interactions. *J. Geophys. Res.* **89**, 4009-4025.

Lewis A. R., Marchant D. R., Kowalewski D. E., Baldwin S. L. and Webb L. E. (2006), The age and origin of the Labyrinth, western Dry Valleys, Antarctica: Evidence for extensive middle Miocene subglacial floods and freshwater discharge to the Southern Ocean. *Geology* **34**, 513-516.

Lu D., Mausel P., Brondizio E. and Moran E. (2002), Assessment of atmospheric correction methods for Landsat TM data applicable to Amazon basin LBA research. *Int. J. Rem. Sens.* **23**(13), 2651-2671.

Marchant D. R. and Head III J. W. (2007), Antarctic dry valleys: Microclimate zonation, variable geomorphic processes, and implications for assessing climate change on Mars. *Icarus* **192**, 187-222.

Marchant D. R., Mackay S., Lamp J. L., Hayden A. T. and Head J. W. (2013), A review of geomorphic processes and landforms in the Dry Valleys of southern Victoria Land: Implications for evaluating climate change and ice-sheet stability. *In* Hambrey M. J., Barker P. F., Barrett P. J., Bowman V., Davies B., Smellie J. L. and Tranter M., *eds. Antarctic Palaeoenvironments and Earth-Surface Processes*. London: Geological Society Special Pub. **381**, *in press*. http://dx.doi.org/10.1144/SP381.10.

Marsh B. (2004), A magmatic mush column Rosetta Stone: The McMurdo Dry Valleys of Antarctica. *Eos Trans. of the Amer. Geophys. Union* **85**, 497-508.

Marsh B. D. and Wheelock M. K. (1994), The vertical variation of composition in the Peneplain and Basement Sills of the McMurdo Dry Valleys: The null hypothesis. *Ant. J. of the U. S.* **29**, 24-25.

Mendenhall J. A., Bernotas L. A., Bicknell W. E., Cerrati V. J., Digenis C. J., Evans J. B., Forman S. E., Hearn D. R., Hoffeld R. H., Lencioni D. E., Nathanson D. M. and Parker A. C. (2000), Earth Observing-1 Advanced Land Imager: Instrument and flight operations overview. *Massachusetts Institute of Technology & Lincoln Laboratory Project Report EO-1-1*.

Murray R. W., Miller D. J. and Kryc K. A. (2000), Analysis of major and trace elements in rocks, sediments, and interstitial waters by Inductively Coupled Plasma-Atomic Emission Spectroscopy (ICP-AES). *Texas A&M University, Ocean Drilling Program Technical Note 29*, 21 pp.

Mustard J. F. and Pieters C. M. (1989), Photometric phase functions of common geologic minerals and applications to quantitative analysis of mineral mixture reflectance spectra. *J. Geophys. Res.* **94**, 13619-13634.

Pieters C. M. (1983), Strength of mineral absorption features in the transmitted component of near-infrared reflected light: First results from RELAB. *J. Geophys. Res.* **88**, 9534-9544.

Ramsey M. S. and Christensen P. R. (1998), Mineral abundance determination: Quantitative deconvolution of thermal emission spectra. *J. Geophys. Res.* **103**, 577-596.

Schenk T., Csatho B., Ahn Y., Yoon T., Shin S. W. and Huh K. I. (2004), DEM generation from the Antarctic LIDAR data: Site report. Available from: http://usarc.usgs.gov/lidar/lidar_pdfs/Site_reports_v5.pdf, 49 pp.

Schwerdtfeger W. (1984), *Weather and climate of the Antarctic*. Amsterdam: Elsevier, 327 pp.

Sugden D. E., Denton G. H. and Marchant D. R. (1995), Landscape evolution of the Dry Valleys, Transantarctic Mountains: Tectonic implications. *J. Geophys. Res.* **100**, 9949-9967.

Zavala K., Leitch A. M. and Fisher G. W. (2011), Silicic segregations of the Ferrar Dolerite sills, Antarctica. *J. Petrol.* **52**(10), 1927-1964.

Figure and Table Descriptions

Figure 1. Spectral parameter map of the McMurdo Dry Valleys. Mafic band strength (MBS) is mapped in red, NIR spectral slope is mapped in green, and the strength of the quartz emissivity peak is mapped in blue (Table 3). Dark object subtraction-regression (DOS-R) locations are marked by orange stars, in situ spectral grid locations are marked by blue stars, and the locations of the four primary study regions in this work are outlined in yellow.

Figure 2. Stratigraphy of the McMurdo Dry Valleys in the area of this study, adapted from Marsh (2004). The stratigraphy of the four primary doleritic sills is shown in purple, whereas the approximate location of the opx-enriched magmatic slurry signatures are shown in yellow. The stratigraphic location of the four study regions are also approximated on the left side of the section.

Figure 3. (a) Visible/near-infrared and (b) thermal infrared spectra of averaged unaltered dolerite interiors (purple) and dolerite surfaces (red) from Beacon Valley. Dolerite surfaces are characterized by strong Fe^{2+}-Fe^{3+} intervalence charge-transfer absorptions at wavelengths shorter than 0.7 μm and an overall higher albedo in the near-infrared. They are also characterized by narrow reststrahlen features in the thermal infrared centered near 1100 cm^{-1} (9.1 μm) and 465 cm^{-1} (21.3 μm), which represent the breakdown of silicate mineralogy into metastable alteration products.

Figure 4. (a) Frequency distributions of measured spectral radiances in each ALI band of image EO1A0581152008022110KG. Data are derived for 3,372 pixels of shadowed regions within the scene, and the plotted frequencies are individually scaled to facilitate comparisons between bands. The measured radiances represent the effect of scattered atmospheric downwelling. Dotted vertical line at 2 W/(m^2 sr μm) is magnified in (b). (b) Frequency distributions of ALI bands 8 – 10. The majority of pixels in band 10 record scattered downwelling radiances of less than 0.1 W/(m^2 sr μm), which is the foundation for our assumption that the scattered radiance component in ALI band 10 is negligible. (c) An example DOS-R regression scatterplot of 42 spectra. The y-intercepts of the modeled regressions for each band represent the scattered atmospheric downwelling radiance values. A total of 18 scattered downwelling radiance spectra were created using this method, which were used in the DOS-R atmospheric removal technique.

Figure 5. Comparison between the dark object subtraction (DOS) atmospheric removal technique used in our spectral mapping (dashed lines) and the use of in situ calibration targets to correct for atmospheric effects in a corresponding Landsat image

(solid lines). Despite the different bandpass positions, the DOS spectra are comparable to the in situ calibration technique, emphasizing the utility of this in-scene atmospheric correction. The absorption features located near 1 μm and 2 μm are associated with the presence of opx and are resolvable only in ALI data and not Landsat data.

Figure 6. (a) VNIR laboratory spectra (dark solid lines) and characteristic ALI spectra (light dashed lines) of different lithologic units. The spectral shapes are largely consistent between laboratory and orbital datasets, while offsets are likely due to sub-pixel mixing and imprecise atmospheric removal. (b) TIR laboratory spectra (dark solid lines) and characteristic ASTER spectra (light dashed lines) of different lithologic units. Data have been scaled and offset for clarity. As with the VNIR data, minor offsets are likely due to sub-pixel mixing and imprecision in the TES atmospheric removal algorithm.

Figure 7. (a) VNIR and (b) TIR spectra of ice and assorted lithologies from throughout the MDV, highlighting the ease of spectrally identifying regions influenced by significant abundances of ice, snow, water, and clouds.

Figure 8. Laboratory TIR emissivity spectra of five rock endmembers in the MDV. The spectra are also resampled to ASTER bandpasses (dots and dashed lines) and plotted with the hyperspectral laboratory data. The top four lithologies were used as spectral endmembers in the linear unmixing algorithm to identify uncontaminated doleritic terrains. The bottom three doleritic spectral endmembers highlight the range of known spectral variation in the dolerite based on laboratory measurements and were used in the linear unmixing of pure doleritic pixels.

Figure 9. The results of a linear unmixing algorithm on the full spectral map of the MDV. The root-mean-square (RMS) error, indicating the goodness of fit of the modeled spectra, shows an overall good fit to the data using the provided endmember spectra. However, slightly increased RMS errors are present in Beacon Valley and other doleritic regions and highlight regions of altered dolerite spectral signatures.

Figure 10. VNIR laboratory spectra of different lithologies found throughout the MDV. The spectra are also resampled to ALI bandpasses (dots and dashed lines) and plotted with the hyperspectral data. The unique shapes of the spectra and positions and strengths of absorption features allows for the identification of individual mineral constituents as well as the discrimination between major lithologic classes.

Figure 11. Scatterplot derived from the spectral map, plotting the strength of the mafic band strength versus the quartz emissivity peak strength. Values derived for representative rock samples measured in the laboratory are shown as colored dots (colors identical to those in Fig. 10; quartzite in blue, granite in green, Mg-poor dolerite in purple, and Mg-rich dolerite in orange). Values derived from type-locations of these lithologies as observed in our spectral dataset are plotted as shaded boxes that are one standard deviation wide in both directions. The offset between the quartzite and Mg-rich laboratory- and orbital-derived values can be explained by sub-pixel mixing, while the offset for the Mg-poor dolerite can be explained by the measurement of quartz-normative dolerites in the laboratory.

Figure 12. VNIR mafic band strength (MBS) maps of (a) the Labyrinth, (b) Victoria Valley, (c) Central Wright Valley, and (d) Beacon Valley. The location of the opx-enriched zones are clearly defined by the areas containing stronger mafic signatures.

Figure 13. Mapping the position of the NIR reflectance peak in (a) the Labyrinth, (b) Victoria Valley, (c) Central Wright Valley, and (d) Beacon Valley. The position of this reflectance peak is associated with the enrichment of opx and nicely maps the distribution of the zones of opx-enrichment identified by Marsh (2004).

Figure 14. Results of linear unmixing of ASTER TIR data of the pure doleritic regions of (a) the Labyrinth, (b) Victoria Valley, (c) Central Wright Valley, and (d) Beacon Valley. Altered doleritic signatures are extensively identified throughout Beacon Valley and are limited elsewhere throughout the MDV.

Figure 15. (a) Mean topographic and mean modeled altered surface abundance profiles of the Labyrinth of Upper Wright Valley. A strong correlation exists between the elevation and the modeled altered surface abundance. (b) A representative topographic profile through the Labyrinth. Background colors are consistent with Figure 2 and represent the approximate elevations and exposures of the Peneplain Sill upper chilled margin and opx-rich interior.

Figure 16. (a) CaO vs. MgO concentrations in rock interiors, as measured by ICP-AES. Samples from the upper sills (represented by the Beacon Valley samples) consistently contain < 7 wt.% MgO and display a positive relationship with CaO, representing more evolved magmatic chemistries. However, in the portions of the lower sills that are influenced by the addition of opx-enriched magmatic slurries, the MgO concentration increases and the relationship with CaO becomes negative, indicating the contribution of more primitive magmatic components. These trends were originally observed by Marsh (2004). (b) VNIR mafic band strength vs. MgO concentration. With the addition of a more primitive magmatic component, a linear relationship exists

between the strength of the 1 μm and 2 μm VNIR mafic bands and the concentration of MgO.

Figure 17. (a) VNIR and (b) TIR laboratory measurements of the surface of sample W10_VV_D1_008. Spectra downsampled to ALI and ASTER bandpasses are also shown. Despite the relatively strong VNIR mafic band strength, TIR data show significantly altered doleritic signatures. These spectral signatures are also found throughout a large portion of central Victoria Valley, which might indicate a region of uniquely altered Mg-rich dolerites.

Figure 18. Comparison of two different ASTER scenes of Victoria Valley, showing the consistency between modeled alteration signatures. This test confirms the spectral variability throughout this region and proves that these signatures are not the result of spectral artifacts present in one particular ASTER image.

Table 1. List of images and information used in the creation of the spectral map of the McMurdo Dry Valleys.

Table 2. Dark object subtraction (DOS) information for the atmospheric correction in Advanced Land Imager data.

Table 3. Spectral parameters used in the creation of the spectral mapping product featured in Figure 1, including the Mafic Band Strength (MBS) parameter.

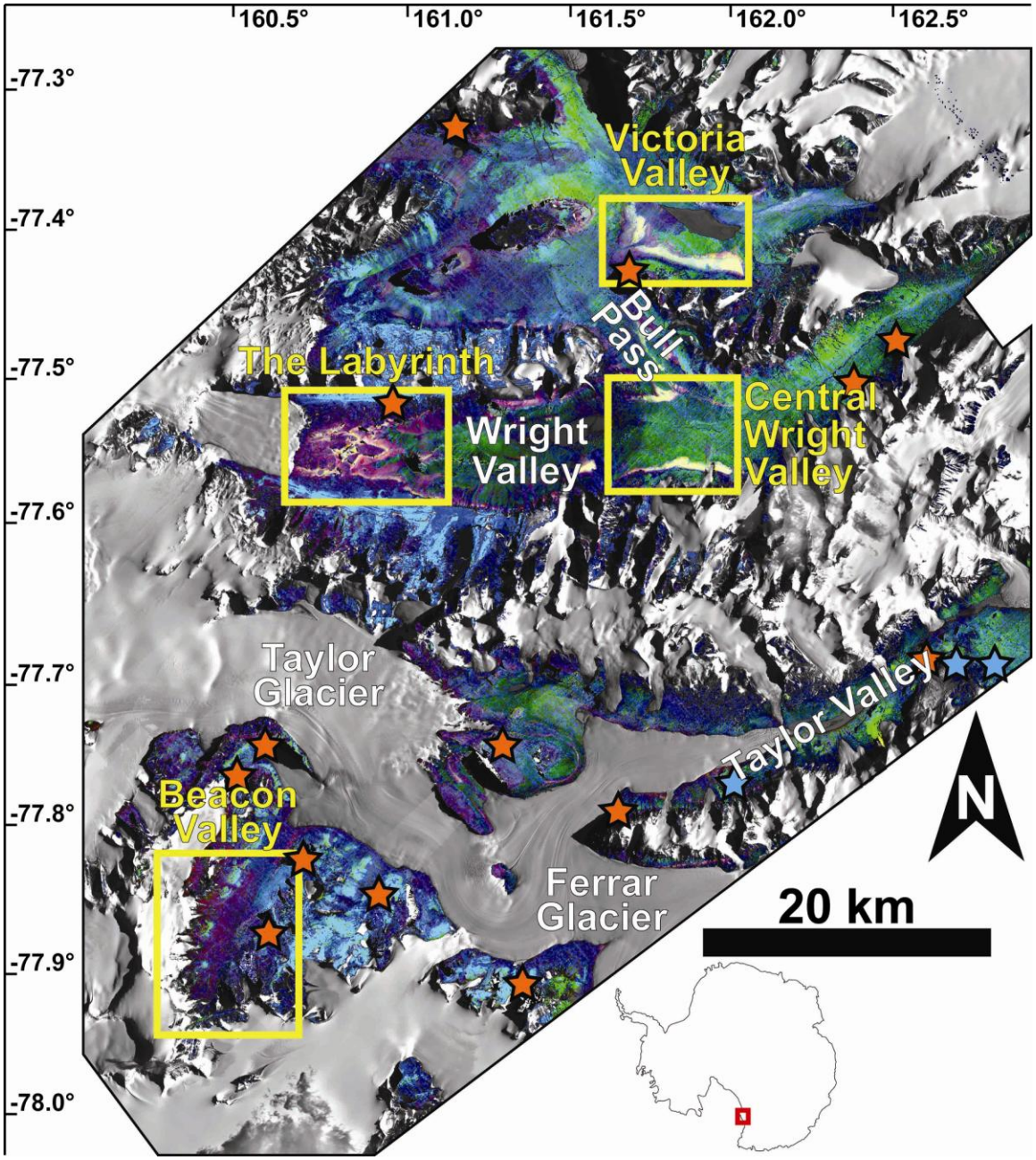

Chapter 3, Figure 1.

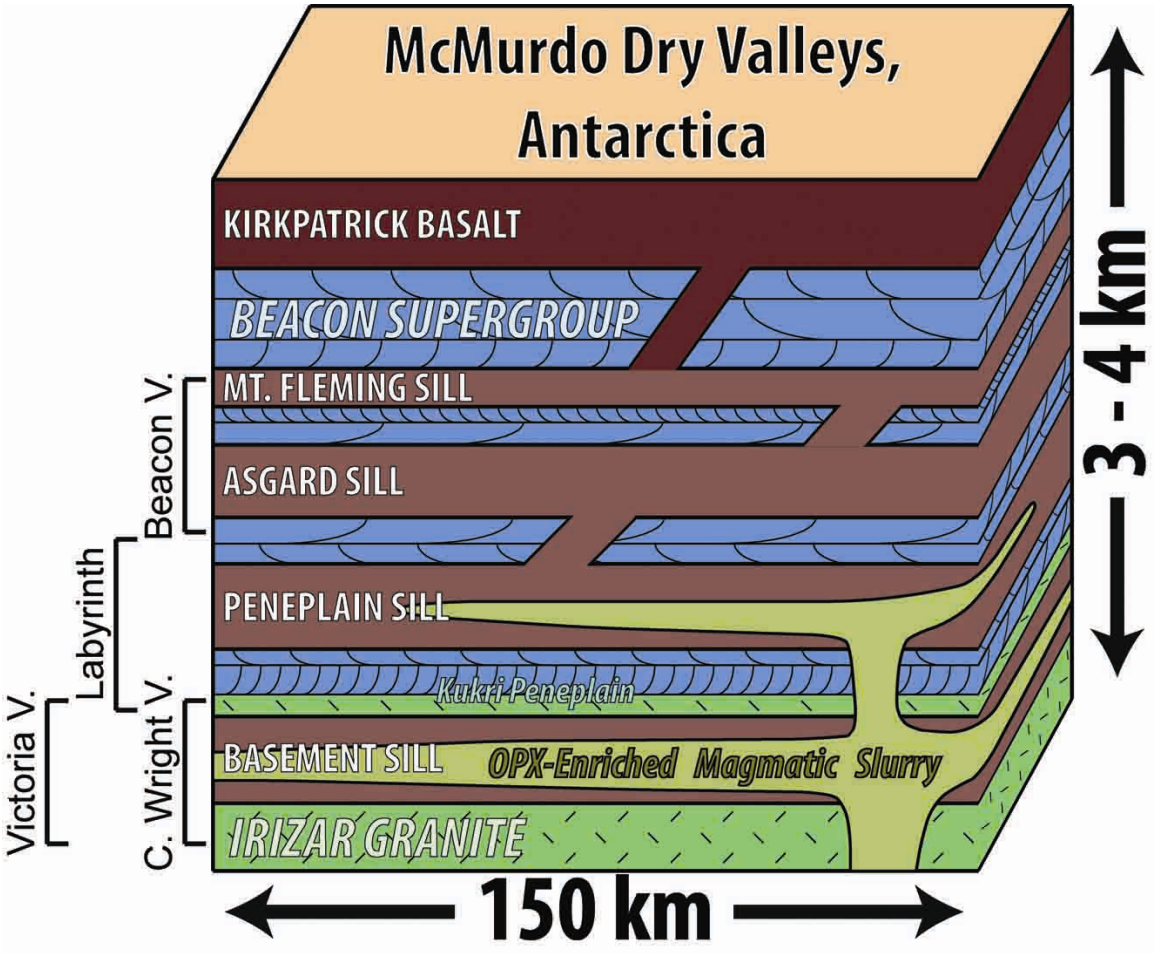

Chapter 3, Figure 2.

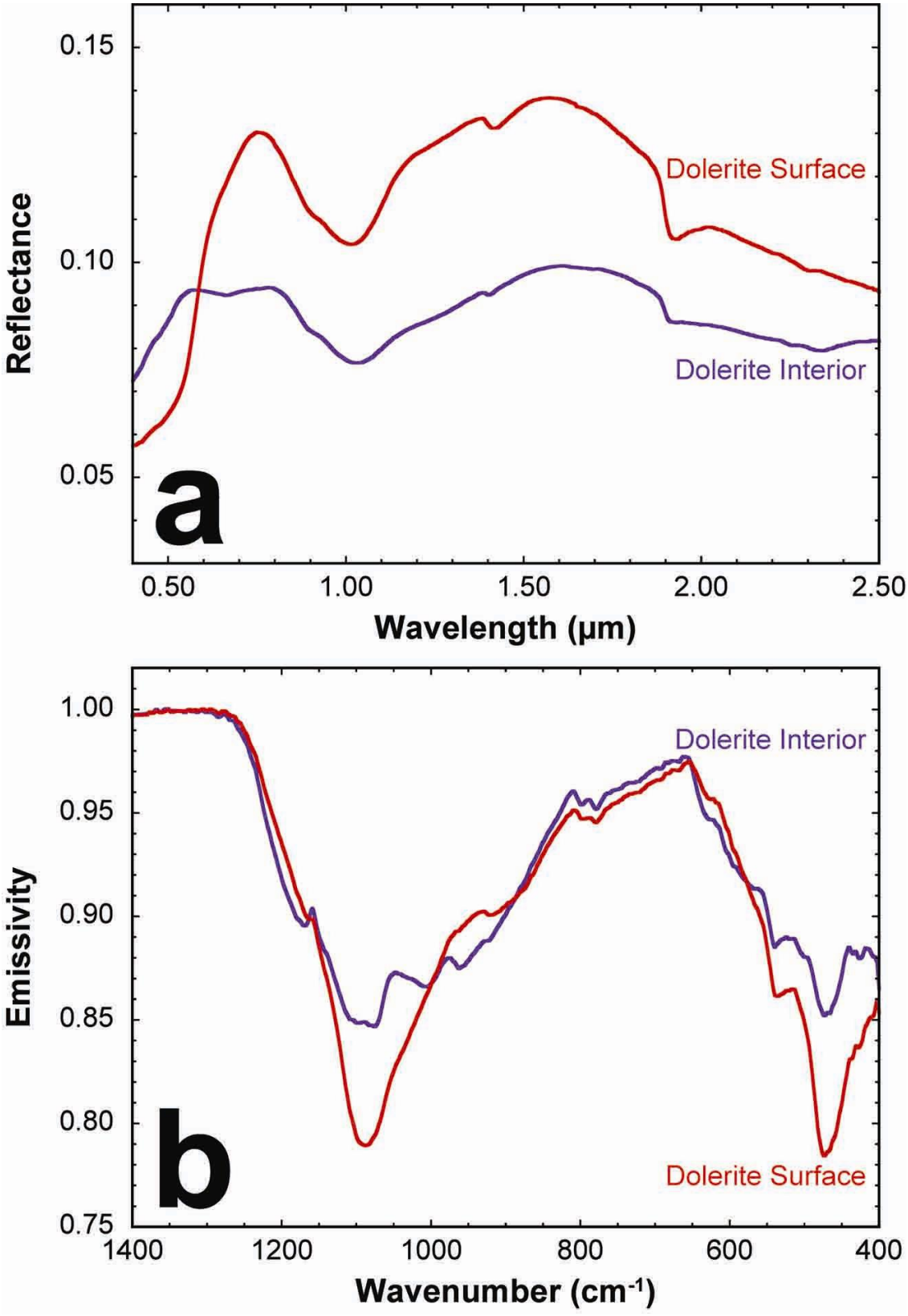

Chapter 3, Figure 3.

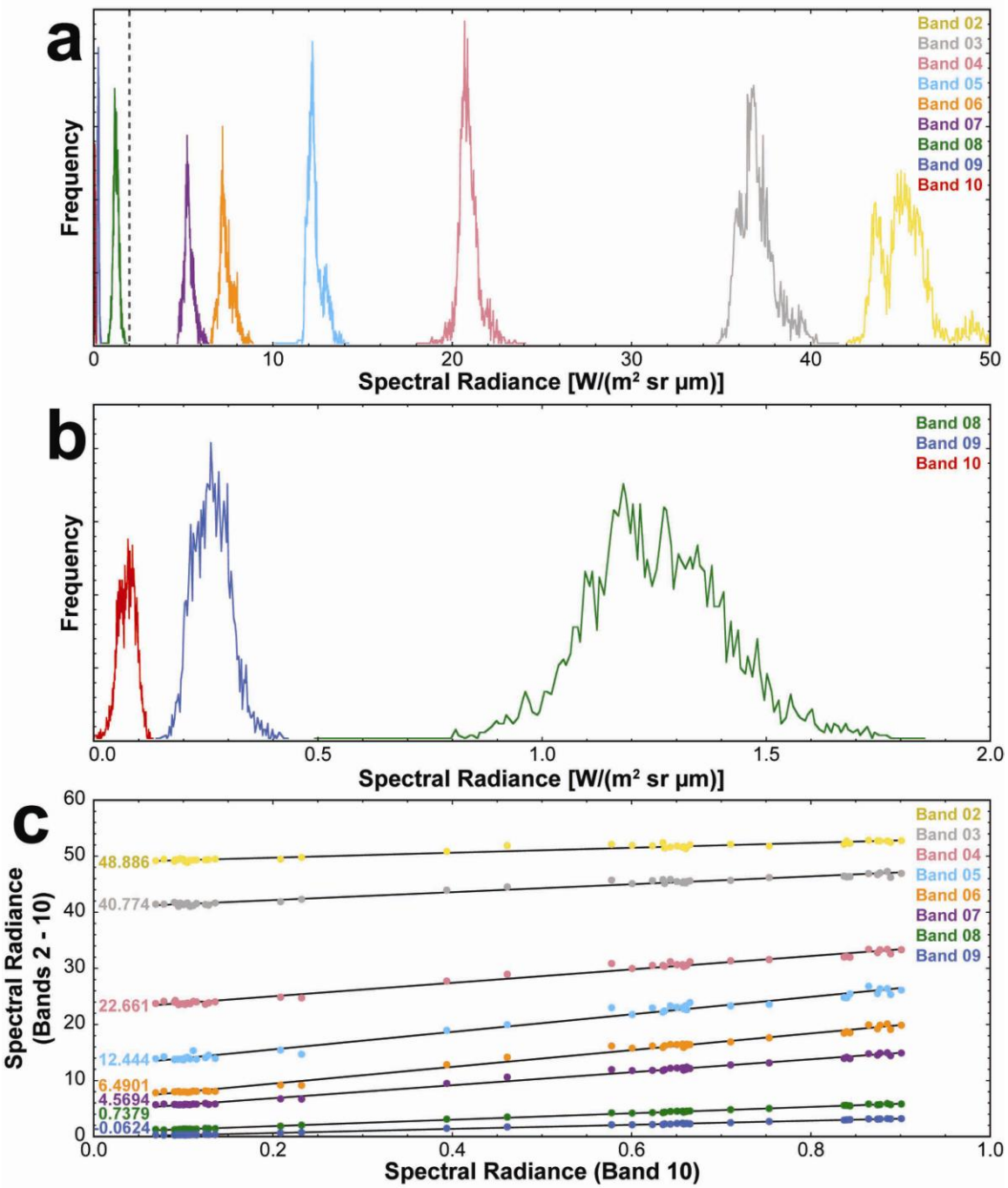

Chapter 3, Figure 4.

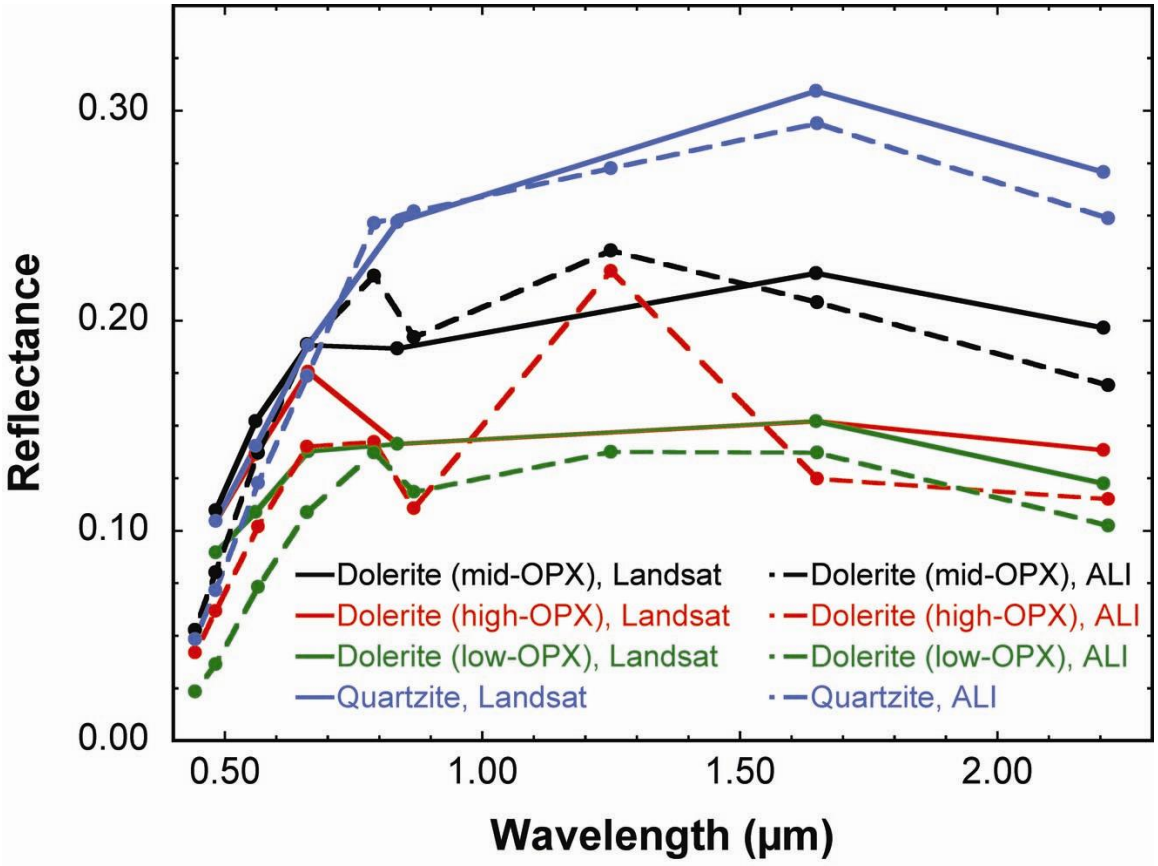

Chapter 3, Figure 5.

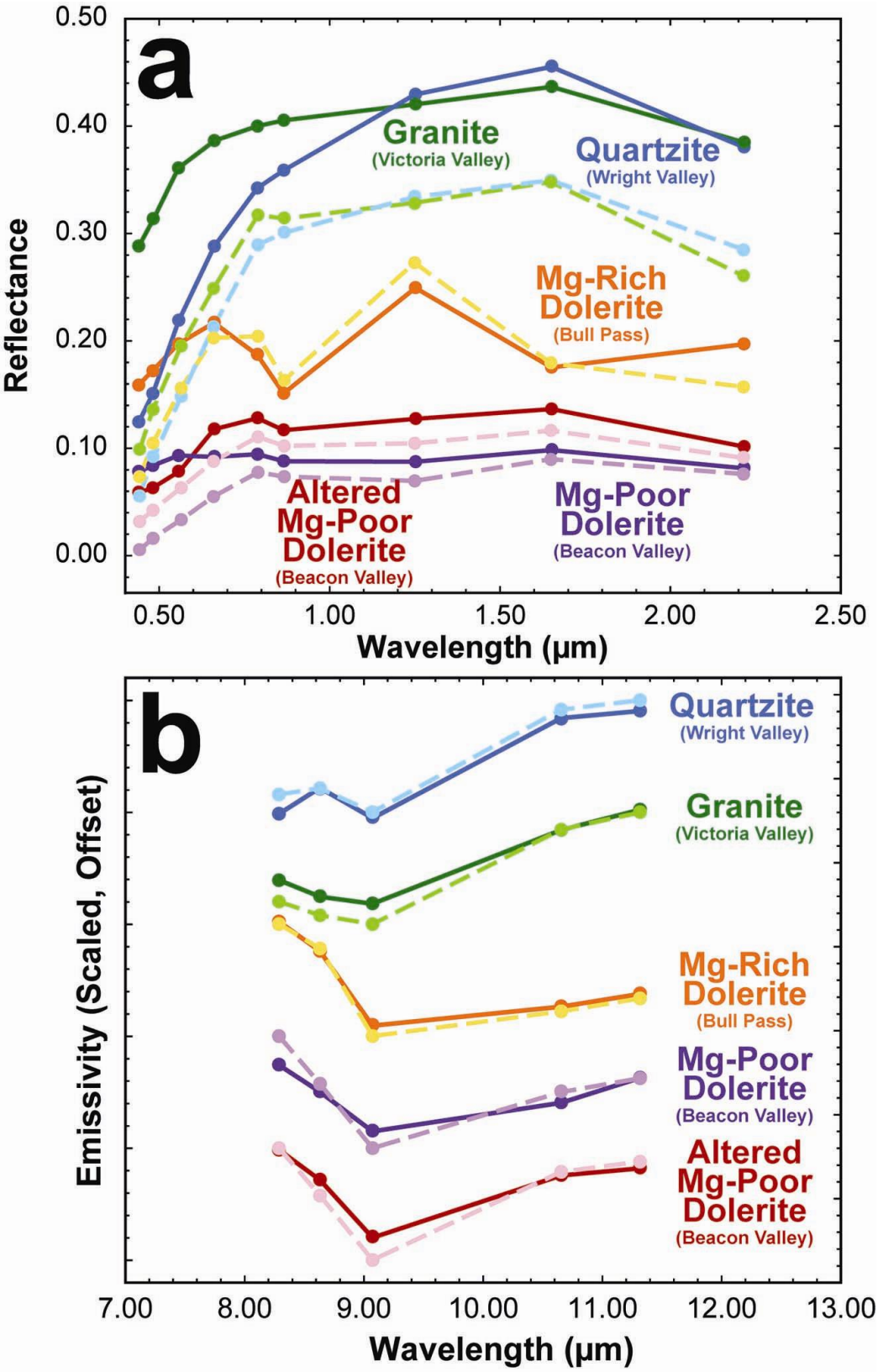

Chapter 3, Figure 6.

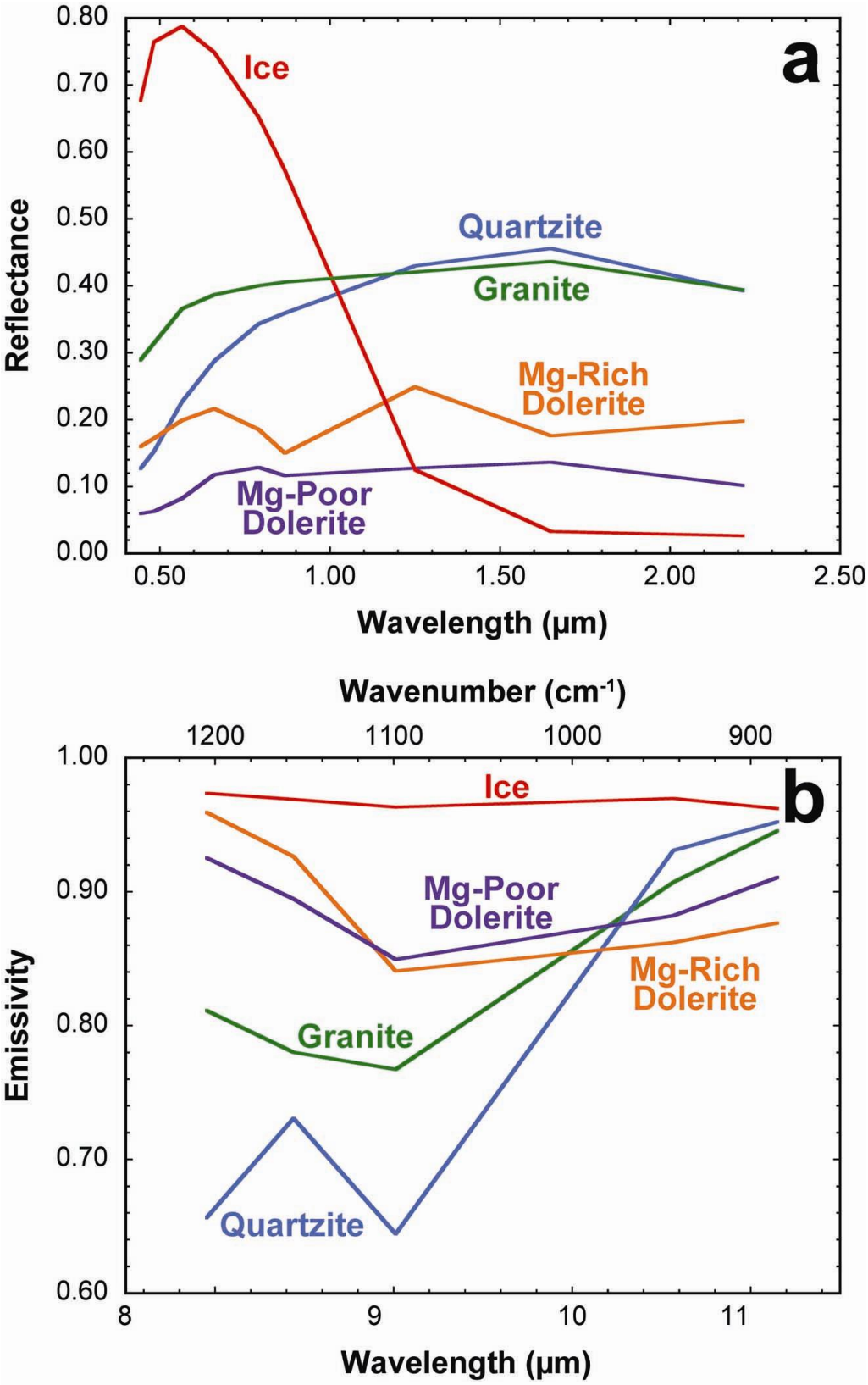

Chapter 3, Figure 7.

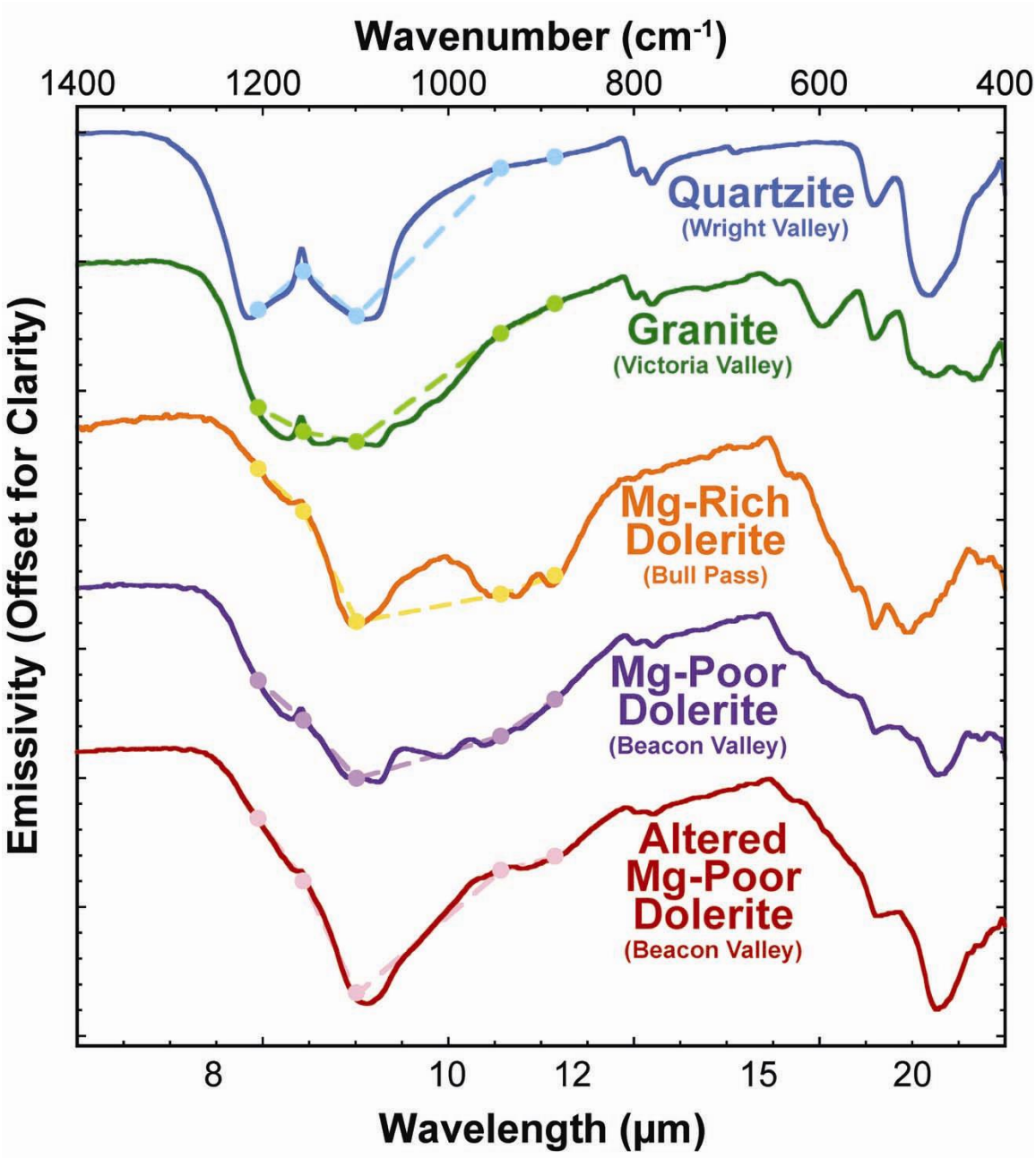

Chapter 3, Figure 8.

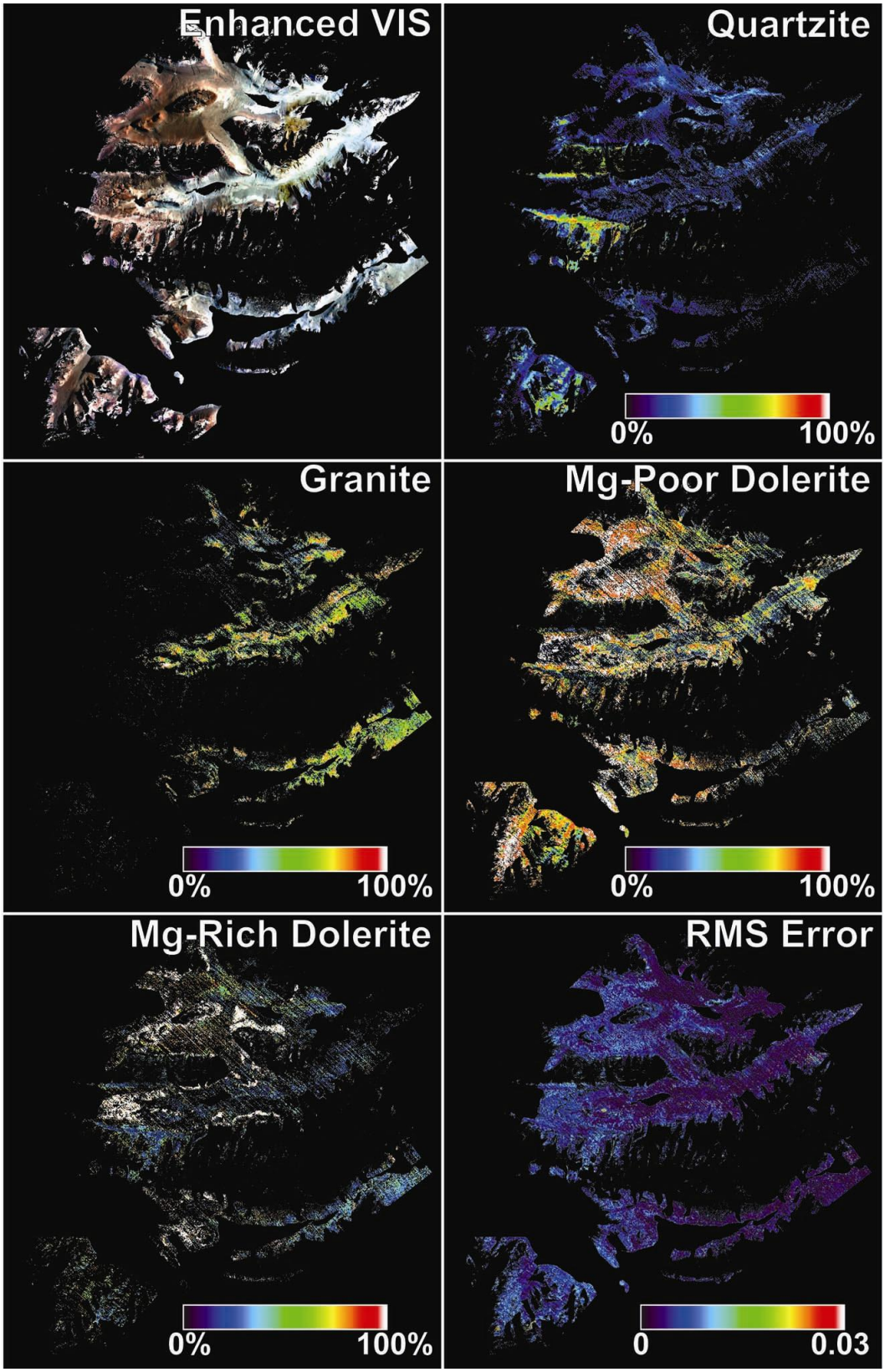

Chapter 3, Figure 9.

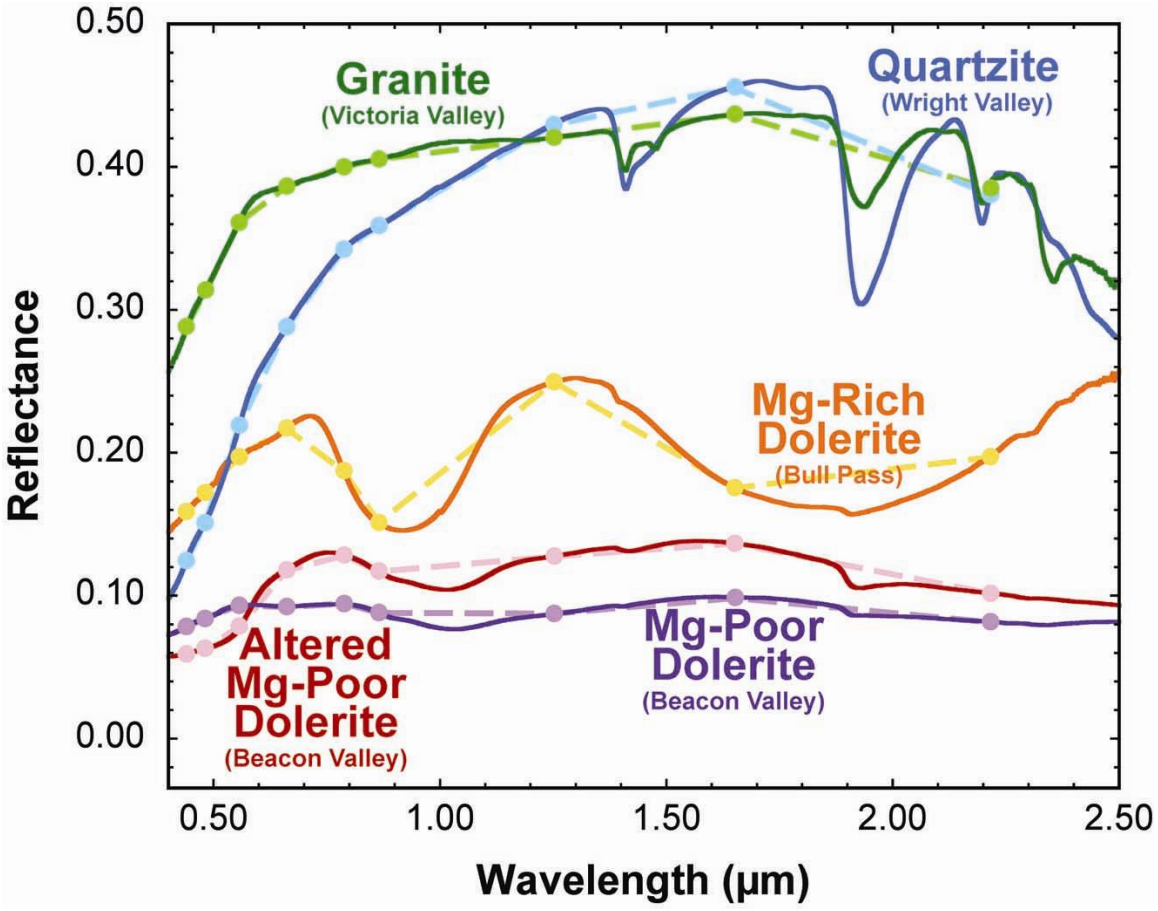

Chapter 3, Figure 10.

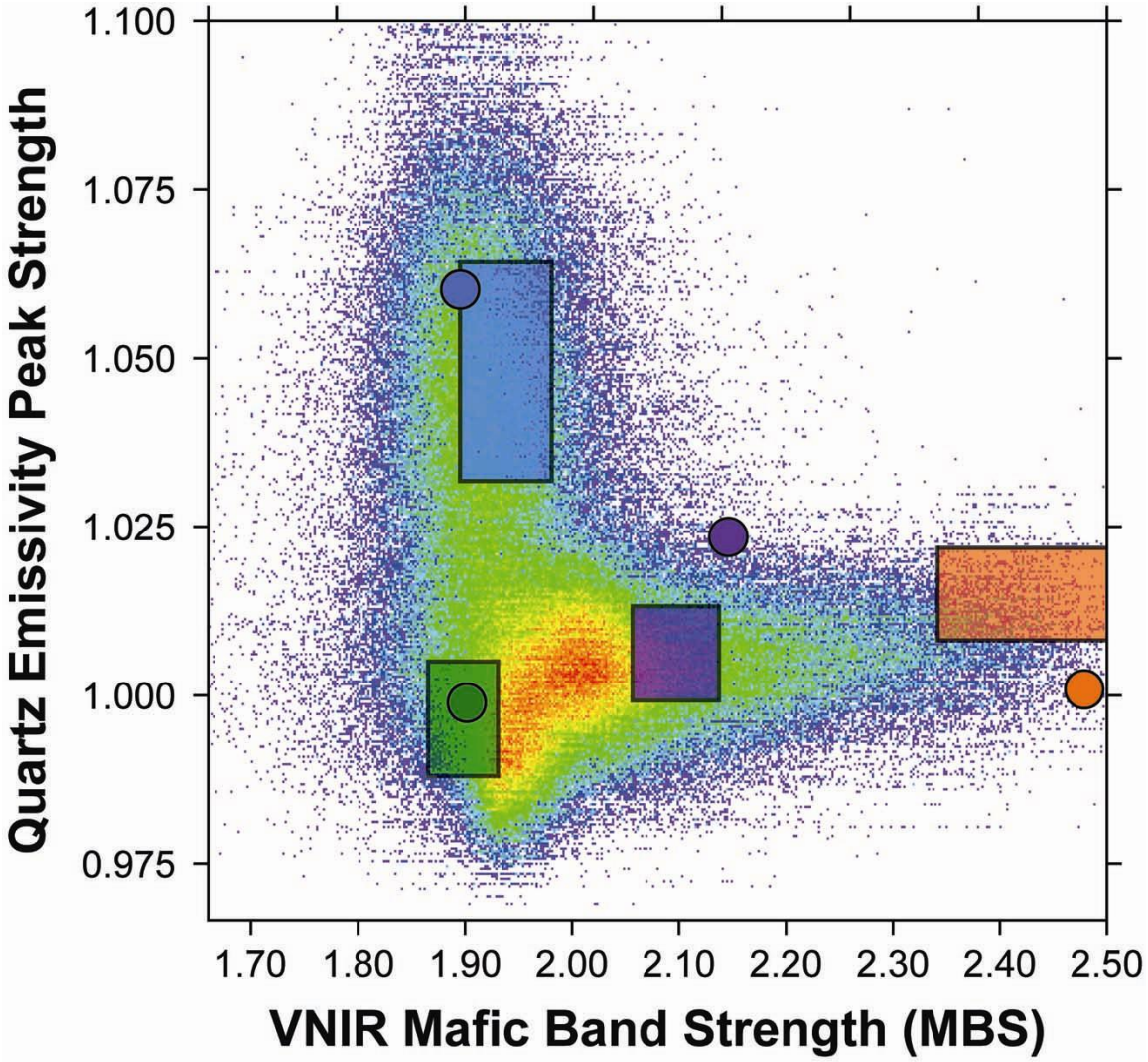

Chapter 3, Figure 11.

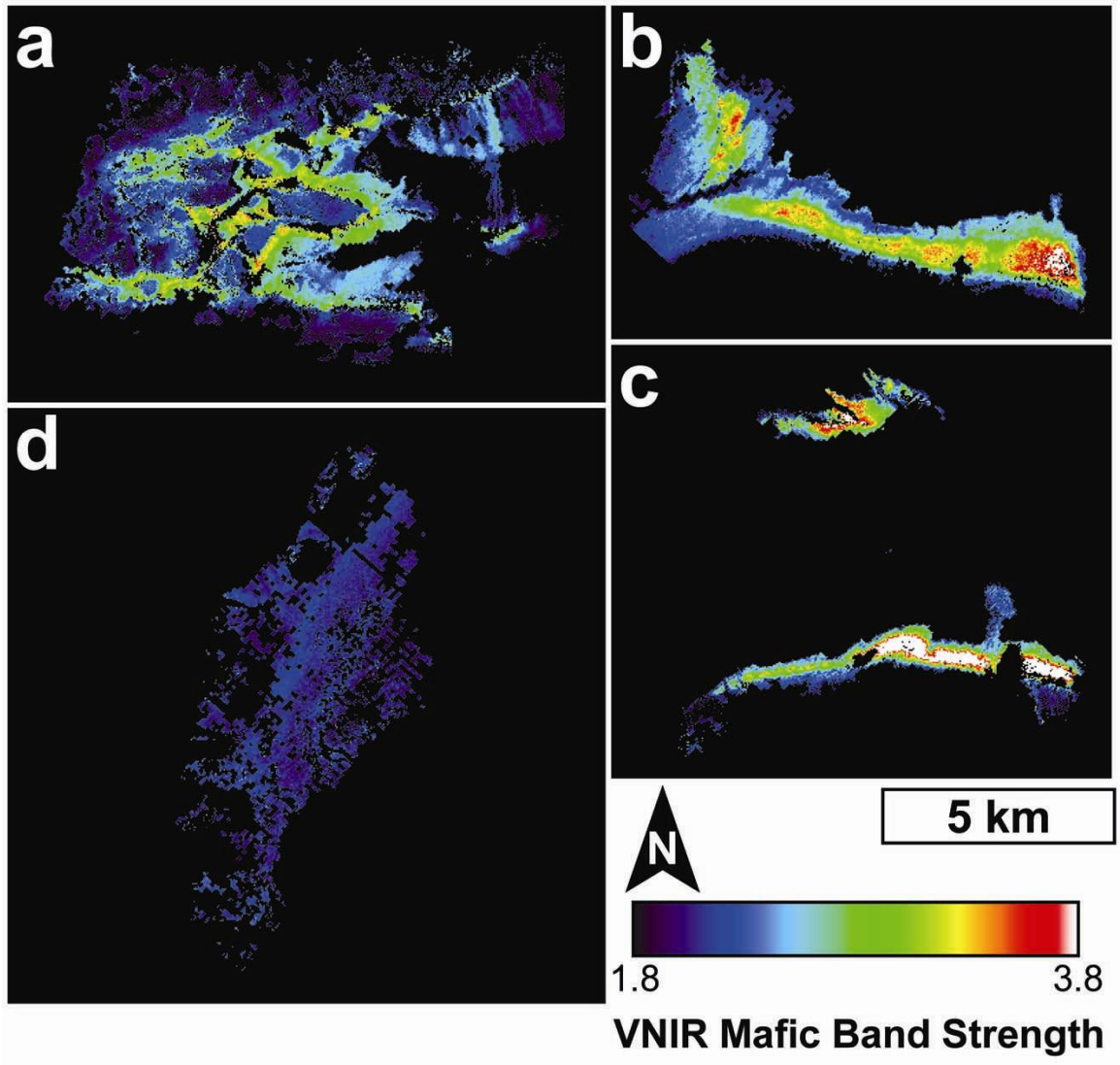

Chapter 3, Figure 12.

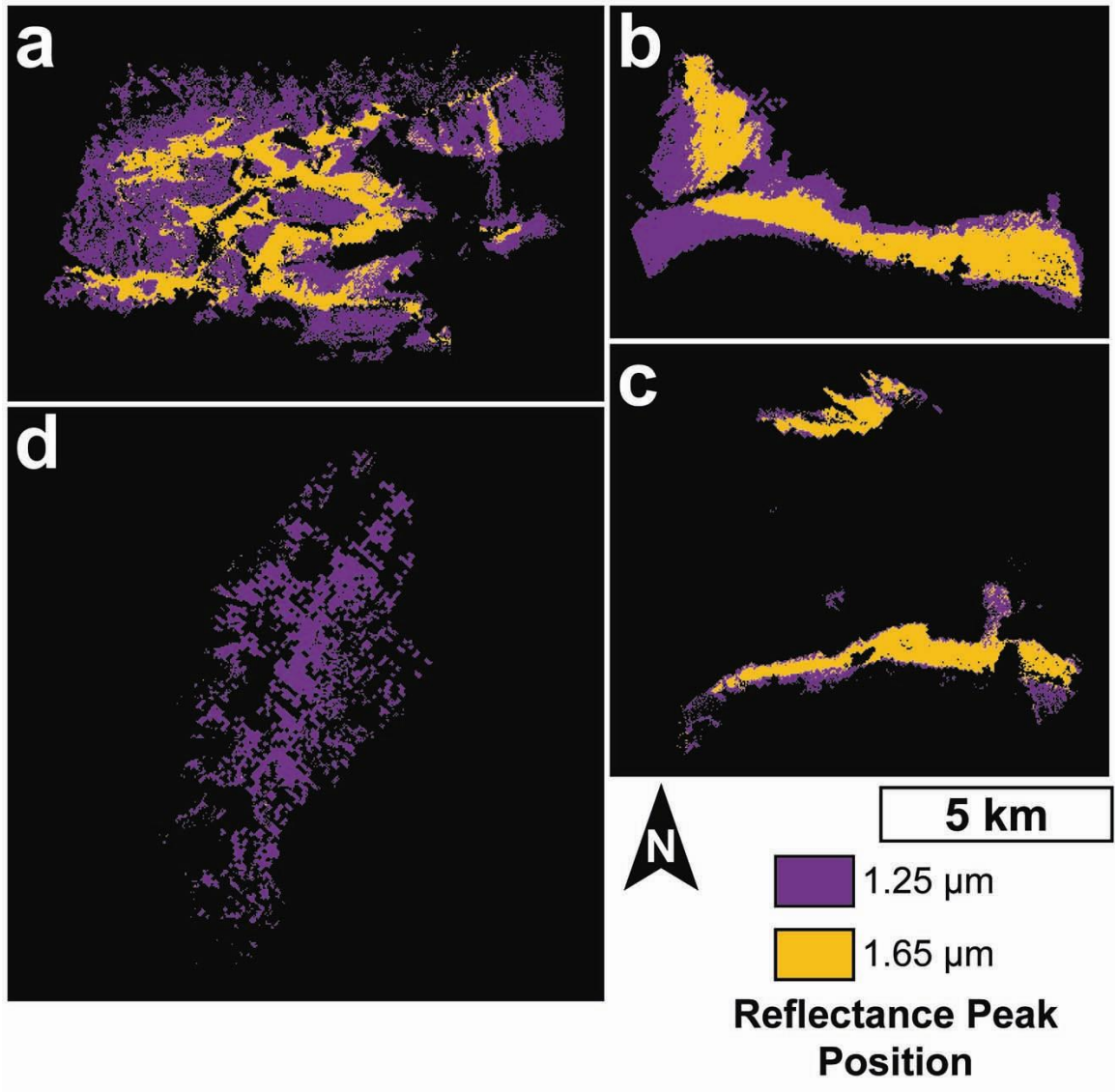

Chapter 3, Figure 13.

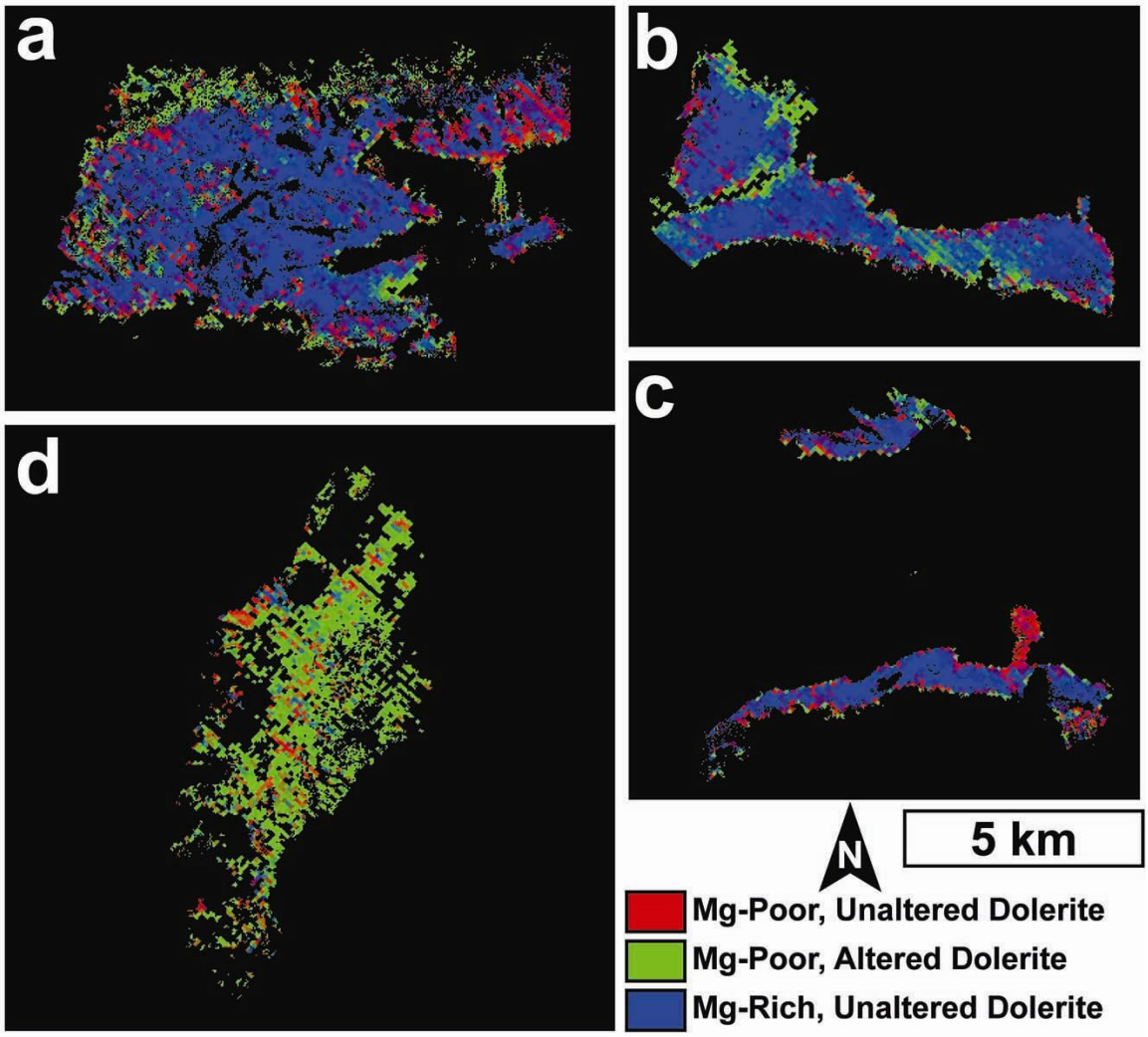

Chapter 3, Figure 14.

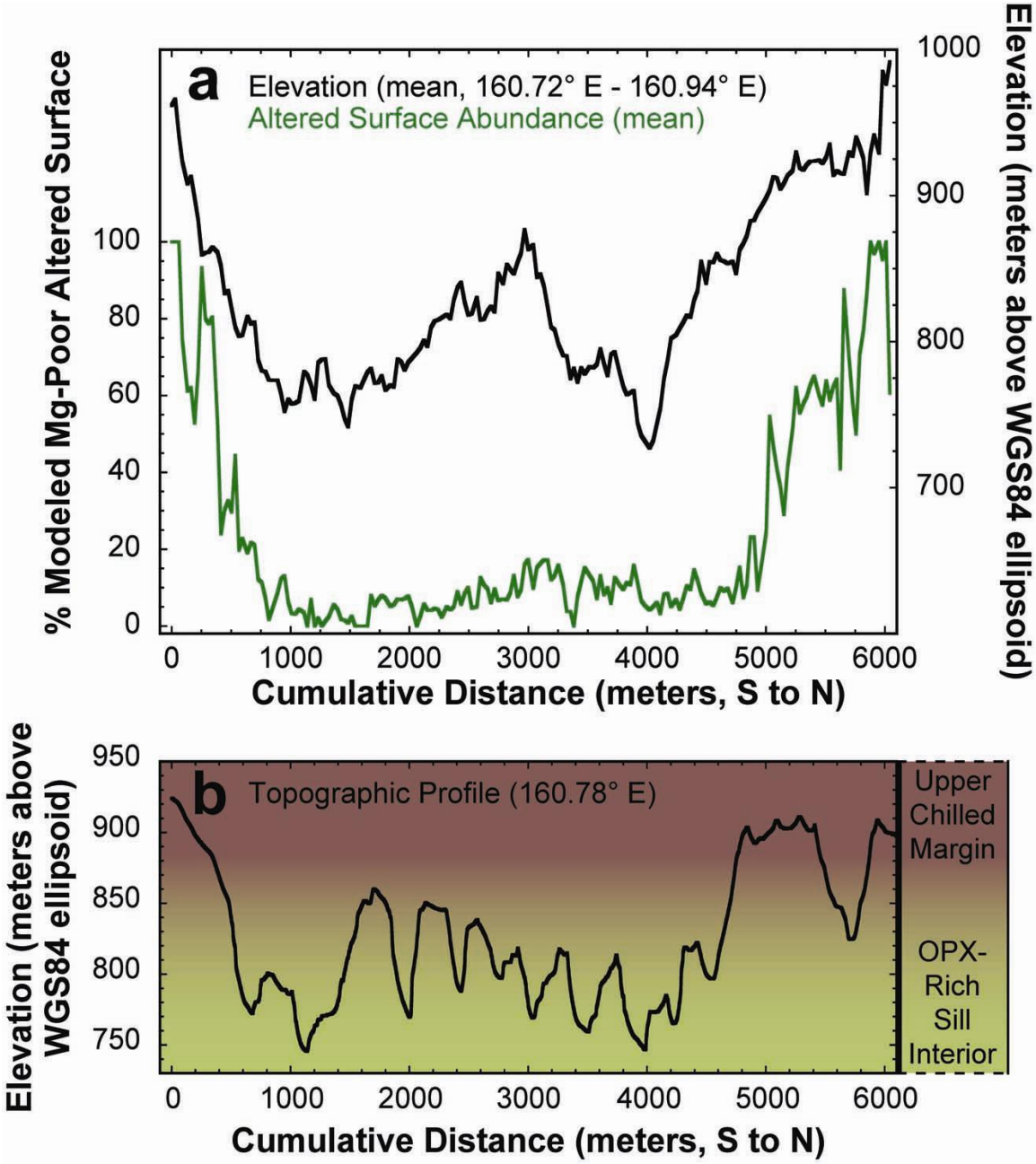

Chapter 3, Figure 15.

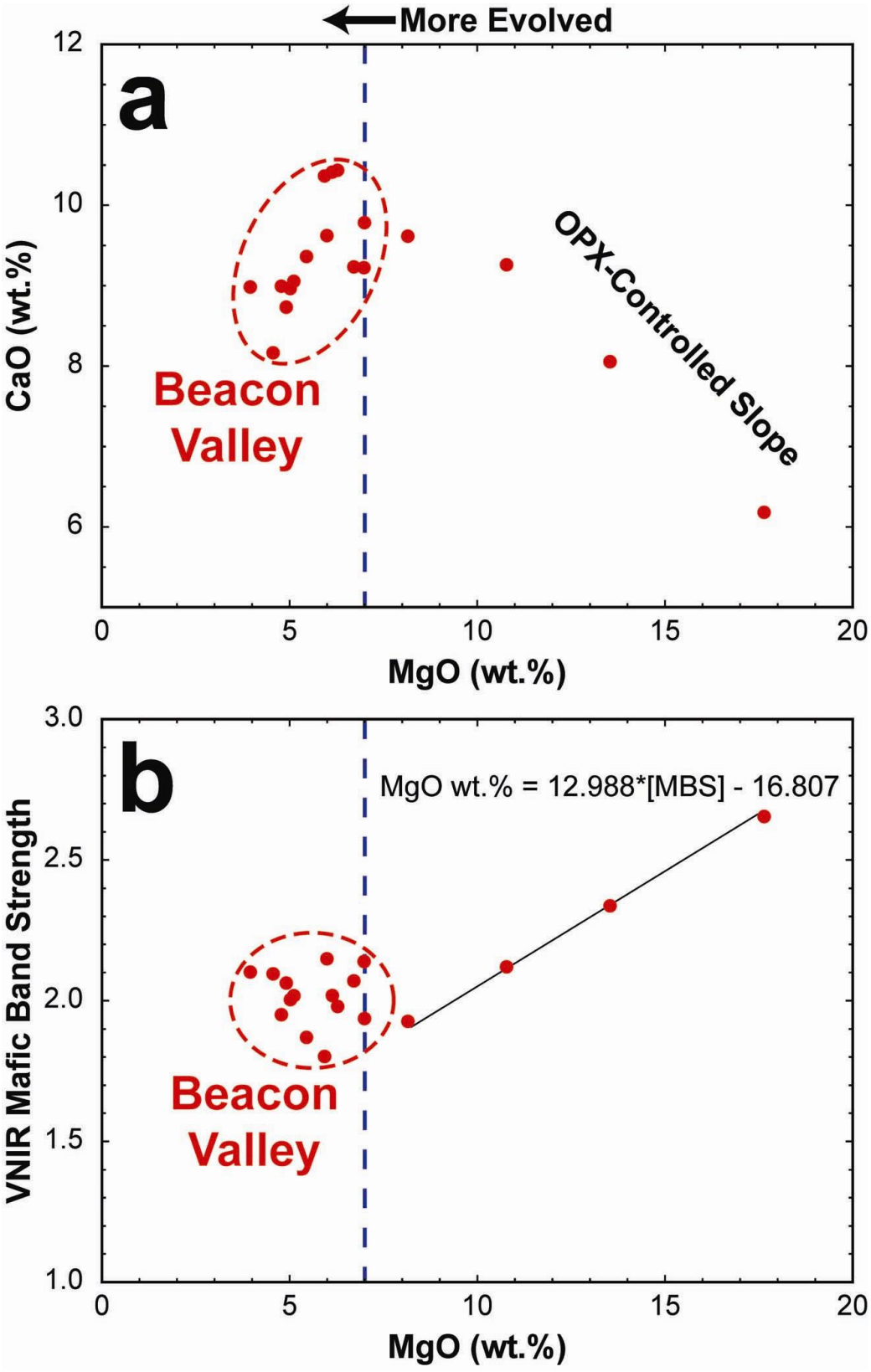

Chapter 3, Figure 16.

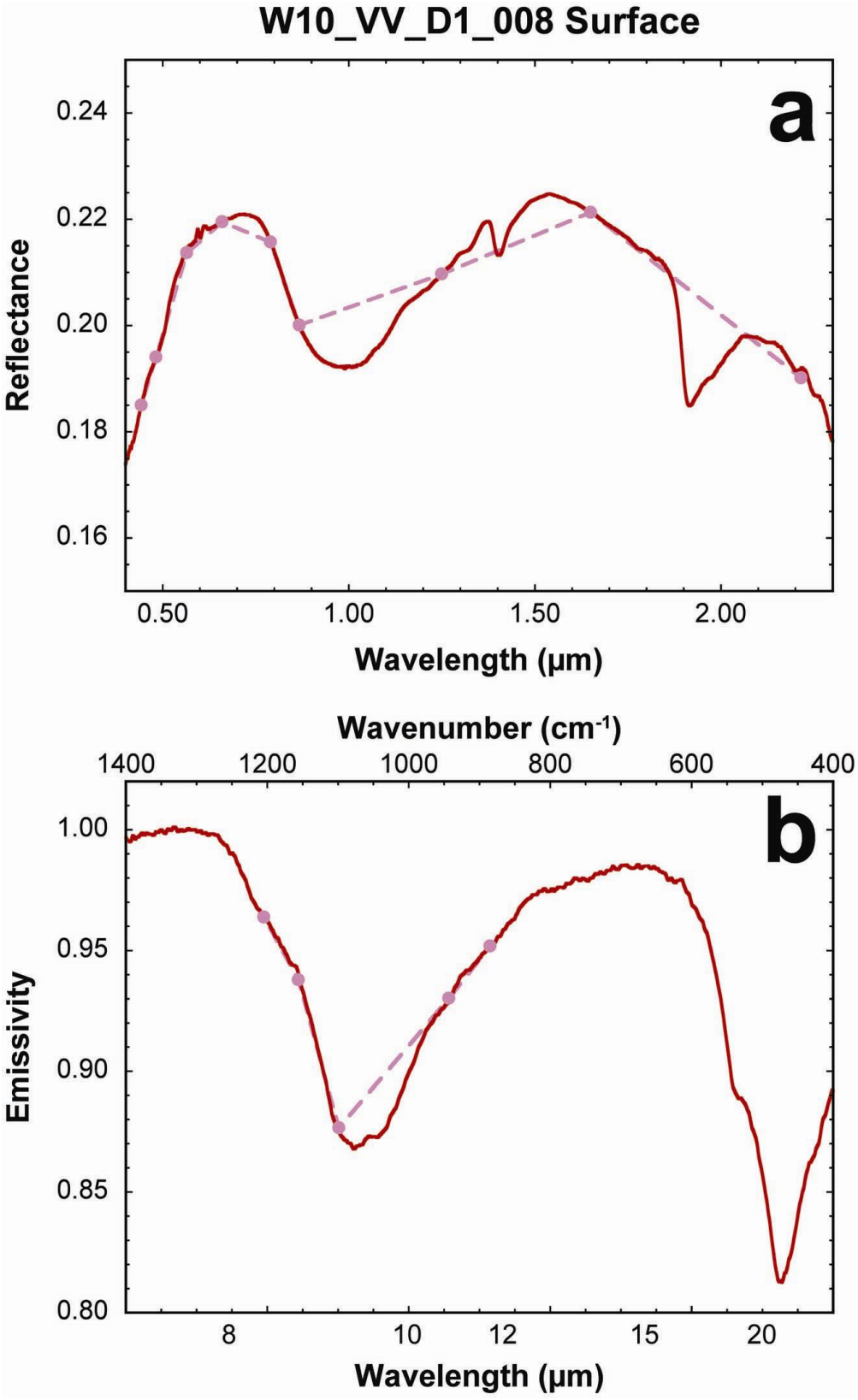

Chapter 3, Figure 17.

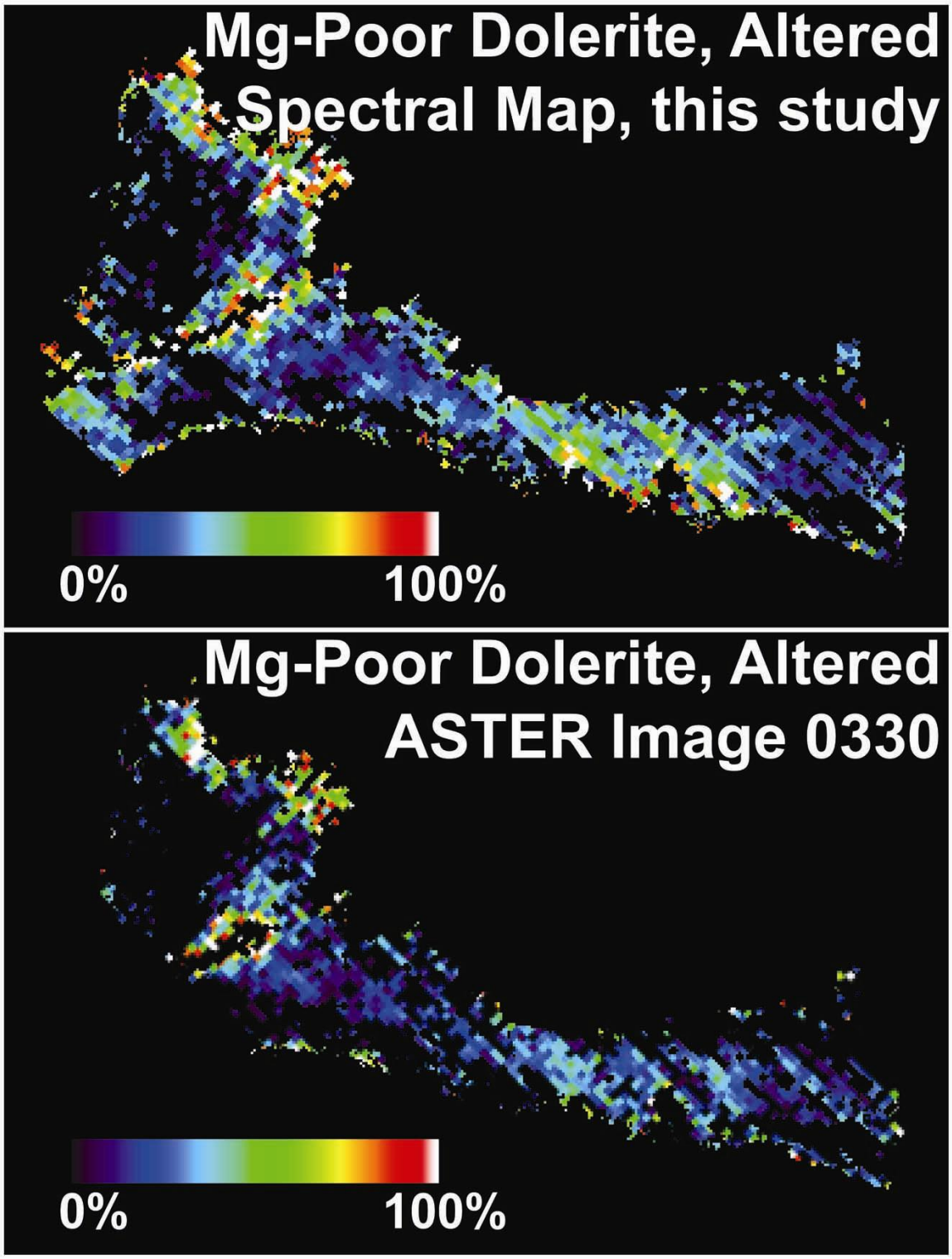

Chapter 3, Figure 18.

Chapter 3, Table 1.

Instrument	Image ID	Date of Acquisition	Location
ALI	EO1A058115200802211OKG	22 Jan 2008	Taylor V., Beacon V.
	EO1A058115201003811OKK	07 Feb 2010	Victoria V., Bull Pass
	EO1A058115200933911OK0	05 Dec 2009	Wright V.
	EO1A058115201004111OK9	10 Feb 2010	Wright V.
	EO1A058115201102711OP1	27 Jan 2011	Wright V.
ASTER	AST_05_00312082002210402	08 Dec 2002	Wright V.
	AST_05_00312112003210330	11 Dec 2003	Wright V.
	AST_05_00312032001211845	03 Dec 2001	Victoria V., Bull Pass
	AST_05_00311292000204446	29 Nov 2000	Taylor V.
	AST_05_00312032001211854	03 Dec 2001	Beacon V.
Landsat	LE70561162012020ASN00	20 Jan 2012	Taylor V., Beacon V., Wright V., Victoria V.

Chapter 3, Table 2.

Image ID	Lat, Lon	# of Pixels	B2 Corr.	B3 Corr.	B4 Corr.	B5 Corr.	B6 Corr.	B7 Corr.	B8 Corr.	B9 Corr.	B10 Corr.
KK	-77.328, 161.275	23	+39.396	+32.464	+18.116	+10.066	+5.6566	+4.0031	+0.6465	-0.0312	0
KK	-77.419, 161.719	43	+39.451	-33.030	+19.196	+10.613	+5.4282	+3.4578	+0.5577	-0.0430	0
KK	-77.514, 161.012	27	+35.924	+29.802	+16.321	+9.0441	+5.1925	+3.6344	+0.7672	-0.0113	0
P1	-77.376, 162.909	36	+57.661	+46.342	+27.043	+15.431	+8.984	+6.4466	+1.1988	+0.0451	0
P1	-77.454, 162.535	40	+49.394	+39.895	+22.502	+12.144	+6.7079	+4.6801	+0.8977	+0.0289	0
P1	-77.487, 162.431	41	+49.384	+40.060	+22.847	+12.528	+7.0322	+5.0108	+0.9542	+0.0715	0
KG	-77.665, 162.689	53	+44.708	+36.051	+20.581	+11.672	+6.6564	+4.8594	+0.8893	-0.0823	0
KG	-77.780, 161.752	48	+49.596	+41.463	+23.411	+13.194	+7.4379	+5.0455	+1.0418	+0.1338	0
KG	-77.747, 160.645	42	+48.886	+40.774	+22.661	+12.444	+6.4901	+4.5694	+0.7379	-0.0624	0
KG	-77.814, 160.774	55	+42.242	+34.726	+19.344	+10.707	+6.0513	+4.2571	+0.8599	+0.0034	0
KG	-77.770, 160.564	42	+46.460	+38.129	+21.106	+11.686	+6.3849	+4.4096	+0.9566	+0.0337	0
KG	-77.871, 160.662	76	+45.082	+35.840	+19.716	+10.746	+5.9421	+4.2567	+0.8239	-0.0175	0
K0	-77.419, 161.719	24	+46.987	+37.133	+20.892	+11.735	+6.3409	+4.5537	+1.0300	-0.0213	0
K0	-77.814, 160.774	46	+49.419	+39.481	+21.851	+12.461	+7.4512	+5.3469	+1.0241	+0.0260	0
K0	-77.741, 161.395	38	+48.622	+39.869	+22.409	+12.949	+7.6412	+5.5942	+1.2831	+0.0741	0
K9	-77.419, 161.719	36	+36.415	+29.663	+16.758	+10.032	+5.8238	+3.9391	+0.6466	-0.0072	0
K9	-77.898, 161.461	21	+40.897	+33.743	+18.691	+10.720	+6.2827	+4.3797	+0.7412	+0.0080	0
K9	-77.845, 161.016	22	+40.548	+32.199	+17.948	+10.051	+5.3748	+3.7179	+0.7420	+0.0032	0

Chapter 3, Table 3.

Parameter Name	Equation	Mapped Color
Mafic Band Strength (MBS)	([0.79 μm] / [0.8675 μm]) + ([1.25 μm] / [1.65 μm])	Red
NIR Spectral Slope	[1.25 μm] / [0.79 μm]	Green
Quartz Emissivity Peak Strength	[8.65 μm] / ((((([9.1 μm] – [8.3 μm]) / 0.80) * 8.65) + ([9.1 μm] – (11.375 * ([9.1 μm] – [8.3 μm]))))	Blue

Chapter Four:

Oxidative weathering in Antarctica and evidence for a cold and dry Amazonian Mars.

M. R. Salvatore[1], J. F. Mustard[1], J. W. Head III[1], and R. F. Cooper[1]

[1]Department of Geological Sciences,

Brown University, Providence, RI 02912, USA

In review in its current form to:

Nature Geoscience

NGS-2013-03-00584

Main Text

Orbital visible/near-infrared (VNIR) reflectance spectroscopy has been used to suggest that global-scale aqueous alteration on Mars ceased near the beginning of the Amazonian epoch (~3.1 Ga; Hartmann and Neukum, 2001), transitioning to an oxidative weathering regime with little or no aqueous alteration (Bibring et al., 2006). Investigations utilizing thermal infrared (TIR) emission spectroscopy, however, have suggested that widespread, latitude-dependent aqueous alteration has occurred during this era (Wyatt and McSween, 2002; Kraft et al., 2003; Michalski et al., 2003; Minitti and Hamilton, 2010; Rampe et al., 2012). Researchers have, until now, been unable to reconcile these seemingly disparate interpretations through a single process that is consistent with our current understanding of martian surface and environmental evolution. Here we show that regional surface spectroscopy of martian mafic terrains spanning the VNIR and TIR wavelength regions (pan-spectral) are consistent with pan-spectral observations of mafic lithologies observed in Beacon Valley of the McMurdo Dry Valleys, Antarctica. In Beacon Valley, oxidative weathering processes are the dominant form of surface alteration, while more mature aqueous alteration phases are absent (Fig. 1) (Salvatore et al., 2012). Significantly, these products of alteration are uniquely preserved in the Mars-like hyper-arid, hypo-thermal, and stable climate of Beacon Valley (Marchant and Head, 2007). The identification of these products of oxidative weathering on Mars and the associated link to a process that is dominant on Mars indicates that substantial amounts of widespread aqueous activity were not present during the Amazonian epoch and provides definitive mineralogical evidence for a cold, dry, and stable martian climate during this time.

High-resolution global spectroscopic studies using the Thermal Emission Spectrometer (TES) instrument (Christensen et al., 2001) on Mars Global Surveyor have identified two widespread surface compositions. Surface Type 1 (ST1) is defined as largely basaltic and minimally altered (Bandfield et al., 2000), while Surface Type 2 (ST2) has been characterized as basaltic with variable amounts of altered materials and is more common at higher latitudes (Wyatt and McSween, 2002; Kraft et al., 2003; Michalski et al., 2003; Minitti and Hamilton, 2010; Rampe et al., 2012). Although substantial TIR spectral variability has been observed within these two regions, their broad distribution has been used to demarcate the extent of post-Noachian alteration across the martian surface. The alteration phases that have been proposed to satisfy these spectral signatures include smectite clays (Wyatt and McSween, 2002), zeolites (Minitti and Hamilton, 2010), allophane (Rampe et al., 2012), and Si-rich mineraloids (Michalski et al., 2003), polymorphs (Michalski et al., 2003), surface coatings (Kraft et al., 2003), and glasses (Fig. 2b) (Koeppen and Hamilton, 2005). The presence of these components implies that significant aqueous alteration has occurred on the martian surface following the emplacement of these Hesperian-aged basaltic units.

Our analyses integrate pan-spectral data for the Syrtis and Northern Acidalia-Utopia spectral regions (Rogers et al., 2007; Rogers and Christensen, 2007), the type localities for ST1 and ST2, respectively (Fig. 2). These locations underscore some of the most significant spectral differences observed in regional-scale thermal emission compositional mapping (Rogers and Christensen, 2007). Using data from the Observatoire pour la Minéralogie, l'Eau, les Glaces et l'Activité (OMEGA) instrument (Bibring et al., 2004) on Mars Express, we generated representative VNIR spectra of

these spectral regions and compare them to their regional TIR emissivity spectra (see Methods section) to assess the nature and composition of primary and secondary phases that may be present.

The OMEGA data for Syrtis exhibit broad 1 μm and 2 μm absorption bands associated with pyroxene, while data for Northern Acidalia-Utopia exhibit a distorted 1 μm band with a significantly weaker 2 μm absorption (Fig. 1c). The strength of the Fe^{3+} crystal field and charge-transfer absorptions in the Syrtis data is weaker than that observed in the Northern Acidalia-Utopia observations, while the Northern Acidalia-Utopia data exhibit an overall higher albedo in the near-infrared in addition to a significant negative slope. These observations are consistent with previous VNIR orbital analyses (e.g. Mustard et al., 2005). Importantly, neither spectrum exhibits vibrational overtones or combination tones near 1.4 μm, 1.9 μm, nor between 2.1 μm and 2.5 μm, indicating that hydrated species are not spectrally abundant phases in these regions.

The lack of evidence for hydrated mineral phases in VNIR reflectance data is seemingly at odds with TIR emission data that have been previously interpreted as containing abundances of these phases at amounts sufficient to be modeled above the detection limits with linear unmixing methods. The recent identification and characterization of oxidative weathering products (OWPs) observed on mafic lithologies in Beacon Valley, Antarctica, though, presents a spectral analog that simultaneously satisfies the key VNIR reflectance and TIR emission spectral properties associated with martian low albedo regions in Syrtis and Northern Acidalia-Utopia (Fig. 1) (Salvatore et al., 2012).

Beacon Valley (77.84º S, 160.63º E) is one of the coldest (mean annual air temperature of -22º C; Doran et al., 2002), driest (mean annual water equivalent precipitation of < 10 mm; Fountain et al., 2009), and most stable (erosion rates of ~15 cm Myr^{-1} and landscape ages of several million years old; Summerfield et al., 1999; Sugden et al., 1995) ice-free surfaces on the planet. The valley surface is dominated by clasts of the Ferrar Dolerite, a shallow intrusive quartz- and hypersthene-normative basaltic unit that has previously been investigated as an analog to martian surface and meteorite compositions (Harvey, 2001; Chevrier et al., 2006). The surfaces of the Ferrar Dolerite are characterized by thin (~0.5 – 5 mm), red alteration rinds that grade into the underlying unaltered rock (Fig. 3). VNIR spectroscopy (Fig. 1c) shows that, compared to their unaltered interiors, altered rock surfaces exhibit weaker 2 μm pyroxene absorptions, stronger Fe^{3+} crystal field and charge-transfer absorptions at wavelengths less than 0.6 μm, and higher albedo and a more pronounced negative spectral slopes in the near-infrared. However, reflectance spectra of dolerite surfaces are not accompanied by significant changes to the strength or presence of absorption features near 1.4 μm, 1.9 μm, or between 2.1 μm and 2.5 μm related to hydrated alteration phases. In the TIR (Fig. 1d), altered surfaces exhibit a narrowing of the reststrahlen features near 1100 cm^{-1} and 470 cm^{-1}, while no evidence exists for the presence of smectite clays in this spectral region. Importantly, mineralogical analyses of these alteration rinds indicate no significant changes in bulk mineralogy as compared to their unaltered interiors, with only subtle variations in chemistry that indicate the migration of cations in response to a dry, oxidizing environment (Salvatore et al., 2012). The process of cation migration and subsequent Fe oxidation modifies the electronic, vibrational, and structural state of the

minerals present at the rock surfaces to significantly modify the reflectance and emission properties. Thus, the OWPs formed in the hyper-arid and hypo-thermal Beacon Valley do not represent a pure mineralogic or alteration endmember, but rather a distinct alteration trend associated with oxidative weathering processes and is a function of the unaltered compositions, environmental conditions, and duration of exposure.

The alteration rinds found ubiquitously throughout the valley represent a metastable phase between unaltered mafic compositions and more mature alteration phases. The hyper-arid and hypo-thermal environmental conditions present in Beacon Valley have effectively arrested chemical alteration at this metastable phase due to the scarcity of liquid water and thermal barriers to alteration processes. Warmer and/or wetter environmental conditions would quickly alter these metastable phases to more mature alteration products, including phyllosilicates. In fact, more mature alteration phases have been found within small pits on dolerite surfaces where liquid water is able to pond following minor snowmelt events, indicating that the ubiquitous rinds are the metastable precursors to these more mature alteration phases (Allen and Conca, 1991).

The sensitivity of VNIR reflectance spectroscopy to the presence of hydrated mineral phases makes this technique an important and requisite tool to constrain the range of possible spectral endmembers present on the martian surface. Our results show that the pan-spectral properties of OWPs are the only known materials that satisfy diagnostic spectral properties in both the VNIR and TIR wavelength regions (Fig. 2). To quantify the contributions of OWPs using regional TIR spectra, we ran a least-squares linear unmixing algorithm (Ramsey and Christensen, 1998) with an endmember library modified from Rogers and Christensen (2007) that is consistent with our regional VNIR

data (Table 1) (see Methods section). Smectite clays, zeolites, high-Si phases, and other hydrated materials were excluded from the endmember library because they were not detected in OMEGA data in these regions of investigation. The unmixing model results suggest that OWPs contribute significantly to the mixing models for both the Syrtis and Northern Acidalia-Utopia TIR emissivity spectra, accounting for roughly 14% and 37% of the modeled mineral abundances, respectively, if the OWPs are treated as a mineral endmember (Fig. 2b, Table 2). The abundances of other modeled endmembers are consistent with previous studies and suggest that the surfaces are largely basaltic in composition (Rogers and Christensen, 2007). The observed goodness of fit of the model results, the absence of coherent signatures in the residual spectra, and the low root-mean-square (RMS) errors confirm that the linear unmixing models provide appropriate fits (Fig. 2b).

Based on analyses from rover landing sites, geologically recent erosion rates of the martian surface have been estimated to be four orders of magnitude slower than those observed in Beacon Valley (Summerfield et al., 1999; Golombek et al., 2006). The widespread distribution and preservation of OWPs throughout Beacon Valley indicate that hyper-arid and hypo-thermal environmental conditions have dominated this valley for an extended period of time. Cosmogenic age dating of dolerite clasts that exhibit well-developed alteration rinds have revealed uncorrected minimum exposure ages of 2.3 Ma and suggest that cold and dry conditions comparable to modern conditions have been present for at least that duration (Schäfer et al., 2000). With similar cold, dry, stable, and oxidizing (Bibring et al., 2006) conditions on Mars, the martian surface is also ideal for the formation and preservation of these early chemical alteration products (during the

proposed “siderikian” era of alteration; Bibring et al., 2006). The identification of OWPs on the martian surface and the dearth of hydrated alteration phases present in VNIR data of post-Noachian basalts requires comparable or more severe hyper-arid and hypo-thermal environmental conditions to be present since their formation. As a result, the preservation of these OWPs on Mars is compelling spectroscopic and mineralogic evidence for the long-term stability of the martian surface as well as the persistent cold and dry conditions that must have been present.

These results elucidate the pan-spectral observations of these critical low albedo regions and resolve the conundrum between previous pan-spectral interpretations. On a regional scale, our results suggest that neither the Syrtis nor Northern Acidalia-Utopia spectral regions have undergone significant post-Noachian aqueous alteration, despite evidence for localized aqueous alteration at or near the surface during this geologic timeframe (e.g. Milliken et al., 2008; Skok et al., 2010). The absence of diagnostic water- and hydroxyl-bearing mineral signatures in VNIR reflectance data suggest that hydrated phases are not present at sufficiently high volume abundances that can be detected using spectroscopic datasets. Additionally, the preservation of the metastable products of oxidative weathering on the martian surface is only possible in the absence of significant aqueous alteration, regardless of pH. Our study suggests that, from a mineralogical and geochemical perspective, liquid water has been an inconsequential component of Amazonian surface processes. The deficiency of aqueous activity during the later stages of martian geologic history provides additional constraints on the evolution of the martian climate and hydrologic system.

Methods

Spectral analyses of dolerite samples

Details regarding sample preparation and analyses can be found in Salvatore et al. (2012). Fourteen dolerite interior and surface fragments were spectrally analyzed using VNIR and TIR spectrometers at the Keck/NASA Reflectance Experiment Laboratory (RELAB) at Brown University and the Vibrational Reflectance Laboratory at Stony Brook University, respectively. VNIR measurements were acquired using a bidirectional reflectance (BDR) spectrometer, which acquires spectra between 0.32 μm and 2.55 μm at a 5 nm spectral sampling interval using a photomultiplier and InSb detectors. Illumination and emergence angles were fixed at 30° and 0°, respectively. Samples were slowly rotated to reduce artifacts associated with viewing or illumination geometries. TIR measurements were acquired using a Nicolet 6700 FTIR Spectrometer, which utilizes a deuterated L-alanine doped triglycine sulfate (DLaTGS) detector and CsI window. Measurements were acquired between 2000 cm^{-1} and 200 cm^{-1} at a sampling interval of 4 cm^{-1} using a CsI beamsplitter. The VNIR spectra presented in this manuscript are of sample MS10_BV_12 and the TIR spectra are the average interior and surface measurements of all fourteen samples (Salvatore et al., 2012).

Orbital data retrieval and calibration

In a fashion similar to TIR data aggregation by Rogers et al. (2007) and Rogers and Christensen (2007), OMEGA data were acquired over broad spectral regions that were classified as belonging to either the N. Acidalia-Utopia or Syrtis surface emissivity groups. All OMEGA data acquired prior to orbit 1600 were consolidated, processed to I/F, corrected for solar incidence angle, and atmospherically calibrated in the same

fashion as Mustard et al. (2005) over the Syrtis and Northern Acidalia-Utopia spectral regions (Fig. 3a). In total, 61,050 and 401,831 OMEGA spectra were acquired and processed over the Syrtis and Northern Acidalia-Utopia spectral regions, respectively. These data were averaged within a single image and then weighted to their appropriate spatial coverage and resolution to produce a single spectrum for each of these two spectral regions (Fig. 3b). This methodology produces VNIR spectra that are comparable to those produced using TIR data over the same spectral regions (Rogers et al., 2007; Rogers and Christensen, 2007), allowing for a pan-spectral investigation of these spectral regions.

TIR data were provided by A. D. Rogers and are identical to those derived for TIR spectral investigations of these particular regions (Rogers et al., 2007; Rogers and Christensen, 2007). Following data acquisition, atmospheric constituents were removed using a linear deconvolution surface-atmosphere separation strategy, as described in Rogers et al. (2007). In this method, an endmember library is built to include both potential surface and atmospheric components; atmospheric components include low- and high-opacity dust, small and large water ice grains, and synthetic CO_2 and water vapor spectra. After the algorithm is run, the atmospheric components are scaled according to their modeled concentrations and removed from the spectrum, producing a surface-only emissivity spectrum. The benefits of this technique, as well as a more detailed description of this and other atmospheric removal techniques, are provided in Rogers et al. (2007). For our study, we utilize the surface-only emissivity spectra of the Syrtis and Northern Acidalia-Utopia surface emissivity groups derived by Rogers et al. (2007).

Assembly of endmember library and linear unmixing

The endmember library used in our linear unmixing models is provided in Table 1. This library is identical to the skeleton library used in Rogers and Christensen (2007) with the addition of quartz and alteration rind endmembers and the exclusion of illite, montmorillonite, K-rich glass, and opal-A endmembers. Justification for the exclusion of these endmembers is provided in the main text. Our models were run between the range of 350 cm^{-1} and 1300 cm^{-1}, excluding the excluded atmospheric CO_2 bands between 518 cm^{-1} and 815 cm^{-1}. All values presented in this manuscript have been normalized to their modeled blackbody components, which are provided in Table 2 along with the modeled endmember abundances.

References

Allen C. C. and Conca J. L. (1991), Weathering of basaltic rocks under cold, arid conditions: Antarctica and Mars. *Proc. Lunar Planet. Sci.* **21**, 711-717.

Bandfield J. L., Hamilton V. E. and Christensen P. R. (2000), A global view of martian surface compositions from MGS-TES. *Science* **287**, 1626-1630.

Bibring J.-P., Soufflot A., Berthé M., Langevin Y., Gondet B., Drossart P., Bouyé M., Combes M., Puget P., Semery A., Bellucci G., Formisano V., Moroz V., Kottsov V. and the OMEGA team (2004), OMEGA: Observatoire pour la Minéralogie, l'Eau, les Glaces et l'Activité. *Eur. Space Agency Spec. Pub.* **1240**, 37 pp.

Bibring J.-P., Langevin Y., Mustard J. F., Poulet F., Arvidson R., Gendrin A., Gondet B., Mangold N., Pinet P., Forget F. and the OMEGA Team (2006), Global

mineralogical and aqueous Mars history derived from OMEGA/Mars Express data. *Science* **312**, 400-404.

Chevrier V., Mathé P.-E., Rochette P. and Gunnlaugsson H. P. (2006), Magnetic study of an Antarctic weathering profile on basalt: Implications for recent weathering on Mars. *Earth Planet. Sci. Lett.* **244**, 501-514.

Christensen P. R., Bandfield J. L., Hamilton V. E., Ruff S. W., Kieffer H. H., Titus T. N., Malin M. C., Morris R. V., Lane M. D., Clark R. L., Jakosky B. M., Mellon M. T., Pearl J. C., Conrath B. J., Smith M. D., Clancy R. T., Kuzmin R. O., Roush T., Mehall G. L., Gorelick N., Bender K., Murray K., Dason S., Greene E., Silverman S. and Greenfield M. (2001), Mars Global Surveyor Thermal Emission Spectrometer experiment: Investigation description and surface science results. *J. Geophys. Res.* **106**(E10), 23823-23871.

Cooper R. F., Fanselow J. B. and Poker D. B. (1996), The mechanism of oxidation of a basaltic glass: Chemical diffusion of network-modifying cations. *Geochim. Cosmochim. Acta* **60**, 3253-3265.

Doran P. T., McKay C. P., Clow G. D., Dana G. L., Fountain A. G., Nylen T. and Lyons W. B. (2002), Valley floor climate observations from the McMurdo dry valleys, Antarctica, 1986-2000. *J. Geophys. Res.* **107**, doi:10.1029/2001JD002045.

Fountain A. G., Nylen T. H., Monaghan A., Basagic H. J. and Bromwich D. (2009), Snow in the McMurdo Dry Valleys, Antarctica. *Int. J. Climatol.* **30**(5), 633-642.

Golombek M. P., Grant J. A., Crumpler L. S., Greeley R., Arvidson R. E., Bell J. F., Weitz C. M., Sullivan R., Christensen P. R., Soderblom L. A. and Squyres S. W.

(2006), Erosion rates at the Mars Exploration Rover landing sites and long-term climate change on Mars. *J. Geophys. Res.* **111**, doi:10.1029/2006JE002754.

Hartmann W. K. and Neukum G. (2001), Cratering chronology and the evolution of Mars. *Space Sci. Rev.* **96**, 165-194.

Harvey R. P. (2001), The Ferrar Dolerite: An Antarctic analog for martian basaltic lithologies and weathering processes. *Wkshp. Mart. Highl. & Moj. Desert Anal.*, abst. 4012.

Hurowitz J. A., McLennan S. M., Tosca N. J., Arvidson R. E., Michalski J. R., Ming D. W., Schröder C. and Squyres S. W. (2006), In situ and experimental evidence for acidic weathering of rocks and soils on Mars. *J. Geophys. Res.* **111**, doi:10.1029/2005JE002515.

Koeppen W. C. and Hamilton V. E. (2005), Discrimination of glass and phyllosilicate minerals in thermal infrared data. *J. Geophys. Res.* **110**, doi:10.1029/2005JE002474.

Kraft M. D., Michalski J. R. and Sharp T. G. (2003), Effects of pure silica coatings on thermal emission spectra of basaltic rocks: Considerations for martian surface mineralogy. *Geophys. Res. Lett.* **30**(24), doi:10.1029/2003GL018848.

Marchant D. R. and Head J. W. (2007), Antarctic dry valleys: Microclimate zonation, variable geomorphic processes, and implications for assessing climate change on Mars. *Icarus* **192**, 187-222.

Michalski J. R., Kraft M. D., Diedrich T., Sharp T. G. and Christensen P. R. (2003), Thermal emission spectroscopy of the silica polymorphs and considerations for remote sensing of Mars. *Geophys. Res. Lett.* **30**(19), doi:10.1029/2003GL018354.

Milliken R. E., Swayze G. A., Arvidson R. E., Bishop J. L., Clark R. N., Ehlmann B. L., Green R. O., Grotzinger J. P., Morris R. V., Murchie S. L., Mustard J. F. and Weitz C. (2008), Opaline silica in young deposits on Mars. *Geology* **36**(11), 847-850.

Minitti M. E. and Hamilton V. E. (2010), A search for basaltic-to-intermediate glasses on Mars: Assessing martian crustal mineralogy. *Icarus* **201**, 135-149.

Mustard J. F., Poulet F., Gendrin A., Bibring J.-P., Langevin Y., Gondet B., Mangold N., Bellucci G. and Altieri F. (2005), Olivine and pyroxene diversity in the crust of Mars. *Science* **307**, 1594-1597.

Rampe E. B., Kraft M. D., Sharp T. G., Golden D. C., Ming D. W. and Christensen P. R. (2012), Allophane detection on Mars with Thermal Emission Spectrometer data and implications for regional-scale chemical weathering processes. *Geology* **40**(11), 995-998.

Ramsey M. S. and Christensen P. R. (1998), Mineral abundance determination: Quantitative deconvolution of thermal emission spectra. *J. Geophys. Res.* **103**(B1), 577-596.

Rogers A. D. and Christensen P. R. (2007), Surface mineralogy of martian low-albedo regions from MGS-TES data: Implications for upper crustal evolution and surface alteration. *J. Geophys. Res.* **112**, doi:10.1029/2006JE002727.

Rogers A. D., Bandfield J. L. and Christensen P. R. (2007), Global spectral classification of martian low-albedo regions with Mars Global Surveyor Thermal Emission Spectrometer (MGS-TES) data. *J. Geophys. Res.* **112**, doi:10.1029/2006JE002726.

Rogers A. D. and Aharonson O. (2008), Mineralogical composition of sands in Meridiani Planum determined from Mars Exploration Rover data and comparison to orbital measurements. *J. Geophys. Res.* **113**, doi:10.1029/2007JE002995.

Salvatore M. R., Mustard J. F., Head J. W., Cooper R. F., Marchant D. R. and Wyatt M. B. (2012), Characterizing widespread oxidation processes on Mars: Alteration rind development and effects on spectroscopic investigations. *Proc. Lunar Planet. Sci. Conf.* **XLIII**, abstract 1597.

Schäfer J. M., Baur H., Denton G. H., Ivy-Ochs S., Marchant D. R., Schlüchter C. and Wieler R. (2000), The oldest ice on Earth in Beacon Valley, Antarctica: New evidence from surface exposure dating. *Earth Planet. Sci. Lett.* **179**, 91-99.

Skok J. R., Mustard J. F., Ehlmann B. L., Milliken R. E. and Murchie S. L. (2010), Silica deposits in the Nili Patera caldera on the Syrtis Major volcanic complex on Mars. *Nature Geosci.* **3**(12), 838-841.

Sugden D. E., Marchant D. R., Potter N., Souchez R. A., Denton G. H., Swisher C. C. and Tison J.-L. (1995), Preservation of Miocene glacier ice in East Antarctica. *Nature* **376**, 412-414.

Summerfield M. A., Stuart F. M., Cockburn H. A. P., Sugden D. E., Denton G. H., Dunai T. and Marchant D. R. (1999), Long-term rates of denudation in the Dry Valleys, Transantarctic Mountains, southern Victoria Land, Antarctica based on in-situ-produced cosmogenic ^{21}Ne. *Geomorph.* **27**, 113-129.

Wyatt M. B. and McSween H. Y. (2002), Spectral evidence for weathered basalt as an alternative to andesite in the northern lowlands of Mars. *Nature* **417**, 263-266.

Figure and Table Descriptions

Figure 1. Lithologic and spectral comparisons between Mars and Beacon Valley, Antarctica. (a) Typical basaltic clast in Gusev Crater, Mars (*Spirit* Pancam P2542_Sol14_L456_zoom-A16R1). (b) Typical doleritic clast in Beacon Valley, Antarctica. Subset shows the unaltered (grey) interior and the thin alteration rind (red). (c) Orbital VNIR reflectance spectra from OMEGA (Bibring et al., 2004) and laboratory VNIR reflectance spectra of dolerite interiors and rinds. (d) Orbital TIR emission spectra from TES (Rogers and Christensen, 2007) and laboratory TIR emission spectra of dolerite interiors and rinds.

Figure 2. Comparison of orbital and laboratory TIR and VNIR spectra. (a) The geographic locations used to derive the regional VNIR reflectance and TIR emission data (Rogers et al., 2007). (b) Martian TIR emission spectra (Rogers and Christensen, 2007) overlain with unmixing model results (green). Model residuals (difference between data and model results) indicate that no significant absorptions fail to be modeled during unmixing. Several laboratory emission spectra are also provided for comparison of spectral features and shapes. References can be found in Rogers and Christensen (2007) and Minitti and Hamilton (2010). (c) Martian VNIR reflectance spectra with a suite of analog materials proposed by this study and by previous studies. Strong hydration bands (marked by vertical dashed lines) are present in all of these analog materials with the exception of the dolerite alteration rind. Spectra from the RELAB spectral database (planetary.brown.edu/relabdocs/relab.htm).

Figure 3. Explanation of oxidative weathering processes. (a) A dolerite alteration rind in thin section. Primary crystal structure is maintained throughout the rind

with no evidence for depositional coatings. (b) A schematic of the alteration process, where divalent cations migrate towards the rock surface – a flux compensated by electron transfer in the mineral valence band – as Fe^{2+} is converted to Fe^{3+}. Friable oxides created during this process are readily removed through erosion, dissolution, and abrasion upon exposure to the environment. Modified from Salvatore et al. (2012) and Cooper et al. (1996).

Table 1. Spectral library of geologically relevant endmembers used in this study. Source information can be found in Rogers and Christensen (2007).

Table 2. Modeled surface abundances for Syrtis and Northern Acidalia-Utopia spectral regions. Statistical errors associated with the reported concentrations are derived from the square root of the diagonal of the estimated vector coefficients covariance matrix (Rogers and Aharonson, 2008). Italicized components are modeled at abundances less than 10%, which is the approximate detection limit of most geological materials. Also included are the blackbody contributions and the root-mean-square (RMS) error, indicative of the goodness of fit of the model.

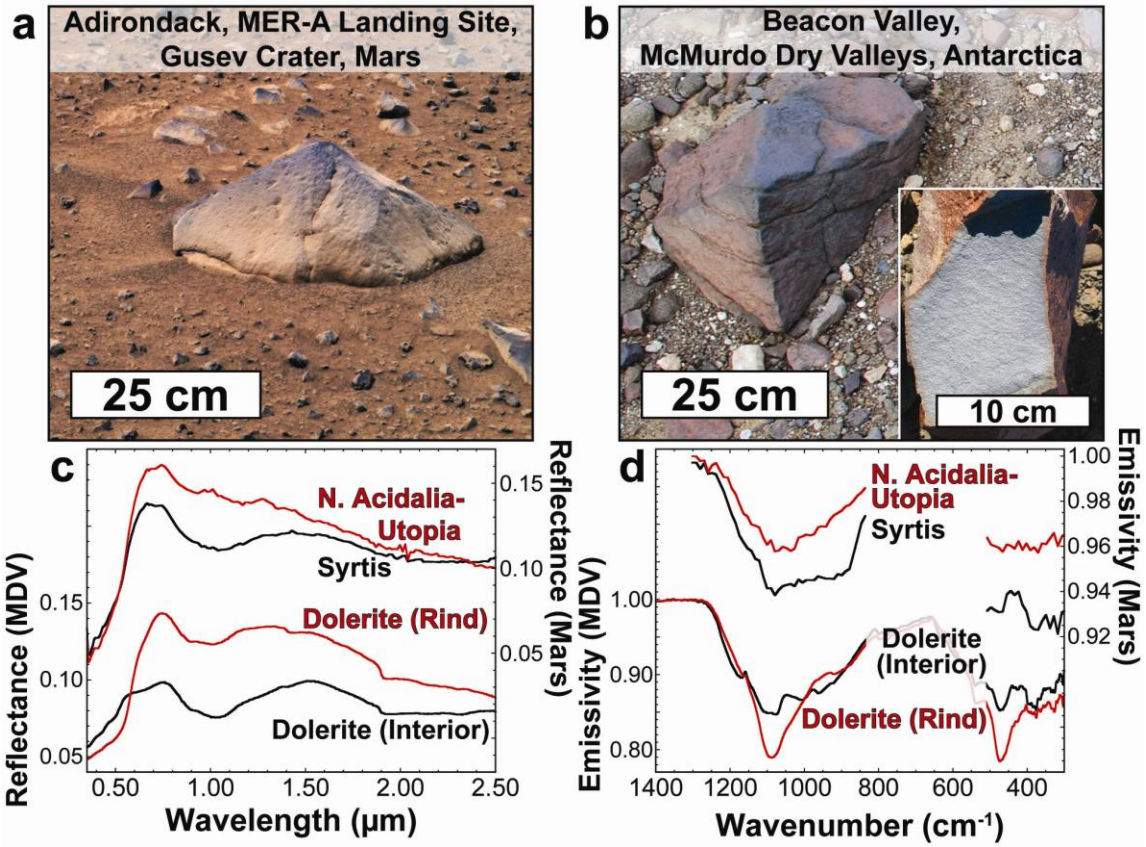

Chapter 4, Figure 1.

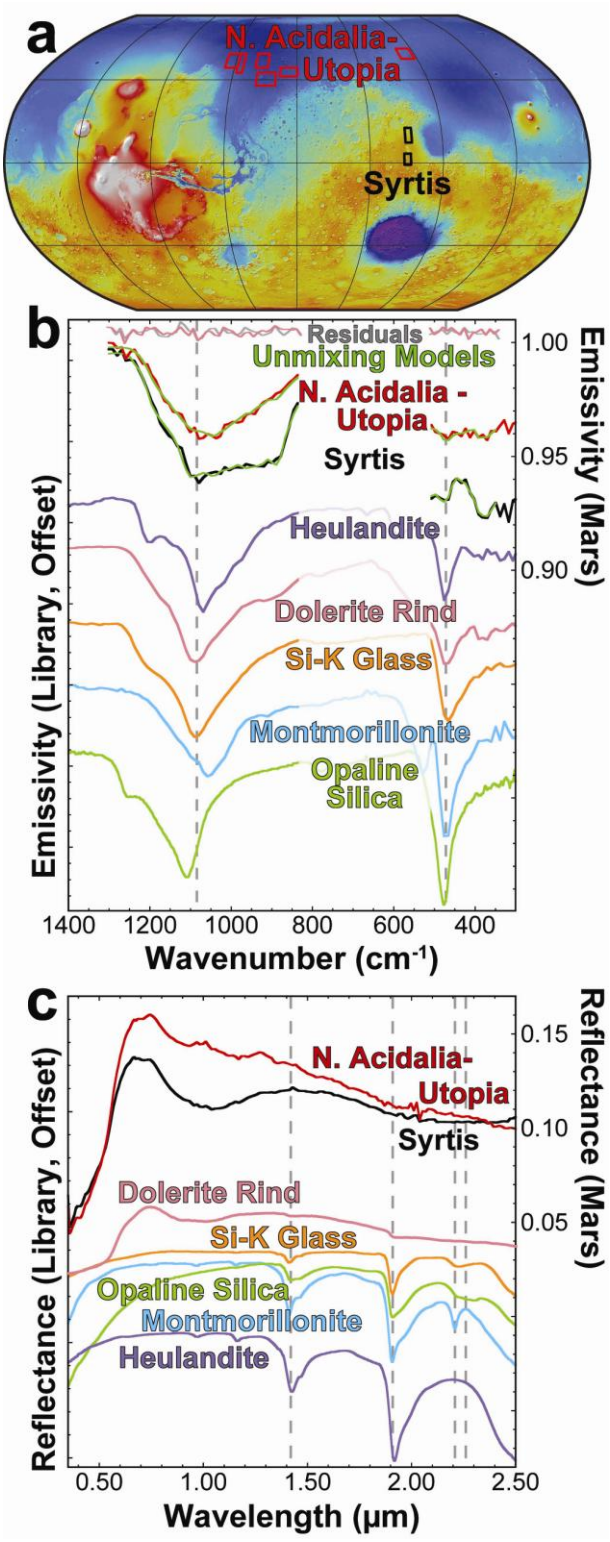

Chapter 4, Figure 2.

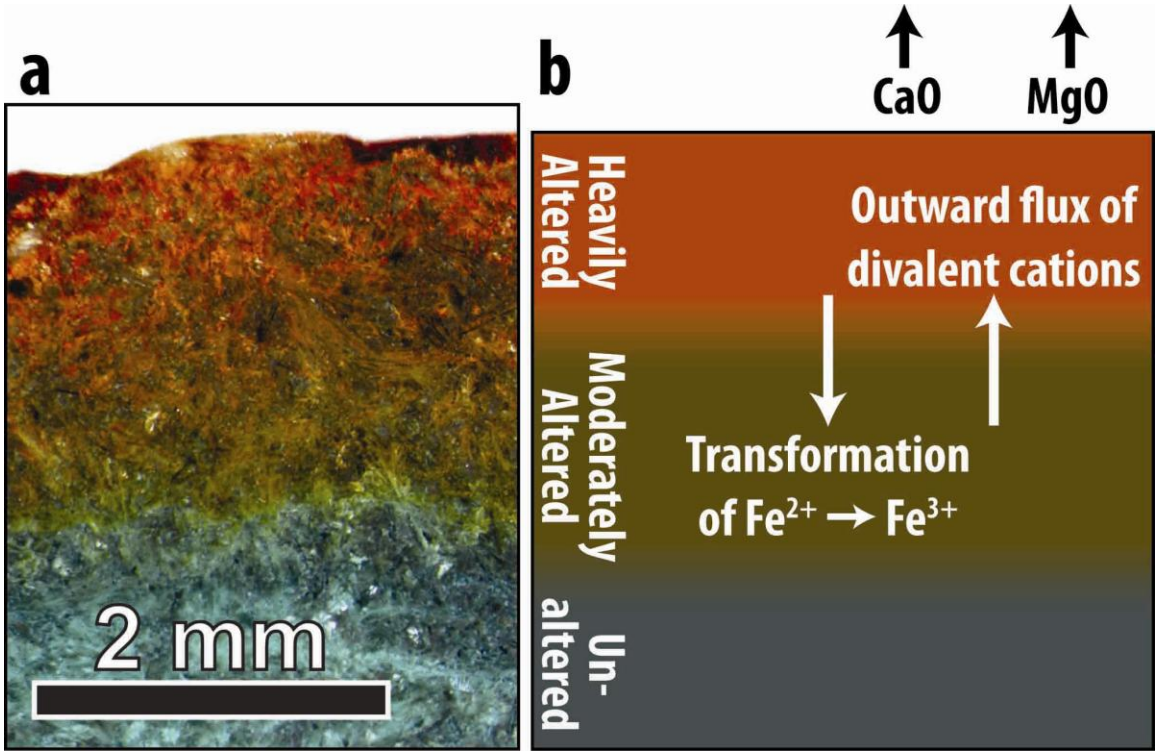

Chapter 4, Figure 3.

Chapter 4, Table 1.

Material (Sample ID or Source)	Classification
Albite (WAR-0244)	Plagioclase
Andesine (BUR-240)	Plagioclase
Anorthite (BUR-340)	Plagioclase
Bronzite (NMNH-93527)	Low-Ca Pyroxene
Enstatite (HS-9.4B)	Low-Ca Pyroxene
Pigeonite (D. Lindsley)	High-Ca Pyroxene
Diopside (WAR-6474)	High-Ca Pyroxene
Augite (NMNH-9780)	High-Ca Pyroxene
Augite (NMNH-122302)	High-Ca Pyroxene
Hedenbergite (DSM-HED01)	High-Ca Pyroxene
Forsterite (BUR-3720A)	Olivine
Fayalite (WAR-RGFAY01)	Olivine
Olivine Fo60 (V. Hamilton)	Olivine
Biotite (BUR-840)	Phyllosilicate
Serpentine (HS-8.4B)	Phyllosilicate
Magnesiohastingsite (HS-115.4B)	Amphibole
Calcite (C40)	Carbonate
Dolomite (C20)	Carbonate
Anhydrite (ML-S9)	Sulfate
Gypsum (ML-S6)	Sulfate
Dolerite Rind (M. Salvatore)	Oxidative Weathering Product
Quartz (BUR-4120)	Quartz
Hematite (TES-derived)	Oxide

Chapter 4, Table 2.

Endmember Group	Syrtis	Northern Acidalia-Utopia
OWPs	14.1% ± 3.7%	37.0% ± 2.9%
Plagioclase	27.3% ± 5.4%	28.7% ± 4.6%
Pyroxene	29.9% ± 4.7%	11.2% ± 3.1%
Olivine	*5.8% ± 3.3%*	*3.3% ± 1.9%*
Quartz	*0.6% ± 0.8%*	*0.0%*
Amphibole	*3.1% ± 3.4%*	*0.0%*
Phyllosilicate	*6.6% ± 2.5%*	*9.4% ± 2.6%*
Sulfate	*6.2% ± 1.7%*	*7.7% ± 1.8%*
Carbonate	*5.7% ± 0.7%*	*2.6% ± 0.7%*
Oxide	*0.7% ± 5.9%*	*0.0%*
Blackbody	35.4% ± 5.3%	67.19% ± 1.3%
RMS Error	0.139%	0.150%

Chapter Five:

The spectral influence of oxidative weathering on martian low albedo terrain.

M. R. Salvatore[1], J. F. Mustard[1], J. W. Head III[1], R. F. Cooper[1], and M. B. Wyatt[1]

[1]Department of Geological Sciences,

Brown University, Providence, RI 02912, USA

Abstract

Thermal infrared (TIR) investigations of the martian surface have revolutionized our understanding of both the primary and secondary mineralogical constituents present at regional spatial scales, revealing a largely basaltic surface with variable amounts of secondary phases. However, the TIR spectral signatures of many alteration phases, including smectites, zeolites, opaline silica, allophane, hydrated glasses, and oxidative weathering products, are indistinguishable in Thermal Emission Spectrometer (TES) investigations. Fortunately, the spectral signatures of these phases in the visible/near-infrared (VNIR) spectrum are distinctive and can provide additional evidence as to the compositions of these martian terrains. In this study, we investigate the VNIR spectral signatures associated with typical martian low albedo regions to constrain the primary and secondary phases that may be present. We also characterize the spectral trends associated with oxidative weathering products, which are uniquely preserved in the hyper-arid and hypo-thermal environments of the McMurdo Dry Valleys. Our results indicate that (1) oxidative weathering of basaltic compositions results in unique VNIR spectral signatures that are indistinguishable from several other alteration phases in the TIR; (2) hydrated alteration phases are not spectrally significant components across regional low albedo terrains on Mars; (3) variations in VNIR spectral shape between 1.5 μm and 2.6 μm are likely to result from the combination of true variations in primary composition as well as spectral indications of chemical weathering; and (4) evidence suggests that oxidative weathering processes and variations in primary composition can account for the majority of observed regional spectral signatures. New linear unmixing models of regional TIR spectra are consistent with the presence of oxidative weathering

products in exchange for hydrated alteration phases. We further explore and substantiate these conclusions by local investigations of surface and subsurface spectral signatures in Acidalia Planitia and Syrtis Major, where unaltered basaltic subsurfaces undergo a similar spectral evolution to more oxidized and less mafic signatures. These analyses confirm the strong spectral influence of hyper-arid and hypo-thermal environmental conditions on remote compositional analyses of the martian surface. Additionally, the ubiquity of oxidative weathering products across the martian surface indicates that the martian climate has been cold and dry for the last ~3.0 Ga of its geologic history.

1.0 Introduction

The dominantly basaltic nature of the martian surface was initially identified through telescopic investigations (e.g. Adams and McCord, 1969; McCord and Adams, 1969) and has been since been confirmed by orbital analyses (e.g. Erard et al., 1990; Mustard et al., 1993; Christensen et al. 2000a). Subsequently, a variety of altered compositions have been identified using orbiting spectroscopic observations (e.g. Poulet et al., 2005; Bibring et al., 2006), analyses of martian meteorites (e.g. Bridges et al., 2001), and landed datasets (e.g. Squyres et al., 2008). This diversity of alteration mineralogies, however, appears to be localized in the oldest geologic terrains (Bibring et al., 2006). Younger and more globally homogeneous units, including martian dust, soils, and post-Noachian (~3.7 Ga to present) volcanic plains, exhibit less spectral and compositional variability than is observed in locally exposed ancient landscapes.

Nonetheless, considerable spectral variations have been observed from orbit across martian low albedo surfaces (Mustard et al., 1993; Mustard and Sunshine, 1995;

Mustard et al., 1997; Bandfield et al., 2000; Christensen et al., 2000a; Bibring et al., 2005; Mustard et al., 2005; Rogers et al., 2007; Rogers and Christensen, 2007). Early thermal infrared (TIR) investigations using the Thermal Emission Spectrometer (TES) instrument identified two unique spectral shapes referred to as Surface Type 1 (ST1) and Surface Type 2 (ST2) (Fig. 1a; Bandfield et al., 2000). These two spectral signatures have since been expanded into 11 unique spectral groups throughout martian low albedo terrain (Rogers et al., 2007; Rogers and Christensen, 2007). While ST1-like signatures have been interpreted as minimally altered basalt, the nature of spectral signatures resembling ST2 has been debated. Initial hypotheses of an andesitic composition (Bandfield et al., 2000) have been largely abandoned in favor of one or several spectrally distinct alteration phases. Wyatt and McSween (2002) initially proposed smectites as a principal ST2 component due to their narrow absorption feature at 1100 cm^{-1}, although later work contested the presence of smectites based on the lack of diagnostic smectite absorption features present at 530 cm^{-1} (Ruff and Christensen, 2007). Other possible alteration components (commonly referred to as "high-silica phases") include thin amorphous silica coatings (Kraft et al., 2003; Minitti et al., 2007), palagonite (Morris et al., 2003), zeolites (Minitti and Hamilton, 2010), Al- or Fe-rich opaline silica (Michalski et al., 2005), Si-rich mineraloids (Michalski et al., 2005), and allophane (Rampe et al., 2012); these have all been proposed as potential contributors to the TIR spectra of ST2 (Fig. 1b). Oxidative weathering processes were recently identified in the McMurdo Dry Valleys of Antarctica, and the resulting spectral signatures were invoked as yet another possible explanation for these unique TIR spectral signatures (Salvatore et al., 2011; 2012; 2013). The anhydrous nature of these oxidative weathering products (OWPs)

precludes the formation of strong vibrational absorption features in the visible/near-infrared (VNIR) associated with hydration and hydrated mineral species, allowing for the remote detection of these phases using a combined VNIR and TIR spectral investigation. By examining the composition and distribution of the primary and secondary phases modeled across the martian surface at a variety of spatial resolutions, we can begin to assess the associated primary and secondary processes that led to their formation as well as the evolution of the martian geologic and climatic systems. This study focuses on answering the following questions: (1) What are the regional VNIR spectral signatures associated with typical martian low albedo terrains? (2) What process(es) can best explain the observed spectral signatures? (3) What are the associated chemical and mineralogical consequences associated with these spectral signatures? (4) What can be inferred about the evolution of the martian climate system based on the distribution of spectral signatures across the surface?

Within the past decade, global VNIR and TIR spectral datasets have been obtained from martian orbit, providing the ability to study these spectral variations across wavelength regions at moderate to high spatial resolutions. In this study, we re-investigate the nature of the low albedo regions initially investigated by Rogers and Christensen (2007) (Fig. 2) using both VNIR and TIR spectroscopic wavelength regions to assess the observed primary and secondary compositions. Data from the Mars Express Observatoire pour la Minéralogie, l'Eau, les Glaces et l'Activité (OMEGA) instrument (Bibring et al., 2004) are regionally averaged to match the low albedo regions studied in Rogers et al. (2007). These data were then subjected to visual inspection and modified Gaussian modeling (MGM; Sunshine et al., 1990) analyses to identify the presence of

spectrally diagnostic phases. Similar analyses are performed on the suite of Antarctic samples discussed in Salvatore et al. (2011; 2012; 2013), which represent the effects of oxidative weathering on basaltic compositions.

Linear unmixing of the regional TIR spectra presented in Rogers and Christensen (2007) was revisited using a subset endmember library that is consistent with regional VNIR observations. Constraining the possible TIR spectral endmembers using VNIR datasets helps to clarify potentially ambiguous spectral signatures. In tandem, these two spectral regions provide complimentary information regarding the potential compositional phases that are present.

Higher resolution spectral analyses of Syrtis Major and Acidalia Planitia were performed to determine the local heterogeneity associated with the observed regional spectral signatures. These analyses supplement previous spectral investigations, which identify small-scale variations in the VNIR spectral signatures throughout both of these regions (Mustard et al., 2005; Baratoux et al., 2007; Salvatore et al., 2010; Skok et al., 2010).

2.0 Methods

2.1 Laboratory spectroscopy

VNIR reflectance spectra of the oxidized alteration rinds and the unaltered interiors of Antarctic dolerites (shallow intrusive basalts) were acquired at the Brown University Keck/NASA Reflectance Experiment Laboratory (RELAB) using a bidirectional reflectance spectrometer, which acquires data between 0.32 and 2.55 μm at a 5 nm sampling interval using a photomultiplier and InSb detectors (Pieters, 1983;

Mustard and Pieters, 1989). Illumination and emergence angles were fixed at 30º and 0º, respectively. MGM analyses were performed on the VNIR spectra of dolerites to identify the relative intensities of the broad crystal field absorptions in the 2 μm region caused by the presence and abundance of pyroxenes. The MGM is an objective analytical technique that does not require a priori information or assumptions about the composition of the material under investigation. In this particular application, the MGM defines and removes a continuum for each individual spectrum and then models the continuum-removed spectrum with a series of modified Gaussian curves (Sunshine et al., 1990). In this study, we utilize the methodology described by Gendrin (2004) and Skok et al. (2010) by which the 2 μm spectral region is subset and modeled using only two modified Gaussians centered at 1.9 μm and 2.3 μm with fixed full width half maximums (FWHM). Spectra are first clipped to include only those data at wavelengths longer than their local reflectance maximum near 1.5 μm. Next, a continuum is defined and removed for each spectrum, and the model is then run until the modeled root-mean-square (RMS) error is below a tolerance of 10^{-5}. These two Gaussians at 1.9 μm and 2.3 μm represent the spectral absorption features of low-calcium pyroxene (LCP) and high-calcium pyroxene (HCP), respectively, and their modeled relative strengths indicate the proportion of each pyroxene endmember to the provided spectrum.

The strength, shape, and position of this 2 μm crystal field absorption band can be influenced by several different factors, most notably the concentration and composition of the pyroxenes present. This absorption feature is caused by the presence of Fe^{2+} in the highly distorted pyroxene M2 site (Burns, 1993). Transitioning from HCP to LCP results in the continued replacement of Ca by Fe^{2+}, causing the M2 site to contract in response to

the presence of a smaller cation and the subsequent shift of the 2 μm band to higher frequencies (shorter wavelengths) (Burns, 1993). As a result, the location of the 2 μm absorption feature shifts from 2.3 μm in HCP to 1.9 μm in LCP, permitting the retrieval of approximate pyroxene composition from the analysis of the relative position and shape of this absorption feature.

This methodology is consistent with previous MGM investigations of martian surface compositions (e.g. Gendrin, 2004; Skok et al., 2010). The 1 μm region was excluded from MGM modeling due to the possible overlapping contributions from several different compositions, including pyroxene, olivine, crystalline plagioclase, ferric iron oxides, and basaltic glass (Kanner et al., 2007). Fortunately, pyroxene is the only common mafic mineral in the dolerite and on Mars that exhibits a significant 2 μm absorption feature. Concern over the influence of strong 1.9 μm vibrational absorption features prompted the exclusion of all dolerite spectra with a 1.9 μm band strength greater than 10% from these analyses.

TIR emission measurements were acquired at the Vibrational Spectroscopy Laboratory at Stony Brook University using a Nicolet 6700 FTIR Spectrometer, which utilizes a deuterated L-alanine doped triglycine sulfate (DLaTGS) detector and CsI window. Measurements were made between 2000 cm^{-1} and 200 cm^{-1} at a resolution of 4 cm^{-1} using a CsI beamsplitter. Linear unmixing was performed used a spectral endmember library that is identical to the skeleton library used in Rogers and Christensen (2007) to ensure consistency between laboratory and orbital analyses. Additional information regarding TIR measurements and calibrations can be found in Ruff et al. (1997).

TIR data were linearly unmixed to determine the abundances of compositional phases present within the samples. The linear unmixing algorithm used in this study is identical to that of Ramsey and Christensen (1998) and consists of a numerical least squares fitting algorithm using a chi-squared minimization (Ramsey, 1996), where the matrix of unknown endmember fractions is solved using a linear regression analysis (Press et al., 1988). Linear unmixing is possible in the TIR due to the high absorption coefficients of most geologically relevant materials, resulting in the dominance of emitted energy from the uppermost surface and the reduction of volumetric interactions and scattering (Ramsey and Christensen, 1998). As a result of this surface interaction, the observed emission spectrum is a linear combination of the areal abundance of phases present on the surface within a given field of view. Unmixing of this spectrum is possible given an endmember library that contains all of the applicable spectral endmembers (Ramsey and Christensen, 1998; Rogers and Christensen, 2007). The spectral unmixing of dolerites was performed using the full wavelength range between 1400 cm^{-1} and 400 cm^{-1}.

2.2 Visible/Near-infrared orbital spectroscopy

To study the observed spectral variability throughout martian low albedo regions and to determine whether significant vibrational absorption features are present throughout these terrains, regional VNIR data were collected, calibrated, and averaged into the same geographic regions described in Rogers et al. (2007). VNIR data were obtained using the OMEGA instrument, which is an imaging reflectance spectrometer that spans the wavelength range of 0.35 μm to 5.1 μm at a sampling resolution of 8 nm – 14 nm and a spatial resolution of 0.3 – 5 km pix^{-1}, depending on the position of the

spacecraft within its highly eccentric orbit (Bibring et al., 2004). Data were acquired from all 61 atmospherically and spectrally clean images obtained over the nine representative spectral regions analyzed in Rogers and Christensen (2007) prior to orbit 1600. Radiance data were corrected to the ratio between the observed radiance and the incoming solar flux (I/F) using the techniques of Bellucci et al. (2006). Atmospheric contributions were removed following the methodologies described in Bibring et al. (2005), where an atmospheric spectrum is derived from spectral observations at the base and summit of Olympus Mons and is scaled by the strength of the CO_2 atmospheric absorption feature measured in the observation. All pixels within these geographic regions were averaged within their individual scene and single channel spikes that are too narrow to be associated with mineralogy were filtered (Ehlmann et al., 2009). Lastly, the average spectrum from each image was weighted according to the area of the footprint of that particular image relative to the total area of the entire spectral region. This process results in nine VNIR spectra, representing the average spectral signature for these representative spectral regions as measured by the OMEGA instrument. Additional high quality OMEGA data up to orbit 2500 were acquired and processed for the detailed investigation of Acidalia Planitia and Syrtis Major.

VNIR data were visually inspected for the presence of electronic and vibrational absorption features associated with primary and secondary compositions. In addition to these visual inspections, MGM was applied to each average spectrum to derive the relative contributions of LCP and HCP in the 2 μm wavelength region in addition to calculating magnitude of the near-infrared spectral slope.

2.3 Thermal infrared orbital spectroscopy

TIR data were gathered from the TES instrument on the Mars Global Surveyor spacecraft to investigate regional and local variations in primary silicate and alteration mineralogy. The TES instrument consists of three subsections, one of which is a Michelson interferometer covering a spectral range from 1650 cm^{-1} to 200 cm^{-1} with a sampling resolution of 5 cm^{-1} – 10 cm^{-1} and an individual pixel size of 3 km by 6 km (Christensen et al., 2001). The emissivity spectra of the nine spectral regions analyzed in this study are identical to those analyzed in Rogers and Christensen (2007) and include Northern Acidalia (NA), Syrtis (SM), Tyrrhena (TT), Cimmeria-Iapygia (CI), Aonium-Phrixi (AP), Hesperia (HP), Mare Sirenum (MS), Meridiani (MP), and Solis (SP). The TIR spectra used in the local investigations of Acidalia Planitia and Syrtis Major were acquired using the TES Data Tool (tes.asu.edu/data_tool; accessed on 26 September 2012) for the spectral regions of interest (Table 1). The local Acidalia Planitia study region was defined as 18º N – 70º N and 310º E – 335º E, whereas the local Syrtis Major study region was defined as 2º S – 28º N and 58º E – 83º E. TES data were acquired between mapping phase orbits 1 to 5317 with a scan length of 10 cm^{-1} and were subset based on target temperature ($\geq$ 255 K), lambert albedo ($<$ 0.15), emission angle ($\leq$ 30º), total ice ($\leq$ 0.04) and dust ($\leq$ 0.15) extinctions, and no solar panel or high gain antenna motions. Following acquisition, only data with sufficient spectral contrast were used (defined as a ratio between emissivity values at 1238 cm^{-1} and 1100 cm^{-1} greater than 10%). The high spectral contrast criterion limited the number of spectra to 9627 for Acidalia Planitia and 32616 for Syrtis Major, which were then individually inspected to identify and remove spectra that exhibited anomalous spectral shapes. Data were then

aggregated into 2 pixel per degree (ppd) bins, where only bins containing 5 or more individual spectra were kept for additional analyses. The resultant data products are two spectral grids (2 ppd) of high quality TES data with high spectral contrast. The average number of spectra included in each bin for Acidalia Planitia and Syrtis major were 14.0 and 27.3, respectively. Unbinned spectra were also used for more detailed spectral investigations and are discussed further in Section 3.3.

Surface emissivity was derived for each of the binned pixels through the use of the linear deconvolution atmospheric removal technique (Ramsey and Christensen, 1998; Smith et al., 2000). This technique uses an additional atmospheric endmember library to distinguish and remove atmospheric components present in the emission spectra. The additional library is forced to fit each individual spectrum (negative values permitted) to return an emissivity spectrum representing only the observed surface. This technique was shown to be effective at removing atmospheric constituents from TES spectra, allowing for the modeling and interpretation of spectral signatures derived from the surface itself (e.g. Wyatt et al., 2003; Rogers et al., 2007). These derived surface emissivity spectra are concurrently unmixed using an endmember library containing geologically pertinent endmembers (Christensen et al., 2000b). Linear unmixing of TES data was performed between 1300 cm^{-1} and 350 cm^{-1} with the exclusion of the wavenumber region of atmospheric CO_2 opacity between 518 cm^{-1} and 815 cm^{-1}.

3.0 Results

3.1 Laboratory analyses (Table 2)

MGM analyses performed on dolerite VNIR reflectance spectra (Fig. 3, Table 2) indicate a systematic decrease in near-infrared spectral slope in dolerite surfaces relative to their interiors, strengthening the negative slope by an average of 9.4º. In addition, the apparent spectral contribution of LCP (indicated by the LCP#, which is calculated as the proportion of LCP relative to total pyroxene, where a value of 1 indicates all LCP and a value of 0 indicates all HCP) is greater in all dolerite surfaces (average LCP# value of 0.46) than for their corresponding interiors (average LCP# value of 0.19). In tandem, there is a clear spectral trend that shows a systematic decrease in spectral slope and increase in LCP# from dolerite interiors to their corresponding surfaces (Fig. 4). Lastly, the strength of the Fe^{3+} intervalence charge transfer (IVCT) absorption feature in the visible wavelengths (<0.6 μm), calculated as the average reflectance surrounding 0.73 μm relative to that near 0.35 μm, is stronger in dolerite surfaces (2.16) relative to dolerite interiors (1.44), indicating a higher degree of oxidation in dolerite surfaces.

Linear unmixing was performed on the same subset of dolerites used in the MGM analyses described above (Fig. 5). The unmixing of these dolerite interiors and surfaces utilizing the skeleton library described in Rogers and Christensen (2007) reveal average LCP# values of 0.25 for dolerite interiors and 0.31 for dolerite surfaces. While the magnitude of modeled LCP enrichment is not equivalent between our VNIR and TIR investigations, it is clear that the oxidation and alteration process at work on dolerite surfaces creates an apparent decrease in the magnitude of HCP spectral contributions relative to that of LCP. This can be observed in the average TIR dolerite spectra (Fig. 5),

which show stronger absorption features between 900 cm^{-1} and 1000 cm^{-1} in the interior spectrum relative to the surface spectrum. These absorptions are due to the second and third critical absorption features in CPX, which are typically weaker than the first characteristic absorption feature in OPX centered near 1050 cm^{-1} (Hamilton, 2000). The reduced strength of these absorption features in the average dolerite surface spectrum results in an apparent decrease in HCP abundance relative to LCP. Additionally, there is a significant spectral misfit between our unmixing model and the measured dolerite surface spectrum in this pyroxene critical absorption region (black arrow, Fig. 5). Emissivity is underestimated between 900 cm^{-1} and 1000 cm^{-1}, indicating that the library may be missing a relevant spectral endmember. Furthermore, it is possible that the modeled pyroxene (particularly HCP) abundances in dolerite surfaces are overestimated, and the inclusion of additional endmembers could potentially increase the LCP# value modeled for dolerite surfaces.

In the unmixing models for both interior and surface spectra, silica- and potassium-rich glass (SiK Glass; Wyatt et al., 2001) is modeled as the most significant "high-silica phase." Dolerite surfaces are also modeled as containing 15.6% smectites. While hydrated interstitial glass may account for the presence of the 1.4 μm and 1.9 μm hydration bands observed in VNIR spectra of both dolerite interiors and surfaces (Fig. 3), its physical abundance at > 15 vol.% in both interiors and surfaces is not supported by this or previous investigations (Salvatore et al., 2013). Additionally, despite these significant spectral differences between dolerite interiors and surfaces, laboratory analyses of the Beacon Valley dolerites using X-ray diffraction reveal no substantial changes in bulk mineralogy (Salvatore et al., 2013). Inductively coupled plasma-atomic

emission spectroscopy via the flux fusion method of sample preparation (Murray et al., 2000) reveals subtle yet diagnostic chemical variations between dolerite interiors and their surfaces that are indicative of the outward migration of divalent cations in response to an oxidation gradient (Salvatore et al., 2013; Cooper et al., 1996) and are not consistent with the presence of significant abundances of hydrated alteration phases.

The modeling of these alteration phases at anomalously high abundances, the significant spectral misfit observed in the unmixing model of dolerite surfaces, and the doubling of the measured RMS error (indicative of the overall goodness of fit of the model; Ramsey and Christensen, 1998), all suggest that the current endmember library is not capable of accurately modeling the components present in dolerite surfaces. The weak to absent chemical and mineralogical variations observed between dolerite interiors and surfaces also imply that a unique compositional endmember is not being excluded from our endmember library at spectrally, chemically, or mineralogically significant abundances. Therefore, we consider dolerite alteration rinds to be unique compositional and spectral endmembers, representing OWPs that form in cold and dry environments. This representative spectrum of oxidative weathering products was added to our linear unmixing library to represent a plausible spectral component of martian low albedo surfaces.

3.2 Orbital analyses (Regional)

VNIR reflectance data of the nine spectral regions reveal the presence of two broad absorption features centered near 1 μm and 2 μm (Fig. 6). These absorptions are the result of crystal field transitions caused primarily by the presence of ferrous iron in the M2 octahedral site in pyroxenes. Additional structure may be present near or within

the 1 μm band due to contributions by Fe^{2+} in the M1 and/or M2 octahedral sites in olivines, Fe^{3+}-bearing components, and basaltic glass (Kanner et al., 2007). All of the spectra also exhibit a strong absorption feature at visible wavelengths (< 0.6 μm) as a result of an Fe^{3+} IVCT absorption. This feature, however, is readily influenced by minute quantities of surface dust (< 1%) and therefore should be interpreted with caution (Roush et al. 1993). Lastly, none of the regional spectra exhibit vibrational absorption features near 1.4 μm (OH^- stretching overtone and combination tones of H_2O), 1.9 μm (stretching and bending combination of H_2O), or between 2.1 and 2.5 μm (structural metal-OH stretching and bending combination). Absorption features at these wavelengths would indicate the presence of hydrated geologic materials, and the absence of these signatures suggests that hydrated phases are not present at spectrally significant abundances.

The MGM-derived outputs indicate substantial spectral variability associated with the 2 μm pyroxene absorptions and the modeled spectral slope (Fig. 7). Most of the regional VNIR spectra exhibit a near-uniform mixture of both the 1.9 μm and 2.3 μm absorption features, as indicated by LCP# values near 0.5. However, the LCP# is substantially higher in the NA spectral region (0.84) and lower in the SM spectral region (0.39). These model results indicate that the majority of the low albedo martian surface is spectrally consistent with a mixture of LCP and HCP, while locales enriched in both LCP and HCP are also present. This observation is consistent with previous regional VNIR investigations of the martian surface (e.g., Mustard et al., 2005).

These laboratory and VNIR spectral investigations indicate that not all of the phases included in the Rogers and Christensen (2007) skeleton library are potential candidates for the observed compositions in martian low albedo regions. Based on the

lack of diagnostic spectral features in the VNIR, we are able to exclude several hydrated phases that are not abundant at spectrally identifiable quantities (~10%, Ehlmann et al., 2012), including illite (IMt-2), montmorillonite (STx-1), SiK Glass, and opal-A (01-011) (Table 3). The non-detection of these phases in the VNIR suggests that their greatest possible abundances are still lower than the estimated TES detection limit of 10% (Ehlmann et al., 2012; Christensen et al., 2000). Their exclusion was also due to their spectral similarity in the TIR, which results in ambiguous model results. Other hydrated phases, including carbonates, sulfates, and amphiboles, were kept in the endmember library because of their unique spectral shapes in the TIR and for their reduction of model RMS errors when modeled at or below TES detection limits. Additionally, a spectrum of enstatite (HS-9.4B; Christensen et al., 2000b) was added to augment the spectral diversity of potential LCP endmembers within the spectral library. Lastly, the spectrum of OWPs (Salvatore et al., 2013) was also included to represent a potential oxidative weathering phase.

Linear unmixing results of the nine low albedo regions utilizing this modified spectral library are presented in Table 4 and are shown graphically in Figure 8. The low RMS errors and the lack of coherent spectral signatures present in residual spectra indicate that our model results appropriately fit the input spectra. In addition, the modeled primary mineral components are largely consistent with previous studies, suggesting largely basaltic substrates with variable amounts of secondary materials.

Several differences exist between our modeled endmember components and those of previous investigations. First, LCP is modeled at much higher abundances than HCP in all of our unmixing models, with the exception of the SM spectrum. This result is at

odds with previous studies, which suggest that the majority of martian low albedo terrains are dominated by HCP (e.g., Bibring et al., 2005; Mustard et al., 2005; Rogers and Christensen, 2007). Second, the modeled plagioclase/pyroxene ratios range from 0.6 (TT) to 2.6 (NA), which is outside the range of those identified in martian meteorites (0.1 – 0.3; Hamilton et al., 1997) and is broader than the range previously modeled by Rogers and Christensen (2007). Third, OWPs are modeled at abundances ranging from 14% to 37%, with an average of 27.9%. This modeled component largely substitutes for the high-silica phases in the endmember libraries of previous studies.

On a plagioclase–(pyroxene + olivine)–OWP ternary diagram (Fig. 9a), all nine regions are widely spread below the 40% plagioclase line, with those regions modeled with higher OWP abundances (e.g., NA, SP, MP) also modeled with less pyroxene and olivine. On a HCP–LCP–olivine ternary diagram (Fig. 9b), most of the regions fall along or near the LCP and olivine join, with TT and SM modeled as having higher HCP abundances. While SM has the lowest modeled LCP abundance, TT has an intermediate modeled LCP abundance, implying that the relative proportion of HCP is not directly associated with the relationship between LCP and olivine abundances. Lastly, on a HCP–LCP–OWP ternary diagram (Fig. 9c), most data plot along the LCP and OWP join. With the exception of MP, those regions modeled with HCP abundances greater than zero are also modeled as having the lowest OWP contributions. This is particularly true for TT and SM, which are the only two regions where HCP is modeled above the traditional TIR detection limits. This suggests that the relative proportion of HCP is linked to the relationship between modeled LCP and OWP abundances. This relationship can also be seen when plotting modeled OWP abundance against LCP# (Fig. 10). Similar to the

trend observed in Figure 9c, the relationship between these two variables does not appear to be linear, although there is a significant logarithmic relationship ($R^2 = 0.87$) that strongly suggests that high OWP abundances are related to high LCP#. Caution must be taken when interpreting TIR-derived LCP#, however, because OWPs are modeled as complex mixtures that contain primary mineral phases that include higher HCP abundances relative to LCP. As a result, HCP spectral signatures may be preferentially masked in OWP spectral signatures. Both VNIR and TIR spectral signatures must be interpreted concurrently to identify where these apparent variations in LCP# are due to either primary igneous or secondary alteration processes.

3.3 Orbital analyses (Local)

Syrtis Major and Acidalia Planitia have long been regarded as spectral endmembers of martian low albedo regions (e.g. Mustard et al., 2005). Our regional analyses confirm the disparities between these two regions in both the visible, near-, and thermal-infrared. Characterization of subsurface compositions throughout these regions was also performed using high resolution VNIR data from the OMEGA and Compact Reconnaissance Imaging Spectrometer for Mars (CRISM) instruments (Baratoux et al., 2007; Salvatore et al., 2010; Skok et al., 2010). These analyses supplement regional surface studies by utilizing impact craters as probes into the shallow subsurface where subaerial alteration processes have likely been minimized relative to the regional surface. Below, we incorporate these detailed investigations of subsurface compositions into our regional surface analyses in an effort to better constrain their relationship.

3.3.1 Acidalia Planitia

In Acidalia Planitia, Salvatore et al. (2010) identified the presence of discrete olivine- and HCP-bearing basaltic components in the shallow subsurface through their identification in crater rims and ejecta deposits. The intact HCP-bearing stratigraphic units are small in scale, on the order of 10^2 m in thickness, precluding the use of the OMEGA instrument to investigate these units in their pristine geologic settings. However, MGM analyses of the CRISM observations presented in Salvatore et al. (2010) confirm the dominance of HCP over LCP (LCP# of 0.34) and suggests the presence of spectrally similar pyroxenes to those observed in Syrtis Major by Skok et al. (2010) (Salvatore et al., unpublished data). This MGM modeling, however, was performed on surface spectra that were ratioed to nearby spectrally neutral terrain (to remove spectral artifacts and remnant atmospheric components; Mustard et al., 2005) and is therefore not equivalent to the MGM analyses performed on the regional unratioed OMEGA data presented elsewhere in this study.

Surface emissivity data for Acidalia Planitia were derived for the binned TES data concurrent with atmospheric removal process and were spectrally unmixed using the modified endmember library. Average model RMS errors were 0.00246 with a standard deviation of 0.00069, and are comparable to the errors associated with the global mineral distributions modeled by Bandfield (2002). Both the shape of the derived surface emissivity spectra as well as the modeled mineral abundances suggest the presence of two distinct terrains within Acidalia Planitia separated north and south of 42º N latitude (hereby referred to as South Acidalia and North Acidalia) (Fig. 11). In South Acidalia, the derived average surface emissivity spectrum exhibits low spectral contrast (~ 4%) and

a slight concave-down feature centered near 950 cm^{-1}, while the derived average surface emissivity spectrum of North Acidalia has higher spectral contrast (~ 6%) and no concave-down feature near 950 cm^{-1} (Fig. 11a). These observations were also made by Rogers et al. (2007), who interpreted the spectral differences to likely be related to small amounts of dust in South Acidalia. Compositionally, total pyroxene, OWP, and carbonate abundances differ between South Acidalia and North Acidalia, although these variations are within the estimated detection limits of the TES instrument (10%, Christensen et al., 2000a) (Fig. 11b, Table 5). The modeled carbonate contribution is due to an unresolved problem associated with linear unmixing of TES data (Fig. 11a; Stockstill-Cahill et al., 2008). Consequently, interpreting these modeled mineral differences is likely inappropriate. Despite these uncertainties, it is evident that LCP is preferred over HCP as the dominant pyroxene phase present in Acidalia Planitia (Fig. 11c).

Higher resolution spectral investigations, however, may be fruitful given the extent of VNIR spectral diversity observed in impact ejecta throughout Acidalia and Chryse planitiae (Tornabene et al., 2006; Salvatore et al., 2010). Several olivine-rich ejecta blankets were identified by Salvatore et al. (2010) and are larger in spatial extent than the discrete subsurface horizons, which permits the use of OMEGA data in their analysis. Grindavik crater (25.4º N, 321.0º E), an 11.7 km crater in southern Acidalia Planitia, is an archetypal example of these olivine-rich ejecta blankets. Ratios of large spectral averages from OMEGA image ORB2079_7 exhibit characteristic olivine absorption features in the VNIR (Fig. 12b), and the absence of olivine absorption features in the surrounding terrain is confirmed through spectral parameterization (Fig. 12a).

In the TIR, fourteen individual TES spectra were extracted from over the ejecta blanket, atmospherically corrected, and unmixed using the methodologies described above. These data were then compared to the regionally binned spectra extracted for the regional terrain south of the crater (Fig. 12c). Although the TES spectra do not overlap entirely with the corresponding OMEGA data, the uniformity of the crater ejecta in Thermal Emission Imaging System (THEMIS) (Christensen et al., 2004) nighttime infrared imagery and its distinct properties relative to the surrounding terrain indicates that the entirety of the ejecta blanket is spectrally distinct. Unmixing results for the crater ejecta confirm the presence of olivine at abundances greater than the estimated detection limits of TES (12.3%), in addition to OWPs (42.9%), plagioclase (18.8%), and other minor phases. On the other hand, binned spectra of the surrounding regional terrain are modeled with olivine at below the TES detection limit (4.0%), while OWPs (51.6%), plagioclase (17.0%), and LCP (11.0%) are the most dominant spectral phases (Table 5).

3.3.2 Syrtis Major

Baratoux et al. (2007) and Skok et al. (2010) characterized the distribution of spectrally distinct ejecta (SDE) in the VNIR across Syrtis Major, which exhibit stronger spectral signatures associated with HCP relative to the surrounding terrain and are largely clustered to the east of Nili Patera (Fig. 13). These data were used to suggest that a regional or global transition in the martian climate occurred roughly 2 Gyr ago (based on extensive crater counting), resulting in the chemical alteration of surface materials prior to this event and the preservation of surface materials exposed since this transition. To further characterize these spectral variations, we assess the regional TIR variability associated with Syrtis Major and compare this with previous VNIR investigations. We

then utilize both VNIR OMEGA and TIR TES data to analyze two archetypal SDEs and compare them to the surrounding regional terrain to compare the modeled mineralogy at a higher spatial resolution.

The average RMS errors associated with atmospheric removal, surface emissivity derivation, and linear unmixing for the 2 ppd TIR Syrtis Major data was 0.00170 with a standard deviation of 0.00028. Two distinct terrains were also identified on the volcanic shield of Syrtis Major, separated by the 69º E line of longitude (hereby referred to as West Syrtis and East Syrtis) (Fig. 14). Both terrains exhibit similar average RMS errors, with West Syrtis modeled at 0.00169 and a standard deviation of 0.00028 and East Syrtis modeled at 0.00170 and a standard deviation of 0.00029. While within the estimated error associated with TES unmixing models, West Syrtis is modeled with 4.6% less pyroxene (primarily HCP) and 4.5% more OWP than East Syrtis (Fig. 14a, Table 5). The modeled LCP# associated with West Syrtis is 0.60, whereas this value is modeled as 0.52 in East Syrtis. The average TIR spectrum of East Syrtis exhibits a stronger absorption between 900 cm^{-1} and 1000 cm^{-1}, similar to that observed in the average dolerite interior TIR spectrum, which indicates a stronger HCP spectral contribution (Fig. 14a, Hamilton 2000). A simple model of adding 5% augite (HCP) to the average West Syrtis spectrum verifies that the addition of an HCP component results in a strengthened absorption feature in this region (Fig. 15). As a result, despite being below the previously accepted detection limits for linear unmixing models, we interpret these mineralogical variations as justifiable.

To investigate these local spectral variations, we acquired 6,527 OMEGA pixels over two SDE in Syrtis Major (associated with craters centered at 8.9º N, 74.3º E, and

5.9º N, 70.5º E, black dashed circles in Fig. 13) from OMEGA images ORB2316_4 and ORB0284_2, respectively. These data were compared to 7,623 OMEGA pixels of the regional terrain near 8.5º N, 68.75º E (grey dashed box, Fig. 13). MGM analyses (Fig. 16) indicate an average LCP# of 0.39 and 0.31 for the regional terrains and the SDE, respectively, which are largely consistent with the values and magnitude of variability observed in Syrtis Major by Skok et al. (2010). The negative VNIR spectral slope of the surrounding terrain is also 0.7º stronger than that of the SDE, which is consistent with the spectral trends observed in the dolerites.

TES spectra were acquired over these two SDE deposits and compared to the surrounding terrain within Syrtis Major. In total, 185 TES spectra were averaged and compared to the TIR spectra of the archetypal regional terrain acquired near 8.5º N, 68.75º E during our regional investigation of binned 2 ppd TES spectra. The results of this study are generally consistent with both previously reported VNIR investigations as well as our analyses of OMEGA data. TIR-derived LCP# is modeled as 0.83 for the surrounding regional terrain and 0.16 for the SDE deposits. While this range of values far exceeds our other analyses as well as those derived from other studies, the trend is identical and indicates the spectral masking of HCP signatures in the surrounding terrains. The spectral variations between SDEs and the surrounding terrain are reported in Figure 17. Particular emphasis is drawn to the modeled 10.8% higher HCP and 4.8% lower OWP abundances in SDE relative to the surrounding regional terrain (Table 5). These modeled trends are consistent with those observed in TIR analyses of dolerite surfaces and interiors, suggesting that similar weathering and resultant spectral processes are at work.

3.4 Summary

VNIR laboratory analyses of weathered dolerites from Beacon Valley, Antarctica, exhibit systematic decreases in NIR spectral slopes. Apparent shifts in the position of the broad 2 μm crystal field absorption band suggests a stronger spectral contribution of LCP relative to HCP, despite no such variations observed in laboratory compositional analyses (Salvatore et al., 2013). Identical VNIR spectral variations are observed regionally across martian low albedo terrains, where regions exhibiting more HCP-dominated spectral signatures have the least negative NIR spectral slopes and regions exhibiting more LCP-dominated spectral signatures have the most negative spectral slopes. Local VNIR analyses are also subject to much more spectral variability than is observed regionally, but where observed, local pyroxene spectral trends appear to be consistent with regional observations. In particular, regional intercrater plains in both Acidalia Planitia and Syrtis Major systematically exhibit more LCP-dominated spectral signatures in the VNIR than the ejecta and subsurface layers exposed in younger impact craters.

TIR spectral measurements of dolerite surfaces are also modeled as being more enriched in LCP than their corresponding unaltered interiors. The significant narrowing of reststrahlen features in the absence of evidence for significant hydration in the VNIR suggests that OWPs are a unique spectral endmember. When added to martian TIR unmixing libraries in exchange for unobserved hydrated phases, OWPs are modeled at spectrally significant abundances in all martian low albedo terrains. Local analyses in Acidalia Planitia and Syrtis Major show identical TIR spectral trends that correspond with VNIR analyses at the same spatial scales. In particular, intercrater plains are

modeled as more enriched in OWPs and exhibit higher LCP# values than younger ejecta deposits.

4.0 Discussion

4.1 Assumptions regarding oxidative weathering products and processes

The oxidation products described in Salvatore et al. (2013) and discussed throughout this manuscript do not represent a pure mineralogic or alteration endmember, but rather a distinct alteration trend associated with the oxidative weathering process observed in Beacon Valley, Antarctica. Additionally, the observed alteration signatures may be strongly dependent upon the composition of the unaltered lithologic material as well as the environment under which oxidation is proceeding. As a result, the applicability of our OWP spectral endmember across the varying primary lithologies observed on Mars is uncertain. Future work must seek to investigate the dependency of the observed spectral signatures of OWPs on the composition of the underlying lithology and the environmental conditions present.

The study by Salvatore et al. (2013) was unable to identify new alteration phases within dolerite alteration rinds, nor were they able to observe the destruction or removal of primary materials inherent to the dolerite within the alteration rind. Based on these analyses, two possibilities exist for the cause of the observed spectral differences between dolerite interiors and alteration rinds. First, the oxidative weathering process results in substantial modification to the electronic and vibrational environment of the dolerite surface, significantly altering the observed spectral signatures in the absence of new phase formation. This possibility is most consistent with the results of Salvatore et al.

(2013). The second possibility is that alteration products are being produced at the sub-micron scale and at abundances below the detection limits of the analytical techniques performed in Salvatore et al. (2013). Possible alteration products include small abundances of hydrated glass replacing plagioclase feldspar or interstitial basaltic matrix materials within the alteration rind, hydrated silica replacing quartz, or small amounts of smectite clays forming within the interstitial basaltic matrix. While current analytical results are unable to definitively rule out any of these possibilities, the combination of x-ray diffraction data, electron microprobe analyses, Mössbauer spectroscopy, and bulk chemical analyses all require the abundances of these phases to be extremely minor with respect to the composition of the unaltered dolerite interiors. As mentioned previously, additional work is required at different relevant field sites to assess the effects of different parent lithology on the observed oxidation products. These additional analyses, including x-ray diffraction at the micron-scale, can also help to potentially identify whether more mature or hydrated alteration products are present at scales that were previously unobservable.

With these caveats aside, our assumption in this analysis that the OWPs observed throughout Beacon Valley are applicable across the martian surface allows us to systematically and uniformly assess each spectral region using the same unmixing library and techniques. The consistency in spectral trends observed throughout the dolerite suite suggests that the result of oxidative weathering is predictable for these specific compositions, which justifies the inclusion of OWPs in our linear unmixing models. Populating our unmixing library with additional OWPs derived from different starting compositions (e.g., dunite, pyroxenite, andesite) is the goal of future research endeavors.

4.2 Effects of oxidative weathering on apparent surface composition

Detailed laboratory characterization of dolerites from Beacon Valley reveals diagnostic spectral trends associated with the production and development of OWPs. In the VNIR, dolerite surfaces exhibit stronger negative spectral slopes than their respective interiors. In addition, MGM analyses of the 2 μm region indicate an apparent enrichment in LCP relative to their interiors. In the TIR, dolerite surfaces are best modeled by a significant increase in amorphous aluminosilicate materials and smectite clays, exhibiting narrowing of the reststrahlen features centered near 1100 cm^{-1} and 465 cm^{-1}. These spectral signatures are not accompanied by mineralogical changes with respect to their unaltered interiors, demonstrating that the observed variations in LCP# are not indicative of bulk mineralogical variations.

This laboratory characterization of OWPs provides a means for remotely assessing the effects of these anhydrous alteration processes where accompanying information about the unaltered lithologies exist. In Acidalia Planitia and Syrtis Major, high-resolution VNIR studies have identified the presence of unaltered olivine- and HCP-bearing basalts in the shallow subsurface (Salvatore et al., 2010; Baratoux et al., 2007; Skok et al., 2010). These identifications were thought to be at odds with broader VNIR and TIR analyses, which reveal spectral signatures that are more enriched in LCP relative to the immediate subsurface. However, the highest modeled abundances of OWPs in these two regions are correlated with the largest apparent enrichment in LCP (Fig. 10). This strong relationship suggests that the observed spectral signatures in these two geographic regions are the result of oxidative weathering processes.

Our understanding of the recent martian climate suggests that oxidative weathering is currently the dominant chemical alteration process on the surface of Mars, which is supported by the spectroscopic variations observed in this study. The lack of hydrated signatures in the VNIR and the abundance of OWPs modeled across martian low albedo terrains confirms that these resultant spectroscopic products are globally distributed. The apparent increase in LCP# in oxidized surfaces relative to their unoxidized interiors is also observed spectroscopically over large geographic regions on Mars.

Local VNIR and TIR measurements are also consistent with the laboratory analyses of oxidized and unoxidized dolerite samples. In Acidalia Planitia, regional spectral signatures reveal a negative slope and weak (if any) mafic signatures in the VNIR, as well as high modeled OWP and LCP# in the TIR, respectively. However, less weathered olivine-rich ejecta blankets exhibit strong olivine spectral signatures in both the VNIR and TIR wavelength regions and a reduction in the apparent LCP#. In Syrtis Major, areas exhibiting spectrally distinct ejecta also reveal low LCP# values, while the surrounding terrain is modeled as having a higher LCP# in the VNIR (Baratoux et al., 2007; Skok et al., 2010) and TIR (this study) in addition to a higher modeled abundance of OWPs. These local spectral observations substantially bolster the argument that the production and distribution of OWPs is a global phenomenon, yet is dependent upon regional and local factors that likely include underlying compositions and regional climate.

As mentioned previously, TIR-derived LCP# values may be significantly influenced by the modeled spectral components within OWPs themselves (Fig. 5). HCP

is modeled as the most abundant pyroxene phase in OWPs, which would likely result in higher LCP# values being modeled for terrains that exhibit strong OWP signatures. The concurrent interpretation of both VNIR and TIR spectral data is necessary to differentiate between spectral artifacts and actual observed mineralogical signatures. Because MGM analyses do not require a priori information about the composition of the material under investigation, these analyses in the VNIR wavelength region provide an objective look into the observed spectral signatures. In tandem with the abilities to estimate modal mineralogy using remote TIR datasets, these two datasets and remote analytical techniques are capable of assessing and clarifying both real and apparent spectral signatures.

Our analyses of both laboratory and remote TIR datasets assume the dominance of linear spectral mixing, which is a fundamental assumption when estimating modal mineralogy. However, the possibility exists that non-linear processes are influencing the observed TIR spectral signatures. Specifically, the minor mineralogical and chemical variations measured during laboratory investigations (e.g. Salvatore et al., 2013) are much smaller than the observed spectral influences. If OWPs are not a true spectral endmember, then the observed spectral signatures are likely the product of non-linear mixing, making the reported modal mineralogies inaccurate. Further spectral and laboratory investigations are currently being designed to assess the assumption of linearity with regards to these spectral signatures.

4.3 Distribution of oxidative weathering products on Mars

Possible explanations for the observed distribution of OWPs across the martian surface include (1) regional- and global-scale climatic variations, (2) age and preservation of the uppermost observable surface, and (3) composition of the underlying substrate:

The substitution of OWPs for smectites, amorphous silica, zeolites, glasses, and other significantly hydrated phases in TIR spectral libraries has important implications for the nature of martian surface materials and the evolution of the martian climate. Our results suggest that hydrated alteration products are not as widespread across the martian surface as were previously hypothesized. This observation relaxes previous climatic constraints that were required to explain their presence across both old and young surfaces. Additionally, while previous TIR studies argued for varying degrees of latitudinal dependence on the distribution of TES ST2 (e.g., Bandfield et al., 2000; Wyatt and McSween, 2002; Rogers et al., 2007), the dependence on latitude observed in our study is unclear. Although the only high-latitude spectral region analyzed in this study is NA, the modeled abundances of OWPs in NA (37%) is not significantly enriched relative to some of the equatorial regions, including MP (35%) and MS (32%). The modeled abundances of OWPs at low latitudes alone varies by more than 20% and can vary considerably even at local scales (e.g., within Syrtis Major), suggesting that OWP abundances are not strictly controlled by regional or latitude-dependent climatic processes.

Could the large variations in OWP abundance be related to discrete shifts in the global climate system? Baratoux et al. (2007) and Skok et al. (2010) found that craters exhibiting spectrally distinct HCP-rich ejecta in Syrtis Major were formed more recently

than ~2 Ga, while older craters exhibit less of a HCP enrichment. They propose that the observed spectral signatures in the Syrtis plains relative to the younger crater ejecta could be the result of "superficial and long-term weathering occurring under the present environmental conditions" (Baratoux et al., 2007). If craters with spectrally distinct ejecta deposits are present in other low albedo terrains, and if these craters are also estimated to be younger than 2 Ga, then evidence for a global-scale shift in climate and alteration history may be preserved. Testing this hypothesis requires (1) identifying whether the presence of SDE is a global phenomenon beyond Syrtis Major and Acidalia Planitia; if so, (2) determining whether the ages of all SDE deposits are younger than 2 Ga; and (3) identifying whether the compositional trends between SDE deposits and the surrounding terrain follow the same tendencies as those observed in Syrtis Major. The disparate subsurface compositions between Syrtis Major and Acidalia Planitia suggests that oxidation processes produce similar spectral results regardless of primary composition, and supports the hypothesis that a shift in global-scale climatic conditions has resulted in the deceleration of oxidative weathering since 2 Ga. However, different trends are observed in crater ejecta in the Tyrrhena Terra region (Rogers, 2011), and the relationship between these different geographic regions must be further investigated.

The identification of OWPs from orbit requires both their formation across the surface as well as the preservation of these materials in the harsh martian environment. As is observed in Beacon Valley, aeolian abrasion effectively scours alteration rinds from the rock surfaces, exposing fresh and unaltered rock in the process (Glasby et al., 1981; Salvatore et al., 2013). The weaker OWP signatures observed in Syrtis Major relative to Acidalia Planitia could potentially indicate greater amounts of physical erosion (likely

related to aeolian abrasion) in Syrtis Major. Evidence exists for widespread and persistent aeolian activity in Syrtis Major based largely on the presence of wind streaks pointing west of most impact craters. The rapid removal of dust in Syrtis Major following global dust storms is also a testament to the heightened aeolian activity (Bell et al., 2012). Therefore, the accumulation of OWPs may be hindered across Syrtis Major relative to other low albedo regions. Regions like Acidalia Planitia and Meridiani exhibit fewer wind streaks than are present in Syrtis Major, indicating that aeolian activity may not be as strong of an erosive force and may explain the higher modeled abundances of OWPs observed in these regions.

Thin coatings of amorphous silica have been previously proposed as contributors to TES ST2 spectral signatures (Kraft et al., 2003; Minitti et al., 2007). However, the preservation of these silica coatings throughout the Amazonian epoch is unlikely in the abrasive martian environment. Whereas oxidative weathering products are able to form under current climatic conditions, the ubiquity of silica-rich coatings across the martian surface would imply either their preservation despite aeolian abrasion and reworking throughout the Amazonian, or the continual renewal and redevelopment of leached layers on rock surfaces and sand grains throughout the Amazonian epoch and into the present. While some studies have shown that silica-rich coatings are moderately resistant to physical erosion (e.g., Kraft and Greeley, 2000), the identification of such coatings on Mars would imply that aqueous activity (which is necessary to produce these types of silica-rich coatings) was present on the martian surface in the very recent geologic past.

Variations in the modeled abundances of OWPs and their relationship to LCP# may be related to differences in primary underlying compositions. Both NA and SM

were previously shown to host olivine- and HCP-bearing basalts in the immediate subsurface (Salvatore et al., 2010; Baratoux et al., 2007; Skok et al., 2010), which may explain their similar alteration pathways and resultant spectral signatures. These other low albedo regions, however, have not been fully investigated using high resolution spectral datasets, and so their subsurface compositions remain largely unconstrained. Instruments on the Mars Exploration Rover *Opportunity* have been used to identify the dominance of LCP at the Meridiani Planum exploration sites, which are located north and west of the locations used to derive the regional Meridiani (MP) VNIR and TIR spectra (Rogers and Aharonson, 2008). This substrate is unique from those identified in NA and SM (e.g., Salvatore et al., 2010; Baratoux et al., 2007; Skok et al., 2010), and the relationship between this disparate starting composition and the observed regional spectral signatures remains uncertain.

4.4 Implications for Amazonian climate

The high modeled abundances of OWPs across the martian surface have implications for the evolution and stability of the martian climate system during the Amazonian epoch. Previous studies (e.g., Cooper et al., 1996; Burkhard and Müller-Sigmund, 2007; Salvatore et al., 2013) have described the metastability and transient nature of these oxidative weathering species, which are far from equilibrium in their current environment and are susceptible to further weathering under most terrestrial conditions. The evidence for similar metastable products on the martian surface implies that conditions on Mars have not been sufficiently warm and/or wet to result in the production of more mature alteration phases since the formation of the OWPs.

Theoretical modeling and geomorphic evidence suggests that the Amazonian climate is akin to that of a cold polar terrestrial desert (e.g., Montmessin, 2006; Marchant & Head, 2007; Carr & Head, 2010). Geochemically, the regional to global production of pre-Amazonian carbonate (e.g. Ehlmann et al., 2008), phyllosilicate (e.g. Poulet et al., 2005), sulfate (e.g. Gendrin et al., 2005; Langevin et al., 2005), and hematite (e.g. Christensen et al., 2000c) represents alteration conditions that are significantly different from those observed during the Amazonian epoch. However, the geochemical effects of Amazonian-era chemical alteration have not been previously studied in detail. This work represents the first attempts at constraining the global geochemical and spectral influences of cold and dry environmental conditions on the alteration of the martian surface. The ubiquity of these alteration processes are substantiated through the agreement between laboratory experiments and orbital observations, particularly the global distributions of OWPs.

Given our current understanding of martian climate and geochemical evolution, the effects of surface oxidation were likely overwhelmed by the production of more mature weathering products through aqueous alteration early in martian history. The formation of carbonates and phyllosilicates epitomize the complex aqueous weathering processes at work during the Noachian epoch (the "Phyllosian" era; Bibring et al., 2006), and required the prolonged contact of geologic materials with liquid water in a variety of chemical environments and at a range of temperatures (Ehlmann et al., 2009). Following a global shift in aqueous geochemistry and alteration environment, martian surface conditions favored the formation of sulfates and other evaporites (the "Theiikian" era; Bibring et al., 2006). Surprisingly, this transition, which approximately coinciding with

the Noachian-Hesperian boundary, also coincides with the formation of valley networks across the martian surface (Fassett & Head, 2008). This association may represent the waning stages of an active hydrologic system, the transition to a desiccating environment, and the termination of extensive physical erosion by fluvial processes.

The later Hesperian-Amazonian boundary, therefore, may represent the transition from a water-limited and evaporite-dominated geochemistry to the hyper-arid, hypo-thermal, and oxidation-dominated environment observed today (the "Siderikian" era; Bibring et al., 2006). This transition would enable the preservation of transient OWPs that would otherwise be overprinted by aqueous processes. The Theiikian-Siderikian boundary was initially thought to have formed rapidly as the last remaining liquid water was sequestered (Bibring & Langevin, 2008). However, more recent studies have suggested that many of the sulfate deposits observed on the martian surface formed episodically in response to a variety of different triggering events (e.g. King & McLennan, 2010; Andrews-Hanna et al., 2007; Murchie et al., 2009; Halevy & Head, 2012), although the average age of these units is thought to be clustered near 3.5 Ga. Finally, should the climate change at ~2 Ga proposed by Baratoux et al. (2007) and Skok et al. (2010) be global in scale, the proposed Theiikian-Siderikian boundary may be much more diffuse and prolonged than previously hypothesized. Together, these studies suggest that the geochemical evolution of Mars, from the Theiikian to the Siderikian, was prolonged and potentially episodic (Head, 2012). The timing and duration of this transition has important implications regarding the cessation of aqueous activity on the martian surface and the duration of oxidative weathering processes modifying the currently observed surface units. Studies to further constrain the martian cratering record

and erosion and weathering rates are required to augment our current understanding of the martian geologic and geochemical history.

5.0 Conclusions

The availability of global VNIR and TIR spectral datasets allows, for the first time, the combined VNIR and TIR spectral analysis of martian low albedo terrain. These investigations ensure that the resultant geologic and geochemical interpretations are consistent throughout both wavelength regions. Regional and local studies provide unique information regarding the abundance and distribution of both primary and secondary phases:

(1) Laboratory VNIR and TIR investigations capture unique spectral properties associated with oxidative weathering products (OWPs), which result from exposure of basaltic compositions to hyper-arid and hypo-thermal terrestrial environments. The characterization of these spectral signatures allows for comparable investigations to be undertaken using martian orbital spectroscopic datasets. These unique spectral properties include an increase in the negative spectral slope in the near-infrared, in addition to an apparent shift to higher LCP abundances relative to their unaltered interiors.

(2) Orbital VNIR spectroscopy of martian low albedo terrains exhibit variability in the strength of the Fe^{2+}-Fe^{3+} charge transfer absorption at wavelengths <0.6 μm, the near-infrared spectral slope, and the position and strength of the 2 μm absorption feature associated with Fe^{2+} in pyroxenes. No vibrational absorption features were observed at 1.4 μm, 1.9 μm, or between 2.0 μm and 2.5 μm,

confirming the absence of hydrated minerals at spectrally observable quantities. MGM analyses of these spectra suggest nearly equal proportions of HCP and LCP throughout these study regions, with the exception of LCP-dominated Northern Acidalia and HCP-dominated Syrtis Major. Northern Acidalia also exhibits the strongest negative spectral slope in the VNIR.

(3) Regional TIR investigations of the martian surface were performed using a modified spectral endmember library, which includes the TIR spectrum of OWPs and excludes spectral phases that are inconsistent with VNIR observations and that are spectrally indistinguishable from OWPs. Linear unmixing models of these TIR spectra exhibit good fits (low RMS errors) and substantial abundances of OWPs, which primarily replace high-silica phases modeled in previous TIR investigations. Other modeled mineralogies are largely consistent with previous studies of these low albedo regions, and indicate that the surfaces are largely basaltic in nature. However, considerable differences in modeled mineral compositions are present and may be a spectral consequence of oxidative weathering.

(4) Localized VNIR spectroscopic investigations uncovered subsurface compositions in both Acidalia Planitia (Salvatore et al., 2010; this study) and Syrtis Major (Baratoux et al., 2007; Skok et al., 2010; this study) identify subsurface compositions that are more enriched in olivine and HCP relative to their apparent surface signatures. Additionally, the distinct spectral signatures in many ejecta deposits confirm that the shallow subsurfaces and observable surfaces of these regions are spectrally inconsistent.

(5) Localized TIR investigations of Acidalia Planitia and Syrtis Major are consistent with our local VNIR investigations. Olivine-bearing ejecta in Acidalia Planitia were identified using OMEGA are also identified in TIR investigations. The surrounding terrains, however, contain higher abundances of OWPs, lower olivine abundances, and higher modeled LCP abundances. Similar trends are observed in Syrtis Major, where HCP-enriched ejecta blankets in East Syrtis contain lower OWP abundances and a lower modeled LCP# than the surrounding regional terrains.

(6) The spectral influences of OWPs are consistent with the observed martian regional and local spectral signatures. The identification of these products indicates that cold and dry conditions have dominated Amazonian Mars, preserving these metastable alteration products. The transition from the Theiikian to the Siderikian climatic eras was likely more gradual than previously thought, based on the spectral and temporal sequences identified in this study and previous studies.

Determining regional variations in primary mineralogy through the use of VNIR and TIR spectroscopy must account for the influence of oxidative weathering on the apparent surface mineralogy. Significant compositional variations have been observed in the mafic mineral components of the martian meteorites as well as localized spectroscopic investigations, indicating that martian basaltic surfaces are, indeed, heterogeneous in composition. However, the ability for oxidative chemical alteration to mimic such primary mineralogical variations can complicate the remote characterization of these mafic surfaces. Additionally, the significant surface heterogeneity observed

between Acidalia Planitia and Syrtis Major, despite their olivine- and HCP-bearing basaltic substrates, may suggest that the composition of the Hesperian Ridged Plains is more homogeneous than previously suspected. Future studies can further substantiate these studies by linking surface observations with subsurface compositions using similar techniques.

References

Adams J. B. and McCord T. B. (1969), Mars: Interpretation of spectral reflectivity of light and dark regions. *J. Geophys. Res.* **74**(20), 4851-4856.

Andrews-Hanna J. C., Phillips R. J. and Zuber M. T. (2007), Meridiani Planum and the global hydrology of Mars. *Nature* **446**, 163-166.

Bandfield J. L. (2002), Global mineral distributions on Mars. *J. Geophys. Res.* **107**(E6), doi:10.1029/2001JE001510.

Bandfield J. L., Hamilton V. E. and Christensen P. R. (2000), A global view of martian surface compositions from MGS-TES. *Science* **287**, 1626-1630.

Baratoux D., Pinet P., Gendrin A., Kanner L., Mustard J., Daydou Y., Vaucher J. and Bibring J.-P. (2007), Mineralogical structure of the subsurface of Syrtis Major from OMEGA observations of lobate ejecta blankets. *J. Geophys. Res.* **112**(E08S05), doi:10.1029/2007JE002890.

Bell J. F., Wellington D. F., Anderson R. B., Wolff M. J., Supulver K. D., Cantor B. A. and Malin M. C. (2012), Three Mars years of surface albedo changes observed by the Mars Reconnaissance Orbiter MARCI investigation. *Proc. AGU Fall Mtg.*, abstract P24B-05.

Bellucci G., Altieri F., Bibring J.-P., Bonello G., Langevin Y., Gondet B. and Poulet F. (2006), OMEGA/Mars Express: Visual channel performances and data reduction techniques. *Planet. Space Sci.* **54**, 675-684, doi:10.1016/j.pss.2006.03.006.

Bibring J.-P., Soufflot A., Berthé M., Langevin Y., Gondet B., Drossart P., Bouyé M., Combes M., Puget P., Semery A., Bellucci G., Formisano V., Moroz V., Kottsov V. and the OMEGA team (2004), OMEGA: Observatoir pour la Minéralogie, l'Eau, les Glaces et l'Activité. *Eur. Space Agency Spec. Pub.* **1240**, 37 pp.

Bibring J.-P., Langevin Y., Gendrin A., Gondet B., Poulet F., Berthé M., Soufflot A., Arvidson R., Mangold N., Mustard J., Drossart P. and the OMEGA team (2005), Mars surface diversity as revealed by the OMEGA/Mars Express observations. *Science* **307**, 1576-1581.

Bibring J.-P., Langevin Y., Mustard J. F., Poulet F., Arvidson R., Gendrin A., Gondet B., Mangold N., Pinet P., Forget F. and the OMEGA team (2006), Global mineralogical and aqueous Mars history derived from OMEGA/Mars Express data. *Science* **312**, 400-404.

Bibring J.-P. and Langevin Y. (2008), Mineralogy of the martian surface from Mars Express OMEGA observations. In *The Martian Surface: Composition, Mineralogy, and Physical Properties* (ed. Bell III J. F.), Cambridge Univ. Press, 153-168.

Bridges J. C., Catling D. C., Saxton J. M., Swindle T. D., Lyon I. C. and Grady M. M. (2001), Alteration assemblages in martian meteorites: Implications for near-surface processes. *Space Sci. Rev.* **96**, 365-392.

Burkhard D. J. M. and Müller-Sigmund H. (2007), Surface alteration of basalt due to cation-migration. *Bull. Volcanol.* **69**, 319-328.

Burns R. G. (1993), *Mineralogic Applications of Crystal Field Theory*. Cambridge Univ. Press, New York, 551 pp.

Carr M. H. and Head III J. W. (2010), Geologic history of Mars. *EPSL* **294**, 185-203.

Christensen P. R., Bandfield J. L., Smith M. D., Hamilton V. E. and Clark R. N. (2000a), Identification of a basaltic component on the martian surface from Thermal Emission Spectrometer data. *J. Geophys. Res.* **105**(E4), 9609-9621.

Christensen P. R., Bandfield J. L., Hamilton V. E., Howard D. A., Lane M. D., Piatek J. L., Ruff S. W. and Stefanov W. L. (2000b), A thermal emission spectral library of rock forming minerals. *J. Geophys. Res.* **105**, 9735-9739.

Christensen P. R., Bandfield J. L., Clark R. N., Edgett K. S., Hamilton V. E., Hoefen T., Kieffer H. H., Kuzmin R. O., Lane M. D., Malin M. C., Morris R. V., Pearl J. C., Pearson R., Roush T. L., Ruff S. W. and Smith M. D. (2000c), Detection of crystalline hematite mineralization on Mars by the Thermal Emission Spectrometer: Evidence for near-surface water. *J. Geophys. Res.* **105**(E4), 9623-9642.

Christensen P. R., Bandfield J. L., Hamilton V. E., Ruff S. W., Kieffer H. H., Titus T. N., Malin M. C., Morris R. V., Lane M. D., Clark R. N., Jakosky B. M., Mellon M. T., Pearl J. C., Conrath B. J., Smith M. D., Clancy R. T., Kuzmin R. O., Roush T., Mehall G. L., Gorelick N., Bender K., Murray K., Dason S., Greene E., Silverman S. and Greenfield M. (2001), Mars Global Surveyor Thermal Emission

Spectrometer experiment: Investigation description and surface science results. *J. Geophys. Res.* **106**(E10), 23823-23871.

Christensen P. R., Jakosky B. M., Kieffer H. H., Malin M. C., McSween Jr. H. Y., Nealson K., Mehall G. L., Silverman S. H., Ferry S., Caplinger M. and Ravine M. (2004), The Thermal Emission Imaging System (THEMIS) for the Mars 2001 Odyssey mission. *Space Sci. Rev.* **110**, 85-130.

Cooper R. F., Fanselow J. B. and Poker D. B. (1996), The mechanism of oxidation of a basaltic glass: Chemical diffusion of network-modifying cations. *Geochim. Cosmochim. Acta* **60**, 3253-3265.

Ehlmann B. L., Mustard J. F., Murchie S. L., Poulet F., Bishop J. L., Brown A. J., Calvin W. M., Clark R. N., Des Marais D. J., Milliken R. E., Roach L. H., Roush T. L., Swayze G. A. and Wray J. J. (2008), Orbital identification of carbonate-bearing rocks on Mars. *Science* **322**, 1828-1832.

Ehlmann B. L., Mustard J. F., Swayze G. A., Clark R. N., Bishop J. L., Poulet F., Des Marais D. J., Roach L. H., Milliken R. E., Wray J. J., Barnouin-Jha O. and Murchie S. L. (2009), Identification of hydrated silicate minerals on Mars using MRO-CRISM: Geologic context near Nili Fossae and implications for aqueous alteration. *J. Geophys. Res.* **114**(E00D08), doi:10.1029/2009JE003339.

Ehlmann B. L., Bish D. L., Ruff S. W. and Mustard J. F. (2012), Mineralogy and chemistry of altered Icelandic basalts: Application to clay mineral detection and understanding aqueous environments on Mars. *J. Geophys. Res.* **117**(E00J16), doi:10.1029/2012JE004156.

Erard S., Bibring J.-P., Langevin Y., Combes M., Hurtrez S., Sotin C., Head J. W. and Mustard J. F. (1990), Determination of spectral units in the Syrtis Major-Isidis Planitia region from Phobos/ISM observations. *Proc. Lunar Planet. Sci. Conf.* **21**, 327-328.

Fassett C. I. and Head III J. W. (2008), The timing of martian valley network activity: Constraints from buffered crater counting. *Icarus* **195**, 61-89.

Gendrin A. (2004), Mineralogie de Mars: L'experience OMEGA. *Ph.D. dissertation*, Université de Paris, Paris.

Gendrin A., Mangold N., Bibring J.-P., Langevin Y., Gondet B., Poulet F., Bonello G., Quantin C., Mustard J., Arvidson R. and LeMouélic S. (2005), Sulfates in martian layered terrains: The OMEGA/Mars Express view. *Science* **307**, 1587-1591.

Glasby G. P., McPherson J. G., Kohn B. P., Johnston J. H., Keys J. R., Freeman A. G. and Tricker M. J. (1981), Desert varnish in southern Victoria Land, Antarctica. *N. Z. J. Geol. Geophys.* **24**(3), 389-397.

Glotch T. D., Morris R. V., Christensen P. R. and Sharp T. G. (2004), Effect of precursor mineralogy on the thermal infrared emission spectra of hematite: Application to martian hematite mineralization. *J. Geophys. Res.* **109**, doi:10.1029/2003JE002224.

Halevy I. and Head J. W. (2012), Punctuated volcanism, transient warming and global change in the Late Noachian–Early Hesperian. *Lunar Planet. Sci. Conf.* **43**, abstract 1908.

Hamilton V. E. (2000), Thermal infrared emission spectroscopy of the pyroxene mineral series. *J. Geophys. Res.* **105**(E4), 9701-9716.

Hamilton V. E., Christensen P. R. and McSween Jr. H. Y. (1997), Determination of martian meteorite lithologies and mineralogies using vibrational spectroscopy. *J. Geophys. Res.* **102**, 25593-25603.

Head J. W. (2012), Mars climate history: A geological perspective. *Lunar Planet. Sci. Conf.* **43**, abstract 2582.

Kanner L. C., Mustard J. F. and Gendrin A. (2007), Assessing the limits of the Modified Gaussian Model for remote spectroscopic studies of pyroxenes on Mars. *Icarus* **187**, 442-456.

King P. L. and McLennan S. M. (2010), Sulfur on Mars. *Elements* **6**(2), 107-112.

Kraft M. D. and Greeley R. (2000), Rock coatings and aeolian abrasion on Mars: Application to the Pathfinder landing site. *J. Geophys. Res.* **105**(E6), 15107-15116.

Kraft M. D., Michalski J. R. and Sharp T. G. (2003), Effects of pure silica coatings on thermal emission spectra of basaltic rocks: Considerations for martian surface mineralogy. *Geophys. Res. Lett.* **30**(24), doi:10.1029/2003GL018848.

Langevin Y., Poulet F., Bibring J.-P. and Gondet B. (2005), Sulfates in the north polar region of Mars detected by OMEGA/Mars Express. *Science* **307**, 1584-1586.

Marchant D. R. and Head III J. W. (2007), Antarctic dry valleys: Microclimate zonation, variable geomorphic processes, and implications for assessing climate change on Mars. *Icarus* **192**, 187-222.

McCord T. B. and Adams J. B. (1969), Spectral reflectivity of Mars. *Science* **163**, 1058-1060.

Michalski J. R., Kraft M. D., Diedrich T., Sharp T. G. and Christensen P. R. (2003), Thermal emission spectroscopy of the silica polymorphs and considerations for remote sensing of Mars. *Geophys. Res. Lett.* **30**(19), doi:10.1029/2003GL018354.

Michalski J. R., Kraft M. D., Sharp T. G., Williams L. B. and Christensen P. R. (2005), Mineralogical constraints on the high-silica martian surface component observed by TES. *Icarus* **174**, 161-177.

Minitti M. E., Weitz C. M., Lane M. D. and Bishop J. L. (2007), Morphology, chemistry, and spectral properties of Hawaiian rock coatings and implications for Mars. *J. Geophys. Res.* **112**, doi:10.1029/2006JE002839.

Minitti M. E. and Hamilton V. E. (2010), A search for basaltic-to-intermediate glasses on Mars: Assessing martian crustal mineralogy. *Icarus* **210**, 135-149.

Montmessin F. (2006), The orbital forcing of climate changes on Mars. *Space Sci. Rev.* **125**, 457-472.

Morris R. V., Graff T. G., Mertzman S. A., Lane M. D. and Christensen P. R. (2003), Palagonitic (not andesitic) Mars: Evidence from the thermal emission and VNIR spectra of palagonitic alteration rinds on basaltic rocks. *Int. Conf. Mars* **6**, abstract 3211.

Morse S. A. (1996), Kiglapait mineralogy: 3. Olivine compositions and Rayleigh fractionation models. *J. Petrol.* **37**(5), 1037-1061.

Murchie S. L., Mustard J. F., Ehlmann B. L., Milliken R. E., Bishop J. L., McKeown N. K., Noe Dobrea E. Z., Seelos F. P., Buczkowski D. L., Wiseman S. M., Arvidson R. E., Wray J. J., Swayze G., Clark R. N., Des Marais D. J., McEwen A. S. and Bibring J.-P. (2009), A synthesis of martian aqueous mineralogy after 1 Mars year

of observations from the Mars Reconnaissance Orbiter. *J. Geophys. Res.* **114**(E00D06), doi:10.1029/2009JE003342.

Murray R. W., Miller D. J. and Kryc K. A. (2000), Analysis of major and trace elements in rocks, sediments, and interstitial waters by inductively coupled plasma-atomic emission spectrometry (ICP-AES). *ODP Tech. Note* **29**, 27 pp., [Available at http://www-odp.tamu.edu/publications/tnotes/tn29/INDEX.HTM].

Mustard J. F. and Pieters C. M. (1989), Photometric phase functions of common geologic minerals and applications to quantitative analysis of mineral mixture reflectance spectra. *J. Geophys. Res.* **94**(B10), 13619-13634.

Mustard J. F., Erard S., Bibring J.-P., Head J. W., Hurtrez S., Langevin Y., Pieters C. M. and Sotin C. J. (1993), The surface of Syrtis Major: Composition of the volcanic substrate and mixing with altered dust and soil. *J. Geophys. Res.* **98**, 3387-3400.

Mustard J. F. and Sunshine J. M. (1995), Seeing through the dust: Martian crustal heterogeneity and links to the SNC meteorites. *Science* **267**, 1623-1626.

Mustard J. F., Murchie S., Erard S. and Sunshine J. (1997), In situ compositions of martian volcanic: Implications for the mantle. *J. Geophys. Res.* **102**(E11), 25605-25615.

Mustard J. F., Poulet F., Gendrin A., Bibring J.-P., Langevin Y., Gondet B., Mangold N., Bellucci G. and Altieri F. (2005), Olivine and pyroxene diversity in the crust of Mars. *Science* **307**, 1594-1597.

Pieters C. M. (1983), Strength of mineral absorption features in the transmitted component of near-infrared reflected light: First results from RELAB. *J. Geophys. Res.* **88**(B11), 9534-9544.

Poulet F., Bibring J.-P., Mustard J. F., Gendrin A., Mangold N., Langevin Y., Arvidson R. E., Gondet B., Gomez C. and the OMEGA team (2005), Phyllosilicates on Mars and implications for early martian climate. *Nature* **438**, 623-627.

Press W. H., Flannery B. P., Teukolsky S. A. and Vetterling W. T. (1988), *Numerical Recipes in C: The Art of Scientific Computing*, 1st ed. Cambridge Univ. Press, New York, pp. 517-539.

Rampe E. B., Kraft M. D., Sharp T. G., Golden D. C., Ming D. W. and Christensen P. R. (2012), Allophane detection on Mars with Thermal Emission Spectrometer data and implications for regional-scale chemical weathering processes. *Geology* **40**(11), 995-998.

Ramsey M. S. (1996), Quantitative analysis of geological surfaces: A deconvolution algorithm for midinfrared remote sensing data. *Ph.D. dissertation*, 276 pp., Ariz. State Univ., Tempe.

Ramsey M. S. and Christensen P. R. (1998), Mineral abundance determination: Quantitative deconvolution of thermal emission spectra. *J. Geophys. Res.* **103**(B1), 577-596.

Rogers A. D. (2011), Crustal compositions exposed by impact craters in the Tyrrhena Terra region of Mars: Considerations for Noachian environments. *Earth Planet. Sci. Lett.* **301**, 353-364.

Rogers A. D. and Christensen P. R. (2007), Surface mineralogy of martian low-albedo regions from MGS-TES data: Implications for upper crustal evolution and surface alteration. *J. Geophys. Res.*, **112**(E01003), doi:10.1029/2006JE002727.

Rogers A. D. and Aharonson O. (2008), Mineralogical composition of sands in Meridiani Planum determined from Mars Exploration Rover data and comparison to orbital measurements. *J. Geophys. Res.* **113**, doi:10.1029/2007JE002995.

Rogers A. D., Bandfield J. L. and Christensen P. R. (2007), Global spectral classification of martian low-albedo regions with Mars Global Surveyor Thermal Emission Spectrometer (MGS-TES) data. *J. Geophys. Res.* **112**(E02004), doi:10.1029/2006JE002726.

Roush T. L., Blaney D. L. and Singer R. B. (1993), The surface composition of Mars as inferred from spectroscopic observations. In *Topics in Remote Sensing 4, Remote Geochemical Analysis: Elemental and Mineralogical Composition* (eds. Pieters C. M. and Englert P. A.), Cambridge Univ. Press, 367-393.

Ruff S. W. (2004), Spectral evidence for zeolite in the dust on Mars. *Icarus* **168**(1), 131-143.

Ruff S. W. and Christensen P. R. (2007), Basaltic andesite, altered basalt, and a TES-based search for smectite clay minerals on Mars. *Geophys. Res. Lett.* **34**(L10204), doi:10.1029/2007GL029602.

Ruff S. W., Christensen P. R., Barbera P. W. and Anderson D. L. (1997), Quantitative thermal emission spectroscopy of minerals: A laboratory technique for measurement and calibration. *J. Geophys. Res.* **102**, 14889-14913.

Salvatore M. R., Mustard J. F., Wyatt M. B. and Murchie S. L. (2010), Definitive evidence of Hesperian basalt in Acidalia and Chryse planitiae. *J. Geophys. Res.* **115**(E07005), doi:10.1029/2009JE003519.

Salvatore M. R., Wyatt M. B., Mustard J. F. and Head III J. W. (2011), Development of alteration rinds on the Ferrar Dolerite of the Antarctic Dry Valleys: Initial characterization. *Proc. Lunar Planet. Sci. Conf.***42**, abstract 1479.

Salvatore M. R., Mustard J. F., Head J. W., Marchant D. R., Cooper R. F. and Wyatt M. B. (2012), Spectral and chemical characterization of hyper-arid and hypo-thermal oxidation processes as an analog for Amazonian alteration on Mars. *AGU Fall Mtg.*, abstract P11F-06.

Salvatore M. R., Mustard J. F., Head J. W., Cooper R. F., Marchant D. R. and Wyatt M. B. (2013), Development of alteration rinds by oxidative weathering processes in Beacon Valley, Antarctica, and Implications for Mars. *Geochim. Cosmochim. Acta*, doi:10.1016/j.gca.2013.04.002.

Skok J. R., Mustard J. F., Murchie S. L., Wyatt M. B. and Ehlmann B. L. (2010), Spectrally distinct ejecta in Syrtis Major, Mars: Evidence for environmental change at the Hesperian-Amazonian boundary. *J. Geophys. Res.* **115**(E00D14), doi:10.1029/2009JE003338.

Smith M. D., Bandfield J. L. and Christensen P. R. (2000), Separation of atmospheric and surface spectral features in Mars Global Surveyor Thermal Emission Spectrometer (TES) spectra. *J. Geophys. Res.* **105**(E4), 9589-9607.

Squyres S. W., Arvidson R. E., Ruff S., Gellert R., Morris R. V., Ming D. W., Crumpler L., Farmer J. D., Des Marais D. J., Yen A., McLennan S. M., Calvin W., Bell J. F., Clark B. C., Wang A., McCoy T. J., Schmidt M. E. and de Souza P. A. (2008), Detection of silica-rich deposits on Mars. *Science* **320**, 1063-1067.

Stockstill-Cahill K. R., Anderson F. S. and Hamilton V. E. (2008), A study of low-albedo deposits within Amazonis Planitia craters: Evidence for locally derived ultramafic to mafic materials. *J. Geophys. Res.* **113**, doi:10.1029/2007JE003036.

Sunshine J. M., Pieters C. M. and Pratt S. F. (1990), Deconvolution of mineral absorption bands: An improved approach. *J. Geophys. Res.* **95**(B5), 6955-6966.

Tornabene L. L., Moersch J. E., McSween Jr. H. Y., Piatek J. L., Milam K. A. and Christensen P. R. (2006), The subsurface geology of Mars via remote sensing of impact craters. *GSA Ann. Mtg. SE Sect.* **38**(3), p. 81.

Wyatt M. B. and McSween H. Y. (2002), Spectral evidence for weathered basalt as an alternative to andesite in the northern lowlands of Mars. *Nature* **417**(6886), 263-266.

Wyatt M. B., Hamilton V. E., McSween Jr. H. Y., Christensen P. R. and Taylor L. A. (2001), Analysis of terrestrial and martian volcanic compositions using thermal emission spectroscopy: 1. Determination of mineralogy, chemistry, and classification strategies. *J. Geophys. Res.* **106**(E7), 14711-14732.

Wyatt M. B., McSween H. Y., Moersch J. E. and Christensen P. R. (2003), Analysis of surface compositions in the Oxia Palus region on Mars from Mars Global Surveyor Thermal Emission Spectrometer observations. *J. Geophys. Res.* **108**(E9), doi:10.1029/2002JE001986.

Figure and Table Descriptions

Figure 1. (a) Representative Surface Type 1 (ST1) and Surface Type 2 (ST2) TIR spectra (from Bandfield et al. 2000). The origin of the narrow reststrahlen feature in ST2

has been widely debated. (b) Proposed spectral contributors to ST2 TIR spectra, including hydrated minerals and mineraloids, Si-rich glasses, and oxidative weathering products (OWPs). Zeolite spectrum from Ruff et al. (2007), OWP spectrum from Salvatore et al. (2013), Si-K glass from Wyatt et al. (2001), montmorillonite spectrum from Christensen et al. (2000b), and opaline silica spectrum from Michalski et al. (2003).

Figure 2. A map of the 9 low albedo regions identified by Rogers et al. (2007) and subsequently analyzed in Rogers and Christensen (2007) and in this study. Regions include Aonium-Phrixi (AP), Cimmeria-Iapygia (CI), Hesperia (HP), Meridiani (MP), Mare Sirenum (MS), N. Acidalia-Utopia (NA), Syrtis (SM), Solis (SP), and Tyrrhena (TT). Background is TES bolometric albedo. The locations of Figure 11 and Figure 14 are outlined by dashed white boxes.

Figure 3. Average dolerite interior (a) and surface (b) that were subset for modified Gaussian model (MGM) analyses. Original data from Salvatore et al. (2013). MGM analysis fits (light grey) and continua (dark grey) are also shown, along with the relative strengths of the modeled 1.9 μm (black, circles) and 2.3 μm (black, squares) absorption features associated with LCP and HCP, respectively. The average dolerite surface is modeled as having a higher LCP abundance relative to HCP (defined as LCP#) than the average dolerite interior.

Figure 4. VNIR spectral slope plotted against LCP# for dolerite interiors (black circles) and surfaces (grey circles), as modeled using MGM techniques. Grey joins and arrows link the interior and surface measurements of the same sample. All pairs show a systematic decrease in spectral slope and increase in LCP# in the sample surface relative to its unaltered interior.

Figure 5. Average TIR emission spectra of the same subset of dolerite interiors (black) and surfaces (light grey) used in MGM analyses. The dolerite surface spectrum is offset by -0.05. The results of linear unmixing are reported and are graphically represented as dashed, dark grey lines. A region of substantial misfit between the measured and modeled surface spectra is highlighted (black arrow).

Figure 6. Average OMEGA data for the 9 spectral regions outlined in Figure 2. Also shown are the MGM fits (light grey), the MGM continua (dark grey), and example LCP (circles, black line) and HCP (squares, black line) modeled Gaussians.

Figure 7. VNIR spectral slope plotted against LCP# for the 9 martian low albedo regions, as modeled using MGM. There is an apparent relationship between the magnitude of the VNIR spectral slope and the modeled LCP#, implying that the two are likely related.

Figure 8. Average TES spectra for the 9 spectral regions outlined in Figure 2 and presented in Rogers and Christensen (2007). Results from our modified endmember library and unmixing analyses are shown as dashed dark grey lines and are presented in Table 4.

Figure 9. Model mineralogy for each spectral region as derived from linear unmixing of TIR data. (a) Plot of plagioclase, pyroxene + olivine, and OWPs, showing a largely even mix between all three components with no clear trends between regions. (b) Plot of HCP, LCP, and olivine. Most regions fall near or along the LCP-olivine join, while SM and TT are significantly enriched in HCP relative to the other spectral regions. (c) Plot of HCP, LCP, and OWPs. Most spectral regions fall along the LCP-OWPs join. However, the regions modeled as having the highest abundances of HCP are also

modeled as having the lowest abundances of OWPs, although the relationship appears to be nonlinear.

Figure 10. Modeled OWP abundance plotted against modeled LCP#, as derived from TIR linear unmixing. There exists a significant logarithmic trend between these two variables ($R^2 = 0.87$), implying that a higher OWP abundance is correlated to a higher modeled LCP#.

Figure 11. (a) Mean spectra of South Acidalia (black) and North Acidalia (grey), as derived from binned TES data. Modeled spectral fits are also shown as dashed dark grey lines and are presented in Table 5. (b) TES data binned at 2 ppd, showing variability in the modeled abundances of pyroxene (red), OWPs (green), and carbonate (blue). The spectral dichotomy can be observed both north and south of roughly 42º N by a transition from dominantly blue colors in the south, to dominantly red colors in the north. (c) Modeled LCP# binned at 2 ppd as derived from TES data, indicating high values across the entirety of Acidalia Planitia and implying the dominance of LCP over HCP.

Figure 12. (a) THEMIS daytime infrared image of Grindavik crater (25.4º N, 321.0º E), overlain with the OLINDEX2 olivine parameter (Salvatore et al. 2010) for OMEGA image ORB2079_7. Cold colors indicate weak olivine VNIR absorption features, while warm colors indicate strong features. Also shown are OMEGA regions of interest (dashed light green and red regions) and the locations of TES data analyses (solid dark green and red regions), the spectra of which are presented in (b) and (c), respectively. (b) OMEGA VNIR spectra of Grindavik ejecta and the regional terrain. The ratioed spectrum (blue) reveals a broad absorption centered near 1 μm and no

absorption feature observed near 2 μm, consistent with a forsterite library spectrum (orange) and the absence of pyroxene within the crater ejecta. (c) TES TIR spectra of Grindavik ejecta and regional terrain. A forsterite library spectrum (orange) is also shown to highlight its consistency with the absorption feature centered near 920 cm^{-1} in the Grindavik ejecta spectrum, as highlighted in the ratioed spectrum (blue). Modeled unmixing results also confirm a stronger olivine contribution in Grindavik ejecta relative to the surrounding terrain, and are presented in Table 5.

Figure 13. A map of LCP# throughout Syrtis Major, highlighting the locations of spectrally distinct ejecta (SDE) blankets concentrated in East Syrtis. Modified from Skok et al. (2010). Black dashed circles highlight the SDE analyzed in Figures 16 and 17, and the grey dashed box highlights the regional terrain to which these SDE were compared.

Figure 14. (a) Mean spectra of West Syrtis (black) and East Syrtis (grey), as derived from binned TES data. Modeled spectral fits are shown as dashed dark grey lines and are presented in Table 5. (b) TES binned data at 2 ppd, showing variability in the modeled abundances of HCP (red), OWPs (green), and olivine (blue). West Syrtis appears more green (stronger OWP signatures), while East Syrtis appears more red (stronger HCP signatures). (c) Modeled LCP# binned at 2 ppd as derived from TES data, showing higher LCP# values in West Syrtis and lower LCP# values in East Syrtis. These results are consistent with VNIR analyses performed by Baratoux et al. (2007) and Skok et al (2010) (Fig. 13).

Figure 15. Average TES spectra of West Syrtis (black) and East Syrtis (light grey), as derived from binned TES data. An additional 5% spectral contribution from augite (HCP) to the West Syrtis spectrum shows good agreement with the East Syrtis

spectrum, suggesting that a slight enrichment in HCP in East Syrtis can account for the majority of the spectral variability observed between these two regions. This is consistent with concurrent and previous VNIR analyses.

Figure 16. Average VNIR spectra of regional terrain (a, grey dashed box in Fig. 13) and SDE deposits (b, black dashed circles in Fig. 13) in Syrtis Major from OMEGA images ORB0284_2 and ORB2316_4. MGM fits and continua are shown as light grey and dark grey lines, respectively. The relative strengths of the LCP (circles, black lines) and HCP (squares, black lines) absorption features are also shown. The regional terrain exhibits a higher LCP# value (0.39) relative to the SDE (0.31) and can be seen as the relative strengths of the LCP and HCP absorptions.

Figure 17. TES TIR spectra derived from archetypal regional terrain in Syrtis Major (grey, grey dashed box in Fig. 13) and the same SDE deposits analyzed in Figure 16 using OMEGA data (black, black dashed circles in Fig. 13). Linear unmixing model results are shown as dashed dark grey lines, and the modeled mineral concentrations are provided in Table 5. SDE are modeled as having higher HCP abundances, lower LCP#, and lower OWP abundances than the archetypal regional terrain.

Table 1. The regions, locations, and number of TES spectra used in local TIR investigations.

Table 2. Modified Gaussian modeling (MGM) results for dolerite interiors and surfaces.

Table 3. Modified skeleton library from Rogers and Christensen (2007). Endmembers in grey were removed due to their non-detection in VNIR wavelengths and

their spectral similarities in the TIR. Italicized endmembers were added to the Rogers and Christensen (2007) skeleton library to provide additional spectral characterization.

Table 4. Modeled mineralogical abundances for the 9 martian low albedo regions, derived from linear unmixing of TIR emission spectra using the modified endmember library provided in Table 3. Abundances, statistical errors, and RMS errors are reported in percent. Statistical errors for the modeled abundances are derived from the square root of the diagonal of the estimated covariance matrix (see Rogers and Aharonson (2008)).

Table 5. Linear unmixing results for Acidalia Planitia and Syrtis Major. Regional 2 ppd unmixing results are highlighted in grey and represent the TIR spectral dichotomy observed in both of these regions. Localized spectrally distinct ejecta deposits in Acidalia Planitia (associated with Grindavik crater) and Syrtis Major (associated with two craters located at 8.9º N, 74.3º E and 5.9º N, 70.5º E) are also modeled. Abundances, statistical errors, and RMS errors are reported in percent.

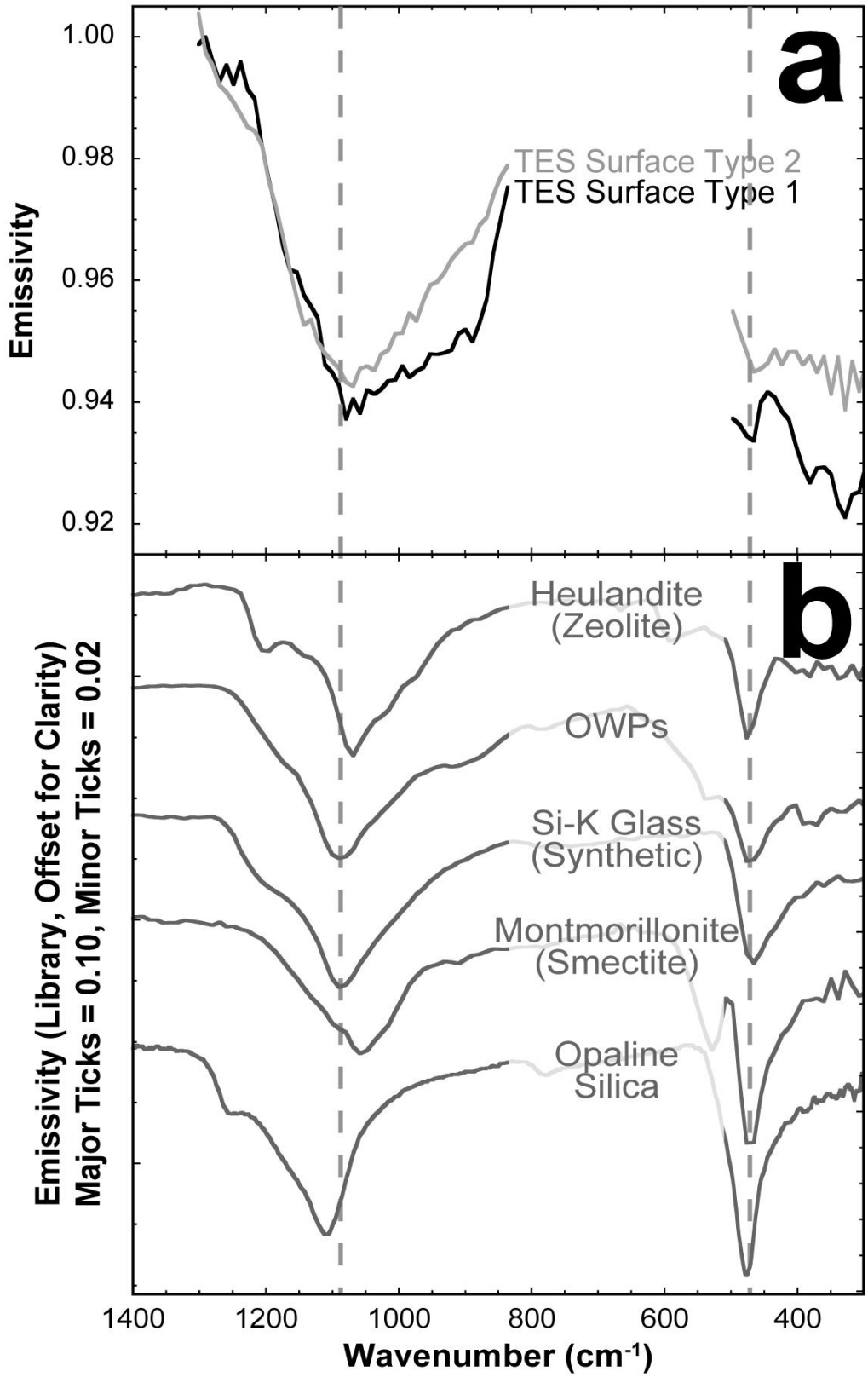

Chapter 5, Figure 1.

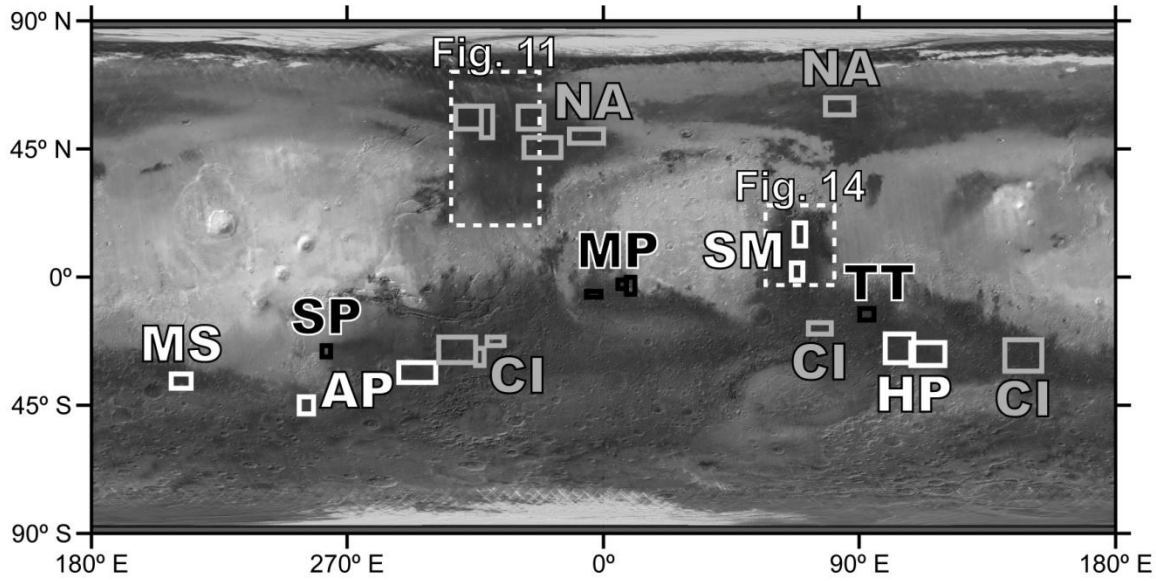

Chapter 5, Figure 2.

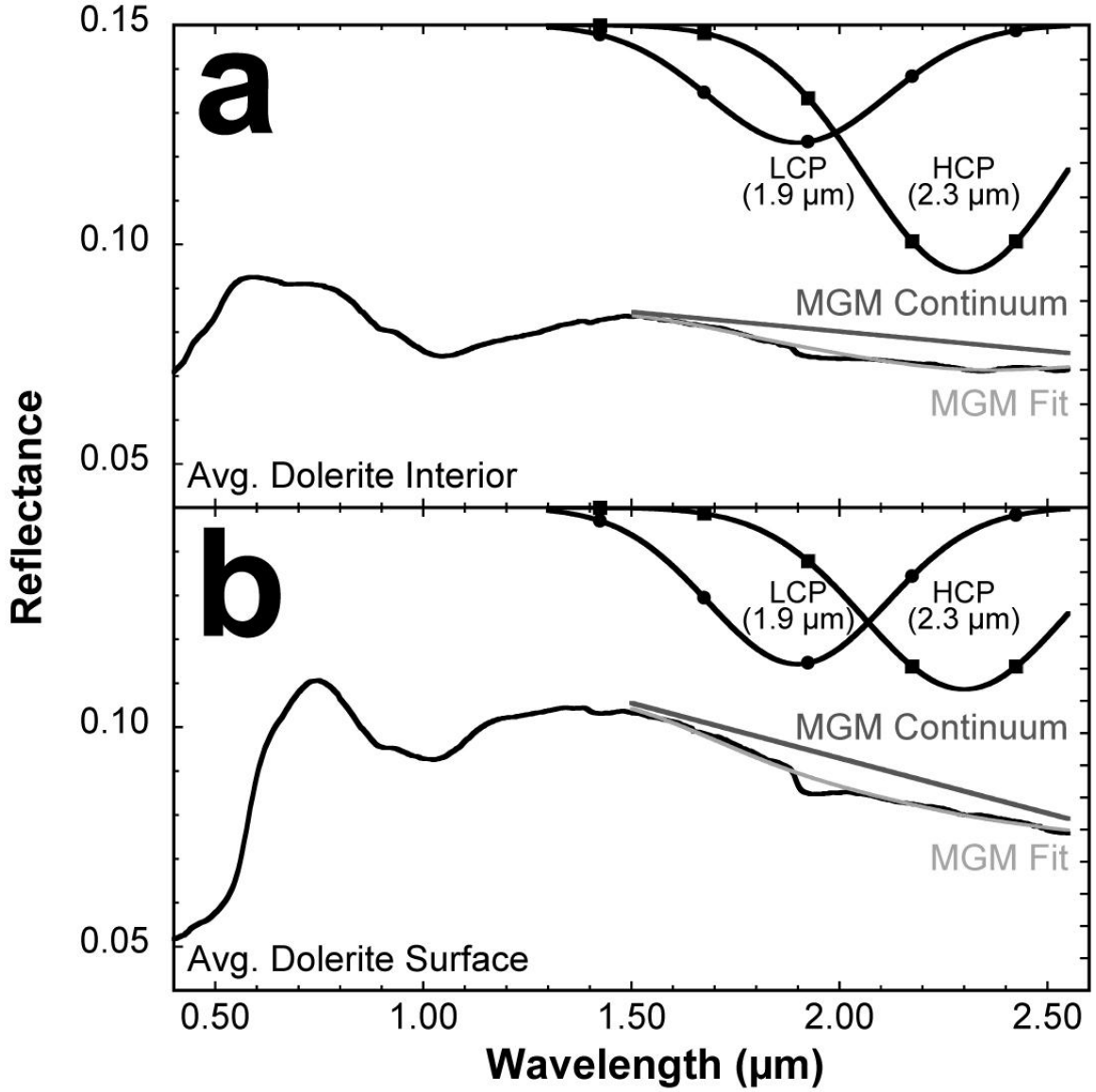

Chapter 5, Figure 3.

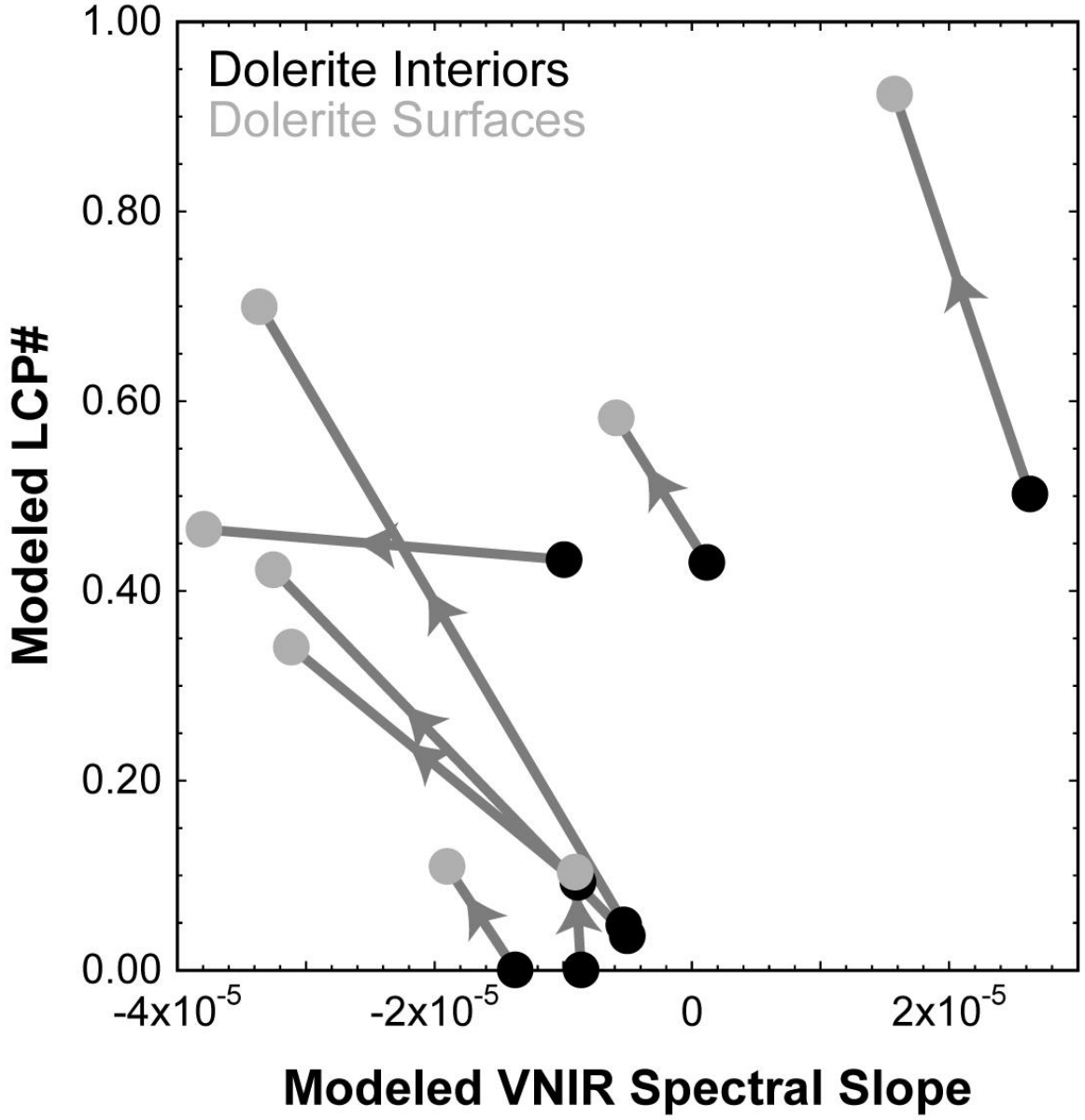

Chapter 5, Figure 4.

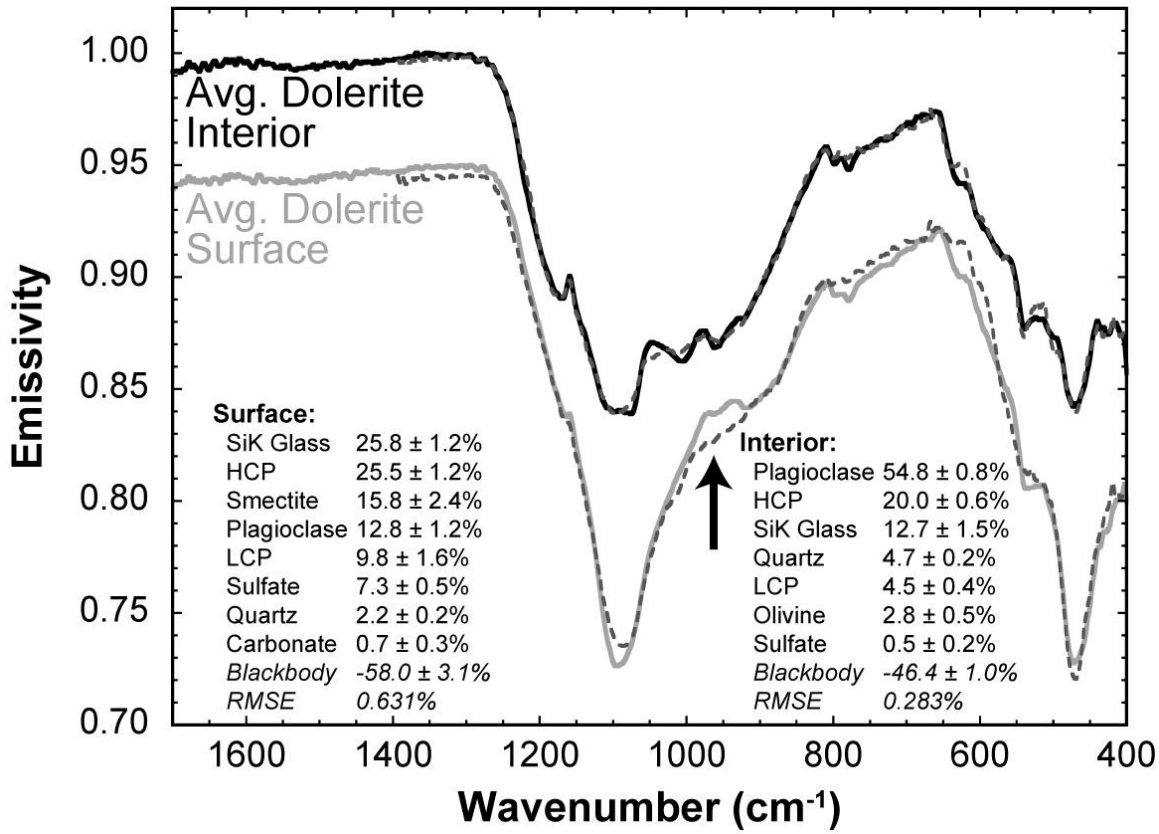

Chapter 5, Figure 5.

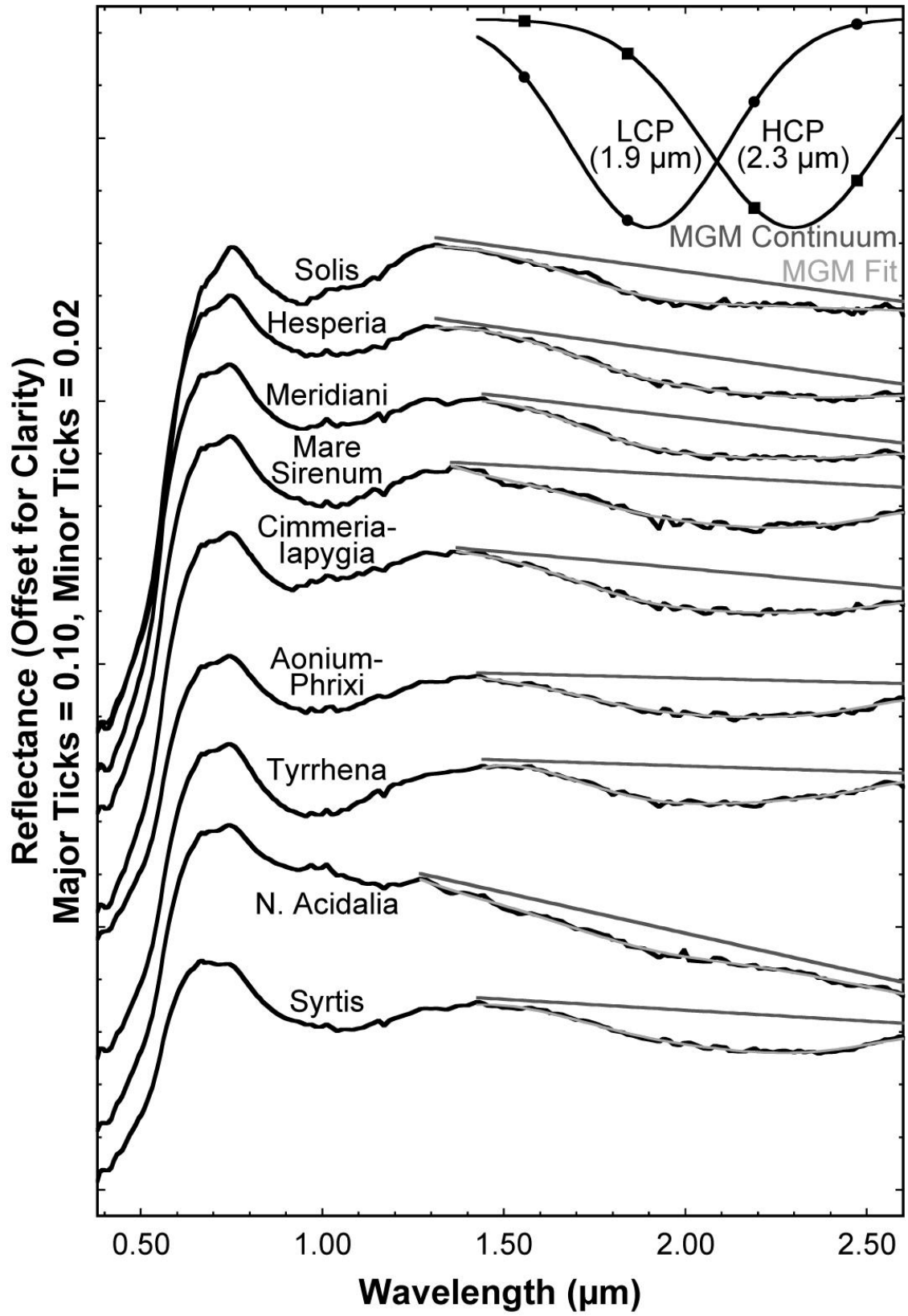

Chapter 5, Figure 6.

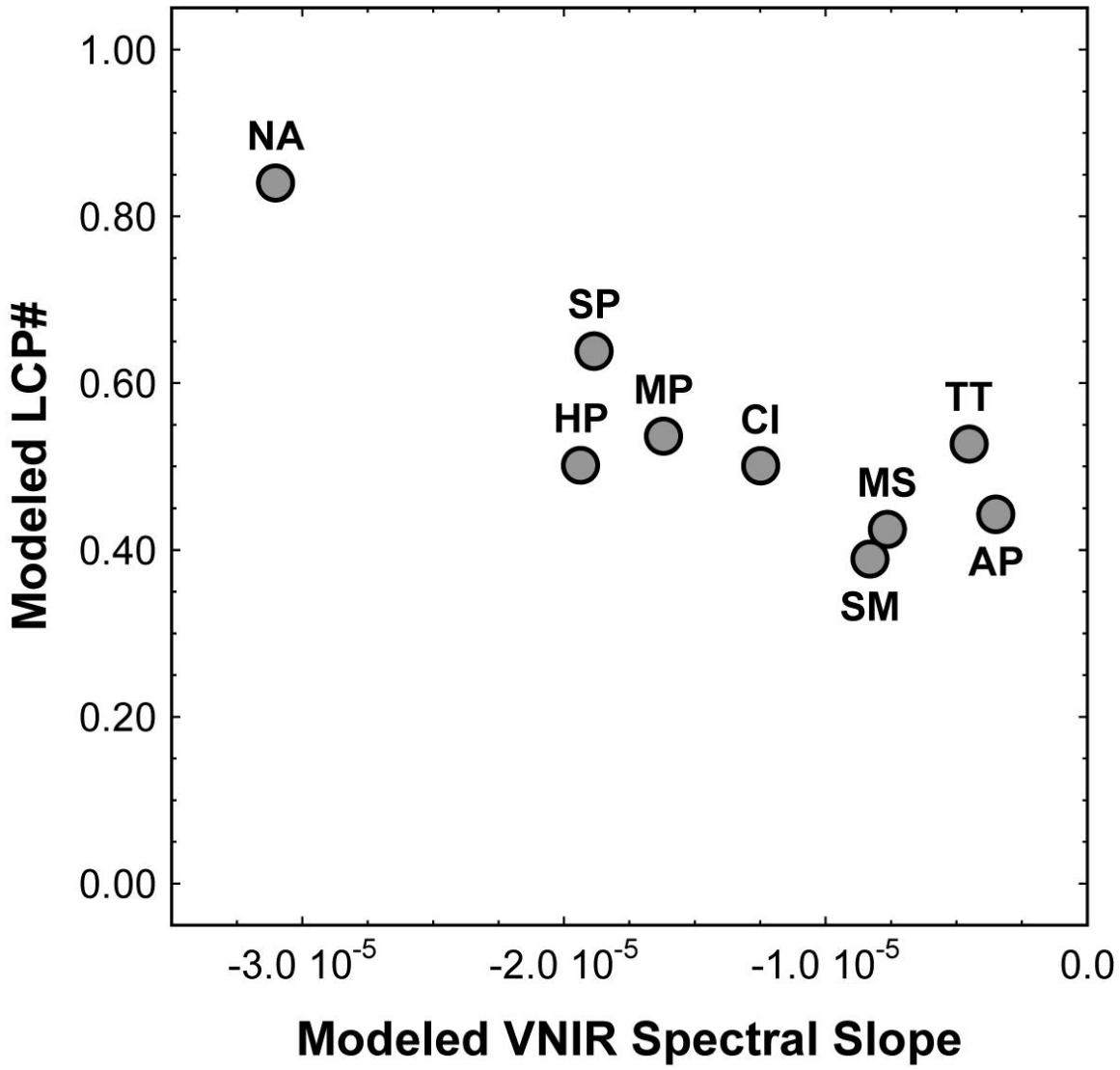

Chapter 5, Figure 7.

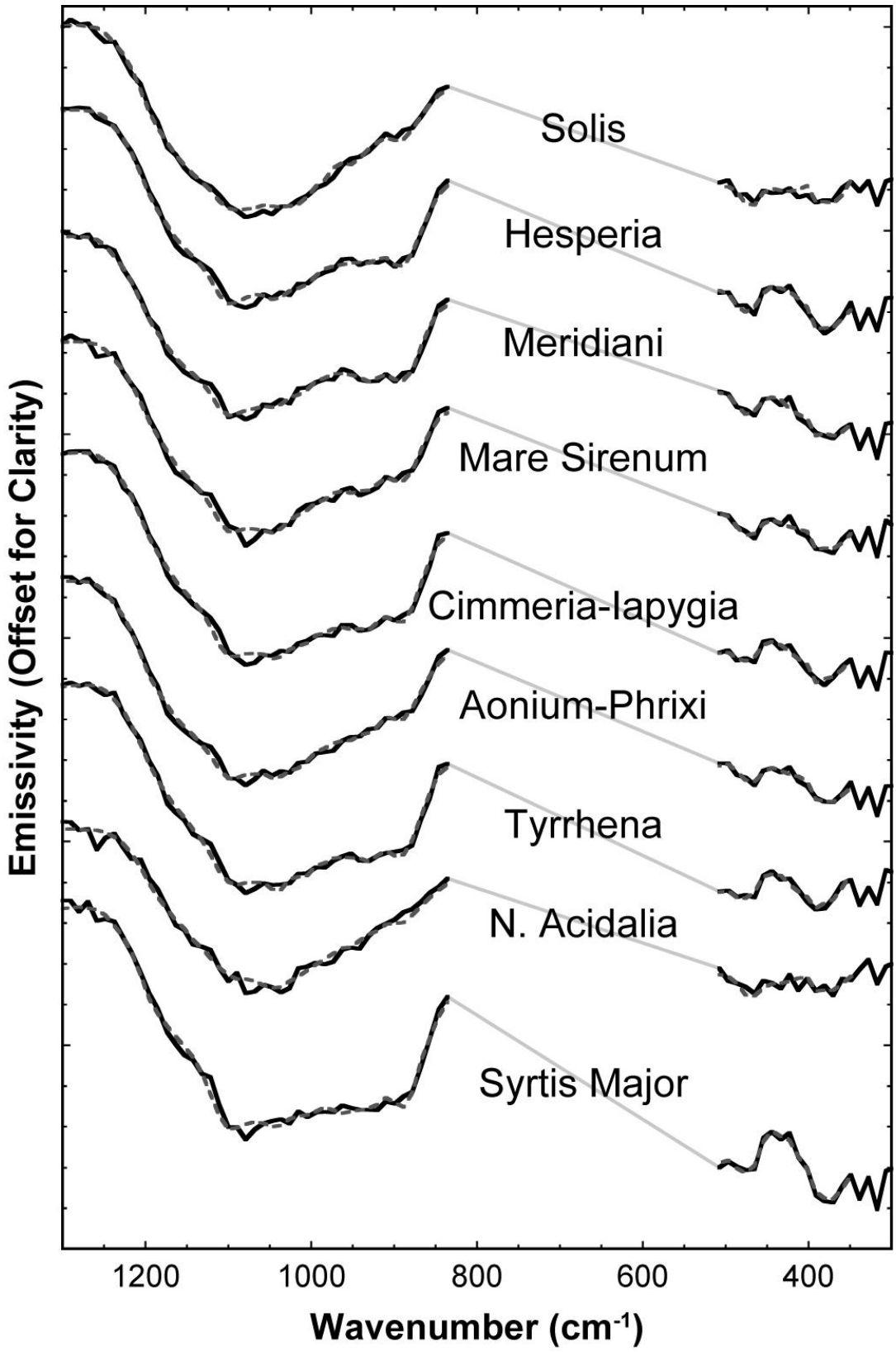

Chapter 5, Figure 8.

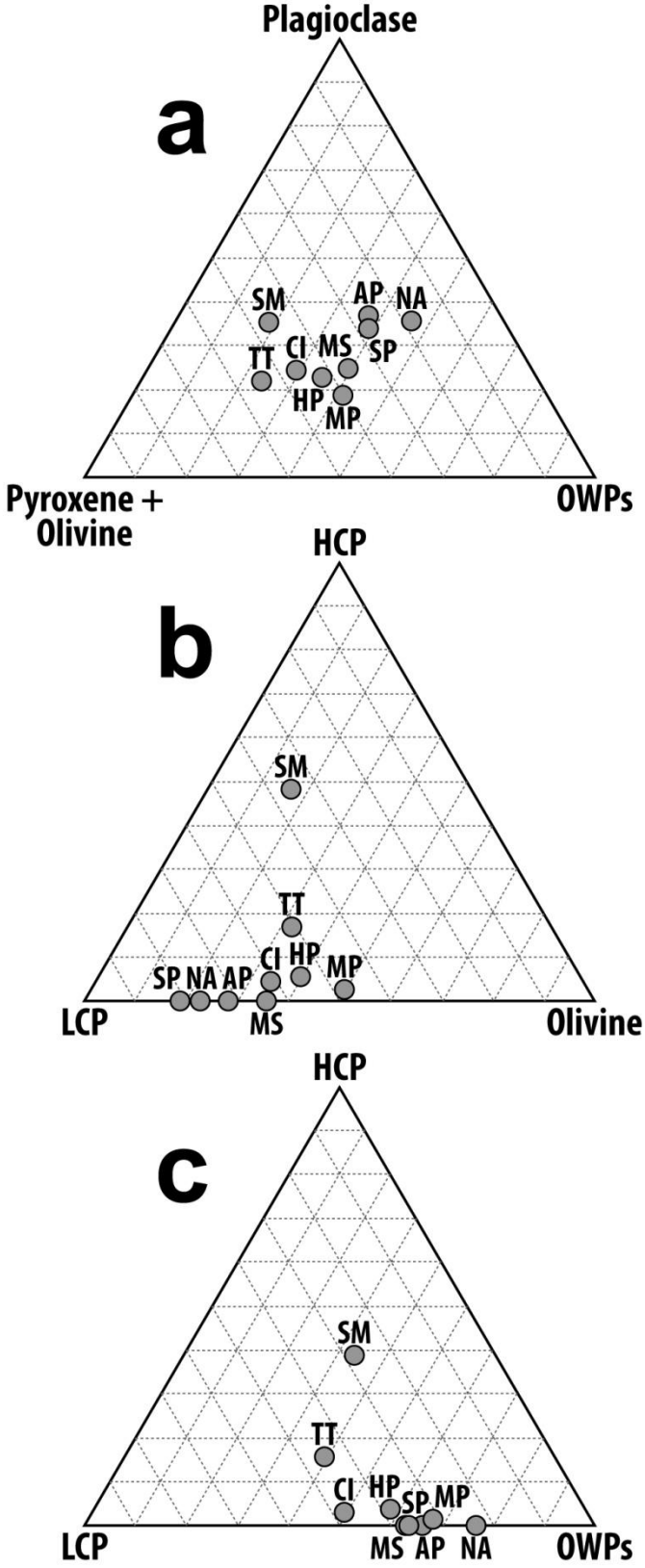

Chapter 5, Figure 9.

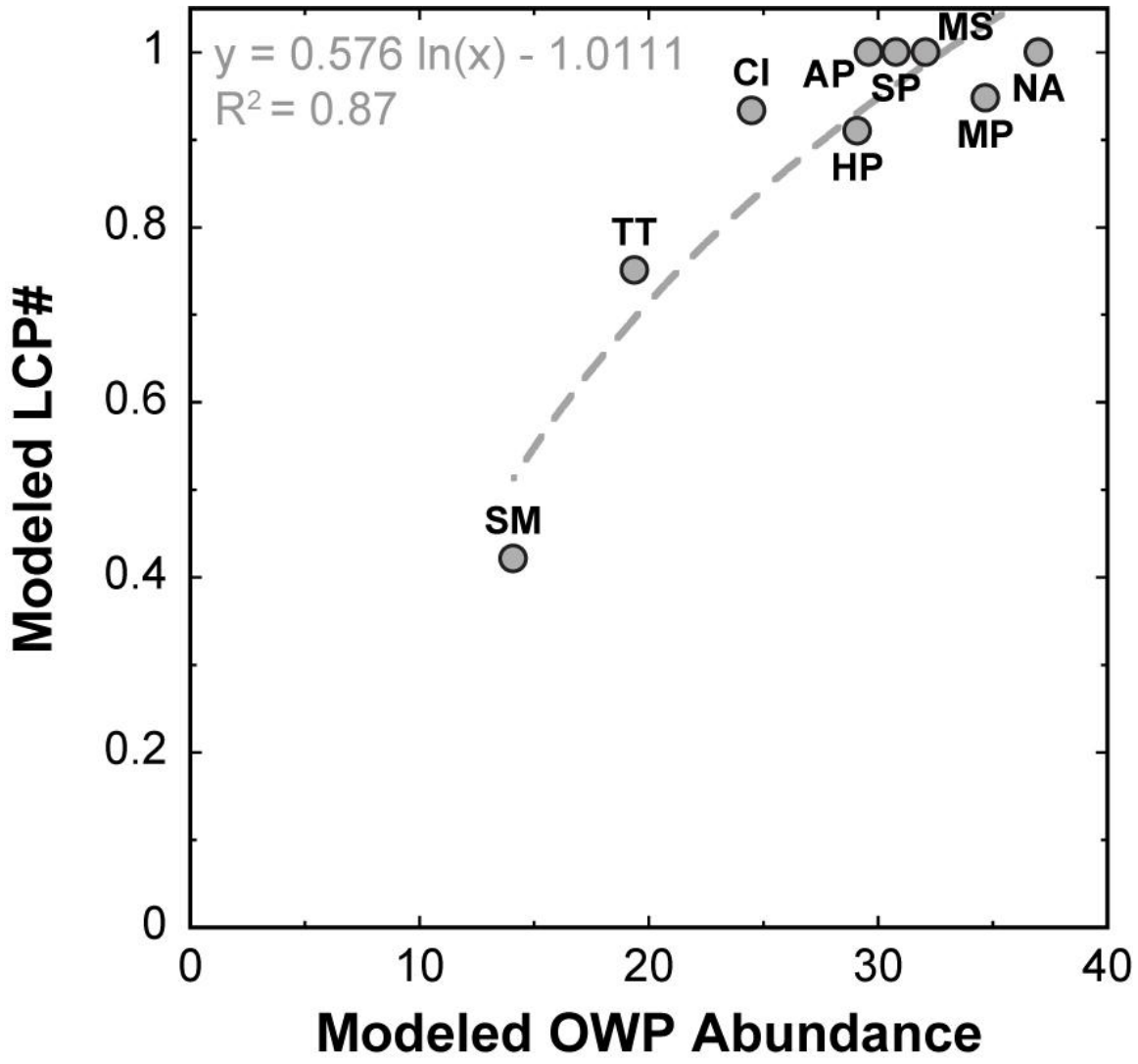

Chapter 5, Figure 10.

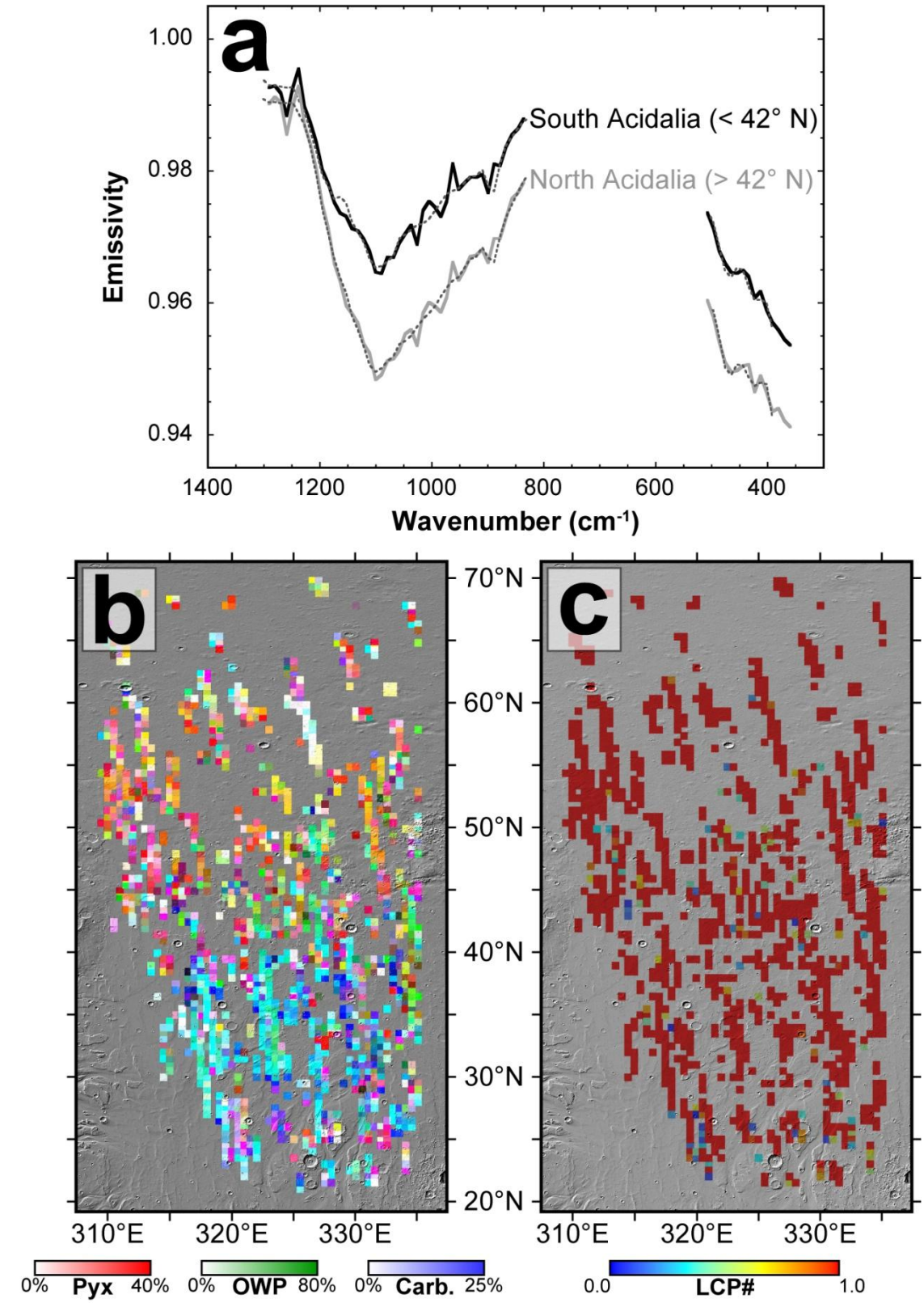

Chapter 5, Figure 11.

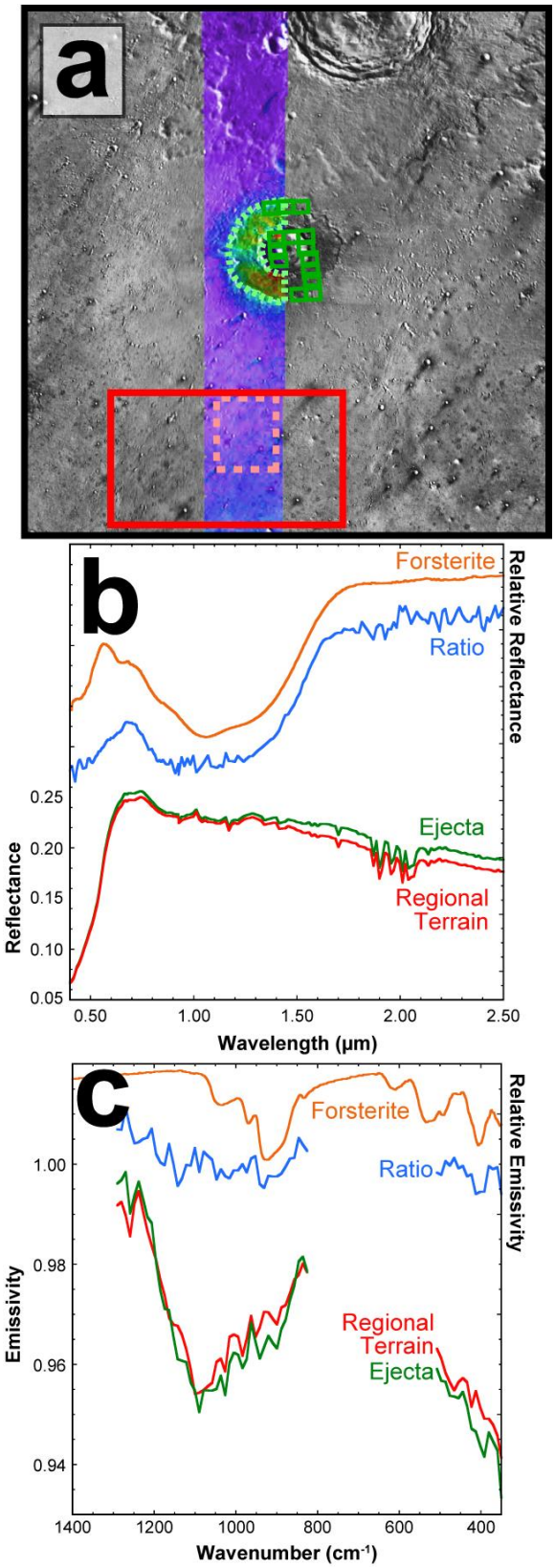

Chapter 5, Figure 12.

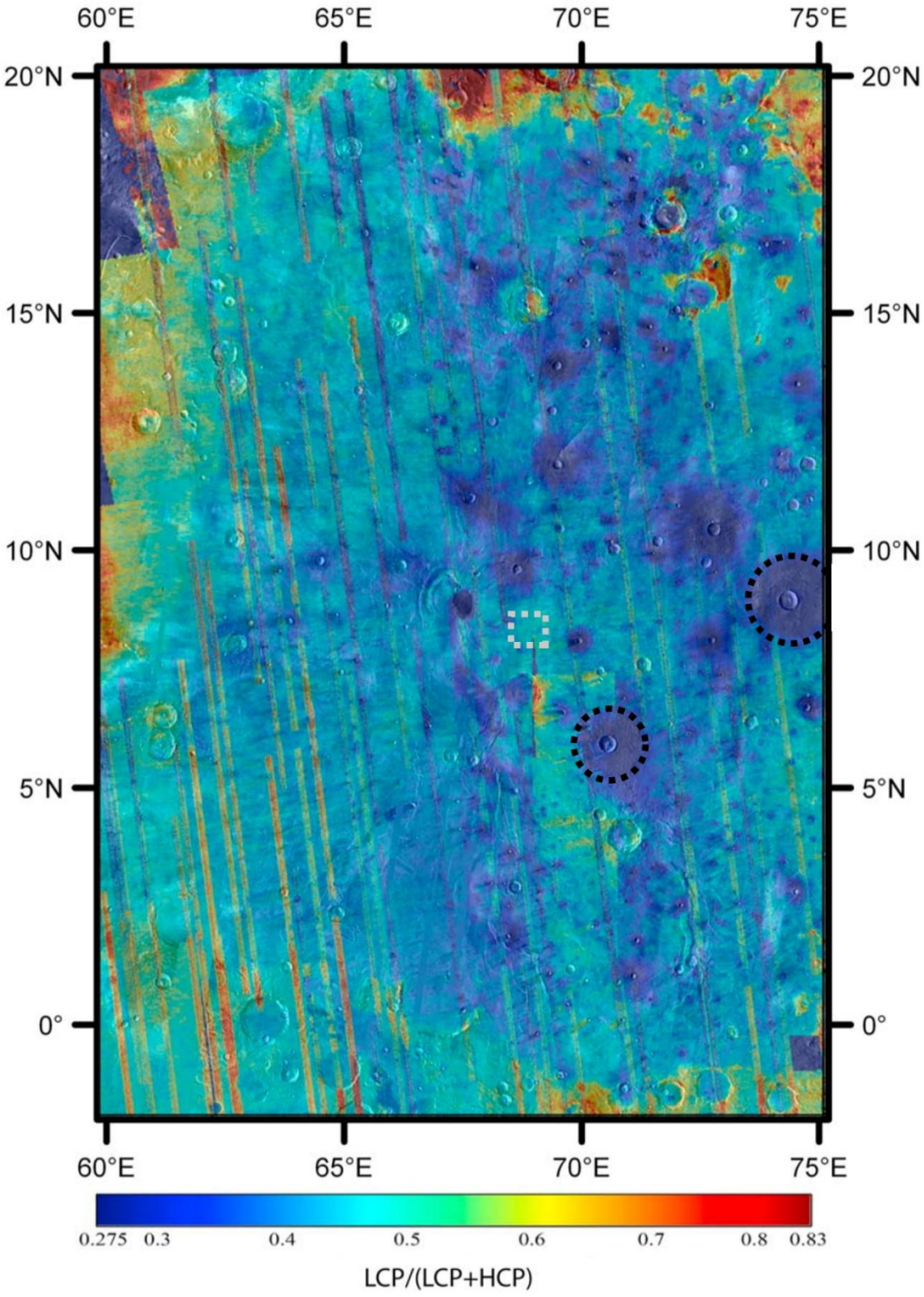

Chapter 5, Figure 13.

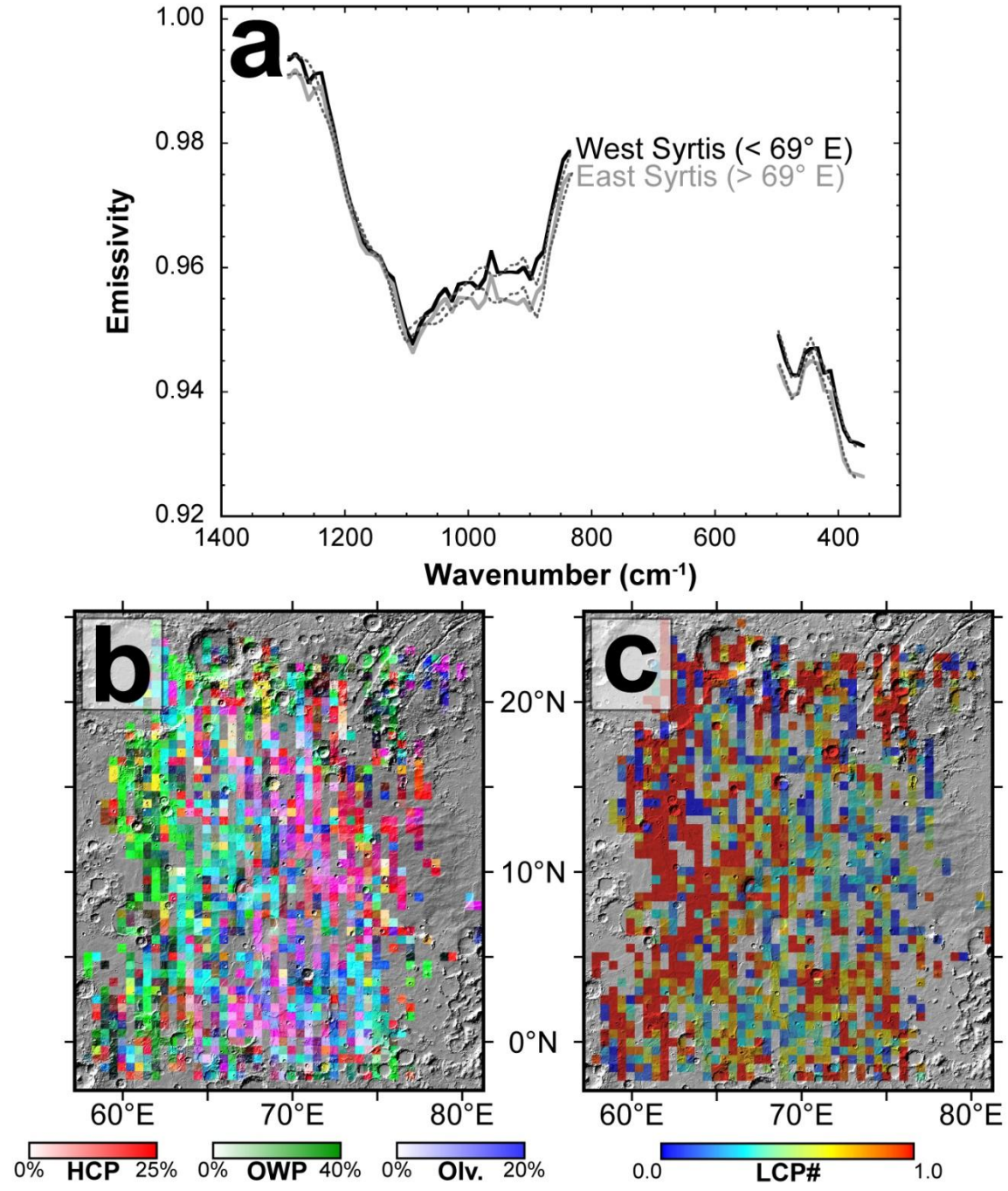

Chapter 5, Figure 14.

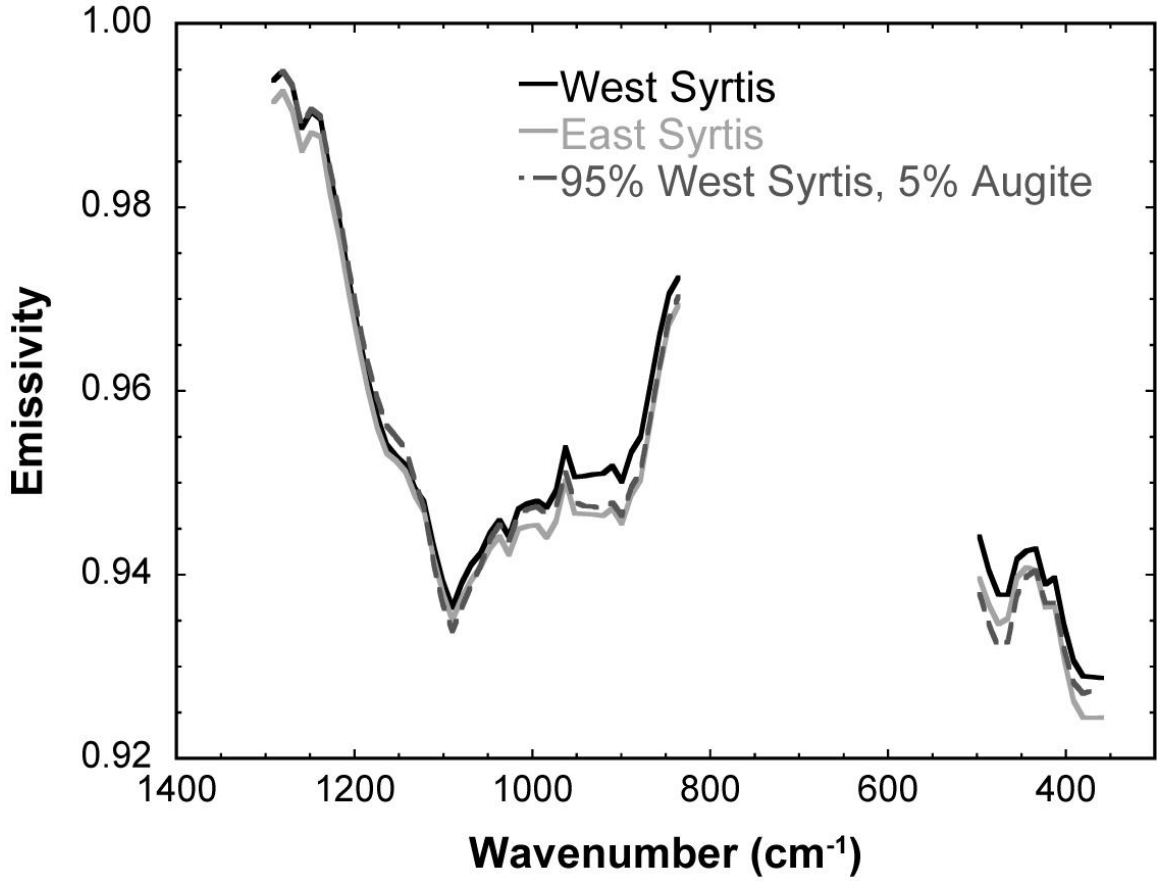

Chapter 5, Figure 15.

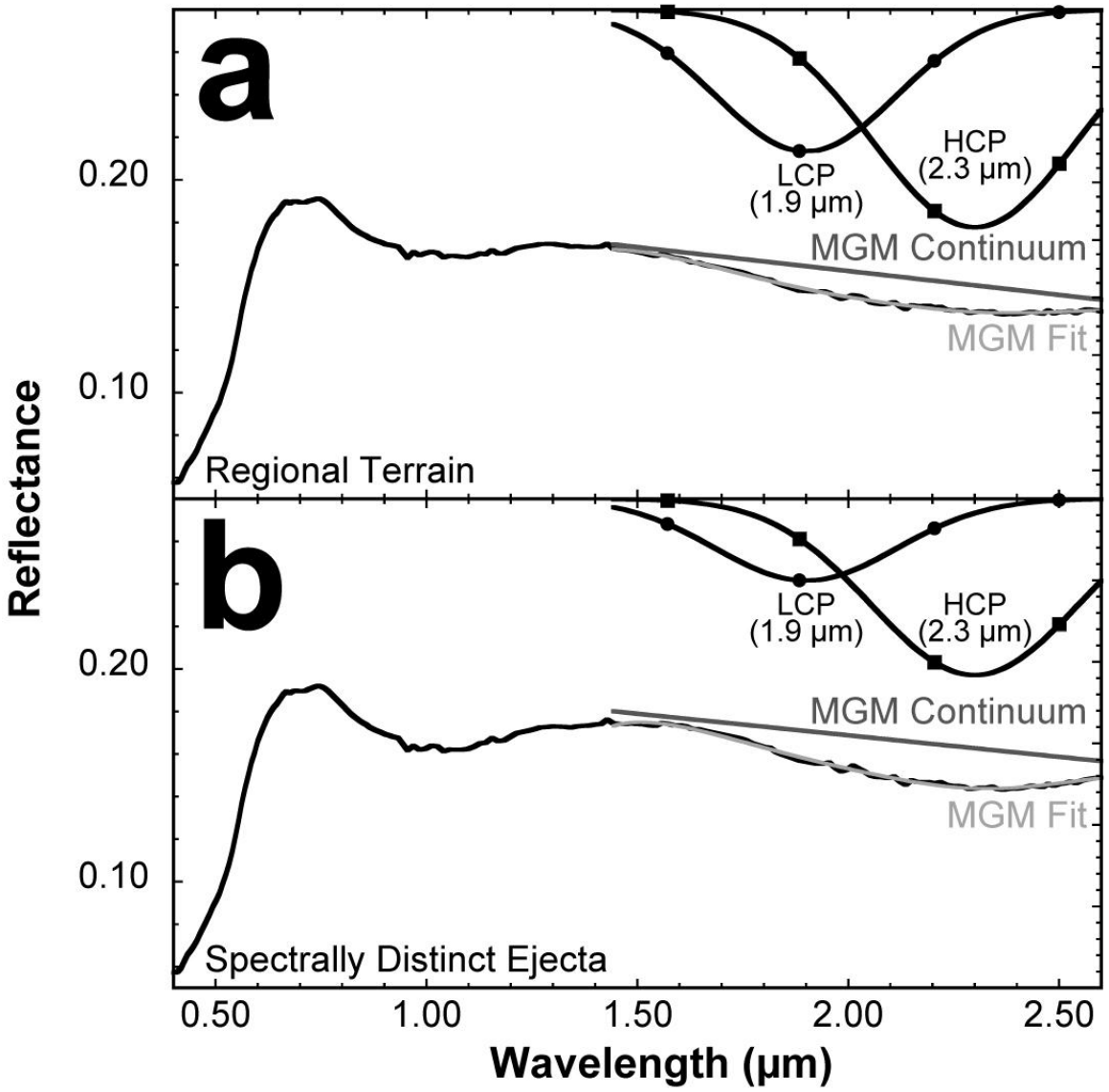

Chapter 5, Figure 16.

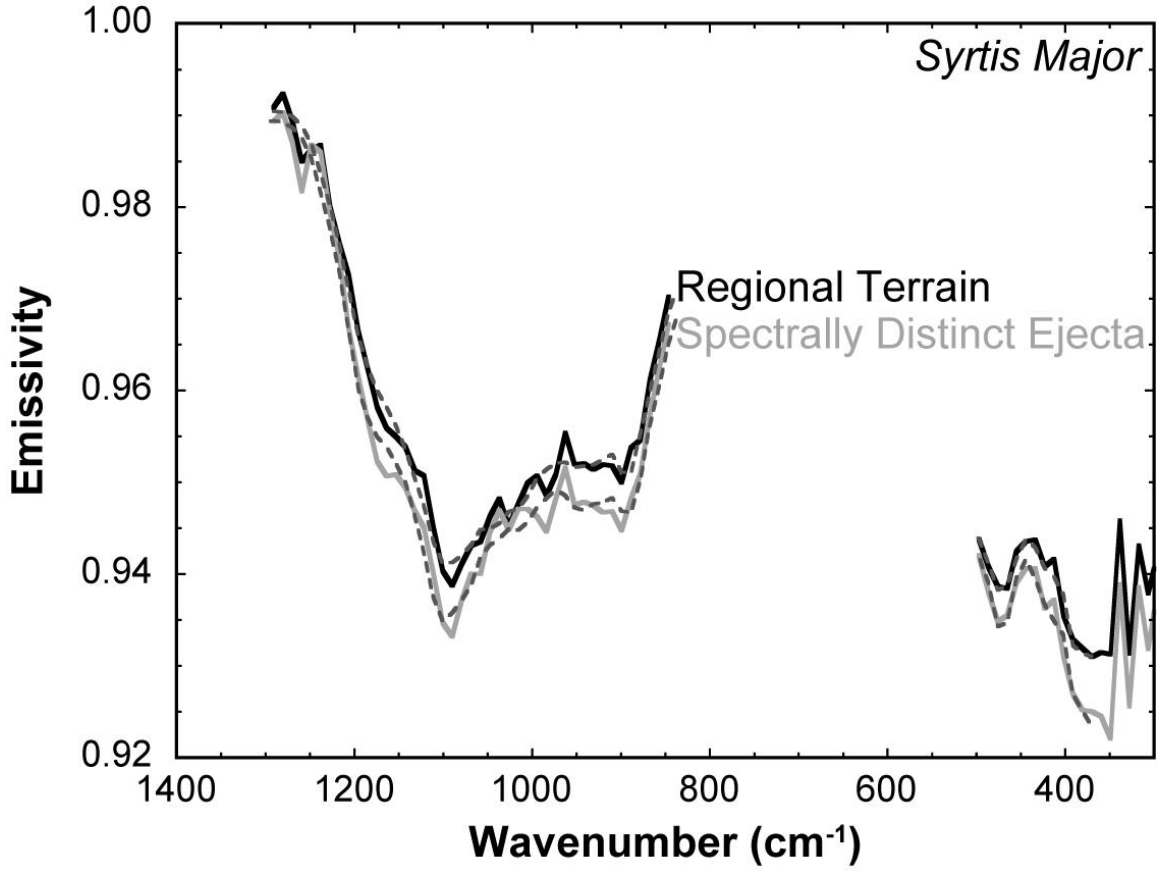

Chapter 5, Figure 17.

Chapter 5, Table 1.

Region	Latitude	Longitude	# of Spectra
Acidalia Planitia	18º N – 70º N	310º E – 335º E	20422
Syrtis Major	2º S – 28º N	58º E – 83º E	38699

Chapter 5, Table 2.

Sample	1.9 µm Strength	2.3 µm Strength	Slope ($x10^{-5}$)	*Slope (°)*	y-intercept ($x10^{-1}$)	RMS Error (%)	LCP#	Fe^{3+} IVCT Strength
MS10_BV_02_int	0.09031	0.08966	2.63	*1.65*	0.41	0.896	0.502	1.45
MS10_BV_02_sur	0.07927	0.00655	1.58	*1.00*	0.62	1.097	0.924	1.74
MS10_BV_03_int	0.07889	0.10464	0.12	*0.08*	0.87	0.916	0.430	1.58
MS10_BV_03_sur	0.09251	0.06639	-0.58	*-0.37*	1.11	1.496	0.582	2.38
MS10_BV_06_int	0.00331	0.06626	-0.53	*-0.33*	0.87	1.047	0.048	1.25
MS10_BV_06_sur	0.01714	0.00737	-3.36	*-2.12*	1.75	1.685	0.699	2.00
MS10_BV_07_int	0.00345	0.09208	-0.50	*-0.32*	0.83	1.335	0.036	1.34
MS10_BV_07_sur	0.07340	0.10049	-3.25	*-2.05*	1.78	1.671	0.422	2.41
MS10_BV_09_int	-0.02703	0.02252	-1.37	*-0.86*	1.08	1.509	0.000	1.25
MS10_BV_09_sur	0.00913	0.07440	-1.90	*-1.20*	1.29	1.847	0.109	1.99
MS10_BV_10_int	-0.00367	0.07931	-0.86	*-0.54*	0.93	1.655	0.000	1.44
MS10_BV_10_sur	0.00562	0.04882	-0.90	*-0.57*	0.64	1.210	0.103	1.64
MS10_BV_11_int	0.00725	0.07102	-0.88	*-0.56*	0.90	0.984	0.093	1.46
MS10_BV_11_sur	0.03242	0.06277	-3.11	*-1.96*	1.44	2.041	0.341	2.19
MS10_BV_12_int	0.11646	0.15275	-0.99	*-0.62*	1.15	2.050	0.433	1.74
MS10_BV_12_sur	0.08068	0.09295	-3.79	*-2.39*	1.91	1.770	0.465	2.89
Interior Average	**0.03362**	**0.08478**	**0.30**	***-0.19***	**0.88**	**1.30**	**0.193**	**1.44**
Surface Average	**0.04877**	**0.05747**	**1.92**	***-1.21***	**1.32**	**1.60**	**0.456**	**2.16**

Chapter 5, Table 3.

Endmember	Mineral Group	Source
Albite WAR-0244	Plagioclase	Christensen et al. (2000b)
Andesine BUR-240	Plagioclase	Christensen et al. (2000b)
Anorthite BUR-340	Plagioclase	Christensen et al. (2000b)
Bronzite NMNH-93527	Low-Ca Pyroxene	Christensen et al. (2000b)
Diopside WAR-6474	High-Ca Pyroxene	Christensen et al. (2000b)
Augite NMNH-9780	High-Ca Pyroxene	Hamilton (2000)
Augite NMNH-122302	High-Ca Pyroxene	Hamilton (2000)
Hedenbergite DSM-HED01	High-Ca Pyroxene	Christensen et al. (2000b)
Pigeonite	Low-Ca Pyroxene	Hamilton (2000)
Forsterite BUR-3720A	Olivine	Christensen et al. (2000b)
Fayalite WAR-RGFAY01	Olivine	Christensen et al. (2000b)
KI 3362 Fo60	Olivine	Morse (1996)
Biotite BUR-840	Phyllosilicate	Christensen et al. (2000b)
Serpentine HS-8.4B	Phyllosilicate	Christensen et al. (2000b)
Illite IMt-2	Phyllosilicate	Christensen et al. (2000b)
Ca-Montmorillonite STx-1	Phyllosilicate	Christensen et al. (2000b)
Si-K Glass	High-Si Phase	Wyatt et al. (2001)
Opal-A (01-011)	High-Si Phase	Michalski et al. (2003)
Magnesiohastingsite HS-115.4B	Amphibole	Christensen et al. (2000b)
Avg. Martian Hematite	Oxide	Glotch et al. (2004)
Calcite C40	Carbonate	Christensen et al. (2000b)
Dolomite C20	Carbonate	Christensen et al. (2000b)
Anhydrite ML-S9	Sulfate	Christensen et al. (2000b)
Gypsum ML-S6	Sulfate	Christensen et al. (2000b)
OWP	*OWP*	*Salvatore et al. (2013)*
Enstatite HS-9.4B	*Low-Ca Pyroxene*	*Christensen et al. (2000b)*
Blackbody	Blackbody	Christensen et al. (2000b)

Chapter 5, Table 4.

GROUP	AP	CI	HP	MP	MS	NA	SM	SP	TT
Plagioclase	29.3 ± 3.8	20.3 ± 4.6	18.9 ± 4.4	15.6 ± 4.3	20.4 ± 3.8	28.7 ± 4.6	27.3 ± 5.4	27.0 ± 3.2	18.0 ± 4.6
Low-Ca Pyx	14.7 ± 4.7	23.7 ± 3.4	19.2 ± 3.2	16.1 ± 3.7	18.9 ± 4.0	11.2 ± 3.1	12.6 ± 4.3	17.6 ± 3.7	22.6 ± 3.1
High-Ca Pyx	0.0	1.7 ± 4.8	1.9 ± 4.4	0.9 ± 4.7	0.0	0.0	17.3 ± 5.1	0.0	7.5 ± 3.6
Olivine	5.8 ± 1.9	13.3 ± 2.7	13.8 ± 2.6	16.7 ± 2.9	10.5 ± 2.1	3.3 ± 1.9	5.8 ± 3.3	4.1 ± 1.1	14.3 ± 2.3
Phyllosilicate	4.6 ± 2.3	3.2 ± 3.0	4.5 ± 2.8	2.4 ± 1.5	6.2 ± 2.5	9.4 ± 2.6	6.6 ± 2.5	2.8 ± 0.8	3.1 ± 2.6
Amphibole	0.0	2.2 ± 2.9	0.3 ± 2.8	0.0	0.0	0.0	3.1 ± 3.4	3.9 ± 2.3	3.6 ± 2.6
Carbonate	4.0 ± 0.6	2.9 ± 0.6	3.6 ± 0.6	4.1 ± 0.6	3.3 ± 0.6	2.6 ± 0.7	5.7 ± 0.7	2.4 ± 0.5	2.3 ± 0.4
Sulfate	8.4 ± 1.5	8.2 ± 1.3	8.9 ± 1.2	9.4 ± 1.4	8.5 ± 1.6	7.7 ± 1.8	6.2 ± 1.7	11.3 ± 1.3	8.8 ± 1.4
OWP	29.6 ± 3.2	24.5 ± 4.3	29.1 ± 4.1	34.7 ± 3.8	32.1 ± 3.4	37.0 ± 2.9	14.1 ± 3.7	30.8 ± 2.2	19.4 ± 3.3
Quartz	0.1 ± 0.8	0.0	0.0	0.0	0.0	0.0	0.6 ± 0.8	0.0	0.4 ± 0.7
Oxide	3.4 ± 6.1	0.0	0.0	0.0	0.0	0.0	0.7 ± 5.9	0.0	0.0
Plag/Pyx	2.0	0.8	0.9	0.9	1.1	2.6	0.9	1.5	0.6
LCP#	1.00	0.93	0.91	0.95	1.00	1.00	0.42	1.00	0.75
Blackbody	52.2 ± 4.6	45.9 ± 1.9	50.7 ± 1.6	56.6 ± 1.5	53.8 ± 1.7	67.2 ± 1.3	35.4 ± 5.3	59.5 ± 1.3	46.8 ± 1.7
RMS Error	0.104	0.118	0.111	0.113	0.136	0.150	0.139	0.160	0.108

Chapter 5, Table 5.

GROUP	North Acidalia	South Acidalia	Grindavik Ejecta	Regional Terrain	West Syrtis	East Syrtis	SDE Deposits	Regional Terrain
Plagioclase	28.6 ± 3.4	25.1 ± 4.6	18.8 ± 4.4	17.0 ± 6.2	27.7 ± 4.4	29.2 ± 4.4	31.7 ± 6.0	24.0 ± 5.7
Low-Ca Pyx	7.3 ± 2.6	1.9 ± 2.4	8.0 ± 3.3	11.0 ± 3.9	7.3 ± 3.0	8.7 ± 2.8	2.4 ± 2.8	7.5 ± 2.8
High-Ca Pyx	0.0	0.0	0.0	0.0	4.8 ± 5.1	8.0 ± 4.7	12.3 ± 6.9	1.5 ± 5.9
Olivine	2.1 ± 1.3	0.6 ± 1.9	12.3 ± 2.0	4.0 ± 2.7	10.8 ± 3.4	10.7 ± 3.0	8.1 ± 4.4	14.2 ± 4.2
Phyllosilicate	0.5 ± 0.7	0.0	1.5 ± 0.9	2.2 ± 3.0	0.6 ± 0.7	0.0	0.0	1.3 ± 1.1
Amphibole	0.0	0.0	0.0	0.0	0.0	0.0	0.0	0.0
Carbonate	4.9 ± 0.6	8.0 ± 0.6	6.5 ± 0.7	8.6 ± 1.1	5.4 ± 0.7	5.5 ± 0.5	6.0 ± 0.7	5.5 ± 0.7
Sulfate	8.6 ± 1.5	8.4 ± 1.7	9.9 ± 1.9	5.5 ± 2.2	5.4 ± 1.5	4.2 ± 1.2	3.8 ± 1.3	5.3 ± 1.9
OWP	48.1 ± 2.5	56.1 ± 3.2	42.9 ± 3.2	51.6 ± 3.8	36.9 ± 3.8	32.4 ± 3.4	34.7 ± 4.5	39.5 ± 4.9
Quartz	0.0	0.1 ± 0.9	0.0	0.0	0.6 ± 0.9	1.3 ± 0.9	0.9 ± 1.2	1.2 ± 1.2
Oxide	0.0	0.0	0.0	0.0	0.0	0.0	0.0	0.0
Plag/Pyx	3.9	13.2	2.3	1.5	2.3	1.7	2.2	2.7
LCP#	1.00	1.00	1.00	1.00	0.60	0.52	0.16	0.83
Blackbody	61.9 ± 0.9	71.7 ± 0.8	62.0 ± 1.2	69.1 ± 1.2	48.6 ± 1.1	46.6 ± 1.1	49.2 ± 1.7	52.9 ± 1.5
RMSE	0.153	0.150	0.195	0.185	0.169	0.170	0.196	0.163

Chapter Six:

On the current and future investigation of pervasive oxidative alteration processes on Earth and Mars.

M. R. Salvatore[1]

[1]Department of Geological Sciences,

Brown University, Providence, RI 02912, USA

1.0 Summary and Significance of Work

This body of work aims to further our understanding of cold and dry chemical alteration processes through the use of terrestrial analogs, laboratory analyses, and remote sensing. We have been fortunate to root our investigations in fundamental laboratory analyses (e.g. Cooper et al., 1996) that thoroughly characterize and quantify the process of oxidative weathering in basaltic glasses at high temperatures. However, in natural settings, the ubiquity of oxidative weathering is typically overwritten by more mature alteration processes, such as the development of amorphous or crystalline alteration phases. As a result, in more than a decade since the process of oxidative weathering has been characterized, only a few studies have identified natural environments where this process is observed and the resultant products are preserved (e.g. Burkhard and Müller-Sigmund, 2007).

Through extensive field work and the identification of these metastable terrestrial weathering products, it soon became obvious that Beacon Valley, Antarctica, experienced pervasive oxidative weathering without the development of more mature alteration phases. This represents the only natural laboratory where oxidative weathering processes are subaerially preserved. In Chapter Two, we characterize a subset of samples from Beacon Valley using a suite of laboratory techniques in an attempt to investigate the chemical, mineralogical, and spectral effects of oxidative weathering on these samples. Our investigations show that spectrally significant modifications occur to the rock surfaces in response to small chemical and immeasurable mineralogical variations. While the electronic and vibrational environments of these samples are clearly distorted

significantly upon weathering, the exact cause and nature of these changes remain uncertain.

These distinct spectral signatures and their spatial distributions throughout the McMurdo Dry Valleys are further investigated in Chapter Three. A multitude of difficulties, largely with respect to atmospheric and geometric corrections, has precluded the widespread use of orbital and aerial spectral datasets over the McMurdo Dry Valleys. Using in-scene atmospheric correction techniques and a wealth of ground-truthed visible/near-infrared (VNIR) and thermal infrared (TIR) data, we have produced the first multispectral data product covering the majority of the McMurdo Dry Valleys (MDV). The first scientific results utilizing this valuable data product are presented in Chapter Three, where the spectral variability observed in the Ferrar Dolerite is characterized from orbit and linked to a range of primary compositions and secondary processes. In particular, variations in the abundance of orthopyroxene are readily observed using VNIR spectral datasets due to the strength of the 1 μm and 2 μm crystal field absorption features caused by Fe^{2+} in pyroxenes. Additionally, the distinct spectral signatures of oxidative weathering are observed in the thermal infrared, and their observed distribution throughout the MDV highlights their unique preservation in Beacon Valley and in only a few other localized regions throughout the MDV. These results confirm that while oxidative weathering is a global and pervasive phenomenon, preservation of these signatures and products is rare in terrestrial environments.

The successful characterization of oxidative weathering products in Beacon Valley, using both laboratory and orbital techniques, has allowed us to apply our observations to martian surface investigations. The wealth of hyperspectral VNIR and

TIR data from orbit are well suited to characterize similar spectral signatures to those observed in the MDV. Chapter Four presents the initial results of our orbital investigation of the martian surface and the spectral similarities to signatures observed in Beacon Valley. The Syrtis and N. Acidalia-Utopia spectral regions, which represent the two distinct low albedo surface endmembers on Mars, can be uniquely characterized as basaltic surfaces that have undergone variable amounts of oxidative weathering. Not only is oxidative weathering a good analog to the spectral signatures observed in both the VNIR and TIR wavelength regions, but it is also consistent with our current understanding of martian surface and climate evolution. For example, thin silica-rich surface coatings have been shown to exhibit spectral similarities to the alteration rinds identified in Beacon Valley and hypothesized for the martian surface (Fig. 1; Kraft et al., 2003; Minitti et al. 2007; Chemtob et al., 2010). However, the dominance of physical erosion on the current martian surface, and ubiquity of these thin coatings that are necessary on the martian surface, makes the presence of these features on the martian surface less likely and supports our hypothesis of oxidative alteration processes being the primary cause of these spectral signatures at regional and global scales. This initial investigation highlights the observed spectral similarities and sets the stage for additional and more detailed VNIR and TIR analyses.

Chapter Five builds upon and expands the research presented in Chapter Four. The nine characteristic low albedo regions initially identified by Rogers et al. (2007) and characterized by Rogers and Christensen (2007) in the TIR were investigated using data from the Observatoire pour la Minéralogie, l'Eau, les Glaces et l'Activité (OMEGA; Bibring et al., 2004) to derive regional hyperspectral VNIR signatures to further

characterize the near-surface mineralogy. Additionally, Syrtis Major and Acidalia Planitia were both investigated at higher spatial resolutions to relate the observed surface signatures to subsurface compositions using impact craters as geologic boreholes into the subsurface. The results from this investigation suggest that hydrated alteration products are not observed at spectrally significant abundances on regional spatial scales. Instead, oxidative weathering processes are capable of explaining the observed spectral signatures and are uniquely consistent across both VNIR and TIR wavelength regions. At higher resolutions, the subsurface compositions of both Syrtis Major and Acidalia Planitia appear to be dominated by high-Ca pyroxene- and olivine-bearing basalts. However, variable amounts of oxidative weathering result in an apparent weakening of these spectral signatures in exchange for an apparent enrichment in low-Ca pyroxene. This work suggests that the interpreted primary compositions of different low albedo regions on Mars may be significantly influenced by oxidative weathering processes. As a result, future spectral investigations of Mars must account for the effects of oxidative weathering processes on apparent surface compositions.

2.0 Outstanding Questions

Although the work presented in this dissertation answers several fundamental questions regarding the alteration process associated with cold desert environments and the distribution of these alteration products on both Earth and Mars, many outstanding questions remain. Here, we highlight a handful of these remaining questions both as a means of organizing relevant future research, but also as a means of appreciating the diversity of the questions that we have worked so tirelessly to address.

2.1 What is the primary mechanism for the migration of cations to rock surfaces during oxidative weathering in Beacon Valley, Antarctica?

The low temperatures in Beacon Valley are critical for the preservation of metastable oxidative weathering products and the retardation of more mature alteration processes. However, these low temperatures and associated slow kinetics raise another question: What are the relative roles of different diffusion mechanisms that result in cation migration and alteration rind formation? As mentioned in Chapter Two, simple extrapolation of high-temperature volume diffusion rates to ambient Antarctic temperatures result in extremely slow rates that are insufficient to generate the observed alteration rind thicknesses. It is likely that diffusion along grain boundaries, dislocations, and other fast paths play an important role in the formation of these alteration rinds via cation migration. Characterizing the relative roles of these different diffusion mechanisms during oxidative weathering can help to constrain the duration and rates of oxidative weathering in Antarctica and provide a more fundamental understanding of how geologic materials weather in oxidizing environments. Further extrapolation can then help to predict oxidative weathering mechanisms and rates on the martian surface.

2.2 What is the cause of the large amount of variability observed in X-ray diffraction data and what is the relationship to spectroscopic measurements?

X-ray diffraction (XRD) is widely considered to be the standard method for mineralogical identification and quantification in geologic samples because it measures fundamental lattice parameters to assess crystal structures. Efforts to characterize powders of both dolerite interiors and surfaces are described in Chapter Two. Measurements were made at three different laboratories using three different preparation

and measurement techniques, none of which resulted in clean and reproducible patterns. Additionally, attempts at quantitative characterization using Reitveld refinements resulted in mineral abundances that were not consistent with other spectral and compositional measurements. For example, the Fe-bearing smectite clay nontronite was modeled at an abundance of roughly 30% in both the interior and surface of a particular dolerite sample. However, VNIR and TIR measurements do not reveal spectral signatures that correspond to the presence of nontronite at these abundances. Additionally, the presence of nontronite at 30 vol.% would result in diagnostic shifts in sample chemistry, although no such shifts are observed (Salvatore et al., 2013). As a result, XRD analyses appear to be incongruous with other laboratory techniques that are all consistent with each other.

While XRD analyses were not critical towards our dolerite characterization described in Chapter Two, this inconsistency is of concern. In particular, while XRD analyses are a standard mineralogical assessment performed on terrestrial samples, the ability to characterize surface mineralogy on other planets, particularly Mars, relies heavily on remote spectroscopy. Disagreements between XRD analyses and spectral measurements on terrestrial samples, like those observed in Chapter Two, create concern regarding the ability to accurately assess sample mineralogy using either method. What is the true relationship between these XRD and spectral analyses? Are the disagreements between the two datasets the result of sample preparation or analytical errors, or is there a property that is fundamental to the Ferrar Dolerite (e.g., amount of interstitial glass or the morphology of individual grains) that precludes the ability to use either technique to accurately assess the mineralogical components that are present? Additional work is currently being designed to meticulously prepare and measure the same dolerite suite

discussed in Chapter Two (i.e., Salvatore et al., 2013) using techniques designed solely for XRD analyses. Should large disagreements continue between analytical techniques, the ability to link spectroscopic studies to mineralogical identifications derived via XRD analyses must be reevaluated.

2.3 What is the origin of the spectral variations observed in oxidative weathering products?

The chemical, mineralogical, and spectral signatures of oxidative weathering described in the preceding chapters represents our current understanding of how basaltic lithologies alter where hyper-arid and hypo-thermal conditions dominate. The subtle yet systematic chemical signatures associated with the oxidized alteration rinds on dolerites are indicative of a unique process with a foundation in chemical diffusion, kinetics, and thermodynamics (Cooper et al. 1996). The cause of the observed spectral variability, however, is less constrained.

VNIR reflectance spectroscopy is sensitive to both the electronic environment associated with transition metals (primarily Fe) as well as the vibrational overtones and combination tones associated with different anion groups and cation-anion pairings. In Chapter Two, we first characterize the VNIR spectral signatures of alteration rinds and the dominant spectral differences between dolerite surfaces and their interiors. To further compare these signatures to the regional VNIR spectral signatures observed across the martian surface, we revisit these VNIR spectra in Chapter Five, where modified Gaussian model (MGM; Sunshine et al., 1990) analyses reveal a systematic decrease in spectral slope and apparent shift in the 2 μm electronic transition associated with pyroxene. Higher H_2O abundances could result in a stronger fundamental vibrational absorption

associated with water near 3 μm, which has been shown to result in decreased NIR spectral slopes in samples of heavily hydrated phases. While the dolerite surfaces are likely more enriched in H_2O relative to their interiors, the slope of dolerite surfaces is more gradual and begins at shorter wavelengths than would be expected by the simple presence of a stronger H_2O fundamental absorption. This imposed spectral slope may also be the cause of the apparent shift in the 2 μm band center. Definitive evidence for the cause of these spectral features, however, is lacking and requires additional macro- and micro-scale spectral measurements to supplement these initial studies.

The narrowing of the reststrahlen features in thermal infrared (TIR) emission spectra of dolerite surfaces is similarly unconstrained with regards to the underlying vibrational processes involved in the production of these signatures. In silicates, absorptions in these wavelength regions are linked to the primary Si-O vibrational frequencies. Variations in these shapes imply that the Si-O vibrational environment has been modified (and, in this instance, simplified) to result in one dominant vibrational frequency (~1100 cm^{-1}). Perhaps the removal of divalent cations, enrichment in monovalent cations, and the associated oxidation of ferrous iron can result in such Si-O homogenization? Additional work must also be undertaken at a variety of spatial scales to clearly identify the extent and cause of these spectral relationships.

2.4 How does oxidative weathering influence the spectral signatures of different primary compositions?

We have shown that the spectral signatures associated with oxidative weathering in Beacon Valley, Antarctica, are comparable to those observed throughout the martian surface. However, while the Ferrar Dolerite is an appropriate analog for many martian

basaltic lithologies, its limited compositional range precludes direct comparison to all observed lithologies across the martian surface. Igneous compositions on Mars range from quartzofeldspathic to ultramafic on both local and regional scales, and understanding the spectral influences of oxidative weathering on these different primary compositions is critical.

The chemical effects of oxidative weathering have been well documented in both laboratory (Cooper et al., 1996) and natural settings (Burkhard & Müller-Sigmund, 2007; Salvatore et al., 2013). In theory, the initial compositions of these materials should not influence the distinct alteration trends associated with the oxidation process, so long as the necessary chemical components (e.g., ferrous iron, divalent and monovalent cations) are present at significant abundances (Cook and Cooper, 2000). However, because the cause of the resultant spectral effects is not completely understood, the influence of primary composition must also be investigated. For example, TIR spectra of oxidized dolerite surfaces exhibit a significant narrowing of the reststrahlen features centered roughly at the same frequency as the dolerite interiors. However, if the primary dolerite were olivine-rich, the reststrahlen features of the unaltered dolerite would shift to lower frequencies. Would the resultant oxidative weathering signatures show a comparable shift to lower frequencies, or is the observed 1100 cm^{-1} center unique to oxidative weathering products regardless of the starting composition?

In Chapter Three, we show that the Ferrar Dolerite has a range of compositions and textures that reflect multiple injections of pyroxene-laden magmatic slurries concurrent with sill emplacement. We also highlight how the preservation of alteration rinds on these more mafic dolerites is thwarted by their increased susceptibility to

physical erosion. The inherent variability and difficulties associated with these natural samples will likely require the identification of additional field sites that contain different primary lithologies exhibiting well-developed oxidation rinds. Care must be taken when selecting appropriate field sites, however, to ensure that oxidative weathering processes dominate over more common chemical alteration processes (e.g., fluvial, periglacial), which introduces our next outstanding question.

2.5 How does oxidative weathering progress under different climatic conditions?

Beacon Valley represents the only known natural laboratory on Earth where such immature oxidative alteration rinds develop and are preserved under ambient climatic conditions. Lasaga (1984) and numerous additional studies have determined that the dominant style of alteration is determined in large part by the temperature and chemistry of the alteration environment. Therefore, one would expect the nature and dominance of oxidative alteration to be dependent upon environmental conditions.

Figure 2 shows the location of Beacon Valley and other terrestrial, martian, and modeled martian environments with respect to mean annual temperature and precipitation. While oxidative weathering has been shown to dominate in Beacon Valley, what is the true extent of this alteration process in temperature-precipitation space? In other words, at what temperature do other alteration processes (e.g., thermal decomposition) begin to overshadow oxidative weathering? This bounding limit is useful for determining the ability to reproduce relevant weathering conditions in laboratory settings. Additionally, how much liquid water is necessary to overprint oxidative weathering products with hydrous alteration products? This information can help to define other potential field sites to investigate oxidative weathering. Should the

bounding environmental coordinates of oxidative weathering be fairly broad, the possibility of constraining the rate and extent of oxidation for many primary compositions is realistic. If not, cautious laboratory experiments may be the only way to study terrestrial oxidative weathering processes in further detail.

2.6 What is the rate of oxidative weathering in terrestrial and martian environments?

The previously described outstanding question has clear implications for understanding the rate of oxidative weathering on Earth and Mars. In Chapter Two, our samples were collected along an age transect defined by Marchant et al. (2007) and represent surface ages of 0.6 Ma and older. We found no clear relationship between alteration rind properties and the position along the predefined age transect. This result is consistent with that of Marchant et al. (2013), who found that alteration rind thickness does not significantly increase beyond a surface exposure age of roughly 10,000 – 15,000 years. While their study was focused primarily on the processes of physical erosion in the MDV, additional work needs to be undertaken to determine the rates and kinetic mechanisms of oxidation, taking grain size and unaltered primary composition into account.

Combining the rate of oxidation rind formation with the climatic conditions present within Beacon Valley will help to constrain oxidation rates in this hyper-arid and hypo-thermal natural environment. Together with previous laboratory studies, the kinetics of oxidative weathering can be estimated and applied to other natural terrestrial and martian environments. However, the rate of weathering rind formation is dependent on both environmental conditions as well as primary composition. In particular, the relative abundance of cations will change each individual transport coefficient and,

hence, the rates at which cations are able to migrate within the material. In terrestrial environments, the primary composition of samples can be easily constrained through field and laboratory studies. On Mars, however, primary mineralogy must be modeled using a variety of analytical datasets at a wide range of spatial resolutions. Therefore, the successful determination of oxidation rates on Mars is heavily dependent upon the successful determination of primary starting compositions. Nonetheless, relative rate estimations are valuable when assessing and comparing the evolutionary history of different martian landscapes.

Determining oxidation rates will require the use of both laboratory analyses of naturally oxidized samples and the oxidation of pristine samples in controlled laboratory environments. While the textures of naturally oxidized materials can hold valuable information regarding the nature and extent of alteration (e.g., Cooper et al. 1996), the ability to study the evolution of these textures on human timescales is not a current possibility. Instead, the oxidation of unaltered samples in a controlled laboratory setting could potentially supplement the study of natural samples. Given the potential sensitivity of this alteration process to the unique environmental conditions found in Beacon Valley, however, caution must be taken to ensure that laboratory-derived oxidation products are comparable to those observed in nature.

3.0 Future Work and Concluding Remarks

3.1 Future work

Future work to explore these outstanding questions will require a similar combination of field, laboratory, and orbital investigations. Graduate student Kevin

Cannon (Brown University, exp. 2017) has been analyzing the spectral, chemical, and mineralogical properties of basalts and basaltic sandstones from Carapace Nunatak, an isolated bedrock exposure along the eastern margin of the East Antarctic Ice Sheet that is located 110 km NNW of Beacon Valley. Preliminary measurements indicate that the samples from Carapace Nunatak have experienced more extensive aqueous alteration than the dolerites in Beacon Valley (Cannon et al., 2013). While mean annual temperatures are likely colder on Carapace Nunatak due to its exposure on top of the East Antarctic Ice Sheet, the amount of melting may be significantly higher due to the availability of snow and ice and the dark albedo of the rocks. The radiating effect of the dark rocks is manifested in the presence of an ice collar surrounding the nunatak (Fig. 3). The result of this effect is that liquid water is likely in more frequent contact with the rocks on Carapace Nunatak than in Beacon Valley. Determining whether these alteration products are the result of subaerial alteration in the current Antarctic environment or whether they are associated with deuteric alteration (volcanic rocks) or allogenic/authigenic alteration (sedimentary rocks) prior to exposure is of critical importance.

Future work on the Carapace Nunatak sample suite will involve additional chemical and mineralogical analyses, including the use of micro-X-ray diffraction (μXRD), micro-X-ray fluorescence (μXRF), elemental mapping, and micro-X-ray Absorption Near Edge Structure (μXANES) analyses, which require the use of synchrotron radiation and has been accepted for study at Brookhaven National Laboratory. Additional work surrounding new field sites and new analytical techniques are also being considered:

3.1.1 Field studies

Future field investigations will be necessary to identify the range of natural environments where oxidative weathering products are currently observed. One potential location for future research is the Nevada National Security Site (N2S2), located approximately 100 km northwest of Las Vegas. Hundreds of nuclear and conventional ordinances were detonated at this location beginning in 1951, creating well-developed and well-preserved craters that excavate underlying geologic materials. Of particular interest are the 81 m diameter crater created during Project Danny Boy resulting from a 0.42 kiloton (kt, of TNT) nuclear device buried at 33.5 m depth into basaltic substrate, and the 260 m diameter Schooner crater resulting from a 30 kt nuclear device buried at 108 m depth into basaltic substrate (DOE, 2000). The excavated and ejected material consists primarily of trachybasalt containing roughly 60% plagioclase, 15% pyroxene, 15% interstitial glass, and 10% olivine, with minor opaques (Nordyke and Wray, 1964; James, 1969).

Studies of the exposed basaltic materials will help to constrain the degree to which oxidative weathering products are preserved in this environment, as well as the extent to which chemical alteration has progressed beyond the effects of oxidation. These types of studies are possible (and are likely better constrained than those performed in the McMurdo Dry Valleys) because of the detailed temporal and environmental records available for this location. For example, the exact times of exposure for the basaltic ejecta associated with the Danny Boy and Schooner craters are precisely known (DOE, 2000). This information provides unique information on the temporal role of chemical alteration in desert environments. Additionally, detailed

weather and climate records are available from both Las Vegas, NV (105 km southeast of N2S2), and Beatty, NV (41 km southwest of N2S2), which provide temperature and precipitation data through the date and time of basalt excavation. Therefore, the extent of alteration observed on these basaltic clasts will allow us to determine whether exposure to the subtropical desert climate of southern Nevada results in significantly different alteration products than those observed in Beacon Valley.

3.1.2 Laboratory analyses

Additional laboratory analyses on the suite of dolerite samples from Beacon Valley can help to further constrain the properties and extent of oxidative weathering throughout each individual sample. One particular analysis that could potentially improve our understanding of the relationship between the spectral, chemical, and optical signatures observed in dolerite alteration rinds is the use of micro-thermal emission imaging, which is currently being developed at the Arizona State University Mars Space Flight Facility (Edwards and Christensen, 2012). This spectrometer is capable of achieving spatial resolutions of ~90 μm pix^{-1} on powders, whole rock, and sectioned samples. Further characterization of dolerite alteration rinds using this technology can help to constrain the depth of the observed thermal emission signatures as well as emissivity variations associated with different mineral groups.

Similarly, preliminary analyses using hyperspectral VNIR imaging spectroscopy (with Dr. Ed Cloutis, University of Winnipeg) has been conducted by graduate student Rebecca Greenberger (Brown University, exp. 2015) on a subset of dolerites from Beacon Valley. These data have a spectral resolution of 5 nm between 0.42 μm and 1.10 μm, and a spectral resolution of 10 nm between 1.20 μm and 2.50 μm. Initial

investigations of the data between 0.42 μm and 1.10 μm show good agreement with measurements made at the Reflectance Experiment Laboratory (RELAB) at Brown University (Fig. 4). Given the sub-millimeter spatial resolution that can be achieved using this imaging system, characterization of the alteration rind and the transition into the unaltered rock interior can be carefully characterized. As of April of 2013, calibration of the near-infrared component of these data is still underway.

Laboratory analyses utilizing transmission electron microscopy (TEM) can help to elucidate nanometer-scale textures within the dolerites. Graduate student Hillary O'Brien (Brown University, exp. 2016) has been spearheading the efforts of analyzing select dolerite samples using TEM analyses to search for new phases that may form within the alteration rinds. These analyses will help to refine the alteration model that we present in Chapter Two. Additional XRD analyses under optimal sample preparation and analytical conditions must also be performed in order to reconcile the conflicting results presented in Chapter Two, and to perform more robust Rietveld refinements on the measurements in order to derive reasonable quantitative mineral abundances. Future work is currently being planned for the summer of 2013.

3.1.3 Remote analyses

Orbital investigations of additional terrestrial field sites will help to establish the link between the weathering processes and the observed spectral signatures. The utility of Advanced Land Imager (ALI; Mendenhall et al., 2000) and Advanced Spaceborne Thermal Emission and Reflection Radiometer (ASTER; ERSDAC, 2005) datasets to study both primary and secondary compositions was shown in Chapter Three. The spatial coverage and proven utility of these datasets will be useful in future investigations

in other relevant terrestrial environments. Orbital and aerial datasets with higher spectral resolution, including Hyperion (220 spectral bands between 0.4 μm and 2.5 μm; Pearlman et al., 2001), Airborne Visible/Infrared Imaging Spectrometer (AVIRIS, 224 spectral bands between 0.4 μm and 2.5 μm; Green et al., 1998), and the Thermal Infrared Multispectral Scanner (TIMS, 6 spectral bands between 8.2 μm and 12.2 μm; Palluconi and Meeks, 1985), can potentially contribute to these analyses, provided appropriate atmospheric corrections can be applied.

Chapters Four and Five of this dissertation focus primarily on the regional-scale spectral analyses of the martian surface, with the investigation of more localized spectral signatures limited only to Syrtis Major and Acidalia Planitia. A quick survey of other low albedo regions revealed little spectral variation observed at the spatial resolutions of the OMEGA and the Thermal Emission Spectrometer (TES) instruments in the VNIR and TIR, respectively. However, high resolution TIR imagery from the Thermal Emission Imaging System (THEMIS; Christensen et al., 2004) may be capable of identifying spectral signatures at high spatial resolutions that would otherwise be invisible using TES. For example, small impact craters in Mare Sirenum are dark in THEMIS daytime infrared imagery and bright in THEMIS nighttime infrared imagery, indicating that they exhibit a lower albedo and a higher thermal inertia than the surrounding terrain, respectively. These craters, which are several hundred meters in diameter and, hence, beyond the spatial resolution of TES, are prime candidates for investigation using the THEMIS multispectral TIR capabilities. Analysis of these craters could reveal both the underlying unaltered composition of Mare Sirenum as well as the potential role of oxidative weathering processes in this unique location. Higher resolution OMEGA and

Compact Reconnaissance Imaging Spectrometer for Mars (CRISM; Murchie et al., 2007) data would complement these THEMIS analyses and help to ascertain the present and absent mineral species.

3.2 Concluding remarks

Since the earliest stages of planetary evolution, oxidative weathering has likely been an active and global component of the terrestrial and martian subaerial alteration regime. As the martian surface began to desiccate, liquid water became sequestered into its current solid surface and subsurface reservoirs. As widespread aqueous activity and alteration ceased, oxidative weathering processes developed into the dominant chemical alteration process on the martian surface. The low temperatures and paucity of liquid water in Beacon Valley has also led to the dominance of oxidative weathering without the subsequent obscuration by more mature chemical alteration. This represents the first natural laboratory where Amazonian-style chemical alteration has been investigated on Earth as well as the first thorough characterization of Amazonian-aged chemical weathering. By constraining the details of chemical alteration under modern martian surface conditions, our work provides a stable foundation upon which to investigate the nature, timing, and influences of climatic transitions on Mars.

References

Bibring J.-P., Langevin Y., Mustard J. F., Poulet F., Arvidson R., Gendrin A., Gondet B., Mangold N., Pinet P., Forget F. and the OMEGA team (2006), Global mineralogical and aqueous Mars history derived from OMEGA/Mars Express data. *Science* **312**, 400-404.

Burkhard D. J. M. and Müller-Sigmund H. (2007), Surface alteration of basalt due to cation-migration. *Bull. Volcanol.* **69**, 319-328.

Cannon K. M., Salvatore M. R. and Mustard J. F. (2013), Weathering rinds on basalts and basaltic sandstones in the Antarctic climate: Spectroscopic implications for Mars. *LPSC* **XLIV**, abstract 1358.

Christensen P. R., Jakosky B. M., Kieffer H. H., Malin M. C., McSween Jr. H. Y., Nealson K., Mehall G. L., Silverman S. H., Ferry S., Caplinger M. and Ravine M. (2004), The Thermal Emission Imaging System (THEMIS) for the Mars 2001 Odyssey mission. *Space Sci. Rev.* **110**, 85-130.

Cook G. B. and Cooper R. F. (2000), Iron concentration and the physical process of dynamic oxidation in an alkaline earth aluminosilicate glass. *Am. Min.* **85**, 397-406.

Cooper R. F., Fanselow J. B. and Poker D. B. (1996), The mechanism of oxidation of a basaltic glass: Chemical diffusion of network-modifying cations. *Geochim. Cosmochim. Acta* **60**, 3253-3265.

DOE (2000), United States Nuclear Tests: July 1945 through September 1992. *U.S. Dept. of Energy* **DOE/NV-209-REV 15**, 162 pp.

Edwards C. S. and Christensen P. R. (2012), Development of a microscopic thermal emission spectrometer: Analysis of primary igneous materials for planetary analogs. *LPSC* **XLIII**, abstract 2658.

ERSDAC, SNM (2005), ASTER Users Guide, Part 1 General, Version 4. http://www.science.aster.ersdac.or.jp/en/documents/users_guide/part1/pdf/Part1_4E.pdf, Date Accessed: 12 June 2012.

Green R. O., Eastwood M. L., Sarture C. M., Chrien T. G., Aronsson M., Chippendale B. J., Faust J. A., Pavri B. E., Chovit C. J., Solis M. and Olah M. R. (1998), Imaging spectroscopy and the Airborne Visible/Infrared Imaging Spectrometer (AVIRIS). *Rem. Sens. Of Env.* **65**(3), doi:10.1016/S0034-4257(98)00064-9.

James O. B. (1969), Shock and thermal metamorphism of basalt by nuclear explosion, Nevada Test Site. *Science* **166**, 1615-1620.

Lasaga A. C. (1984), Chemical kinetics of water-rock interactions. *J. Geophys. Res.* **89**(B6), 4009-4025.

Marchant D. R., Phillips W. M., Fastook J. L., Head III J. W., Schaefer J. M., Shean D. E. and Kowalewski D. E. (2007), Dating the world's oldest debris-covered glacier: Implications for interpreting viscous-flow features on Mars. *LPSC* **38**, abstract 1895.

Marchant D. R., Mackay S., Lamp J. L., Hayden A. T. and Head J. W. (2013), A review of geomorphic processes and landforms in the Dry Valleys of southern Victoria Land: Implications for evaluating climate change and ice-sheet stability. *In* Hambrey M. J., Barker P. F., Barrett P. J., Bowman V., Davies B., Smellie J. L. and Tranter M., *eds. Antarctic Palaeoenvironments and Earth-Surface Processes*. London: Geological Society Special Pub. **381**, *in press*. http://dx.doi.org/10.1144/SP381.10.

Mendenhall J. A., Bernotas L. A., Bicknell W. E., Cerrati V. J., Digenis C. J., Evans J. B., Forman S. E., Hearn D. R., Hoffeld R. H., Lencioni D. E., Nathanson D. M. and Parker A. C. (2000), Earth Observing-1 Advanced Land Imager: Instrument

and flight operations overview. *Massachusetts Institute of Technology & Lincoln Laboratory Project Report EO-1-1*.

Minitti M. E., Weitz C. M., Lane M. D. and Bishop J. L. (2007), Morphology, chemistry, and spectral properties of Hawaiian rock coatings and implications for Mars. *J. Geophys. Res.* **112**, doi:10.1029/2006JE002839.

Murchie S., Arvidson R., Bedini P., Beisser K., Bibring J.-P., Bishop J., Boldt J., Cavender P., Choo T., Clancy R. T., Darlington E. H., Des Marais D., Espiritu R., Fort D., Green R., Guinness E., Hayes J., Hash C., Heffernan K., Hemmler J., Heyler G., Humm D., Hutcheson J., Izenberg N., Lee R., Lees J., Lohr D., Malaret E., Martin T., McGovern J. A., McGuire P., Morris R., Mustard J., Pelkey S., Rhodes E., Robinson M., Roush T., Schaefer E., Seagrave G., Seelos F., Silverglate P., Slavney S., Smith M., Shyong W.-J., Strohbehn K., Taylor H., Thompson P., Tossman B., Wirzburger M. and Wolff M. (2007), Compact Reconnaissance Imaging Spectrometer for Mars (CRISM) on Mars Reconnaissance Orbiter (MRO). *J. Geophys. Res.* **112**, doi:10.1029/2006JE002682.

Nordyke M. D. and Wray W. (1964), Cratering and radioactivity results from a nuclear cratering detonation in basalt. *J. Geophys. Res.* **69**, 675-689.

Palluconi F. D. and Meeks G. R. (1985), Thermal Infrared Multispectral Scanner (TIMS): An investigator's guide to TIMS data. *NASA STI/Recon Tech. Rep. N* **85**, 28286.

Pearlman J., Carman S., Segal C., Jarecke P., Barry P. and Browne W. (2001), Overview of the Hyperion Imaging Spectrometer for the NASA EO-1 mission. *IGARSS 2001*.

Rogers A. D. and Christensen P. R. (2007), Surface mineralogy of martian low-albedo regions from MGS-TES data: Implications for upper crustal evolution and surface alteration. *J. Geophys. Res.*, **112**(E01003), doi:10.1029/2006JE002727.

Rogers A. D., Bandfield J. L. and Christensen P. R. (2007), Global spectral classification of martian low-albedo regions with Mars Global Surveyor Thermal Emission Spectrometer (MGS-TES) data. *J. Geophys. Res.* **112**(E02004), doi:10.1029/2006JE002726.

Salvatore M. R., Mustard J. F., Head J. W., Cooper R. F., Marchant D. R. and Wyatt M. B. (2013), Development of alteration rinds by oxidative weathering processes in Beacon Valley, Antarctica, and Implications for Mars. *Geochim. Cosmochim. Acta, in review.*

Sunshine J. M., Pieters C. M. and Pratt S. F. (1990), Deconvolution of mineral absorption bands: An improved approach. *J. Geophys. Res.* **95**(B5), 6955-6966.

Figure Descriptions

Figure 1. Back-scattered electron (BSE) micrograph of a dolerite surface (a; sample MS10_BV_05A, see Chapter Two for additional sample details) compared to the silica-rich basaltic coatings studied in Minitti et al. (2007) (b; Figure 13a from Minitti et al., 2007). The dashed line in the scale bar of (a) indicates 20 μm, which is approximately the thickness of the silica-rich coating studied in Minitti et al. (2007). No evidence exists for the presence of thin coatings on dolerites from Beacon Valley, which would be observable should they be present at the same scale as those identified by Minitti et al. (2007). While spectral similarities exist between these two distinct surface

textures, the physical manifestations are drastically different. White arrows indicate sample surfaces.

Figure 2. Mean annual precipitation plotted against mean annual temperature for three terrestrial analog locations (light and dark blue), current martian locations (dark green), and modeled martian environments (light green). Characterizing oxidative weathering in other analog environments will help to determine the rates and relative importance of this process under different climatic conditions.

Figure 3. Oblique aerial photograph of Carapace Nunatak, looking towards the west. Considerable amounts of snow and ice are present on and around the exposed bedrock. The ice collar on the left portion of the image is largely due to thermal radiation emitted from the dark and high thermal inertia bedrock, which prevents significant ice accumulations from forming immediately adjacent to the exposed bedrock. For scale, the distance between the vertical cliff face and the summit of the annotated ice collar is approximately 75 meters. Photograph taken by M. R. Salvatore.

Figure 4. (a) A hyperspectral image of dolerite sample MS10_BV_01 (see Chapter Two for additional chemical, mineralogical, and spectral information on this sample). The alteration rind, unaltered interior, and the transition between these two are clearly visible. Surface pitting is also visible on the rock surface. Boxes represent the locations of the spectra shown in (b), with colors corresponding to the respective spectra. (b) Spectra derived from the hyperspectral image. Shown for comparison are the laboratory-derived RELAB spectra, which are in good agreement with the spectra derived from the hyperspectral image.

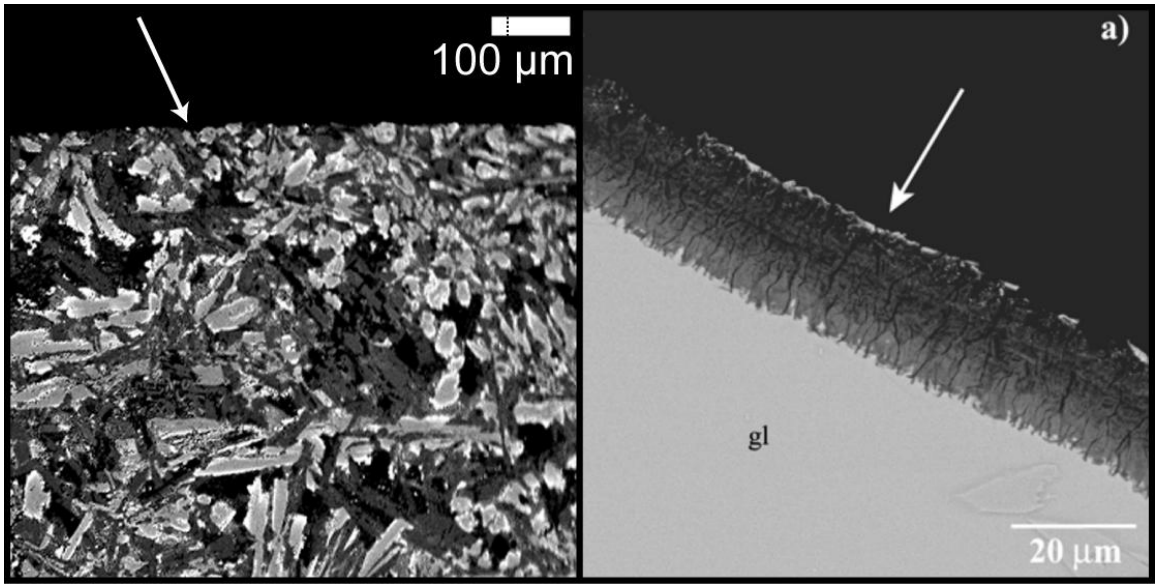

Chapter 6, Figure 1.

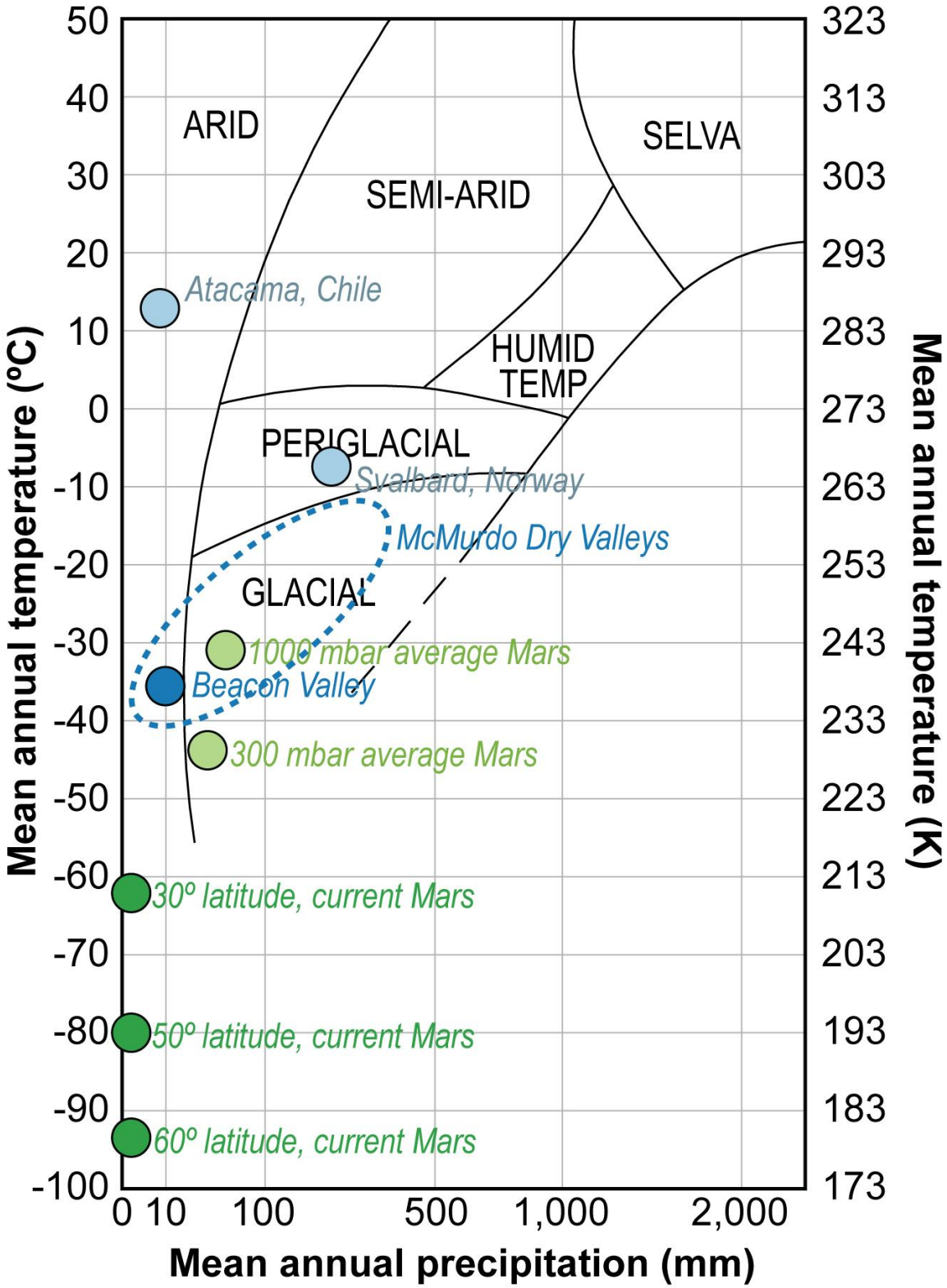

Chapter 6, Figure 2.

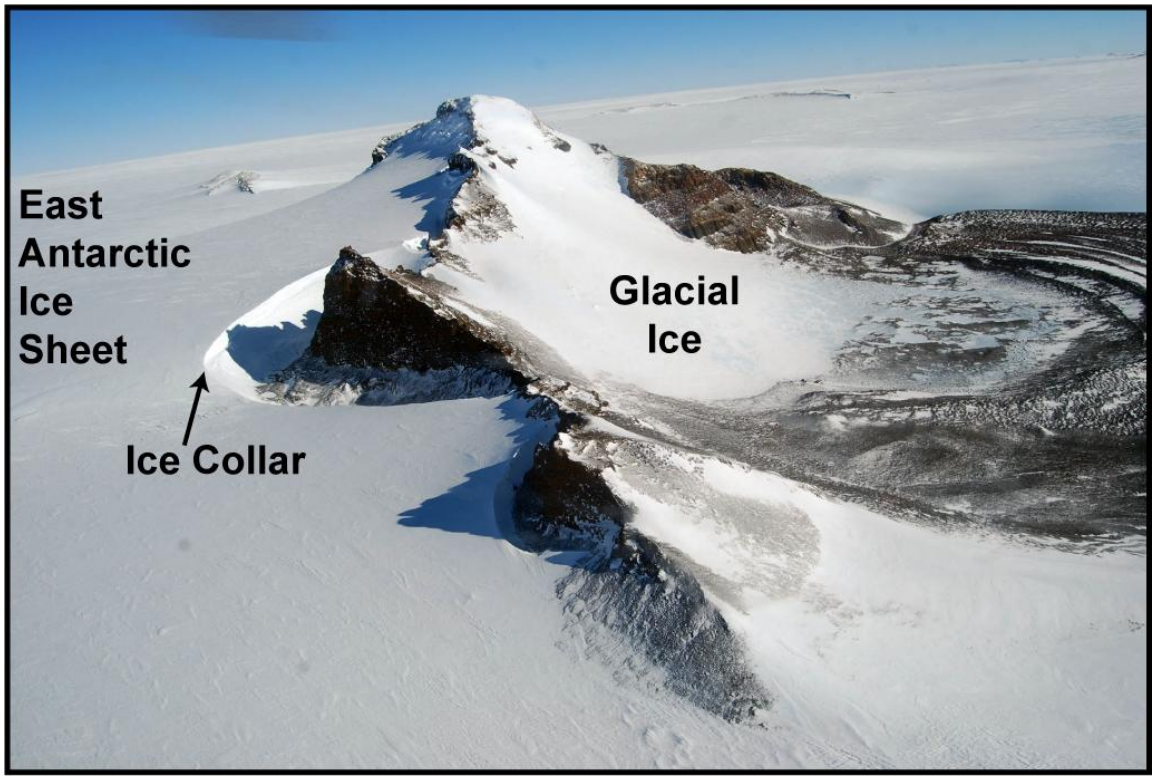

Chapter 6, Figure 3.

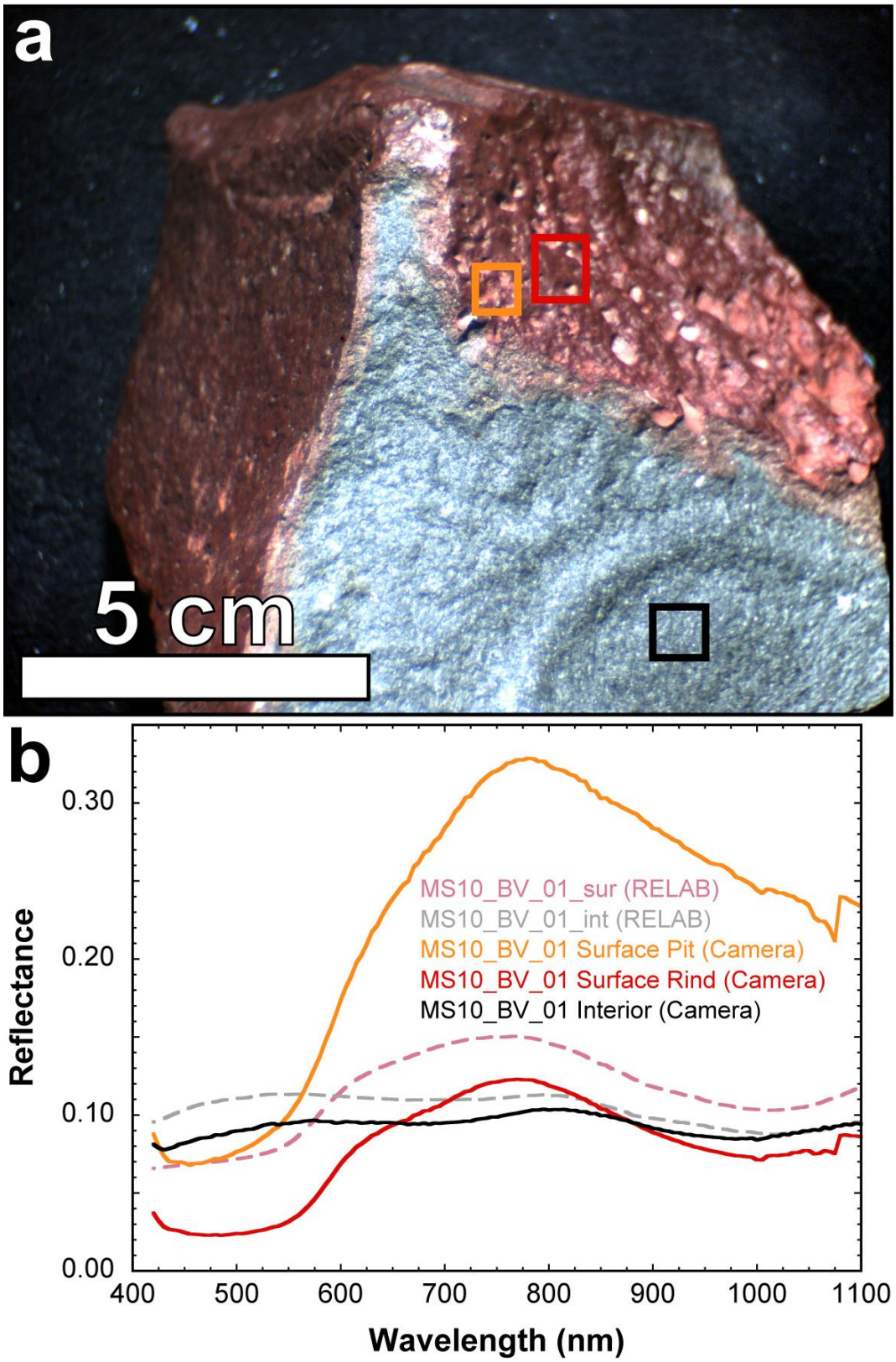

Chapter 6, Figure 4.

Appendix A:

Multispectral map of the McMurdo Dry Valleys: Description, methodology, and parameterization.

M. R. Salvatore[1]

[1]Department of Geological Sciences,

Brown University, Providence, RI 02912, USA

Main Text

The McMurdo Dry Valleys (MDV) of Antarctica are some of the most geologically diverse ice- and vegetation-free terrains on Earth. The geology of this unique region has been extensively studied since their discovery in the early 20th century and has revolutionized our understanding of the tectonic (e.g., Gleadow and Fitzgerald, 1987; Denton et al., 1993; Sugden et al., 1995), volcanic (e.g., Gunn, 1962; Armstrong, 1978; Marsh 2004), and climatic history (e.g., Denton et al., 1993; Marchant and Denton, 1996) of Antarctica. The United States Navy began a detailed aerial photographic campaign of key locations on the Antarctic continent in 1946 (including the MDV; PGC 2013), which was followed by rigorous geologic mapping of the region, completed in the mid-1990s (McElroy et al., 1987; Kirk et al., 1989; Allibone and Heron, 1991; Pocknall et al., 1994; Turnbull et al., 1994; Isaac et al., 1995). This mapping was substantiated with ground observations and use of aerial photography.

While aerial photography and (more recently) orbital imagery have been used to investigate regional and local geomorphology, spectral datasets have not been thoroughly investigated. The likely reasons behind the limited use of these datasets are the geometric and atmospheric difficulties associated with polar observations. The low solar elevation ($\leq 35.9^{o}$) and long solar path length through the atmosphere (proportional to cosine θ, where θ is the solar elevation in degrees) equate to low irradiances and large atmospheric contributions, respectively. In contrast, tropical remote sensing benefits from high solar elevations and short atmospheric path lengths, resulting in large solar irradiances and minimized atmospheric contributions (although heightened atmospheric H_2O contents are often problematic).

Since the 1980s, radiative transfer modeling has been used to estimate atmospheric contributions so that they can be removed from remote datasets. However, these models require the input of atmospheric parameters coinciding with the time of image acquisition. Reasonable estimates of atmospheric information can be made across much of the populated landmasses, thanks in large part to the dense distributions of regional and international airports. The isolation of the MDV makes the frequent and robust collection of atmospheric information difficult. McMurdo Station is the closest location of consistent atmospheric data collection, but the volatility of atmospheric conditions along the Transantarctic Mountains makes these data largely inapplicable to the MDV (Doran et al., 2002). The difficulties in constraining atmospheric parameters throughout the MDV make traditional radiative transfer modeling unsuitable for atmospherically correcting remote datasets. This is especially true for the visible and near-infrared (VNIR) wavelengths, where both the incoming solar irradiance as well as the exiting radiance from the target of interest must pass through the atmosphere. To mitigate these issues, we used an in-scene hybrid dark object subtraction and regression (DOS-R) method to atmospherically correct our VNIR dataset (more information provided in Chapter Three). Thermal infrared (TIR) emission spectroscopy, on the other hand, does not have to correct for atmospheric effects on incoming solar irradiance which, due to the long path length of low-elevation solar irradiance, is the largest source of atmospheric contributions. As a result, after confirming the efficacy of the standard Temperature/Emissivity Separation (TES) algorithm (Gillespie et al., 1998) using laboratory-derived emissivity values of relevant lithological endmembers, it was

determined that the publically available atmospherically corrected data were suitable for use in our MDV spectral mapping product.

The benefits of remote spectral mapping are prodigious. Spectral mapping supplements traditional geologic mapping through the addition of compositional information and unobstructed spatial coverage. VNIR data are sensitive to Fe^{2+}-Fe^{3+} intervalence charge transfer absorptions at visible wavelengths, in addition to Fe^{2+} crystal field absorptions in the near-infrared. The TIR is sensitive to variations in silicate mineral structure in addition to the effects of oxidative chemical alteration processes. In tandem, these two wavelength regions are able to distinguish between all of the exposed primary lithologies throughout the MDV as well as select altered components.

In the creation of this spectral mapping product, multispectral VNIR and TIR datasets were used due to their coverage, ease of access and processing, and high signal to noise. Advanced Land Imager (ALI; Mendenhall et al., 2000) and Advanced Spaceborne Thermal Emission and Reflection Radiometer (ASTER; ERSDAC, 2005) datasets were utilized and provide broad spatial coverage at 30 m pix^{-1} and 90 m pix^{-1}, respectively. In total, this combined spectral product contains 1.57×10^{-6} multispectral pixels of ice-, snow-, water-, and cloud-free terrain, providing geomorphic and compositional information to supplement traditional geologic mapping products. However, while the improved spatial coverage is an obvious benefit to geologic investigations of the MDV, the relatively coarse spatial footprint precludes the detailed investigation of sub-pixel features. For example, variations in mineralogy and texture are aggregated into a single spectral signature. Additionally, if contributing below the masking thresholds described in Chapter Three, the presence of sub-pixel ice, snow,

water, clouds, or shadows can substantially alter the observed spectral signature, resulting in misinterpretation. Nonetheless, in conjunction with traditional geologic mapping, multispectral orbital data provide an additional tool for geologic interpretations.

Detailed sensor information and data calibration techniques are outlined in Chapter Three of this dissertation. In this Appendix, we present additional details regarding the images utilized in the production of the spectral map as well as additional calibration and atmospheric removal information.

The completed spectral map can be downloaded from the following website: http://planetary.brown.edu/grad_pages/Salvatore/MDV_spectral_map_2013.zip (subject to change, please contact M. R. Salvatore for additional information), which includes an image file and a README file with additional information. Provided below are approximate true color images of the spectral map with the outlines of the individual ALI (Fig. 1) and ASTER (Fig. 2) images used in the final mosaic. Figure 3a through Figure 3n display single band images of the completed mosaic. Figure 4 is a contextual figure and represents the range of spectral diversity observed throughout the MDV (see Chapter 3, Figure 1). Table 1 lists the names, date of acquisition, and locations of each image used in the spectral map. Table 2 provides information necessary for the radiometric calibration of ALI data (see Chapter Three for additional details). Table 3 provides the hybrid dark object subtraction and regression (DOS-R) atmospheric removal values for each pixel used in the derivation of the VNIR atmospheric correction and supplements the averaged DOS-Rvalues found in Chapter Three, Table 2. Lastly, Table 4 lists the Earth-Sun distance (d) in astronomical units and the solar elevation (θ) in degrees for the date and time that each ALI image was acquired.

References

Allibone A. H. and Heron D. W. (1991), Geology of the Thundergut area, southern Victoria Land, Antarctica. Scale 1:50,000. *New Zeal. Geol. Surv.*, Misc. Map Series 21.

Armstrong R. L. (1978), K-Ar dating: Late Cenozoic McMurdo Volcanic Group and dry valley glacial history, Victoria Land, Antarctica. *New Zealand J. Geol. & Geophys.* **21**, 685-698.

Chander G., Markham B. L. and Helder D. L. (2009), Summary of current radiometric calibration coefficients for Landsat MSS, TM, ETM+, and EO-1 ALI sensors. *Rem. Sens. of Env.* **113**, 893-903.

Denton G. H., Sugden D. E., Marchant D. R., Hall B. L. and Wilch T. I. (1993), East Antarctic Ice Sheet sensitivity to Pliocene climate change from a Dry Valleys perspective. *Geograf. Annal.* **75**A, 155-204.

Doran P. T., McKay C. P., Clow G. D., Dana G. L., Fountain A. G., Nylen T. and Lyons W. B. (2002), Climate observations from the McMurdo Dry Valleys, Antarctica, 1986-2000. *J. Geophys. Res.* **107**, doi:10.1029/2001JD002045.

ERSDAC, SNM (2005), ASTER Users Guide, Part 1 General, Version 4. http://www.science.aster.ersdac.or.jp/en/documents/users_guide/part1/pdf/Part1_4E.pdf, Date Accessed: 12 June 2012.

Gillespie A., Rokugawa S., Matsunaga T., Cothern S., Hook S. and Kahle A. B. (1998), A temperature and emissivity separation algorithm for Advanced Spaceborne Thermal Emission and Reflection radiometer (ASTER) images. *Inst.Elect. & Electr. Eng. Trans. on Geosci. & Rem. Sens.* **36**, 1113-1126.

Gleadow A. J. W. and Fitzgerald P. G. (1987), Uplift history and structure of the Transantarctic Mountains – New evidence from fission track dating of basement apatites in the Dry Valleys area, southern Victoria Land. *Earth & Planet. Sci. Lett.* **82**, 1-14.

Gunn B. M. (1962), Differentiation in Ferrar Dolerites. *New Zeal. J. Geol. & Geophys.* **5**, 820-863.

Isaac M. J., Chinn T. J., Edbrooke S. W. and Forsyth P. J. (1995), Geology of the Olympus Range area, southern Victoria Land, Antarctica. Scale 1:50,000. *N. Z. Inst. of Geol. & Nucl. Sci.*, geol. map 20.

Kirk P. A., Sherwood A. M., Woolfe K. J., Allibone A. M., Anckorn J. F. and Morrison A. D. (1989), Geology of the Knobhead Area, southern Victoria Land, Antarctica. Scale 1:50,000. *New Zeal. Geol. Surv.*, Misc. Map Series 19.

Marchant D. R. and Denton G. H. (1996), Miocene and Pliocene paleoclimate of the Dry Valleys region, southern Victoria Land: A geomorphological approach. *Marine Micropaleo.* **27**, 253-271.

Marsh B. (2004), A magmatic mush column Rosetta Stone: The McMurdo Dry Valleys of Antarctica. *Eos Trans. of the Amer. Geophys. Union* **85**, 497-508.

McElroy C. T. and Rose G. (1987), Geology of the Beacon Heights area, southern Victoria Land, Antarctica. *New Zeal. Geol. Surv.*, Misc. Map Series 15.

Mendenhall J. A., Bernotas L. A., Bicknell W. E., Cerrati V. J., Digenis C. J., Evans J. B., Forman S. E., Hearn D. R., Hoffeld R. H., Lencioni D. E., Nathanson D. M. and Parker A. C. (2000), Earth Observing-1 Advanced Land Imager: Instrument

and flight operations overview. *Massachusetts Institute of Technology & Lincoln Laboratory Project Report EO-1-1*.

PGC (2013), Polar Geospatial Center at the University of Minnesota. www.pgc.umn.edu, accessed on 04 January 2013.

Pocknall D. T., Chinn T. J., Sykes R. and Skinner D. N. B. (1994), Geology of the Convoy Range area, southern Victoria Land, Antarctica. Scale 1:50,000. *Inst. of Geol. & Nucl. Sci.*, geol. map 11.

Sugden D. E., Denton G. H. and Marchant D. R. (1995), Landscape evolution of the Dry Valleys, Transantarctic Mountains: Tectonic implications. *J. Geophys. Res.* **100**, 9949-9967.

Turnbull I. M., Allibone A. H., Forsyth P. J. and Heron D. W. (1994), Geology of the Bull Pass-St. John Range area, southern Victoria Land, Antarctica. Scale 1:50,000. *Inst. of Geol. & Nucl. Sci.*, geol. map 14.

Figure and Table Descriptions

Figure 1. Outlines of subset Advanced Land Imager (ALI) images used in the creation of the spectral mapping product. Image names are abbreviated to the final two characters.

Figure 2. Outlines of subset Advanced Spaceborne Thermal Emission and Reflection Radiometer (ASTER) images used in the creation of the spectral mapping product. Image names are abbreviated to the final four numbers.

Figure 3. Single band images of the completed spectral mosaic of the McMurdo Dry Valleys. (a) Band 1 (0.4430 μm), (b) Band 2 (0.4825 μm), (c) Band 3 (0.5650 μm),

(d) Band 4 (0.6600 μm), (e) Band 5 (0.7900 μm), (f) Band 6 (0.8675 μm), (g) Band 7 (1.2500 μm), (h) Band 8 (1.6500 μm), (i) Band 9 (2.2150 μm), (j) Band 10 (8.2910 μm), (k) Band 11 (8.6340 μm), (l) Band 12 (9.0750 μm), (m) Band 13 (10.6570 μm), (n) Band 14 (11.3180 μm).

Figure 4. Spectral parameter map of the McMurdo Dry Valleys. Mafic band strength (MBS) is mapped in red, NIR spectral slope is mapped in green, and the strength of the quartz emissivity peak is mapped in blue. Dark object subtraction-regression (DOS-R) locations are marked by orange stars, in situ spectral grid locations are marked by blue stars, and the locations of the four primary study regions highlighted in Chapter Three are outlined in yellow.

Table 1. List of images used to create the spectral map of the McMurdo Dry Valleys.

Table 2. Band-specific rescaling gain factor ($G_{rescale}$, [(W/(m^2 sr μm))/DN]), band-specific rescaling bias factor ($B_{rescale}$, [W/(m^2 sr μm)]), and mean exoatmospheric solar irradiance ($ESUN_{\lambda}$, [W/(m^2 μm)]) for each ALI band used in the production of this spectral map. Data from Chander et al. (2009).

Table 3. Pixel values used in the hybrid dark object subtraction and regression (DOS-R) atmospheric removal technique.

Table 4. Earth-Sun distance (d) in astronomical units and the solar elevation (θ) in degrees for the date and time of ALI image acquisition.

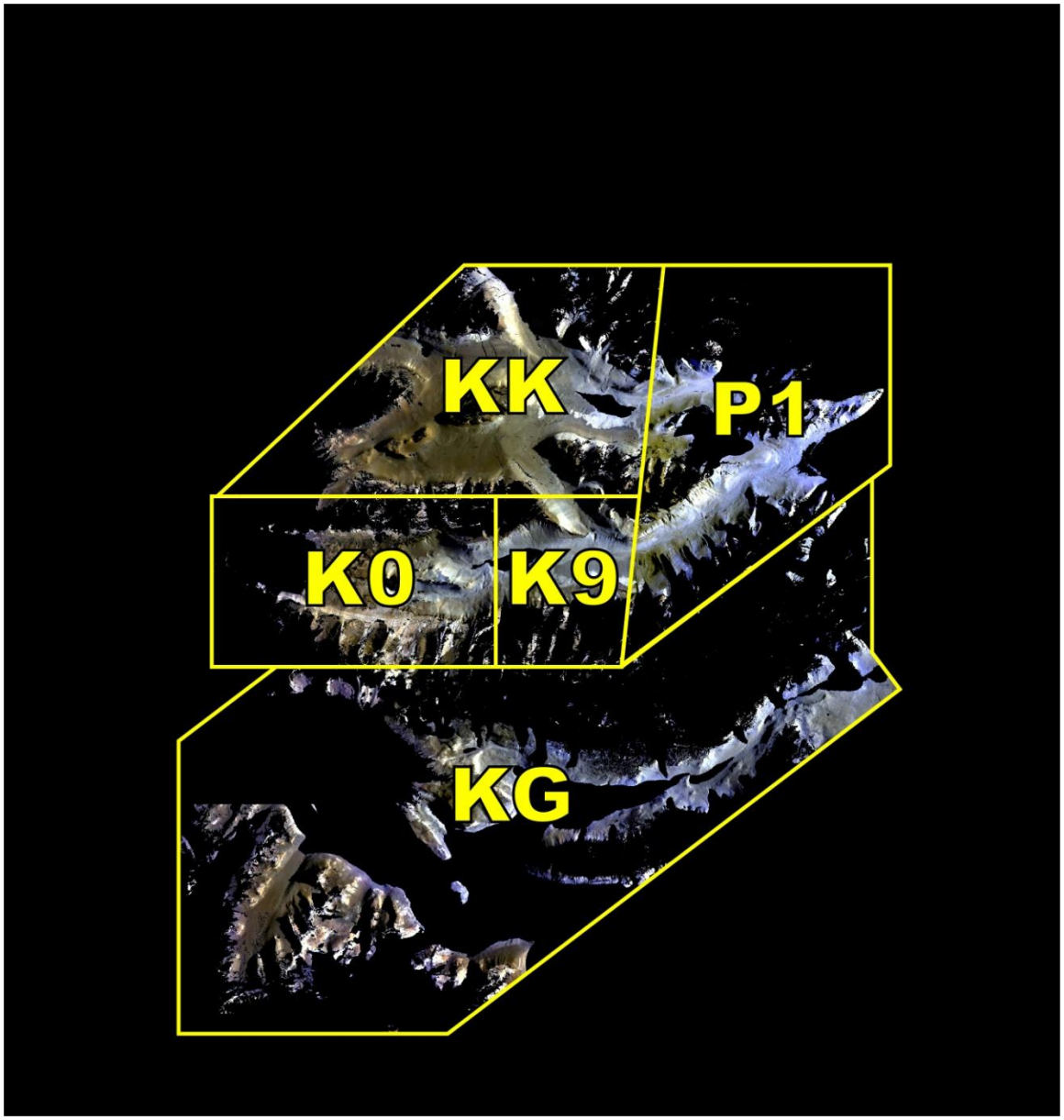

Appendix A, Figure 1.

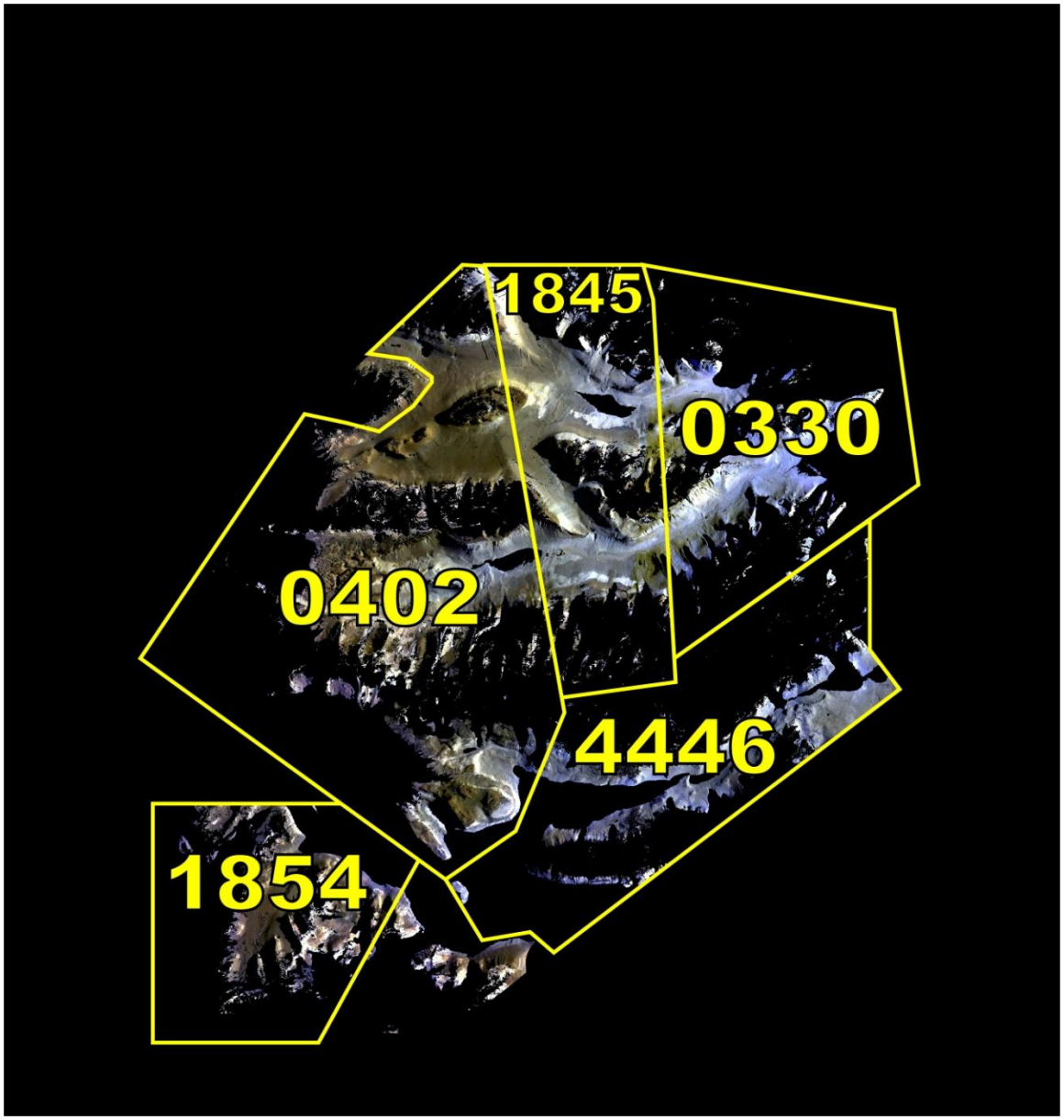

Appendix A, Figure 2.

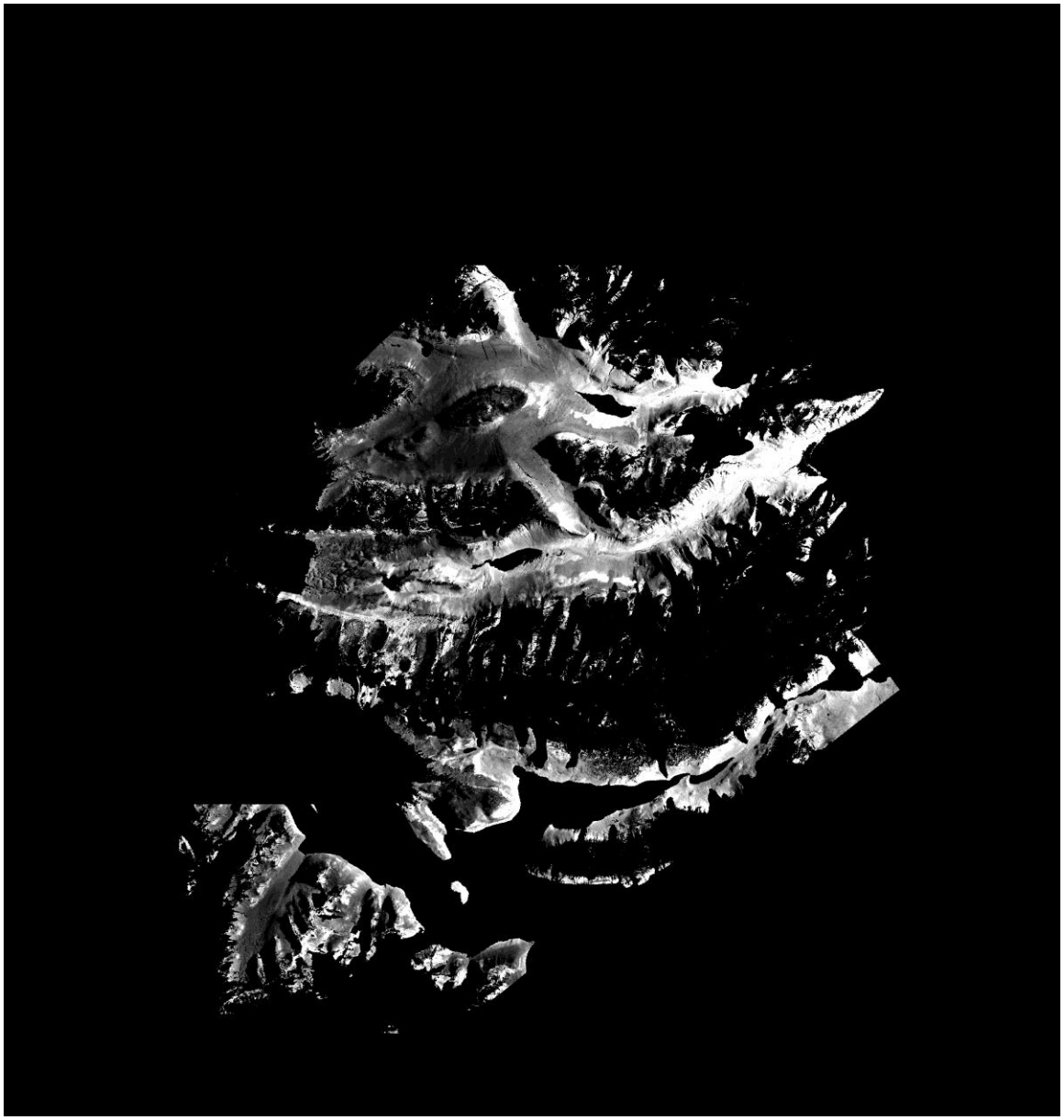

Appendix A, Figure 3a.

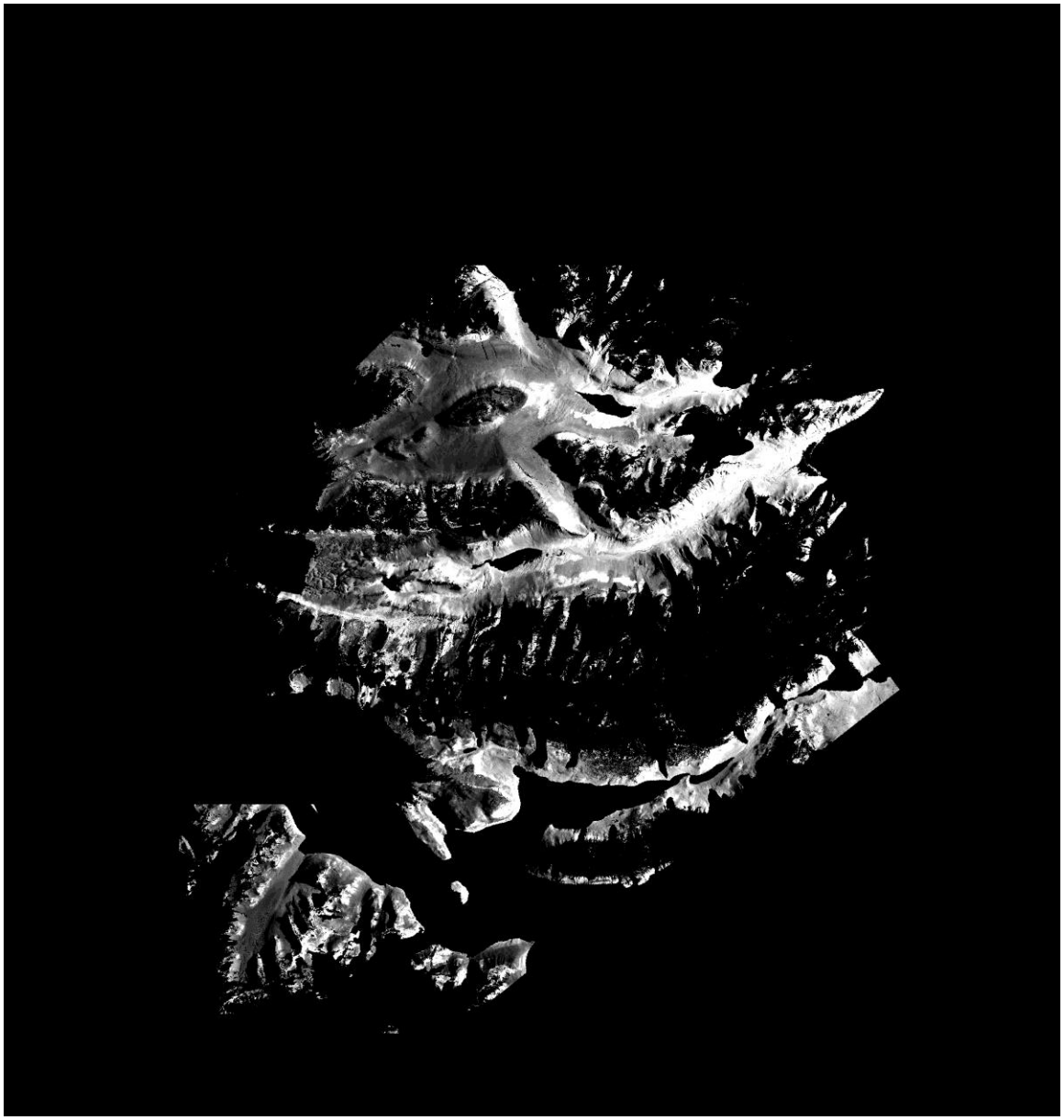

Appendix A, Figure 3b.

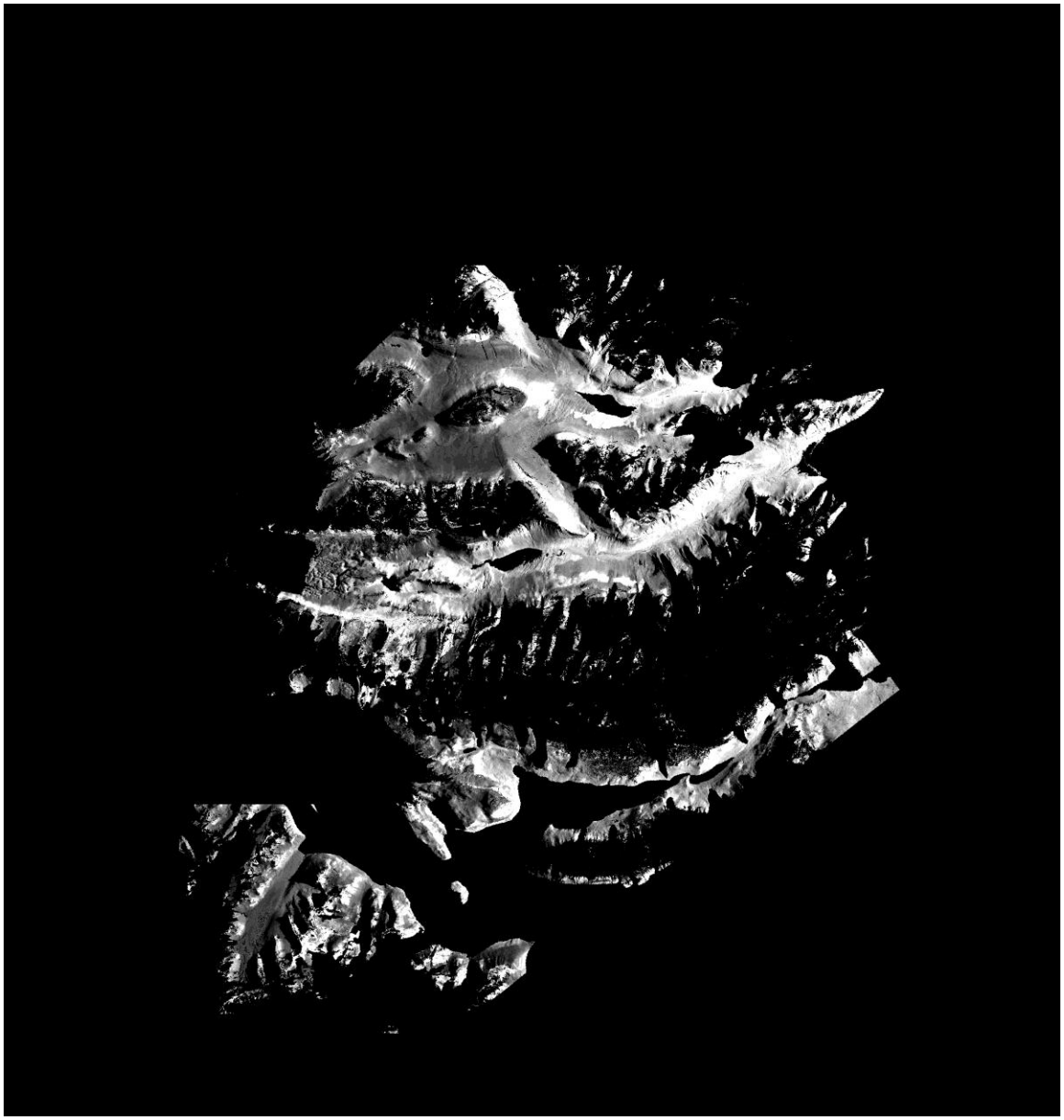

Appendix A, Figure 3c.

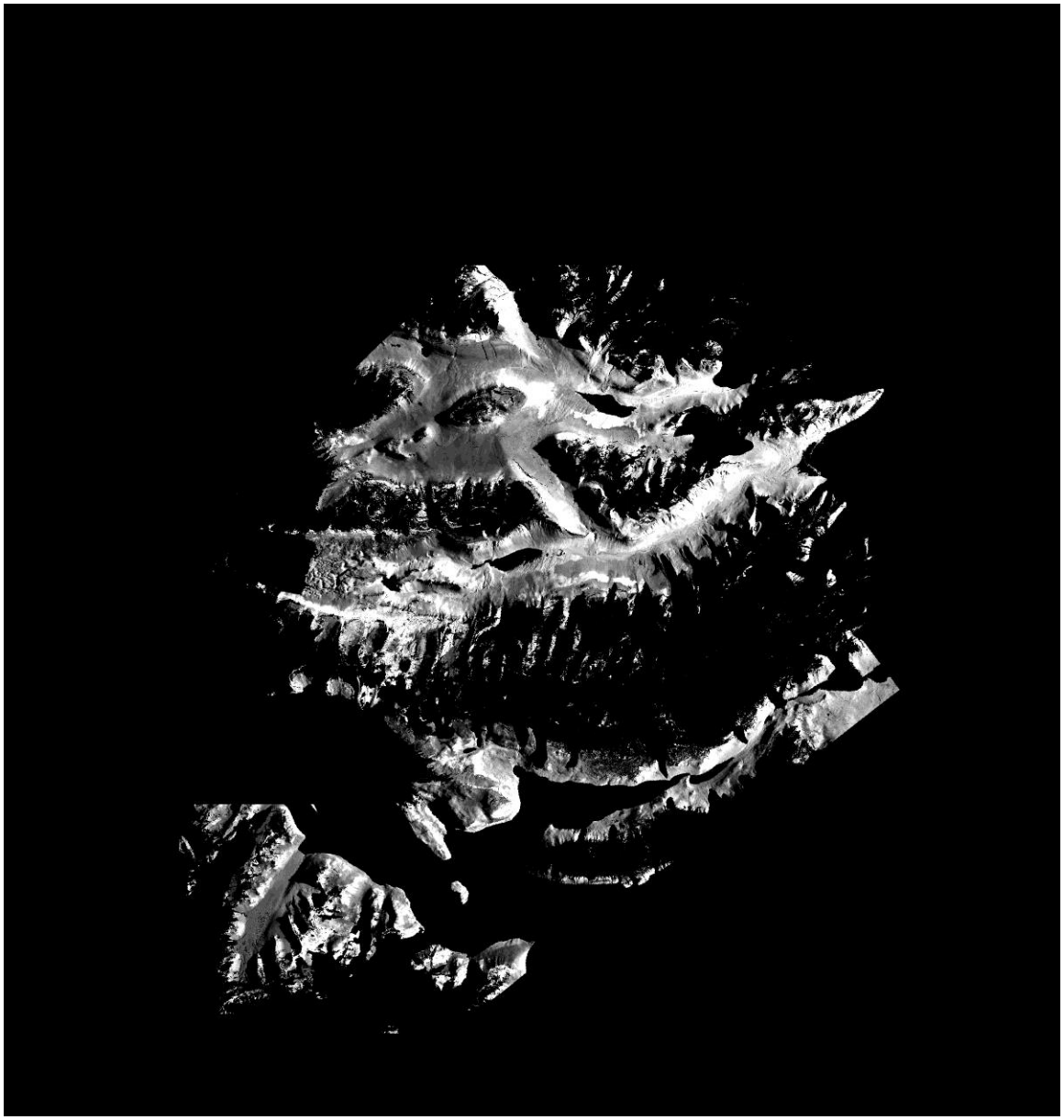

Appendix A, Figure 3d.

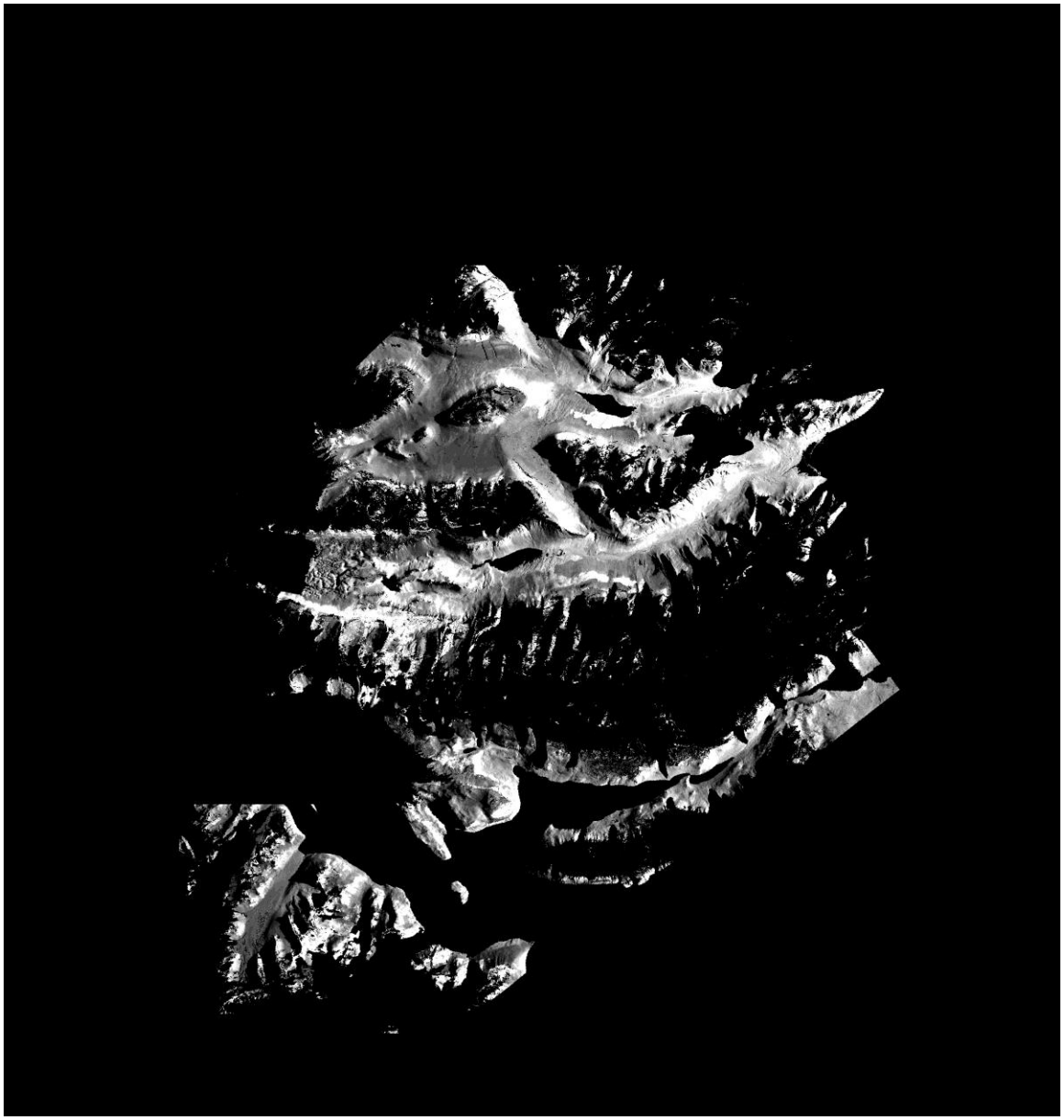

Appendix A, Figure 3e.

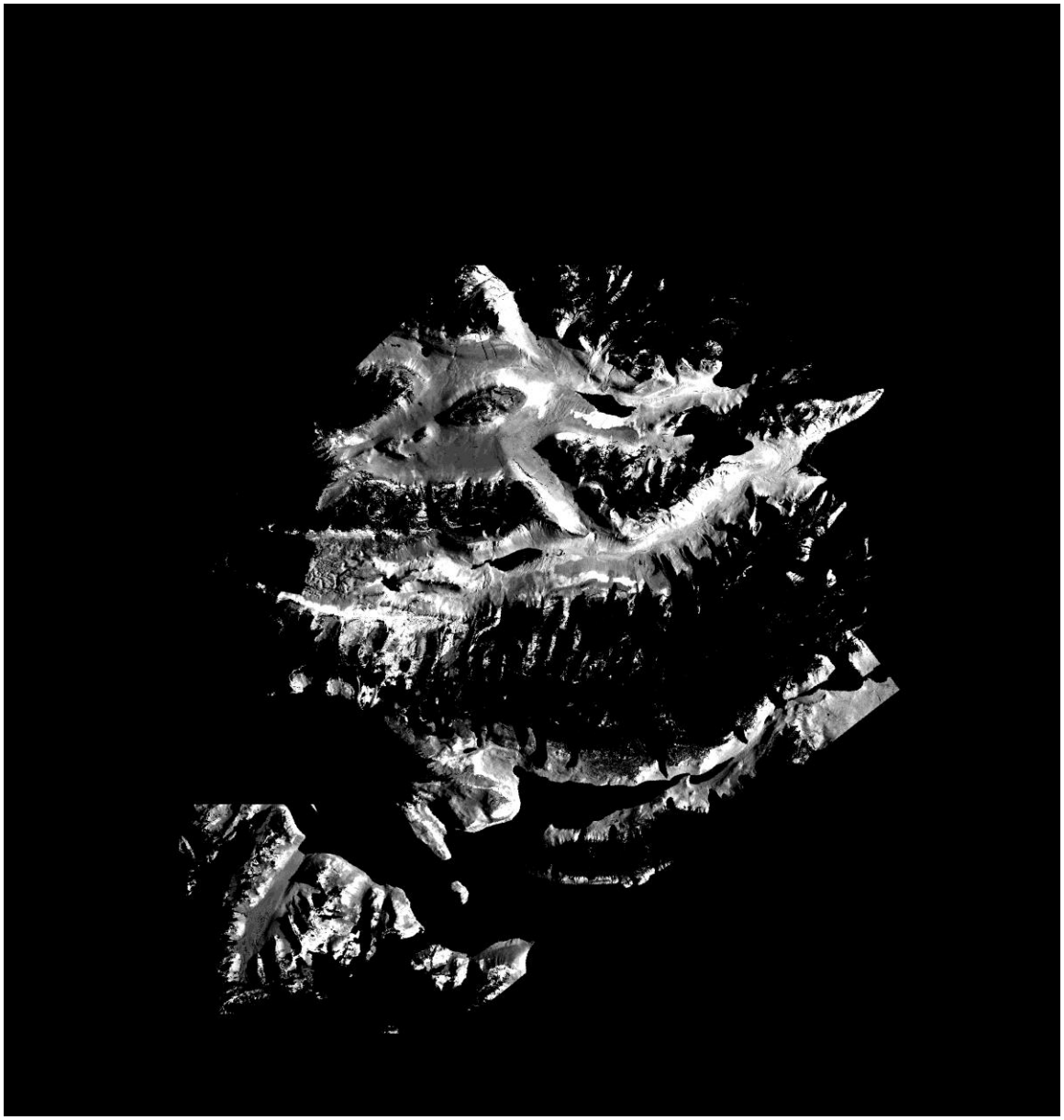

Appendix A, Figure 3f.

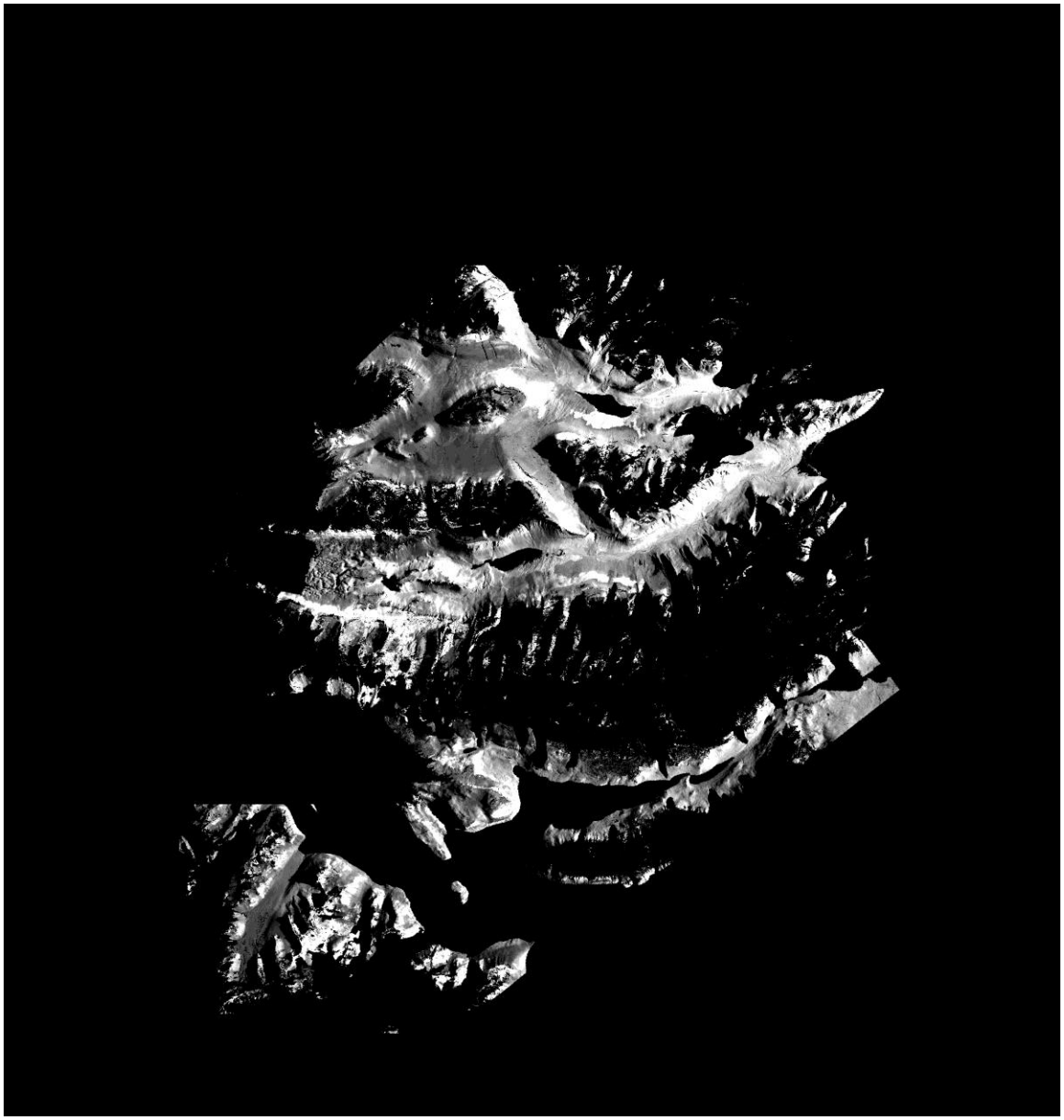

Appendix A, Figure 3g.

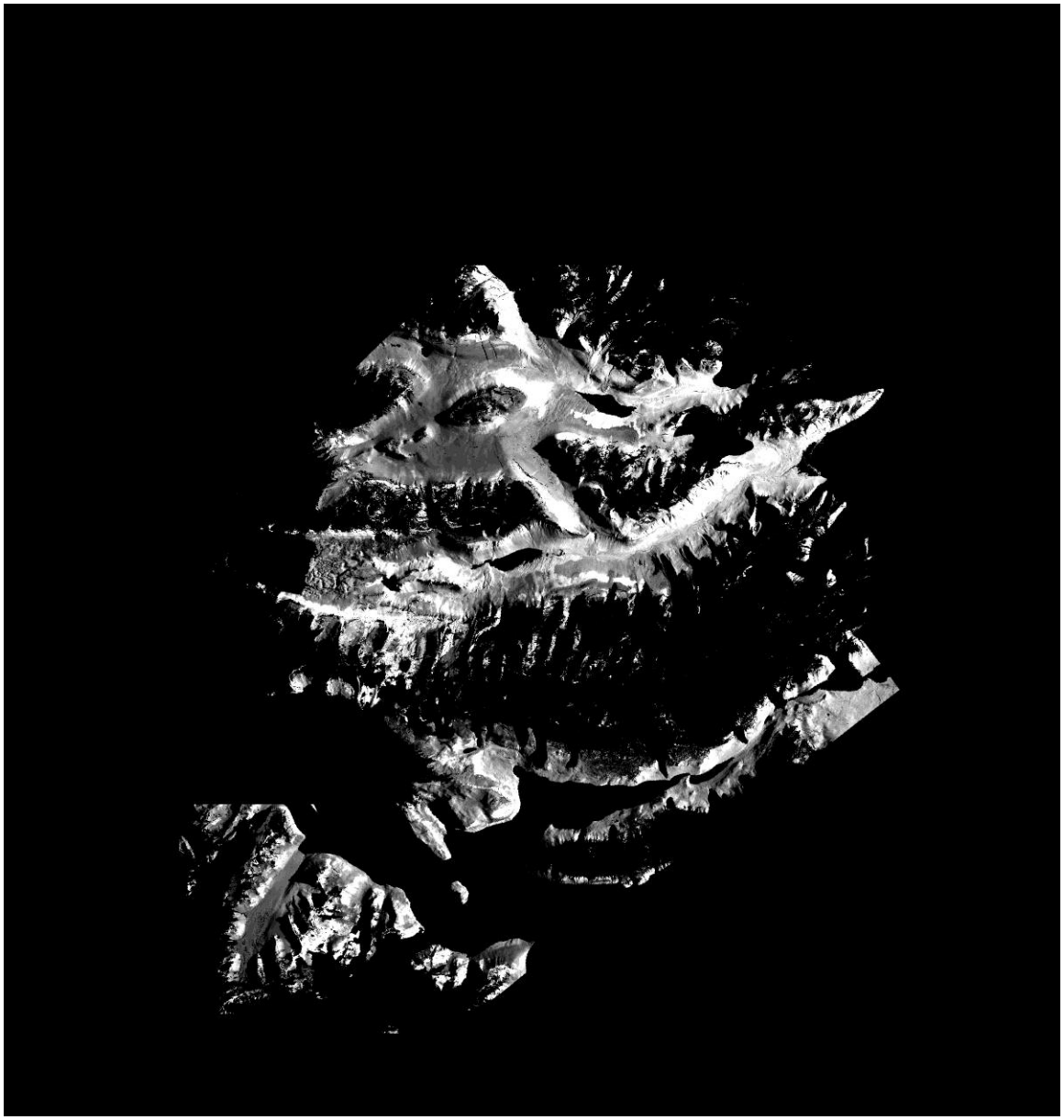

Appendix A, Figure 3h.

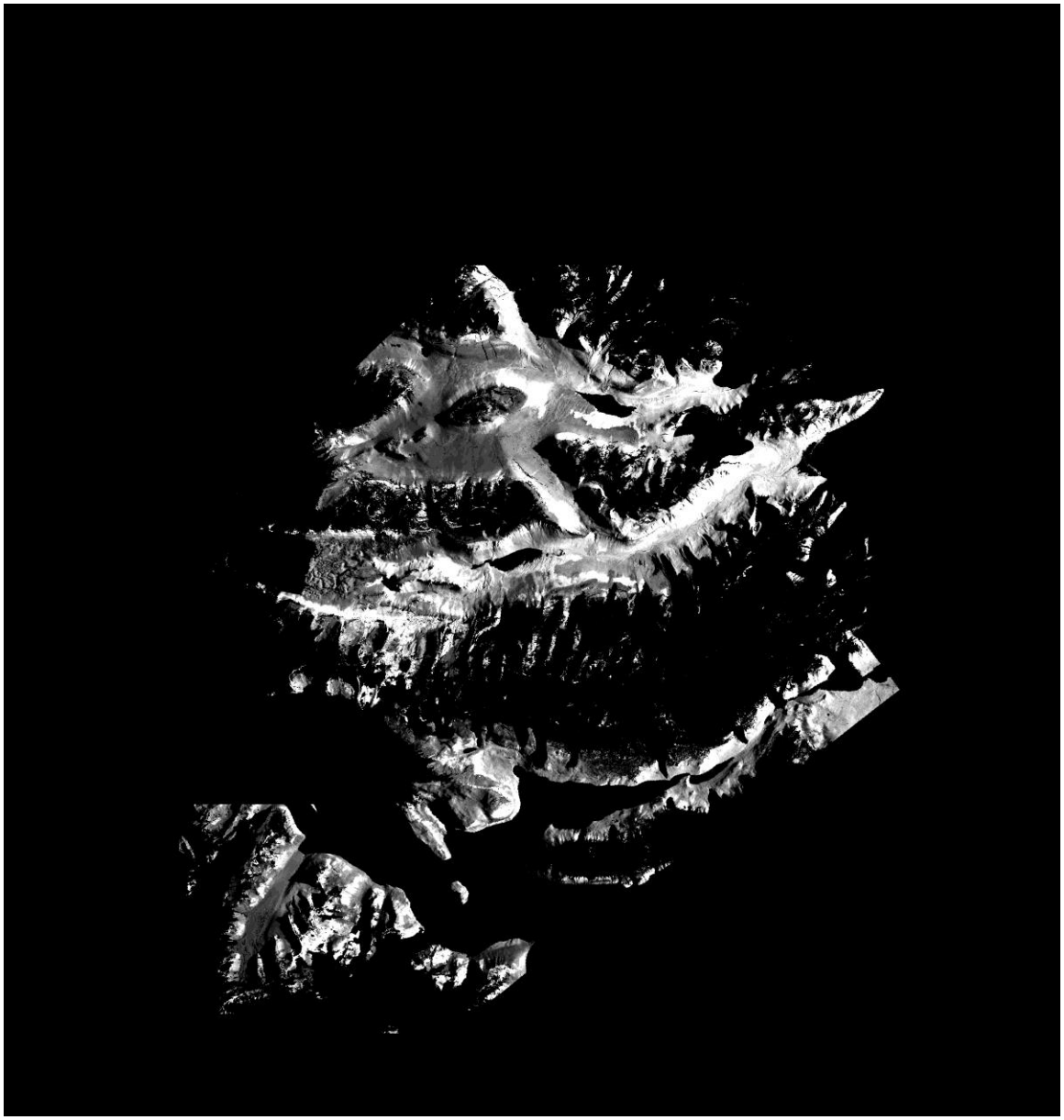

Appendix A, Figure 3i.

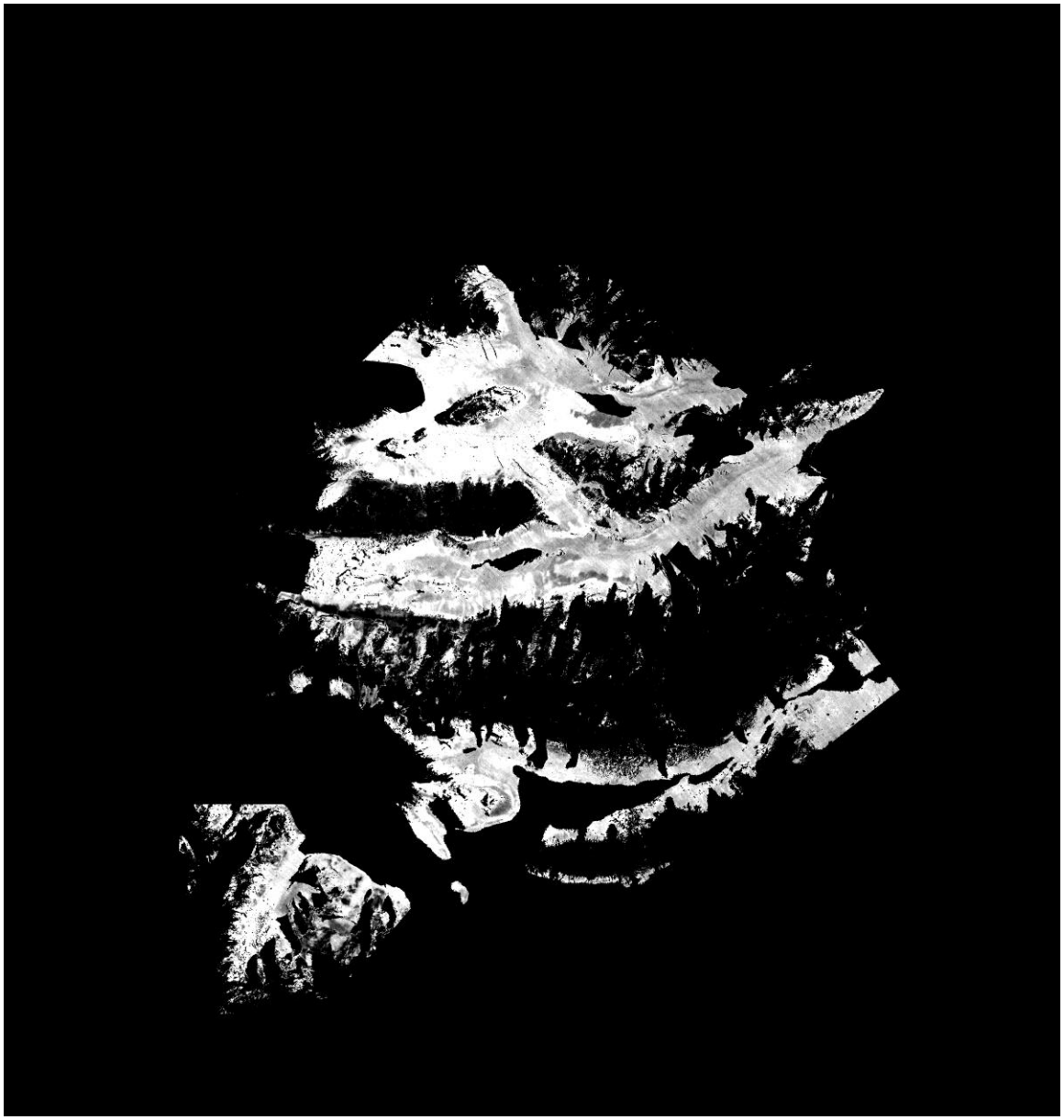

Appendix A, Figure 3j.

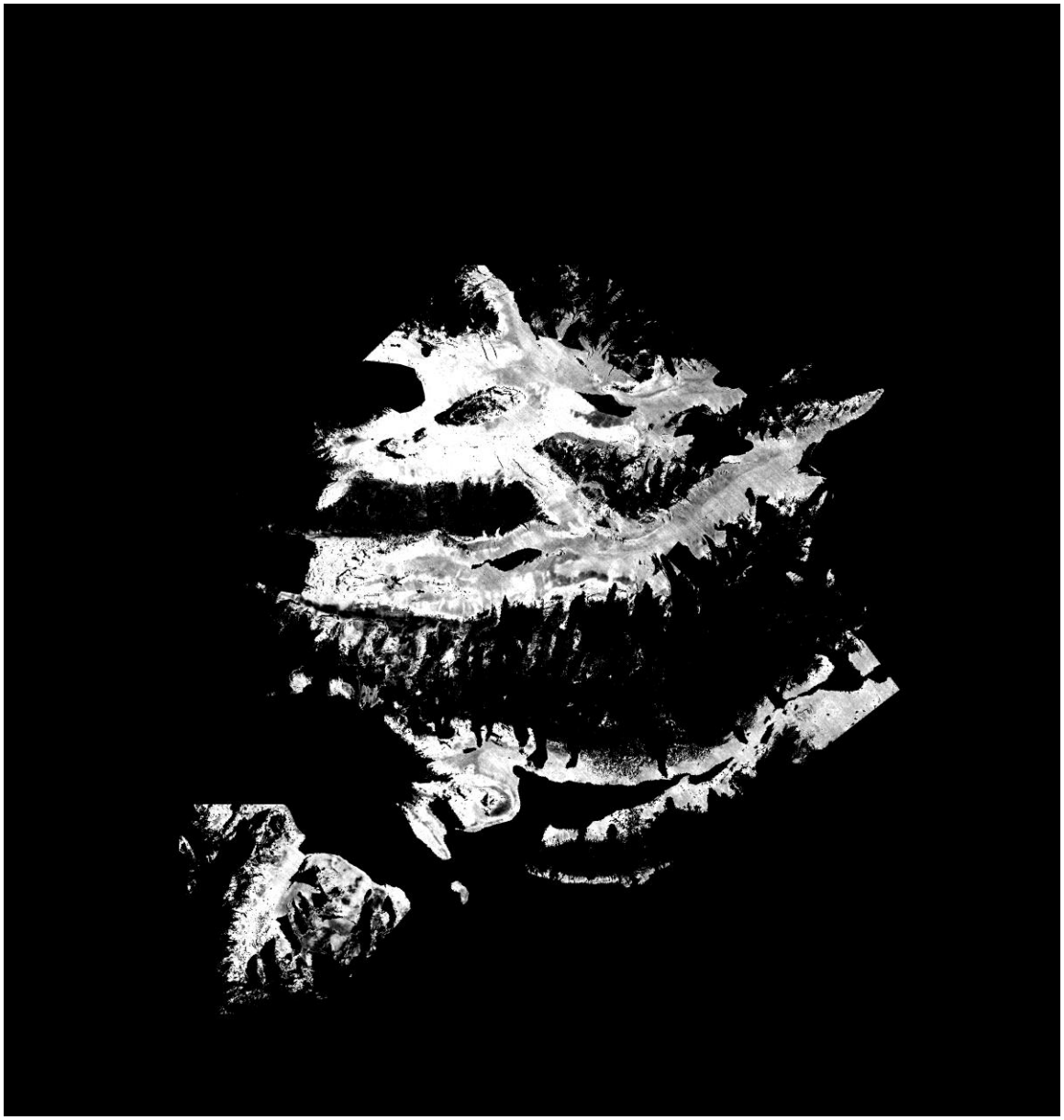

Appendix A, Figure 3k.

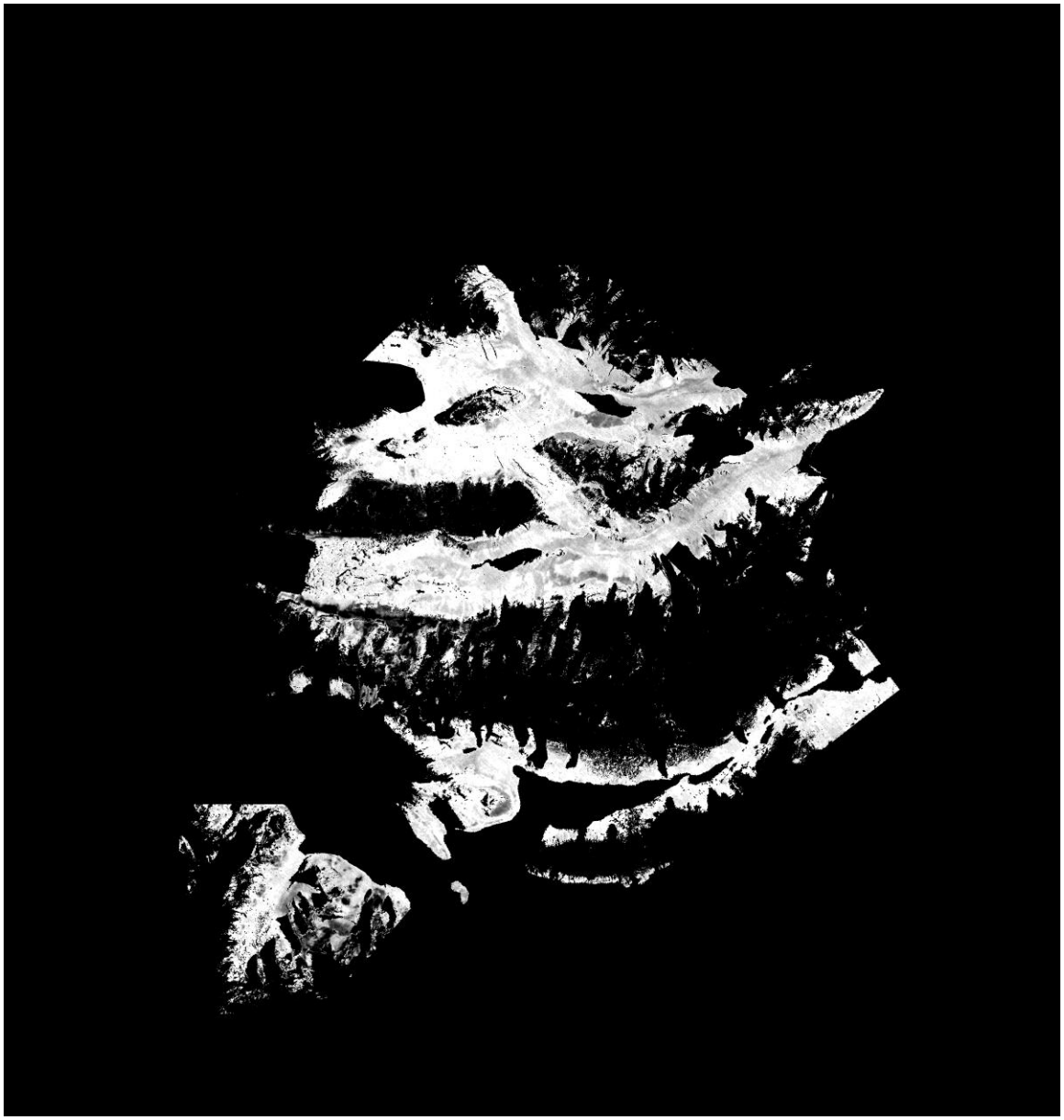

Appendix A, Figure 3l.

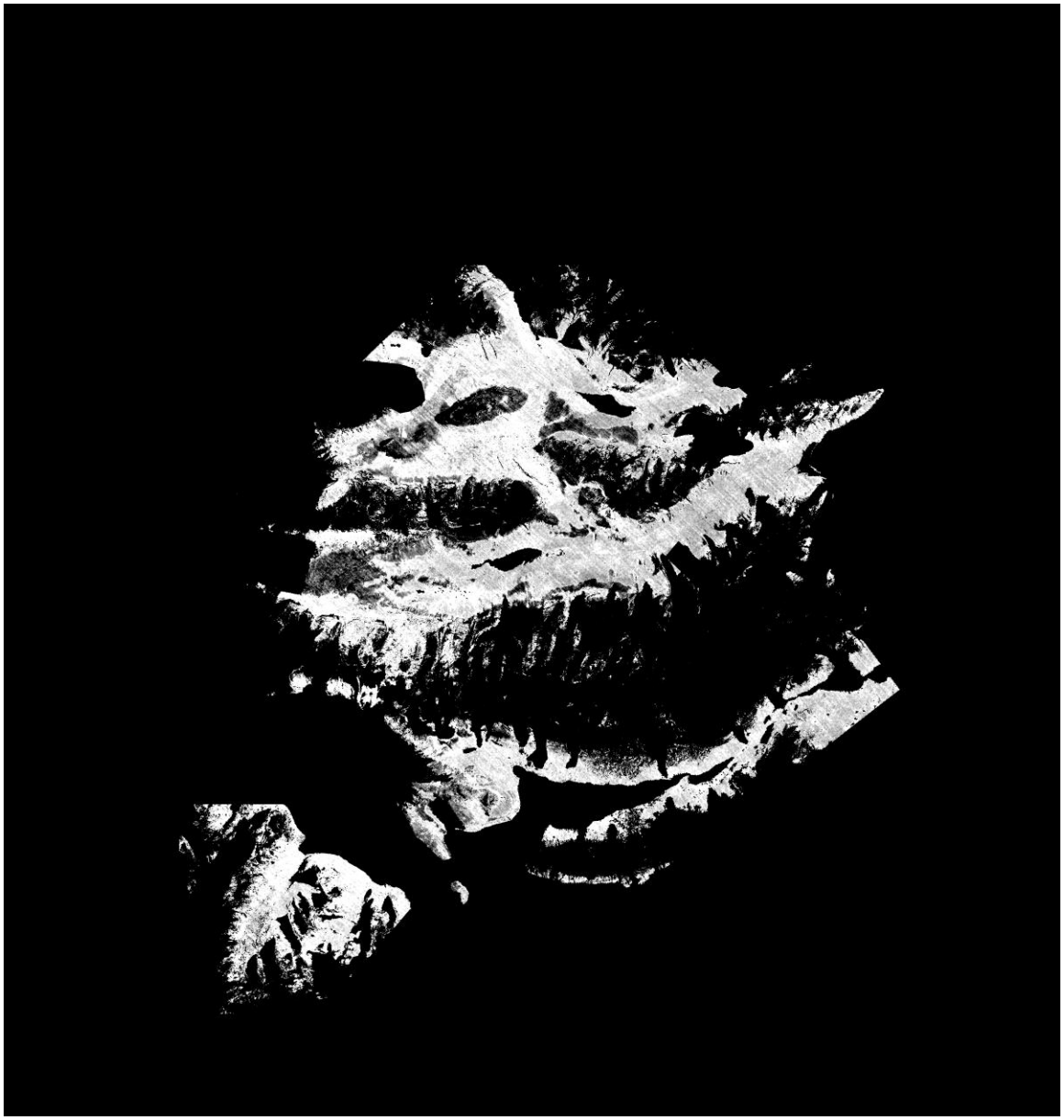

Appendix A, Figure 3m.

Appendix A, Figure 3n.

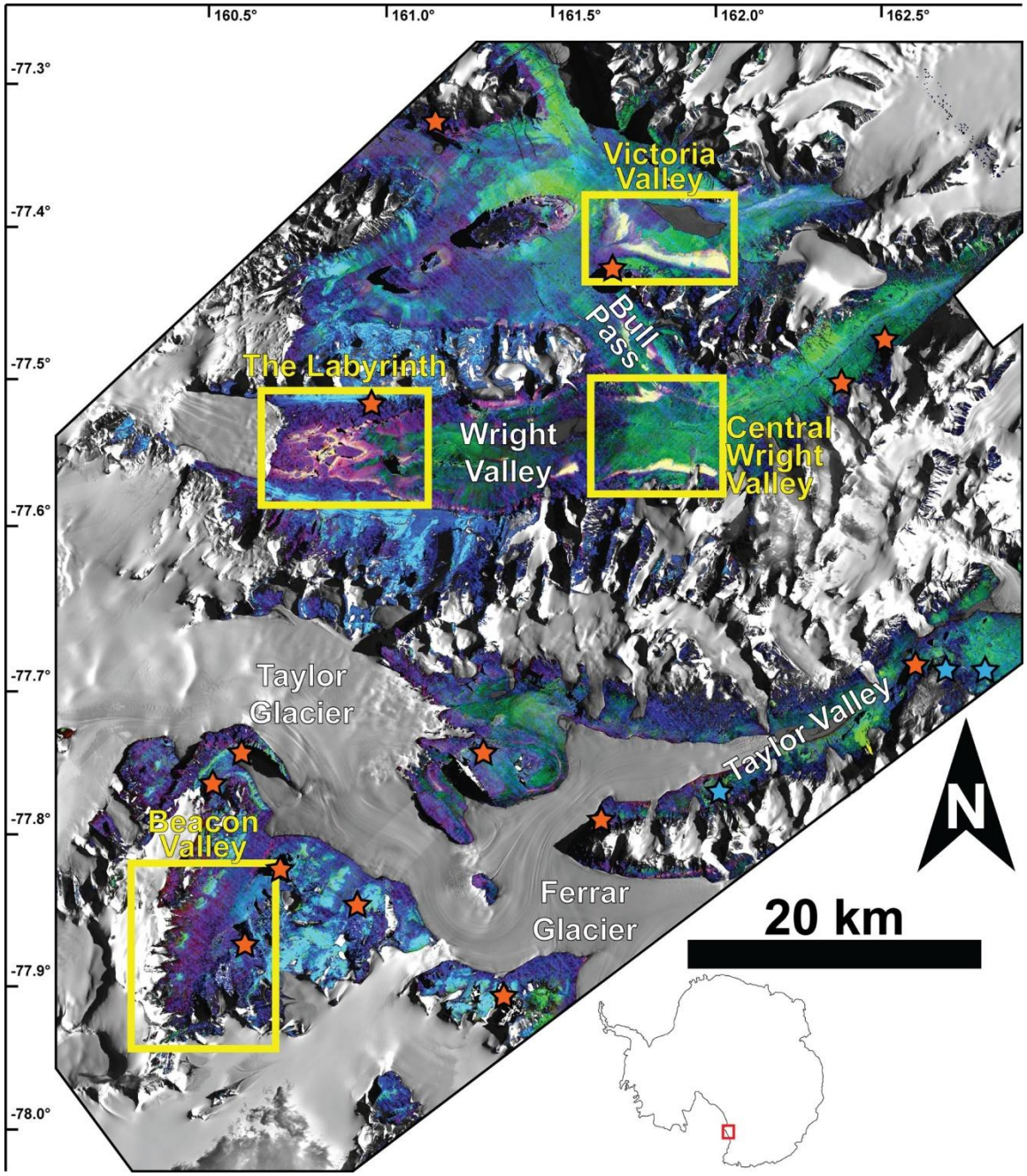

Appendix A, Figure 3.

Appendix A, Table 1.

Instrument	Image ID	Date of Acquisition	Location
ALI	EO1A0581152008022110KG	22 Jan 2008	Taylor V., Beacon V.
	EO1A0581152010038110KK	07 Feb 2010	Victoria V., Bull Pass
	EO1A0581152009339110K0	05 Dec 2009	Wright V.
	EO1A0581152010041110K9	10 Feb 2010	Wright V.
	EO1A0581152011027110P1	27 Jan 2011	Wright V.
ASTER	AST_05_00312082002210402	08 Dec 2003	Wright V.
	AST_05_00312112003210330	11 Dec 2003	Wright V.
	AST_05_00312032001211845	03 Dec 2001	Victoria V., Bull Pass
	AST_05_00311292000204446	29 Nov 2000	Taylor V.
	AST_05_00312032001211854	03 Dec 2001	Beacon V.

Appendix A, Table 2.

Band	$G_{rescale}$	$B_{rescale}$	$ESUN_{\lambda}$
B1P	0.045	-3.4	1857
B1	0.043	-4.4	1996
B2	0.028	-1.9	1807
B3	0.018	-1.3	1536
B4	0.011	-0.85	1145
B4P	0.0091	-0.65	955.8
B5P	0.0083	-1.3	452.3
B5	0.0028	-0.6	235.1
B7	0.00091	-0.21	82.38

Appendix A, Table 3.

Image	X-Pixel	Y-Pixel	B2	B3	B4	B5	B6	B7	B8	B9	B10
KK	1305	1238	41.645	36.579	24.868	17.312	12.394	8.750	3.116	1.455	0.372
KK	1304	1239	41.915	37.009	24.700	17.492	12.713	8.969	3.273	1.601	0.402
KK	1303	1239	42.185	36.880	24.784	17.312	12.460	8.750	3.174	1.483	0.372
KK	1303	1238	41.105	35.719	23.888	15.764	11.118	7.758	2.825	1.198	0.311
KK	1302	1238	41.375	35.676	23.188	15.566	10.843	7.658	2.576	1.164	0.300
KK	1302	1237	40.790	35.031	22.628	15.080	10.436	7.276	2.269	0.996	0.246
KK	1302	1236	40.655	34.472	22.012	14.684	10.018	6.912	2.244	0.920	0.237
KK	1301	1236	40.115	33.612	20.416	12.686	8.170	5.638	1.597	0.503	0.148
KK	1301	1235	40.295	34.042	21.312	13.154	8.599	6.157	1.879	0.657	0.165
KK	1300	1235	40.025	33.741	21.004	12.560	7.961	5.656	1.497	0.453	0.115
KK	1300	1236	39.935	33.612	20.220	12.560	7.939	5.602	1.597	0.498	0.119
KK	1299	1236	39.845	33.569	20.332	12.110	7.675	5.383	1.398	0.394	0.111
KK	1299	1237	40.700	34.816	21.760	13.712	9.094	6.475	1.962	0.755	0.185
KK	1298	1237	40.385	34.988	21.480	13.766	9.116	6.503	1.904	0.744	0.180
KK	1298	1236	40.205	33.526	20.332	12.308	7.862	5.483	1.381	0.442	0.122
KK	1297	1236	40.340	34.128	20.668	12.686	8.148	5.756	1.564	0.551	0.146
KK	1297	1237	40.925	34.945	21.704	13.838	9.050	6.357	1.862	0.761	0.189
KK	1296	1237	40.655	34.859	21.088	13.568	8.819	6.157	1.721	0.699	0.185
KK	1296	1236	40.475	34.859	20.472	13.388	8.709	6.275	1.721	0.638	0.166
KK	1296	1235	40.070	33.483	19.716	11.714	7.125	5.174	1.273	0.344	0.095
KK	1295	1235	40.160	33.612	19.296	11.930	7.466	5.220	1.215	0.391	0.099
KK	1295	1234	39.800	33.182	19.128	11.282	6.806	4.783	1.115	0.237	0.069
KK	1294	1234	40.250	33.440	19.100	11.156	6.751	4.710	1.057	0.206	0.067
KK	1692	1556	50.825	50.425	43.292	36.572	31.435	25.958	11.507	6.313	1.812
KK	1692	1557	50.690	50.425	43.180	36.374	31.259	25.849	11.681	6.285	1.799
KK	1691	1557	48.755	48.361	40.240	32.972	27.871	22.801	10.171	5.451	1.575
KK	1691	1558	49.790	48.619	39.876	32.738	27.552	22.500	10.096	5.378	1.562
KK	1690	1558	48.845	47.372	38.392	31.352	26.287	21.736	9.764	5.277	1.566
KK	1690	1559	49.565	48.619	40.660	33.548	28.454	23.492	10.727	5.608	1.623
KK	1689	1559	49.070	49.178	40.968	33.746	28.619	23.602	10.627	5.736	1.667
KK	1689	1560	48.800	47.587	39.456	32.378	27.442	22.619	10.411	5.574	1.618
KK	1688	1560	49.070	47.845	39.764	32.702	27.783	22.628	10.204	5.602	1.632
KK	1687	1560	48.080	46.340	37.496	30.002	25.231	20.881	8.610	5.174	1.519
KK	1687	1561	48.485	48.103	39.876	32.594	27.552	22.482	9.980	5.294	1.572
KK	1686	1561	47.765	45.953	37.944	31.190	26.144	21.691	9.573	5.227	1.539
KK	1686	1560	47.585	45.695	36.684	29.732	24.747	20.207	8.984	4.762	1.395
KK	1686	1559	47.360	46.082	36.712	29.300	23.999	19.434	8.785	4.448	1.306
KK	1685	1559	46.730	44.319	34.304	26.744	21.007	17.031	7.332	3.956	1.145
KK	1685	1560	46.055	44.405	34.444	27.410	22.503	18.333	7.921	4.216	1.203

KK	1684	1560	46.505	43.674	33.716	25.844	20.501	16.585	7.282	3.681	1.079
KK	1684	1559	46.505	43.330	33.660	25.880	20.666	16.995	7.515	4.180	1.228
KK	1683	1559	46.055	42.513	32.624	24.674	19.709	15.857	6.859	3.818	1.144
KK	1683	1560	45.830	43.244	33.184	25.826	20.710	16.777	7.282	3.883	1.138
KK	1682	1560	44.480	41.567	31.672	23.828	18.279	14.283	5.846	3.090	0.959
KK	1682	1559	44.570	41.309	30.468	22.424	17.333	13.901	5.797	3.202	0.998
KK	1682	1560	44.480	41.567	31.672	23.828	18.279	14.283	5.846	3.090	0.959
KK	1681	1560	42.950	38.729	27.528	19.184	14.033	10.989	4.327	2.340	0.756
KK	1681	1561	42.635	37.912	26.800	18.626	13.032	9.879	3.738	1.763	0.537
KK	1680	1561	42.275	37.224	25.512	17.348	12.097	9.333	3.398	1.847	0.580
KK	1680	1562	43.085	37.525	25.596	17.168	11.833	8.860	3.257	1.508	0.480
KK	1679	1562	43.130	37.912	25.932	17.510	12.471	9.524	3.431	1.769	0.554
KK	1679	1563	42.275	37.310	25.820	17.492	12.449	9.378	3.514	1.704	0.536
KK	1678	1563	41.420	36.149	23.748	15.620	10.205	7.758	2.634	1.116	0.355
KK	1678	1564	40.475	34.558	21.648	13.262	8.159	5.984	1.671	0.677	0.234
KK	1677	1564	40.295	33.827	20.584	12.182	6.960	5.001	1.074	0.397	0.108
KK	1677	1563	40.430	34.988	21.648	13.370	8.071	5.729	1.746	0.582	0.152
KK	1676	1563	40.115	34.386	20.808	11.750	7.268	4.983	1.464	0.366	0.098
KK	1676	1564	39.935	34.085	20.416	11.822	6.927	4.810	1.190	0.332	0.094
KK	1675	1564	39.665	33.655	20.304	12.092	6.905	4.701	1.256	0.321	0.087
KK	1675	1563	39.980	34.214	20.640	12.146	6.993	4.892	1.339	0.310	0.087
KK	1674	1563	40.160	34.386	20.584	12.236	6.872	4.783	1.373	0.321	0.088
KK	1674	1564	40.070	33.827	20.360	11.930	6.806	4.683	1.306	0.282	0.082
KK	1673	1564	40.295	34.042	20.332	11.948	6.861	4.737	1.232	0.304	0.080
KK	1673	1563	40.250	34.386	20.472	12.506	7.235	4.956	1.232	0.307	0.088
KK	1672	1563	40.250	34.601	20.640	12.326	7.301	4.983	1.323	0.327	0.087
KK	1672	1564	40.340	34.386	20.780	12.470	7.312	5.001	1.240	0.335	0.088
KK	1106	1912	40.925	35.805	25.540	18.644	14.253	10.661	3.531	1.657	0.476
KK	1105	1912	40.430	35.805	24.980	18.554	14.110	10.798	3.738	1.704	0.484
KK	1105	1911	39.575	35.074	23.580	17.294	12.603	9.396	3.174	1.366	0.404
KK	1105	1910	39.170	34.214	22.544	16.394	11.877	8.805	2.858	1.262	0.367
KK	1104	1910	39.755	34.386	23.020	16.412	12.108	8.887	2.991	1.209	0.343
KK	1104	1911	40.025	35.375	23.888	17.348	12.603	9.669	3.165	1.374	0.384
KK	1104	1912	40.520	35.848	24.896	18.176	13.736	10.316	3.605	1.609	0.463
KK	1104	1913	39.935	35.461	24.784	18.734	14.231	10.598	3.730	1.811	0.519
KK	1103	1913	40.115	35.332	24.280	17.942	13.527	10.124	3.697	1.716	0.474
KK	1103	1912	40.115	35.074	23.692	17.258	13.197	9.933	3.290	1.528	0.434
KK	1103	1911	38.990	34.085	22.236	15.512	11.437	8.477	2.734	1.150	0.325
KK	1103	1910	37.910	32.451	20.444	14.198	10.051	7.349	2.410	0.887	0.260
KK	1102	1910	37.100	31.333	18.876	12.434	7.983	5.884	1.705	0.582	0.162
KK	1102	1911	37.820	32.537	20.724	13.928	9.567	7.176	2.161	0.848	0.237

KK	1102	1912	38.945	33.397	22.012	15.710	11.415	8.659	2.867	1.265	0.369
KK	1102	1913	39.755	34.945	23.356	16.628	12.680	9.497	3.190	1.464	0.426
KK	1101	1913	39.125	34.472	22.516	15.818	11.602	8.541	2.709	1.167	0.339
KK	1101	1912	38.180	33.182	21.004	14.234	10.150	7.449	2.360	0.898	0.261
KK	1101	1911	37.955	32.494	20.024	12.866	9.072	6.694	2.003	0.708	0.205
KK	1101	1910	37.370	31.505	18.736	11.660	7.631	5.593	1.680	0.498	0.148
KK	1101	1909	37.100	30.989	17.896	10.994	6.861	4.901	1.339	0.304	0.098
KK	1100	1909	36.920	30.989	17.924	10.706	6.894	4.947	1.273	0.299	0.080
KK	1100	1908	36.830	31.075	17.896	10.814	6.553	4.737	1.356	0.282	0.086
KK	1099	1908	36.515	30.559	17.616	10.040	6.542	4.674	1.173	0.254	0.078
KK	1099	1907	36.920	30.989	17.756	10.526	6.575	4.646	1.124	0.243	0.074
KK	1098	1907	36.290	30.688	17.756	10.310	6.553	4.683	1.273	0.268	0.078
KK	1098	1906	36.425	30.473	17.532	10.562	6.542	4.746	1.124	0.268	0.073
P1	1660	1522	68.150	62.508	52.112	42.314	35.230	28.170	11.889	6.624	2.091
P1	1659	1522	68.015	61.605	50.572	40.892	33.932	27.524	11.598	6.375	1.985
P1	1659	1523	68.465	61.906	51.272	41.432	34.251	27.433	11.532	6.369	2.018
P1	1658	1523	66.890	60.229	48.220	38.372	31.424	25.340	10.171	5.641	1.798
P1	1658	1524	67.565	60.745	48.472	38.318	31.479	25.576	10.569	5.700	1.813
P1	1657	1524	66.710	59.154	46.876	36.500	29.565	23.875	9.507	4.978	1.583
P1	1657	1525	65.900	59.068	45.700	35.222	28.663	23.074	9.249	4.913	1.559
P1	1656	1525	65.810	57.778	45.084	34.520	27.486	21.873	8.452	4.376	1.392
P1	1656	1526	65.135	57.778	44.272	33.656	26.837	21.590	8.552	4.381	1.384
P1	1655	1526	65.090	57.305	44.580	33.440	26.089	20.617	7.697	3.984	1.261
P1	1655	1527	65.180	57.176	42.592	31.856	24.956	19.707	7.457	3.743	1.187
P1	1655	1528	64.505	57.090	42.144	31.082	23.889	18.897	6.942	3.502	1.102
P1	1654	1528	64.010	55.499	40.212	29.300	21.986	17.040	6.137	2.976	0.906
P1	1654	1529	63.020	54.209	38.532	27.374	20.314	15.712	5.597	2.642	0.814
P1	1654	1530	62.525	53.607	37.328	26.312	19.522	15.084	5.315	2.357	0.730
P1	1653	1530	61.265	52.231	35.732	24.602	17.674	13.755	4.701	2.049	0.655
P1	1653	1531	61.175	51.070	34.584	23.360	16.640	12.736	4.211	1.780	0.555
P1	1653	1532	60.905	50.425	32.848	21.560	14.803	11.244	3.497	1.424	0.437
P1	1653	1533	59.915	48.877	31.140	19.544	12.889	9.569	2.759	0.915	0.285
P1	1652	1533	58.970	48.533	29.852	18.302	11.756	8.778	2.427	0.752	0.220
P1	1652	1534	58.340	47.673	28.704	17.510	10.799	7.931	2.028	0.531	0.150
P1	1651	1534	58.160	48.318	28.872	17.456	10.777	7.968	2.053	0.489	0.139
P1	1651	1535	58.835	47.673	28.536	16.970	10.425	7.813	1.763	0.442	0.107
P1	1651	1536	58.295	46.899	28.004	16.574	10.084	7.558	1.771	0.383	0.115
P1	1650	1536	58.250	47.157	28.396	16.790	10.425	7.677	1.788	0.433	0.132
P1	1650	1537	58.025	47.286	28.396	16.808	10.271	7.549	1.713	0.397	0.122
P1	1649	1537	58.340	47.243	28.676	17.042	10.546	7.758	1.721	0.439	0.146
P1	1649	1538	58.340	47.071	28.284	16.592	10.293	7.576	1.663	0.402	0.128

P1	1649	1539	57.800	46.598	27.808	16.448	10.051	7.349	1.746	0.391	0.109
P1	1648	1539	58.115	46.727	27.780	16.538	10.150	7.413	1.713	0.402	0.127
P1	1648	1540	57.980	46.598	27.724	16.430	10.117	7.449	1.829	0.380	0.119
P1	1647	1540	57.980	46.899	28.004	16.574	10.194	7.449	1.788	0.428	0.102
P1	1647	1541	57.440	46.254	28.004	16.376	10.106	7.458	1.837	0.405	0.118
P1	1646	1541	57.665	46.727	27.724	16.286	10.095	7.476	1.572	0.422	0.099
P1	1646	1542	58.070	46.469	27.528	16.340	10.018	7.367	1.647	0.405	0.112
P1	1645	1542	56.990	45.910	27.696	16.160	9.974	7.212	1.622	0.397	0.098
P1	1367	1833	61.940	59.627	47.408	36.410	28.487	22.428	8.951	5.820	1.987
P1	1367	1834	60.815	58.208	46.008	35.384	27.706	21.809	8.826	5.683	1.968
P1	1366	1834	61.085	58.595	45.168	34.322	26.375	20.981	8.112	5.370	1.858
P1	1366	1835	60.500	57.434	44.580	34.124	26.309	20.817	8.295	5.302	1.832
P1	1365	1835	59.645	55.671	42.732	32.108	24.384	19.297	7.714	4.936	1.715
P1	1364	1835	57.980	53.564	39.568	28.706	21.810	17.159	6.477	4.222	1.499
P1	1363	1835	56.855	50.898	36.488	26.078	19.049	14.765	5.448	3.410	1.190
P1	1363	1836	55.550	50.210	35.452	24.872	18.345	14.219	5.257	3.236	1.143
P1	1362	1836	54.470	48.361	33.240	22.874	16.178	12.463	4.543	2.600	0.925
P1	1362	1837	55.280	48.318	32.344	21.866	15.705	12.108	4.327	2.502	0.888
P1	1361	1837	54.245	46.598	31.056	20.372	14.099	10.943	3.688	2.150	0.754
P1	1360	1837	53.030	45.437	29.516	18.680	12.493	9.588	3.091	1.665	0.579
P1	1360	1838	52.535	44.362	28.088	17.582	11.756	8.869	2.892	1.475	0.512
P1	1359	1838	51.860	43.846	27.108	16.430	10.777	8.050	2.460	1.153	0.412
P1	1359	1839	50.870	42.685	26.212	15.836	10.249	7.604	2.153	0.990	0.308
P1	1359	1840	50.960	42.298	25.204	14.990	9.270	7.076	2.086	0.803	0.292
P1	1359	1841	49.970	41.954	24.840	14.396	8.654	6.403	1.547	0.565	0.211
P1	1358	1841	49.970	41.008	23.916	13.838	8.159	6.048	1.663	0.506	0.162
P1	1358	1842	50.240	41.352	24.308	13.892	8.379	6.093	1.505	0.506	0.197
P1	1358	1843	50.330	41.782	24.784	14.198	8.511	6.202	1.182	0.517	0.189
P1	1358	1844	50.825	41.782	24.532	14.252	8.456	6.166	1.298	0.512	0.144
P1	1359	1844	49.610	41.610	24.672	14.090	8.533	6.166	1.431	0.503	0.142
P1	1359	1845	50.375	41.739	24.476	14.162	8.566	6.120	1.721	0.464	0.159
P1	1358	1845	50.240	41.696	24.504	14.144	8.456	6.102	1.505	0.509	0.145
P1	1357	1845	50.735	41.782	24.588	14.180	8.511	6.130	1.406	0.500	0.146
P1	1357	1846	49.880	41.696	24.532	14.072	8.324	6.111	1.489	0.481	0.139
P1	1357	1847	50.465	41.782	24.784	14.090	8.456	6.157	1.638	0.492	0.146
P1	1358	1847	50.870	41.696	24.588	14.396	8.467	6.120	1.738	0.500	0.168
P1	1358	1848	50.825	41.696	24.476	14.144	8.489	5.993	1.771	0.478	0.170
P1	1358	1849	50.420	41.309	24.308	14.018	8.412	6.093	1.464	0.509	0.162
P1	1357	1849	50.600	41.524	24.308	14.036	8.291	5.993	1.771	0.489	0.164
P1	1357	1850	50.285	41.438	24.280	13.946	8.456	5.957	1.705	0.492	0.150
P1	1358	1850	50.465	41.438	24.308	14.018	8.456	6.111	1.564	0.506	0.149

P1	1358	1851	50.240	41.567	24.560	14.252	8.467	6.184	1.680	0.470	0.136
P1	1359	1851	50.600	40.750	24.924	14.324	8.599	6.148	1.464	0.475	0.157
P1	1360	1851	50.915	41.782	24.364	14.180	8.357	6.066	1.514	0.433	0.167
P1	1360	1852	50.105	41.524	24.504	14.072	8.456	5.993	1.464	0.416	0.169
P1	1359	1852	50.240	41.266	24.616	14.126	8.511	6.039	1.373	0.478	0.153
P1	1358	1852	50.510	40.406	24.728	14.018	8.511	5.911	1.564	0.492	0.135
P1	1358	1853	50.150	40.664	24.140	14.054	8.434	5.948	1.464	0.475	0.143
P1	1277	1950	57.305	52.446	38.084	27.950	20.820	16.140	6.079	3.681	1.297
P1	1277	1951	57.800	52.145	37.664	26.906	20.160	15.712	6.004	3.552	1.265
P1	1278	1951	57.440	52.747	38.056	27.302	20.666	16.403	6.328	3.726	1.263
P1	1278	1952	57.305	53.048	38.420	28.112	21.260	16.804	6.469	3.984	1.366
P1	1279	1952	59.780	56.789	43.684	32.990	25.649	20.380	8.345	4.849	1.689
P1	1279	1953	59.375	53.994	42.396	31.568	24.274	19.143	7.656	4.558	1.581
P1	1280	1953	60.905	56.617	44.132	33.170	25.770	20.398	8.079	4.994	1.760
P1	1280	1954	59.690	56.015	42.508	31.334	24.076	19.124	7.614	4.583	1.654
P1	1281	1954	61.625	58.724	46.820	35.906	28.311	22.446	9.150	5.644	1.973
P1	1281	1955	61.490	58.638	45.840	34.880	27.508	21.727	8.643	5.392	1.908
P1	1280	1955	58.790	54.811	41.388	30.650	23.581	18.415	7.166	4.278	1.547
P1	1280	1956	58.160	53.607	39.680	28.670	21.986	17.277	6.560	3.939	1.423
P1	1279	1956	57.395	53.220	39.344	28.346	21.513	16.849	6.378	3.748	1.352
P1	1279	1957	56.315	51.500	36.936	26.042	19.357	15.220	5.730	3.320	1.210
P1	1278	1957	55.280	48.834	33.464	22.748	16.101	12.691	4.618	2.486	0.896
P1	1278	1958	53.570	47.028	31.896	20.930	14.979	11.635	3.813	2.091	0.709
P1	1277	1958	52.580	45.265	29.488	19.580	13.219	10.325	3.448	1.878	0.616
P1	1277	1959	51.140	43.115	26.548	15.818	9.853	7.331	1.846	0.803	0.262
P1	1276	1959	50.375	41.825	24.868	14.594	8.951	6.666	1.746	0.506	0.190
P1	1276	1958	51.095	42.341	26.380	16.088	9.996	7.422	1.854	0.904	0.323
P1	1276	1957	51.680	43.889	28.956	18.464	12.482	9.533	3.116	1.427	0.449
P1	1275	1957	51.095	42.771	25.848	15.620	9.644	7.276	2.211	0.806	0.241
P1	1275	1958	50.510	40.879	25.120	14.720	9.050	6.594	1.862	0.556	0.166
P1	1275	1957	51.095	42.771	25.848	15.620	9.644	7.276	2.211	0.806	0.241
P1	1274	1957	50.105	41.825	25.008	14.630	9.061	6.666	1.622	0.671	0.193
P1	1274	1958	50.240	41.524	24.924	14.432	8.863	6.475	1.821	0.548	0.170
P1	1274	1957	50.105	41.825	25.008	14.630	9.061	6.666	1.622	0.671	0.193
P1	1273	1957	50.375	41.610	24.588	14.450	8.797	6.512	1.688	0.534	0.166
P1	1273	1958	50.510	42.040	24.672	14.288	8.973	6.512	1.588	0.551	0.179
P1	1273	1959	50.825	41.739	24.868	14.486	8.830	6.466	1.680	0.542	0.177
P1	1272	1959	50.195	41.395	24.588	14.414	8.764	6.430	1.622	0.534	0.158
P1	1272	1960	49.835	41.266	24.532	14.360	8.731	6.348	1.647	0.573	0.157
P1	1273	1960	50.510	41.438	24.812	14.576	8.819	6.321	1.738	0.512	0.148
P1	1273	1961	50.060	40.535	24.840	14.486	8.775	6.439	1.572	0.503	0.172

P1	1274	1961	50.600	41.567	24.784	14.360	8.742	6.357	1.547	0.495	0.162
P1	1274	1962	50.645	41.997	24.868	14.288	8.687	6.302	1.638	0.475	0.144
P1	1273	1962	50.465	41.438	24.896	14.324	8.621	6.403	1.497	0.461	0.179
P1	1274	1962	50.645	41.997	24.868	14.288	8.687	6.302	1.638	0.475	0.144
P1	1275	1962	50.870	41.739	24.784	14.522	8.786	6.439	1.597	0.481	0.156
P1	1275	1963	51.365	42.255	24.812	14.234	8.643	6.284	1.439	0.461	0.151
P1	1276	1963	50.420	42.298	24.952	14.396	8.797	6.393	1.422	0.470	0.155
KG	2562	1503	49.097	42.528	30.801	22.911	17.200	13.498	4.821	2.262	0.758
KG	2563	1503	50.042	45.108	34.245	26.583	19.982	15.627	6.099	2.996	0.943
KG	2564	1503	49.997	45.108	34.021	26.277	20.016	15.754	5.825	2.755	0.911
KG	2565	1503	47.297	40.335	26.797	18.429	12.349	9.093	2.937	1.016	0.408
KG	2566	1503	45.407	37.368	22.401	13.641	8.543	6.354	1.750	0.367	0.168
KG	2567	1503	45.182	36.465	21.729	13.011	8.146	6.136	1.418	0.314	0.147
KG	2568	1503	44.912	37.067	21.953	13.101	8.191	6.136	1.492	0.308	0.127
KG	2569	1503	45.272	36.852	22.121	13.119	8.333	6.181	1.467	0.280	0.159
KG	2570	1503	45.092	37.153	22.037	13.209	8.191	6.172	1.227	0.280	0.150
KG	2571	1503	45.497	36.895	22.009	13.155	8.179	6.081	1.484	0.288	0.149
KG	2572	1503	45.497	36.852	22.009	13.173	8.224	6.163	1.625	0.283	0.145
KG	2573	1503	45.182	36.852	22.009	13.389	8.257	6.245	1.716	0.302	0.147
KG	2574	1503	44.867	36.637	21.953	13.389	8.224	6.218	1.609	0.322	0.162
KG	2574	1502	45.137	36.594	21.981	13.641	8.323	6.272	1.725	0.344	0.156
KG	2573	1502	44.822	36.852	21.813	13.155	8.036	6.099	1.609	0.283	0.145
KG	2572	1502	45.542	36.981	21.897	13.119	8.158	6.145	1.418	0.258	0.149
KG	2571	1502	45.632	37.368	21.925	13.245	8.234	6.181	1.227	0.297	0.151
KG	2570	1502	45.317	37.153	21.981	13.245	8.201	6.245	1.061	0.314	0.159
KG	2569	1502	45.227	36.637	21.981	13.119	8.113	6.145	1.393	0.300	0.110
KG	2568	1502	45.182	37.067	22.121	13.389	8.411	6.327	1.517	0.353	0.112
KG	2567	1502	46.037	37.798	23.353	14.343	9.059	6.654	1.907	0.456	0.232
KG	2566	1502	46.982	40.249	27.245	18.825	12.854	9.466	3.011	1.131	0.438
KG	2565	1502	48.827	43.173	31.193	23.559	17.827	13.716	4.821	2.260	0.800
KG	2564	1502	51.167	47.129	36.653	28.905	22.336	17.738	6.904	3.464	1.107
KG	2563	1502	50.312	45.237	34.077	26.169	20.126	15.818	6.223	3.058	0.992
KG	2562	1502	49.232	42.872	30.857	22.263	15.891	12.633	4.696	2.282	0.756
KG	2562	1501	48.917	42.528	30.129	21.705	16.176	12.779	4.746	2.139	0.738
KG	2563	1501	50.042	44.807	33.153	25.089	19.322	15.281	5.684	2.862	0.977
KG	2564	1501	50.267	45.667	35.029	27.123	21.016	16.655	6.688	3.346	1.090
KG	2565	1501	49.772	44.936	34.329	25.827	19.707	15.509	6.066	2.982	0.979
KG	2566	1501	49.367	43.087	31.417	23.055	17.089	13.215	4.538	2.170	0.740
KG	2567	1501	47.702	41.109	28.561	20.463	14.669	11.041	3.509	1.456	0.550
KG	2568	1501	46.712	39.131	24.921	16.233	10.413	7.637	2.414	0.647	0.285
KG	2569	1501	45.632	37.540	22.877	14.055	8.807	6.618	1.833	0.398	0.185

KG	2570	1501	45.497	37.411	22.233	13.425	8.366	6.172	1.443	0.316	0.095
KG	2571	1501	45.767	36.809	21.981	13.155	8.146	6.181	1.252	0.302	0.102
KG	2572	1501	45.317	36.895	21.953	13.245	8.125	6.127	1.534	0.300	0.158
KG	2573	1501	45.227	37.110	21.869	13.137	7.981	6.045	1.509	0.274	0.142
KG	2574	1501	45.362	37.196	21.785	13.137	8.234	6.145	1.526	0.288	0.160
KG	2575	1501	45.137	36.852	22.065	13.407	8.300	6.281	1.750	0.311	0.161
KG	2575	1500	45.137	36.981	22.177	13.533	8.300	6.299	1.550	0.325	0.166
KG	2574	1500	45.542	36.938	21.897	13.137	8.158	6.108	1.658	0.266	0.159
KG	2573	1500	45.407	37.067	21.981	13.155	8.003	6.172	1.858	0.252	0.131
KG	2572	1500	44.957	37.067	22.009	13.209	8.224	6.208	1.542	0.294	0.042
KG	2571	1500	45.632	37.712	22.989	14.037	8.642	6.472	1.633	0.389	-0.010
KG	2570	1500	45.767	39.088	23.969	15.549	10.038	7.564	2.389	0.689	0.252
KG	2569	1500	46.397	38.787	25.341	16.629	11.028	8.274	2.397	0.854	0.348
KG	2568	1500	47.747	40.550	27.553	18.717	13.427	10.513	3.451	1.434	0.496
KG	2567	1500	48.692	42.786	30.465	22.317	16.506	12.724	4.588	2.114	0.715
KG	2566	1500	49.772	44.850	33.321	24.855	18.575	14.662	5.609	2.649	0.846
KG	2565	1500	50.357	45.194	34.273	25.899	19.696	15.618	5.875	2.920	0.953
KG	2564	1500	50.582	45.968	35.001	26.853	20.192	15.700	6.157	3.080	1.002
KG	2564	1499	50.807	46.054	34.553	27.339	21.610	16.965	6.638	3.270	1.109
KG	2565	1499	50.267	45.237	34.525	26.709	20.379	15.955	6.049	3.108	1.029
KG	2566	1499	49.502	45.108	33.517	25.449	18.860	14.926	5.435	2.794	0.913
KG	2567	1499	49.097	43.302	31.025	22.551	16.484	12.815	4.696	2.204	0.725
KG	2568	1499	47.702	41.539	28.113	19.239	13.954	10.722	3.617	1.526	0.541
KG	2569	1499	47.387	40.980	27.441	18.843	12.800	10.058	3.235	1.389	0.457
KG	2570	1499	47.657	39.303	25.817	17.493	12.349	9.366	2.920	1.042	0.418
KG	2571	1499	46.487	38.658	25.285	16.989	11.722	8.920	2.779	1.000	0.367
KG	2572	1499	46.577	39.604	26.069	17.277	10.995	8.047	2.223	0.711	0.146
KG	2573	1499	45.407	37.927	22.485	13.389	8.290	6.281	1.617	0.330	0.034
KG	2574	1499	44.957	37.153	21.869	13.011	8.158	6.117	1.725	0.269	0.159
KG	2575	1499	45.992	37.325	22.205	13.407	8.311	6.309	1.517	0.328	0.169
KG	2576	1499	45.677	36.981	22.009	13.371	8.191	6.208	1.401	0.314	0.151
KG	2576	1498	44.867	37.153	21.925	13.389	8.378	6.281	1.509	0.322	0.167
KG	2575	1498	45.452	36.809	22.261	13.461	8.389	6.263	1.418	0.367	0.136
KG	2574	1498	46.262	38.056	23.269	14.469	8.630	6.345	1.584	0.370	0.027
KG	2573	1498	47.882	41.797	30.885	22.713	15.846	11.741	3.883	1.604	0.465
KG	2572	1498	47.837	41.281	28.645	20.931	15.561	12.396	4.331	2.044	0.673
KG	2571	1498	46.487	38.357	23.577	14.307	9.533	7.555	2.273	0.748	0.290
KG	2570	1498	45.992	39.389	25.537	17.043	11.326	8.529	2.746	1.098	0.383
KG	2569	1498	47.657	40.851	27.189	19.023	13.394	10.458	3.376	1.414	0.492
KG	2568	1498	48.017	41.539	28.925	20.409	14.637	11.459	3.908	1.747	0.589
KG	2567	1498	48.827	42.743	31.333	22.911	16.891	13.270	4.721	2.313	0.776

KG	2567	1497	49.142	43.646	31.137	22.533	16.980	13.106	4.804	2.226	0.746
KG	2568	1497	48.332	42.442	29.597	21.003	15.461	11.951	3.916	1.879	0.649
KG	2569	1497	47.792	41.066	27.889	19.113	13.207	10.203	3.318	1.534	0.517
KG	2570	1497	46.442	39.518	25.453	16.953	12.040	9.503	2.995	1.126	0.400
KG	2571	1497	46.397	39.776	26.489	18.069	12.172	9.111	2.970	1.064	0.402
KG	2572	1497	49.142	42.184	28.113	18.915	12.712	9.666	3.459	1.378	0.469
KG	2573	1497	50.177	44.291	32.649	24.063	18.091	14.189	5.294	2.400	0.850
KG	2574	1497	47.972	41.625	30.409	22.281	15.429	11.741	4.074	1.814	0.634
KG	2575	1497	46.532	39.045	24.697	15.675	9.698	7.109	1.866	0.546	0.044
KG	2576	1497	45.182	37.239	22.429	13.659	8.620	6.454	1.642	0.378	0.038
KG	2577	1497	44.867	37.153	22.289	13.389	8.521	6.299	1.750	0.305	0.168
KG	2578	1497	45.767	37.368	21.925	13.227	8.201	6.218	1.526	0.325	0.152
KG	1828	1874	54.200	48.748	34.696	26.654	20.655	15.776	5.846	2.760	0.756
KG	1828	1875	54.110	49.651	35.844	28.328	21.887	16.786	6.461	3.068	0.810
KG	1827	1875	54.380	49.092	35.704	27.590	21.326	16.021	6.037	2.917	0.803
KG	1827	1876	53.975	48.662	34.948	27.140	21.084	15.766	5.987	2.816	0.772
KG	1826	1876	53.615	48.576	34.752	26.528	20.237	15.157	5.813	2.757	0.772
KG	1826	1877	54.605	49.092	35.256	27.140	20.963	15.921	5.954	2.861	0.818
KG	1825	1877	54.155	49.178	35.732	27.734	21.040	15.703	6.162	2.998	0.901
KG	1825	1878	53.570	49.092	34.556	26.672	20.721	15.776	5.863	2.808	0.856
KG	1824	1878	53.165	48.232	33.632	25.088	18.290	13.755	5.373	2.581	0.779
KG	1824	1879	53.525	47.501	32.904	23.936	17.652	13.200	4.759	2.320	0.665
KG	1823	1879	56.045	51.371	38.588	30.164	23.086	17.486	6.842	3.426	0.816
KG	1823	1880	55.370	51.027	37.412	28.310	21.777	16.831	6.178	3.118	0.914
KG	1822	1880	55.370	50.941	37.524	29.678	22.690	17.386	6.693	3.278	0.927
KG	1822	1881	55.190	50.511	37.328	28.526	22.008	16.777	6.029	3.018	0.830
KG	1821	1881	53.165	47.630	33.100	24.926	18.675	14.056	5.033	2.424	0.726
KG	1821	1882	53.660	48.060	33.548	24.764	18.235	13.810	4.875	2.318	0.617
KG	1820	1882	53.300	48.189	33.744	24.998	18.290	13.501	4.676	2.351	0.642
KG	1820	1883	53.660	47.931	32.680	23.684	17.355	12.782	4.311	2.071	0.599
KG	1819	1883	52.625	47.458	32.372	23.288	17.014	12.536	4.477	2.150	0.579
KG	1819	1884	52.805	46.770	32.064	23.360	16.816	12.500	4.253	2.032	0.561
KG	1818	1884	53.525	47.587	33.212	24.692	18.026	13.619	4.875	2.390	0.658
KG	1818	1885	53.345	47.157	32.232	22.982	16.134	11.799	4.178	1.892	0.505
KG	1817	1885	52.355	46.426	30.720	21.668	14.880	11.053	3.531	1.662	0.468
KG	1817	1886	50.825	43.760	26.856	16.556	10.579	7.613	2.236	0.755	0.220
KG	1816	1886	51.140	43.373	25.960	16.052	9.809	7.131	1.887	0.649	0.181
KG	1816	1887	50.195	42.298	24.448	14.090	8.368	5.784	1.489	0.338	0.062
KG	1815	1887	50.510	43.889	27.108	17.222	10.755	7.413	2.302	0.817	0.118
KG	1815	1888	51.185	43.631	26.492	16.862	11.140	7.922	2.261	0.769	0.147
KG	1814	1888	50.960	43.717	26.632	16.700	10.568	7.549	2.244	0.769	0.082

KG	1814	1889	50.465	43.244	25.540	15.638	9.710	6.794	1.796	0.540	0.129
KG	1813	1889	49.835	42.169	24.504	14.360	8.555	5.857	1.547	0.363	-0.005
KG	1813	1890	49.835	42.040	24.028	13.838	8.225	5.647	1.273	0.282	0.066
KG	1812	1890	49.880	42.470	24.028	13.928	8.170	5.593	1.414	0.304	-0.042
KG	1812	1891	49.610	41.696	24.000	13.928	8.027	5.629	1.190	0.251	0.078
KG	1811	1891	49.385	41.825	24.112	13.874	8.049	5.520	1.306	0.279	-0.036
KG	1811	1892	49.475	41.395	23.608	13.640	7.895	5.493	1.165	0.248	0.058
KG	1810	1892	49.745	41.094	23.580	13.586	7.928	5.474	1.223	0.246	-0.013
KG	1810	1893	49.250	41.309	23.356	13.478	7.950	5.456	1.198	0.229	0.057
KG	1809	1893	49.745	41.567	23.496	13.352	7.785	5.402	1.248	0.218	0.039
KG	1809	1894	49.385	41.094	23.552	13.514	7.785	5.447	1.256	0.232	0.073
KG	1808	1894	49.565	40.750	23.412	13.316	7.719	5.256	1.182	0.226	0.063
KG	1808	1895	49.250	40.836	23.244	13.298	7.763	5.356	1.323	0.229	0.065
KG	1807	1895	49.160	41.567	23.468	13.388	7.763	5.429	0.900	0.243	0.060
KG	1807	1896	50.240	41.739	23.720	13.586	7.961	5.502	1.323	0.246	0.070
KG	1806	1896	50.195	42.169	23.720	13.730	7.829	5.411	1.223	0.220	0.070
KG	1806	1897	50.195	41.825	23.776	13.766	8.082	5.474	1.348	0.246	0.074
KG	1805	1897	50.330	42.126	23.748	13.730	7.950	5.493	1.157	0.237	0.079
KG	1805	1898	49.790	41.868	24.560	14.180	8.214	5.647	1.240	0.268	0.088
KG	936	1724	52.490	46.211	32.596	25.358	19.115	14.456	5.689	3.144	0.889
KG	937	1724	52.715	46.297	32.148	24.728	18.697	14.128	5.572	2.973	0.840
KG	938	1724	52.085	45.695	31.336	23.324	16.893	12.782	4.801	2.486	0.711
KG	939	1724	51.680	45.437	30.328	22.784	15.881	11.872	4.361	2.253	0.658
KG	940	1724	51.455	45.136	30.356	22.388	16.167	11.935	4.361	2.287	0.637
KG	941	1724	51.590	45.265	30.636	23.036	16.497	12.281	4.527	2.379	0.657
KG	942	1724	52.040	45.609	31.168	23.882	16.387	12.163	4.552	2.281	0.665
KG	943	1724	51.860	45.652	30.524	22.946	16.134	11.826	4.278	2.150	0.624
KG	944	1724	52.400	45.824	30.524	22.190	15.903	11.781	4.261	2.166	0.635
KG	945	1724	51.950	45.093	29.992	21.776	15.782	11.762	4.186	2.122	0.601
KG	946	1724	51.905	44.534	28.928	19.940	14.165	10.589	3.489	1.713	0.462
KG	947	1724	49.790	42.298	24.728	14.684	9.149	6.703	2.012	0.724	0.232
KG	948	1724	49.295	41.395	23.608	14.054	8.148	5.929	1.489	0.391	0.125
KG	949	1724	49.385	41.051	23.524	13.784	8.071	5.638	1.265	0.318	0.095
KG	950	1724	49.250	41.051	23.692	13.856	7.950	5.675	1.356	0.318	0.108
KG	951	1724	49.565	41.653	23.664	13.802	7.950	5.684	1.323	0.304	0.097
KG	952	1724	49.205	41.438	23.720	13.892	7.796	5.675	1.281	0.293	0.069
KG	952	1725	48.845	41.653	23.804	14.144	7.884	5.738	1.323	0.310	0.105
KG	953	1725	49.430	41.352	23.692	13.694	7.983	5.629	1.348	0.307	0.100
KG	953	1726	49.430	41.438	24.112	14.216	8.082	5.793	1.198	0.271	0.078
KG	952	1726	49.070	41.438	23.552	13.982	7.983	5.784	1.339	0.288	0.102
KG	951	1726	49.295	41.567	24.028	13.820	8.071	5.775	1.348	0.310	0.115

KG	950	1726	49.340	41.653	24.280	13.766	7.983	5.738	1.223	0.260	0.091
KG	949	1726	49.115	41.782	23.972	13.748	7.994	5.738	1.223	0.285	0.090
KG	948	1726	49.475	41.653	24.000	13.928	8.082	5.802	1.422	0.346	0.136
KG	947	1726	49.385	41.266	23.860	14.522	8.071	5.738	1.422	0.344	0.129
KG	946	1726	49.295	41.180	24.112	15.296	8.093	5.802	1.290	0.341	0.111
KG	945	1726	49.475	41.911	24.840	15.422	9.204	6.721	1.846	0.643	0.209
KG	944	1726	50.870	43.932	27.724	18.932	12.812	9.469	3.124	1.469	0.394
KG	943	1726	52.085	45.738	30.860	22.982	16.156	11.926	4.244	2.122	0.578
KG	942	1726	51.635	45.867	31.196	23.306	16.442	12.208	4.485	2.245	0.644
KG	941	1726	51.590	45.480	30.552	22.586	16.475	12.399	4.502	2.340	0.662
KG	940	1726	51.815	45.480	30.636	23.072	16.387	12.217	4.518	2.346	0.651
KG	939	1726	51.365	45.222	30.440	23.342	16.189	11.990	4.419	2.304	0.661
KG	938	1726	51.815	46.168	31.560	23.594	17.586	13.164	5.025	2.693	0.754
KG	937	1726	52.085	46.426	32.036	24.818	18.455	13.946	5.548	2.953	0.837
KG	936	1726	52.265	46.340	31.980	25.448	18.510	13.910	5.498	3.029	0.844
KG	935	1726	52.760	46.727	32.792	25.538	19.236	14.520	5.631	3.104	0.875
KG	934	1726	52.760	46.942	33.324	26.096	19.841	14.902	5.821	3.194	0.901
KG	934	1727	52.715	47.028	33.324	26.348	19.841	14.893	5.738	3.149	0.877
KG	933	1727	52.715	47.286	33.408	26.384	20.105	14.929	5.896	3.177	0.886
KG	933	1728	52.850	46.899	33.380	26.816	19.907	14.784	5.813	3.127	0.865
KG	1071	1982	45.290	39.546	26.688	19.922	15.221	11.171	4.062	2.169	0.571
KG	1071	1983	45.830	39.202	26.604	19.886	15.067	11.153	4.153	2.248	0.595
KG	1071	1984	45.290	39.761	26.940	20.426	15.617	11.963	4.469	2.483	0.674
KG	1071	1985	45.650	39.890	27.500	20.930	16.541	12.563	4.892	2.822	0.766
KG	1070	1985	45.380	39.417	26.492	19.940	15.342	11.508	4.394	2.410	0.667
KG	1070	1984	45.020	38.729	26.660	19.544	15.221	11.508	4.336	2.348	0.634
KG	1070	1983	44.705	39.202	26.856	20.030	15.265	11.235	4.195	2.278	0.600
KG	1069	1983	44.750	39.417	25.904	19.526	14.627	10.889	4.103	2.158	0.573
KG	1069	1984	44.795	38.643	25.428	18.770	13.956	10.397	3.697	1.984	0.527
KG	1069	1985	44.705	37.955	24.644	17.852	12.350	9.260	3.431	1.716	0.477
KG	1068	1985	43.400	36.106	22.012	13.334	9.534	6.930	1.929	0.850	0.236
KG	1068	1984	43.895	37.267	23.048	15.638	10.656	7.840	2.634	1.240	0.318
KG	1067	1984	43.355	35.848	20.920	12.254	8.060	5.766	1.688	0.512	0.132
KG	1067	1985	43.130	35.375	20.360	11.714	7.345	5.411	1.422	0.344	0.088
KG	1067	1986	42.680	35.031	20.248	10.202	7.323	5.238	1.339	0.352	0.088
KG	1067	1987	42.725	35.332	20.136	11.966	7.367	5.383	1.348	0.341	0.089
KG	1067	1988	42.455	35.375	20.220	11.858	7.356	5.329	1.356	0.335	0.096
KG	1066	1988	42.410	35.418	20.248	12.110	7.323	5.356	1.422	0.332	0.093
KG	1066	1987	42.860	35.418	20.416	11.912	7.367	5.320	1.331	0.341	0.089
KG	1066	1986	42.815	35.461	20.332	11.534	7.345	5.283	1.339	0.355	0.089
KG	1065	1986	42.905	35.633	20.528	12.236	7.246	5.320	1.331	0.318	0.097

KG	1065	1987	42.815	35.504	20.528	12.470	7.411	5.101	1.281	0.324	0.086
KG	1065	1988	42.725	35.289	20.360	12.380	7.312	5.229	1.414	0.307	0.091
KG	1064	1988	42.635	35.719	20.388	12.632	7.323	5.210	1.281	0.324	0.086
KG	1064	1987	43.175	35.848	20.472	12.182	7.389	5.229	1.339	0.316	0.087
KG	1063	1987	42.545	35.590	20.584	12.416	7.356	5.265	1.256	0.313	0.084
KG	1063	1988	42.995	35.418	20.528	12.290	7.389	5.201	1.290	0.313	0.078
KG	1063	1989	42.365	35.289	20.444	12.398	7.235	5.165	1.298	0.335	0.071
KG	1062	1989	42.590	35.418	20.472	12.290	7.455	5.320	1.248	0.352	0.082
KG	1062	1988	42.860	35.461	20.360	12.164	7.345	5.365	1.364	0.313	0.081
KG	1061	1988	43.085	35.891	20.360	12.164	7.246	5.265	1.281	0.299	0.073
KG	1061	1989	42.590	35.418	20.388	12.092	7.356	5.301	1.431	0.338	0.070
KG	1061	1990	42.635	35.461	20.668	12.722	7.642	5.538	1.522	0.436	0.108
KG	1060	1990	42.455	35.160	20.612	12.146	7.455	5.311	1.306	0.344	0.088
KG	1060	1991	42.410	35.246	20.192	11.948	7.290	5.138	1.232	0.324	0.078
KG	1060	1992	42.050	35.117	20.332	11.804	7.202	5.174	1.348	0.346	0.089
KG	1059	1992	42.320	35.332	20.192	12.020	7.048	5.156	1.265	0.302	0.093
KG	1059	1993	42.725	35.762	20.976	13.118	7.983	5.957	1.813	0.545	0.143
KG	1058	1993	43.310	36.708	22.404	15.116	10.777	7.986	2.576	1.184	0.337
KG	1057	1993	44.345	38.041	25.176	17.816	13.186	9.924	3.439	1.878	0.504
KG	1057	1992	44.435	38.041	24.784	17.726	13.032	9.642	3.390	1.688	0.457
KG	1057	1991	44.480	38.385	24.644	16.988	12.724	9.378	3.207	1.643	0.429
KG	1056	1991	44.435	38.643	26.100	18.734	14.275	10.325	3.838	2.043	0.503
KG	1056	1992	44.345	38.772	26.072	18.878	14.605	10.962	3.846	2.077	0.573
KG	1056	1993	44.390	38.170	24.924	18.086	12.768	9.906	3.564	1.833	0.517
KG	1056	1994	43.670	36.794	23.272	15.260	11.206	8.177	2.676	1.450	0.407
KG	1055	1994	42.635	35.676	20.612	12.470	7.851	5.857	1.572	0.478	0.170
KG	1055	1993	43.580	36.235	22.712	14.216	10.282	7.285	2.344	1.086	0.292
KG	1054	1993	42.545	35.289	20.220	11.588	7.411	5.329	1.414	0.321	0.121
KG	1053	1993	42.365	35.289	20.164	11.714	7.180	5.001	1.240	0.288	0.078
KG	1053	1994	42.995	34.902	20.304	11.516	7.224	5.138	1.298	0.279	0.078
KG	1053	1995	42.545	35.246	20.304	11.930	7.268	5.147	1.339	0.316	0.078
KG	1053	1996	42.545	34.988	20.108	12.020	7.290	5.119	1.331	0.307	0.085
KG	1052	1996	42.050	35.160	20.248	11.840	7.257	5.201	1.306	0.313	0.084
KG	1051	1996	42.500	35.246	20.332	11.786	7.191	5.156	1.265	0.299	0.084
KG	906	1773	49.385	41.782	26.632	18.068	12.944	9.679	3.356	1.508	0.441
KG	906	1774	48.890	42.513	26.744	18.266	12.922	9.588	3.423	1.475	0.434
KG	906	1775	48.755	41.997	26.184	17.708	12.240	9.123	2.983	1.298	0.368
KG	906	1776	48.935	41.653	25.680	17.132	11.657	8.486	2.941	1.195	0.351
KG	905	1776	48.710	40.707	24.644	16.178	10.557	7.786	2.377	0.934	0.262
KG	905	1777	48.485	40.578	24.196	15.476	9.809	7.313	2.286	0.856	0.270
KG	904	1777	47.900	40.879	24.224	15.368	9.974	6.867	2.261	0.836	0.232

KG	904	1776	47.900	40.621	24.168	15.296	9.831	7.258	2.269	0.853	0.260
KG	904	1775	48.035	40.707	24.532	15.890	10.128	7.649	2.510	0.951	0.306
KG	903	1775	48.530	41.137	24.924	16.088	10.546	7.768	2.402	1.010	0.274
KG	903	1776	48.170	40.664	24.196	15.440	10.205	7.376	2.385	0.926	0.283
KG	903	1777	48.350	40.922	24.504	16.016	10.711	7.940	2.427	0.948	0.282
KG	903	1778	49.025	40.879	24.784	16.538	10.612	7.931	2.560	0.926	0.291
KG	902	1778	48.170	40.191	23.636	14.828	9.314	6.776	2.053	0.657	0.184
KG	902	1779	47.675	39.761	23.132	14.018	8.731	6.330	1.804	0.565	0.166
KG	901	1779	47.765	39.675	23.552	14.792	8.907	6.557	1.970	0.702	0.223
KG	901	1780	47.855	40.062	24.000	14.990	9.490	6.666	2.028	0.685	0.224
KG	900	1780	49.115	41.868	26.324	17.438	12.460	9.651	3.033	1.452	0.441
KG	900	1781	48.395	40.191	23.804	14.396	8.940	6.148	1.896	0.545	0.169
KG	900	1782	47.495	39.417	22.768	13.388	8.126	5.820	1.580	0.411	0.109
KG	900	1783	46.910	39.116	22.628	13.424	8.027	5.911	1.580	0.425	0.123
KG	899	1783	46.820	39.159	22.516	13.280	8.005	5.793	1.505	0.386	0.109
KG	898	1783	47.180	39.245	22.600	13.334	8.104	5.820	1.597	0.433	0.121
KG	897	1783	47.090	39.460	22.432	13.316	8.104	5.857	1.588	0.428	0.131
KG	897	1784	47.045	39.073	22.348	13.226	8.115	5.784	1.597	0.388	0.121
KG	897	1785	47.315	39.331	22.376	13.532	8.027	5.811	1.481	0.411	0.120
KG	897	1786	47.405	39.460	22.824	13.712	8.621	6.266	1.804	0.514	0.159
KG	896	1786	47.405	39.503	22.936	13.892	8.379	6.139	1.671	0.478	0.139
KG	896	1787	47.135	39.675	22.964	13.856	8.720	6.330	1.896	0.554	0.153
KG	896	1788	47.135	39.245	22.572	13.496	8.005	5.756	1.489	0.400	0.112
KG	895	1788	47.405	39.589	22.656	13.658	8.313	6.139	1.705	0.484	0.136
KG	894	1788	47.540	39.288	22.600	13.586	8.236	6.011	1.680	0.447	0.140
KG	893	1788	46.910	38.987	22.432	13.316	8.016	5.665	1.555	0.405	0.103
KG	893	1787	47.135	39.159	22.712	13.316	8.049	5.829	1.655	0.428	0.105
KG	892	1787	47.090	38.987	22.516	13.244	7.950	5.784	1.580	0.414	0.114
KG	891	1787	47.135	39.030	22.460	13.298	8.005	5.738	1.530	0.405	0.101
KG	890	1787	46.910	39.030	22.460	13.424	8.082	5.747	1.580	0.405	0.101
KG	889	1787	47.000	39.073	22.600	13.406	8.137	5.693	1.638	0.425	0.107
KG	889	1788	47.405	39.030	22.600	13.478	8.049	5.747	1.406	0.402	0.106
KG	888	1788	47.180	39.245	22.628	13.442	8.181	5.702	1.588	0.461	0.133
KG	887	1788	47.360	39.202	22.824	13.496	8.280	5.875	1.630	0.470	0.139
KG	886	1788	47.450	39.288	22.656	13.352	8.346	5.957	1.597	0.461	0.134
KG	955	2220	50.735	44.448	32.008	25.358	20.237	15.202	5.697	2.903	0.804
KG	956	2220	50.330	44.061	31.560	24.818	19.115	14.320	5.406	2.721	0.763
KG	957	2220	50.060	44.319	31.924	25.142	19.423	14.647	5.398	2.735	0.749
KG	958	2220	50.555	43.975	31.364	25.178	19.555	14.229	5.307	2.768	0.762
KG	959	2220	49.745	42.599	29.348	21.452	15.749	12.308	4.352	1.970	0.542
KG	959	2219	46.910	38.858	24.336	15.980	9.776	7.294	2.493	1.058	0.242

KG	959	2218	46.055	36.923	21.004	12.794	7.840	5.465	1.265	0.369	0.129
KG	958	2218	47.450	39.245	24.672	16.088	10.293	7.886	2.609	1.007	0.250
KG	957	2218	48.935	41.782	27.948	20.966	15.210	10.752	3.979	1.914	0.519
KG	956	2218	49.790	43.717	31.336	23.846	18.433	14.110	5.299	2.533	0.717
KG	955	2218	50.510	43.932	31.280	25.412	19.445	14.411	5.506	2.819	0.756
KG	954	2218	50.510	44.491	32.204	25.304	19.588	14.947	5.581	2.712	0.766
KG	954	2217	50.555	43.846	31.756	24.494	18.422	14.028	5.423	2.631	0.723
KG	954	2216	49.475	41.911	29.348	22.568	16.387	11.808	4.352	2.208	0.576
KG	955	2216	46.550	38.858	23.944	15.044	10.469	8.059	2.468	0.906	0.287
KG	956	2216	45.605	36.880	21.116	12.722	7.466	5.229	1.539	0.436	0.090
KG	956	2215	45.515	36.923	20.668	12.002	7.345	5.156	1.182	0.195	0.095
KG	956	2214	45.785	36.665	20.808	12.074	7.290	5.247	1.298	0.285	0.095
KG	956	2213	45.515	36.536	20.836	12.164	7.301	5.238	1.348	0.265	0.092
KG	955	2213	45.650	36.536	20.612	12.074	7.158	5.210	1.207	0.234	0.087
KG	954	2213	45.650	36.450	20.584	12.038	7.224	5.201	1.198	0.248	0.078
KG	953	2213	45.155	36.579	20.696	12.002	7.466	5.183	1.190	0.288	0.087
KG	952	2213	45.290	37.181	21.648	12.794	7.752	5.866	1.647	0.436	0.119
KG	951	2213	47.675	39.374	24.252	16.916	11.404	7.804	2.452	1.181	0.337
KG	950	2213	48.620	42.126	29.012	21.020	15.397	11.972	4.203	1.979	0.539
KG	949	2213	49.475	43.287	30.916	24.044	18.752	13.728	5.282	2.606	0.716
KG	948	2213	49.115	43.717	31.000	24.224	19.379	14.574	5.373	2.718	0.740
KG	948	2212	48.035	41.997	29.236	21.362	15.683	11.881	4.485	2.152	0.550
KG	948	2211	45.650	38.385	24.140	16.214	10.799	7.922	2.692	1.105	0.275
KG	948	2210	47.540	40.320	25.568	17.492	13.065	9.724	2.975	1.147	0.353
KG	949	2210	45.470	37.439	22.572	14.234	9.468	6.985	1.846	0.590	0.167
KG	949	2209	48.440	40.492	25.764	18.374	13.417	10.079	3.298	1.419	0.430
KG	950	2209	46.100	37.826	22.460	13.856	9.028	6.939	1.954	0.523	0.179
KG	950	2208	47.675	40.062	25.960	18.410	13.472	10.379	3.597	1.606	0.472
KG	951	2208	47.315	39.288	23.888	15.530	10.920	8.095	2.269	0.702	0.229
KG	951	2207	49.295	41.825	28.004	20.804	16.046	12.126	4.161	2.029	0.607
KG	952	2207	47.675	38.901	23.608	15.098	10.117	7.749	2.344	0.747	0.231
KG	952	2206	47.360	38.815	24.308	16.664	11.437	8.004	2.601	1.055	0.305
KG	953	2206	46.010	36.536	20.724	12.056	7.400	5.456	1.256	0.274	0.105
KG	952	2206	47.360	38.815	24.308	16.664	11.437	8.004	2.601	1.055	0.305
KG	951	2206	49.025	42.169	29.600	21.470	15.914	12.081	4.236	2.032	0.553
KG	951	2205	47.675	39.589	25.484	17.582	11.448	8.314	2.933	1.343	0.323
KG	950	2205	48.755	42.040	28.872	21.344	16.266	12.181	4.352	2.116	0.619
KG	950	2204	46.910	39.632	25.876	17.006	11.459	8.896	3.041	1.240	0.312
KG	949	2204	49.070	42.427	29.376	21.902	16.618	12.381	4.485	2.178	0.580
KG	949	2203	49.070	41.825	28.788	21.326	15.562	11.499	4.095	1.909	0.486
KG	948	2203	49.745	44.147	31.084	23.396	17.949	13.428	4.709	2.228	0.629

KG	948	2202	49.925	43.889	30.720	22.442	16.750	12.945	4.527	2.066	0.583
KG	947	2202	50.195	42.943	29.572	23.000	17.520	13.046	4.676	2.320	0.656
KG	947	2201	48.980	42.298	29.432	21.758	16.310	12.381	4.435	2.066	0.576
KG	947	2200	48.170	40.707	27.080	19.400	13.043	9.706	3.597	1.522	0.369
KG	947	2199	45.965	37.095	22.068	13.658	8.291	5.729	1.638	0.559	0.158
KG	948	2199	45.605	36.536	21.060	12.218	7.312	5.456	1.256	0.282	0.054
KG	948	2200	46.325	38.428	22.656	14.324	9.611	6.885	1.896	0.772	0.190
KG	949	2200	45.020	36.966	21.172	12.146	7.037	5.220	1.290	0.276	0.045
KG	949	2201	46.190	37.396	22.152	13.298	8.863	6.348	1.555	0.528	0.172
KG	950	2201	45.830	36.751	20.976	12.164	6.993	5.083	1.348	0.260	0.065
KG	950	2202	46.190	37.826	22.376	13.370	8.302	6.357	1.763	0.453	0.112
KG	951	2202	46.235	36.665	20.836	12.254	7.136	5.074	1.232	0.260	0.055
KG	951	2203	45.650	36.794	20.920	11.912	7.213	5.274	1.256	0.240	0.069
KG	952	2203	45.740	36.837	20.920	11.894	7.257	5.238	1.273	0.248	0.074
KG	952	2204	46.010	36.493	20.808	12.038	6.960	5.292	1.323	0.240	0.066
KG	953	2204	45.650	36.794	20.724	12.002	7.092	5.156	1.339	0.226	0.084
KG	953	2205	45.380	36.278	21.004	12.020	7.114	5.038	1.256	0.237	0.061
KG	954	2205	45.605	36.450	20.640	12.056	7.169	5.101	1.190	0.223	0.055
KG	954	2206	45.335	36.407	20.696	12.074	7.103	5.183	1.198	0.240	0.083
KG	954	2207	45.290	36.192	20.752	12.056	7.235	5.283	1.232	0.274	0.061
KG	953	2207	45.605	36.536	21.004	12.416	7.598	5.429	1.315	0.316	0.083
KG	952	2207	47.675	38.901	23.608	15.098	10.117	7.749	2.344	0.747	0.231
KG	952	2208	45.830	36.579	21.340	12.776	8.148	5.948	1.630	0.419	0.129
KG	951	2208	47.315	39.288	23.888	15.530	10.920	8.095	2.269	0.702	0.229
KG	951	2209	45.695	36.622	20.864	12.236	7.620	5.474	1.456	0.360	0.116
KG	950	2209	46.100	37.826	22.460	13.856	9.028	6.939	1.954	0.523	0.179
KG	950	2210	45.515	36.493	20.948	12.308	7.554	5.356	1.406	0.335	0.092
KG	949	2210	45.470	37.439	22.572	14.234	9.468	6.985	1.846	0.590	0.167
KG	948	2210	47.540	40.320	25.568	17.492	13.065	9.724	2.975	1.147	0.353
K0	1745	1367	54.065	47.845	35.032	27.104	20.182	15.120	5.855	2.743	0.699
K0	1745	1368	53.210	46.985	34.052	26.528	19.533	14.456	5.315	2.500	0.614
K0	1744	1368	53.075	46.555	33.128	25.034	18.004	13.319	5.199	2.270	0.552
K0	1744	1369	51.680	44.921	31.616	23.432	16.563	12.154	4.610	2.015	0.475
K0	1745	1369	53.030	45.867	32.288	24.368	17.839	13.355	5.008	2.197	0.544
K0	1745	1370	52.490	45.308	31.924	23.324	16.453	11.954	4.560	1.802	0.458
K0	1744	1370	51.590	44.104	30.636	21.938	15.331	10.971	4.020	1.539	0.371
K0	1744	1369	51.680	44.921	31.616	23.432	16.563	12.154	4.610	2.015	0.475
K0	1743	1369	50.960	43.029	28.732	20.336	13.780	10.097	3.522	1.503	0.390
K0	1743	1370	49.160	41.739	26.884	18.230	12.174	9.069	3.041	1.175	0.299
K0	1742	1370	50.105	41.438	26.884	17.906	11.701	8.723	2.883	1.077	0.286
K0	1742	1369	50.240	41.739	27.472	18.932	12.944	9.406	3.248	1.354	0.334

K0	1741	1369	49.340	41.180	26.716	17.870	11.778	8.587	2.875	1.186	0.341
K0	1741	1370	49.475	40.234	25.652	16.790	10.733	7.704	2.203	0.822	0.235
K0	1741	1371	49.025	39.073	23.384	14.558	8.621	6.575	1.896	0.542	0.151
K0	1741	1372	47.360	38.901	23.020	14.180	8.643	6.211	1.597	0.447	0.107
K0	1742	1372	48.530	39.288	23.972	14.882	9.061	6.585	1.970	0.517	0.130
K0	1743	1372	49.160	39.804	24.700	16.124	10.524	7.995	2.800	0.747	0.195
K0	1743	1373	48.485	39.503	24.532	15.548	10.007	7.176	2.203	0.548	0.152
K0	1742	1373	48.170	38.686	22.908	14.000	8.335	6.075	1.671	0.327	0.079
K0	1742	1374	47.765	38.729	22.684	13.712	8.016	5.738	1.647	0.302	0.056
K0	1741	1374	47.945	38.772	22.712	13.676	8.137	6.029	1.763	0.369	0.091
K0	1741	1375	47.585	38.643	22.908	14.144	8.467	6.048	1.738	0.366	0.092
K0	1740	1375	48.170	38.643	22.404	13.622	7.994	5.784	1.721	0.310	0.076
K0	927	2803	50.105	42.341	25.764	16.736	11.415	8.514	2.618	0.853	0.234
K0	927	2804	49.880	41.954	25.652	16.484	11.228	8.350	2.626	0.803	0.198
K0	926	2804	50.195	42.126	25.792	16.754	11.239	8.450	2.626	0.820	0.221
K0	926	2805	49.835	41.868	25.428	16.466	11.162	8.304	2.601	0.786	0.214
K0	927	2805	49.790	41.825	25.260	16.268	10.986	8.141	2.477	0.775	0.196
K0	927	2806	49.790	41.739	25.008	16.070	10.832	8.077	2.194	0.764	0.189
K0	926	2806	49.565	41.825	24.896	16.124	10.898	8.086	2.418	0.713	0.203
K0	926	2807	48.800	41.180	24.392	15.260	10.238	7.504	1.854	0.593	0.166
K0	925	2807	48.710	40.922	24.028	14.846	9.754	7.185	2.145	0.495	0.129
K0	925	2808	49.160	40.707	23.468	14.432	9.182	6.894	1.580	0.405	0.110
K0	924	2808	49.340	40.664	23.244	14.126	9.061	6.566	1.705	0.332	0.096
K0	924	2809	49.295	40.449	23.300	14.036	8.973	6.539	1.572	0.366	0.087
K0	923	2809	48.890	40.234	23.132	14.036	8.984	6.448	1.804	0.271	0.093
K0	922	2809	49.385	40.492	23.580	13.892	8.830	6.475	1.613	0.307	0.085
K0	922	2808	49.430	40.664	23.552	14.414	9.160	6.776	1.638	0.372	0.099
K0	922	2807	49.385	40.922	23.888	14.864	9.776	7.103	1.896	0.428	0.139
K0	922	2806	49.250	41.395	24.000	15.026	9.963	7.376	1.995	0.531	0.174
K0	922	2805	49.970	41.696	24.840	15.800	10.612	7.868	2.178	0.663	0.218
K0	922	2804	50.555	42.470	25.596	16.790	11.624	8.514	2.518	0.870	0.248
K0	922	2803	50.735	43.545	26.744	17.762	12.548	9.424	2.875	1.114	0.317
K0	922	2802	51.320	43.975	27.864	18.986	13.648	10.297	3.323	1.315	0.374
K0	923	2802	51.005	43.502	27.864	18.500	13.252	10.070	3.265	1.242	0.331
K0	923	2801	51.185	43.545	27.444	18.572	13.076	9.815	3.232	1.184	0.325
K0	924	2801	50.690	42.986	26.352	17.510	12.130	9.078	2.750	0.985	0.266
K0	924	2800	51.275	43.201	26.520	17.708	12.361	9.178	2.684	1.030	0.277
K0	925	2800	50.465	42.556	26.044	17.096	11.899	8.960	2.402	0.926	0.246
K0	926	2800	49.970	42.040	25.120	16.052	10.942	8.204	2.344	0.741	0.209
K0	927	2800	49.025	40.750	23.692	14.666	9.644	7.103	1.497	0.458	0.158
K0	927	2799	49.385	40.836	23.748	14.666	9.688	7.158	1.937	0.458	0.159

K0	928	2799	49.025	40.879	23.720	14.450	9.270	6.748	1.223	0.374	0.143
K0	929	2799	49.070	41.438	24.784	15.854	11.052	8.405	2.394	0.814	0.250
K0	929	2798	49.835	41.868	25.456	16.448	11.063	8.204	2.294	0.794	0.251
K0	930	2798	50.375	42.599	26.632	18.338	13.164	9.942	3.174	1.212	0.365
K0	930	2797	50.330	43.158	26.604	17.888	12.427	9.396	2.883	1.094	0.336
K0	931	2797	49.835	42.642	25.792	16.844	11.668	8.850	2.651	0.912	0.268
K0	931	2796	49.475	42.341	25.680	16.844	11.602	8.623	2.427	0.862	0.260
K0	932	2796	49.295	41.739	25.260	16.322	11.118	8.523	2.468	0.822	0.200
K0	932	2795	50.465	42.943	27.108	18.194	12.790	9.660	3.016	1.178	0.352
K0	933	2795	50.870	44.276	28.676	20.804	15.518	11.772	4.054	1.573	0.448
K0	933	2794	51.365	44.792	28.676	19.796	14.451	11.034	3.697	1.497	0.461
K0	934	2794	51.500	43.803	28.088	19.220	14.044	10.534	3.456	1.290	0.387
K0	934	2793	51.050	43.717	27.780	18.932	13.593	10.197	3.439	1.279	0.392
K0	935	2793	50.780	43.717	27.696	19.076	13.714	10.343	3.381	1.307	0.389
K0	935	2792	51.185	44.147	28.480	19.814	14.198	10.825	3.605	1.396	0.430
K0	935	2791	51.275	44.448	28.900	20.336	14.902	11.326	3.755	1.503	0.436
K0	936	2791	51.635	44.792	29.684	21.290	15.782	11.954	4.020	1.724	0.493
K0	1418	2521	53.345	47.114	33.324	25.952	20.072	15.011	5.971	2.906	0.781
K0	1418	2522	53.210	47.157	33.184	26.096	19.984	15.211	6.062	2.992	0.788
K0	1417	2522	53.570	47.372	33.492	26.222	20.039	15.011	5.863	2.850	0.802
K0	1416	2522	53.750	48.103	34.052	26.672	20.479	15.612	5.888	2.990	0.851
K0	1416	2523	52.220	45.953	30.916	23.378	17.300	13.255	4.908	2.379	0.625
K0	1416	2524	51.050	43.760	28.144	19.688	14.154	10.834	3.846	1.671	0.430
K0	1416	2525	49.970	42.427	26.044	17.744	11.998	8.941	3.024	1.035	0.251
K0	1416	2526	50.870	42.728	26.184	16.970	11.217	8.450	2.759	0.965	0.232
K0	1416	2527	50.645	42.341	25.988	17.474	11.932	8.951	2.643	1.046	0.262
K0	1416	2528	50.195	41.997	25.652	16.574	10.799	7.804	2.460	0.730	0.173
K0	1416	2529	49.880	41.524	24.560	15.728	10.194	7.431	2.128	0.649	0.167
K0	1416	2530	50.195	41.911	24.812	15.800	10.205	7.576	2.053	0.677	0.178
K0	1417	2530	50.285	41.868	24.700	15.692	10.282	7.595	2.103	0.643	0.123
K0	1417	2531	50.510	42.685	25.680	16.682	11.239	8.341	2.402	0.800	0.179
K0	1417	2532	50.915	43.029	26.912	18.392	12.746	9.560	3.058	1.158	0.321
K0	1417	2533	51.545	43.975	28.256	19.796	14.110	10.479	3.572	1.371	0.378
K0	1418	2533	51.410	43.975	28.480	20.318	14.198	10.534	3.746	1.480	0.419
K0	1418	2534	51.365	44.448	28.844	20.282	14.396	10.962	3.829	1.629	0.453
K0	1418	2535	51.320	44.448	28.648	19.922	14.253	10.825	3.921	1.570	0.452
K0	1418	2536	51.455	44.061	28.060	19.796	13.868	10.316	3.365	1.441	0.397
K0	1419	2536	51.455	45.050	28.844	20.606	14.990	11.408	3.780	1.758	0.485
K0	1419	2537	50.600	43.373	27.192	19.580	13.967	10.407	3.705	1.385	0.400
K0	1420	2537	51.095	43.416	27.640	19.346	13.714	10.243	3.431	1.430	0.402
K0	1420	2538	49.340	41.266	25.232	16.556	11.107	8.213	2.377	0.864	0.258

K0	1421	2538	49.970	41.696	24.924	16.160	10.645	7.895	2.493	0.867	0.220
K0	1422	2538	49.385	41.266	25.064	16.052	10.337	7.667	2.103	0.775	0.145
K0	1422	2539	48.890	40.535	23.412	13.982	8.621	6.657	1.829	0.338	0.113
K0	1423	2539	50.150	41.696	24.056	14.738	9.270	6.894	2.078	0.444	0.149
K0	1423	2540	48.800	40.320	23.160	13.982	8.654	6.448	1.837	0.391	0.118
K0	1423	2541	49.070	40.750	23.636	14.414	9.083	6.867	1.979	0.388	0.109
K0	1424	2541	48.890	40.406	23.580	14.576	9.105	6.721	1.837	0.419	0.114
K0	1425	2541	48.125	39.804	23.132	14.072	8.720	6.512	1.912	0.450	0.053
K0	1426	2541	48.260	40.234	24.028	14.648	9.578	6.730	1.871	0.408	0.118
K0	1426	2542	49.295	41.782	24.840	15.710	10.568	7.977	2.576	0.822	0.205
K0	1427	2542	50.645	42.857	27.220	18.626	12.790	9.415	3.074	1.172	0.299
K0	1428	2542	51.365	44.319	28.760	20.030	14.572	11.098	3.763	1.590	0.389
K0	1428	2543	51.545	44.835	29.096	20.696	14.803	11.171	3.672	1.693	0.446
K0	1429	2543	51.635	45.695	30.076	21.866	15.309	11.735	4.244	1.982	0.483
K9	1717	639	39.080	33.741	22.992	16.736	12.097	8.750	3.024	1.380	0.353
K9	1716	639	38.675	33.268	21.816	15.620	10.986	7.786	2.526	1.116	0.283
K9	1716	640	38.225	32.924	20.164	14.756	10.106	7.149	2.252	0.918	0.228
K9	1717	640	38.225	32.881	21.340	15.116	10.513	7.558	2.410	1.038	0.260
K9	1717	641	38.000	31.892	19.716	12.938	8.467	5.984	1.754	0.635	0.180
K9	1718	641	38.495	33.010	21.424	15.836	11.261	7.849	2.750	1.156	0.290
K9	1718	642	38.180	32.021	20.444	14.198	9.809	6.976	2.178	0.884	0.228
K9	1717	642	37.685	31.591	19.744	13.172	8.687	5.902	1.680	0.562	0.149
K9	1716	642	37.730	31.247	19.044	12.344	7.939	5.593	1.406	0.484	0.122
K9	1715	642	37.280	30.860	18.512	11.462	7.026	4.856	1.132	0.262	0.062
K9	1715	643	36.785	30.645	18.372	11.138	6.696	4.755	0.924	0.246	0.060
K9	1714	643	36.785	30.559	17.588	10.904	6.553	4.628	0.958	0.234	0.061
K9	1714	644	36.785	30.473	17.700	10.814	6.630	4.601	1.007	0.206	0.068
K9	1715	644	37.055	30.215	17.504	10.994	6.762	4.701	1.107	0.237	0.069
K9	1715	643	36.785	30.645	18.372	11.138	6.696	4.755	0.924	0.246	0.060
K9	1716	643	37.010	30.860	18.400	11.264	6.839	4.728	1.099	0.237	0.068
K9	1717	643	38.090	31.505	19.828	13.118	8.819	6.221	1.771	0.621	0.159
K9	1717	642	37.685	31.591	19.744	13.172	8.687	5.902	1.680	0.562	0.149
K9	1718	642	38.180	32.021	20.444	14.198	9.809	6.976	2.178	0.884	0.228
K9	1719	642	40.295	35.805	25.316	21.038	15.848	11.453	3.971	1.732	0.429
K9	1719	641	39.935	35.117	25.120	19.778	14.803	10.498	3.763	1.702	0.432
K9	1720	641	42.410	39.030	30.720	24.260	18.752	13.592	5.191	2.441	0.624
K9	1721	638	42.725	39.288	30.272	24.566	19.060	13.901	5.456	2.570	0.673
K9	1721	637	42.275	38.686	29.180	23.576	18.048	13.137	5.166	2.519	0.645
K9	1722	637	42.815	39.159	30.160	24.314	18.807	13.701	5.531	2.768	0.702
K9	1722	638	43.040	39.589	30.608	25.070	19.533	14.238	5.780	2.836	0.713
K9	1723	638	42.860	39.847	31.728	25.790	20.391	14.856	6.178	3.071	0.781

K9	1723	637	43.265	39.417	30.748	25.034	19.467	14.411	5.797	3.015	0.770
K9	1724	637	42.815	39.804	31.392	25.448	19.995	14.784	6.004	3.202	0.817
K9	1724	636	42.995	39.460	30.720	24.764	19.368	14.310	5.780	3.130	0.796
K9	1725	636	42.635	40.191	31.728	25.844	20.424	15.184	6.203	3.432	0.894
K9	1443	2365	43.355	38.213	24.840	17.564	12.834	9.305	3.016	1.542	0.400
K9	1443	2366	42.860	38.084	24.336	17.528	12.680	9.278	2.726	1.494	0.387
K9	1442	2366	42.995	37.181	23.776	17.024	12.064	8.896	2.858	1.391	0.360
K9	1441	2366	42.545	37.181	23.468	16.214	11.558	8.368	2.551	1.237	0.305
K9	1440	2366	42.590	36.665	22.768	15.494	10.689	7.622	1.896	1.021	0.260
K9	1440	2367	42.410	36.235	22.040	15.026	10.238	7.313	1.945	0.906	0.236
K9	1440	2368	42.320	36.364	21.956	14.504	9.644	7.040	2.020	0.845	0.222
K9	1439	2368	42.320	35.891	21.228	13.784	9.116	6.448	1.688	0.666	0.169
K9	1439	2369	41.555	34.945	20.556	12.956	8.346	5.857	1.514	0.475	0.125
K9	1438	2369	41.285	34.558	20.108	12.092	7.510	5.402	1.306	0.313	0.078
K9	1437	2369	41.285	34.429	19.604	12.002	7.521	5.338	1.306	0.282	0.073
K9	1437	2370	41.060	34.128	19.380	11.696	7.334	5.201	1.049	0.271	0.058
K9	1436	2370	41.240	34.773	19.828	11.804	7.345	5.201	0.841	0.251	0.069
K9	1103	2124	49.070	43.975	33.548	26.924	21.876	17.341	7.008	3.967	1.151
K9	1102	2124	48.125	42.470	31.140	24.800	19.874	15.448	6.137	3.379	1.034
K9	1101	2124	47.855	41.868	30.608	23.990	18.928	14.693	5.390	3.026	0.906
K9	1101	2125	47.450	41.309	30.020	23.270	18.345	14.165	5.423	2.984	0.883
K9	1101	2126	47.945	41.180	29.908	22.856	17.674	13.737	5.124	2.718	0.815
K9	1100	2126	46.370	40.105	28.368	21.182	16.387	12.882	4.635	2.416	0.716
K9	1100	2127	46.280	39.718	27.752	20.462	15.133	11.571	4.045	2.088	0.642
K9	1099	2127	44.165	37.353	24.700	17.744	13.043	9.806	3.406	1.699	0.517
K9	1098	2127	43.085	35.848	22.488	15.350	10.491	7.904	2.717	1.217	0.349
K9	1098	2128	42.455	34.644	21.256	14.198	9.303	6.858	1.879	0.890	0.279
K9	1097	2128	42.455	34.128	20.808	13.370	8.467	6.221	1.929	0.705	0.196
K9	1097	2129	42.095	33.655	19.884	11.840	7.246	5.156	1.215	0.433	0.125
K9	1096	2129	42.230	33.526	19.576	11.552	6.729	4.874	1.398	0.341	0.096
K9	1096	2130	41.645	33.569	19.576	11.696	6.894	4.828	1.165	0.335	0.095
K9	1095	2130	41.825	33.440	19.408	11.444	6.740	4.965	1.381	0.355	0.103
K9	1095	2131	40.745	33.397	19.296	11.426	6.883	4.810	1.132	0.346	0.101
K9	1094	2131	41.375	32.967	19.044	11.300	6.542	4.801	1.306	0.304	0.102
K9	1094	2132	40.925	33.053	19.128	11.462	6.839	4.856	1.140	0.324	0.094
K9	1093	2132	41.735	32.881	19.016	11.318	6.586	4.846	1.331	0.316	0.089
K9	1093	2133	40.385	33.225	18.988	11.282	6.696	4.801	1.290	0.318	0.082
K9	1092	2133	40.565	33.053	19.044	11.282	6.564	4.801	1.414	0.296	0.098
K9	1092	2134	40.700	32.838	19.268	11.354	6.718	4.774	1.248	0.321	0.101

Appendix A, Table 4.

Image ID	Date of Acquisition	d	θ
EO1A0581152008022110KG	22 Jan 2008	0.98419	20.759
EO1A0581152010038110KK	07 Feb 2010	0.98628	17.600
EO1A0581152009339110K0	05 Dec 2009	0.98547	26.761
EO1A0581152010041110K9	10 Feb 2010	0.98680	17.425
EO1A0581152011027110P1	27 Jan 2011	0.98472	21.773

Appendix B:

Database of samples collected during the 2009-2010 and 2010-2011 field seasons supporting National Science Foundation grant ANT-0739702.

M. R. Salvatore[1]

[1]Department of Geological Sciences,

Brown University, Providence, RI 02912, USA

Main Text

The following data were collected as a component of the National Science Foundation grant entitled "Orbital Spectral Mapping of Surface Compositions in the Antarctic Dry Valleys: Regional Distributions of Secondary Mineral-Phases as Climate Indicators" (ANT-0739702, James Head (Principal Investigator), Michael Wyatt (Former Principal Investigator), and John Mustard (Co-Principal Investigator)). Additional information regarding the objectives of this award can be found at the following website: www.nsf.gov/awardsearch/showAward?AWD_ID=0739702. More than 600 rock and sediment samples (totaling more than 4,200 lbs) were collected for the primary purpose of ground-truthing orbital spectral signatures observed across the McMurdo Dry Valleys (MDV) of Antarctica. This appendix includes a description of the samples collected for the purposes of ground-truthing remote sensing datasets in addition to the complete database of all samples collected from the MDV and returned to Brown University.

As per the objectives of the funded grant, the majority of the samples were collected to ground-truth orbital spectroscopic datasets. Fifty-five sampling grids and 4 sampling transects were collected in regions that were designated unique based on ASTER imagery. Aside from a select few spectral grids, each grid consists of 9 individual sampling locations in a square-shaped pattern, with each sample located 30 meters from its neighboring sample; sampling transects were also optimally designed with 30 meter spacing between sampling locations. Some grids were designed to contain 25 samples in a square-shaped pattern to better characterize a large and spectrally homogeneous area. In addition, few sampling grids in Beacon Valley were designed with 60 meter spacing between sampling locations to test whether grids with higher spatial

coverage yet lower spatial resolution can better characterize the average spectral properties of the surfaces under investigation.

The naming designation for the grid and transect samples was developed to help to quickly identify the season, geographic location, and lithology under investigation. Each sample name follows the following format: W##_XX_$$_@@@. The initial "W" designates the samples as belonging to (former) Principal Investigator Michael **W**yatt. The numbers ##, either "09" or "10", indicate the year that the samples were collected; all samples labeled "09" were collected during the 2009-2010 field season, while all samples labeled "10" were collected during the 2010-2011 field season. The letters "XX" were used to designate the geographic location within the MDV where the samples were collected. For example, "BV" indicates that the samples were collected in **B**eacon **V**alley, while "BP" indicates that the samples were collected in **B**ull **P**ass. The alphanumeric "$$" were used to designate the lithology under investigation and a unique identifier for that particular sampling grid or transect. For example, "Gd2" indicates the **second g**rano**d**iorite grid, "D3" indicates the **third d**olerite grid, and "T1" indicates the **first t**ransect. In some rare occasions, the indicated lithology incorrectly represents the lithology that was observed in the field. For example, the samples that begin with "W10_VV_S…" were labeled as indicating a sandstone (quartzite) sampling location. This interpretation was based on initial ASTER investigations that indicated a quartz-rich spectral signature. However, in situ field investigations indicated that this unit is a quartz-rich granitic lithology. However, to maintain consistency within our naming rubric, the sample names were not changed. Lastly, the numbers "@@@" were used to designate the unique sample identifier within that particular grid or transect. To

summarize this naming scheme, sample "W10_BP_D1_003" indicates the third sample of the first dolerite grid in Bull Pass during the 2010-2011 field season, while "W09_WV_T3_004" indicates the fourth sample of the third sampling transect in Wright Valley during the 2009-2010 field season. Samples collected for purposes other than ground-truthing were designated with other names and labels. All names are consistent with those written on the sampling bags.

The strategic goal at each sampling location was to collect a clast and sediment sample that was representative of the surface in the immediate vicinity of the sampling location. Therefore, samples collected for ground-truthing purposes typically consist of a single clast in addition to approximately 500 cm^3 of surface sediments. Clast sizes vary, but are typically representative of the average clast size on the surface. Where only massive clasts or exposed bedrock exists, however, sample sizes can vary depending on the size of the clast fractured using a rock hammer or the size of the only loose rock fragments in the vicinity of the sampling location. The amount of collected sediment also varies depending on the abundance of sediment near the sampling location.

Each sample is typically accompanied by four photographs (Fig. 1): one low-magnification image of the sample before collection, one high-magnification image of the sample before collection, one low-magnification image of the sample location after collection, and one high-magnification image of the sample location after collection. Each of the four photographs also contains the labeled sampling bag within the field of view, providing both confirmation of the sample being collected as well as a means of determining scale within the image. Lastly, the date and time of collection are also indicated on the sampling bag. In the absence of time to identify the geographic

orientation of each sample, we chose to include the date and time of each measurement in our sampling photographs to provide the information necessary to calculate solar azimuth using measurements of shadows present within the image. As of the time of writing, there has been no need to determine the geographic orientation of each sample or image, but the necessary data are available should the necessity arise. In total, nearly 2,300 sample photographs were acquired, totaling 5.59 GB of data. As a result of this large file size, sample photographs are available upon request to the Principal Investigator and are not currently stored online.

All of the samples returned to Brown University from McMurdo Station, Antarctica, are listed in the table below. Where available, the latitude and longitude of the sampling location and the date and time of collection are also provided. The numerical identifier of the box that each sample was transported in is also provided, in addition to any comments regarding sampling, handling, or documentation. All samples are currently stored in Metcalf Laboratory at Brown University and are available upon request to the Principal Investigator.

Figure and Table Descriptions

Figure 1. A typical photographic documentation sequence for the collected spectral grids. This sequence is for sample W09_BV_F05_006. (a) Low magnification, before collection. (b) High magnification, before collection. (c) Low magnification, after collection. (d) High magnification, after collection.

Table 1. Sample database with sample name, latitude and longitude of the sample, date and time of collection, and storage box name. Additional comments are provided in the "comments" field.

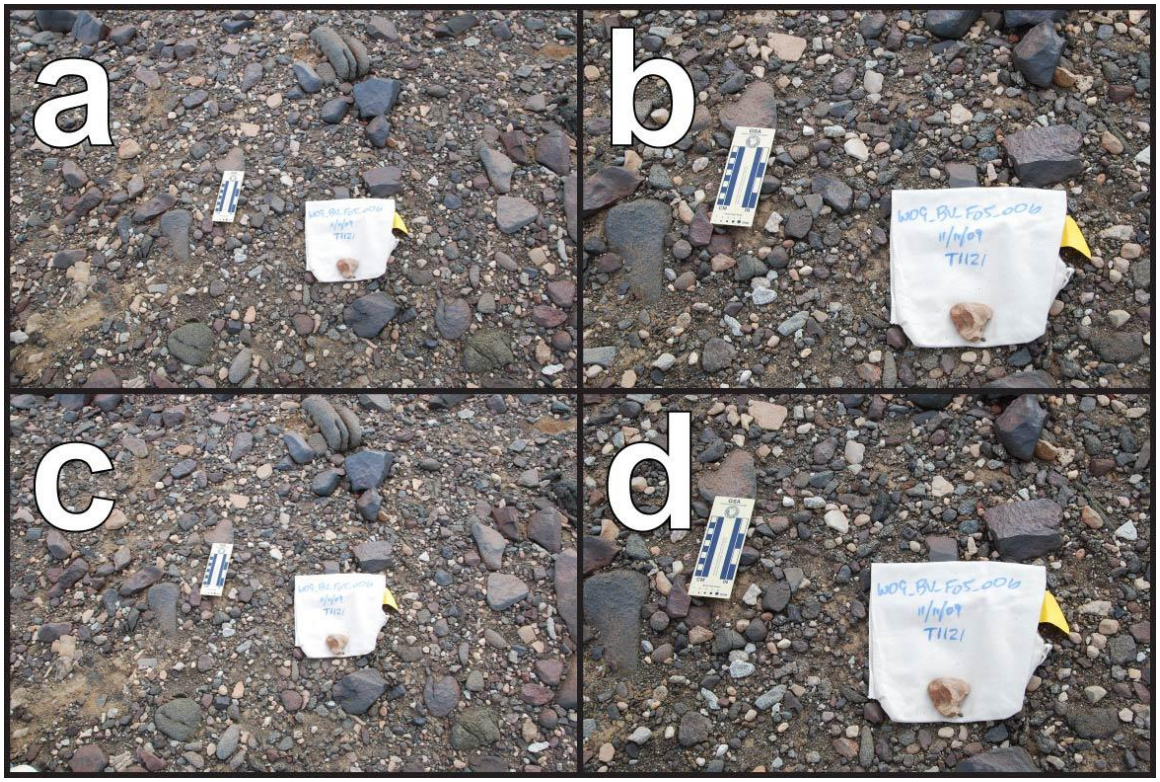

Appendix B, Figure 1.

Appendix B, Table 1.

SAMPLE NAME	LAT (ºN)	LON (ºE)	DATE	TIME	BOX	COMMENTS
W09_WV_Gd2_001	-77.564357	161.303184	11/23/2009	1542	1	
W09_WV_Gd2_002	-77.564895	161.303282	11/23/2009	1603	1	
W09_WV_Gd2_003	-77.565432	161.30338	11/23/2009	1600	1	
W09_WV_Gd2_004	-77.564336	161.305678	11/23/2009	1545	1	
W09_WV_Gd2_005	-77.564873	161.305776	11/23/2009	1606	1	
W09_WV_Gd2_006	-77.565411	161.305874	11/23/2009	1558	1	
W09_WV_Gd2_007	-77.564315	161.308172	11/23/2009	1547	1	
W09_WV_Gd2_008	-77.564852	161.30827	11/23/2009	1552	1	
W09_WV_Gd2_009	-77.565389	161.308368	11/23/2009	1555	1	
W09_WV_T1_001	-77.564972	161.309999	11/23/2009	1804	1	
W09_WV_T1_005	-77.566759	161.310825	11/23/2009	1750	1	
W09_WV_T1_007	-77.567652	161.311239	11/23/2009	1743	1	
W09_WV_T1_010	-77.568992	161.311859	11/23/2009	1735	1	
W09_WV_T1_013	-77.570332	161.312479	11/23/2009	1727	1	
W09_WV_T1_016	-77.571671	161.313099	11/23/2009	1719	1	
W09_WV_T1_017	-77.572118	161.313306	11/23/2009	1716	1	
W09_WV_T1_018	-77.572565	161.313513	11/23/2009	1713	1	
W09_WV_T1_019	-77.573011	161.31372	11/23/2009	1710	1	
W09_WV_T1_020	-77.573258	161.313926	11/23/2009	1706	1	
W09_WV_Gd1_001	-77.56347	161.244122	11/22/2009	1645	2	
W09_WV_Gd1_002	-77.563738	161.24417	11/22/2009	1647	2	
W09_WV_Gd1_003	-77.564007	161.244217	11/22/2009	1707	2	
W09_WV_Gd1_004	-77.564275	161.244265	11/22/2009	1709	2	
W09_WV_Gd1_005	-77.564544	161.244313	11/22/2009	1735	2	
W09_WV_Gd1_006	-77.563459	161.245369	11/22/2009	1643	2	
W09_WV_Gd1_007	-77.563728	161.245417	11/22/2009	1649	2	
W09_WV_Gd1_010	-77.564534	161.24556	11/22/2009	1733	2	
W09_WV_Gd1_011	-77.563449	161.246616	11/22/2009	1641	2	
W09_WV_Gd1_012	-77.563718	161.246664	11/22/2009	1651	2	
W09_WV_Gd1_013	-77.563986	161.246711	11/22/2009	1702	2	
W09_WV_Gd1_015	-77.564524	161.246807	11/22/2009	1731	2	
W09_WV_Gd1_016	-77.563439	161.247863	11/22/2009	1639	2	
W09_WV_Gd1_017	-77.563707	161.247911	11/22/2009	1654	2	
W09_WV_Gd1_018	-77.563976	161.247958	11/22/2009	1700	2	
W09_WV_Gd1_019	-77.564245	161.248006	11/22/2009	1716	2	
W09_WV_Gd1_020	-77.564513	161.248054	11/22/2009	1729	2	
W09_WV_Gd1_022	-77.563697	161.249157	11/22/2009	1656	2	
W09_WV_Gd1_023	-77.563966	161.249205	11/22/2009	1658	2	

W09_WV_Gd1_025	-77.564503	161.249301	11/22/2009	1721	2	
BV alt? 11/16/09			11/16/2009		3	
BV G-070 collected soils					3	
BV Mullins alteration?					3	
BV north/south rocks					3	
BV representative surface samples					3	
BV surface fines					3	
BV Uly core tubes / syringes					3	
BV Unlabelled whirl pack					3	
W09_WV_D3_001	-77.569302	161.279349	11/26/2009	1326	4	
W09_WV_D3_002	-77.569839	161.279446	11/26/2009	1257	4	
W09_WV_D3_003	-77.570376	161.279543	11/26/2009	1250	4	
W09_WV_D3_004	-77.569281	161.281844	11/26/2009	1322	4	
W09_WV_D3_005	-77.569818	161.281941	11/26/2009	1302	4	
W09_WV_D3_006	-77.570355	161.282038	11/26/2009	1245	4	
W09_WV_D3_007	-77.56926	161.284339	11/26/2009	1314	4	
W09_WV_D3_008	-77.569797	161.284436	11/26/2009	1306	4	
W09_WV_D3_009	-77.570334	161.284533	11/26/2009	1240	4	
W09_WV_G2_003	-77.548257	161.216229	11/27/2009	1209	4	
W09_WV_G2_004	-77.548526	161.216276	11/27/2009	1206	4	
W09_WV_G2_008	-77.548247	161.217474	11/27/2009	1157	4	
W09_WV_G2_009	-77.548516	161.217521	11/27/2009	1159	4	
W09_WV_G2_010	-77.548784	161.217568	11/27/2009	1201	4	
W09_WV_G2_015	-77.548774	161.218814	11/27/2009	1139	4	
W09_WV_T3_001	-77.5453	161.262763	11/27/2009	1313	4	
W09_WV_T3_002	-77.545563	161.263516	11/27/2009	1316	4	
W09_WV_T3_003	-77.545826	161.26427	11/27/2009	1318	4	
W09_WV_T3_005	-77.546351	161.265777	11/27/2009	1323	4	
W09_WV_T3_006	-77.546614	161.266531	11/27/2009	1325	4	
W09_BV_F01_002	-77.80232	160.70711	11/11/2009	1455	5	
W09_BV_F01_003	-77.80205	160.70707	11/11/2009	1457	5	
W09_BV_F01_004	-77.80258	160.70842	11/11/2009	1503	5	
W09_BV_F01_005	-77.80231	160.70838	11/11/2009	1501	5	
W09_BV_F01_007	-77.80258	160.70969	11/11/2009	1505	5	
W09_BV_F01_008	-77.80231	160.70965	11/11/2009	1506	5	
W09_BV_F03_001	-77.81209	160.69004	11/11/2009	1327	5	
W09_BV_F03_002	-77.81182	160.69	11/11/2009	1324	5	
W09_BV_F03_003	-77.81155	160.68996	11/11/2009	1316	5	
W09_BV_F03_004	-77.81208	160.69131	11/11/2009	1330	5	
W09_BV_F03_005	-77.81181	160.69127	11/11/2009	1344	5	
W09_BV_F03_006	-77.81154	160.69124	11/11/2009	1342	5	

W09_BV_F03_008	-77.81181	160.69254	11/11/2009	1336	5	
W09_BV_F03_009	-77.81154	160.69251	11/11/2009	1339	5	
W09_BV_F04_002	-77.81895	160.66549	11/11/2009	1226	5	
W09_BV_F04_003	-77.81868	160.66546	11/11/2009	1222	5	
W09_BV_F04_004	-77.81921	160.6668	11/11/2009	1214	5	
MRS misc. loose rocks					5	
W09_WV_D1_001	-77.55063	161.13527	11/20/2009	1153	6	
W09_WV_D1_002	-77.5509	161.13532	11/20/2009	1156	6	
W09_WV_D1_003	-77.55116	161.13536	11/20/2009	1158	6	
W09_WV_D1_004	-77.55143	161.13541	11/20/2009	1201	6	
W09_WV_D1_005	-77.5517	161.13545	11/20/2009	1203	6	
W09_WV_D1_006	-77.55062	161.13652	11/20/2009	1150	6	
W09_WV_D1_007	-77.55088	161.13656	11/20/2009	1147	6	
W09_WV_D1_008	-77.55115	161.13661	11/20/2009	1145	6	
W09_WV_D1_009	-77.55142	161.13665	11/20/2009	1142	6	
W09_WV_D1_010	-77.55169	161.1367	11/20/2009	1139	6	
W09_WV_D1_011	-77.55061	161.13776	11/20/2009	1122	6	
W09_WV_D1_012	-77.55088	161.13781	11/20/2009	1124	6	
W09_WV_D1_013	-77.55114	161.13785	11/20/2009	1127	6	
W09_WV_D1_014	-77.55141	161.1379	11/20/2009	1128	6	
W09_WV_D1_015	-77.55168	161.13794	11/20/2009	1132	6	
W09_WV_D1_016	-77.5506	161.13901	11/20/2009	1118	6	
W09_WV_D1_017	-77.55087	161.13905	11/20/2009	1116	6	
W09_WV_D1_018	-77.55113	161.1391	11/20/2009	1112	6	
W09_WV_D1_021	-77.55059	161.14025	11/20/2009	1054	6	
W09_WV_D1_022	-77.55086	161.1403	11/20/2009	1058	6	
W09_WV_D1_023	-77.55112	161.14034	11/20/2009	1100	6	
W09_WV_D1_024	-77.55139	161.14039	11/20/2009	1102	6	
W09_WV_D1_025	-77.55166	161.14044	11/20/2009	1105	6	
W09_BV_M1_001	-77.90202	160.59067	11/16/2009	1205	7	Points mislabeled in ArcMap and Excel. Other data correct.
W09_BV_M1_002	-77.90226	160.59097	11/16/2009	1202	7	Points mislabeled in ArcMap and Excel. Other data correct.
W09_BV_M1_003	-77.90269	160.59176	11/16/2009	1144	7	Points mislabeled in ArcMap and Excel. Other data correct.
W09_BV_M1_004	-77.90191	160.59154	11/16/2009	1207	7	Points mislabeled in ArcMap and Excel. Other data correct.
W09_BV_M1_005	-77.90224	160.59229	11/16/2009	1159	7	Points mislabeled in ArcMap and Excel. Other data correct.
W09_BV_M1_006	-77.90257	160.59272	11/16/2009	1148	7	Points mislabeled in ArcMap and Excel. Other data correct.
W09_BV_M1_007	-77.90182	160.59246	11/16/2009	1209	7	Points mislabeled in ArcMap and Excel. Other data

						correct.
W09_BV_M1_008	-77.9022	160.59342	11/16/2009	1157	7	Points mislabeled in ArcMap and Excel. Other data correct.
W09_BV_M1_009	-77.90244	160.59377	11/16/2009	1151	7	Points mislabeled in ArcMap and Excel. Other data correct.
W09_BV_M2_001	-77.89739	160.5825	11/16/2009	1330	7	Points mislabeled in ArcMap and Excel. Other data correct.
W09_BV_M2_002	-77.89767	160.58339	11/16/2009	1327	7	Points mislabeled in ArcMap and Excel. Other data correct.
W09_BV_M2_003	-77.89799	160.58351	11/16/2009	1313	7	Points mislabeled in ArcMap and Excel. Other data correct.
W09_BV_M2_004	-77.89728	160.58364	11/16/2009	1333	7	Points mislabeled in ArcMap and Excel. Other data correct.
W09_BV_M2_005	-77.8976	160.5849	11/16/2009	1325	7	Points mislabeled in ArcMap and Excel. Other data correct.
W09_BV_M2_006	-77.89788	160.58484	11/16/2009	1316	7	Points mislabeled in ArcMap and Excel. Other data correct.
W09_BV_M2_007	-77.8972	160.58486	11/16/2009	1336	7	Points mislabeled in ArcMap and Excel. Other data correct.
W09_BV_M2_008	-77.89748	160.58619	11/16/2009	1321	7	Points mislabeled in ArcMap and Excel. Other data correct.
W09_BV_M2_009	-77.89777	160.58645	11/16/2009	1318	7	Points mislabeled in ArcMap and Excel. Other data correct.
W09_BV_M3_003	-77.89207	160.5692	11/16/2009	1440	7	Points mislabeled in ArcMap and Excel. Other data correct.
W09_BV_M3_002	-77.89176	160.56849	11/16/2009	1432	7	Points mislabeled in ArcMap and Excel. Other data correct.
W09_BV_M3_004	-77.89138	160.56903	11/16/2009	1438	7	Points mislabeled in ArcMap and Excel. Other data correct.
W09_BV_M3_005	-77.89165	160.56944	11/16/2009	1429	7	Points mislabeled in ArcMap and Excel. Other data correct.
W09_BV_M3_006	-77.89192	160.57019	11/16/2009	1421	7	Points mislabeled in ArcMap and Excel. Other data correct.
W09_BV_M3_008	-77.8915	160.57043	11/16/2009	1427	7	Points mislabeled in ArcMap and Excel. Other data correct.
W09_BV_M3_007	-77.89124	160.56986	11/16/2009	1418	7	Points mislabeled in ArcMap and Excel. Other data correct.
W09_BV_M4_001	-77.88833	160.5565	11/16/2009	1521	7	Points mislabeled in ArcMap and Excel. Other data correct.
W09_BV_M4_002	-77.88851	160.55728	11/16/2009	1518	7	Points mislabeled in ArcMap and Excel. Other data correct.
W09_BV_M4_003	-77.88877	160.55797	11/16/2009	1505	7	Points mislabeled in ArcMap and Excel. Other data correct.
W09_BV_M4_004	-77.88818	160.55737	11/16/2009	1524	7	Points mislabeled in ArcMap and Excel. Other data correct.

W09_BV_M4_005	-77.88839	160.5584	11/16/2009	1516	7	Points mislabeled in ArcMap and Excel. Other data correct.
W09_BV_M4_006	-77.88859	160.55889	11/16/2009	1508	7	Points mislabeled in ArcMap and Excel. Other data correct.
W09_BV_M4_007	-77.88803	160.55899	11/16/2009	1526	7	Points mislabeled in ArcMap and Excel. Other data correct.
W09_BV_M4_008	-77.88826	160.55921	11/16/2009	1513	7	Points mislabeled in ArcMap and Excel. Other data correct.
W09_BV_M4_009	-77.88847	160.56015	11/16/2009	1510	7	Points mislabeled in ArcMap and Excel. Other data correct.
UWV North Fork Coatings			12/4/2009		8	
UWV North Fork Dolerite Coatings			12/4/2009		8	
UWV North Fork Salt Lake Samples	-77.53295	161.16464	12/4/2009		8	
UWV South Slope Orientation Study Site 1	-77.53234	161.14431	12/3/2009		8	
UWV South Slope Orientation Study Site 2	-77.53121	161.15907	12/3/2009		8	
UWV South Slope Orientation Study Site 3	-77.53215	161.14951	12/3/2009		8	
UWV Unlabelled					8	
UWV "Dol Top Tongue Soil"	-77.57827	161.2725	11/30/2009		9	
UWV "Top Gully Dol"	-77.57827	161.2725	11/30/2009		9	
UWV Dolerite "Ashtray"					9	
UWV Site 1J Transects	-77.56859	161.2905	11/30/2009		9	
UWV Site 2J Transects	-77.56719	161.29009	12/6/2009		9	
UWV Site 5G Transects	-77.5659	161.29491	12/6/2009		9	
UWV "Dol TOP Gareth Gully"	-77.57992	161.28033	11/30/2009		10	
UWV JWH South Fork Eolian Samples					10	
UWV JWH_09_DJP_01					10	
UWV North Slope Orientation Study Site 1	-77.56961	161.28707	12/4/2009		10	
UWV North Slope Orientation Study Site 2	-77.56997	161.2863	12/4/2009		10	
UWV North Slope Orientation Study Site 3	-77.56998	161.28893	12/4/2009		10	
W09_BV_F06_001	-77.8405	160.6156	11/10/2009	1518	11	
W09_BV_F06_002	-77.84023	160.61556	11/10/2009	1522	11	
W09_BV_F06_003	-77.83996	160.61553	11/10/2009	1525	11	
W09_BV_F06_004	-77.84049	160.61688	11/10/2009	1539	11	
W09_BV_F06_005	-77.84022	160.61684	11/10/2009	1535	11	
W09_BV_F06_006	-77.83996	160.6168	11/10/2009	1531	11	
W09_BV_F06_007	-77.84049	160.61815	11/10/2009	1544	11	
W09_BV_F06_008	-77.84022	160.61812	11/10/2009	1550	11	
W09_BV_F06_009	-77.83995	160.61808	11/10/2009	1553	11	
W09_BV_F07_001	-77.84697	160.58491	11/10/2009	1336	11	
W09_BV_F07_002	-77.8467	160.58487	11/10/2009	1333	11	

W09_BV_F07_003	-77.84643	160.58484	11/10/2009	1330	11	
W09_BV_F07_004	-77.84696	160.58618	11/10/2009	1319	11	
W09_BV_F07_005	-77.84669	160.58615	11/10/2009	1322	11	
W09_BV_F07_006	-77.84642	160.58611	11/10/2009	1326	11	
W09_BV_F07_007	-77.84696	160.58746	11/10/2009	1316	11	
W09_BV_F07_008	-77.84669	160.58742	11/10/2009	1312	11	
W09_BV_F07_009	-77.84642	160.58739	11/10/2009	1308	11	
W09_BV_F09_001	-77.87098	160.52731	11/9/2009	1343	11	
W09_BV_F09_002	-77.87071	160.52728	11/9/2009	1347	11	
W09_BV_F09_003	-77.87044	160.52724	11/9/2009	1349	11	
W09_BV_F09_004	-77.87098	160.52859	11/9/2009	1331	11	
W09_BV_F09_005	-77.87071	160.52855	11/9/2009	1336	11	
W09_BV_F09_006	-77.87044	160.52852	11/9/2009	1338	11	
W09S_BV_001B			11/9/2009	1213	11	
W09S_BV_003			11/9/2009		11	
W09S_BV_006			11/9/2009		11	
W09S_BV_008			11/9/2009		11	
UWV JWH_09_JG_600_0					12	
UWV JWH_09_JG_600_10					12	
UWV JWH_09_JG_600_20					12	
UWV JWH_09_JG_650_0					12	
UWV JWH_09_JG_650_10					12	
UWV JWH_09_JG_650_14					12	
UWV JWH_09_JG_790_Channel					12	
UWV JWH_09_JG_790_Fan					12	
UWV JWH_09_JG_790_Gravel					12	
UWV JWH_09_JG_796.2_16					12	
UWV JWH_09_SS_01_21					12	
UWV JWH_09_SS_01_5					12	
UWV JWH_DJP_01					12	
UWV JWH_DJP_02					12	
UWV JWH_DJP_03					12	
UWV JWH_NF_G5_01					12	
UWV JWH_S1_09					12	
UWV LK09_TwnPks_A+B+C					12	
UWV LK09_TwnPks_D+E					12	
JLS001-007 sed. samples for GWC					12	
LWV AP2	-77.52695	162.16405	12/20/2009		13	2 halves of lava bomb.
LWV BP1	-77.52542	162.16112	12/20/2009		13	
LWV CC2	-77.5255	162.16851	12/20/2009		13	

LWV CP1	-77.52532	162.16858	12/20/2009		13	
BV Unlabelled dolerite					14	
W09_BV_BF2_001	-77.87563	160.48548	11/12/2009	1253	14	
W09_BV_BF2_002	-77.87536	160.48544	11/12/2009	1251	14	
W09_BV_BF2_003	-77.87509	160.48541	11/12/2009	1248	14	
W09_BV_BF2_004	-77.87562	160.48676	11/12/2009	1256	14	
W09_BV_BF2_005	-77.87535	160.48672	11/12/2009	1304	14	
W09_BV_BF2_006	-77.87508	160.48669	11/12/2009	1246	14	
W09_BV_BF2_007	-77.87561	160.48804	11/12/2009	1259	14	
W09_BV_BF2_008	-77.87534	160.488	11/12/2009	1302	14	
W09_BV_BF2_009	-77.87508	160.48797	11/12/2009	1242	14	
W09_BV_F10_001	-77.88552	160.50738	11/12/2009	1448	14	
W09_BV_F10_002	-77.88525	160.50735	11/12/2009	1446	14	
W09_BV_F10_003	-77.88498	160.50731	11/12/2009	1443	14	
W09_BV_F10_004	-77.88552	160.50866	11/12/2009	1451	14	
W09_BV_F10_005	-77.88525	160.50863	11/12/2009	1453	14	
W09_BV_F10_006	-77.88498	160.50859	11/12/2009	1456	14	
W09_BV_F10_007	-77.88551	160.50994	11/12/2009	1503	14	
W09_BV_F10_008	-77.88524	160.50991	11/12/2009	1500	14	
W09_BV_F10_009	-77.88497	160.50987	11/12/2009	1458	14	
W09_BV_M7_001	-77.87867	160.53509	11/12/2009	1632	14	
W09_BV_M7_002	-77.8784	160.53506	11/12/2009	1630	14	
W09_BV_M7_003	-77.87813	160.53502	11/12/2009	1622	14	
W09_BV_M7_004	-77.87866	160.53637	11/12/2009	1644	14	
W09_BV_M7_005	-77.87839	160.53634	11/12/2009	1646	14	
W09_BV_M7_006	-77.87812	160.5363	11/12/2009	1634	14	
W09_BV_M7_007	-77.87865	160.53765	11/12/2009	1642	14	
W09_BV_M7_008	-77.87838	160.53762	11/12/2009	1639	14	
W09_BV_M7_009	-77.87812	160.53758	11/12/2009	1637	14	
W09S_BV_001A			11/9/2009		14	
BV Central/East Taylor Moraine Samples	-77.80704	160.69931	11/11/2009	1428	15	
BV Unlabelled whirl pack					15	
W09_BV_F01_001	-77.80259	160.70715	11/11/2009	1453	15	
W09_BV_F01_006	-77.80204	160.70834	11/11/2009	1459	15	
W09_BV_F01_009	-77.80204	160.70962	11/11/2009	1508	15	
W09_BV_F03_007	-77.81155	160.68996	11/11/2009	1332	15	
W09_BV_F04_001	-77.81922	160.66553	11/11/2009	1228	15	
W09_BV_F04_005	-77.81894	160.66676	11/11/2009	1217	15	
W09_BV_F04_006	-77.81868	160.66673	11/11/2009	1219	15	
W09_BV_F04_007	-77.81921	160.66807	11/11/2009	1209	15	

W09_BV_F04_008	-77.81894	160.66804	11/11/2009	1206	15	
W09_BV_F04_009	-77.81867	160.668	11/11/2009	1204	15	
W09_BV_F05_001	-77.826	160.64485	11/11/2009	1129	15	
W09_BV_F05_002	-77.82574	160.64482	11/11/2009	1126	15	
W09_BV_F05_003	-77.82547	160.64478	11/11/2009	1123	15	
W09_BV_F05_004	-77.826	160.64613	11/11/2009	1116	15	
W09_BV_F05_005	-77.82573	160.64609	11/11/2009	1118	15	
W09_BV_F05_006	-77.82546	160.64606	11/11/2009	1121	15	
W09_BV_F05_007	-77.82599	160.6474	11/11/2009	1114	15	
W09_BV_F05_008	-77.82572	160.64737	11/11/2009	1111	15	
W09_BV_F05_009	-77.82545	160.64733	11/11/2009	1108	15	
W09_BV_MT3_001	-77.80633	160.69445	11/11/2009	1427	15	
LWV AP4	-77.52713	162.16343	12/20/2009		16	
LWV BC2	-77.52552	162.16132	12/20/2009		16	
LWV DC1	-77.53147	162.18308	12/21/2009		16	
LWV AC1	-77.52682	162.16317	12/20/2009		17	
LWV BC1	-77.52488	162.15835	12/20/2009		17	
W09_LWV_D1_003	-77.51984	162.1375	12/19/2009	1352	17	
W09_LWV_D1_007	-77.5187	162.1422	12/19/2009	1338	17	
W09_BV_F08_001	-77.86266	160.55244	11/9/2009	1727	18	
W09_BV_F08_002	-77.86239	160.55241	11/9/2009	1732	18	
W09_BV_F08_003	-77.86212	160.55238	11/9/2009	1734	18	
W09_BV_F08_004	-77.86265	160.55372	11/9/2009	1724	18	
W09_BV_F08_005	-77.86238	160.55369	11/9/2009	1721	18	
W09_BV_F08_006	-77.86212	160.55365	11/9/2009	1716	18	
W09_BV_F08_007	-77.86264	160.555	11/9/2009	1704	18	
W09_BV_F08_008	-77.86238	160.55497	11/9/2009	1706	18	
W09_BV_F08_009	-77.86211	160.55493	11/9/2009	1712	18	
W09_BV_F09_007	-77.87097	160.52986	11/9/2009	1327	18	
W09_BV_F09_008	-77.8707	160.52983	11/9/2009	1323	18	
W09_BV_M8_001	-77.87087	160.54938	11/9/2009	1521	18	
W09_BV_M8_002	-77.8706	160.54935	11/9/2009	1517	18	
W09_BV_M8_003	-77.87033	160.54932	11/9/2009	1453	18	
W09_BV_M8_004	-77.87086	160.55066	11/9/2009	1524	18	
W09_BV_M8_005	-77.87059	160.55063	11/9/2009	1528	18	
W09_BV_M8_006	-77.87032	160.5506	11/9/2009	1531	18	
W09_BV_M8_007	-77.87086	160.55194	11/9/2009	1541	18	
W09_BV_M8_008	-77.87059	160.55191	11/9/2009	1538	18	
W09_BV_M8_009	-77.87032	160.55188	11/9/2009	1535	18	
W09S_BV_001B			11/9/2009	1213	18	
W09S_BV_002			11/9/2009	1246	18	

W09S_BV_004			11/9/2009	1321	18	
W09S_BV_007			11/9/2009	1806	18	
W09S_BV_005			11/9/2009		18	Bag ID: W09S_BV_2nd ash deposit
LWV "Upslope Vent"	-77.52738	162.30093	12/16/2009		19	
LWV Unlabelled					19	
LWV Unlabelled soil & rocks in whirl packs (3)					19	
W09_LWV_D1_001	-77.51876	162.13723	12/19/2009	1359	19	
W09_LWV_D1_002	-77.5193	162.13736	12/19/2009	1356	19	
W09_LWV_D1_008	-77.51924	162.14233	12/19/2009	1335	19	
W09_LWV_D1_009	-77.51978	162.14246	12/19/2009	1331	19	
LWV AP3	-77.527	162.16352	12/20/2009		20	
LWV BP2	-77.52533	162.16095	12/20/2009		20	
LWV Unlabelled canvas bags (2)					20	
W09_LWV_D1_004	-77.51873	162.13971	12/19/2009	1341	20	
W09_LWV_D1_005	-77.51927	162.13984	12/19/2009	1345	20	
W09_LWV_D1_006	-77.51981	162.13998	12/19/2009	1348	20	
W09_WV_D5_001	-77.53124	161.13374	12/4/2009	1358	21	
W09_WV_D5_002	-77.53177	161.13384	12/4/2009	1354	21	
W09_WV_D5_003	-77.53231	161.13393	12/4/2009	1350	21	
W09_WV_D5_004	-77.53122	161.13623	12/4/2009	1337	21	
W09_WV_D5_007	-77.5312	161.13872	12/4/2009	1330	21	
W09_WV_D5_008	-77.53173	161.13881	12/4/2009	1326	21	
W09_WV_D5_009	-77.53227	161.1389	12/4/2009	1322	21	
W09_WV_T8_001	-77.53132	161.15269	12/4/2009	1131	21	
W09_WV_T8_002	-77.5316	161.15407	12/4/2009	1135	21	
W09_WV_T8_003	-77.53187	161.15544	12/4/2009	1142	21	
W09_WV_T8_004	-77.53215	161.15682	12/4/2009	1146	21	
W09_WV_T8_005	-77.53242	161.15819	12/4/2009	1150	21	
W09_WV_T8_006	-77.5327	161.15957	12/4/2009	1155	21	
W09_WV_T8_007	-77.53298	161.16094	12/4/2009	1200	21	
W09_WV_T8_008	-77.53325	161.16232	12/4/2009	1208	21	
W09_WV_T8_009	-77.53353	161.1637	12/4/2009	1212	21	
W09_WV_T8_010	-77.5338	161.16507	12/4/2009	1215	21	
W09_WV_T8_011	-77.53408	161.16645	12/4/2009	1218	21	
LWV "Upslope Vent"	-77.52738	162.30093	12/16/2009		22	
LWV CC3	-77.52555	162.16875	12/20/2009		22	
LWV AP5	-77.52686	162.16442	12/20/2009		23	
LWV Unlabelled					23	
LWV CC1	-77.52543	162.16835	12/20/2009		23	
Mike <3 Air					23	

JLD Hand Samples					23	
LK09-WV JFS-creep					23	
LWV AP1	-77.52698	162.16358	12/20/2009		24	
LWV AP6	-77.52652	162.16337	12/20/2009		24	
LWV DC2	-77.53317	162.1854	12/21/2009		24	
UWV Top Dais Weird					25	
UWV Sandstone Level 3	-77.58727	161.28229			25	
UWV Highest up dolerite tongue rocks					25	
UWV Dolerite in stream on lobe with algae			12/5/2009		25	
UWV Don Juan lobe fine dolerite?			12/5/2009		25	
UWV Walk from Don Juan to camp, fine grained dol			12/5/2009		25	
UWV Eastern dolerite tongue			12/7/2009		25	
UWV High up dolerite tongue					25	
UWV Eastern dolerite tongue FAN			12/7/2009		25	
L-09					26	
L-07					26	
L-06					26	
L-01					26	
L-08					26	
L-05					26	
L-04					26	
L-10					26	
L-03					26	
L-02					26	
L-11					26	
GMT-1-4					26	
GMT-1-3					26	
GMT-1-0					26	
GMT-1-2					26	
GMT-1--2					26	
GMT-1--1					26	
GMT-1-5					26	
GMT-1-1					26	
GMT-2-1					26	
GMT-2-3					26	
GMT-2-2					26	
GMT-2-5					26	
GMT-2-1					26	
GMT-2-0					26	
GMT-2--2					26	

GMT-2-4					26	
GMT-3-3					26	
GMT-3-1					26	
GMT-3-5					26	
GMT-3--2					26	
GMT-3-1					26	
GMT-3-0					26	
GMT-3-2					26	
GMT-3-4					26	
LVS-01					27	
LVS-04					27	
LVS-03					27	
LK WV Sample #3					27	
LK WV Sample #4					27	
LVS-02					27	
LK WV Sample #5					27	
LK09 WV Sample #8					27	
Unlabelled canvas bag					27	Whirl Paks labelled "JWH09-##"
UWV-Dolerite outcrop 1 (column)					27	
LK Saltation Trap					28	
LK Beacon Samples 1					28	
LK Coarse Grained Ripple Experiment					28	
LK N.F. Samples Dais Rocks					28	
LK Beacon Samples #2					28	
LK09 Labyrinth Box Sample					28	
GRANO					28	
LVS-08					28	
LVS-10					28	
LVS-06					28	
LVS-05					28	
LVS-07					28	
LVS-09					28	
UWV-Dolerite outcrop (weathered)					28	
W09_WV_D2_004	-77.55438	160.74805	11/25/2009	1412	29	
W09_WV_D2_005	-77.55491	160.74805	11/25/2009	1420	29	
W09_WV_D2_001	-77.55439	160.74548	11/25/2009	1407	29	
W09_WV_D2_007	-77.55436	160.75047	11/25/2009	1443	29	
W09_WV_D1_020	-77.55167	161.13919	11/20/2009	1107	29	
W09_WV_D1_019	-77.5514	161.13914	11/20/2009	1110	29	
W09_WV_Gd1_014	-77.56426	161.24676	11/22/2009	1714	29	

W09_WV_Gd1_009	-77.56426	161.24551	11/22/2009	1711	29	
W09_WV_Gd1_008	-77.564	161.24546	11/22/2009	1704	29	
W09_WV_Gd1_021	-77.56343	161.24911	11/22/2009	1635	29	
W09_WV_Gd1_024	-77.56423	161.24925	11/22/2009	1718	29	
UWV Dais Special Rocks			11/20/2009		29	
W09_WV_T2_005	-77.54809	161.14685	11/20/2009	1504	29	
W09_WV_T2_001	-77.54903	161.14202	11/20/2009	1516	29	
W09_WV_T2_003	-77.54856	161.14444	11/20/2009	1510	29	
W09_WV_T2_008	-77.54739	161.15048	11/20/2009	1456	29	
W09_WV_T2_002	-77.54879	161.14323	11/20/2009	1512	29	
W09_WV_T2_004	-77.54833	161.14565	11/20/2009	1507	29	
W09_WV_T2_006	-77.54786	161.14806	11/20/2009	1501	29	
W09_WV_T2_009	-77.54716	161.15168	11/20/2009	1453	29	
W09_WV_T2_007	-77.54762	161.14927	11/20/2009	1459	29	
W09_WV_T2_010	-77.54692	161.15289	11/20/2009	1445	29	
UWV Labyrinth pitted rock surface & orange alt.	-77.555163	160.74604	11/25/2009		30	Lat/Lon of Labyrinth Helo Pad
UWV Seussville dolerites	-77.41783	161.41783	11/24/2009		30	
UWV Labyrinth surface till	-77.555163	160.74604			30	Lat/Lon of Labyrinth Helo Pad
UWV Labyrinth core bags	-77.555163	160.74604			30	Lat/Lon of Labyrinth Helo Pad
UWV Dais alt. pebbles & soil			12/1/2009		30	
UWV Special soils			12/1/2009		30	
UWV Labyrinth orange rocks	-77.555163	160.74604	11/25/2009		30	Lat/Lon of Labyrinth Helo Pad
LWV camp dolerite	-77.52698	162.16763	12/22/2009		30	
W09_WV_T3_009	-77.5474	161.26879	11/27/2009	1332	31	
W09_WV_T3_008	-77.54714	161.26804	11/27/2009	1329	31	
W09_WV_G2_025	-77.54875	161.2213	11/27/2009	1113	31	
W09_WV_G2_002	-77.54799	161.21618	11/27/2009	1211	31	
W09_WV_G2_014	-77.5485	161.21877	11/27/2009	1142	31	
W09_WV_G2_018	-77.54823	161.21996	11/27/2009	1131	31	
W09_WV_G2_005	-77.54879	161.21632	11/27/2009	1204	31	
W09_WV_G2_012	-77.54797	161.21867	11/27/2009	1146	31	
W09_WV_G2_007	-77.54798	161.21743	11/27/2009	1154	31	
W09_WV_G2_013	-77.54824	161.21872	11/27/2009	1144	31	
W09_WV_G2_011	-77.5477	161.21863	11/27/2009	1149	31	
W09_WV_G2_021	-77.54768	161.22112	11/27/2009	1123	31	
W09_WV_G1_008	-77.57265	161.31186	11/26/2009	1721	31	
W09_WV_G1_002	-77.57269	161.30687	11/26/2009	1648	31	
W09_WV_G1_006	-77.5732	161.30946	11/26/2009	1713	31	
W09_WV_G1_003	-77.57323	161.30696	11/26/2009	1707	31	
W09_WV_G1_004	-77.57213	161.30926	11/26/2009	1729	31	

W09_WV_G1_009	-77.57318	161.31196	11/26/2009	1717	31	
LK09 Saltation Experiment					31	
UWV Site 1G Transects	-77.57835	161.27957			32	
UWV Site 5J Transects (x2)	-77.56335	161.28033	12/6/2009		32	
UWV Site 4J Transects	-77.56342	161.28921	12/6/2009		32	
Boldt Samples					32	
LK09 Saltation Trap					32	
LK09 Sample #7					33	
Boldt Beacon Valley Samples					33	
Boldt Upper Wright Water Samples					33	
W09_WV_G1_001	-77.57215	161.30677	11/26/2009	1642	33	
W09_WV_G1_005	-77.57267	161.30936	11/26/2009	1725	33	
W09_WV_G1_007	-77.57211	161.31176	11/26/2009	1732	33	
W09_WV_D2_003	-77.55547	160.74563	11/25/2009	1357	33	
W09_WV_D2_009	-77.55544	160.75062	11/25/2009	1434	33	
W09_WV_D2_002	-77.55493	160.74555	11/25/2009	1402	33	
W09_WV_D2_006	-77.55545	160.74812	11/25/2009	1425	33	
W09_WV_D2_008	-77.5549	160.75054	11/25/2009	1438	33	
W09_WV_T3_007	-77.54688	161.26728	11/27/2009	1327	34	
W09_WV_T3_004	-77.54609	161.26502	11/27/2009	1321	34	
W09_WV_T3_010	-77.54766	161.26955	11/27/2009	1334	34	
W09_WV_G2_022	-77.54795	161.22116	11/27/2009	1121	34	
W09_WV_G2_019	-77.5485	161.22001	11/27/2009	1134	34	
W09_WV_G2_017	-77.54796	161.21992	11/27/2009	1129	34	
W09_WV_G2_020	-77.54876	161.22006	11/27/2009	1136	34	
W09_WV_G2_023	-77.54822	161.22121	11/27/2009	1119	34	
W09_WV_G2_016	-77.54769	161.21987	11/27/2009	1126	34	
W09_WV_G2_024	-77.54848	161.22126	11/27/2009	1116	34	
W09_WV_G2_001	-77.54772	161.21614	11/27/2009	1214	34	
W09_WV_G2_006	-77.54771	161.21738	11/27/2009	1151	34	
W09_WV_T1_004	-77.56631	161.31061	11/23/2009	1754	34	
W09_WV_T1_015	-77.57122	161.31289	11/23/2009	1722	34	
W09_WV_T1_002	-77.56541	161.3102	11/23/2009	1801	34	
W09_WV_T1_008	-77.56809	161.31144	11/23/2009	1742	34	
W09_WV_T1_012	-77.56988	161.31227	11/23/2009	1729	34	
W09_WV_T1_011	-77.56943	161.31206	11/23/2009	1732	34	
W09_WV_T1_009	-77.56854	161.31165	11/23/2009	1739	34	
W09_WV_T1_003	-77.56586	161.31041	11/23/2009	1758	34	
W09_WV_T1_014	-77.57077	161.31268	11/23/2009	1725	34	
W09_WV_T1_006	-77.5672	161.31103	11/23/2009	1747	34	

W09_WV_D4_008	-77.56491	161.14293	12/5/2009	1652	35	
W09_WV_D4_006	-77.56439	161.14034	12/5/2009	1701	35	
W09_WV_D4_005	-77.56493	161.14043	12/5/2009	1717	35	
W09_WV_D5_005	-77.53175	161.13632	12/4/2009	1341	35	
W09_WV_D5_006	-77.53229	161.13641	12/4/2009	1346	35	
JWH-09 NF-R02	-77.5284	161.21716			35	
JWH-09 NF_R01	-77.5285	161.20798			35	
UWV unlabelled soil whirl pak	-77.53113	161.13854			35	
UWV unlabelled soil whirl pak					35	
UWV Labyrinth special salt	-77.555163	160.74604	11/25/2009		35	Lat/Lon of Labyrinth Helo Pad
UWV Labyrinth alteration at depth ~10-30 cm	-77.555163	160.74604	11/25/2009		35	Lat/Lon of Labyrinth Helo Pad
JWH-09 DAIS-1					35	
JWH-09 DAIS-2					35	
UWV Labyrinth surface Si	-77.555163	160.74604	11/25/2009		35	Lat/Lon of Labyrinth Helo Pad
Beacon Valley cores 2 different			11/17/2009		36	
Ice Lake 1 rock samples (under ice)			12/7/2009		36	
Ice Lake 2 (rock under ice)			12/7/2009		36	
Slope streaks "yes + no"			12/3/2009		36	
Uly BV 1 surficial rocks with core 1			11/17/2009		36	
W09_BV_M3_001	-77.89148	160.56788	11/16/2009	1435	36	Points mislabeled in ArcMap and Excel. Other data correct.
W09_BV_M3_009	-77.89179	160.57135	11/16/2009	1423	36	Points mislabeled in ArcMap and Excel. Other data correct.
W09_WV_D4_001	-77.56548	161.13803	12/5/2009	1724	36	
W09_WV_D4_002	-77.56495	161.13794	12/5/2009	1728	36	
W09_WV_D4_003	-77.56441	161.13785	12/5/2009	1732	36	
W09_WV_D4_004	-77.56547	161.14052	12/5/2009	1721	36	
W09_WV_D4_007	-77.56545	161.14302	12/5/2009	1645	36	
W09_WV_D4_009	-77.56437	161.14283	12/5/2009	1657	36	
UWV Site 1J Transects	-77.56859	161.2905	11/30/2009		37	
UWV Site 2J Transects	-77.56719	161.29009	12/6/2009		37	
UWV Site 3J Transects (x3)	-77.56526	161.29021	12/1/2009		37	
UWV Site 4G Transects	-77.5673	161.29466	12/2/2009		37	
Beacon Grain Size Variety					1001	
Dolerite Weathering, Nussbaum Riegal	-77.66886	162.80523			1001	
MS10_BV_01	-77.85974	160.57317			1001	
MS10_BV_03	-77.86214	160.56693			1001	
MS10_BV_04	-77.8635	160.56302			1001	
MS10_BV_06	-77.86619	160.55724			1001	
MS10_BV_07	-77.86845	160.55149			1001	

MS10_BV_08	-77.87171	160.54582			1001	
MS10_BV_09	-77.87321	160.54404			1001	
MS10_BV_10	-77.87539	160.54128			1001	
MS10_BV_11	-77.8783	160.5354			1001	
MS10_BV_12	-77.8795	160.53381			1001	
MS10_BV_13	-77.88074	160.53367			1001	
MS10_BV_SANDSTONE_ALT	-77.58734	161.28286			1001	
Taylor Valley Alteration Samples					1001	
INT_GRID Soils	-77.66031	162.81522			1002	
INT2_GRID Soil	-77.66014	162.9232			1002	
MRS B3 & B4 Science					1002	
MRS Granite Weathering					1002	
MRS Nussbaum Dolerite Alt. Rind					1002	
Mustard Sampling Alteration					1002	
PQX Rhone					1002	
PQX Rhone					1002	
W10_TV_B4_001	-77.75792	162.11696	11/19/2010	1220	1002	
W10_TV_B4_002	-77.75738	162.11683	11/19/2010	1223	1002	
W10_TV_B4_003	-77.75684	162.1167	11/19/2010	1226	1002	
W10_TV_B4_004	-77.75789	162.1195	11/19/2010	1214	1002	
W10_TV_B4_005	-77.75735	162.11936	11/19/2010	1241	1002	
W10_TV_B4_006	-77.75681	162.11922	11/19/2010	1232	1002	
W10_TV_B4_007	-77.75786	162.12203	11/19/2010	1208	1002	
W10_TV_B4_008	-77.75732	162.12189	11/19/2010	1238	1002	
W10_TV_B4_009	-77.75679	162.12176	11/19/2010	1235	1002	
W10_TV_DS001	-77.67587	162.79213			1002	
W10_TV_DS002	-77.67587	162.79213			1002	
W10_TV_DS003	-77.67587	162.79213			1002	
W10_TV_DS004	-77.67587	162.79213			1002	
W10_TV_DS005	-77.67587	162.79213			1002	
W10_TV_DS006	-77.67587	162.79213			1002	
W10_TV_DS007	-77.67587	162.79213			1002	
W10_TV_DS008	-77.67587	162.79213			1002	
JFM Wright Valley Samples					1003	
JWH 2010 Samples - COMAIR					1003	
LABY_GRID Rocks JFM	-77.54884	160.95442			1003	
W10_TV_B1_002	-77.69994	162.69626	11/27/2010	1204	1004	
W10_TV_B1_003	-77.69941	162.6961	11/27/2010	1201	1004	
W10_TV_B1_004	-77.70056	162.69894	11/27/2010	1211	1004	
W10_TV_B1_006	-77.69937	162.69862	11/27/2010	1158	1004	

W10_TV_B1_008	-77.69988	162.7013	11/27/2010	1218	1004	
W10_TV_B1_009	-77.69934	162.70114	11/27/2010	1155	1004	
W10_TV_U1_001	-77.67478	162.81472	11/27/2010	1418	1004	
W10_TV_U1_002	-77.67425	162.81455	11/27/2010	1439	1004	
W10_TV_U1_003	-77.67371	162.81439	11/27/2010	1434	1004	
W10_TV_U1_005	-77.67421	162.81706	11/27/2010	1437	1004	
W10_TV_U1_006	-77.67367	162.8169	11/27/2010	1431	1004	
W10_TV_U1_009	-77.67364	162.81941	11/27/2010	1429	1004	
W10_TV_U2_002	-77.68294	162.79512	11/27/2010	1329	1004	
W10_TV_U2_003	-77.6824	162.79495	11/27/2010	1326	1004	
W10_TV_U2_004	-77.68344	162.79779	11/27/2010	1334	1004	
W10_TV_U2_005	-77.6829	162.79763	11/27/2010	1346	1004	
W10_TV_U2_006	-77.68237	162.79747	11/27/2010	1344	1004	
W10_TV_U2_008	-77.68287	162.80014	11/27/2010	1339	1004	
W10_TV_U2_009	-77.68233	162.79998	11/27/2010	1342	1004	
Rhone Basalt	-77.7	162.26357			1005	Location is approximate.
Rhone Basalt	-77.7	162.26357			1005	Location is approximate.
Rhone Basalt	-77.7	162.26357			1005	Location is approximate.
Rhone Basalt	-77.7	162.26357			1005	Location is approximate.
Rhone Basalt	-77.7	162.26357			1005	Location is approximate.
Rhone Basalt	-77.7	162.26357			1005	Location is approximate.
Rhone Basalt	-77.7	162.26357			1005	Location is approximate.
Rhone Basalt	-77.7	162.26357			1005	Location is approximate.
Rhone Basalt	-77.7	162.26357			1005	Location is approximate.
Rhone Basalt	-77.7	162.26357			1005	Location is approximate.
Rhone Basalt	-77.7	162.26357			1005	Location is approximate.
Rhone Basalt	-77.7	162.26357			1005	Location is approximate.
Rhone Basalt	-77.7	162.26357			1005	Location is approximate.
Rhone Basalt	-77.7	162.26357			1005	Location is approximate.
BV_JFM					1006	
BV_JFM					1006	
BV_JFM					1006	
CN 002	-76.8874	159.41236			1006	Location is approximate.
INT_GRID Rocks	-77.66031	162.81522			1006	
INT2_GRID Pebbles from Surface	-77.66014	162.9232			1006	
Loose Rocks (x9)					1006	
Taylor Valley Grid					1006	
TV_JFM_03					1006	
Unlabelled Bag					1006	
MRS Basalt/Dolerite Fragments					1007	

MRS Nussbaum Mntn. Samples					1007	
MRS Random from Nussbaum					1007	
MS_TV_003					1007	
Salvatore KB					1007	
W10_TV_B1_001	-77.70048	162.69642	11/27/2010	1207	1007	
W10_TV_B1_005	-77.69991	162.69878	11/27/2010	1216	1007	
W10_TV_B1_007	-77.70041	162.70146	11/27/2010	1213	1007	
W10_TV_U1_004	-77.67475	162.81723	11/27/2010	1421	1007	
W10_TV_U1_007	-77.67471	162.81974	11/27/2010	1423	1007	
W10_TV_U1_008	-77.67418	162.81958	11/27/2010	1426	1007	
W10_TV_U2_001	-77.68347	162.79528	11/27/2010	1331	1007	
W10_TV_U2_007	-77.6834	162.80031	11/27/2010	1336	1007	
Carapace Basalt	-76.8874	159.41236			1008	Location is approximate.
Carapace Basalt	-76.8874	159.41236			1008	Location is approximate.
Carapace Basalt	-76.8874	159.41236			1008	Location is approximate.
Carapace Basalt	-76.8874	159.41236			1008	Location is approximate.
Talyor Valley Basalt					1008	
Talyor Valley Basalt					1008	
Talyor Valley Basalt					1008	
Talyor Valley Basalt					1008	
Talyor Valley Basalt					1008	
Talyor Valley Basalt					1008	
Talyor Valley Basalt					1008	
Talyor Valley Basalt					1008	
Talyor Valley Basalt					1008	
Victora Valley Dike Material					1008	
Victora Valley Mafic Sample					1008	
Victora Valley Mafic Sample					1008	
Victora Valley Mafic Sample					1008	
JFM South Fork					1009	
MRS Rhone Glacier Volcanic Samples					1009	
Mustard Alteration (Ship)					1009	
Talyor Valley Basalt					1009	
Carapace Basalt	-76.8874	159.41236			1010	Location is approximate.
Carapace Basalt	-76.8874	159.41236			1010	Location is approximate.
Carapace Basalt	-76.8874	159.41236			1010	Location is approximate.
Carapace Basalt	-76.8874	159.41236			1010	Location is approximate.
Carapace Basalt	-76.8874	159.41236			1010	Location is approximate.
Talyor Valley Basalt					1010	
Talyor Valley Basalt					1010	

Talyor Valley Basalt					1010	
Talyor Valley Basalt					1010	
Talyor Valley Basalt					1010	
Talyor Valley Basalt					1010	
Talyor Valley Basalt					1010	
Talyor Valley Basalt					1010	
Talyor Valley Basalt					1010	
Upper Wright Mafic Sample					1010	
Rhone Basalt	-77.7	162.26357			1011	Location is approximate.
Rhone Basalt	-77.7	162.26357			1011	Location is approximate.
Rhone Basalt	-77.7	162.26357			1011	Location is approximate.
Rhone Basalt	-77.7	162.26357			1011	Location is approximate.
Rhone Basalt	-77.7	162.26357			1011	Location is approximate.
Rhone Basalt	-77.7	162.26357			1011	Location is approximate.
Rhone Basalt	-77.7	162.26357			1011	Location is approximate.
Rhone Basalt	-77.7	162.26357			1011	Location is approximate.
Rhone Basalt	-77.7	162.26357			1011	Location is approximate.
Beacon Mafic Sample					1012	
Carapace Basalt	-76.8874	159.41236			1012	Location is approximate.
Carapace Basalt	-76.8874	159.41236			1012	Location is approximate.
Carapace Basalt	-76.8874	159.41236			1012	Location is approximate.
Garnet-Bearing Dike	-77.67587	162.79213			1012	
Spectral Mix					1012	
Talyor Valley Basalt					1012	
Talyor Valley Basalt					1012	
Talyor Valley Basalt					1012	
Talyor Valley Basalt					1012	
Talyor Valley Basalt					1012	
Talyor Valley Basalt					1012	
Talyor Valley Basalt					1012	
Talyor Valley Basalt					1012	
Talyor Valley Basalt					1012	
Talyor Valley Basalt					1012	
Talyor Valley Basalt					1012	
Talyor Valley Basalt					1012	
Talyor Valley Basalt					1012	
Carapace Basalt	-76.8874	159.41236			1013	Location is approximate.
Carapace Basalt	-76.8874	159.41236			1013	Location is approximate.
Carapace Basalt	-76.8874	159.41236			1013	Location is approximate.
Carapace Basalt	-76.8874	159.41236			1013	Location is approximate.
Carapace Basalt	-76.8874	159.41236			1013	Location is approximate.

Carapace Basalt	-76.8874	159.41236			1013	Location is approximate.
Carapace Basalt	-76.8874	159.41236			1013	Location is approximate.
Carapace Basalt	-76.8874	159.41236			1013	Location is approximate.
Talyor Valley Basalt					1013	
Talyor Valley Basalt					1013	
Talyor Valley Basalt					1013	
Talyor Valley Basalt					1013	
Talyor Valley Basalt					1013	
Talyor Valley Basalt					1013	
Talyor Valley Basalt					1013	
Talyor Valley Basalt					1013	
Talyor Valley Basalt					1013	
Talyor Valley Basalt					1013	
Talyor Valley Basalt					1013	
Talyor Valley Basalt					1013	
Piqueux Victoria Dune Sand Sample					1014	
Piqueux Victoria Dune Sand Sample					1014	
W10_VV_D2_003	-77.40415	161.83224	11/7/2010	1323	1014	
W10_VV_D2_007	-77.40518	161.8374	11/7/2010	1312	1014	
W10_VV_D2_009	-77.4041	161.83717	11/7/2010	1328	1014	
W10_VV_S1_001	-77.40425	161.8782	11/7/2010	1242	1014	
W10_VV_S1_004	-77.40422	161.88066	11/7/2010	1235	1014	
W10_VV_S1_005	-77.40368	161.88054	11/7/2010	1238	1014	
W10_VV_S1_007	-77.4042	161.88312	11/7/2010	1232	1014	
W10_LWV_F2_001	-77.47074	162.42657	10/28/2010	1344	1015	
W10_LWV_F2_005	-77.47017	162.4289	10/28/2010	1408	1015	
W10_LWV_F2_006	-77.46964	162.42876	10/28/2010	1352	1015	
W10_LWV_F2_007	-77.47068	162.43152	10/28/2010	1402	1015	
W10_LWV_F2_008	-77.47014	162.43137	10/28/2010	1359	1015	
W10_LWV_F3_001	-77.47717	162.39627	10/28/2010	1258	1015	
W10_LWV_F3_005	-77.4766	162.39861	10/28/2010	1253	1015	
W10_LWV_F3_006	-77.47606	162.39846	10/28/2010	1250	1015	
W10_LWV_F3_007	-77.4771	162.40122	10/28/2010	1314	1015	
W10_LWV_F3_008	-77.47657	162.40108	10/28/2010	1311	1015	
W10_LWV_F3_009	-77.47603	162.40094	10/28/2010	1308	1015	
W10_LWV_F4_004	-77.47875	162.3585	10/28/2010	1149	1015	
W10_LWV_F4_005	-77.47821	162.35836	10/28/2010	1145	1015	
W10_LWV_F4_007	-77.47872	162.36098	10/28/2010	1152	1015	
W10_LWV_F4_008	-77.47818	162.36083	10/28/2010	1154	1015	
W10_LWV_F4_009	-77.47765	162.36069	10/28/2010	1157	1015	

W10_LWV_F5_001	-77.49041	162.33731	10/27/2010	1227	1015	
W10_LWV_F5_002	-77.48987	162.33717	10/27/2010	1230	1015	
W10_LWV_F5_003	-77.48934	162.33703	10/27/2010	1206	1015	
W10_LWV_F5_004	-77.49038	162.33979	10/27/2010	1224	1015	
W10_LWV_F5_005	-77.48984	162.33965	10/27/2010	1234	1015	
W10_LWV_F5_006	-77.48931	162.33951	10/27/2010	1210	1015	
W10_LWV_F5_007	-77.49035	162.34226	10/27/2010	1220	1015	
W10_LWV_F5_008	-77.48981	162.34212	10/27/2010	1216	1015	
W10_LWV_F5_009	-77.48928	162.34198	10/27/2010	1213	1015	
"Piqueux"					1016	
"Piqueux"					1016	
MRS TV Dolerite Alt. Rind #1					1016	
MRS TV Dolerite Alt. Rind #2					1016	
MRS TV Dolerite Alt. Rind #3					1016	
MRS TV Dolerite Alt. Rind #4					1016	
MRS TV Dolerite Alt. Rind #5					1016	
MRS TV Dolerite Alt. Rind #6					1016	
MRS TV Dolerite Alt. Rind #7					1016	
MRS TV Dolerite Alt. Rind #8					1016	
MRS TV Dolerite Alt. Rind #9					1016	
PQX Nussbaum Riegal					1016	
"PQX TV"					1017	
"PQX TV"					1017	
MRS Dunes Samples					1017	
MRS VV Dolerite Trench #1					1017	
MRS VV Dolerite Trench #2					1017	
W10_BP_G2_002	-77.4998	161.91548	11/11/2010	1238	1017	
W10_BP_G2_003	-77.49926	161.91536	11/11/2010	1234	1017	
W10_BP_G2_006	-77.49923	161.91784	11/11/2010	1231	1017	
W10_BP_G2_009	-77.49921	161.92032	11/11/2010	1229	1017	
W10_BP_G3_001	-77.50457	161.8881	11/11/2010	1327	1017	
W10_BP_G3_003	-77.50349	161.88785	11/11/2010	1312	1017	
W10_BP_G3_004	-77.50454	161.89058	11/11/2010	1325	1017	
W10_BP_G3_005	-77.504	161.89046	11/11/2010	1329	1017	
W10_BP_G3_008	-77.50398	161.89294	11/11/2010	1321	1017	
W10_BP_D1_001	-77.47781	161.83462	11/9/2010	1131	1018	
W10_BP_D1_002	-77.47728	161.8345	11/9/2010	1133	1018	
W10_BP_D1_003	-77.47674	161.83438	11/9/2010	1115	1018	
W10_BP_D1_004	-77.47779	161.8371	11/9/2010	1128	1018	
W10_BP_D1_005	-77.47725	161.83698	11/9/2010	1135	1018	
W10_BP_D1_008	-77.47723	161.83945	11/9/2010	1123	1018	

W10_BP_D1_009	-77.47669	161.83933	11/9/2010	1120	1018	
W10_BP_D2_004	-77.45458	161.75072	11/9/2010	1312	1018	
W10_BP_D2_006	-77.4535	161.75049	11/9/2010	1256	1018	
W10_BP_G1_001	-77.47607	161.79772	11/9/2010	1205	1018	
W10_BP_G1_002	-77.47554	161.7976	11/9/2010	1207	1018	
W10_BP_G1_003	-77.475	161.79748	11/9/2010	1210	1018	
W10_BP_G1_004	-77.47605	161.80019	11/9/2010	1202	1018	
W10_BP_G1_005	-77.47551	161.80008	11/9/2010	1215	1018	
W10_BP_G1_006	-77.47497	161.79996	11/9/2010	1212	1018	
W10_BP_G1_007	-77.47602	161.80267	11/9/2010	1159	1018	
W10_BP_G1_008	-77.47548	161.80255	11/9/2010	1156	1018	
W10_BP_G1_009	-77.47495	161.80243	11/9/2010	1154	1018	
W10_BP_U3_001	-77.47243	161.73308	11/9/2010	1113	1018	
W10_BP_U3_002	-77.47189	161.73297	11/9/2010	1110	1018	
W10_BP_U3_003	-77.47135	161.73285	11/9/2010	1106	1018	
W10_BP_U3_005	-77.47187	161.73544	11/9/2010	1139	1018	
W10_BP_U3_006	-77.47133	161.73533	11/9/2010	1136	1018	
W10_LWV_F1_001	-77.46269	162.4638	10/27/2010	1626	1019	
W10_LWV_F1_002	-77.46216	162.46365	10/27/2010	1629	1019	
W10_LWV_F1_003	-77.46162	162.46351	10/27/2010	1632	1019	
W10_LWV_F1_004	-77.46266	162.46627	10/27/2010	1623	1019	
W10_LWV_F1_006	-77.46159	162.46598	10/27/2010	1635	1019	
W10_LWV_F1_007	-77.46263	162.46874	10/27/2010	1619	1019	
W10_LWV_F1_008	-77.46209	162.46859	10/27/2010	1641	1019	
W10_LWV_F1_009	-77.46156	162.46845	10/27/2010	1638	1019	
W10_LWV_F2_002	-77.47021	162.42643	10/28/2010	1347	1019	
W10_LWV_F2_003	-77.46967	162.42628	10/28/2010	1350	1019	
W10_LWV_F2_004	-77.470711	162.42904	10/28/2010	1404	1019	
W10_LWV_F2_009	-77.46961	162.43123	10/28/2010	1355	1019	
W10_LWV_F3_002	-77.47663	162.39613	10/28/2010	1302	1019	
W10_LWV_F3_003	-77.47609	162.39599	10/28/2010	1304	1019	
W10_LWV_F4_001	-77.47878	162.35603	10/28/2010	1141	1019	
W10_LWV_F4_002	-77.47824	162.35588	10/28/2010	1206	1019	
W10_LWV_F4_003	-77.47771	162.35574	10/28/2010	1204	1019	
W10_LWV_F4_006	-77.47768	162.35822	10/28/2010	1201	1019	
Piqueux Ash/Clay (Black Bag)					1020	
W10_TV_D1_004	-77.65618	162.87367	11/14/2010	1455	1020	
W10_TV_D1_006	-77.65511	162.87334	11/14/2010	1445	1020	
W10_TV_D2_004	-77.64947	162.93686	11/14/2010	1240	1020	
W10_TV_G1_001	-77.67269	162.75122			1020	
W10_TV_G1_002	-77.67215	162.75106			1020	

W10_TV_G1_005	-77.67212	162.75358			1020	
W10_TV_G1_008	-77.67208	162.75609			1020	
W10_TV_S1_002	-77.67748	162.7424			1020	
W10_TV_S1_004	-77.67799	162.74508			1020	
W10_TV_S1_008	-77.67742	162.74743			1020	
W10_TV_S1_009	-77.67688	162.74727			1020	
W10_TV_U3_004	-77.65953	162.7556			1020	
W10_TV_U3_007	-77.65949	162.75811			1020	
W10_LWV_F3_004	-77.47713	162.39875	10/28/2010	1255	1021	
W10_TV_D1_002	-77.65568	162.871	11/14/2010	1440	1021	
W10_TV_D1_005	-77.65565	162.87351	11/14/2010	1457	1021	
W10_TV_D1_007	-77.65615	162.87618	11/14/2010	1452	1021	
W10_TV_D2_005	-77.64894	162.93669	11/14/2010	1243	1021	
W10_TV_D2_006	-77.6484	162.93652	11/14/2010	1232	1021	
W10_TV_D2_007	-77.64944	162.93937	11/14/2010	1238	1021	
W10_TV_D2_009	-77.64837	162.96903	11/14/2010	1234	1021	
W10_TV_G1_004	-77.67265	162.75374			1021	
W10_TV_G1_007	-77.67262	162.75625			1021	
W10_TV_S1_003	-77.67695	162.74224			1021	
W10_TV_S1_005	-77.67745	162.74492			1021	
W10_TV_S1_006	-77.67691	162.74475			1021	
W10_TV_S1_007	-77.67795	162.74759			1021	
W10_TV_U3_002	-77.65902	162.75293			1021	
W10_TV_U3_006	-77.65845	162.75528			1021	
W10_TV_U3_008	-77.65896	162.75795			1021	
W10_TV_U3_009	-77.65842	162.75778			1021	
W10_TV_U4_001	-77.6618	162.92368	11/14/2010	1350	1021	
W10_TV_U4_004	-77.66176	162.92619	11/14/2010	1348	1021	
W10_TV_U4_007	-77.66172	162.9287	11/14/2010	1346	1021	
W10_TV_U4_008	-77.66119	162.92853	11/14/2010	1344	1021	
W10_TV_U4_009	-77.66065	162.92836	11/14/2010	1342	1021	
MRS Dolerites (CTZ)					1022	
W10_BP_D3_001	-77.50286	161.8541	11/11/2010	1058	1022	
W10_BP_D3_002	-77.50233	161.85398	11/11/2010	1055	1022	
W10_BP_D3_003	-77.50179	161.85386	11/11/2010	1053	1022	
W10_BP_D3_004	-77.50284	161.85658	11/11/2010	1101	1022	
W10_BP_D3_005	-77.5023	161.85646	11/11/2010	1114	1022	
W10_BP_D3_007	-77.50281	161.85906	11/11/2010	1103	1022	
W10_BP_D3_008	-77.50227	161.85894	11/11/2010	1105	1022	
W10_BP_D3_009	-77.50174	161.85882	11/11/2010	1108	1022	
W10_BP_G2_001	-77.50033	161.9156	11/11/2010	1218	1022	

W10_BP_G2_004	-77.50031	161.91808	11/11/2010	1222	1022	
W10_BP_G2_005	-77.49977	161.91796	11/11/2010	1236	1022	
W10_BP_G2_007	-77.50028	161.92056	11/11/2010	1224	1022	
W10_BP_G2_008	-77.49974	161.92044	11/11/2010	1226	1022	
W10_BP_G3_002	-77.50403	161.88798	11/11/2010	1331	1022	
W10_BP_G3_006	-77.50346	161.89034	11/11/2010	1317	1022	
W10_BP_G3_007	-77.50451	161.89306	11/11/2010	1323	1022	
W10_BP_G3_009	-77.50344	161.89282	11/11/2010	1319	1022	
Carapace Nunatak 001	-76.8874	159.41236			1023	Location is approximate.
Carapace Nunatak 003	-76.8874	159.41236			1023	Location is approximate.
Carapace Nunatak 004	-76.8874	159.41236			1023	Location is approximate.
Carapace Nunatak 005	-76.8874	159.41236			1023	Location is approximate.
Carapace Nunatak 006	-76.8874	159.41236			1023	Location is approximate.
Carapace Nunatak 007	-76.8874	159.41236			1023	Location is approximate.
Carapace Nunatak 007B	-76.8874	159.41236			1023	Location is approximate.
Carapace Nunatak 010	-76.8874	159.41236			1023	Location is approximate.
Carapace Nunatak 0105	-76.8874	159.41236			1023	Location is approximate.
Carapace Nunatak 010A	-76.8874	159.41236			1023	Location is approximate.
Carapace Nunatak 010C	-76.8874	159.41236			1023	Location is approximate.
Carapace Nunatak 010E	-76.8874	159.41236			1023	Location is approximate.
Carapace Nunatak 011	-76.8874	159.41236			1023	Location is approximate.
Carapace Nunatak Float 1	-76.8874	159.41236			1023	Location is approximate.
Garnets on Dike Swarm	-77.67587	162.79213			1023	
Unlabelled Bag					1023	
MRS Carapace Sandstone/Conglomerate					1024	
MS_CN_001	-76.8874	159.41236			1024	Location is approximate.
MS_CN_002	-76.8874	159.41236			1024	Location is approximate.
MS_CN_003	-76.8874	159.41236			1024	Location is approximate.
MS_CN_004	-76.8874	159.41236			1024	Location is approximate.
MS_CN_005	-76.8874	159.41236			1024	Location is approximate.
MS_CN_006	-76.8874	159.41236			1024	Location is approximate.
MS_CN_007	-76.8874	159.41236			1024	Location is approximate.
MS_CN_008A	-76.8874	159.41236			1024	Location is approximate.
MS_CN_008B	-76.8874	159.41236			1024	Location is approximate.
MS_CN_010	-76.8874	159.41236			1024	Location is approximate.
MS_CN_011	-76.8874	159.41236			1024	Location is approximate.
MS_CN_012A-E	-76.8874	159.41236			1024	Location is approximate.
MS_CN_013	-76.8874	159.41236			1024	Location is approximate.
MS_CN_014	-76.8874	159.41236			1024	Location is approximate.
MS_CN_015	-76.8874	159.41236			1024	Location is approximate.

MS_CN_016	-76.8874	159.41236			1024	Location is approximate.
MS_CN_017	-76.8874	159.41236			1024	Location is approximate.
MS_CN_018	-76.8874	159.41236			1024	Location is approximate.
MS_CN_019	-76.8874	159.41236			1024	Location is approximate.
MS_CN_020	-76.8874	159.41236			1024	Location is approximate.
MS_CN_021	-76.8874	159.41236			1024	Location is approximate.
MS_CN_022	-76.8874	159.41236			1024	Location is approximate.
MS_CN_023	-76.8874	159.41236			1024	Location is approximate.
MS_CN_024	-76.8874	159.41236			1024	Location is approximate.
MS_CN_025	-76.8874	159.41236			1024	Location is approximate.
W10_VV_C1_001	-77.36862	161.8007	11/2/2010	1445	1025	
W10_VV_C1_003	-77.36754	161.80046	11/2/2010	1449	1025	
W10_VV_C1_008	-77.36803	161.80549	11/2/2010	1456	1025	
W10_VV_C1_004	-77.36859	161.80315	11/2/2010	1501	1025	
W10_VV_D1_001	-77.39529	161.7506	11/4/2010	1425	1025	
W10_VV_D1_002	-77.39476	161.75049	11/4/2010	1422	1025	
W10_VV_D1_003	-77.39422	161.75037	11/4/2010	1420	1025	
W10_VV_D1_004	-77.39527	161.75306	11/4/2010	1428	1025	
W10_VV_D1_005	-77.39473	161.75295	11/4/2010	1443	1025	
W10_VV_D1_006	-77.3942	161.75283	11/4/2010	1441	1025	
W10_VV_D1_007	-77.39524	161.75552	11/4/2010	1431	1025	
W10_VV_D1_008	-77.39471	161.75541	11/4/2010	1434	1025	
W10_VV_D1_009	-77.39417	161.75529	11/4/2010	1437	1025	
W10_VV_DS1_002	-77.40008	161.92985			1025	
W10_VV_DS1_001	-77.40264	161.92167			1025	
W10_VV_DS1_006	-77.39859	161.9411	11/3/2010	1319	1025	
W10_VV_S2_001	-77.40273	161.95554	11/3/2010	1245	1025	
W10_VV_S2_002	-77.40219	161.95541	11/3/2010	1247	1025	
W10_VV_S2_004	-77.4027	161.958	11/3/2010	1242	1025	
W10_VV_S2_005	-77.40216	161.95788	11/3/2010	1239	1025	
W10_VV_S2_006	-77.40163	161.95775	11/3/2010	1229	1025	
W10_VV_S2_007	-77.40267	161.96046	11/3/2010	1236	1025	
W10_VV_S2_008	-77.40214	161.96034	11/3/2010	1233	1025	
W10_VV_S2_009	-77.4016	161.96021	11/3/2010	1231	1025	
W10_LWV_F1_005	-77.46212	162.46612	10/27/2010	1644	1026	
W10_LWV_U1_001	-77.42539	162.6838	10/30/2010	1251	1026	
W10_LWV_U1_002	-77.42486	162.68365	10/30/2010	1243	1026	
W10_LWV_U1_003	-77.42432	162.6835	10/30/2010	1240	1026	
W10_LWV_U1_004	-77.42536	162.68627	10/30/2010	1248	1026	
W10_LWV_U1_005	-77.42482	162.68611	10/30/2010	1246	1026	
W10_LWV_U1_006	-77.42429	162.68596	10/30/2010	1238	1026	

W10_LWV_U1_007	-77.42533	162.68873	10/30/2010	1230	1026	
W10_LWV_U1_008	-77.42479	162.68858	10/30/2010	1232	1026	
W10_LWV_U1_009	-77.42425	162.68842	10/30/2010	1235	1026	
W10_LWV_U3_001	-77.41878	162.67222	10/30/2010	1115	1026	
W10_LWV_U3_002	-77.41825	162.67206	10/30/2010	1135	1026	
W10_LWV_U3_003	-77.41771	162.67191	10/30/2010	1132	1026	
W10_LWV_U3_004	-77.41875	162.67468	10/30/2010	1118	1026	
W10_LWV_U3_005	-77.41821	162.67452	10/30/2010	1138	1026	
W10_LWV_U3_006	-77.41768	162.67437	10/30/2010	1129	1026	
W10_LWV_U3_007	-77.41872	162.67714	10/30/2010	1121	1026	
W10_LWV_U3_008	-77.41818	162.67699	10/30/2010	1123	1026	
W10_LWV_U3_009	-77.41764	162.67683	10/30/2010	1126	1026	
W10_VV_A1_001	-77.36784	161.7407	11/2/2010	1111	1027	
W10_VV_A1_002	-77.3673	161.74059	11/2/2010	1114	1027	
W10_VV_A1_003	-77.36677	161.74047	11/2/2010	1116	1027	
W10_VV_A1_004	-77.36781	161.74316	11/2/2010	1109	1027	
W10_VV_A1_005	-77.36728	161.74304	11/2/2010	1124	1027	
W10_VV_A1_006	-77.36674	161.74293	11/2/2010	1118	1027	
W10_VV_A1_007	-77.36779	161.74561	11/2/2010	1107	1027	
W10_VV_A1_008	-77.36725	161.7455	11/2/2010	1122	1027	
W10_VV_A1_009	-77.36672	161.74538	11/2/2010	1120	1027	
W10_VV_C1_002	-77.36808	161.80058	11/2/2010	1447	1027	
W10_VV_C1_005	-77.36806	161.80304	11/2/2010	1503	1027	
W10_VV_C1_006	-77.36752	161.80292	11/2/2010	1451	1027	
W10_VV_C1_007	-77.36857	161.80561	11/2/2010	1458	1027	
W10_VV_C1_009	-77.36749	161.80537	11/2/2010	1454	1027	
W10_VV_DS1_003	-77.3981	161.93597	11/3/2010	1323	1027	
W10_VV_DS1_004	-77.40303	161.92621	11/3/2010	1307	1027	
W10_VV_DS1_005	-77.39859	161.9411	11/3/2010	1313	1027	
W10_VV_S2_003	-77.40165	161.95529	11/3/2010	1226	1027	
W10_BP_D1_006	-77.47671	161.83686	11/9/2010	1117	1028	
W10_BP_D1_007	-77.47776	161.83957	11/9/2010	1126	1028	
W10_BP_D2_001	-77.4546	161.74825	11/9/2010	1310	1028	
W10_BP_D2_003	-77.45353	161.74802	11/9/2010	1300	1028	
W10_BP_D2_007	-77.45455	161.75319	11/9/2010	1247	1028	
W10_BP_D2_008	-77.45402	161.75308	11/9/2010	1250	1028	
W10_BP_D2_009	-77.45348	161.75296	11/9/2010	1253	1028	
W10_BP_U3_004	-77.4724	161.73556	11/9/2010	1117	1028	
W10_BP_U3_007	-77.47238	161.73803	11/9/2010	1120	1028	
W10_BP_U3_008	-77.47184	161.73792	11/9/2010	1124	1028	
W10_BP_U3_009	-77.4713	161.7378	11/9/2010	1133	1028	

W10_VV_D2_001	-77.40523	161.83248	11/7/2010	1317	1028	
W10_VV_D2_002	-77.40469	161.83236	11/7/2010	1320	1028	
W10_VV_D2_004	-77.4052	161.83494	11/7/2010	1315	1028	
W10_VV_D2_005	-77.40466	161.83482	11/7/2010	1332	1028	
W10_VV_D2_006	-77.40413	161.83471	11/7/2010	1326	1028	
W10_VV_D2_008	-77.40464	161.83729	11/7/2010	1309	1028	
W10_VV_S1_002	-77.40371	161.87808	11/7/2010	1219	1028	
W10_VV_S1_003	-77.40317	161.87796	11/7/2010	1222	1028	
W10_VV_S1_006	-77.40315	161.88042	11/7/2010	1224	1028	
W10_VV_S1_008	-77.40366	161.883	11/7/2010	1230	1028	
W10_VV_S1_009	-77.40312	161.88288	11/7/2010	1227	1028	
Loose Rocks (x2)					1029	
PQX (B)					1029	
Unbagged Sandstone with Layering					1029	
W10_TV_D1_001	-77.65622	162.87116	11/14/2010	1438	1029	
W10_TV_D1_003	-77.65515	162.87083	11/14/2010	1443	1029	
W10_TV_D1_008	-77.65561	162.87601	11/14/2010	1450	1029	
W10_TV_D1_009	-77.65508	162.87585	11/14/2010	1447	1029	
W10_TV_D2_001	-77.64951	162.93435	11/14/2010	1248	1029	
W10_TV_D2_002	-77.64897	162.93418	11/14/2010	1245	1029	
W10_TV_D2_003	-77.64844	162.93402	11/14/2010	1230	1029	
W10_TV_D2_008	-77.6489	162.9392	11/14/2010	1236	1029	
W10_TV_G1_003	-77.67161	162.7509			1029	
W10_TV_G1_006	-77.67158	162.75341			1029	
W10_TV_G1_009	-77.67154	162.75593			1029	
W10_TV_S1_001	-77.67802	162.74256			1029	
W10_TV_U3_001	-77.65956	162.75309			1029	
W10_TV_U3_003	-77.65849	162.75276			1029	
W10_TV_U3_005	-77.65899	162.75544			1029	
W10_TV_U4_002	-77.66126	162.92351	11/14/2010	1351	1029	
W10_TV_U4_003	-77.66072	162.92334	11/14/2010	1338	1029	
W10_TV_U4_005	-77.66122	162.92602	11/14/2010	1353	1029	
DB Samples					1030	
JLD Hand Samples					1030	
JLD Hand Samples					1030	
MRS TV Dolerite ("Genesis Rock")	-77.66422	162.80101			1001	
MS10_BV_02	-77.86028	160.57066			1001	
MS10_BV_05A&B	-77.86455	160.56027			1001	